MACROMOLECULES CONTAINING METAL and METAL-LIKE ELEMENTS

VOLUME 9

Supramolecular and Self-Assembled Metal-Containing Materials

Edited by

ALAA S. ABD-EL-AZIZ

CHARLES E. CARRAHER, Jr.

CHARLES U. PITTMAN, Jr.

MARTEL ZELDIN

Macromolecules Containing Metal and Metal-Like Elements

Volume 9

Supramolecular and Self-Assembled Metal-Containing Materials

Edited by

Alaa S. Abd-El Aziz
University of British Columbia Okanagan, Kelowna, British Columbia, Canada

Charles E. Carraher, Jr.
Department of Chemistry and Biochemistry, Florida Atlantic University, Boca Raton, Florida, and Florida Center fior Environmental Studies, Palm Beach Gardens, Florida

Charles U. Pittman, Jr.
Department of Chemistry, Mississippi State University, Mississippi State, Mississippi

Martel Zeldin
Department of Chemistry, University of Richmond, Richmond, Virginia

A JOHN WILEY & SONS, INC., PUBLICATION

Macromolecules Containing Metal and Metal-Like Elements

Volume 9

Macromolecules Containing Metal and Metal-Like Elements

Volume 9

Supramolecular and Self-Assembled Metal-Containing Materials

Edited by

Alaa S. Abd-El Aziz
University of British Columbia Okanagan, Kelowna, British Columbia, Canada

Charles E. Carraher, Jr.
Department of Chemistry and Biochemistry, Florida Atlantic University, Boca Raton, Florida, and Florida Center fior Environmental Studies, Palm Beach Gardens, Florida

Charles U. Pittman, Jr.
Department of Chemistry, Mississippi State University, Mississippi State, Mississippi

Martel Zeldin
Department of Chemistry, University of Richmond, Richmond, Virginia

A JOHN WILEY & SONS, INC., PUBLICATION

Published by John Wiley & Sons, Inc., Hoboken, New Jersey
Published simultaneously in Canada

Library of Congress Cataloging-in-Publication Data:

ISBN 978-0-470-25144-7
ISSN 1545-438X

Printed in the United States of America

10 9 8 7 6 5 4 3 2 1

Contributors

Alaa S. Abd-El-Aziz, University of British Columbia, Okanagan, Kelowna, British Columbia V1V 1V7, Canada

Somobrata Acharya, World Premier International (WPI), Research Center for Materials Nanoarchitectonics (MANA) and Supermolecules Group, National Institute for Materials Science (NIMS), Tsukuba 305-0044, Japan

Pilar Amo-Ochoa, Departamento de Tecnología Industrial, Universidad Alfonso X EI Sabio, Madrid, E-28691, Spain

Marius Andruh, Inorganic Chemistry Laboratory, University of Bucharest, Bucharest, Romania

Shamindri M. Arachchige, Department of Chemistry, Virginia Polytechnic Institute and State University, Blacksburg, Virginia 24061-0212

Katsuhiko Ariga, World Premier International (WPI), Research Center for Materials Nanoarchitectonics (MANA) and Supermolecules Group, National Institute for Materials Science (NIMS), Tsukuba 305-0044, Japan

Ana Belén Descalzo, Instituto de Química Molecular Aplicada, Departamento de Química, Universidad Politécnica de Valencia, Valenica E-46022, Spain

Jitendra K. Bera, Department of Chemistry, Indian Institute of Technology, Kanpur 208016, India

Karen J. Brewer, Department of Chemistry, Virginia Polytechnic Institute and State University, Blacksburg, Virginia 24061-0212

Charles E. Carraher, Jr. Department of Chemistry and Biochemistry, Florida Atlantic University, Boca Raton, Florida 33431; and Florida Center for Environmental Studies, Palm Beach Gardens, Florida 33410

Oscar Castillo, Departamento de Química Inorgánica, Facultad de Ciencia y Tecnologia, Universidad del País Vasco, Bilbao E-48080, Spain

Samar K. Das, School of Chemistry, University of Hyderabad, Hyderabad 500046, India

Juan P. Garcia Terán, Departamento de Química Inorgánica, Facultad de Ciencia y Technología, Universidad del País Vasco, Bilbao E-48080, Spain

Jonathan P. Hill, World Premier International (WPI), Research Center for Materials Nanoarchitectonics (MANA) and Supermolecules Group, National Institute for Materials Science (NIMS), Tsukuba 305-0044, Japan

Qingmin Ji, World Premier International (WPI), Research Center for Materials Nanoarchitectonics (MANA) and Supermolecules Group, National Institute for Materials Science (NIMS), Tsukuba 305-0044, Japan

Melissa L. Kistler, Department of Chemistry, Lehigh University, Bethlehem, Pennsylvania 18015

Laura M. Lanni, Department of Chemistry and Biochemistry, University of South Carolina, Columbia, South Carolina 29208

John J. Lavigne, Department of Chemistry and Biochemistry, University of South Carolina, Columbia, South Carolina 29208

Jie Liu, Department of Chemistry and Biochemistry, University of South Carolina, Columbia, South Carolina 29208

Tianbo Liu, Department of Chemistry, Lehigh University, Bethlehem, Pennsylvania 18015

Antonio Luque, Departamento de Química Inorgánica, Facultad de Ciencia y Technología, Universidad del País Vasco, Bilbao E-48080, Spain

Moumita Majumdar, Department of Chemistry, Indian Institute of Technology, Kanpur 208016, India

Ramón Martínez-Máñez, Instituto de Química Molecular Aplicada, Departamento de Química, Universidad Politécnica de Valencia, Valencia E-46022, Spain

Joe Pigga, Department of Chemistry, Lehigh University, Bethlehem, Pennsylvania 18015

Charles U. Pittman, Jr. Department of Chemistry, Mississippi State University, Mississippi State, Mississippi 39762

Brett M. Rambo, Department of Chemistry and Biochemistry, University of South Carolina, Columbia, South Carolina 29208

Catalina Ruiz-Pérez, Laboratorio de Rayos X y Materiales Moleculares, Departamento de Física Fundamental II, Facultad de Fisica de la Universidad de La Laguna, La Laguna 38204, Spain

Knut Rurack, Bundesanstalt fur Materialforschung und -prüfung (BAM), Berlin 12489, Germany

Félix Sancenón, Instituto de Química Molecular Aplicada, Departamento de Química, Universidad Politecnica de Valencia, Valenica E-46022, Spain

George K. H. Shimizu, Department of Chemistry, University of Calgary, Calgary, Alberta T2N 1N4, Canada

Pavuluri Srinivasu, World Premier International (WPI), Research Center for Materials Nanoarchitectonics (MANA) and Supermolecules Group, National Institute for Materials Science (NIMS), Tsukuba 305-0044, Japan

Jared M. Taylor, Department of Chemistry, University of Calgary, Calgary, Alberta T2N 1N4, Canada

R. William Tilford, Department of Chemistry and Biochemistry, University of South Carolina, Columbia, South Carolina 29208

Ramanathan Vaidhyanathan, Department of Chemistry, University of Calgary, Calgary, Alberta T2N 1N4, Canada

Ajayan Vinu, World Premier International (WPI), Research Center for Materials Nanoarchitectonics (MANA) and Supermolecules Group, National Institute for Materials Science (NIMS), Tsukuba 305-0044, Japan

Martel Zeldin, Department of Chemistry, University of Richmond, Gottwald Science Center, Richmond, Virginia 23173

Contents

Preface

This book series, *Macromolecules Containing Metal and Metal-Like Elements*, is our attempt to bring to the chemical community new concepts and developments in the titled area of research. Volume 9 focuses attention on the area of supramolecular chemistry, supramolecular architecture, and supramolecular self-assemblies that involve materials containing metals and metal-like elements and the potential applications of these interesting hybrid materials.

Supramolecular chemistry may be defined as the formation of large complex assemblies (i.e., clusters) of species composed of two or more small, intermediate, and/or large molecules that are held together by noncovalent bonds. By noncovalent bonds we essentially mean hydrogen bonds, van der Waals interactions, metal coordination (donor–acceptor) interactions, π–π interactions, hydrophobic interactions, electrostatic forces, and/or combinations of these forces. Such interacting complex species are characterized by their spatial features, which include their architecture, as well as by the interactions, which hold the various components into a superstructure. The intermolecular interactions may be *weak,* as in hydrogen bonding, or *strong,* as in the case of metal-ion coordination. Very simple examples of the former are the vapor phase dimerization of acetic acid, which is held together by two hydrogen bonds; clathrates, which consist of one type of molecule that traps and contains a second type of molecule (i.e., host–guest complexes, inclusion compounds); and catenanes and rotaxanes, which are composed of two or more macrocyclic molecules that form a mechanically interlocked molecular architecture. An example of a strong intermolecular interaction is ferritin, which is a natural, iron-containing, globular complex of 24-protein subunits arranged as a hollow sphere with six channels that are used for intracellular storage and mobility of iron.

Supramolecular science has grown considerably over the past several decades, particularly with the pioneering discoveries by D. J. Cram, C. J. Pederson and Jean-Marie Lehn.[1,2] The field is now highly interdisciplinary and has developed to such an extent that it presently encompasses all the subdisciplines of chemistry in addition to significant contributions from the other physical and biological sciences and numerous engineering technologies. It is important that supramolecular systems are beginning to display valuable commercial applications in catalysis, nanotechnology, electro-optical devices, molecular

sensing and recognition, and biomedicine. For example, several inventions involving supramolecular assemblies have recently been reported in the patent literature.[3] Some scientists have proposed that supramolecular systems will be the chemical *building blocks* of the future, thereby affecting everything from quantum dots to artificial intelligence.[4] For those who wish to learn more about the field, we recommend the several recent reviews[5] in addition to the series, *Advances in Supramolecular Chemistry*, edited by G. W. Gokel.[6]

In this volume we have collected 10 review chapters from distinguished scientists who have contributed extensively to the study and development of supramolecular assemblies that contain metals and metal-like elements with unusual structures and morphologies and possess potentially useful (and applicable) physical and biological properties. The first chapter by K. Ariga et al. is a general discussion of supramolecular structures that contain inorganic building blocks for hybrid lipid thin films, layer-by-layer assemblies, structure transcription, and functional mesoporous hybrids. This is followed by two chapters, the first by M. L. Kistler et al., who describe the self-assembly of hydrophilic polyoxometalate (POM) macro-anions and examine the structure and behavior of POM macro-ions in solution. This is followed by a chapter by S. K. Das, who provides an overview of the supramolecular features of POM-supported transition metal complexes, POM-crown ether complexes with supramolecular cations, and supramolecular water clusters associated with POMs.

Chapter 4, by G. K. H. Shimizu et al., discusses work using metal-containing sulfonates and phosphonates as building blocks (linkers) to supramolecular networks. They describe the disruption of layered solids to form open-framework solids and examine the structure and dynamic behavior of these porous materials.

In Chapter 5, M. Majumdar and J. K. Bera describe the properties of and synthetic protocols for preparing extended linear metal (Cr, Co, Ni and Cu) chain compounds that contain at least three metal ions and are supported by ligand systems. In addition, they describe bent Pd chains that are sandwiched between unsaturated hydrocarbons and unsupported linear metal chain compounds.

In Chapter 6, B. M. Rombo et al. delve into the formation of boronate-linked supramolecular architectures based on boronate ester formation—for example, small molecule diesters form supramolecular self-assemblies in the solid state based on a phenyl-boron-phenyl sandwich motif in which these small oligomers link together to generate macrocycles and other polymers. The polymeric macrocyclics and linear structures demonstrate self-repair capabilities and constitute a new class of wide band-gap semiconducting materials. Through the incorporation of polyvalent boronates, covalent organic frameworks are described, which create highly crystalline, porous network materials.

In Chapter 7, S. M. Arachchige and K. J. Brewer concentrate on the coupling of light-absorbing metal centers to reactive Rh(III), Pt(II), and Pd(II) centers. This chapter highlights the recent progress and basic methods used to

study such reactive metal-containing assemblies. The authors examine different structural motifs and their chemical and photo-physical properties, which give rise to the coupling of ruthenium and osmium light absorbers because recent findings indicate their promise in solar energy conversion, emission-based sensing, spectroscopic probes of biomolecules, DNA modification, DNA photo-cleavage agents, anticancer drug development, and photodynamic therapy.

In Chapter 8, R. Martínez-Máñez et al. discuss the use of supramolecular and hybrid organic–inorganic systems in the development of novel sensing and signaling concepts through a shift or intensity change in color, fluorescence, or redox wave. The chapter highlights the general concept of supramolecular signaling as applied to the development of chromo-fluorogenic chemosensors and focuses attention on new functional sensing concepts that have an improved level of performance with special attention to hybrid systems that show synergic functional effects that are not found in molecular-based systems or with unmodified nanoscopic solids.

O. Castillo et al. in Chapter 9 provide an overview of various aspects of molecular recognition that takes place between nucleobases and artificial receptors. The authors focus attention on metal-oxalato frameworks that are involved in the molecular recognition process. These metal-oxalato fragments present great efficiency by acting as receptors of neutral and cationic nucleobases and even supramolecular nucleobase aggreates; where anchoring to these receptors takes place by coordinative bonding to the metal centers through endocyclic nitrogen atoms or by means of hydrogen bonding interactions between the organic bases and the inorganic fragments.

Finally, in Chapter 10, M. Andruh and C. Ruiz-Pérez discuss synthetic approaches to the crystal engineering of coordination polymers. They address important questions concerning architecture and packing arrangements; i.e., cavities or channels, because such empty spaces may be filled by host anions, solvent molecules, uncoordinated ligand molecules—and interpenetration in which voids associated with one framework are occupied by one or more independent frameworks.

Thus, Volume 9 covers a wide array of subjects in the titled area. The discussions along with the plethora of references in each chapter should enable the reader to obtain a basic understanding of this frontier area of research.

I. REFERENCES

1. E.g., D. J. Cram and J. M. Cram, *Science*, **1974**, *183*, 803; C. J. Pedersen, *Science*, **1988**, *241*, 536; J.-M. Lehn, *Supramolecular Chemistry: Concepts and Perspectives*, Wiley, Hoboken, N. J., **1995.**
2. J.-M. Lehn, *Interdisciplinary Sci. Rev.*, **1985**, *10*, 72; J.-M. Lehn, *Science*, **1985**, *227*, 849; M. Ruben, J.-M. Lehn, and P. Mueller, *Chem. Soc. Rev.*, **2006**, *35* (11), 1056.

3. Three examples in 2008: B. Xu, Z. Yang, G. Liang, and Q. Wang, U.S. Patent 2007224273 (**2008**); M. Pouzot, C. J. E. Schmitt, and R. Mezzenga, Eur. Patent WO2008025784 (**2008**), K. Cho and D. H. Kim, U.S. Patent 20080041300 (**2008**).
4. F. Zhao and M. Zhao, *Recent Res. Devel. Physics*, **2005**, *6*(5), 1.
5. A. Y. Tsivadze, G. V. Ionova, V. K. Mikhalko, and Y. N. Kostrubov, *Rus. Chem. Rev.*, **2007**, *76*(3), 213; A. Harada and K. Kataoka, *Prog. Polym. Sci.*, **2006**, *31*(11), 949; M. D. Ward, *Coord. Chem. Rev.*, **2006**, *250*, 312; M. J. W. Ludden, D. N. Reinhoudt, and J. Huskens, *Chem. Soc. Rev.*, **2006**, *35*(11), 1122; A. Scarso and J. Rebek Jr., *Topics Current Chem.*, **2006**, *265*, 1; P. L. Barthelemy, J. Stephen, and M. Grinstaff, *Pure Appl. Chem.*, **2005**, *77*(12), 2133; M. Schmittel and V. Kalsani, *Topics Current Chem.*, **2005**, *245*, 1; F. J. M. Hoeben, P. Jonkheijm, E.W. Meijer, and A. P. H. J. Schenning, *Chem. Rev.*, **2005**, *105*(4), 1491; K. Bhattacharyya, *Acct. Chem. Res.*, **2003**, *36*(2), 95; J. T. Groves, *Proc. Nat. Acad. Sci.*, **2003**, *100*(7), 3569.
6. G. W. Gokel, *Advances in Supramolecular Chemistry*, vols. *1–9*, Cerberus Press, South Miami, FL (1990–2003).

Series Preface

Most traditional macromolecules are composed of less than 10 elements (mainly C, H, N, O, S, P, C1, F), whereas metal and semi-metal-containing polymers allow properties that can be gained through the inclusion of nearly 100 additional elements. Macromolecules containing metal and metal-like elements are widespread in nature with metalloenzymes supplying a number of essential physiological functions including respiration, photosynthesis, energy transfer, and metal ion storage.

Polysiloxanes (silicones) are one of the most studied classes of polymers. They exhibit a variety of useful properties not common to non-metal-containing macromolecules. They are characterized by combinations of chemical, mechanical, electrical, and other properties that, when taken together, are not found in any other commercially available class of materials. The initial footprints on the moon were made by polysiloxanes. Polysiloxanes are currently sold as high-performance caulks, lubricants, antifoaming agents, window gaskets, O-rings, contact lens, and numerous and variable human biological implants and prosthetics, to mention just a few of their applications.

The variety of macromolecules containing metal and metal-like elements is extremely large, not only because of the large number of metallic and metalloid elements, but also because of the diversity of available oxidation states, the use of combinations of different metals, the ability to include a plethora of organic moieties, and so on. The appearance of new macromolecules containing metal and metal-like elements has been enormous since the early 1950s, with the number increasing explosively since the early 1990s. These new macromolecules represent marriages among many disciplines, including chemistry, biochemistry, materials science, engineering, biomedical science, and physics. These materials also form bridges between ceramics, organic, inorganic, natural and synthetic, alloys, and metallic materials. As a result, new materials with specially designated properties have been made as composites, single- and multiple-site catalysts, biologically active/inert materials, smart materials, nanomaterials, and materials with superior conducting, nonlinear optical, tensile strength, flame retardant, chemical inertness, superior solvent resistance, thermal stability, solvent resistant, and other properties.

There also exist a variety of syntheses, stabilities, and characteristics, which are unique to each particular material. Further, macromolecules containing metal and metal-like elements can be produced in a variety of geometries, including linear, two-dimensional, three-dimensional, dendritic, and star arrays.

In this book series, macromolecules containing metal and metal-like elements will be defined as large structures where the metal and metalloid atoms are (largely) covalently bonded into the macromolecular network within or pendant to the polymer backbone. This includes various coordination polymers where combinations of ionic, sigma-, and pi-bonding interactions are present. Organometallic macromolecules are materials that contain both organic and metal components. For the purposes of this series, we will define metal-like elements to include both the metalloids as well as materials that are metal-like in at least one important physical characteristic such as electrical conductance. Thus the term includes macromolecules containing boron, silicon, germanium, arsenic, and antimony as well as materials such as poly(sulfur nitride), conducting carbon nanotubes, polyphosphazenes, and polyacetylenes.

The metal and metalloid-containing macromolecules that are covered in this series will be essential materials for the twenty-first century. The first volume is an overview of the discovery and development of these substances. Succeeding volumes will focus on thematic reviews of areas included within the scope of metallic and metalloid-containing macromolecules.

Alaa S. Abd-El-Aziz
Charles E. Carraher Jr.
Charles U. Pittman Jr.
Martel Zeldin

CHAPTER 1

Supramolecular Structures and Functions with Inorganic Building Blocks

Katsuhiko Ariga, Ajayan Vinu, Jonathan P. Hill, Pavuluri Srinivasu, Somobrata Acharya, and Qingmin Ji

World Premier International (WPI) Research Center for Materials Nanoarchitectonics (MANA), National Institute for Materials Science (NIMS), Japan

CONTENTS

Macromolecules Containing Metal and Metal-Like Elements, Volume 9: Supramolecular and Self-Assembled Metal-Containing Materials,
Edited by Alaa S. Abd-El Aziz, Charles E. Carraher Jr., Charles U. Pittman Jr., and Martel Zeldin.

I. INTRODUCTION

Fabrication of nanometer-scale structures for ultra-small devices has been paid a great deal of attention because small machines could provide many societal benefits, such as optimization of energy consumption and waste discharge. Several excellent top-down approaches, including photolithography and electron-beam lithography, have been so far used to provide fine microstructures. However, these methods have several drawbacks, including size limitation and the paucity of applicable materials. Therefore, an alternate means, known as the bottom-up approach, has been recently intensively investigated. Methods of bottom-up fabrication rely on molecular self-assembly in supramolecular processes. Supramolecular chemistry, which was originally a branch of fundamental science, has now become an important concept in nanotechnology.

Most of the well-known or well-investigated supramolecular objects are assembled from organic molecules. The class of organic molecules possesses huge structural diversity and thus can exhibit many interesting chemical, physical, and biological functions. Probably the main drawback presented by organic species is their relative physical instability under the harsh conditions currently required for precise fabrication. This is in contrast to the high mechanical strengths and stabilities of most inorganic substances, which make them suitable for material applications. Unfortunately, inorganic materials have not been well investigated in terms of their potential in supramolecular chemistry. A combination of the two worlds of organic supramolecular chemistry and inorganic materials science should create useful nano-structured materials concurrently possessing various functionality, fine structural precision, and high mechanical stability. Supramolecular nanofabrication with inorganic building blocks, including organic–inorganic nano-hybrids and structure-transcribed materials, could be one of the most powerful methodologies for satisfying the current demands of nanotechnology.

As has been widely reported, metal-organic complexes, including metal-organic framework materials, are representative examples of supermolecules containing inorganic building blocks.[1,2] Because this subject has been extensively discussed in many forms, we here concentrate on supramolecular objects consisting of inorganic building blocks that are based on soft supramolecular assemblies. In this chapter, various recent topics in hybrid lipid thin films, layer-by-layer assemblies, structure transcription, and functional mesoporous hybrids are described (Fig. 1). Of course, not all of the recent work can be introduced here but the reader should be able to sense the essential recent trends in the corresponding fields from those examples that have been selected.

II. HYBRID LIPID THIN FILMS

Lipid thin films have been used in many applications, such as permeation control, drug delivery, and other medical applications because of their

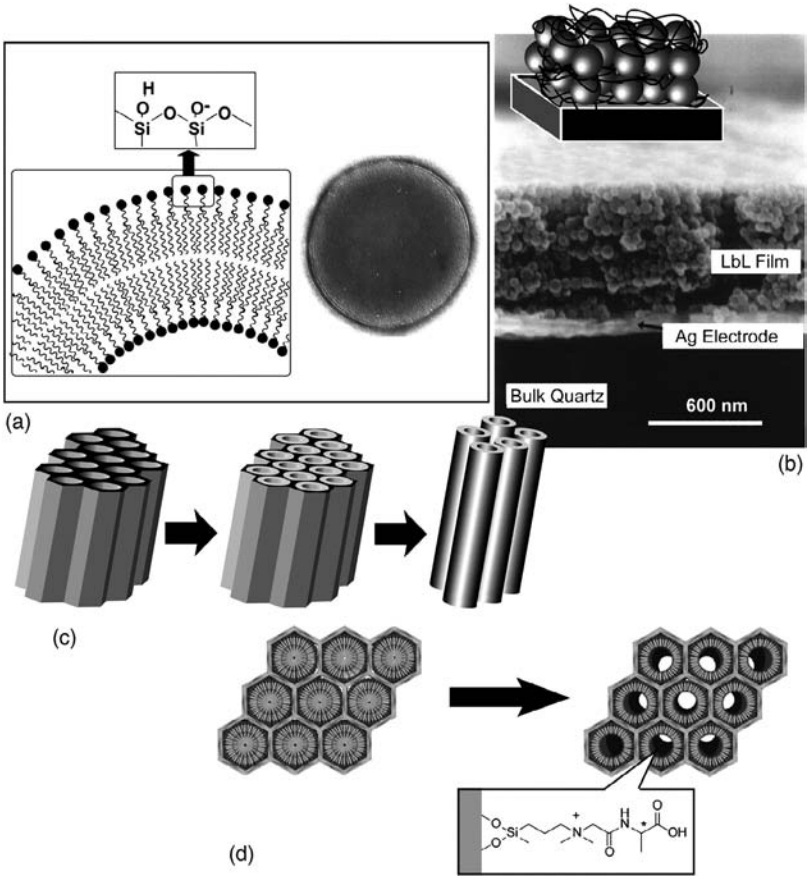

FIGURE 1. Supramolecular objects consist of inorganic building blocks mainly based on soft supramolecular assemblies. (a) Hybrid lipid thin films. (b) Layer-by-layer assemblies. (c) Structure transcription. (d) Functional mesoporous hybrid.

biocompatibility and ease of control under physicochemical conditions. However, a limited mechanical strength is sometimes apparent so that the hybrids of lipid thin films and strong inorganic frameworks are anticipated. In this section, several examples of lipid-inorganic hybrid thin films are described.

As stable lipid monolayer structures, self-assembled monolayers (SAMs) have been used widely where covalent bonding between the monolayer and the substrate afford a satisfactory mechanical strength. Typically, organosilane compounds such as *n*-octadecyltrichlorosilane (OTS) have been used for the preparation of SAM structures through the formation of covalent Si—O—Si linkages between hydrolyzed silane moieties and solid surfaces, such as glass plates or metal oxide layers. For example, Okahata and co-workers prepared a SAM of dialkylorganosilane on a porous glass plate, and successfully regulated

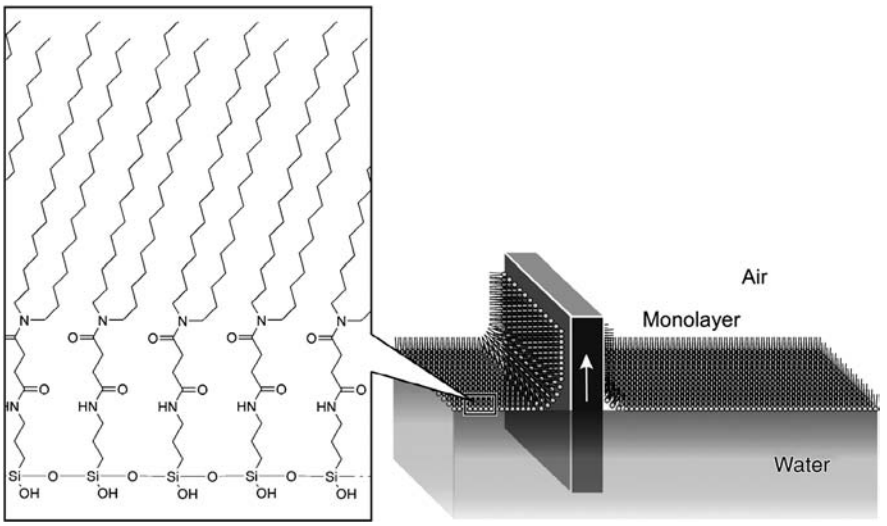

FIGURE 2. Technique for use of organosilane compounds.

material permeation through the glass.[3] The SAM structures developed deeply within the pores, where permeation of molecules dissolved in water could be regulated by variation of the physical state of the SAM structure.

The same research group developed a more sophisticated technique to realize the first example of permeation control through a single monolayer.[4,5] To immobilize a single monolayer on a porous glass surface, the SAM concept and the Langmuir-Blodgett (LB) technique were combined (Fig. 2). An organosilane monolayer was first prepared and polymerized on an air–water interface and was then transferred for immobilization on a solid substrate. The surface pressure-molecular area (π-A) isotherm of dialkylalkoxysilane depended significantly on the pH condition of the water subphase. Condensation at acidic pH 2 induced the formation of a well-condensed monolayer with a limiting area of 0.54 nm^2, which is rather close to the corresponding values from the conventional monolayers of dialkyl compounds such as phospholipids. The LB films that were prepared under acidic conditions showed peaks in the infrared spectra at 1026 and 1095 cm^{-1}, which are assignable to Si—O—Si and indicate the presence of an acid catalyst in the subphase, enabling the monolayer to polymerize.

For permeation control experiments, the polymerized monolayer was transferred onto a porous glass with 5-nm-diameter pores. From the unit area and degree of polymerization, the area occupied by a single polymer molecule was estimated to be $\sim$150 nm^2, which is apparently larger than the pore area of the 5-nm glass (20 nm^2). The transferred monolayer was covalently immobilized on the porous glass plate by heat treatment. As illustrated in Figure 3, the glass plate with the immobilized monolayer was attached to the bottom of a polyethylene tube and soaked in a 1-cm quartz cell. Permeation of a water-soluble

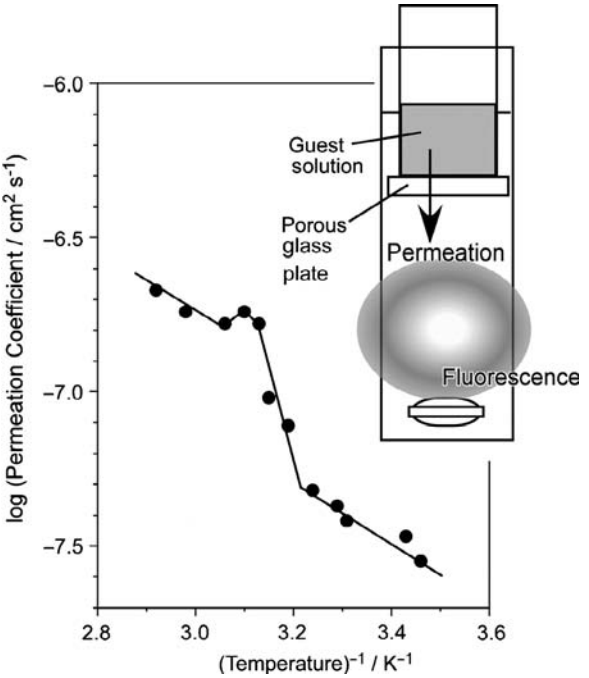

FIGURE 3. Permeation of water-soluble fluorescent probe through a glass plate with the immobilized monolayer.

fluorescent probe was estimated by the increase in fluorescence intensity of the lower solution. It is interesting that permeation through the monolayer exhibited a discontinuity at around 45°C (Fig. 3), which is very close to the phase transition temperature (crystal state to liquid crystalline state) of the polymerized monolayer. This was the first example of permeation control using a 2-nm-thick monolayer, and so far, it is the thinnest lipid film that operates as a permeation valve. This demonstration of control of organic thin film permeation became possible only through hybridization of the fragile monolayer with the mechanically stable inorganic substrate.

Permeation control through monolayer structures has also been demonstrated using electrochemical means (Fig. 4). The same research group similarly immobilized monolayers of dialkyl organosilane compounds on SnO_2 electrodes by forming covalent linkages; permeability of an electrochemically active probe ($Fe(CN)_6^{4-}/Fe(CN)_6^{3-}$) through the monolayer was monitored.[6] This monolayer-hybridized electrode suppressed dramatically the redox response of the Fe probe and was hardly affected by repeated measurements. In sharp contrast, the electrode covered noncovalently with monolayers of conventional fatty acids could not continuously block permeation of the probe molecule. Permeation profiles of $Fe(CN)_6^{4-}/Fe(CN)_6^{3-}$ probe were evaluated at different temperatures, indicating that the redox response of the probe increased

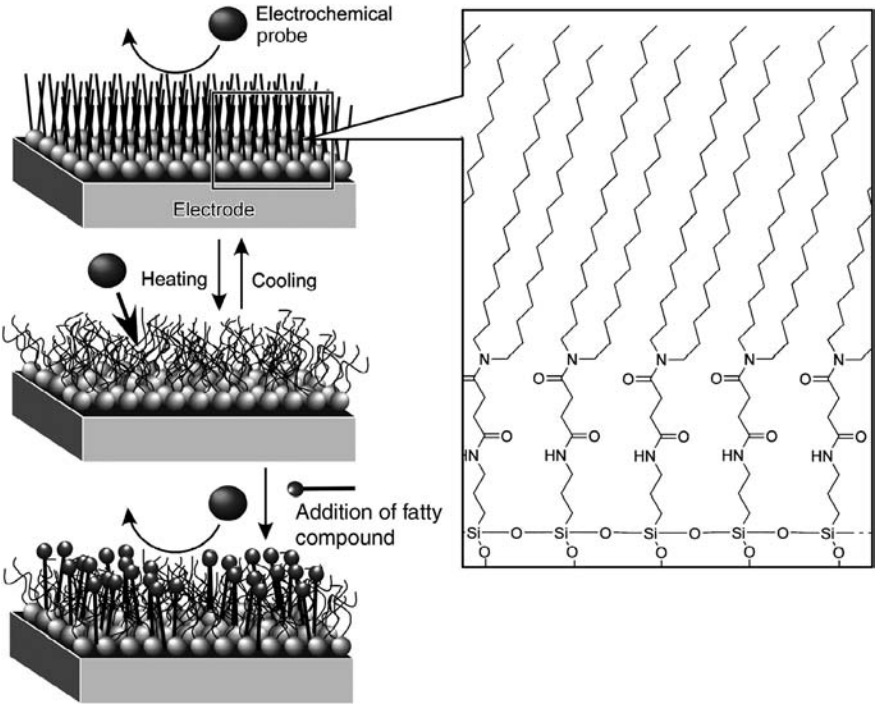

FIGURE 4. Electrochemical investigation of permeation control through monolayer structure.

drastically near the phase transition temperature. Maximum permeability to the probe molecule near the phase transition temperature was probably due to alkyl chain disorder during a period of unstable coexistence of crystalline and liquid crystalline states of the monolayer phase. It is interesting that the addition of alcohol molecules to the solution blocks the permeation of probe molecules, with a significant dependence on the identity of the added alcohol. It is likely that the alcohol molecules fill the pinholes formed on the monolayer and shape discrimination occurs upon alcohol insertion into the monolayer.

The concept of the hybrid electrode was extended to a vitamin-immobilized system by Hisaeda and co-workers (Fig. 5), in which heptapropyl and heptaoctyl esters of vitamin B_{12} derivatives with a Co(II) or Co(III) center were used.[7] Investigation of π-A isotherms of these compounds with the alkoxysilane monolayers suggested that stable accommodation of the vitamin B_{12} functionality in the lipid monolayer can be achieved by the introduction of long chains at the vitamin B_{12} core. The mixed monolayers of the long chain–substituted vitamin B_{12} and organosilane amphiphile were transferred as an *x*-type LB film onto a quartz plate and showed reasonable UV absorbance. Monolayers similarly immobilized on an indium-tin-oxide (ITO) electrode possessed a

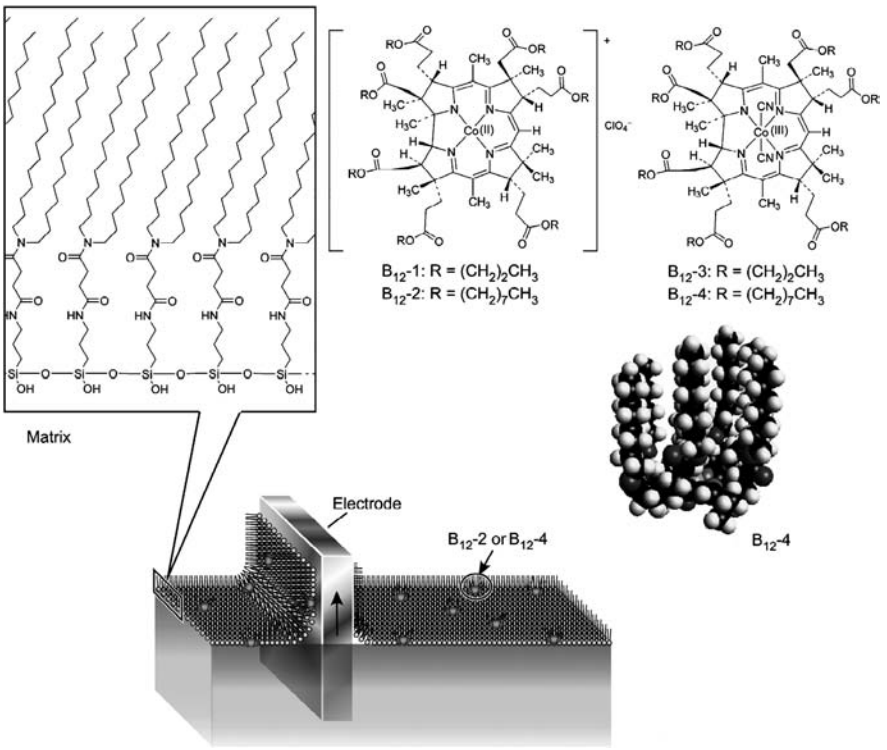

FIGURE 5. Vitamin B_{12}-immobilized monolayer.

Co(II)/Co(I) redox couple. This indicates that the modified electrode can be used as a reactive electrode with a vitamin B_{12} function. To demonstrate this possibility, the vitamin B_{12} derivative was hybridized into thicker films, obtained by the sol-gel process.[8] The modified electrode complex exhibited the Co(II)/Co(I) redox couple, and the controlled-potential electrolysis of benzyl bromide in aqueous solution containing 0.1M KCl afforded dehalogenated products, bibenzyl and toluene, with a total turnover number of >1000 for 1 h.

The form of silica-based hybrid lipid assemblies is not limited to planar thin films. Katagiri co-workers have developed the silica-based hybrid vesicle, cerasome (Fig. 6),[9,10] which is quite distinct from the above-mentioned approaches. The unusual term *cerasome* originates from "*cera*mics + *som*a" by analogy with *liposome* ("lipo + soma"). The cerasome was prepared by vortex mixing of aqueous dispersions of a silane-bearing amphiphile (Si-lipid 1 or Si-lipid 2; Fig. 6). Formation of a silica network at the polar head group upon sol-gel reaction together with spontaneous formation of a bilayer structure resulted in cell-like vesicle structures containing a silica network at the outer and inner surfaces. Transmission electron microscopy (TEM) confirmed the formation of multilamellar vesicles (Fig. 7) with a diameter $\sim$ 200 nm. Aggregated

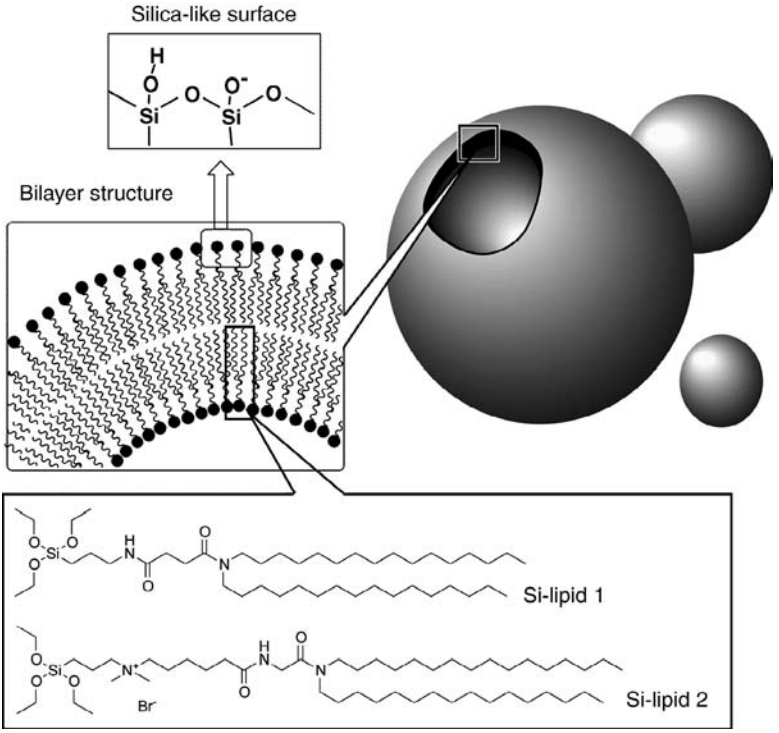

FIGURE 6. Silica-based hybrid vesicle, cerasome.

vesicle structures were often observed without structural collapse (Fig. 7b), suggesting the superior structural stability of cerasome due to the inorganic framework structure formed at the surface.

III. LAYER-BY-LAYER ASSEMBLIES

To obtain structure-controlled nano-hybrids, preparation of layered structures in designed sequences is one of the most practical solutions. Among several methods for the preparation of layered structures, alternate layer-by-layer (LbL) assembly,[11–13] which has been rapidly developed, is suitable for inclusion of a variety of organic and inorganic substances. The LbL assembly was first realized and established by Decher and co-workers[14] some time after a suggestive report by Iler.[15] An outline of this technique is shown in Figure 8, illustrating that the LbL assembly is conducted mainly through electrostatic interaction. Excess adsorption of the substances to an oppositely charged

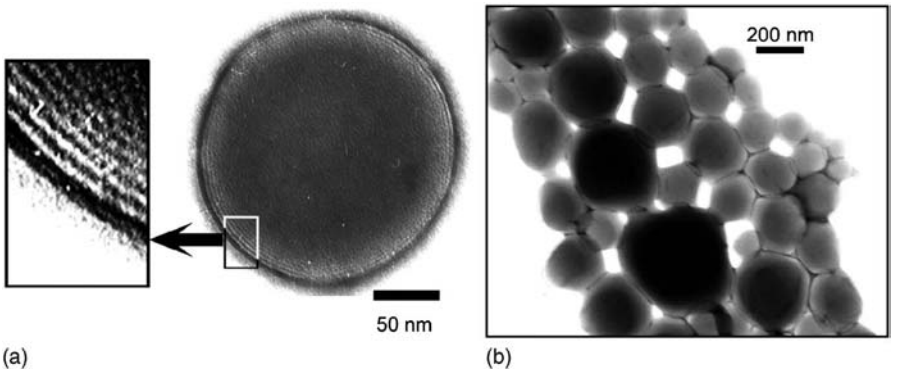

FIGURE 7. (a) TEM images of cerasome, (b) Its assembly.

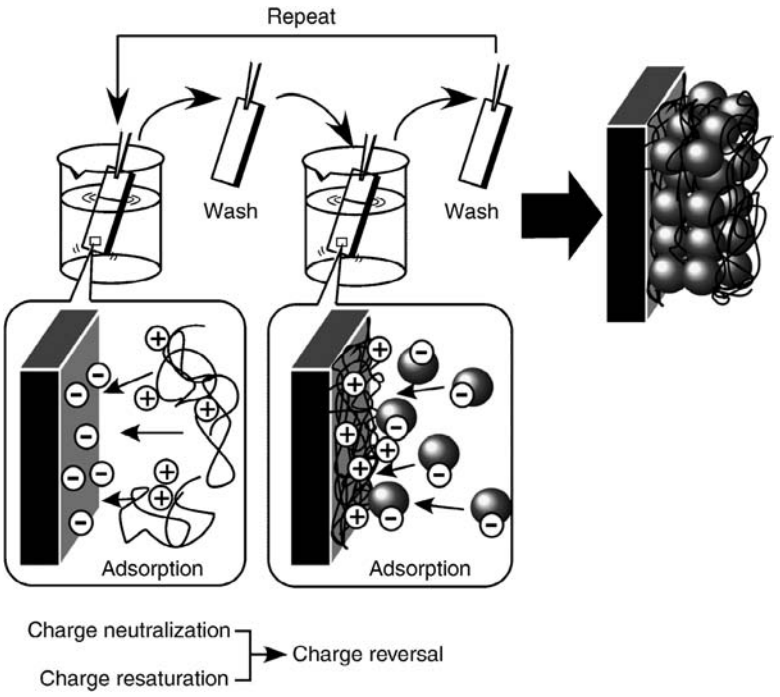

FIGURE 8. Outline of LbL assembly.

surface leads to charge neutralization and resaturation and results in charge reversal. Therefore, continuous assembly between oppositely charged materials can be conducted continuously with great freedom in the number of layers and layering sequence. The variability in applicable materials is another of the most pronounced advantages of this method. Applicable materials are not limited to conventional polyelectrolytes so that not only biochemical materials (including

proteins, DNA strands, and virus particles) but also charged inorganic substances (such as colloidal nanoparticles, clay, nanosheets, modified zeolite crystals, two-dimensional perovskite, and polyoxometalates) have been included. Furthermore, charged supramolecular assemblies, such as bolaamphiphile monolayers, lipid bilayers, LB films, and stacked dye molecules, have also been used in layer-by-layer approaches. Assemblies with other interactions such as hydrogen bonding, metal coordination, and charge transfer interactions have also been demonstrated.

Typical examples of LbL films containing inorganic building blocks are given in Figure 9. The figure shows responses of a quartz crystal microbalance (QCM) on the assembling processes of three sizes of SiO_2 particles (25, 45, and 78 nm in diameter), where larger and smaller steps correspond to the adsorption of SiO_2 particles and poly(diallyldimethylammonium chloride) (PDDA), respectively.[16,17] Stepwise regular increases in the film mass were observed for all kinds of SiO_2 particles. Figure 10 displays scanning electron microscopy (SEM) images of the SiO_2-PDDA LbL film. The SiO_2 particles are closely packed in the layer, but there is no long-range ordering.

This technique can be applied to LbL assembly of cerasomes because, like silicas, they possess surface charge. Initial attempts entailed LbL assembly between cationic polyelectrolyte and anionic cerasomes with monitoring by using QCM, and where reasonable frequency shifts in the QCM response were observed.[18] Morphology of the assembled structure was also confirmed

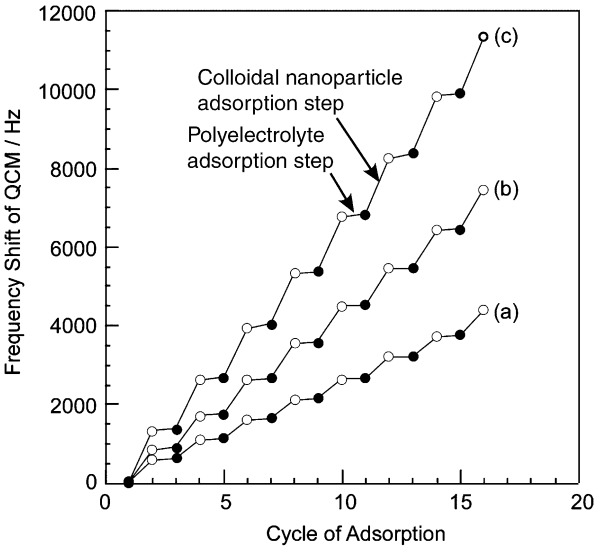

FIGURE 9. QCM responses of the assembling processes of SiO_2 particles with polyelectrolytes. line a, a 25-nm SiO_2 particle; line b, a 45-nm SiO_2 particle; and line c, a 78-nm SiO_2 particle.

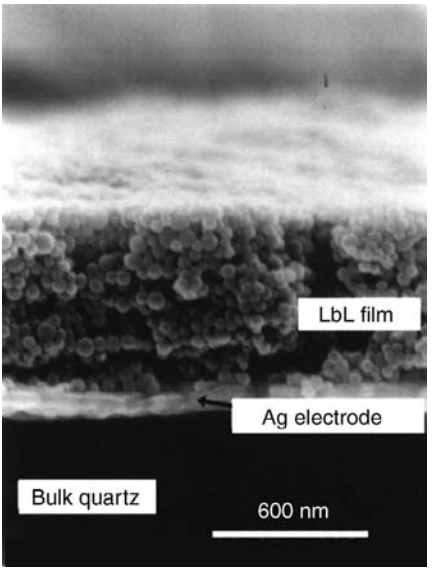

FIGURE 10. A SEM image of the SiO_2-PDDA LbL film. (Reprinted with permission from ref. 17.)

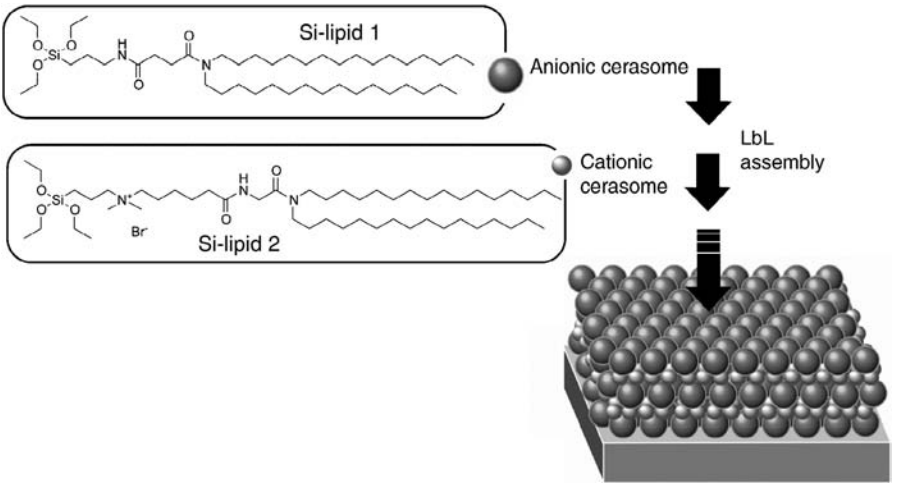

FIGURE 11. LbL assembly between cationic and anionic cerasomes.

by atomic force microscopy (AFM). Appropriate design of the silane-bearing amphiphiles, for example Si-lipid 1 and Si-lipid 2, led to the successful preparation of both cationic and anionic cerasomes, which enabled direct assembly of cerasome particles, thereby avoiding use of interlayer polyelectrolytes (Fig. 11).[19] Formation of a smaller size of cationic cerasomes (20–100 nm)

and a larger size of anionic cerasomes (70–300 nm) was confirmed by TEM observation. Detailed QCM observation revealed large steps and small steps in frequency change corresponding to adsorption of the anionic and the cationic cerasome, respectively. AFM observations of the surface of the assembled structures indicated close packing of the cerasome particles like a stone pavement, where the difference in the particle size for each layer clearly confirmed successful preparation of layered structures of the cationic and anionic cerasomes. The structures presented can be regarded as novel types of artificial multicellular systems for use as bioreactors or biosensors. Further functionalization of the cerasome surface could be used for immobilization of various biomolecules, such as enzymes and antibodies, to create novel bioorganic–inorganic nanohybrids.

Appropriate selection of solid supports for the LbL assembly enables us to prepare free-standing films through selective etching of the solid support (sacrificial layer) (Fig. 12). For example, Mamedov and Kotov demonstrated preparation of free-standing LbL films through assembling films on a cellulose acetate layer that was selectively dissolved later.[20] Tsukruk and co-workers used a similar strategy for fabrication of freely suspended, multilayered nanocomposite membranes containing gold nanoparticles.[21–24] The films that were obtained possessed very stable micromechanical characteristics and a sensitivity far surpassing any existing pressure sensors. Preparation of free-standing films of poly(ethylene oxide) (PEO) and poly(acrylic acid) (PAA), which interact with each other through hydrogen bonding, was realized by Hammond and co-workers.[25] In the films obtained, crystallization of PEO

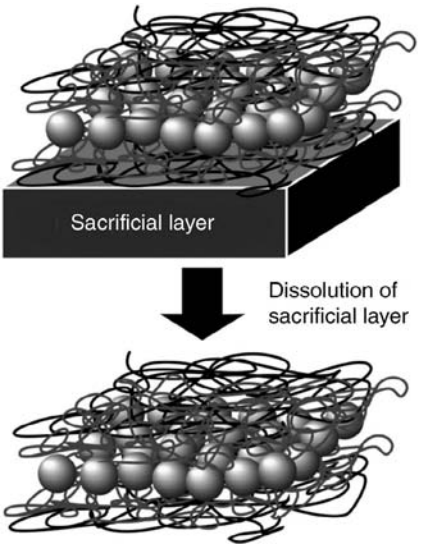

FIGURE 12. Preparation of free-standing LbL films.

moieties was suppressed and exhibited properties advantageous for use as ultrathin hydrogel membranes and solid-state polymer electrolytes.

The LbL technique is even useful for more advanced microfabrication. An excellent example was report by Lvov and co-workers[26] and is summarized in Figure 13, which illustrates the preparation of an LbL self-assembled ultrathin micro-cantilever consisting of clay/polymer nanocomposites. The researchers used sequenced procedures, including patterning, photo-treatment, etching, and LbL assembly. The same research group also proposed a microfluidic approach for the complex formation of polyelectrolytes and polyelectrolyte/protein microstrips on a glass surface.[27] These studies are excellent examples of research into the development of organic–inorganic nanohybrids.

Use of the LbL technique is not restricted to the preparation of planar thin films. One of the most outstanding strategy modifications of the LbL technique involves assembly on colloidal particles followed by hollow capsule formation. For example, Caruso and co-workers reported the formation of hollow silica vesicles through LbL assembly on colloidal nanoparticle templates (Fig. 14).[28] Polyelectrolytes and smaller silica particles were initially formed on a larger colloidal core, which was subsequently selectively destroyed. Calcination of the hybrid vesicles resulted in a hollow vesicle composed of silica. Formation of controlled organic–inorganic layer structures on colloidal particles by LbL assembly also provides media appropriate for investigation of fundamental phenomena.

Decher and co-workers exploited the superiority of LbL assembly for structural design and synthesis to understand energy transfer processes (Fig. 15).[29] They prepared LbL films on gold colloids with a diameter of 13 nm to fabricate metal-core polymer shell capsules, in which the fluorescent organic dyes fluorescein isothiocyanate (FITC) and lissamine rhodamine B (LISS) are placed at various distances from the gold core. The gold nanocore quenches the fluorescence of the fluorescein and lissamine dyes situated in the outer polymer layers of the core-shell nanoparticles. Systematic investigation with control of the distance between dye and metal core provides a direct method to assess the effect of the metal core on the radiative rates, which revealed strongly distance-dependent fluorescence quenching and reduction in the transition probability for radiative transitions by gold nanoparticles.

IV. STRUCTURE TRANSCRIPTION

Supramolecular structures self-assembled from organic molecules often provide finely tuned structures. Transcription of these structures into mechanically stable inorganic substances should be a productive approach for the preparation of novel functional materials. This concept is sometimes known as structure transcription. Transcription of fibrous and tubular structures of organic gels into inorganic substances have has been extensively reported by

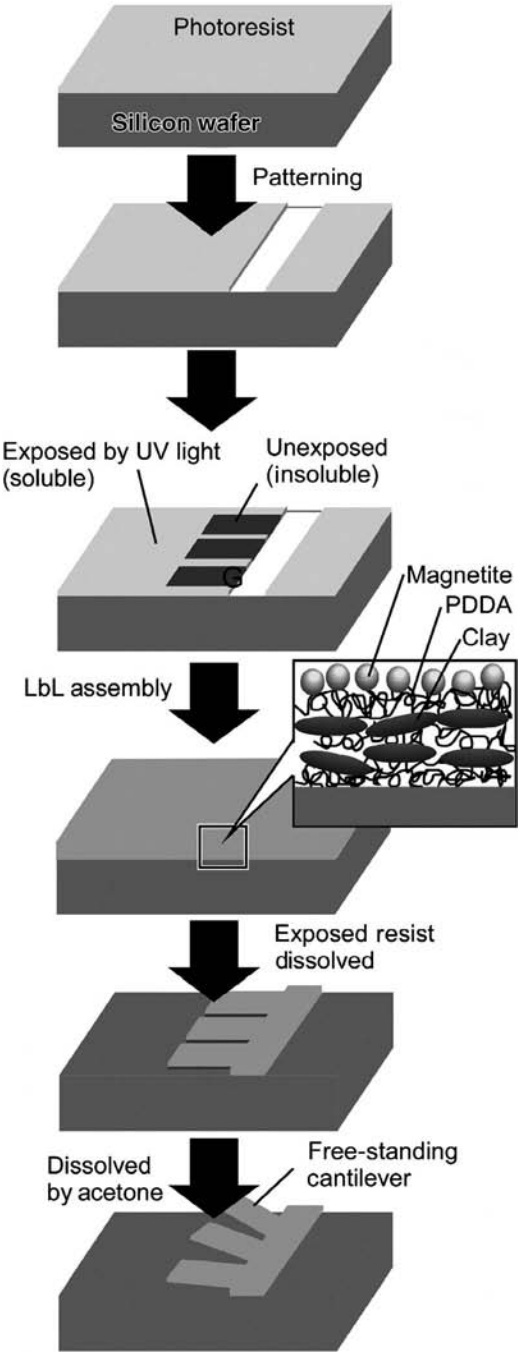

FIGURE 13. Fabrication of LbL self-assembled ultra-thin microcantilever consisting of clay/polymer nanocomposites.

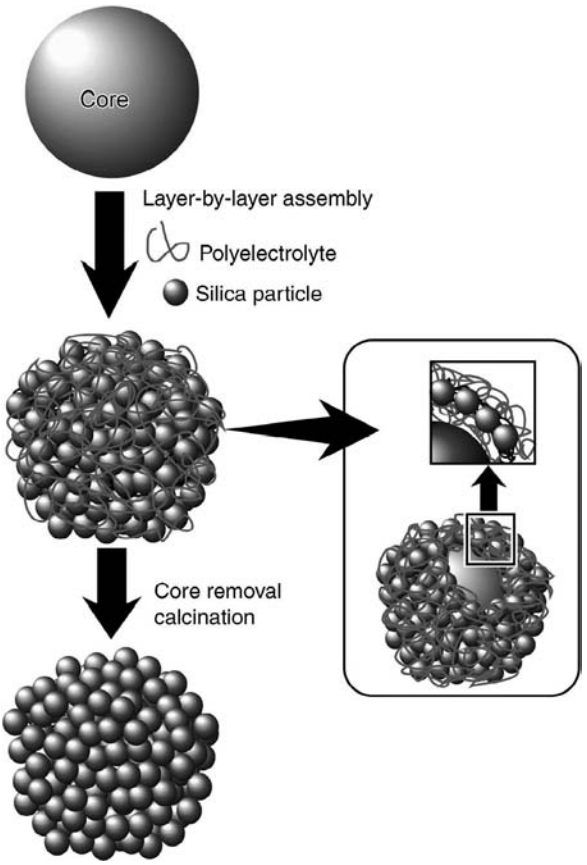

FIGURE 14. Hollow capsule formation by the LbL method.

groups lead by Shinkai, Shimizu, and Hanabusa.[30–32] For example, the compound shown in Figure 16 forms tubular structures in appropriate media, which can be transcribed as double-walled silica nanotubes through the sol-gel condensation of the co-reactant tetraethyl orthosilicate, followed by calcination treatment.[33] Shimizu and co-workers reported metal nanowire formation, by which a synthetic glycolipid *N*-(11-*cis*-octadecennoyl)-β-D-glucopyranosylamine was employed for the fabrication of organic tubular structures with a circular hollow cylinder 30–50 nm wide.[34] Gold or silver nanoparticles were first encapsulated in the hollow cylinders of lipid nanotubes using capillary force, followed by removal of the organic components by firing the nanocomposite, which result in gold nanowires with controlled width.

Yamashita demonstrated the use of a biomolecular array for structure transcription (Fig. 17).[35] A Langmuir monolayer of ferritin, which is composed of 24 self-assembled peptide subunits and is capable of including iron oxide,

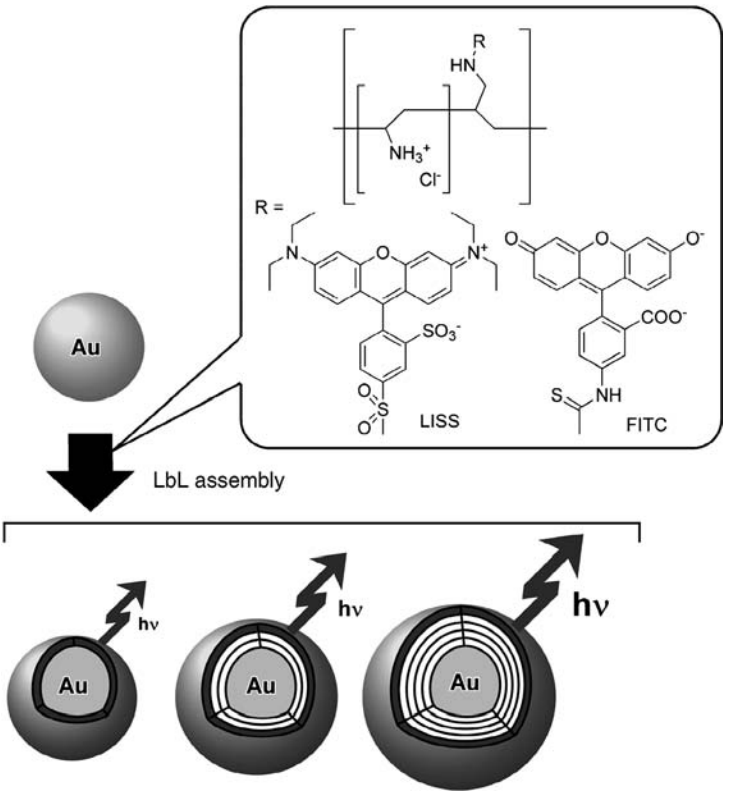

FIGURE 15. LbL films on a gold colloid in which the fluorescent organic dyes fluorescein isothiocyanate (FITC) and lissamine rhodamine B (LISS) are placed at various distances from the gold core.

was first transferred onto a hydrophobized silicon substrate to form a two-dimensional hexagonal array of ferritin. Destruction of organic components by UV/ozone treatment and heat treatment under hydrogen flow left iron particles with diameters < 6 nm in a hexagonal arrangement. Supramolecular arrays prepared from inorganic substances can be used for device preparation. Immobilization of such arrayed structures, for instance as the gate part of a transistor, could lead to the preparation of a floating quantum dot gate transistor for multilevel logic gates capable of room temperature operation.

Apart from the previously mentioned approaches, regular inorganic structures such as porous alumina can be also used as templates for preparation of fine bioorganic structures. As depicted in Figure 18, LbL assembly of organic components such as polymers, lipids, and proteins within inorganic pores followed by selective removal of the inorganic components results in the formation of self-standing tubular structures. Li et al. applied this concept to the fabrication of microtubes from biocomponents such as

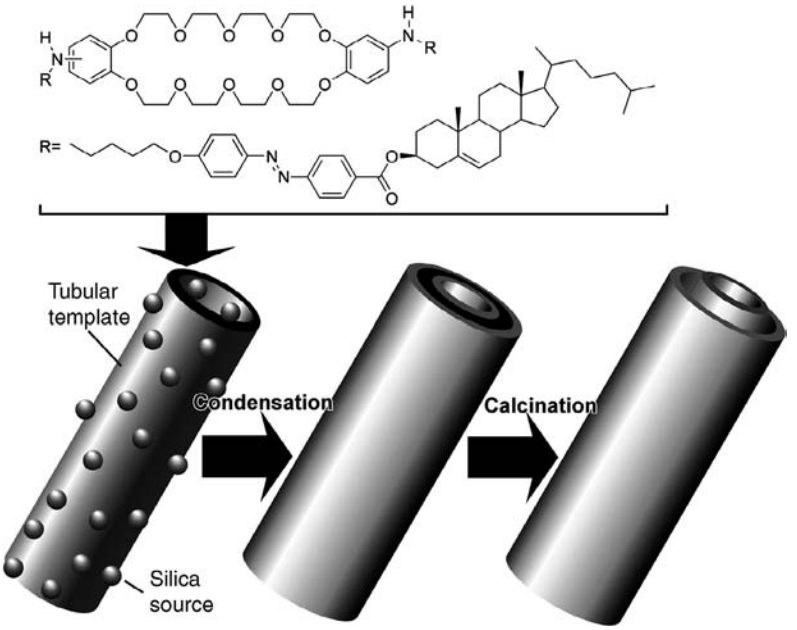

FIGURE 16. Preparation of a double-walled silica nanotube through the sol-gel reaction using an organic tube as a template.

proteins and phospholipids.[36] For example, the surface charge of human serum albumin (HSA) can be modified by variation of pH to be either more positive or more negative so that pure protein tubes can be prepared by the LbL assembly of HSA under controlled pH conditions. These synthetic HSA microtubes have smooth and clean surfaces with a wall thickness of $\sim$ 30 nm. The length of the tubes is $\sim$ 60 μm, and they possess a flexibility that is tolerant to free bending.

One of the most popular and influential examples of structure transcription is given by the preparation of mesoporous materials. Mesoporous materials with regular geometries have recently gained much attention because of their great potential for practical uses such as catalysis, adsorption, separation, sensing, medical usages, environmental applications, and nanotechnology.[37,38] Mesoporous silica, which is the most representative mesoporous structure, is synthesized by structure transcription using micelle supramolecular assemblies (Fig. 19a). In 1990, Kuroda and co-workers first reported the preparation of mesoporous silica of uniform pore size distribution from the layered polysilicate kanemite (FSM-16; folded sheet materials).[39,40] A significant breakthrough in mesoporous materials research came when Mobil scientists disclosed the M41S family of materials, which have large uniform pore structures; high specific surface areas; and specific pore volumes, including hexagonal-MCM-41,[41,42] cubic-MCM-48,[43] and lamellar-MCM-50.[44] These pioneering discoveries were

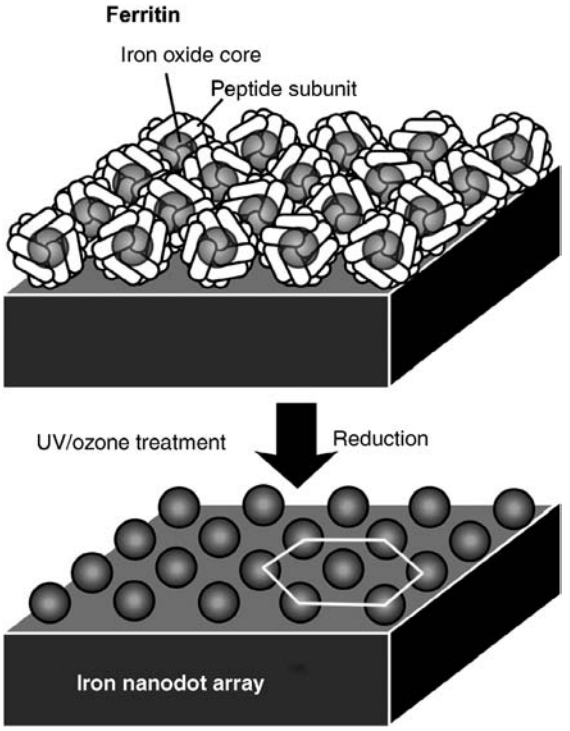

FIGURE 17. Preparation of iron particles arrays from a Langmuir monolayer of ferritin.

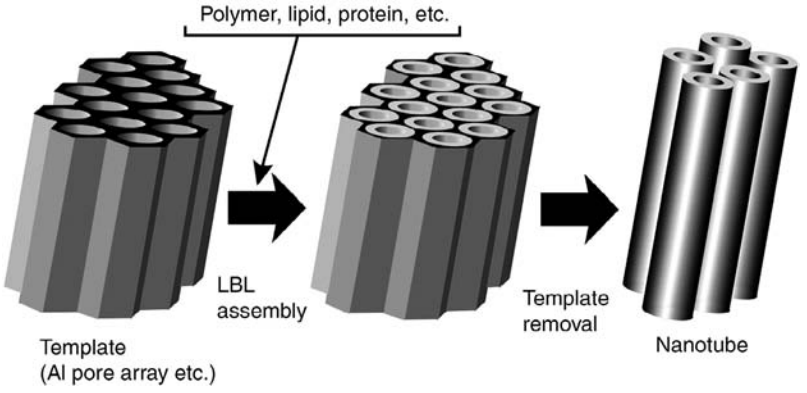

FIGURE 18. Fabrication of microtubes from biocomponents using inorganic pore structures.

followed by various other kinds of mesoporous materials—for example, hexagonal mesoporous silica (HMS) prepared using neutral amine as the template[45] and MSU-1 (Michigan State University) using polyethylene oxide as a structure directing agent.[46] The widely used, highly ordered, large pore mesoporous

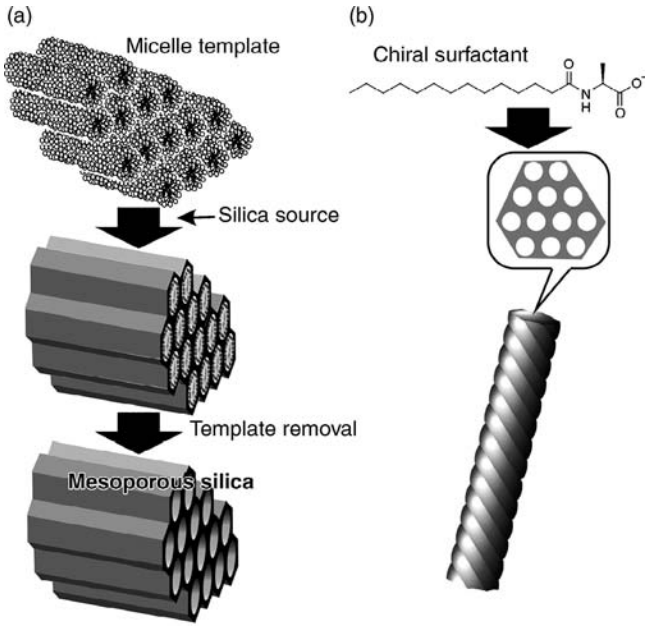

FIGURE 19. (a) General concept for synthesis of mesoporous silica. (b) Formation of mesoporous silica materials with a chiral morphological aspect.

silica-15, SBA-15 (Santa Barbara amorphous), with thicker pore walls and two-dimensional hexagonal structure, was prepared using an amphiphilic triblock copolymer of poly(ethylene oxide) and poly(propylene oxide), P123 (Pluronic) as the structure: directing reagent in a highly acidic media.[47,48] Mesocellular form (MCF) materials can be prepared by using triblock copolymer stabilized oil in water, giving aerogel-like structures, which offer potential as catalyst supports and separation media.[49] One recent and unique example introduced chirality as an important morphological aspect of mesoporous materials by using a chiral surfactant template (Fig. 19b).[50]A novel synthetic *N*-acetyl-type alanine-based surfactant was used as the structure-directing reagent, resulting in mesoporous silica materials with regularly twisted rod-like structures of diameter 130–180 nm and length 1–6 mm. In the structure obtained, hexagonally aligned mesoscopic channels of diameter 2.2 nm were wound together in one particular direction.

Several other synthetic strategies have been used for the preparation of mesoporous materials with various components. In particular, production of carbon materials containing regular mesopores was begun in the late 1990s through a carbonization procedure using mesoporous silica as a regularly structured template followed by removal of the template silica (Fig. 20). Mesoporous carbon structures were first reported by Ryoo using sucrose as a carbon source and mesoporous silicates, such as MCM-48, SBA-1, and SBA-15,

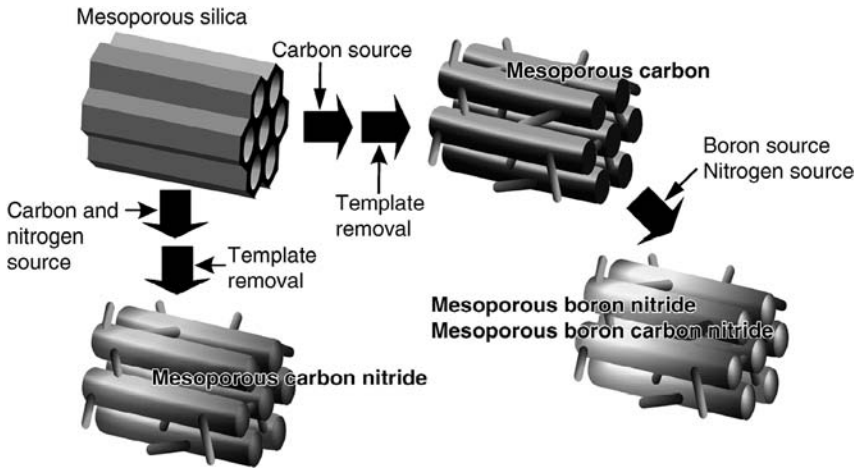

FIGURE 20. Syntheses of mesoporous carbon, mesoporous carbon nitride, mesoporous boron nitride, and mesoporous boron carbon nitride.

as template. These materials are now known as CMK-*x*.[51,52] Hyeon et al. independently and somewhat later reported a similar approach to well-ordered mesoporous carbon materials with a different designation, SNU-*x*.[53] More recently, Vinu and co-workers[54] applied this concept to the synthesis of mesoporous carbon nitride for which combined carbon and nitrogen sources were used (Fig. 20). They also pioneered a third method for the synthesis of mesoporous materials, which they call the "elemental substitution method."[55] In this method, component elements are substituted by other elements with the retention of the mesoporous structure. For example, they successfully realized the first synthesis of mesoporous boron nitride and mesoporous boron carbon nitride (Fig. 20).[56]

V. FUNCTIONAL MESOPOROUS HYBRIDS

The pore sizes of mesoporous materials are compatible with those of complex organic molecules and biological materials. Therefore, supramolecular nanofabrication based on mesoporous materials, such as functionalization at the interiors of mesopores, could be one of the best methods for the creation of functional materials using media for supramolecular interactions within a well-defined geometry.

To modify the mesoporous materials with organic functional groups, the two major methods of co-condensation and grafting are usually used.[57,58] In the co-condensation method, a silica source containing an organic functional group is mixed with a conventional silica source, such as tetraethyl orthosilicate,

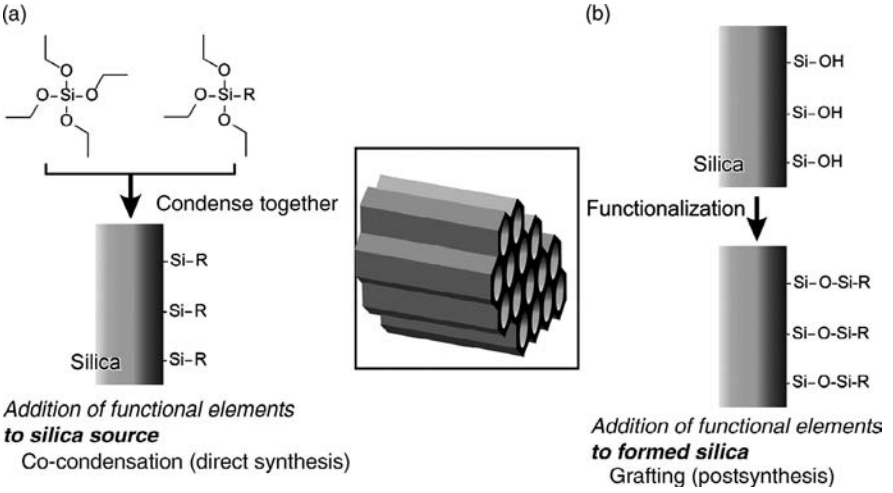

FIGURE 21. Modification of mesoporous silica by (a) co-condensation and (b) grafting.

during mesoporous silica synthesis (Fig. 21a). This method provides a homogeneous distribution of organic functional groups within mesopores. Modification of presynthesized mesoporous silica can be achieved by grafting and is also known as postsynthesis modification (Fig. 21b). Organic functional groups can be introduced by direct reaction of organosilanes at the silica surface, and different functionalities can be then attached to the already introduced groups through covalent bonding and/or molecular recognition. Similarly, the preintroduced functionalities are often converted to other groups by chemical reaction. Such functionalization of mesoporous silica has been used in the development of various functional materials. One example is shown in Figure 22, in which photocontrolled regulation of drug storage and release from mesoporous silica was achieved in the pioneering work by Fujiwara et al.[59] They prepared MCM-41 mesoporous silica, which was functionalized with photoactive coumarin that was grafted only at the pore outlet. Cholestane (guest drug) was incorporated into the mesopores of silica upon exposure to the guest solution. Irradiation by UV light (> 310 nm) caused dimerization of coumarin for trapping of the guest cholestane in the stable form and blocked the leaching of the guest from the mesopores. The dimerized coumarin was cleaved upon irradiation at a different UV wavelength (-250 nm) and resulted in the release of the trapped cholestane.

Ariga and co-workers proposed the synthesis of a mesoporous silica structure possessing amino acid residues densely packed in its pores using a carefully designed surfactant (Fig. 23).[60] During the synthesis of the mesoporous structure, an amphiphile containing a condensable alkoxysilane group was used as a template and sol-gel reactions together with tetraethyl orthosilicate resulted in mesoporous silica whose channels are filled with the covalently attached organic groups (alanine residue) of the template. Cleavage and removal of the

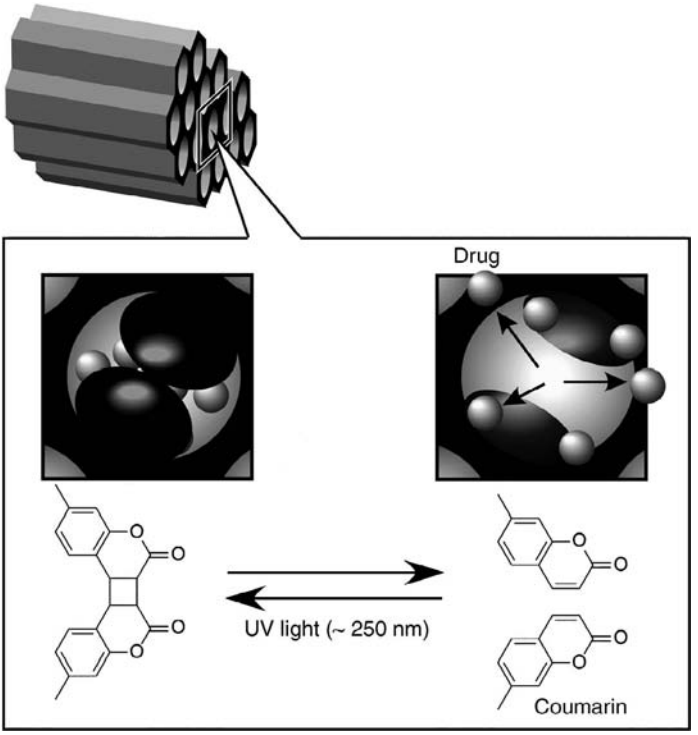

FIGURE 22. Photo-controlled regulation of drug storage and release from mesoporous silica.

alkyl tail by selective hydrolysis of the ester at the C-terminal leaves open pores with a surface covalently functionalized by the alanine residue. In this process, the template behaves like a "lizard" because it could be said that it bites the silica surface with the later cleavage of its tail, which is a defensive mechanism employed by some species of lizard. Aida and co-workers used the hybrid structure for reactor applications and demonstrated the catalytic capability of unhydrolyzed materials on the acetalization of ketones, such as cyclohexanone, in ethanol under mild conditions.[61] According to their proposed mechanism, hydrophobic and hydrophilic reactants can be incorporated simultaneously into the amphiphilic core–shell architecture of the immobilized rod-like micelle within silica channels and then can be activated through hydrogen-bonding interactions with the peptidic functionalities located at the core–shell interface. The lizard templating method is expected to be used for the fabrication of mesoporous silica with a variety of biofunctional groups. It could provide artificial active sites for a wide range of biological functions.

Mesoporous pores are interesting media for confinement of functional organic molecules under restricted motion and orientation. In particular, confinement of polymeric substances is an attractive research subject because

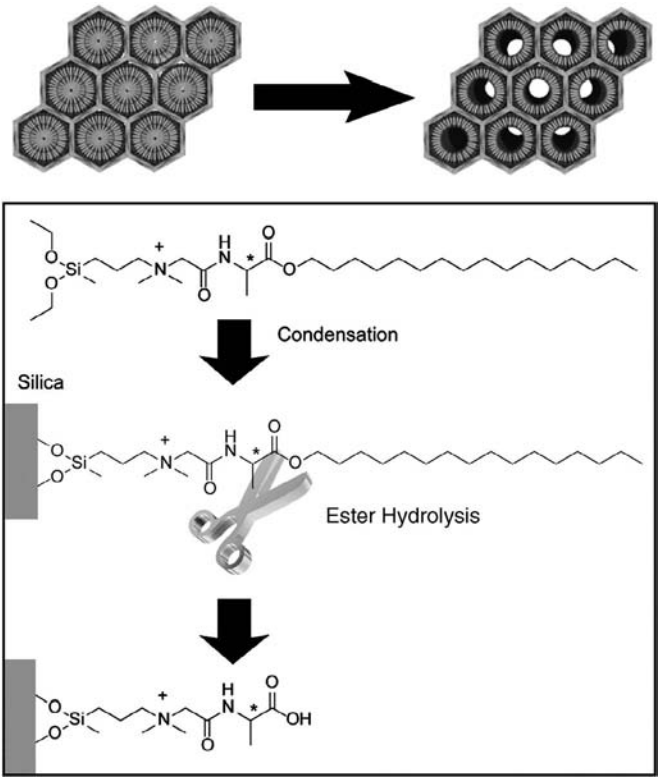

FIGURE 23. Lizard templating method. (Reprinted with permission from ref. 60.)

the dimensions of many polymers far exceed the dimensions of mesopores, especially the diameter; therefore, their motion would be highly restricted, perhaps resulting in peculiar physicochemical properties. One example of direct incorporation of organic polymers into mesoporous silica was reported by Schwartz and co-workers, who incorporated a poly[phenylenevinylene] derivative from solution into a calcined mesoporous silica.[62] They demonstrated that energy migration along the incorporated polymer is slower than Förster energy transfer between the polymer chains. Because there remains the difficulty of diffusion of large polymer molecules into the small mesopores, introduction of monomers and subsequent polymerization of them within the silica nanochannels should be a more reliable method for confinement of the polymers in the mesopores. Ozin and co-workers reported ring-opening polymerization of [1]silaferrocenophane in MCM-41 to provide poly(ferrocenylsilanes).[63] Pyrolysis of the composite resulted in the formation of iron nanoparticles with superparamagnetic properties.

However, postloading methods do not always guarantee confinement of the materials. A more efficient method for confining polymeric structures

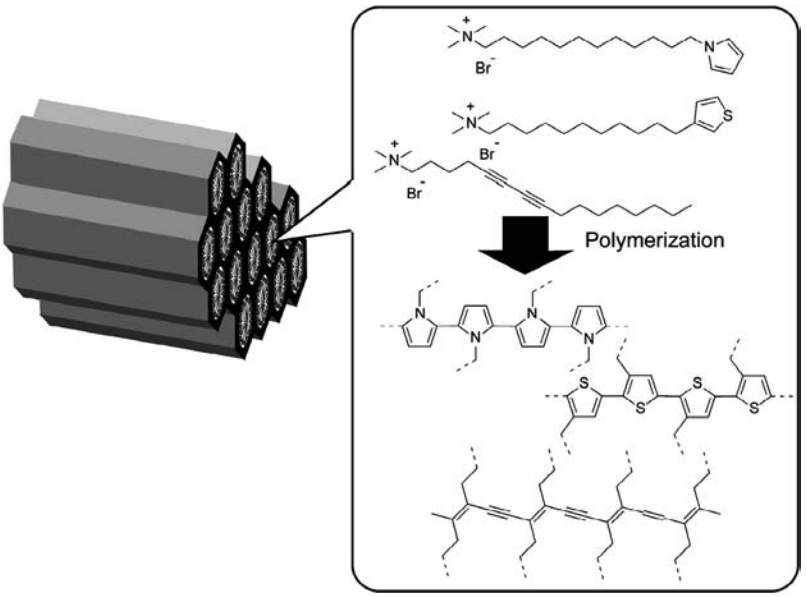

FIGURE 24. Polymerization of template monomers within a mesoporous silica channel.

within mesopores is the introduction of monomer moieties to the template structure because template surfactants are definitely located within the mesopore (Fig. 24). For example, Aida and Tajima used a few kinds of hexadecadiynyltrimethylammonium bromide as templates to synthesize mesoporous silica containing poly(diacetylene) as micro-fibers.[64] The electronic spectra of the silica-polymer composite that were obtained were red shifted possibly due to confinement of the poly(diacetylene) and an elongated effective conjugation within the silica nanochannel. Lu et al. used oligo(ethyleneglycol)-functionalized diacetylenic surfactants as structure-directing reagents for mesoporous silica films through casting, spin-coating, or dip-coating methods.[65] Aida and co-workers developed poly(pyrrole)-containing mesoporous silica films.[66] Differences were apparent between the hexagonal and lamellar composites from their spectroscopic behavior. The polypyrrole chains are highly constrained and insulated when incorporated within hexagonal nanoscopic channels and the possibility of the polarons recombining into bipolarons is significantly suppressed. In contrast, the two-dimensional lamellar phase affords spatial freedom for electron recombination. Similarly, Fuhrhop and co-workers reported thiophene polymerization in mesoporous silica channels.[67]

Inorganic mesoporous channels also provide a unique environment for supramolecular assembly. Aida and co-workers reported the first example of immobilization of one-dimensional columnar charge-transfer (CT) assemblies in mesoporous silica films through a sol-gel reaction with CT complexes of amphiphilic triphenylene donors and various acceptors (Fig. 25).[68]

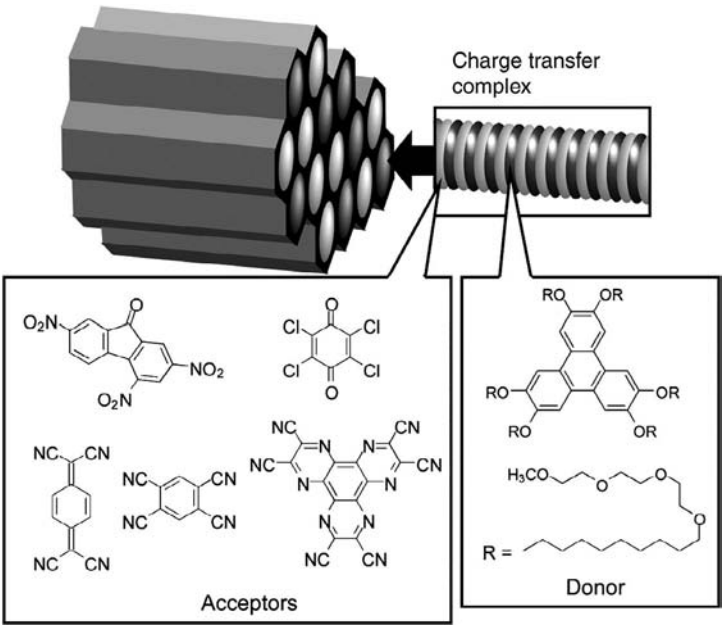

FIGURE 25. Immobilization of one-dimensional columnar charge-transfer assemblies within mesoporous silica channels.

The prepared films are highly transparent and their apparent color can be tuned by varying the concentration and/or identity of the intercalating acceptor. It is interesting that the donor/acceptor molar ratio can be adjusted over a wide range from 1:1 to 9:1, which is advantageous for exploration of their photoconductive properties. The mesoporous silica wall segregates the individual CT columns so that the composite films display neither solvatochromism nor guest exchange activity and exhibit red-shifted absorption bands. The latter phenomenon may reflect a long-range structural ordering.

Ariga and co-workers developed mesoporous silica with densely packed peptide segments that are known as proteosilica (Fig. 26).[69,70] This nanocomposite material provides an asymmetric medium for photochemical reactions.[71] Photochromic dye molecules such as spiropyran and diarylethene can be doped into the chiral environments of the proteosilica films, from which asymmetric photoreaction were demonstrated. Alanylalanine-type surfactants were used as the host peptides, and the spiropyran guest was co-doped with the surfactant at various mixing ratios. Isomerization between the spiropyran form and the merocyanine form can be repeated upon alternate irradiation of the films with visible light (420 nm) and UV light (280 nm), respectively. Circular dichroism (CD) spectra of the hybrid films containing 5 mol % of spiropyran were measured. Only negligible CD signals originating from the guest could be observed for the film containing the merocyanine form, implying that induced

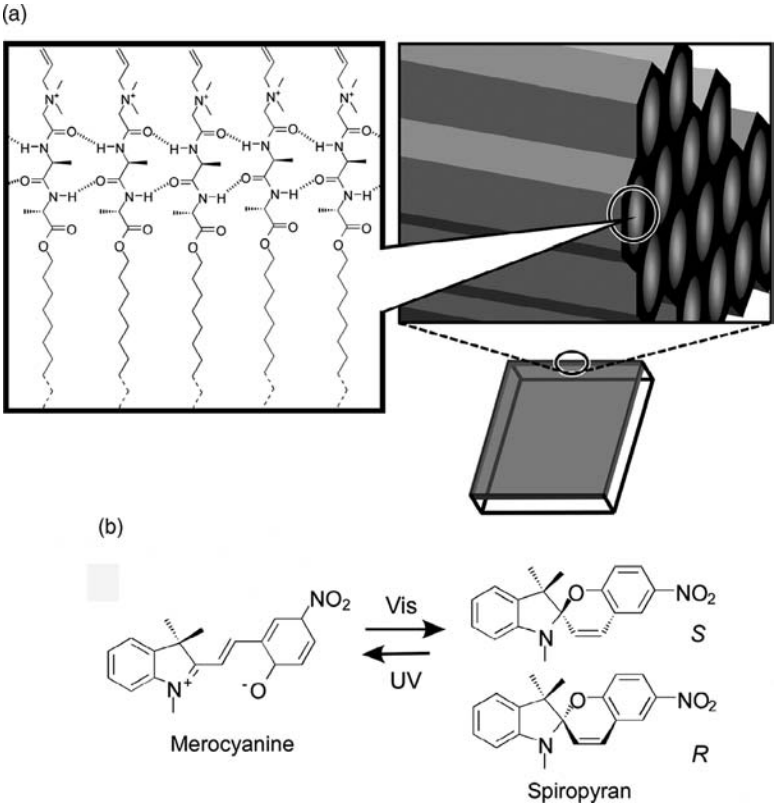

FIGURE 26. (a) Structure of proteosilica. (b) Photochromic reaction within the composite.

CD of the nonchiral merocyanine was not significant, even in the chiral peptide environment. In contrast, the film with the spiropyran form showed clear CD activity in the region from 250 nm to 400 nm for the L-peptide host. A complete mirror image of the CD spectrum was obtained when the D-peptide host was used as the host surfactant, indicating that the CD signals from the guest were driven by the chiral environment of the surrounding host. Alternate irradiation with UV and visible light induced repeated changes in the CD spectra with a small degradation in the intensity. The reported system could be applied for development of nondestructive memory devices.

Another unique approach for introduction of organic functionalities into inorganic mesoporous frameworks can be seen in the synthesis of periodic mesoporous organosilicates (PMOs) (Fig. 27).[72–74] This series of materials possess organic functionalities within a silica framework in their mesoporous structure and can be synthesized using organic molecules bearing multiple alkoxysilane groups, such as bis(triethoxysilyl)ethene and bis(triethoxysilyl)-benzene. Introduction of various organic components has been reported. One

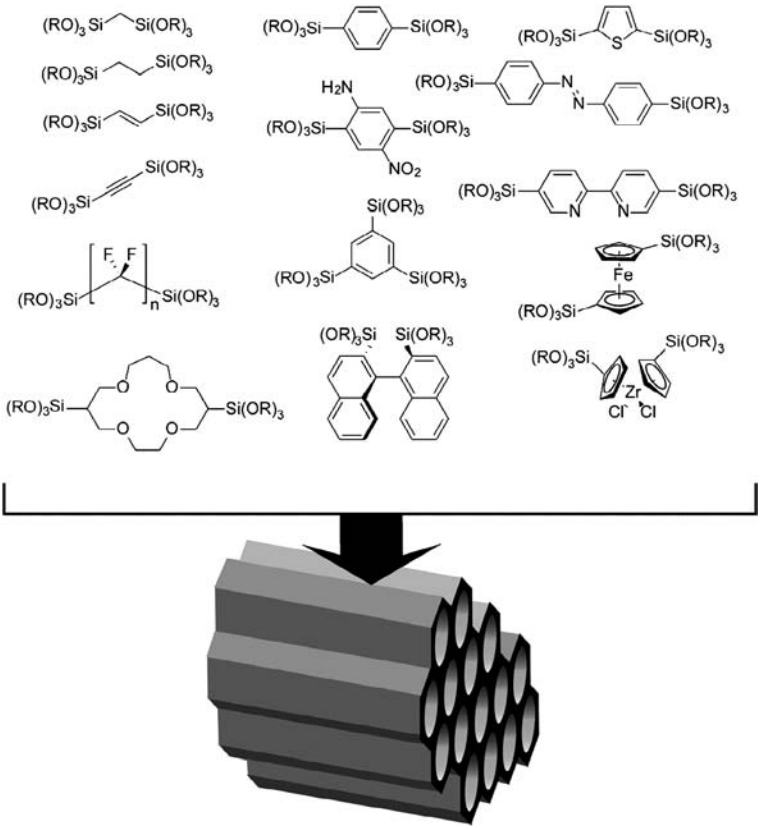

FIGURE 27. Periodic mesoporous organosilicates with various organic functionalities.

of the most impressive findings in PMO technology is formation of a crystalline pore wall.[75] Inagaki et al. synthesized PMO materials using benzene-bridged organosilane, 1,4-bis(triethoxysilyl)benzene.[75] The powder x-ray diffraction (XRD) patterns and a detailed TEM observation confirmed formation of a crystal-like pore-wall structure in which hydrophilic silicate layers and hydrophobic benzene layers are alternately arrayed.

It is possible to immobilize large biomolecules such as proteins and DNA strands within mesoporous materials to provide inorganic-bionanohybrids. These materials have been investigated by several research groups. For example, Vinu et al. undertook systematic research on protein adsorption onto mesoporous materials including mesoporous silica and mesoporous carbon. The results indicated that protein adsorption capability increased as pore volume and/or pore diameter of mesopore materials increased (Fig. 28).[76–80] Of various physical parameters, the charge state of the proteins seriously affected adsorption capacities. Proteins lose their net charge at their isoelectric point, and at this point most of the proteins exhibit maximum adsorptions.

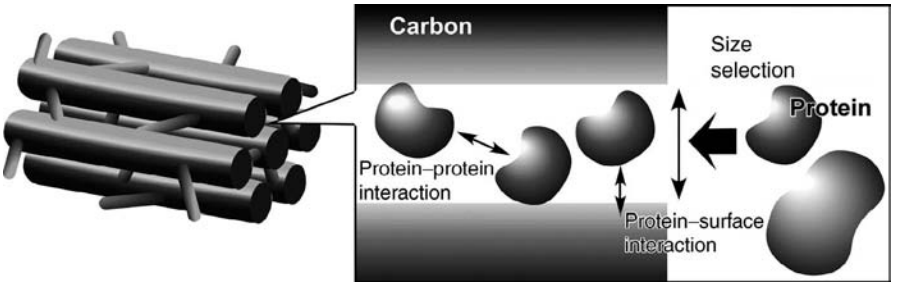

FIGURE 28. Protein adsorption onto mesoporous carbon.

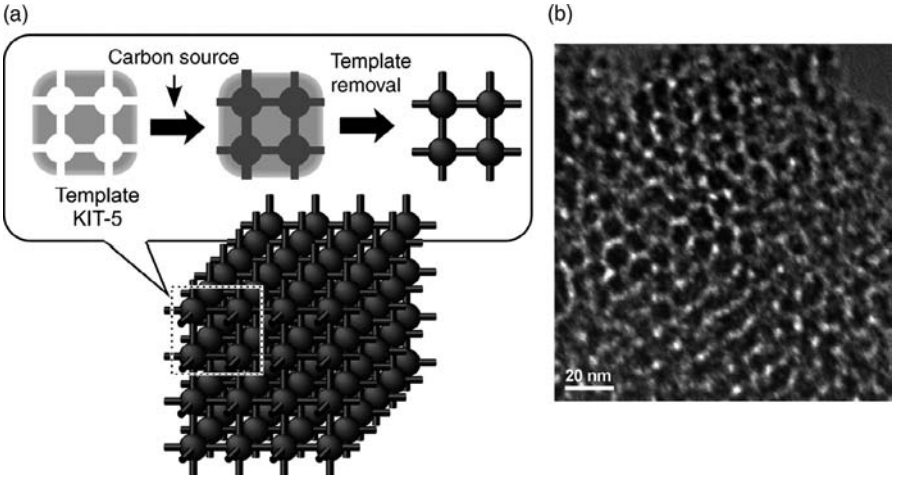

FIGURE 29. (a) Synthesis of the carbon nanocage. (b) Its TEM image. (Reprinted with permission from ref. 83.)

Also, hydrophobic mesoporous carbons often display superior adsorption capabilities to hydrophilic mesoporous silicates.

Careful selection of the template structure can provide geometrically engineered carbon materials. Vinu and co-workers recently reported the synthesis of the novel nanocarbon, "carbon nanocages"[81,82] through template synthesis using large three-dimensional cage-type face-centered cubic mesoporous silica materials (KIT-5) as inorganic templates (Fig. 29). The specific surface area and specific pore volume of carbon nanocage greatly exceed those reported for conventional mesoporous carbon materials. Therefore, the capacity for lysozyme adsorption on the carbon nanocage is much larger than that observed with mesoporous carbon CMK-3. The carbon nanocage also exhibits excellent capability for separation of small molecules.[83] In Figure 30a, the superior adsorption capability of the carbon nanocage in the removal of a dyestuff (Alizarin Yellow) is demonstrated. With the application of slight pressure, an aqueous solution was passed through a bed of the respective

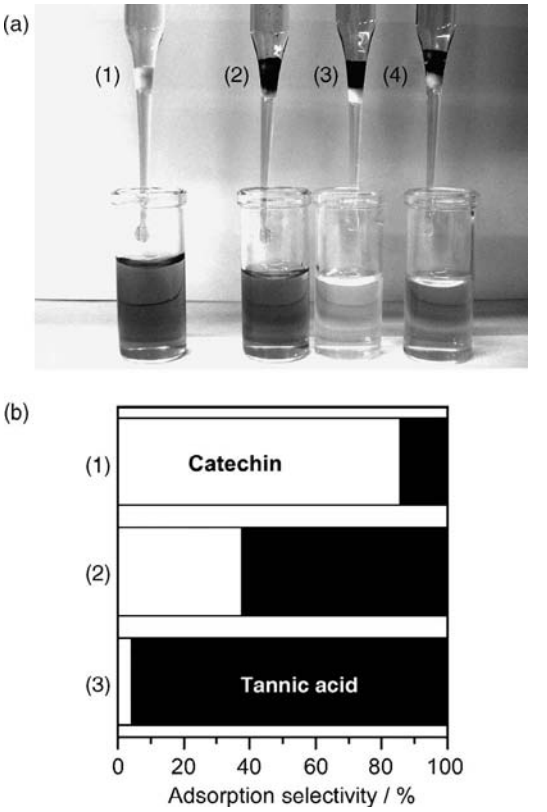

FIGURE 30. (a) Adsorption experiment of Alizarin Yellow through carbon materials: (1) without carbon materials, (2) through activated carbon, (3) through a carbon nanocage, (4) through CMK-3. (b) Selective separation of catechin and tannic acid upon adsorption: (1) activated carbon, (2) with CMK-3, (3) carbon nanocage. (Reprinted with permission from ref. 83.)

carbon material that was deposited on top of a cotton plug in a pipette. When compared with the control test without carbon (1) the carbon nanocage materials completely removed the dye (3), while activated carbon powder (2) and CMK-3 (4) were not effective for removal of the dye under these conditions. A highly selective separation of catechin and tannic acid by the carbon nanocage material in a one-pot process was also found. Adsorption ratios between these tea components at 1 g L^{-1} are summarized in Figure 30b, where complete inversion in the selectivities for catechin and tannic acid is demonstrated in passing from activated carbon, CMK-3, to the carbon nanocage. It is surprising that the use of a carbon nanocage as adsorbent provided a highly selective adsorption of tannic acid ($\sim$ 95%) in a simple one-pot process. This result could originate in the unique geometry of the carbon nanocage materials.

VI. FUTURE PERSPECTIVES

In this chapter, we have described various examples of recent research on supramolecular structure and function involving inorganic building blocks. Although these examples were limited to the four topics of hybrid lipid thin films, layer-by-layer assemblies, structure transcription, and functional mesoporous hybrid, a variety of possibilities in their structural designs and functions are presented. These supramolecular structures will certainly contribute to future nanotechnologies. However, we not only must pursue dreams for the far future but also must demonstrate the importance of such supramolecular systems for uses in the present. For example, the final topic of the final section, tea-component separation by using a nanoengineered carbon nanocage, is a good example for promoting the usefulness of supramolecular structures to general audiences. These demonstrations are related to potential real-life applications and are of paramount importance for public understanding and support. Sciences and technology in these fields must function practically to ensure improvements in our lifestyles and in our society at large.

VII. ACKNOWLEDGMENTS

The research studies described in this chapter were partially supported by Grant-in-Aid for Scientific Research in Priority Area Chemistry of Coordination Space and a Grant-in-Aid for Science Research in Priority Area Super-Hierarchical Structures from the Ministry of Education, Science, Sports, and Culture, Japan, and a Grant-in-Aid for Scientific Research (B) from the Japan Society for the Promotion of Science.

VIII. REFERENCES

1. O. M. Yaghi, M. O'Keeffe, N. W. Ockwig, H. K. Chae, M. Eddaoudi, and J. Kim, *Nature,* **2003**, *423*, 705.
2. S. Kitagawa, R. Kitaura, and S. Noro, *Angew. Chem. Int. Ed.*, **2004**, *43*, 2334.
3. Y. Okahata, K. Ariga, and O. Shimizu, *Langmuir*, **1986**, *2*, 538.
4. Y. Okahata, K. Ariga, H. Nakahara, and K. Fukuda, *J. Chem. Soc., Chem. Commun.*, **1986**, 1069.
5. K. Ariga and Y. Okahata, *J. Am. Chem. Soc.*, **1989**, *111*, 5618.
6. Y. Okahata, M. Yokobori, Y. Ebara, H. Ebato, and K. Ariga, *Langmuir*, **1990**, *6*, 1148.
7. K. Ariga, K. Tanaka, K. Katagiri, J. Kikuchi, H. Shimakoshi, E. Oshima, and Y. Hisaeda, *Phys. Chem. Chem. Phys.*, **2001**, *3*, 3442.
8. H. Shimakoshi, A. Nakazato, M. Tokunaga, K. Katagiri, K. Ariga, J. Kikuchi, and Y. Hisaeda, *Dalton Trans.*, **2003**, 2308.
9. K. Katagiri, K. Ariga, and J. Kikuchi, *Chem. Lett.*, **1999**, 661.

10. K. Katagiri, M. Hashizume, K. Ariga, T. Terashima, and J. Kikuchi, *Chem. Eur. J.*, **2007**, *13*, 5272.
11. G. Decher, *Science*, **1997**, *277*, 1232.
12. P. T. Hammond, *Adv. Mater.*, **2004**, *16*, 1271.
13. K. Ariga, J. P. Hill, and Q. Ji, *Phys. Chem. Chem. Phys.*, **2007**, *9*, 2319.
14. G. Decher, J. D. Hong, and J. Schmitt, *Thin Solid Films*, **1992**, *210*, 831.
15. R. K. Iler, *J. Colloid Interface. Sci.*, **1966**, *21*, 569.
16. K. Ariga, Y. Lvov, M. Onda, I. Ichinose, and T. Kunitake, *Chem. Lett.*, **1997**, 125.
17. Y. Lvov, K. Ariga, M. Onda, I. Ichinose, and T. Kunitake, *Langmuir*, **1997**, *13*, 6195.
18. K. Katagiri, R. Hamazaki, K. Ariga, and J. Kikuchi, *Langmuir*, **2002**, *18*, 6709.
19. K. Katagiri, R. Hamazaki, K. Ariga, and J. Kikuchi, *J. Am. Chem. Soc.*, **2002**, *124*, 7892.
20. A. A. Mamedov and N. A. Kotov, *Langmuir*, **2000**, *16*, 5530.
21. C. Jiang, S. Markutsya, and V. V. Tsukruk, *Adv. Mater.*, **2004**, *16*, 157.
22. C. Jiang, S. Markutsya, Y. Pikus, and V. V. Tsukruk, *Nat. Mater.*, **2004**, *3*, 721.
23. S. Markutsya, C. Jiang, Y. Pikus and V. V. Tsukruk, *Adv. Funct. Mater.*, **2005**, *15*, 771.
24. C. Jiang and V. V. Tsukruk, *Adv. Mater.*, **2006**, *18*, 829.
25. J. L. Lutkenhaus, K. D. Hrabak, K. McEnnis, and P. T. Hammond, *J. Am. Chem. Soc.*, **2005**, *127*, 17228.
26. F. Hua, T. Cui, and Y. M. Lvov, *Nano Lett.*, **2004**, *4*, 823.
27. D. G. Shchukin, D. S. Kommireddy, Y. Zhao, T. Cui, G. B. Sukhorukov, and Y. M. Lvov, *Adv. Mater.*, **2004**, *16*, 389.
28. F. Caruso, R. A. Caruso, and H. Möhwald, *Science*, **1998**, *282*, 1111.
29. G. Schneider, G. Decher, N. Nerambourg, R. Praho, M. H. V. Werts, and M. Blanchard-Desce, *Nano Lett.*, **2006**, *6*, 530.
30. Y. Ono, K. Nakashima, M. Sano, Y. Kanekiyo, K. Inoue, J. Hojo, and S. Shinkai, *Chem. Commun.*, **1998**, 1477.
31. J. Hwa Jung, Y. Ono, K. Hanabusa, and S. Shinkai, *J. Am. Chem. Soc.*, **2000**, *122*, 5008.
32. J. H. Jung, H. Kobayashi, M. Masuda, T. Shimizu, and S. Shinkai, *J. Am. Chem. Soc.*, **2001**, *123*, 8785.
33. J. H. Jung, S.-H. Lee, J. S. Yoo, K. Yoshida, T. Shimizu, and S. Shinkai, *Chem. Eur. J.*, **2003**, *9*, 5307.
34. B. Yang, S. Kamiya, Y. Shimizu, N. Koshizaki, and T. Shimizu, *Chem. Mater.*, **2004**, *16*, 2826.
35. I. Yamashita, *Thin Solid Films*, **2001**, *393*, 12.
36. G. Lu, S. Ai, and J. Li, *Langmuir*, **2005**, *21*, 1679.
37. A. Corma, *Chem. Rev.*, **1997**, *97*, 2373.
38. M. E. Davis, *Nature*, **2002**, *417*, 813.
39. T. Yanagisawa, T. Shimizu, K. Kuroda, and C. Kato, *Bull. Chem. Soc. Jpn.*, **1990**, *63*, 988.
40. S. Inagaki, Y. Fukushima, and K. Kuroda, *J. Chem. Soc., Chem. Commun.*, **1993**, 680.
41. C. T. Kresge, M. E. Leonowicz, W. J. Roth, J. C. Vartuli, and J. S. Beck, *Nature*, **1992**, *359*, 710.
42. J. S. Beck, J. C. Vartuli, W. J. Roth, M. E. Leonowicz, C. T. Kresge, K. D. Schmitt, C. T. W. Chu, D. H. Olson, E. W. Sheppard, S. B. McCullen, J. B. Higgins, and J. L. Schlenker, *J. Am. Chem. Soc.*, **1992**, *114*, 10834.
43. J. C. Vartuli, K. D. Schmitt, C. T. Kresge, W. J. Roth, M. E. Leonowicz, S. B. McCullen, S. D. Hellring, J. S. Beck, J. L. Schlenker, D. H. Olson, and E. W. Sheppard, *Chem. Mater.*, **1994**, *6*, 2317.

44. M. Dubois, T. Gulik-Krzywicki, and B. Cabane, *Langmuir*, **1993**, *9*, 673.
45. P. T. Tanev and T. J. Pinnavaia, *Science*, **1995**, *267*, 865.
46. S. A. Bagshaw, E. Prouset, and T. J. Pinnavaia, *Science*, **1995**, *269*, 1242.
47. D. Zhao, J. Feng, Q. Huo, N. Melosh, G. H. Fredickson, B. F. Chmelka, and G. D. Stucky, *Science*, **1998**, *279*, 548.
48. D. Zhao, Q. Huo, J. Feng, B. F. Chmelka, and G. D. Stucky, *J. Am. Chem. Soc.*, **1998**, *120*, 6024.
49. P. Schmidt-Winkel, W. W. Lukens, D. Zhao, P. Yang, B. F. Chmelka, and G. D. Stucky, *J. Am. Chem. Soc.*, **1999**, *121*, 254.
50. S. Che, Z. Liu, T. Ohsuna, K. Sakamoto, O. Terasaki, and T. Tatsumi, *Nature*, **2004**, *429*, 281.
51. R. Ryoo, S. H. Joo, and S. Jun, *J. Phys. Chem. B*, **1999**, *103*, 7743.
52. S. Jun, S. H. Joo, R. Ryoo, M. Kurk, M. Jaroniec, Z. Liu, T. Ohsuna, and O. Terasaki, *J. Am. Chem. Soc.*, **2000**, *122*, 10712.
53. J. Lee, S. Yoon, T. Hyeon, S. M. Oh, and K. B. Kim, *Chem. Commun.*, **1999**, 2177.
54. A. Vinu, K. Ariga, T. Mori, T. Nakanishi, S. Hishita, D. Golberg, and Y. Bando, *Adv. Mater.*, **2005**, *17*, 1648.
55. A. Vinu, T. Mori, and K. Ariga, *Sci. Technol. Adv. Mater.*, **2006**, *7*, 753.
56. A. Vinu. M. Terrones, D. Golberg, S. Hishita, K. Ariga, and T. Mori, *Chem. Mater.*, **2005**, *17*, 5887.
57. A. Vinu, K. Z. Hossain, and K. Ariga, *J. Nanosci. Nanotechnol.*, **2005**, *5*, 347.
58. K. Ariga, A. Vinu, J. P. Hill, and T. Mori, *Coord. Chem. Rev.*, **2007**, *251*, 2562.
59. N. K. Mal, M. Fujiwara, and Y. Tanaka, *Nature*, **2003**, *421*, 350.
60. Q. Zhang, K. Ariga, A. Okabe, and T. Aida, *J. Am. Chem. Soc.*, **2004**, *126*, 988.
61. W. Otani, K. Kinbara, Q. Zhang, K. Ariga, and T. Aida, *Chem. Eur. J.*, **2007**, *13*, 1731.
62. T.-Q. Nguyen, J. Wu, V. Doan, B. J. Schwartz, and S. H. Tolbert, *Science*, **2000**, *288*, 652.
63. M. J. MacLachlan, M. Ginzburg, N. Coombs, N. P. Raju, J. E. Greedan, G. A. Ozin, and I. Manners, *J. Am. Chem. Soc.*, **2000**, *122*, 3878.
64. T. Aida and K. Tajima, *Angew. Chem. Int. Ed.*, **2001**, *40*, 3803.
65. Y. Lu, Y. Yang, A. Sellinger, M. Lu, J. Huang, H. Fan, R. Haddad, G. Lopez, A. R. Burns, D. Y. Sasaki, J. Shelnutt, and C. J. Brinker, *Nature*, **2001**, *410*, 913.
66. M. Ikegame, K. Tajima, and T. Aida, *Angew. Chem. Int. Ed.*, **2003**, *42*, 2154.
67. G. Li, S. Bhosale, T. Wang, Y. Zhang, H. Zhu, and J.-H. Fuhrhop, *Angew. Chem. Int. Ed.*, **2003**, *42*, 3818.
68. A. Okabe, T. Fukushima, K. Ariga, and T. Aida, *Angew. Chem. Int. Ed.*, **2002**, *41*, 3414.
69. K. Ariga, Q. Zhang, M. Niki, A. Okabe, and T. Aida, *Stud. Surf. Sci. Catal.*, **2003**, *146*, 427.
70. K. Ariga, *Chem. Rec.*, **2004**, *3*, 297.
71. K. Ariga, T. Aimiya, Q. Zhang, A. Okabe, M. Niki, and T. Aida, *Int. J. Nanosci.*, **2002**, *1*, 521.
72. S. Inagaki, S. Guan, Y. Fukushima, T. Ohsuna, and O. Terasaki, *J. Am. Chem. Soc.*, **1999**, *121*, 9611.
73. T. Asefa, M. J. MacLachlan, N. Coombs, and G. A. Ozin, *Nature*, **1999**, *402*, 867.
74. B. J. Melde, B. T. Holland, C. F. Blanford, and A. Stein, *Chem. Mater.*, **1999**, *11*, 3302.
75. S. Inagaki, S. Guan, T. Ohsuna, and O. Terasaki, *Nature*, **2002**, *416*, 304.
76. A. Vinu, C. Streb, V. Murugesan, and M. Hartmann, *J. Phys. Chem. B*, **2003**, *107*, 8297.
77. A. Vinu, V. Murugesan, and M. Hartmann, *J. Phys. Chem. B*, **2004**, *108*, 7323.

78. A. Vinu, V. Murugesan, O. Tangermann, and M. Hartmann, *Chem. Mater.*, **2004**, *16*, 3056.
79. A. Vinu, M. Miyahara, and K. Ariga, *J. Phys. Chem. B*, **2005**, *109*, 6436.
80. A. Vinu, M. Miyahara, and K. Ariga, *J. Nanosci. Nanotechnol.*, **2006**, *6*, 1510.
81. A. Vinu, M. Miyahara, V. Sivamurugan, T. Mori, and K. Ariga, *J. Nanosci. Nanotechnol.*, **2005**, *15*, 5122.
82. P. Srinivasu, V. V. Balasubramanian, L. Kumaresan, D. P. Sawant, X. Jin, S. Alam, K. Ariga, T. Mori, and A. Vinu, *J. Nanosci. Nanotechnol.*, **2007**, *7*, 3250.
83. K. Ariga, A. Vinu, M. Miyahara, J. P. Hill, and T. Mori, *J. Am. Chem. Soc.*, **2007**, *129*, 11022.

CHAPTER 2

Self-Assembly of Hydrophilic Polyoxometalate Macroanions in Dilute Solutions

Melissa L. Kistler, Joe Pigga, and Tianbo Liu

Department of Chemistry, Lehigh University, Bethlehem, Pennsylvania 18015

CONTENTS

Macromolecules Containing Metal and Metal-Like Elements, Volume 9: Supramolecular and Self-Assembled Metal-Containing Materials,
Edited by Alaa S. Abd-El Aziz, Charles E. Carraher Jr., Charles U. Pittman Jr., and Martel Zeldin.

I. INTRODUCTION

Polyoxometalates (POMs) are a large group of inorganic metal oxide clusters, which include some of the largest inorganic molecules known so far. Such giant molecular clusters are formed by the connection of metal-oxygen polyhedral building blocks via covalent bondings as illustrated in Figure 1. The central metal atoms are usually transition metals such Mo, W, V, etc.

The discovery of various POM clusters represents tremendous and continuous efforts from synthetic inorganic chemists. Some POMs also exist in nature. For example, Native Americans first observed the mysterious "blue water" centuries ago near present day Idaho Springs and the Valley of Ten Thousand Smokes.[1,2] These blue waters actually contained naturally soluble molybdenum blue, which is formed from partially oxidized molybdenite. Molybdenum blues represent only one example of the many types of polyoxometalate complexes now known. Such solutions present challenges in understanding the composition and structure of the nanoscaled polyoxometalates in solution and have intrigued several prominent scientists.[3,4] In 1783, Carl W. Scheele reported a soluble molybdenum blue species. In 1826, J. J. Berzelius discovered the first polyoxomolybdate: Mo_5O_{14}. However, it took scientists almost 200 years to finally identify the chemical compositions and molecular structures of those species in molybdenum blue solutions, due to their high solubility in water (difficult to crystallize) and very complex structures (difficult to resolve their structures). They are a group of giant polyoxomolybdate molecular clusters with beautiful geometrical structures and very high symmetry.[5–20]

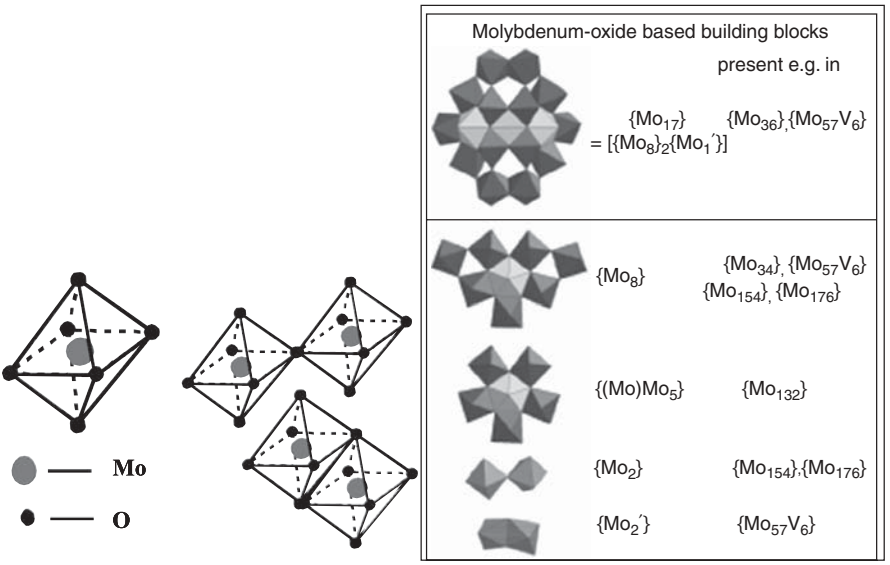

FIGURE 1. Metal oxide polyhedrals are the building blocks of various POMs. The large polyoxomolybdate clusters are assembled via a limited number of building blocks[7] (Reprinted with permission from ref. 13.)

Among the nanometer-scaled, anionic POM clusters are the wheel-shaped $\{Mo_{154}\}$[16] and $\{Mo_{176}\}$,[9] the lemon-shaped "hedgehog" $\{Mo_{368}\}$,[10] and hollow spherical "Keplerate" $\{Mo_{132}\}$[11] and $\{Mo_{72}Fe_{30}\}$[12] (Fig. 2). Their detailed chemical compositions are listed in Table 1. The spherically shaped Keplerate POMs have icosahedral symmetry, which are composed of 12 $\{Mo(Mo)_5\}$ pentagonal building blocks connected by 30 linkers. The basic assembly based on these building blocks form the basic skeleton $\{Pentagon\}_{12}\{Linker\}_{30}$. The linkers are $Fe^{(III)}(H_2O)^{3+}$ in $\{Mo_{72}Fe_{30}\}$ and $\{Mo_2\}$ in $\{Mo_{132}\}$. The $\{Mo_2\}$ fragment has been described as resembling the Buckminsterfullerene C_{60}.

The giant POM clusters provide a variety of features of transferable building blocks, versatile redox chemistry, integration of hetero-elements and exchange ligands, tuneable charge-to-size ratio, and template functionality, which have allowed for the synthesis of nanostructured species with well-defined structural units from simple metal oxide building blocks.[7] POMs also exhibit many unique structural, electrical, and optical properties. Also, POMs have very interesting applications in medicine, catalysis, and nanofabrication.[7]

The large POMs can be synthesized by partially reducing molybdate salts (containing Mo^{VI}) in acidic aqueous solutions. Depending on the reaction pH and other conditions, different types of polyoxomolybdates can be obtained. For example, $\{Mo_{132}\}$ is synthesized by reducing an aqueous solution of ammonium molybdate to generate pentagonal bipyramidal $\{MoO_7\}$ groups.[11] High

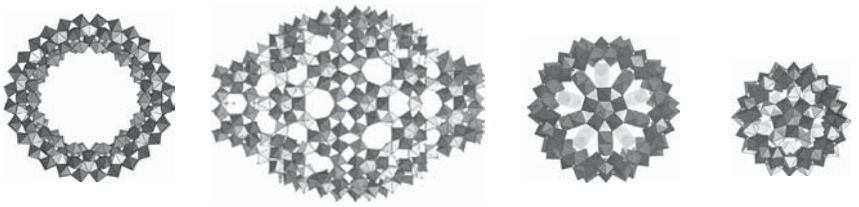

FIGURE 2. Some large, hydrophilic polyoxometalate clusters. From left: $\{Mo_{132}\}$,[11] $\{Mo_{368}\}$,[10] $\{Mo_{154}\}$,[16] and $\{Mo_{72}Fe_{30}\}$.[12] Detailed molecular formulae are listed in Table 1.

TABLE 1. Several POM Clusters

Abbreviation	Formula	Reference
$\{Mo_{132}\}$(ac)	$[\{(Mo)Mo_5O_{21}(H_2O)_6\}_{12}\{Mo_2O_4(CH_3COOH)\}_{30}]^{42-}$	11
$\{Mo_{72}Fe_{30}\}$	$[Mo^{VI}{}_{72}Fe^{III}{}_{30}O_{252}(CH_3COO)_{12}$ $\{Mo_2O_7(H_2O)\}_2\{H_2Mo_2O_8(H_2O)\}(H_2O)_{91}]$	12
$\{Mo_{72}V_{30}\}$	$Na_8K_{14}(VO)_2[\{(Mo^{VI})Mo^{VI}{}_5O_{21}(H_2O)_3\}_{10}\{(Mo^{VI})$ $Mo^{VI}{}_5O_{21}(H_2O)_3(SO_4)\}_2\{V^{VI}O(H_2O)\}_{20}$ $\{V^{VI}O\}_{10}(\{KSO_4\}_5)_2]\cdot\sim 150H_20$	14
$\{Mo_{72}Cr_{30}\}$	$Na_2[(H_2O)_{12}\subset(\{Mo^{VI}{}_{72}Cr^{III}{}_{30}O_{252}(CH_3COO)_{20}$ $(H_2O)_{92}\}]\cdot 120H_20$	15
$\{Mo_{154}\}$	$Na_{15}[Mo_{154}O_{462}H_{14}(H_2O)_{70}]_{0.5}[Mo_{152}O_{457}H_{14}(H_2O)_{68}]_{0.5}$	16
$\{Mo_{176}\}$	$K_{16}[Mo_{176}O_{528}H_{16}(H_2O)_{80}]$	17
$\{Mo_{368}\}$	$Na_{48}[H_xMo_{368}O_{1032}(H_2O)_{240}(SO_4)_{48}]$	10

concentrations of bidentate acetate ligand is used to stabilize $\{Mo_2{}^{V}\}$ linker groups to form the crystalline salt of Mo_{132}. $\{Mo_{72}Fe_{30}\}$ is synthesized by reacting $FeCl_3$ with $\{Mo_{132}\}$.[12] The $\{Mo_2\}$ spacers of $\{Mo_{132}\}$ are subsequently replaced by 30 $Fe^{(III)}(H_2O)$ linkers. Both POMs show very unusual solution behavior, which will be described in more detail. Other POM clusters are easily synthesized by the acidification or reduction of aqueous molybdate solutions.

II. SOLUTION BEHAVIOR OF POM MACROIONS: SOLUBLE BUT STILL AGGREGATE

The surface of the POMs clusters is considerably hydrophilic due to many water ligands chemically attached to the central metal ions. The hydrophilic surface, together with the negative charges on the POMs, makes the macroions very soluble in water and other polar solvents, such as methanol, ethanol, and acetone. The POMs can be categorized into two groups, depending on the nature of their charges: strong electrolytes and weak electrolytes. $\{Mo_{154}\}$, $\{Mo_{132}\}$, and

$\{Mo_{368}\}$ are typical strong electrolytes. These clusters carry inherent charges due to existence of Mo^{V} centers and the ligands incorporated in their skeleton. In crystals and in solution, such clusters exist as macroanions, balanced by multiple small cations such as Na^+, NH_4^+, and H^+. Some charges are delocalized (in the case of $\{Mo_{154}\}$ and $\{Mo_{368}\}$), and the electrons can travel on the skeleton of the clusters. Meanwhile, $\{Mo_{72}Fe_{30}\}$ is a typical weak electrolyte, which exists as neutral molecules in crystals but carry some charges when dissolved in water due to the partial deprotonation of their water layers.[21] In other words, $\{Mo_{72}Fe_{30}\}$ behaves like a type of weak acid. We will describe its solution properties later in the text.

POM macroions allow a connection between simple ions and colloidal systems to be established. Similar to simple ions, POM macroions are highly soluble, thermodynamically stable, and form "real solutions." However POMs macroanions are significantly larger than common simple ions, leading to a large size disparity between cations and anions. At the same time, the sizes of POM are close to some small colloids. Colloidal systems are insoluble, thermodynamically unstable, and form suspensions, but POMs do not display any of these characteristics. Instead, they form stable real solutions.

A commonly accepted fact is that soluble inorganic ions should distribute homogeneously in dilute solutions. However this fact may not be true for POM macroanions in polar solvents. Water-soluble POMs usually do not exist as single ions in water or other polar solvents (Figure 3). Instead, the Tyndall effect was observed from the solution. The Tyndall effect is the result of scattered visible light from suspended particles of colloidal size. Thus the Tyndall effect is not expected to appear in common solutions of homogeneously distributed soluble inorganic ions. Dynamic light scattering (DLS) and scanning electron microscopy (SEM) studies[22] indicate that the POM macroions tend to form large, spherical aggregates that display a relatively narrow size distribution. More interesting, a large amount of solvent is found inside the supramolecualr aggregates, and the aggregates tend to burst when exposed in

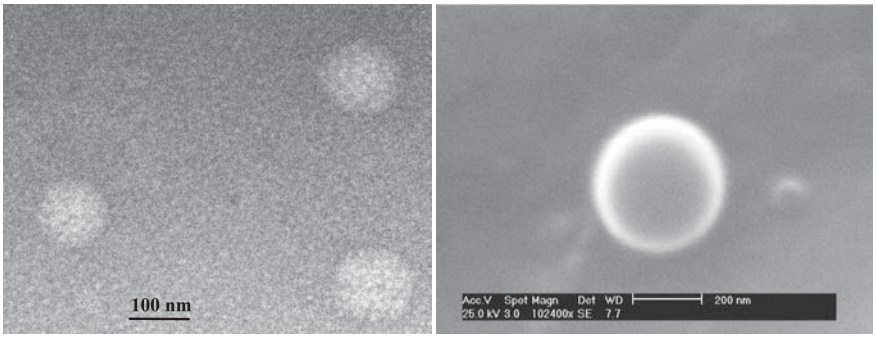

(a) (b)

FIGURE 3. SEM and TEM images obtained from POM blackberry solutions. (a) TEM image of $\{Mo_{154}\}$ in aqueous solution. (Reprinted with permission from ref. 23.) (b) SEM image of $\{Mo_{132}\}$ in water/acetone mixture[24] (Reprinted with permission from ref. 25.)

vacuum. Such evidence indicates that the spherical aggregates might have a hollow nature. Obviously, the large assemblies do not behave like regular aggregates formed by less-soluble species because the latter is not stable and tend to further aggregate and precipitate from the solution. Considering that POMs are highly soluble, they are not expected to aggregate and precipitate. This observation triggered us to further examine the mysterious POM solutions.[23]

III. CHARACTERIZATION OF THE SUPRAMOLECULAR STRUCTURES

Laser light scattering (LLS) techniques, including both static light scattering (SLS) and dynamic light scattering (DLS) are useful tools for obtaining information about the POM macroionic solutions. LLS is best suited for studying polymer and colloidal particles with sizes ranging from 1 to 1000 nm. LLS allows for the determination of physical properties of the solute properties, including particle molar mass, size, shape, and internal structure.

SLS measures the absolute scattered intensities of sample solutions at different scattering angles and concentrations. Information about the particles in solution, such as the weight-average molar mass (M_w) and the radius of gyration (R_g), as well as the nature of interparticle interactions, can be determined by using a Zimm plot. DLS measures the intensity-intensity correlation curve, which can review the information regarding the diffusion of the particles in solution. By using the Stokes-Einstein equation, the hydrodynamic radius (R_h) and the size distribution of the particles in solution can be determined with the help of special software, such as CONTIN.[24]

Detailed SLS and DLS studies on the supramolecular structures in POM solution are described by using the wheel-shaped macroion $\{Mo_{154}\}^{16}$ as an example.[23] A small amount of $\{Mo_{154}\}$ is dissolved in aqueous solution at pH 2.3. A CONTIN analysis of the DLS measurements shows that macroanions of $\{Mo_{154}\}$ form large, monodispersed structures with an average R_h of 45 nm (Fig. 4). At the same time, SLS measurements show that the average R_g of the supramolecular structures is 45.2 $\pm$ 1.4 nm (Fig. 4). For spherical objects (Fig. 3a), the relation of $R_h = R_g$ implies that the supramolecular structure is hollow. (For a solid sphere, $R_g = 0.77R_h$; increasing the ratio of R_g/R_h indicates that more mass in a sphere is distributed closer to the surface.) More evidence comes from the M_w of the supramolecular structures determined by SLS, which is $\sim 2.54 \pm 0.25 \times 10^7$ g/mol, corresponding to $\sim$1165 single $\{Mo_{154}\}$ wheels in each large sturcture. These POMs are barely enough to cover a single layer of a 45-nm-radius sphere (and the POMs are still not touching each other). Therefore, we can conclude that the $\{Mo_{154}\}$ macroions form spherical, single-layer, vesicle-like structures.[23] Figure 5 shows the structure based on LLS and TEM.

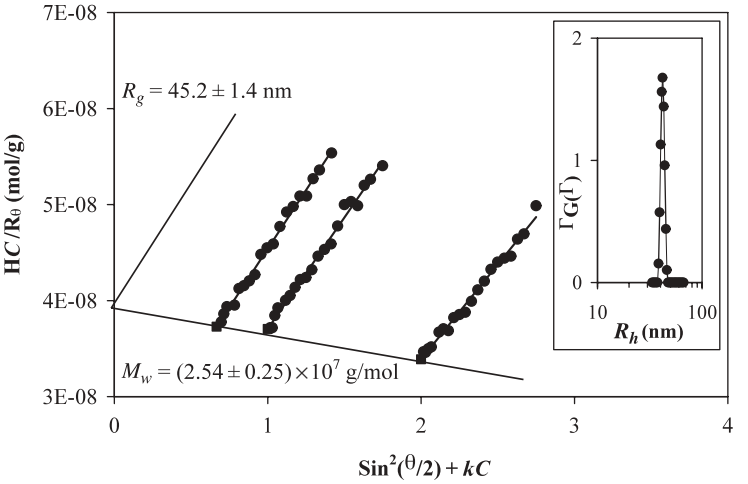

FIGURE 4. Typical Zimm plot based on measurements of a SLS study. Three different solution concentrations (0.03, 0.015, 0.01 mg/mL) all at pH 2.3 are measured. The R_g and M_w can be calculated from the plot. *Inset*: Typical CONTIN results from a DLS study of 0.01 mg/mL aqueous POM solution at pH 2.3, scattering angle of 60°. Here R_h = 45 nm, with a very narrow size distribution [23] (Reprinted with permission from ref. 23.)

Bilayer vesicle structures are very common in surfactant solutions, driven by the hydrophobic interaction due to the surfactant tails. Here the vesicle-like POM supramoelcular structures are completely different from surfactant bilayer vesicles because the POM macroions are fully hydrophilic. Furthermore, the POM macroions do not touch each other in the assemblies due to the electrostatic repulsions. We have given the new structure the nickname *blackberry* because of the similar shapes of the blackberry fruit and the self-assembled structures formed by POM macroions.

The self-assembly of POM anions into large, single-layer, hollow, spherical vesicles, which resemble a blackberry-type structure in very dilute solutions is unique. Though made up of inorganic clusters, the blackberries are very soft and even membrane-like, as broken blackberries have been observed by TEM imaging.[23] There is no long-range packing of POMs on the blackberry surface but only some short-range packing in local areas, as shown in Figure 6.

IV. CONTROLLING THE BLACKBERRY FORMATION AND BLACKBERRY SIZE BY CHANGING SOLVENT QUALITY

It is important to determine the driving forces responsible for the blackberry formation in dilute solutions. Because the POMs do not have any hydrophobic regions, hydrophobic interaction can be excluded. We first examine

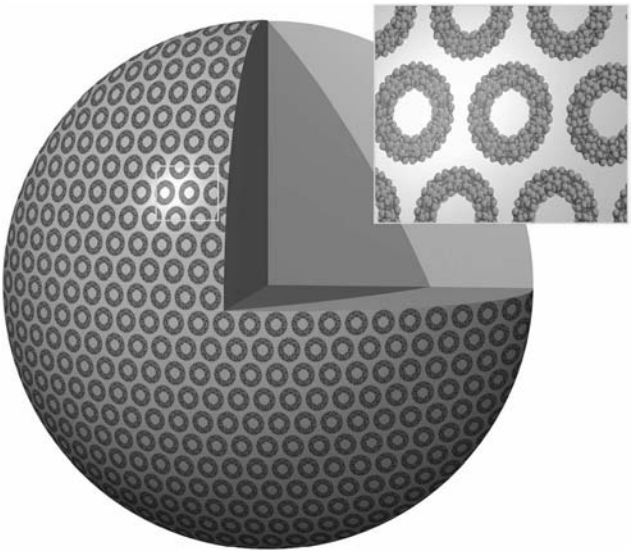

FIGURE 5. Spherical vesicle-like "blackberry" structure (90 nm in diameter at pH 2.3) formed by $\{Mo_{154}\}$ giant-wheel POMs in aqueous solution, as determined by various techniques. (Reprinted with permission from ref. 23.)

the possible contribution from the van der Waals forces, which are responsible for the aggregation of colloidal particles, according to the DLVO theory.

We choose $\{Mo_{132}\}$ macroions for this study. Each $\{Mo_{132}\}$ cluster carries 42 inherent charges in crystals, balanced by 42 NH_4^+ cations. $\{Mo_{132}\}$ can be dissolved into different solvents of water, acetone, and their mixtures with volume percentages of acetone ranging from 0 to 100% to make 1.0 mg/mL solutions.[25] It is very interesting that no blackberry formation is observed in either pure aqueous solution or in highly acetone-rich ($>$ 70 vol %) solutions (Fig. 7a). In water, $\{Mo_{132}\}$ macroions are highly charged so that the strong electrostatic repulsion prevents any self-association. Whereas in mixed solvents containing $>$ 70 vol % acetone, the $\{Mo_{132}\}$ clusters are almost uncharged because acetone is a solvent with much lower dielectric constant. $\{Mo_{132}\}$ clusters can still be soluble in such solvents and exist as (almost) neutral molecules. Blackberry formation is observed in the middle range, where acetone accounts for 3–70 vol % of the solvent. This is unusual because when more water is added into the mixed solvent, it will make $\{Mo_{132}\}$ clusters more charged, and therefore $\{Mo_{132}\}$ macroions should further repel one another. However, the blackberry formation indicates that a stronger attractive force is generated with the process. Similarly, adding more acetone into the blackberry solution should decrease the charge density of $\{Mo_{132}\}$, and the $\{Mo_{132}\}$ ions should be closer each other due to the decrease of electrostatic repulsion. Instead,

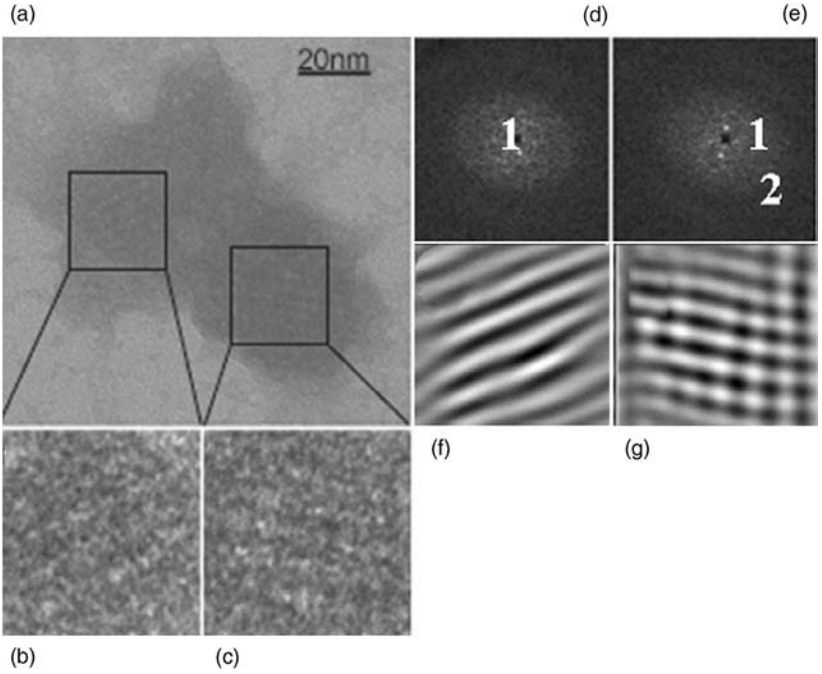

FIGURE 6. High-resolution TEM images on a small piece of a $\{Mo_{154}\}$ blackberry showing ordered local packing of $\{Mo_{154}\}$ macroanions on a blackberry surface. One-dimensional packing is shown in panel d and two-dimensional packing in panel e[23] (Reprinted with permission from ref. 23.)

we observe the opposite phenomenon—the blackberries will fall apart if enough acetone is added, indicating the loss of attraction among them.

Such unusual experimental results indicate that the van der Waals forces, which do not change with the changing solvent quality, cannot be the major attractive forces for the blackberry formation.[25,26] Instead, the presence of a moderate amount of charge on $\{Mo_{132}\}$ clusters is critical. Therefore, we should seriously consider the role of counterions and their mediated attractive forces.

Furthermore, we found that the average blackberry R_h increased monotonically with increasing acetone content, from $\sim$30 nm in 5 vol % acetone solution to $\sim$100 nm in 70 vol % acetone solution (Fig. 7a). The size distributions of the blackberry structures formed in different solvents are very similar, per the CONTIN results. A linear relationship between the R_h of the blackberries and the solvent quality (as the inverse dielectric constant, $1/\varepsilon$) is obtained, as shown in Figure 7b.

This linear relation indicates that the blackberry formation is a free-energy-favored process because the blackberry size (i.e., the preferred curvature for the blackberry surface) is determined by the solvent quality. Recently,

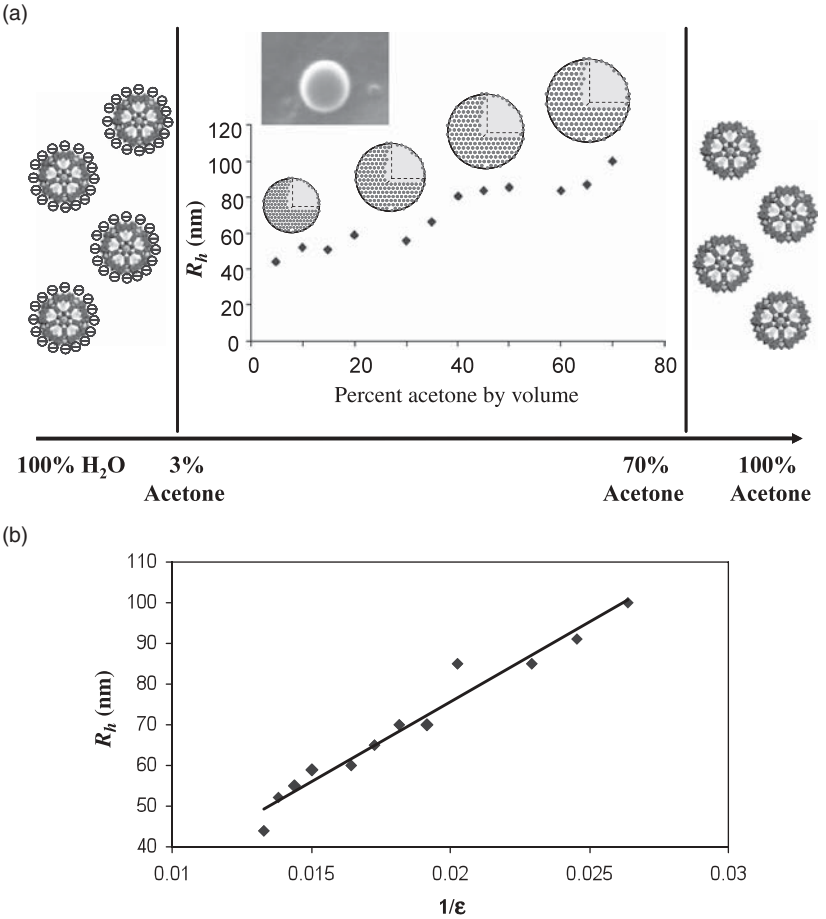

FIGURE 7. (a) A typical discrete macroion-blackberry-discrete macorion/neutral cluster transition observed in 1.0 mg/mL $\{Mo_{132}\}$ water–acetone solutions with different acetone compositions. In the blackberry region, the average hydrodynamic radii (R_h) of the $\{Mo_{132}\}$ blackberries in water–acetone solvents measured by DLS are plotted. Experiments were performed at a 90° scattering angle. (b) Average hydrodynamic radius (R_h) of the $\{Mo_{132}\}$ blackberries in water–acetone solvents measured by DLS vs. the inverse dielectric constant of the solvent, ε. (Reprinted with permission from ref. 25. Copyright [2008] American Chemical Society.)

we presented an equation to describe the factors that determine blackberry size:[27]

$$R \approx -\frac{48\lambda_B u}{\Psi^2} \tag{1}$$

with λ_B, u, Φ being the Bjerrum length, the magnitude of the attractive force between macroanions, and the zeta potential of the blackberries, respectively. The parameter λ_B is defined as:

$$\lambda_B = \frac{e^2}{4\pi\varepsilon_0\varepsilon_R kT} \tag{2}$$

with e, ε_0, ε_R, k, T being the unit charge, the permittivity of vacuum, the solvent dielectric constant, the Boltzmann constant, and absolute temperature, respectively. Obviously, a linear relationship was found between the $\{Mo_{132}\}$ blackberry size and $1/\varepsilon_R$. Basically, the blackberry size is controlled by the charge regulation. Three parameters are important: solvent quality (in dielectric constant), change density of POM macroions (in the zeta potential of blackberries), and the strength of the attractive forces among POM macroions.

Blackberry structures are not easy to form due to the high energy barrier between the two states of single macroanions and supramolecular structures. Furthermore, it is even more difficult to break the blackberry structure.[25] However, it is possible to cause the breaking or reassembly of blackberry structures by simply changing solvent composition. Furthermore the blackberry size can be changed by tuning the solvent quality. For example, take $\{Mo_{132}\}$ blackberries formed in water–acetone solvents: After adding water or acetone to change the composition of the solvent and after mild heating at 30°C, the blackberry size will change accordingly. The new size is consistent with the size of blackberries formed directly in such a solvent. The reproducible formation of the $\{Mo_{132}\}$ blackberry clearly indicates that the blackberry formation is a thermodynamically favored process and that the sizes of blackberries reported in Figure 7a are in thermodynamically stable states.

V. COUNTERION ASSOCIATION AROUND DISCRETE POM MACROIONS

By realizing the importance of the counterions and the charge on POM macroions for blackberry formation, we need to systematically clarify the state of small countercations in POM solutions and their role for the blackberry formation. It is well known in polyelectrolyte solutions, due to the large size and high electric field of the macroions (long-chain polyelectrolytes), a large part of the counterions remain closely associated. This ''counterion association'' phenomenon has been observed in many systems, including DNA and protein solutions.[25,26] The counterion condensation around large colloidal particles is very significant. The POMs are soluble ions and much smaller than the colloids. On the other hand, these macroanions are much larger than the small cations—that is, an obvious disparity between anions and cations

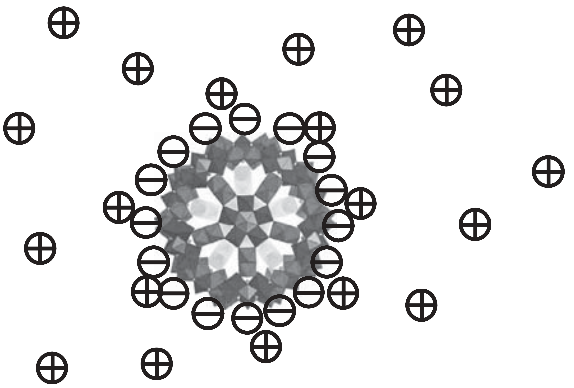

FIGURE 8. In dilute aqueous solution, cations such as NH_4^+ are found to be closely associated with macroanions. The degree of association increases with increasing POM concentration[24] (Reprinted with permission from ref. 28.)

exists in POM solution. Consequently, the cation–anion interaction is more complicated than that in simple ionic solutions, where caitons and anions can be treated as free ions in dilute solution regime.

We used simple conductivity measurements to determine the degree of counterion association around discrete $\{Mo_{132}\}$ macroions in aqueous solution.[28] In aqueous solution, $\{Mo_{132}\}$ macroions remain as discrete ions due to the repulsive interactions among the highly charged anions.[22] Each $\{Mo_{132}\}$ macroion is balanced by 42 NH_4^+ cations when dissolved in water, according to its chemical formula; in addition, $\{Mo_{132}\}$ also releases a small number of H^+ into solution (< 0.5 per cluster). In dilute solutions, the degree of counterion association in $\{Mo_{132}\}$ aqueous solution is about 20%. Furthermore, the degree of counterion association also depends on macroion concentration. At low macroion concentrations, nearly all of the counterions are free in solution, but at higher macroion concentrations, the degree of counterion association increases (Fig. 8). Compared to colloidal systems, the counterion association in POM solutions is weaker because the POMs have smaller sizes.

VI. COUNTERION CONDENSATION AROUND BLACKBERRIES

When blackberries are formed, most of the counterions are found to be absorbed around them. POM blackberries exist in solution as large, highly charged species. To determine the charge carried by the macroions and the blackberries, zeta potential analysis has been applied. Zeta potential analysis is a measurement of the electrical potential that exists at the surface of a charged particle in solution. To determine the charge of the POM blackberries, the ion mobility must be

determined and can be obtained from zeta potential measurements. The ion mobility is related to the charge on particles via the Hückel equation:[29]

$$\mu_o = q/6\pi\eta r \tag{3}$$

where μ_o, η, q, and r are the absolute mobility of particles at zero buffer ionic strength, the solvent viscosity, the charge on particles, and the particle radius, respectively.[18,19] In our current case, the solution contains no buffer ions, thus the measured mobility is μ_o. Our results indicate that in various blackberry solutions, $> 99\%$ of the small countercations are closely associated with blackberries.[29] In other words, the blackberries have very strong capability in attracting cations from dilute solutions.

VII. IDENTIFICATION OF THE DRIVING FORCES RESPONSIBLE FOR THE BLACKBERRY FORMATION

The driving forces of the blackberry self-assembly process are unique and differ from many types of traditional systems that have been well studied. Unlike surfactant micelles and vesicles, hydrophobic interactions do not contribute to the blackberry formation because the POMs have no hydrophobic moieties. In colloidal systems, self-assembly occurs by van der Waals forces. As previously mentioned, van der Waals forces do not contribute significantly to POM self-assembly.[25,26]

The role of the counterions is important to the POM self-assembly process if hydrophobic interactions and van der Waals forces do not drive the blackberry formation. Past studies have shown that the counterions are effective in the self-assembly process with some contribution from hydrogen bonding.[21,25,26] The counterions associated with the large POM macroions are most likely shared between neighboring macroions. In this manner, the like-charged POM macroions, which are expected to repel one another, actually exist close to other POMs. Thus the observation is that there exists an attraction among the like-charged POM macroions. To determine how counterions contribute to blackberry formation, studies were performed to determine the effect of cationic valent state and hydrated size on the blackberry formation, which is described later.[15]

VIII. SOFT NATURE OF THE BLACKBERRIES—EFFECT OF ADDITIONAL HYDROGEN BONDING

Hydrogen bonding may be important to the blackberry structure because there is a large distance ($\sim 0.9 \pm 0.4$ nm) between the neighboring POMs that cover the surface of blackberries; the space is most likely filled with the

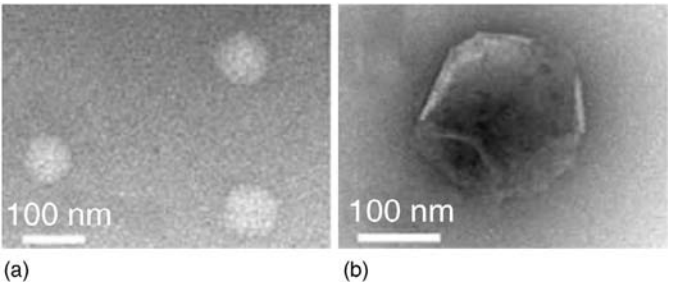

FIGURE 9. TEM studies of $\{Mo_{154}\}$ blackberries formed in aqueous solutions. (a) A broken blackberry flattened on a carbon support film demonstrating wrinkle feature[23] (Reprinted with permission from ref. 23.)

solvent—in most cases water. The water molecules that occupy this space on the surface may be linked together by additional hydrogen bonding.[30]

The contribution from the hydrogen bonds can be observed from the soft biomembrane-like nature of blackberries. In Figure 9b, a blackberry is shown to retain its morphology after bursting in vacuum. This behavior was also observed using an atomic force microscope to tap the surface of a blackberry.[31] When the blackberry surface is tapped by the atomic force microscopy (AFM) cantilever, it behaves like a soft sphere, absorbing the cantilever tip but maintaining the spherical structure. The soft nature of blackberries is unusual because POMs are made up of "hard" inorganic spheres.[31]

IX. WEAK ELECTROLYTE TYPE POMS

The solution behavior of weak electrolyte POMs, such as $\{Mo_{72}Fe_{30}\}$,[12,21,31–34] is different from those strong electrolytes. As previously discussed, $\{Mo_{72}Fe_{30}\}$ is neutral in crystals but behaves as a weak acid and carries 7–8 negative charges when dissolved in pure water due to partial deprotonation of the 30 $Fe^{III}(H_2O)$ centers.[21] Consequently, the solution becomes acidic (pH $\sim$ 3.4 for 1.0 mg/mL $\{Mo_{72}Fe_{30}\}$), and the $\{Mo_{72}Fe_{30}\}$ clusters become hydrophilic macroanions carrying localized charges. The deprotonation scheme is show in Figure 10. A pH-titration experiment confirms the weak acid nature of $\{Mo_{72}Fe_{30}\}$. Its degree of depronotation depends on solution pH, with more H^+ being released into solution at a higher pH. The moderate number of charges and the water layer of $\{Mo_{72}Fe_{30}\}$ make the POM clusters highly soluble in polar solvents.

At pH $<$ 2.7 the POMs are nearly uncharged in aqueous solution. Such neutral clusters are found to exist as soluble molecules in solution and do to self-assemble into the blackberry structure. With increasing pH value to $>$ 3.0, the slightly charged $\{Mo_{72}Fe_{30}\}$ macroions start to form blackberries; even the electrostatic repulsion among them becomes stronger. This again confirms that

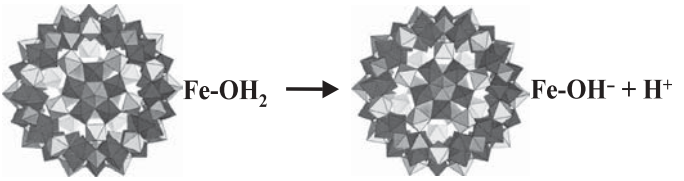

FIGURE 10. $\{Mo_{72}Fe_{30}\}$: A weak acid type of 2.5-nm diameter, C_{60}-shaped spherical hydrophilic polyoxometalate molecular cluster formed by Mo-O polyhedrals (blue) and Fe-O polyhedrals (yellow). It can partially deprotonate the water ligands attached to its Fe centers (Reprinted with permission from ref. 21.)

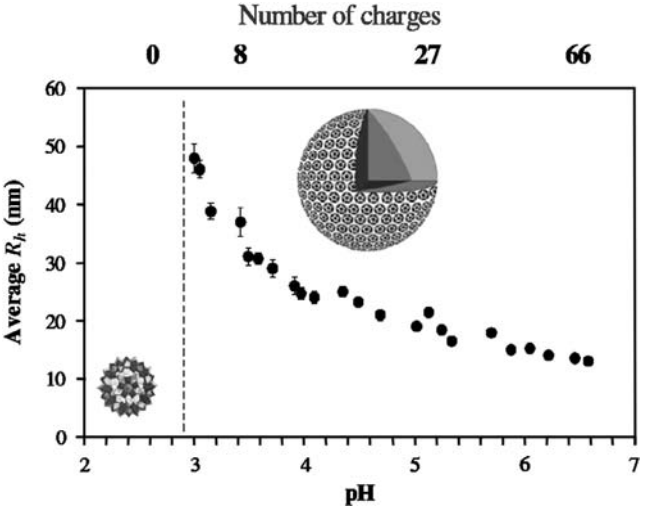

FIGURE 11. For $\{Mo_{72}Fe_{30}\}$ macroanions in dilute aqueous solution, the degree of association depends on pH. At pH $>$ 3.0, blackberries form as the $\{Mo_{72}Fe_{30}\}$ are charged, and the blackberry size decreases with increasing pH[21] (Reprinted with permission from ref. 21.)

the van der Waals forces are not responsible for the blackberry formation. The blackberry size decreases monotonically with increasing solution pH from R_h = 50 nm at pH 3.0 to R_h = 17 nm at pH 6.6 (i.e., increasing charge density on $\{Mo_{72}Fe_{30}\}$), which is consistent with the conclusion in Eq. (1) (Fig. 11).[21] At pH $>$ 6.6 the $\{Mo_{72}Fe_{30}\}$ macroions will decompose. Also, the size of the blackberries can be accurately and reversibly tuned by simply adjusting the solution pH.

X. EFFECT OF ADDITIONAL ELECTROLYTES

Counterion association appears to be an important aspect in blackberry formation.[21] Therefore, it is important to understand the effects of adding extra electrolytes to POM solutions (either before or after) the blackberry formation,

and examine how the additional salts affect the process and the structures of the final assemblies. We use $\{Mo_{72}Fe_{30}\}$ clusters as an example because of their very high stability in solution. Initially in aqueous solution $\{Mo_{72}Fe_{30}\}$ macroions are balanced by protons and trace amounts of extra electrolytes remaining from the $\{Mo_{72}Fe_{30}\}$ synthesis.

The experiments were performed by adding predetermined amounts (0–50 mM) of chloride salts (e.g., LiCl, NaCl, KCl, RbCl, $CaCl_2$, $MgCl_2$, $BaCl_2$, and $NiCl_2$) to freshly prepared 0.5-mg/mL $\{Mo_{72}Fe_{30}\}$ aqueous solutions (ones where no blackberries are present).[35]

This was done to determine

- How the salt concentration affects blackberry formation and stability. Blackberries have a critical flocculation concentration for additional cations, which is the minimum amount of added cations required to precipitate the blackberries (this is a typical colloidal behavior following the DLVO theory—that is, the added salts decrease the screening length of the blackberries; therefore, the blackberries, precipitate due to the dominant van der Waasl forces). Once the blackberries precipitate, $\sim$80% of the original POM anions present are still in solution.[31] This may be partly due to the break up of some blackberries, but also shows that the large POM anions are stable in high salt concentrations. This may be a useful property of POMs for applications like ion exchange and heavy-metal waste sequesterization.
- The effect of valent state of the added cations on blackberry formation and stability and size.
- The effect of cation size (ionic radius, hydrated radius, or hydration number) on blackberry size.

After heating several weeks at 40°C, the hydrodynamic radius (R_h) of the $\{Mo_{72}Fe_{30}\}$ blackberries was measured using DLS. For each type of added salt, a general trend is observed: up to a specific critical salt concentration (CSC), the blackberry size does not change significantly. Once this CSC is reached, the blackberry size gradually increases with increasing salt concentration. The CSC is about 100 times lower for divalent cations than for monovalent ones, due to the much stronger interaction between divalent cations and POM anions. The interesting observation is that the CSC for Rb^+ ions occurs at an intermediate point between that of divalent and monovalent cations, much lower than for other monovalent cations (Fig. 12). This is likely due to the fact that the large Rb^+ ions are less hydrated than the other types of monovalent cations, thus having a more positive hydration enthalpy. This property of Rb^+ ions allows them to more effectively screen the interactions among macroions.

If the small counterions are involved in the blackberry formation process as shared counterions between POM macroions, it is possible that the size of the counterions would affect their capability of attracting adjacent POMs. Because Rb^+ is less hydrated, its size is smaller than the other types of cations

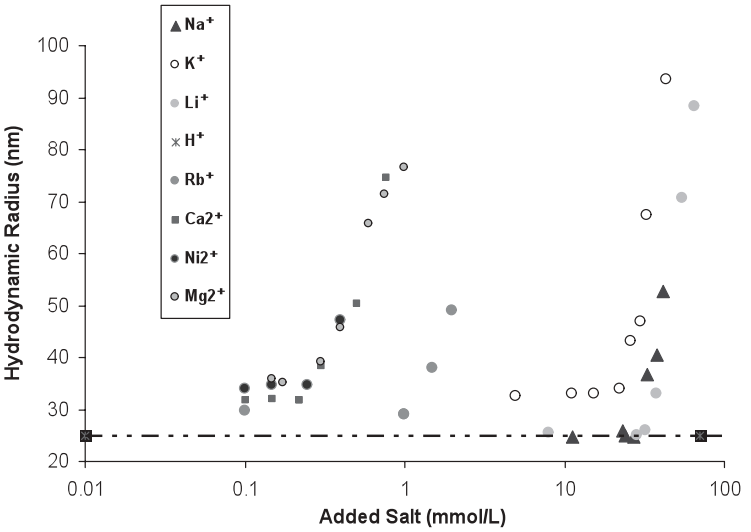

FIGURE 12. The effects of extra added electrolytes are shown on $\{Mo_{72}Fe_{30}\}$ blackberry formation. CSCs are clearly seen as the R_h of the blackberries stays constant for each salt and then gradually increases once the critical salt concentration is reached.

shown in Figure 12, although its atomic mass is the highest. Therefore, it is easier for the Rb^+ ions to function as "bridging cations" between POMs than the more hydrated monovalent cations.

The dehydration idea is supported by the fact that a longer time period was required for blackberries to form in solutions containing the more highly hydrated cations like Ni^{2+} and Zn^{2+}, whereas solutions containing less hydrated cations like Ba^{2+} and Rb^+ formed aggregates almost immediately.

Another observation is that for all other cations besides Li^+ and Na^+, the blackberry radius before the CSC is larger than that without additional salts (then the only counterions are H^+ cations), as shown in Figure 12. This observation suggests that the Li^+ and Na^+ cannot replace the shared protons originally existing among the POMs on the blackberry surface. However blackberries formed in NaCl and LiCl still exhibit a CSC owing to a screening effect due to counterion condensation from the excess salt. Likewise, when other types of cations are introduced into blackberry solution, they will increase the blackberry size before CSC. The possible reason is that these cations have stronger affinity to the POMs than to protons. Therefore, they will (at least partially) replace the protons between POMs and act as "bridging cations." This stronger attractive force between POMs will lead to larger blackberry sizes, as predicted by Eq. (1).

The effects of added salt were found to be reversible in solutions containing monovalent cations like Na^+, K^+, and Rb^+. Blackberry formation was allowed to complete in solutions containing amounts of KCl that exceeded the CSC. Then these solutions were diluted to decrease the salt concentration to a point

below the CSC, while keeping the macroion concentration the same. This was done by adding the appropriate amount of freshly prepared, salt-free, 0.5 mg/mL $\{Mo_{72}Fe_{30}\}$ to achieve the correct dilution. When this was done, the average blackberry size decreased according per the amount of dilution. For example, at 45 mM KCl, the average blackberry R_h is $\sim$90 nm. When the KCl concentration was diluted from 45 to 15 mM, the sample was allowed to equilibrate for several weeks at 40°C. After the blackberry radius stopped changing, the radius was $\sim$33 nm, which is about the same size as a sample prepared in 15 mM KCl. Therefore, the blackberry formation processes in the presence of additional salts as shown in Figure 12 are all free-energy favored processes.

XI. KINETIC PROCESS OF BLACKBERRY FORMATION

Time-resolved DLS and SLS studies can be used to study the mechanism of the blackberry formation process.[33,34] SLS measurements can monitor the change in scattered intensity of the solutions. As shown in Figure 13, the scattered intensity from a series of $\{Mo_{72}Fe_{30}\}$ solutions are very low at the beginning, showing that all the clusters exist as discrete macroions in solution immediately after the dissolution. DLS results confirm this conclusion by showing no mode corresponding to large R_h values. The scattered intensity increases continuously but also slowly with time at room temperature, indicating the continuous formation of supramolecualr structures in solution. The intensity increment continues for months until finally reaches equilibrium at a quite high level. The growth of the scattered intensity becomes faster at higher

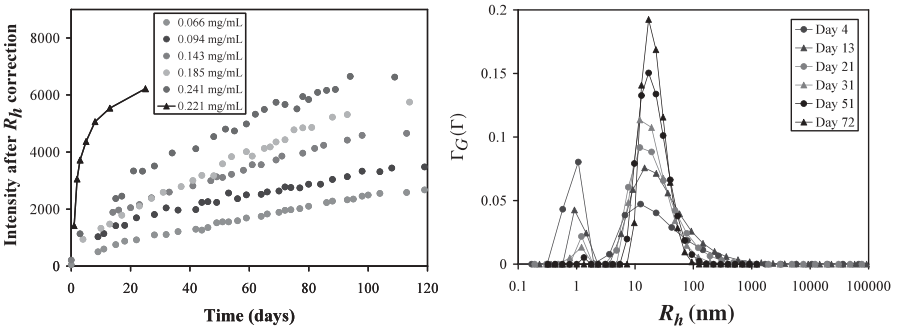

FIGURE 13. SLS (a) and DLS (b) measurements to monitor the slow blackberry formation in dilute aqueous solutions of $\{Mo_{72}Fe_{30}\}$. All experiments were performed at 25°C, except the filled triangles in panel a, which were carried out at 45°C. (Reprinted with permission from ref. 33. Copyright [2008] American Chemical Society.)

temperatures. The increment of the scattered intensity may arise from two sources, based on the simplified Rayleigh-Gans-Debye equation:[33]

$$I\alpha C \cdot M_w = C \cdot R_n^2 \tag{4}$$

where I, C, M_w are the scattered intensity from blackberry solution, the blackberry concentration and mass, respectively. The M_w is proportional to the square of R_h because the blackberries have a hollow nature. From Eq. (4), it is clear that the intensity increment could be the result of (a) the blackberries size increasing with time or (b) the number of blackberries in solution with time. We can use DLS measurements (Fig. 13b) to identify which factor is more dominant. DLS results clearly indicate that the size of blackberries does not change significantly from day 4 to day 72. The peak due to blackberries increases continuously with time, suggesting that more and more blackberries have been formed. At the same time, the peak due to discrete macroions becomes smaller and smaller, suggesting that the single macroions have been continuously consumed for the blackberry formation. Combining the SLS and DLS results, we can conclude that the increase in scattered intensity with time is mainly due to the increase of the number of the blackberries. Also, once the blackberries are formed, they will maintain a preferred size and will not grow bigger.

Such results help us to build a reasonable model to explain the kinetics of the blackberry formation, as shown in Figure 14.[29,34] When the $\{Mo_{72}Fe_{30}\}$ single crystals are just dissolved in water, almost all the clusters exist as discrete macroanions. Very slowly, they will attract with each other to form blackberries. There are two possible routes for the blackberry formation process, as shown in Figure 14: (a) Once the blackberries start to form, they quickly reach the final size and stop growing; meanwhile, the remaining discrete macroions will start to form new blackberries. (b) Many small blackberries are formed simultaneously, and they slowly and continuously grow into larger ones. The DLS studies clearly

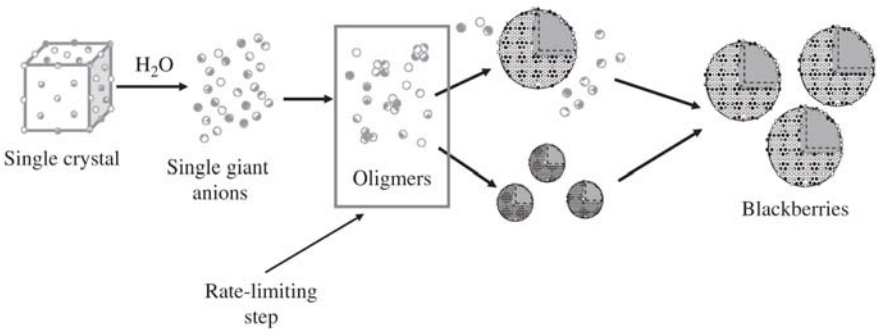

FIGURE 14. The mechanism of blackberry self-assembly process. The oligomer formation is the rate-limiting step (Reprinted with permission from ref. 29.)

indicate that the first route is correct in this case because the average R_h of the blackberries does not change with time from day 4 to day 72. This also suggests that for the blackberry formation, there exists a very high energy barrier, which is responsible for the slow process at the beginning. Once the blackberry formation starts, the blackberries will quickly reach the final size (free-energy favored size).

The initial stage of the blackberry formation can be monitored by the change of the total scattered intensity from the solutions by SLS measurements. Because the blackberry size almost does not change with time, the increment of scattered intensity is proportional to the number of blackberries in solution. In Figure 15, the time-resolved intensity curves roughly follow the rule for first-order reactions and the reaction rate k can be directly determined. By studying the temperature dependence of the blackberry formation rate, we can estimate the energy barrier (activation energy for the blackberry formation) by using the Arrhenius equation:[34]

$$k = A \cdot e^{-E_a/RT} \tag{5}$$

where A, E_a, R, and T are a preexponential factor, the activation energy, the universal gas constant, and the temperature, respectively. The Eq. (5) can also be written as:

$$\ln k = -E_a/RT + \ln A \tag{6}$$

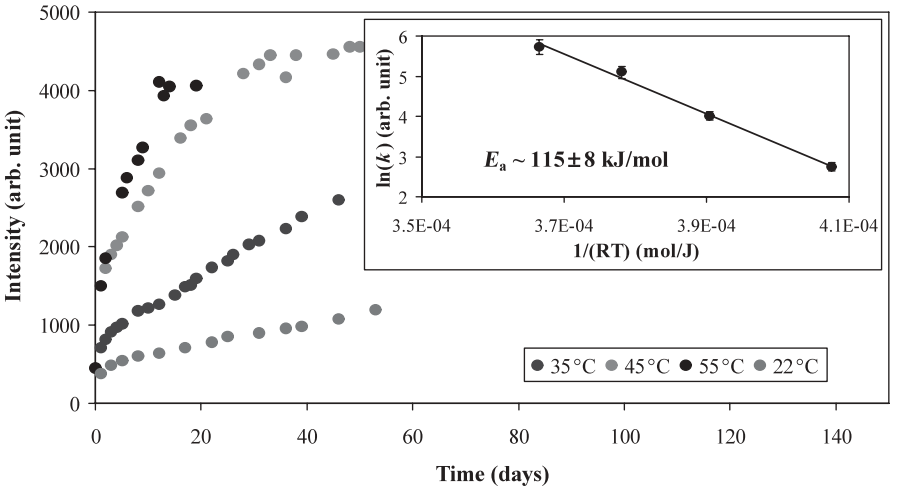

FIGURE 15. Determination of the blackberry formation rate at the initial stage at different temperatures by monitoring the change of the total scattered intensity from SLS experiments. The curves follow the patterns for first-order reactions. The temperature dependence of the reaction rate provides the information regarding the activation energy of the blackberry formation[34] (Reprinted with permission from ref. 34.)

Because the blackberry formation process can be monitored with the change of scattered intensity I from SLS measurements, we can calculate the E_a of this transformation by LLS. For the $\{Mo_{72}Fe_{30}\}$ blackberries formed in aqueous solution, the activation energy is determined as $\sim$115 kJ/ml, which is a very high value, considering that the process is a physical process (Fig. 15). This helps explain why the blackberry formation is so slow at room temperature. This high energy barrier should come from the fact that the individual POM anions are very difficult to come to each other and form oligmers at the beginning. Once the oligmers are formed, the blackberry formation process will be accelerated significantly.[34]

XII. CATION TRANSPORT OVER THE ANIONIC BLACKBERRY MEMBRANE

The blackberries have a negatively charged surface formed by a single layer of macroanions. Considering that the POM anions are not touching each other on the blackberry surface due to electrostatic repulsion, and the small cations might stay between the POMs, it is reasonable to speculate that the blackberry walls might be permeable to small cations. With the help of hydrogen bonds, the blackberry walls show soft, robust and membrane features. Such inorganic membranes are different from bilayer membranes formed by amphiphiles because they do not have any compact, hydrophobic regions. Studying the cation transport process across the blackberry membrane and comparing it to corresponding processes across cell membranes would be very interesting.

We explored whether the nature of water (e.g., polarity or viscosity) inside the blackberries is different from that in bulk solution; and whether the conserved and soft blackberry membrane is permeable to various ions (i.e., achieving passive transportation) by using cation-sensitive fluorophore chlorotetracycline (CTC) and two anion-sensitive fluorophores, 6-methoxyquinoline (6-MQ) and coumarin 1 (Fig. 16).[36] After the fluorophores are incorporated into $\{Mo_{72}Fe_{30}\}$ blackberries, a wavelength blue shift in fluorescence maxima is observed, which clearly indicates that the fluorophores have experienced a different water environment than in bulk water. This evidence shows that the water inside the blackberries possesses a higher viscosity than that in bulk, possibly due to additional hydrogen bondings with the hydrophilic POMs. Therefore, blackberry formation is a process capable of creating micrometer-scaled water droplets with features different from the bulk.

Once the fluorophore-containing blackberries are formed, extra salts are added into the solution. CTC can bind to Ca^{2+} and Mg^{2+} with enhanced fluorescence by forming fluorescent chelates. We observe a continuous increase (for 12–14 h) in fluorescence quantum yield (Φ_f) of CTC over time when Ca^{2+} or Mg^{2+} are added (Fig. 17), followed by a blue shift (4 nm for Ca^{2+}; 5 nm for Mg^{2+}). The slow increase of Φ_f indicates that some fluorophores cannot be

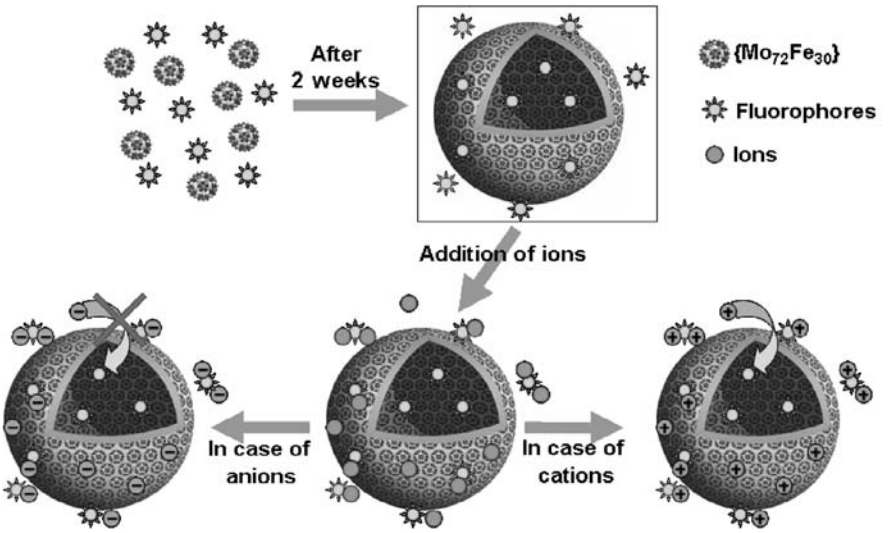

FIGURE 16. Formation of fluorophore-containing $\{Mo_{72}Fe_{30}\}$ blackberries in solution. The additional cations, once added into solution, instantly interact with fluorophores in bulk solution and on blackberry surface. They subsequently enter into the blackberries and interact with the fluorophores inside. The anions could not cross the membrane.[36] (Reprinted with permission from ref. 36. Copyright [2008] American Chemical Society.)

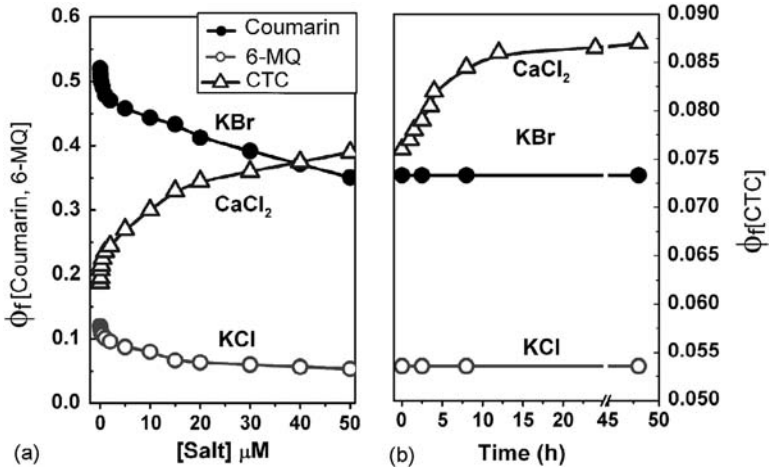

FIGURE 17. The change in fluorescence quantum yield of coumarin 1, 6-MQ, and CTC with addition of KBr, KCl and $CaCl_2$, respectively. (a) Instantaneous change occurs with the addition of salts. (b) Change in fluorescence quantum yield with time, once the addition of salt is stopped.[36] (Reprinted with permission from ref. 36. Copyright [2008] American Chemical Society).

accessed by those divalent cations when they are just introduced into the solution, but the change of the cation environment leads to more and more cation-fluorophore interactions. A reasonable explanation is that the Ca^{2+} or Mg^{2+} ions first quickly interact with the fluorophores in bulk solution and on the external blackberry surface, until all the initial available fluorophores are saturated. The slow increase of Φ_f suggests that more and more fluorophores become accessible with those divalent cations with time, which clearly shows that the cations move slowly across the blackberry membrane and interact with the fluorophores present inside. Therefore, we conclude that the anionic blackberry membrane is permeable to small cations, without the help of any specific carriers. The curves (Φ_f vs. time) for Ca^{2+} and Mg^{2+} are almost identical, suggesting that the cation transport across the blackberry membrane does not show obvious dependence on cationic size at least for small ions, because the inter-POM spacing on blackberry surface is broad enough.[36]

On the contrary, the small anions, such as Cl^- and Br^-, cannot move across the blackberry wall, due to the electrostatic repulsion between them and the anionic blackberry surface (Fig. 16).[36]

XIII. MACROIONS IN SOLUTION: AN IMPORTANT LINKAGE AMONG SIMPLE IONS, POLYMERS, COLLOIDS, AND BIOSYSTEMS

The POM macroionic solutions are different from the traditional ionic solutions containing small inorganic ions because the soluble ions do not distribute homogeneously in dilute solutions. However, the POM solutions are still free-energy favored real solutions, which distinguishes them from colloidal suspensions.

The POMs show some similarities with long-chain polyelectrolytes, including proteins and DNAs. Macromolecular polyelectrolytes show a much more complex solution behavior that has not been totally understood. It is known that the polyelectrolyte chains tend to interact strongly with each other to form long-range ordered structures in salt-free solutions. For most of the polyelectrolytes, the solution behavior is complicated due to variable chain conformations and entanglements. In contrast, the inorganic macroions have fixed size, shape, number of charges on each ion and manifold of well-defined functionalities with options for further modifications. Therefore, they can be treated as ideal model systems for understanding polyelectrolyte solutions. Particularly, the self-assembly of POM macroions shows similarities to the formation of many types of virus shells formed by the ordered assembly of capsid proteins.[37–39] With similar size and other features (e.g., charge), the connection between inorganic macroionic assemblies and biosystems should be intriguing.

XIV. CONCLUSIONS

In summary, the recent discovery of various structurally well-defined, nanometer-scale, hydrophilic POM species has successfully pushed the size limit of inorganic ions into the nanometer scale. This progress provides new opportunities in different fields—for example, physical chemistry of solutions—as a new type of self-assembly behavior is observed in such soluble macroionic solutions. The POM macroanions show totally different solution behaviors when compared to regular inorganic ions, owing to their size and surface charges, while even significant differences among these giant anions occur. The POMs tend to self-associate into uniform, single-layer, hollow, spherical blackberry structures, and the blackberry size can be accurately tuned by solvent quality, solution pH, and the charge density of macroions. The blackberry formation is also fundamentally different from the well-known self-assembly behaviors like polymers, surfactant micelles, and colloids, because the driving forces are not due to hydrophobic interactions or van der Waals forces. On the contrary, the counter-ion-mediated attraction and hydrogen bonds must be important. Based on our new discoveries, some widely accepted concepts, such as "Soluble inorganic ions distribute homogeneously in solutions" and "Soluble ions reach equilibrium state quickly in dilute solutions" may not always be correct when the ions are large enough.

The macroionic solution represents a bridge connecting the traditional areas of simple ions and colloids. Now we can address some fundamental questions, such as What happens when soluble ions reach the nanometer scale? by studying such novel solution systems.

XV. ACKNOWLEDGMENTS

T. L. thanks supports from the NSF (CHE-0545983), ACS-PRF (46294-G3), and Lehigh University (startup fund and FRG).

XVI. REFERENCES

1. *Gmelins Handbuch der Anorganischen Chemie*, no. 53, 8th ed., Verlag Chemie, Berlin, 1935. Completely references the older literature after Scheele.
2. A. Müller and C. Serain, *Acc. Chem. Res.*, **2000**, *33*, 2.
3. (a) C. W. Scheele, in *Sämtliche Physische und Chemische Werke*, vol. 1, ed. D. S. F. Hermbstädt, Martin Sändig oHG; Niederwalluf/Wiesbaden, **1971**, pp. 185–200 (originally published 1793). (b) J. A. Schufle, *Torbern Bergman: A Man before His Time*, Coronado Press, Lawrence, KS, **1985**.
4. J. J. Berzelius, *Poggend. Ann. Phys. Chem,* **1826**, *6*, 369.
5. A. Müller, J. Meyer, E. Krickenmeyer, and E. Diemann, *Angew. Chem. Int. Ed. Engl.*, **1998**, *35*, 1206.

6. A. Müller and S. Roy, *Coord. Chem. Rev.*, **2003**, *245*, 153.
7. A. Müller, P. Kogerler, and A. W. M. Dress, *Coord. Chem. Rev*, **2001**, *222*, 193.
8. C. L. Hill, ed. *Polyoxometalates, Chem. Rev.*, **1998**, *98*, 17.
9. A. Müller, S. K. Das, V. P. Fedin, E. Krickemeyer, C. Beugholt, H. Bögge, M. Schmidtmann, and B. Hauptfleisch, *Anorg. Allg. Chem.*, **1998**, *625*, 1187.
10. A. Müller, E. Beckmann, H. Bogge, M. Schmidtmann, and A. Dress, *Angew. Chem. Int. Ed.*, **2002**, *41*, 1162.
11. A. Müller, E. Krichemeyer, H. Bogge, M. Schmidtmann, and F. Peters, *Agnew. Chem. Int. Ed.*, **1998**, *37*, 3359.
12. A. Müller, S. Sabyasachi, Q. N. S. Syed, H. Bögge, M. Schmidtmann, S. Sarkar, P. Kögerler, B. Hauptfleisch, A. Trautwein, V. Schünemann, *Angew. Chem. Int. Ed.*, **1999**, *3*, 3238.
13. A. Müller, P. Kögerler, and C. Kuhlmann, *Chem. Comm.*, **1999**, 1347.
14. B. Botar, P. Kögerler, A. Müller, R. Garcia-Serres, and C. Hill, *Chem Commun.*, **2005**, *45*, 5621.
15. A. M. Todea, A. Merca, H. Bögge, J. van Slageren, M. Dressel, L. Engelhardt, M. Luban, T. Glaser, M. Henry, and A. Müller, *Angew. Chem., Int. Ed.*, **2007**, *46*, 6106.
16. A. Müller, E. Krickenmeyer, J. Meyer, H. Bögge, F. Peters, W. Plass, E. Diemann, S. Dillinger, F. Nonnebruch, M. Randerath, and C. Menke, *Angew. Chem. Int. Ed.*, **1995**, *34*, 2122.
17. A. Müller, E. Krickemeyer, H. Bögge, M. Schmidtmann, C. Beugholt, P. Kögerler, and C. Z. Lu, *Angew. Chem., Int. Ed.*, **1998**, *37*, 1220.
18. B. Botar, P. Kogerler, and C. Hill, *Chem Commun.*, **2005**, *25*, 3138.
19. B. Botar, P. Kogerler, and C. Hill, *J. Am. Chem. Soc.*, **2006**, *128*, 5336.
20. L. Cronin, P. Kogerler, and A. Müller, *J. Solid State Chem.,* **2000**, *152*, 57.
21. T. Liu, B. Imber, E. Diemann, E. Liu, K. Cokleski, H. Li, Z. Chen, and A. Müller, *J. Am. Chem. Soc.*, **2006**, *128*, 15914.
22. A. Müller, E. Diemann, C. Kuhlmann, W. Eimer, C. Serain, T. Tak, A. Knöchel, and P. K. Pranzas, *Chem. Commun.*, **2001**, *19*, 1928.
23. T. Liu, E. Diemann, H. Li, A. W. M. Dress, and A. Müller, *Nature*, **2003**, *426*, 59.
24. S. W. Provencher, *Biophys. J.*, **1976**, *16*, 29.
25. M. L. Kistler, A. Bhatt, G. Liu, D. Casa, and T. Liu, *J. Am. Chem. Soc.* **2007**, *129*, 6453.
26. G. Liu, and T. Liu, *J. Am. Chem. Soc.* **2005**, *127*, 6942.
27. L. Verhoeff, M. L. Kistler, A. Bhatt, J. Pigga, J. Groenewold, M. Klokkenburg, S. Veen, S. Roy, T. Liu, and W. K. Kegel, *Phys. Rev. Lett.*, **2007**, *99*, 66104.
28. G. Liu, M. L. Kistler, T. Li, A. Bhatt, and T. Liu, *J. Cluster Sci.*, **2006**, *17*, 427.
29. G. Liu, T. Liu, S. S. Mal, and U. Kortz, *J. Am. Chem. Soc.*, **2006**, *128*, 10103.
30. A. Oleinikova, H. Weingaertner, M. Chaplin, E. Diemann, H. Bögge, and A. Müller, *Chem Phys Chem.*, **2007**, *8*, 646.
31. G. Liu, Y. Cai, and T. Liu, *J. Am. Chem. Soc.*, **2004**, *126*, 16690.
32. T. Liu, *J. Am. Chem. Soc.*, **2002**, *124*, 10942.
33. T. Liu, *J. Am. Chem. Soc.*, **2003**, *125*, 312.
34. G. Liu, and T. Liu, *Langmuir*, **2005**, *21*, 2713.
35. J. Pigga, and T. Liu, unpublished results.
36. P. P. Mishra, J. Pigga, and T. Liu, *J. Am. Chem. Soc.*, **2008**, *130*, 1548.
37. I. Morfin, F. Horkay, P. Basser, F. Bley, A. Hecht, and C. Rochas, *Biophys. J.*, **2004**, *87*, 2897.
38. A. C. Steven, B. L. Trus, F. P. Booy, N. Cheng, A. Zlotnick, J. R. Caston, and J. F. Conway, *FASEB J.*, **1997**, *11*, 733.
39. P. Ceres, and A. Zlotnick, *Biochemistry,* **2002**, *41*, 11525.

CHAPTER 3

Supramolecular Structures and Polyoxometalates

Samar K. Das

School of Chemistry, University of Hyderabad, India

CONTENTS

Macromolecules Containing Metal and Metal-Like Elements,
Volume 9: Supramolecular and Self-Assembled Metal-Containing Materials,
Edited by Alaa Abd-El Aziz, Charles E. Carraher, Charles U. Pittman, and Martel Zeldin.

I. INTRODUCTION

The polyoxometalate (POM) is defined to a large group of generally anionic clusters formed from early transition metals—for example, (V(V), Nb(V), Ta(V)), Mo(VI) and W(VI)—oxo anions linked by shared oxide ions.[1] Thus POMs represent a distinctive class of inorganic compounds that are so important in terms of their electronic versatility and structural variation that they are fascinating to many areas of science and technology, such as chemical, materials, biological, and medical sciences and catalysis.[2] In the last few years, significant attention continued to focus on POMs on account of their intriguing architectures because POMs have successfully been employed as inorganic building units for the aesthetic construction of supramolecular arrays.[3–7] The spherical surface of most of the POM anions gives a better opportunity of forming hydrogen bonding interactions with the organic–inorganic moieties because the terminal and bridging oxygen atoms of POM anions are good hydrogen bond acceptors.[8] Thus O−H · · · O, N−H · · · O, C−H · · · O and O−H · · · N hydrogen bonding interactions, which can be called *supramolecular cements* in terms of the crystal engineering of supramolecular assemblies,[9,10] are often observed among POM anions, crystal waters, and other organic–inorganic coordination complexes present in relevant crystalline molecular solids.

Detailed discussions on supramolecular structures of giant polyoxometalate clusters have been reported by Müller and co-workers.[11–15] The number of ionic lattices formed from anionic POM clusters and organic cations–coordination complex cations resulting in supramolecular structures is substantial and literally more than hundreds of new compounds in this class appear annually.[2,12,16–22] In this overview, the supramolecular features of POM-based systems will be discussed mainly under three headings: (a) supramolecular features of polyoxometalate supported transition metal complexes, (b) polyoxometalate-crown ether complexes with supramolecular cations, and (c) supramolecular water clusters associated with polyoxometalates.

II. SUPRAMOLECULAR FEATURES OF POLYOXOMETALATE-SUPPORTED TRANSITION-METAL COMPLEXES

An important advance in POM chemistry is POM-supported transition-metal complexes.[23] Such metal oxide-based inorganic compounds provide functional materials with interesting optical, electronic, and magnetic properties and serve as structural models for understanding the multiple functions of oxide-supported catalysts.[1,24] Keggin-type anions have mostly been used to support inorganic complexes because the charge density of Keggin surface oxygen atoms

can be increased either by reducing some of their metal centers (e.g., Mo^{VI} to Mo^{V}) or by replacing higher valent metal centers with lower valent metal centers (e.g., Mo^{VI} by V^{IV}).[25,26] Wang and co-workers have contributed significantly in this direction. They reported the hydrothermal synthesis and crystal structures of reduced and capped Keggin derivatives decorated by transition-metal complexes.[27] One of these modified polyoxometalates is $[PMo_6^{VI}Mo_2^{V}V_8^{IV}O_{44}\{Co(2,2'\text{-bipy})_2(H_2O)\}_4][PMo_4^{VI}Mo_4^{V}V_8^{IV}O_{44}\{Co(2,2'\text{-bipy})_2(H_2O)\}_2]\cdot 4H_2O$, which consists of $[PMo_6^{VI}Mo_2^{V}V_8^{IV}O_{44}\{Co(2,2'\text{-bipy})_2(H_2O)\}_4]^{3+}$ polyoxocations and $[PMo_4^{VI}Mo_4^{V}V_8^{IV}O_{44}\{Co(2,2'\text{-bipy})_2(H_2O)\}_2]^{3-}$ polyoxoanions, in which mixed-metal tetra-capped $[PMo_8V_8O_{44}]$ subunits are covalently linked to four and two cobalt coordination complexes $[Co(2,2'\text{-bpy})_2(H_2O)]^{2+}$, respectively, via the terminal oxo groups of the capping vanadium atoms as shown in Figures 1 and 2, respectively.

In the POM-supported cationic species, $[PMo_6^{VI}Mo_2^{V}V_8^{IV}O_{44}\{Co(2,2'\text{-bipy})_2(H_2O)\}_4]^{3+}$, the mixed-valent heteropolyanion, $[PMo_6^{VI}Mo_2^{V}V_8^{IV}O_{44}]^{5-}$, act as multidentate ligands that are covalently linked to four cobalt coordination complexes, $[Co(2,2'\text{-bipy})_2(H_2O)]^{2+}$, resulting in a paddlewheel type of arrangement (Fig. 1a). The unique feature of this system can be described by the presence of a same heteropolyanion, $[PMo_8V_8O_{44}]^{n-}$, in both cations and anions in the same crystal at the same time. This became possible because of the modifying effect of the transition-metal complexes on the surface of polyoxometalates and different extents of reduction of the heteropolyanion in the polyoxocation and polyoxoanion. The bipyridine ring of the POM-supported cobalt coordination complex can exert π-π stacking interactions with its nearby bipyridine ring of the neighboring POM-supported cobalt complexes, and the surface of the POM cluster is a good hydrogen bond acceptor. Thus, through the linkages of π-π stacking interactions and hydrogen bond contacts, an extended three-dimensional supramolecular network is formed in the solid-state structure of $[PMo_6^{VI}Mo_2^{V}V_8^{IV}O_{44}\{Co(2,2'\text{-bipy})_2(H_2O)\}_4][PMo_4^{VI}Mo_4^{V}V_8^{IV}O_{44}\{Co(2,2'\text{-bipy})_2(H_2O)\}_2]\cdot 4H_2O$.

Recently, Niu and co-workers reported an interesting example of a Keggin unit–supported transition-metal complex in compound $[Cu(4,4'\text{-bipy})]_2[SiW_{12}O_{40}\{Cu(4,4'\text{-bipy})\}_4](OH)_2\cdot H_2O$ (4,4′-bipy = 4,4′-bipydine) that consists of a neutral polyoxometalate $[Cu(4,4'\text{-bipy})]_2[SiW_{12}O_{40}\{Cu(4,4'\text{-bipy})\}_4]$, two $[Cu(4,4'\text{-bipy})]^{+}$ cations, two hydroxyls, and one water molecule (Fig. 3a) in which the Keggin anion $[SiW_{12}O_{40}]^{4-}$ is covalently bonded to four copper-bipyridine complex fragments $[Cu(4,4'\text{-bipy})]^{+}$ through the terminal oxygen atoms of the Keggin anions.[28] As shown in Figure 3b, the four copper ions, which are covalently linked to each Keggin anion, form four one-dimensional $[Cu(4,4'\text{-bipy})]_n^{n+}$ chains along the crystallographic *a* axis through the N, N terminals of 4,4′-bipy. Thus each polyoxometalate cluster is covalently bonded to four Cu-bipy chains via Cu–O_t bonds. This results in the formation of a new type of one-dimensional, fourfold, chain-like structure formed from the Keggin $[SiW_{12}O_{40}]^{4-}$ clusters and polymeric $[Cu(4,4'\text{-bipy})]_n^{n+}$ chains (Fig. 3b).

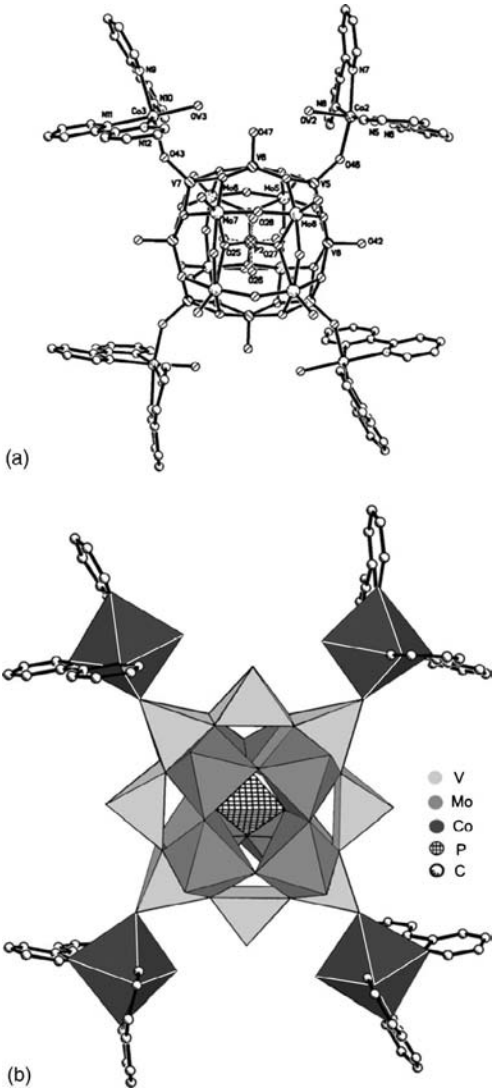

FIGURE 1. (a) POM-supported cobalt coordination complexes in the polyoxocation, $[PMo_6^{VI}Mo_2^{V}V_8^{IV}O_{44}\{Co(2,2'\text{-bipy})_2(H_2O)\}_4]^{3+}$, showing the tetra-capping and tetra-supporting connection mode and disordered P tetrahedron. (b) The same is shown in the polyhedral representation of the polyoxocation. (Reprinted with permission from ref. 27.).

Other examples of Keggin heteropolyanion-supported transition metal complexes that are structurally characterized, include $[Cu^{I}(phen)_2]_4[PMo_8^{VI}V_6^{IV}O_{42}\{Cu^{I}(phen)_2\} \cdot H_5O_2$,[27] $[Ni(phen)_3][PMo_9^{VI}Mo_3^{V}O_{40}\{Ni(phen)\}_2]$,[27] $[Ni(2,2'\text{-bipy})_3]_{1.5}[PW_{10}^{VI}W_2^{V}O_{40}Ni(2,2'\text{-bipy})_2(H_2O)] \cdot 0.5H_2O$,[29] and $[Co(1,10'\text{-phen})_3]_{1.5}[PMo_{10}^{VI}Mo_2^{V}O_{40}Co(1,10'\text{-phen})_2(H_2O)] \cdot 0.5H_2O$[29].

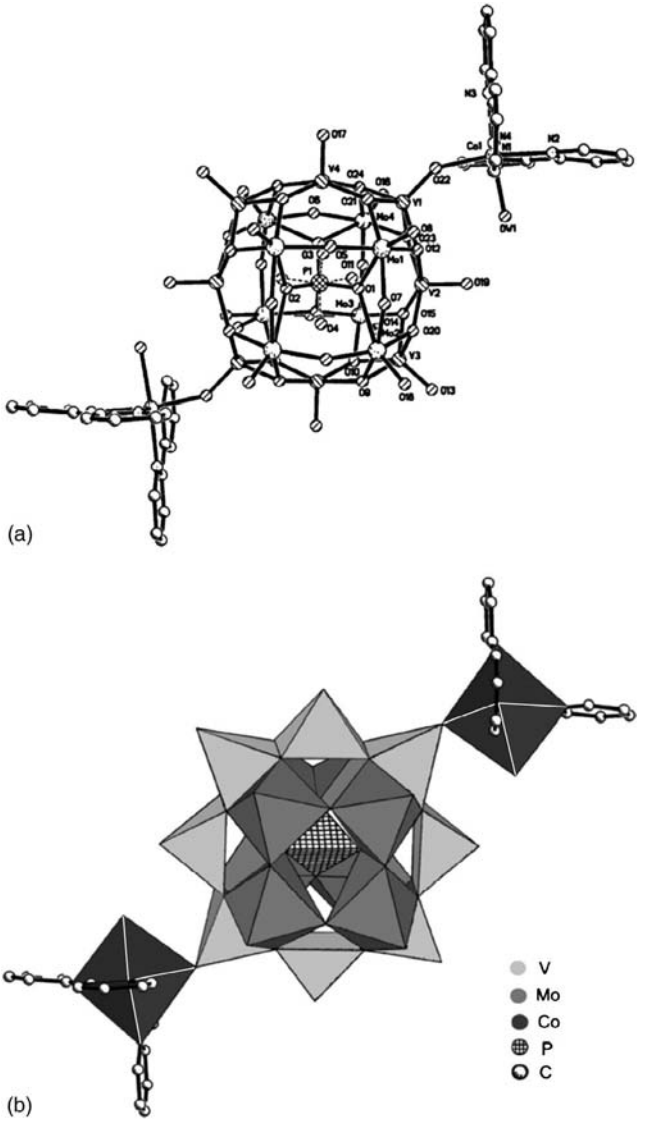

FIGURE 2. (a) View of the polyoxoanion in 1, $[PMo_4^{VI}Mo_4^{V}V_8^{IV}O_{44}\{Co(2,2'\text{-bipy})_2(H_2O)\}_4]^{3-}$, showing the tetra-capping and bisupporting connection mode. (b) Polyhedral representation of the polyoxoanion in 1, showing the coordination environments around Mo, V, and Co atoms. (Reprinted with permission from ref. 270.)

Octamolybdate, $[Mo_8O_{26}]^{4-}$, a common isopolyanion, is now well established for supporting transition-metal complexes that exhibit diversity in supramolecular structures. In this isopolyanion, eight isomeric forms are known based on different types of polyhedral and oxo-groups present in these isomers (Table 1).[30]

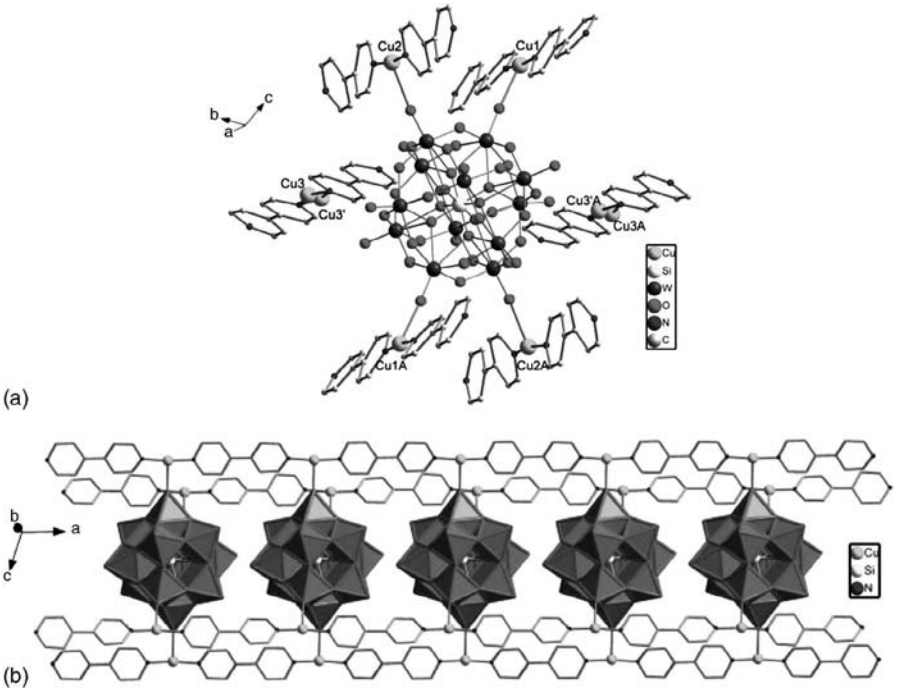

FIGURE 3. (a) View of the asymmetric unit in compound $[Cu(4,4'\text{-bipy})]_2[SiW_{12}O_{40}\{Cu(4,4'\text{-bipy})\}_4] \cdot (OH)_2 \cdot H_2O$. (b) Polyhedral representation of the one dimensional, fold four, chain-like structure viewed along the *b* axis. (Reprinted with permission from ref. 28.)

TABLE 1. Descriptions of Eight Isomeric Forms of $[Mo_8O_{26}]^{4-}$ Based on Oxo-Group Types and Polyhedral Components

Isomer	Types of Oxo Groups	Polyhedra
α-$[Mo_8O_{28}]^{4-}$	$6\mu^2$, $6\mu^3$, 14t	6 octahedra, 2 tetrahedra
β-$[Mo_8O_{28}]^{4-}$	$6\mu^2$, $4\mu^3$, $2\mu^5$, 14t	8 octahedra
γ-$[Mo_8O_{28}]^{4-}$	$10\mu^2$, $2\mu^3$, 14t	6 octahedra, 2 square pyramids
δ-$[Mo_8O_{28}]^{4-}$	$10\mu^2$, $2\mu^3$, 14t	4 octahedra, 4 tetrahedra
ε-$[Mo_8O_{28}]^{4-}$	$4\mu^2$, $6\mu^3$, 16t	2 octahedra, 6 square pyramids
ζ-$[Mo_8O_{28}]^{4-}$	$6\mu^2$, $6\mu^3$, 14t	4 octahedra, 4 square pyramids
η-$[Mo_8O_{28}]^{4-}$	$4\mu^2$, $8\mu^3$, 14t	6 octahedra, 2 square pyramids
θ-$[Mo_8O_{28}]^{4-}$	$8\mu^2$, $4\mu^3$, 14t	4 octahedra, 2 square pyramids, 2 tetrahedra

Seven isomers of $[Mo_8O_{28}]^{4-}$, α through η, are found to support transition-metal coordination complexes via coordinate covalent bonds. The θ-$[Mo_8O_{28}]^{4-}$ isomer, which is unique in the sense that it has a maximum number of polyhedral, is not known to coordinate a transition-metal complex. Among

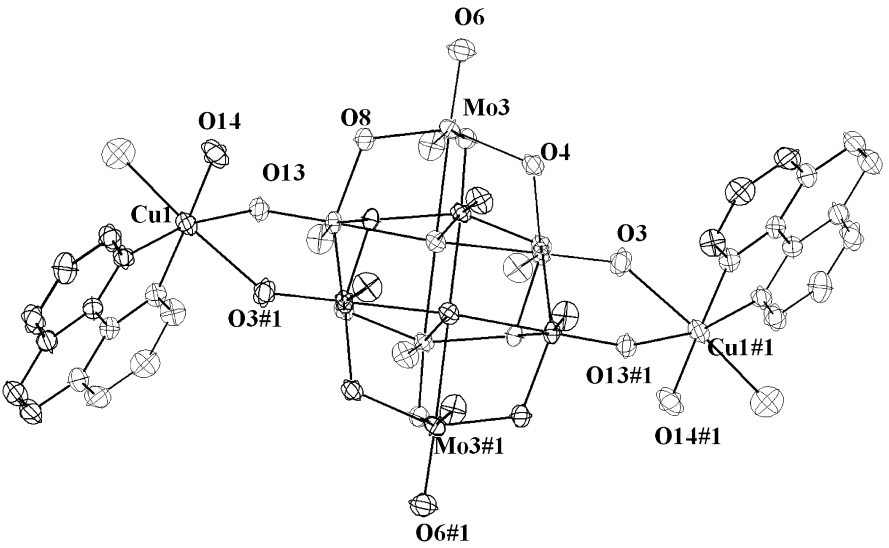

FIGURE 4. Thermal ellipsoidal representation of $[\{Cu(phen)(H_2O)_2\}_2(Mo_8O_{26})]$ in compound $[\{Cu(phen)(H_2O)_2\}_2(Mo_8O_{26})]\cdot 8H_2O$ (50% probability). The symmetric transformation was used to generate equivalent atoms: #1, 2-*x*, 2-*y*, -*z*. (Reprinted with permission from ref. 31.)

these isomers, the β isomer is commonly found to be decorated by metal coordination complexes. We have shown that the β-$[Mo_8O_{28}]^{4-}$ octamolybdate coordinates to two bis(aqua)copper phenanthroline complexes through its terminal oxygen atoms (Fig. 4).[31]

As expected, the β-$[Mo_8O_{26}]^{4-}$ consists of eight edge-sharing octahedral $\{MoO_6\}$ units. The Mo-O distances can be grouped into four categories. These are 14Mo-O_t (O_t = terminal oxygen atoms) groups with the bond lengths in the range of 1.658–1.745 Å; six bridged Mo-O_b distances that fall in the range of 1.871–2.352 Å; four $\{\mu_3\}$-type bridging distances with 1.918–2.365 Å; and two $\{\mu_5\}$-type bridging distances, which are in the range of 2.317–2.521 Å. The structure of the isopolyanion can also be described as two sets of four $\{Mo\text{-}O_6\}$ octahedra lying one above the other and joined by sharing an edge. The copper complex in this system is a monophenanthroline Cu(II) complex with two aqua ligands, which is rarely known in the literature.

A similar octamolybdate-supported copper monophenanthroline complex was reported, but with copper ions in the 1+ oxidation state.[32] The octahedral coordination geometry around each copper is filled by the two nitrogen atoms of the phenanthroline ligands (N(1) and N(2), with an average bond length of 2 Å, two water (O(14) and O(15)) molecules (as monodentate ligands) and two terminal oxygen atoms (O(13) and O(3)) of the isopolyanion (Fig. 4). The axial positions are occupied by a terminal oxygen of the cluster

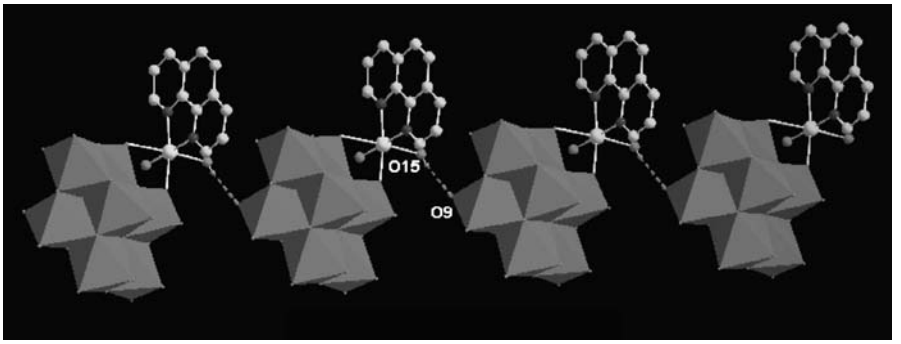

FIGURE 5. An extended one-dimensional chain formed by hydrogen bonding interactions that include copper-coordinated water O(15) and a terminal oxygen atom O(9) of the isopolyanion. *Color code*: isopolyanion, red polyhedral; C, green; N, blue; copper coordinated water O, purple. The hydrogen bonds are shown as dashed purple lines.

(O(3)) and a coordinated water O(15) in the bond length range of 2.306–2.477 Å, which is expectedly longer due to Jahn-Teller distortion for a Cu^{2+} ion. In this system, the copper-coordinated water O(15) undergoes a hydrogen bonding interaction with the terminal oxygen atom O(9) of the isopolyanion and thereby results in the formation of a one-dimensional chain (Fig. 5).

In the relevant crystal structure, these one-dimensional chains are laterally linked by a supramolecular water octamer (vide infra) resulting in a two-dimensional layer-like arrangement as shown in Figure 6. The other transition-metal complexes that are supported by the octamolybdate isopolyanion are also known in the literature.[33,34]

Heptamolybdate isopolyanion, $[Mo_7O_{24}]^{6-}$, is also an attractive metal oxide-based support because of its easy availability as an ammonium salt and its use as a potential catalyst for organic oxidation. The recent literature shows that $[Mo_7O_{24}]^{6-}$ isopolyanion can be functionalized by transition-metal complexes. Neumann and co-workers reported a new type of heptamolybdate that supports $[M^{II}(DMSO)_3]^{2+}$(M = Ru^{2+} and Os^{2+}) in compounds $[NH_4]_4[Ru^{II}(DMSO)_3Mo_7O_{24}]$ and $[NH_4]_4[Os^{II}(DMSO)_3Mo_7O_{24}]$, respectively.[35] This heptamolybdate is an example of new structural type in the sense that it has one approximately tetrahedral coordinate oxygen atom and one pentacoordinated oxygen atom in a nearly pyramidal configuration (Fig. 7). This is in contrast to the structure of normal heptamolybdate–paramolybdate, which is a type II polyoxometalate with a *cis*-dioxo configuration at all molybdenum sites and has seven condensed edge-sharing $\{MoO_6\}$ octahedra and two tetracoordinating bridging oxygens.[36] It is remarkable that these two POM-supported transition-metal complexes exhibit selective catalysis for the aerobic oxidation of alcohols to ketones–aldehydes with high turn over numbers.[35] A new heptamolybdate-supported supramolecular cobalt complex, $[Hapy]_4[Co(H_2O)_5Mo_7O_{24}] \cdot 9H_2O$, has been reported by Cao and co-workers[37] (Fig. 8).

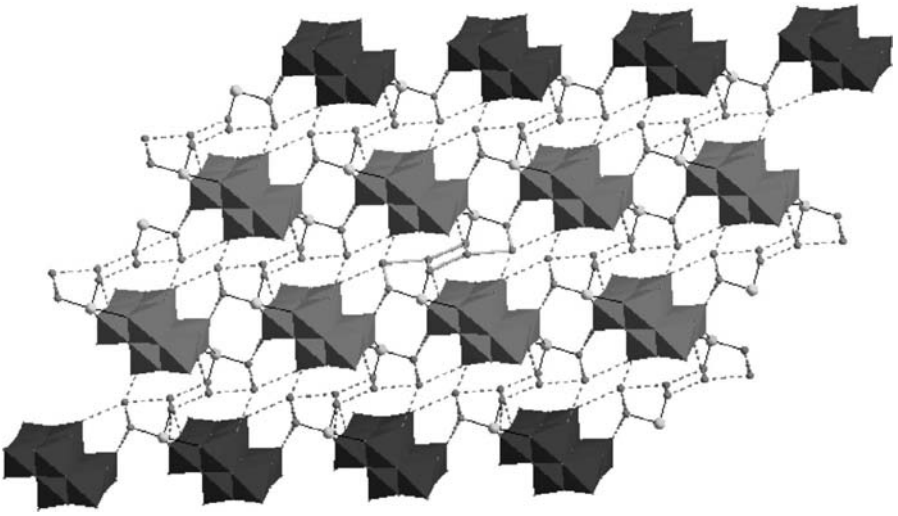

FIGURE 6. Two-dimensional supramolecular hydrogen bonded array in compound $[\{Cu(phen)(H_2O)_2\}_2(Mo_8O_{26})]\cdot 8H_2O$ that is exclusively formed by lateral hydrogen bonding interactions between one-dimensional chains. One of the water octamers is shown in solid lines (center of structure) for clarity. The polyhedral representations of the octamolybdates are given for a clear view of the water octamer.

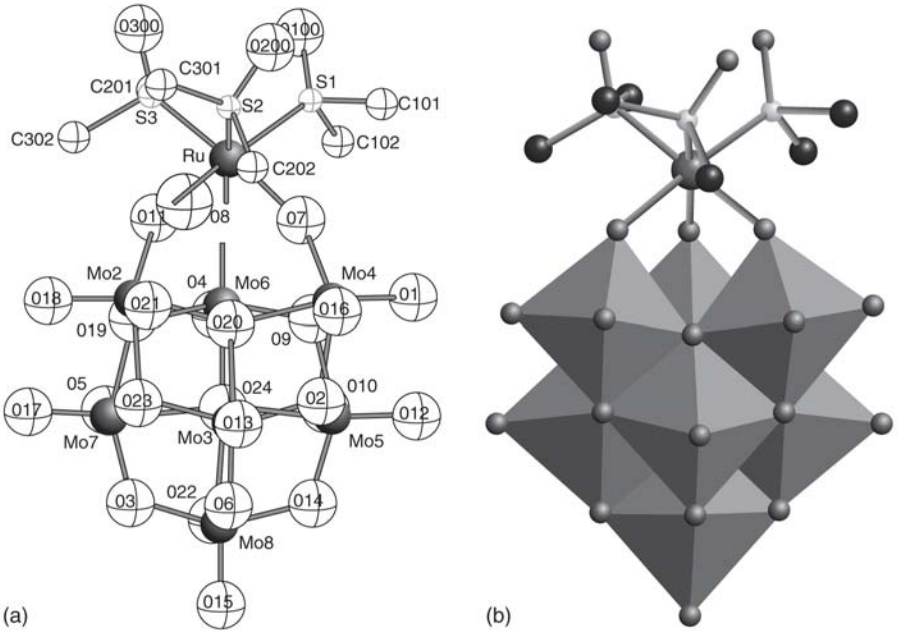

FIGURE 7. Structural representation of $[Ru^{II}(DMSO)_3Mo_7O_{24}]^{4-}$. (a) Ball and stick. (b) Polyhedral. (Reprinted with permission from ref. 35.)

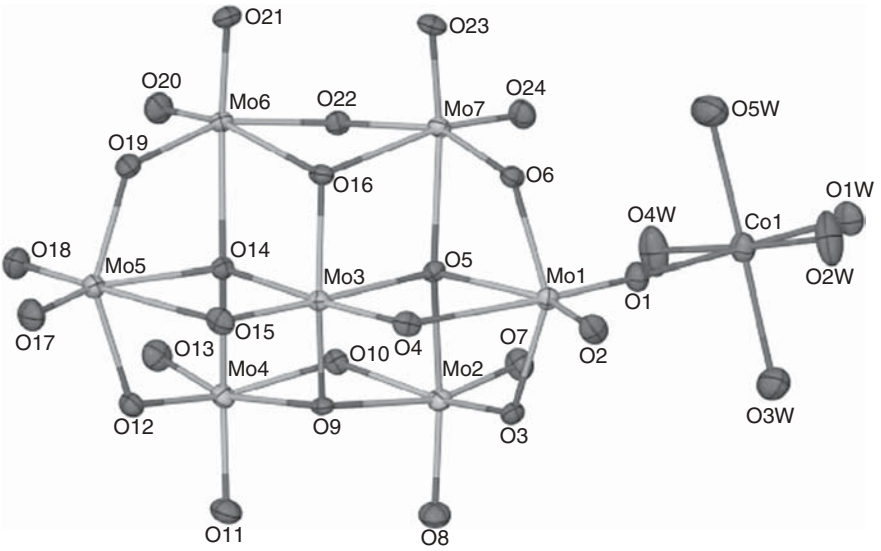

FIGURE 8. Thermal ellipsoidal plot of $[Co(H_2O)_5Mo_7O_{24}]^{4-}$ in compound $[Hapy]_4[Co(H_2O)_5Mo_7O_{24}] \cdot 9H_2O$. (Reprinted with permission from ref. 37.)

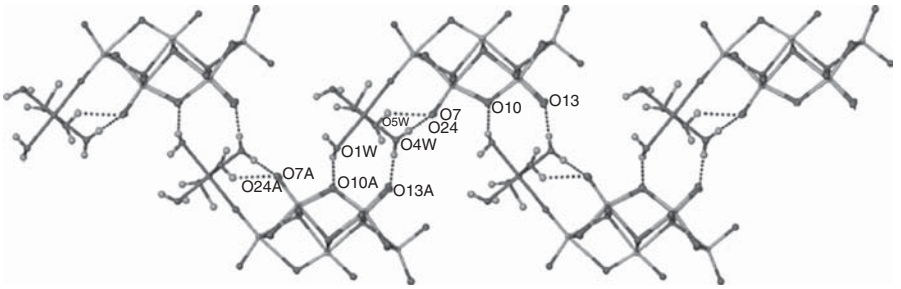

FIGURE 9. A representation of a one-dimensional supramolecular zigzag chain found in a crystal of $[Hapy]_4[Co(H_2O)_5Mo_7O_{24}] \cdot 9H_2O$. (Reprinted with permission from ref. 37.)

In the crystal structure of $[Hapy]_4[Co(H_2O)_5Mo_7O_{24}] \cdot 9H_2O$, the $[Co(H_2O)_5Mo_7O_{24}]^{4-}$ anion undergoes intermolecular supramoelcular hydrogen bonding interactions of the type $O(W)\cdots H\cdots O(POM)$, resulting in the formation of one-dimensional supramolecular zigzag chains (Fig. 9). These chains are linked laterally by the associated cation (protonated 2-aminopyridine) through $N-H\cdots O$ and $C-H\cdots O$ hydrogen bond interactions to form a heptamolybdate-based inorganic-organic hybrid material, $[Hapy]_4[Co(H_2O)_5Mo_7O_{24}] \cdot 9H_2O$, with alternating layers of inorganic anions and organic cations (Fig. 10).

Cronin and co-workers have demonstrated that a highly charged POM anion, $[H_2Mo_4^{V}Mo_{16}^{VI}O_{52}]^{10-}$ (Mo16 cluster), which represents a new structural type,[38] decomposes in the presence of divalent transition metal cations (Fe^{2+} and Mn^{2+}} in high concentrations to produce the isostructural $\{Mo_7M_2\}$-type

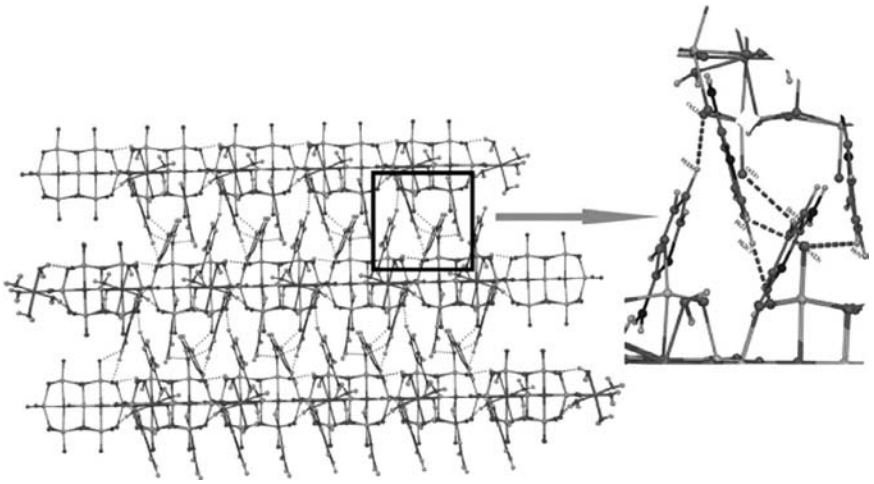

FIGURE 10. Two-dimensional supramolecular layer of alternating anions and cations. (Reprinted with permission from ref. 37.)

compounds, $(HMTAH^+)_2[Fe_2(H_2O)_9Mo_7O_{24}] \cdot 2H_2O$ and $(HMTAH^+)_2[Mn_2(H_2O)_9Mo_7O_{24}] \cdot 2H_2O$, which are based on individual heptamolybdate fragments.[39] We have recently synthesized the zinc analog of this system, $[HMTAH]_2[\{Zn(H_2O)_5\}\{Zn(H_2O)_4\{Mo_7O_{24}\}] \cdot 2H_2O$, in a simple one-pot wet synthesis.[40] Its crystal structure shows that two different Zn(II)-aqua complexes, $[Zn(H_2O)_5]^{2+}$ and $[Zn(H_2O)_4]^{2+}$, are covalently coordinated to a heptamolybdate anion, $[Mo_7O_{24}]^{6-}$, resulting in an anionic species of polyoxometalate-supported zinc–aqua complex, $[\{Zn(H_2O)_5\}\{Zn(H_2O)_4\}\{Mo_7O_{24}\}]^{2-}$, which is stabilized with two protonated hexamethylenetetramine cations (Fig. 11) in the compound $[HMTAH]_2[\{Zn(H_2O)_5\}\{Zn(H_2O)_4\{Mo_7O_{24}\}] \cdot 2H_2O$.

The compound was synthesized starting from sodium molybdate, zinc nitrate, and hexamethylenetetramine in an aqueous medium of pH 3.0. The overall reaction for this cluster formation is shown in Eq. (1). The zinc aqua-complexes, $[Zn(H_2O)_5]^{2+}$ and $[Zn(H_2O)_4]^{2+}$, formed in situ from zinc nitrate and water and, in this reaction, are subsequently coordinated to the POM cluster anion $[Mo_7O_{24}]^{6-}$, resulting in the POM-supported zinc–aqua complex $[\{Zn(H_2O)_5\}\{Zn(H_2O)_4\{Mo_7O_{24}\}]^{2-}$ (Eq. (2)). In principle, the cyclic amine (hexamethylenetetramine) (HMTA) is capable of coordinating to the Zn^{2+} ion through its nitrogen donors. However, low pH (3.0) is not favorable for such metal–nitrogen bond because the metal–nitrogen bond undergoes facile acid hydrolysis.

$$7[MoO_4]^{2-} + 8H^+ \rightarrow [Mo_7O_{24}]^{6-} + 4H_2O \quad (1)$$

$$[Mo_7O_{24}]^{6-} + [Zn(H_2O)_5]^{2+} + [Zn(H_2O)_4]^{2+} \rightarrow [\{Zn(H_2O)_5\}\{Zn(H_2O)_4\{Mo_7O_{24}\}]^{2-} \quad (2)$$

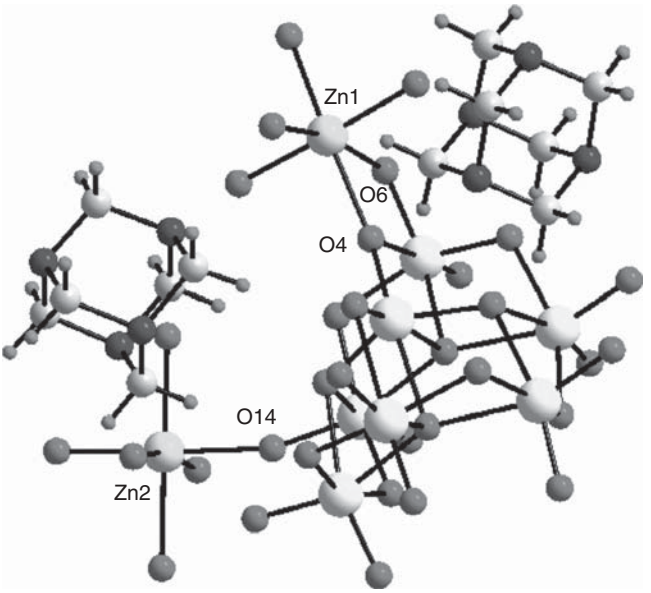

FIGURE 11. The molecular structure of $[HMTAH]_2[\{Zn(H_2O)_5\}\{Zn(H_2O)_4\{Mo_7O_{24}\}] \cdot 2H_2O$ (ball and stick model). *Color code:* O, red; Mo, yellow; C, gray; H, purple; Zn, cyan; N, blue. (Reprinted with permission from ref. 40.)

HMTA is known to be a versatile component in metallo-supramolecular chemistry because of its possible hydrogen bond donor and acceptor sites. On the other hand, the nucleophilic surface of the octamolybdate can act as hydrogen bond acceptor sites. In its crystal structure, four types of hydrogen bonding interactions are expected: N–H···O/O–H···N, O–H···O, C–H···O, and N–H···N. Because the hydrogen atoms on the nitrogen base and the oxygen atoms in the water could not be located, and only one nitrogen of each organic amine is protonated, it would not be possible to distinguish between N–H···O and O–H···N hydrogen bonds around the organic amine cation.

As shown in Figure 12, the heptamolybdate anion is hydrogen bonded to five surrounded zinc–aqua complexes besides two zinc–aqua complexes that are supported by the cluster anion through coordinate covalent bonds. The organic amine cations, $[HMTAH]^+$, use their C–H bonds to form C–H···O hydrogen bonds with surrounding octamolybdate anions. Figure 13 shows that the organic amines "N1N2N3N4" and "N5N6N7N8" in $[HMTAH]_2[\{Zn(H_2O)_5\}\{Zn(H_2O)_4\{Mo_7O_{24}\}] \cdot 2H_2O$ are hydrogen bonded with five and four surrounding heptamolybdate anions, respectively. In addition, the aqua complexes undergo both O–H···O and N–H···O / O–H···N hydrogen bonding interactions with both the surrounding heptamolybdate anion and organic amine cations. The combination of all these supramolecular interactions (N–H···O/O–H···N,

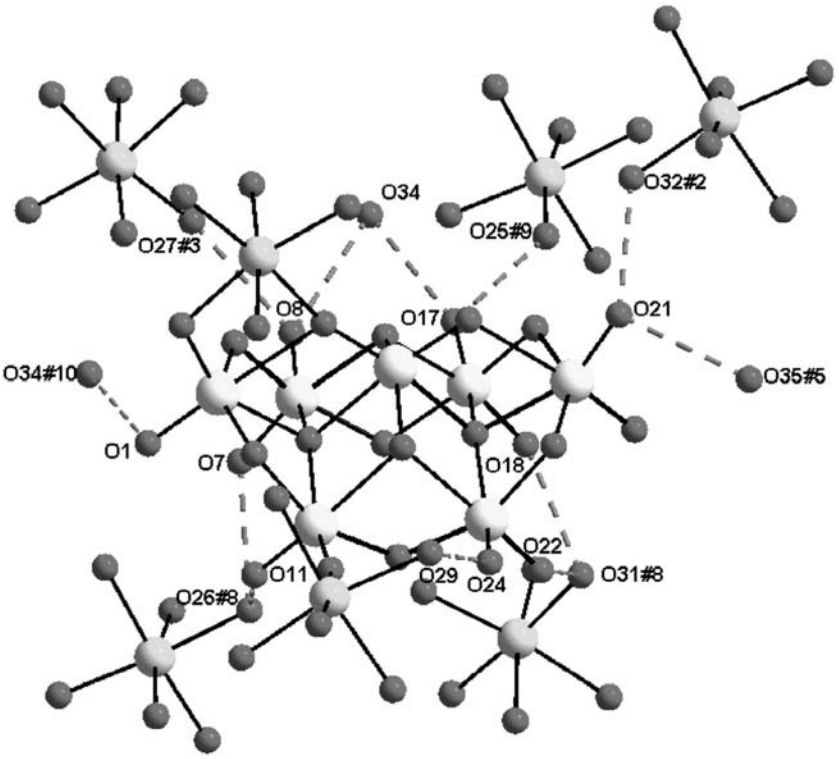

FIGURE 12. The hydrogen bonding situation around the $[Mo_7O_{24}]^{6-}$ cluster anion. *Color code:* O, red; Mo, yellow; C, gray; Zn, cyan. The purple dotted lines represent the O–H · · · O hydrogen bonding interaction. (Reprinted with permission from ref. 40.)

O−H · · · O, C−H · · · O, and N−H · · · N) results in an intricate three-dimensional supramolecular network with a well-defined channels as viewed by looking down to the crystallographic *c* axis (Fig. 14).

Strandberg-type heteropolyanion, formulated as $[X_2Mo_5O_{23}]^{n-}$ ($n = 6$ when $X = P(V)$ and $n = 4$ when $X = S(VI)$), can be viewed as two $\{XO_4\}$ tetrahedrons capping either side of an irregular ring of five $\{MoO_6\}$ octahedra that are linked by one corner-shared and four edge-shared contacts (Fig. 15). The maximum possible symmetry of this anion is, C_2 and the structure is, therefore, dissymmetric. We have reported the optical resolution of this heteropolyanion $[X_2Mo_5O_{23}]^{n-}$ by using the Pfeiffer effect, an effect in which the displacement of a racemate equilibrium occurs in favor of one enantiomer on treatment with an enantiopure optically active compound (known as an environment substance).[41] Wang and co-workers described the transition-metal complexes supported by this class of heteropolyanion—namely, $(H_2bpy)_{0.5}\{[Ni(H_2O)_5][Ni(Hbpy)(H_2O)_4][Mo_5P_2O_{23}]\}$ and $(H_2bpy)0.5\{[Co(H_2O)_5][Co(Hbpy)(H_2O)_4][Mo_5P_2O_{23}]\}$.[42] The novelty of this system lies in the fact that two distinct transition-metal complex cation fragments, $[Ni(H_2O)_5]^{2+}$ and $[Ni(Hbpy)(H_2O)_4]^{3+}$, are supported

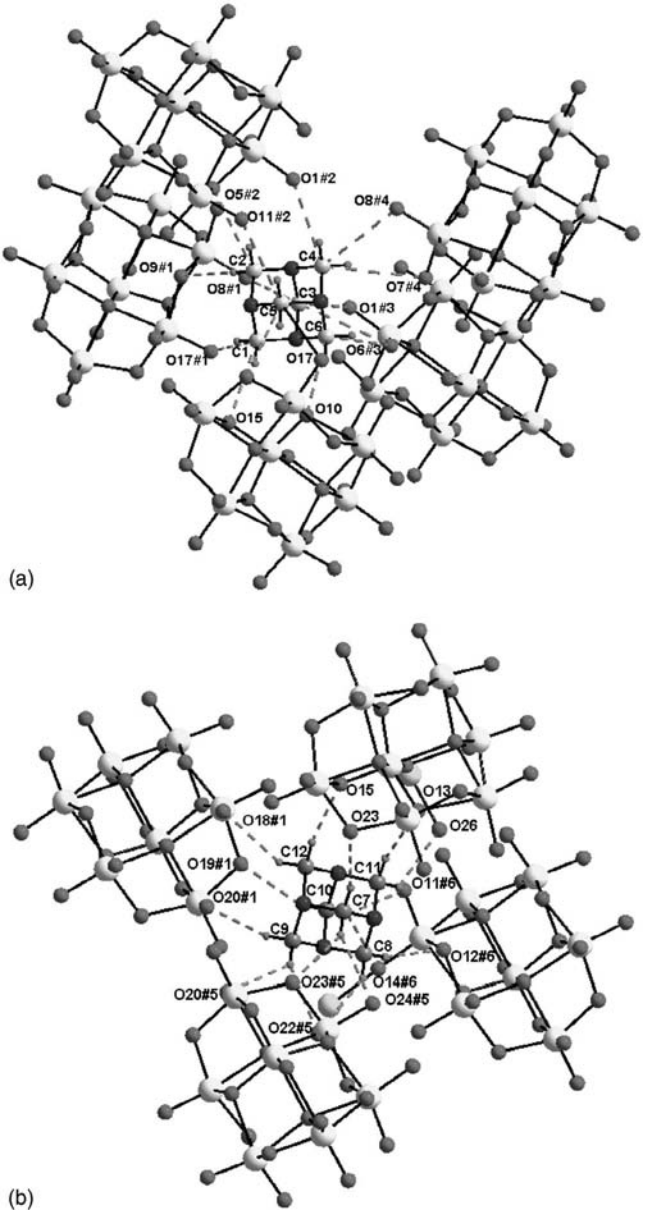

FIGURE 13. The C–H · · · O hydrogen bonding interactions of organic amine cations with a surrounding POM cluster anion. (a) "N1N2N3N4." (b) "N5N6N7N8." *Color code:* O, red; Mo, yellow; C, gray; H, purple; Zn, cyan; N, blue. Purple dotted lines represent the hydrogen bonding interactions.

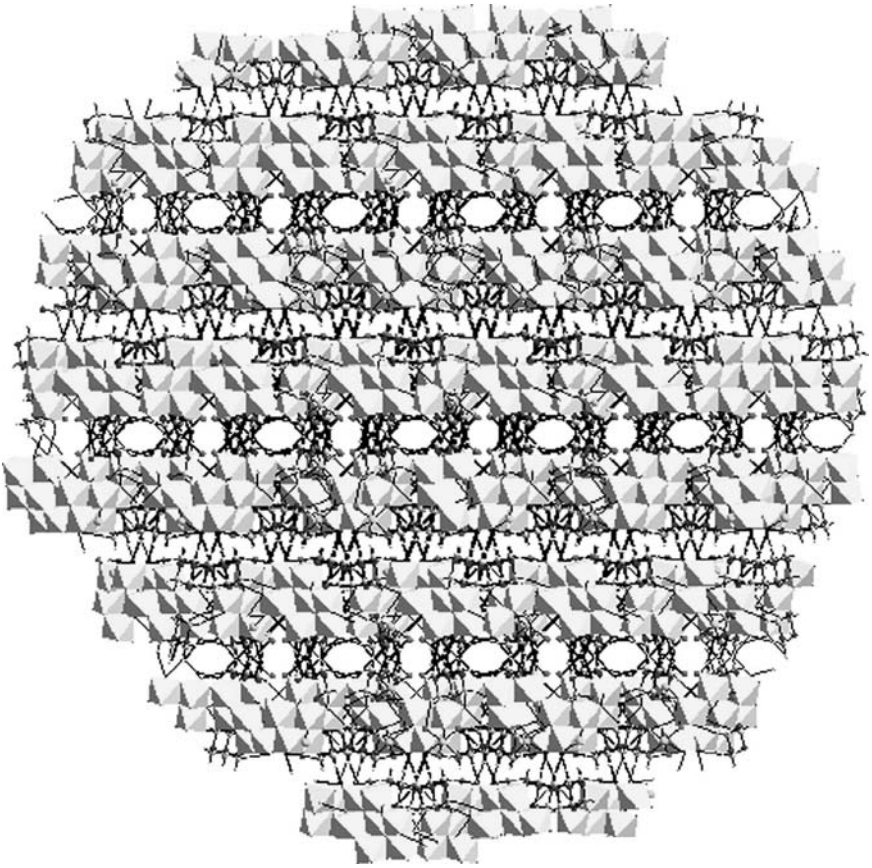

FIGURE 14. Three-dimensional supramolecular network (formed by N–H···O/O–H···N, O–H···O, C–H···O and N–H···N hydrogen bonding interactions) having well-defined channels as viewed by looking down to the crystallographic c axis. (Reprinted with permission from ref. 40.)

on the same diphosphopentamolybdate cluster anion, $[Mo_5P_2O_{23}]^{6-}$, as shown in Figure 16. It is interesting that the bisupporting polyoxometalate clusters of these two compounds form layers via a hydrogen bonding interaction, and these layers are, in turn, parallel-stacked to generate a three-dimensional network with one-dimensional channels (Fig. 17).

During the past several years we have been working on an Anderson-type heteropolyanion, $[Al(OH)_6Mo_6O_{18}]^{3-}$ and exploiting its linking propensity with metal ions–metal complex cations to obtain extended structures of new metal oxide–based materials. We have demonstrated a chain-like extended structure based on an Anderson-type polyanion and a lanthanide cation linker in the compound $[La(H_2O)_7Al(OH)_6Mo_6O_{18}]_n \cdot 4nH_2O$.[43] The structure of this

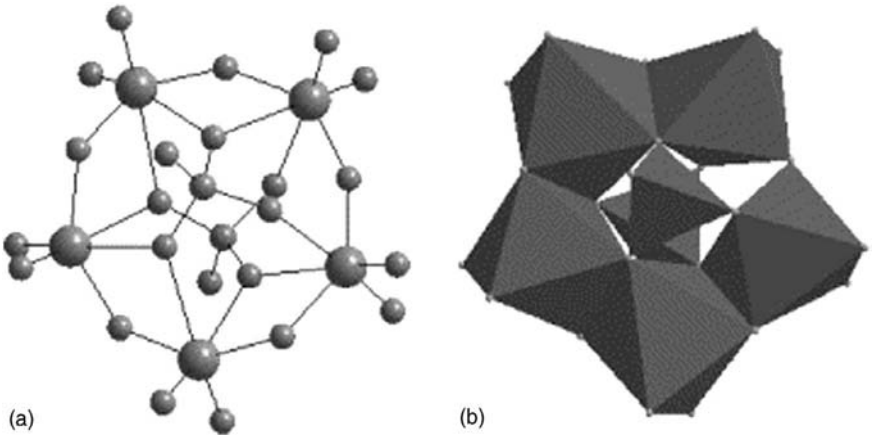

FIGURE 15. (a) Ball and stick model. (b) Polyhedral representation of the Strandberg anion $[S_2Mo_5O_{23}]^{4-}$. (Reprinted with permission from ref. 41.)

compound is formed by Anderson-type anions $[Al(OH)_6Mo_6O_{18}]^{3-}$ linked by La^{3+} cations to yield a polymer chain running parallel to the crystallographic *b* axis (Fig. 18). The structure of the Anderson anion $[Al(OH)_6Mo_6O_{18}]^{3-}$ in this coordination polymer is similar to the structures reported for other Anderson-type anions.[1] This consists of seven edge-shared octahedra, six of which are Mo-octahedra arranged hexagonally around the central octahedron containing hetero metal ion, which is Al^{3+} in the present case (Fig. 18b). In the crystal structure of $[La(H_2O)_7Al(OH)_6Mo_6O_{18}]_n \cdot 4nH_2O$., the molybdenum–oxygen distances can be divided into four groups: molybdenum-terminal oxygen (1.68–1.73 Å), molybdenum-oxygen linked to lanthanum (1.72 Å), molybdenum-bridging oxygen (1.88–1.99 Å), and molybdenum-internal oxygen common to two molybdenum atoms and an aluminium atom (2.26–2.33 Å).

In the polymer chain the Anderson anion acts as a bidentate ligand coordinating two lanthanum(III) ions through the terminal oxygen atoms (Fig. 18) of two nonadjacent MoO_6 octahedra. Along the chain, lanthanum(III) has a coordination number of nine and is in the center of a tricapped-trigonal prism (Fig. 18b) formed by two terminal oxygen atoms from two $[Al(OH)_6Mo_6O_{18}]^{3-}$ units (average La–O 2.604 Å) and by seven water molecules (average La–OH_2 2.546 Å). It is interesting that these $[La(H_2O)_7Al(OH)_6Mo_6O_{18}]_n$ polymeric chains, which are arranged parallel to the crystallographic *b* axis, are linked by an extensive hydrogen bonded network between the zigzag polymer chains (Fig. 18) to a two-dimensional (2D) network and then to a three-dimensional (3D) network by hydrogen-bonded interactions between the zigzag layers (Fig. 19). This extensive hydrogen-bonded network is constructed by the interaction of the water molecules coordinated to the lanthanum ion, the coordinated hydroxide ions of the central $Al(OH)_6$ moiety, and four solvent water molecules, all of which interact with the peripheral terminal and bridging oxygen atoms of the heteropolyanion.

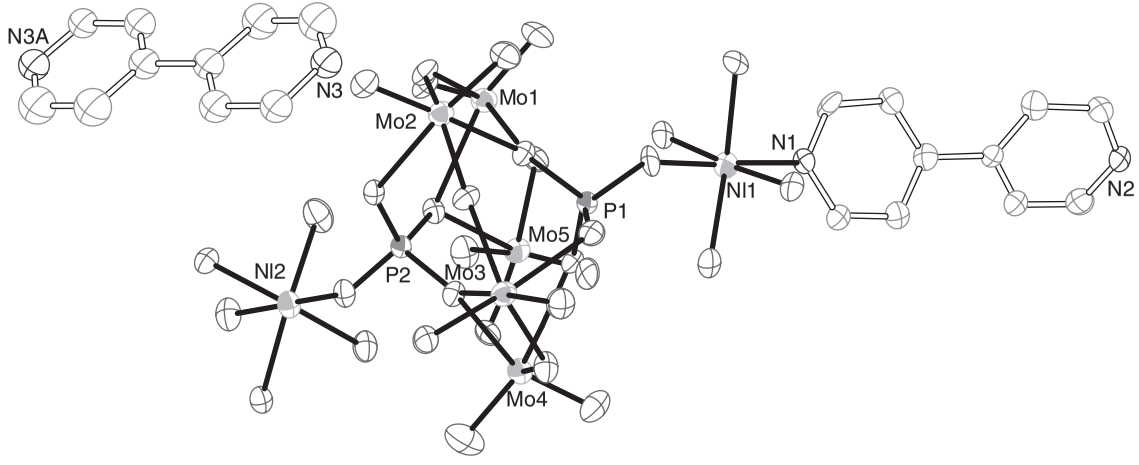

FIGURE 16. Thermal ellispsoidal plot of $(H_2bpy)_{0.5}\{[Ni(H_2O)_5][Ni(Hbpy)(H_2\text{-}O)_4][Mo_5P_2O_{23}]\}$. (Reprinted with permission from ref. 42.)

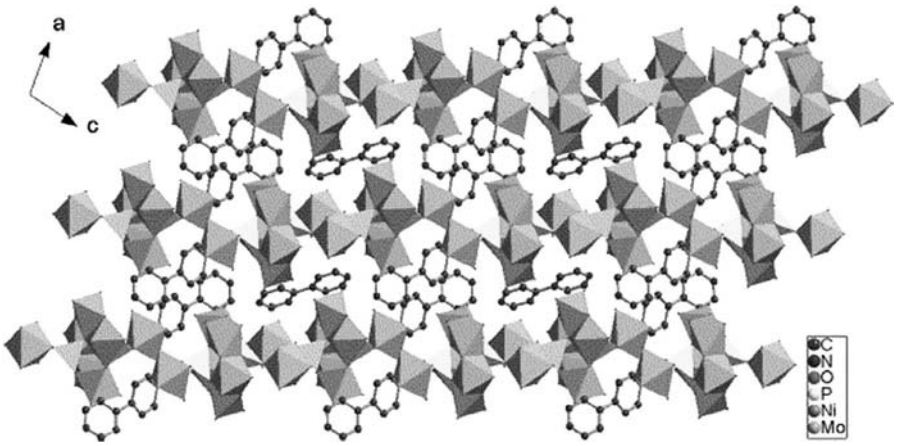

FIGURE 17. Three-dimensional supramolecular network (viewed down the crystallographic *b* axis) in $(H_2bpy)_{0.5}\{[Ni(H_2O)_5][Ni(Hbpy)(H_2\text{-}O)_4][Mo_5P_2O_{23}]\}$. (Reprinted with permission from ref. 42.)

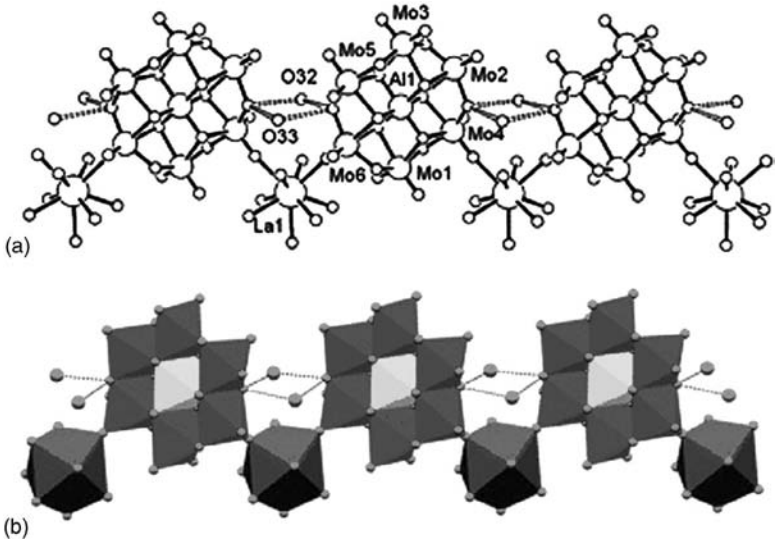

FIGURE 18. (a) An ORTEP representation showing the linked Anderson anions to lanthanum cations in a head-to-tail fashion in compound $[La(H_2O)_7Al(OH)_6\text{-}Mo_6O_{18}]_n \cdot 4nH_2O$. The Anderson anions are additionally linked through hydrogen bonding via O(32) and O(33) waters along the chain. (b) Polyhedral representation of the one-dimensional zigzag chain running parallel to the crystallographic *b* axis. *color code:* La, purple; Mo, blue; Al, cyan; O, red). (Reprinted with permission from ref. 43.)

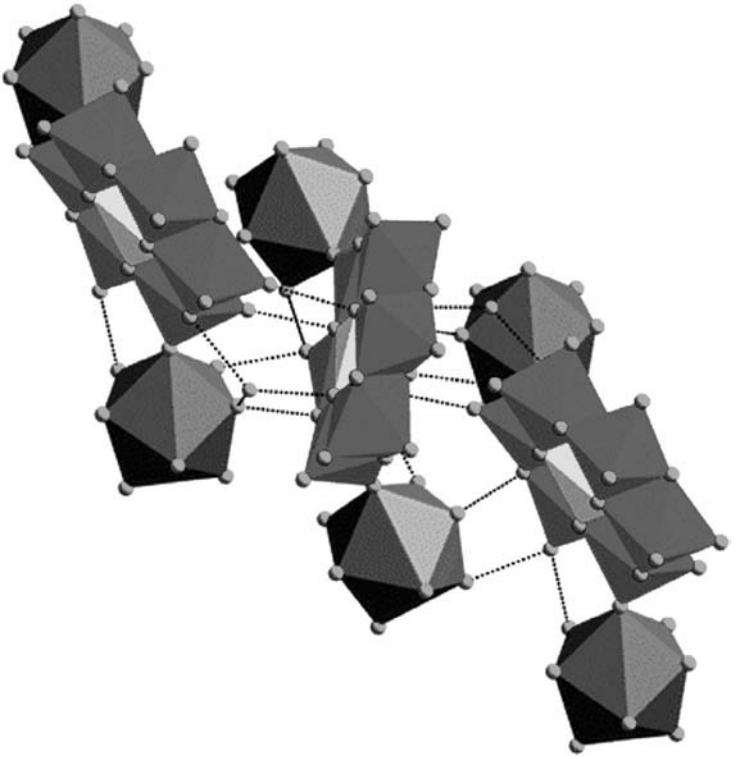

FIGURE 19. Polyhedral representation of $[La(H_2O)_7Al(OH)_6Mo_6O_{18}]_n \cdot 4nH_2O$ showing a supramolecular three-dimensional network, in which lanthanum-Anderson anion chains are interlinked via hydrogen bonding. *Color code:* La, purple; Mo, blue; Al, cyan; O, red. Solvent waters are omitted for clarity. (Reprinted with permission from ref. 43.)

The construction of this material, $[La(H_2O)_7Al(OH)_6Mo_6O_{18}]_n \cdot 4nH_2O$, from well-defined discrete building blocks provides the opportunity to synthesize a new class of one-dimensional (1D) inorganic solids simply by replacing La^{3+} with other rare earth metal ions such as Sm^{3+}, Eu^{3+}, and Gd^{3+}. Krebs and coworkers reported a series of lanthanide Anderson one-dimensional chain compounds of the formula $K_{6n}(TeMo_6O_{24})_n[(Ln(H_2O)_7)_2(TeMo_6O_{24})]_n \cdot 16nH_2O$ (Ln = Eu, Gd) and $K_{3n}[Ln(H_2O)_5(TeMo_6O_{24})]_n \cdot 6nH_2O$ (Ln = Tb, Dy, Ho, Er).[44] They found that the solid-state structures of $Ln/(TeMo_6O_{24})^{6-}$ compounds strongly depend on the lanthanide cations as evidenced by the fact that in the case of Eu^{3+} and Gd^{3+} cations the lanthanides attain ninefold coordination by seven water molecules and two terminal oxygen atoms of the $[TeMo_6O_{24}]^{6-}$ anions (Fig. 20a) resulting in an infinite one-dimensional chain for $[(Ln(H_2O)_7)_2(TeMo_6O_{24})]_n$ of staircase type that has two linkers between two Anderson anions. On the other hand, the Tb^{3+}, Dy^{3+}, Ho^{3+}, and Er^{3+} cations are

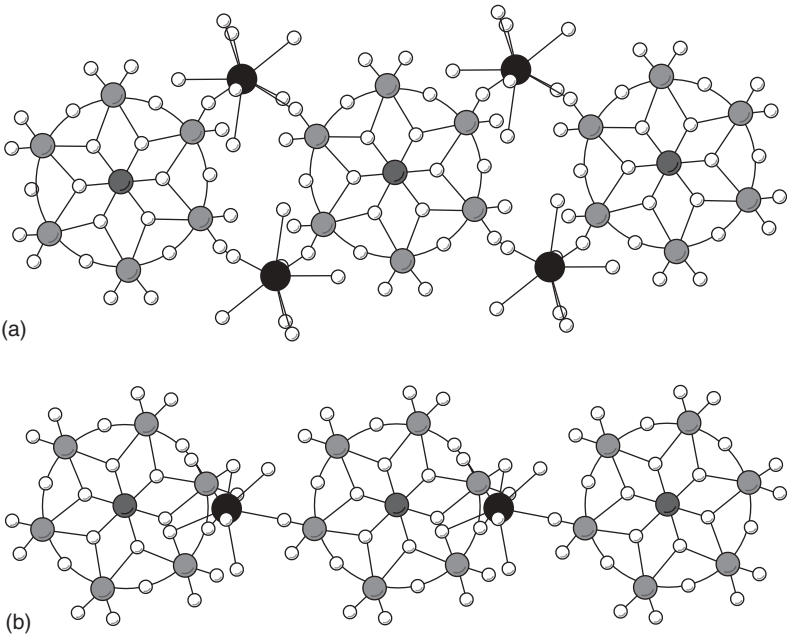

FIGURE 20. Infinite one-dimensional chains of (a) $[(Ln(H_2O)_7)_2(TeMo_6O_{24})]_n$(Ln = Eu, Gd) and (b) $[Ln(H_2O)_5(TeMo_6O_{24})]_n^{3n-}$(Ln = Tb, Dy, Ho, Er). *Color code:* Mo, light gray; Te, middle gray; Ln, dark gray; O, white. (Reprinted with permission from ref. 44.)

coordinated by five water molecules, two terminal oxygen atoms, and one molybdenum-bridging oxygen atom belonging to the $[TeMo_6O_{24}]^{6-}$ anion (Fig. 20b) bringing about anionic chains of $[Ln(H_2O)_5(TeMo_6O_{24})]_n^{3n-}$, in which there is one linker between two $[TeMo_6O_{24}]^{6-}$ anions.

After success with an "f" block metal cation as linker in assembling an Anderson-type heteropolyanion, we attempted to use a "d" block metal complex cation as a connector to assemble this heteropolyanion. We succeeded in connecting this versatile building unit (Anderson-type POM anion) with a Cu(II)-complex ion, $\{Cu^{II}(2,2'\text{-bipy})(H_2O)_2\}^{2+}$, to form a new type of chain in the compound $[Cu^{II}(2,2'\text{-bipy})(H_2O)_2Cl][Cu^{II}(2,2'\text{-bipy})(H_2O)_2Al(OH)_6Mo_6O_{18}]\cdot 4H_2O$.[45] The crystal structure shows that this compound is made up of spiral-type chains with $[Cu^{II}(2,2'\text{-bipy})(H_2O)_2Al(OH)_6Mo_6O_{18}]_n^{n-}$ as anions, chloro-copper complexes, $[Cu^{II}(2,2'\text{-bipy})(H_2O)_2Cl]_n^{n+}$ as cations, and lattice waters. The chain is formed by Anderson anions, $[Al(OH)_6Mo_6O_{18}]^{3-}$, linked to $[Cu^{II}(2,2'\text{-bipy})(H_2O)_2]^{2+}$ complexes as shown in Figures 21 and 22.

In the polymer chain in compound $[Cu^{II}(2,2'\text{-bipy})(H_2O)_2Cl][Cu^{II}(2,2'\text{-bipy})(H_2O)_2Al(OH)_6Mo_6O_{18}]\cdot 4H_2O$, each cluster anion acts as a bidentate ligand coordinating two $\{Cu^{II}(2,2'\text{-bipy})(H_2O)_2\}^{2+}$ complex fragments through the terminal oxygen atoms (Fig. 21) of two nonadjacent MoO_6 octahedra. There

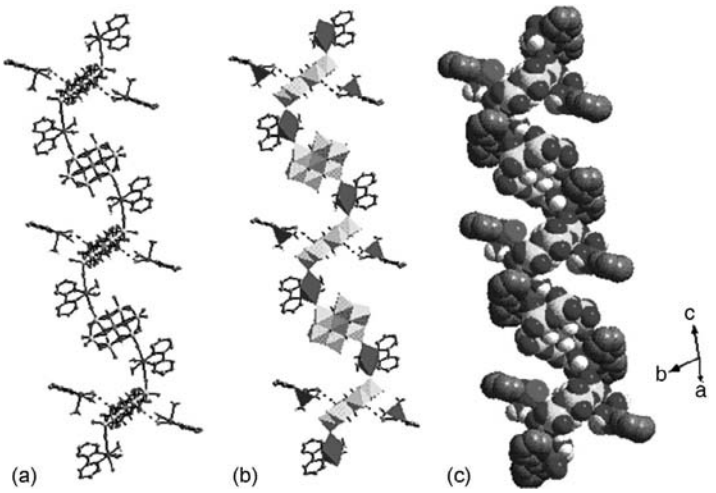

FIGURE 21. The structure of $[Cu^{II}(2,2'\text{-bipy})(H_2O)_2Cl][Cu^{II}(2,2'\text{-bipy})(H_2O)_2Al(OH)_6Mo_6O_{18}]$, showing a spiral-type chainlike array of $\{Al(OH)_6Mo_6O_{18}\}^{3-}$ cluster anions interconnected through $\{Cu^{II}(bipy)(H_2O)_2\}^{2+}$ bridging copper complex fragments. Two chloro-copper complexes are hydrogen bonded, alternatively, to only one type of Anderson anion in the chain. (a) Ball-and-stick representation. (b) Polyhedral representation. (c) Space-filling plot. *Color code:* Al, cyan; Mo, yellow; O, red; Cu, purple; Cl, green; N, blue; C, gray; H, white. (Reprinted with permission from ref. 45.)

are two crystallographically independent copper sites making up two different coordination environments around copper. In the first one, the linker of the chain is a distorted octahedron (Figs. 21 and 22a and c), which is defined by two nitrogen coordinations from the 2,2′-bipyridine ligand (Cu(1)-N(1) = 1.986(3), Cu(1)-N(2) = 1.980(3)), two water ligations (Cu(1)-O(24) = 1.945(3), Cu(1)-O(26) = 1.986(3)), and two *trans* terminal oxygen atoms from two different Anderson anions (Cu(1)-O(6) = 2.738(3), Cu(1)-O(17) = 2.283(3)). The second copper site (Fig. 22b) is coordinated by two nitrogen atoms from 2,2′-bipyridine ligand (Cu(2)-N(3) = 1.989(3), Cu(2)-N(4) = 2.012(4)), two water molecules (Cu(2)-O(27) = 1.960(4), Cu(2)-O(28) = 2.206(3)), and a chloride anion (Cu(2)-Cl(1) = 2.2899(16)) to complete the roughly square pyramidal geometry of $[Cu^{II}(2,2'\text{-bipy})(H_2O)_2Cl]^+$. Two such chloro complexes are always associated with only Al(1) containing an Anderson anion via hydrogen bonding in the chain (Figs. 21 and 22b middle).

The O–H · · · Cl hydrogen bonding interactions of two chloro-copper complex cations with one Anderson anion (alternatively in the chain) instead of each Anderson anion interacting one cation, $[Cu^{II}(2,2'\text{-bipy})(H_2O)_2Cl]^+$, are surprising and unusual. This is possibly the result of optimal crystal packing. Supramolecular analysis of this crystal structure shows that both intrachain and interchain O–H · · · O hydrogen-bonding interactions are present. We believe that the spiral-type structure of the present chain is governed by the proposed

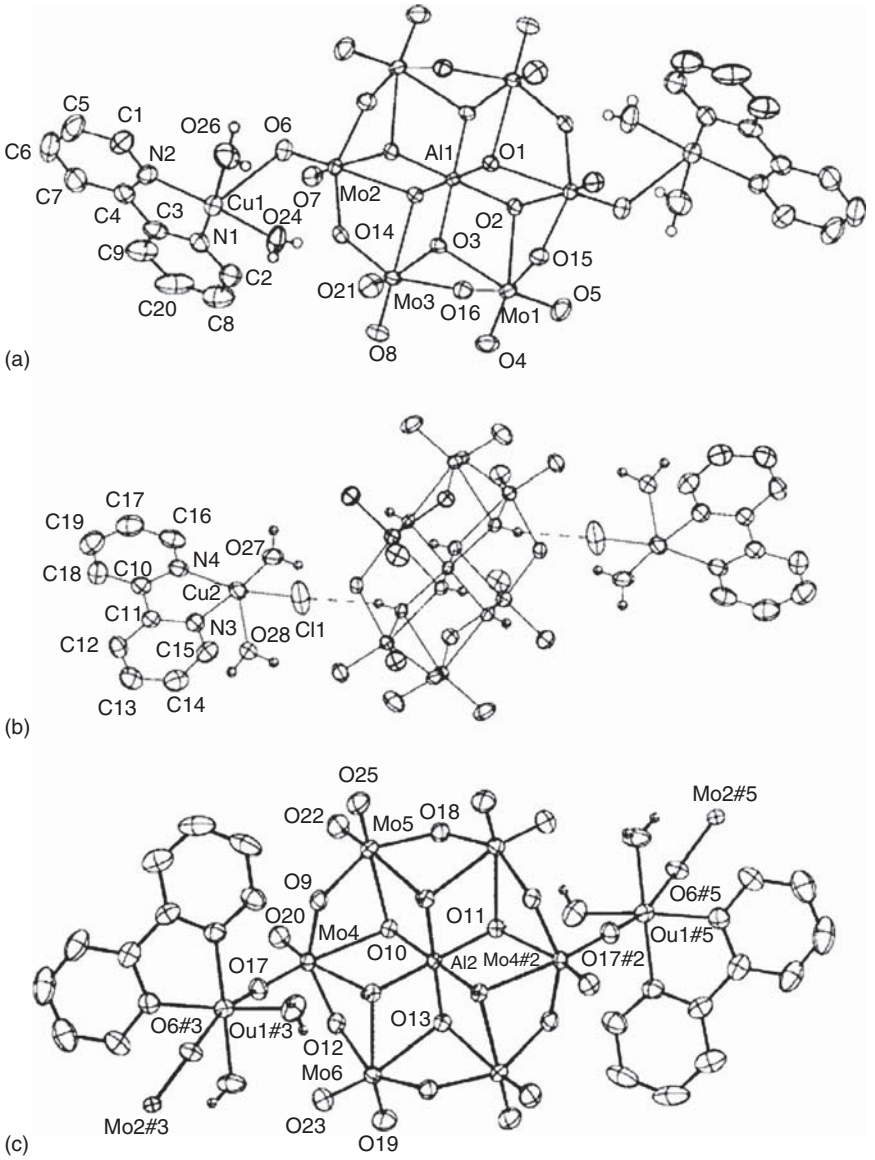

FIGURE 22. (a) Coordination of an Anderson anion via terminal oxygen atoms on molybdenum to $\{Cu(bipy)(H_2O)_2^{2+}\}$ complex fragments in compound $[Cu^{II}(2,2'\text{-bipy})(H_2O)_2Cl][Cu^{II}(2,2'\text{-bipy})(H_2O)_2Al(OH)_6Mo_6O_{18}]\cdot 4H_2O$. (b) Hydrogen-bonding interaction of the cation $\{Cu(bipy)(H_2O)_2Cl\}^{1+}$ via O–H $\cdots$ Cl bonds to the same Anderson anion. (c) Linked Anderson heteropolyanion to $\{Cu(bipy)(H_2O)_2\}^{2+}$ complex fragments resulting in the formation of a chain. Thermal ellipsoid plots with 50% probability (Reprinted with permission from ref. 45.)

interchain hydrogen bonding because this involves a terminal oxygen atom from one Anderson anion and a bridging oxygen atom from other Anderson anion (Figs. 22 and 23). This, in turn, results in two types of orientations of the Anderson anions along the chain. The spiral nature of the chain is also influenced by the (lateral) interchain O–H · · · O hydrogen-bonding interactions. This includes three types of hydrogen bonds. The resulting hydrogen bonding supramolecular network is presented in Figure 23.

In most of the POM-supported transition-metal compounds, the charge of the POM-linked inorganic entity is either neutral or negative; the negative charge in most cases is balanced by transition-metal complex cations. There are few examples of POM-supported metal ions–metal complexes that act as cations with halide, acetate, hydroxyl, and POM anions that counterbalance the positive charges. Such structurally characterized compounds are [ε-$PMo_{12}O_{36}(OH)_4\{La(H_2O)_4\}_4]Br_5 \cdot 16H_2O$,[46] $[Mn^{II}V_6^{IV}O_6\{(OCH_2CH_2)_2N(CH_2CH_2OH)\}_6]Cl_2$,[47] $[Ag_6(PMo_{10}V_2O_{40})](CH_3COO) \cdot 8H_2O$,[48] $[(V^VO_4)Mo^{VI}O_{12}O_{36}(V^{IV}O)_6][(OH)_9] \cdot 16H_2O$,[49] K_3[ε-$PMo_{12}O_{36}(OH)_4\{La(H_2O)_{4.25}Cl_{0.75}\}_4$][α-$PMo_{12}O_{40}] \cdot 28H_2O$,[46] and $[NH_4]_2[\{Gd(DMF)_7\}_2(Mo_8O_{26})][Mo_8O_{26}]$.[50]

However, the examples in which POM-supported transition metal complexes act both as cation and anion (as ion pair components) are very scarce in the literature. Two such reported compounds are $\{[Ni(phen)_2(H_2O)]_2[Ni(phen)_2][V_8^{IV}Mo_6^{VI}Mo_2^VO_{40}(PO_4)]\}$ $\{[Ni(phen)_2(H_2O)]_2[V_8^{IV}Mo_6^{VI}Mo_2^VO_{40}(PO_4)_2]\} \cdot 5H_2O \cdot 2EtOH$[51] and $[PMo_6^{VI}Mo_2^VV_8^{IV}O_{44}\{Co(2,2'\text{-bpy})_2(H_2O)\}_4][PMo_4^{IV}Mo_4^VV_8^{IV}O_{44}\{Co(2,2'\ bpy)_2(H_2O)\}_2] \cdot 4H_2O$.[27] In the former compound, the charge difference (of one) between the two ion pairs became possible because of the different numbers of phosphate anions present in the cation and anion. In the latter compound, the difference in the oxidation states of molybdenum in the cation and anion makes the charge difference. In both compounds, a Keggin-type POM anion has been used to support the transition metal complexes.

We have recently established a unique example in which a ''discrete'' Anderson-type heteropolyanion-supported copper phenanthroline complex was obtained by varying its coordination mode from ''water'' to ''chloride'', which can act both as cation and anion in the same compound.[52] The following two compounds exhibit such charge complementarity: $[Al(OH)_6Mo_6O_{18}\{Cu(phen)(H_2O)_2\}_2][Al(OH)_6Mo_6O_{18}\{Cu(phen)(H_2O)Cl\}_2] \cdot 5H_2O$ and $[Cr(OH)_6Mo_6O_{18}\{Cu(phen)(H_2O)_2\}_2][Cr(OH)_6Mo_6O_{18}\{Cu(phen)(H_2O)Cl\}_2] \cdot 5H_2O$. These two compounds have been synthesized by a procedure similar to that of the compound $[Cu^{II}(2,2'\text{-bipy})(H_2O)_2Cl][Cu^{II}(2,2'\text{-bipy})(H_2O)_2Al(OH)_6Mo_6O_{18}] \cdot 4H_2O$, discussed earlier. We believe that changing the organic ligand from bipyridine to *o*-phenanthroline results in the formation of a discrete charge complementariy system instead of the chain-like arrangements in $[Cu^{II}(2,2'\text{-bipy})(H_2O)_2Cl][Cu^{II}(2,2'\text{-bipy})(H_2O)_2Al(OH)_6Mo_6O_{18}] \cdot 4H_2O$. We have isolated compounds $[Al(OH)_6Mo_6O_{18}\{Cu(phen)(H_2O)_2\}_2][Al(OH)_6Mo_6O_{18}\{Cu(phen)(H_2O)Cl\}_2] \cdot 5H_2O$ and $[Cr(OH)_6Mo_6O_{18}\{Cu(phen)(H_2O)_2\}_2][Cr(OH)_6Mo_6O_{18}\{Cu(phen)(H_2O)Cl\}_2] \cdot 5H_2O$ using a simple wet synthesis. The synthesis is performed in a mixed aqueous-organic medium. The following synthesis scheme

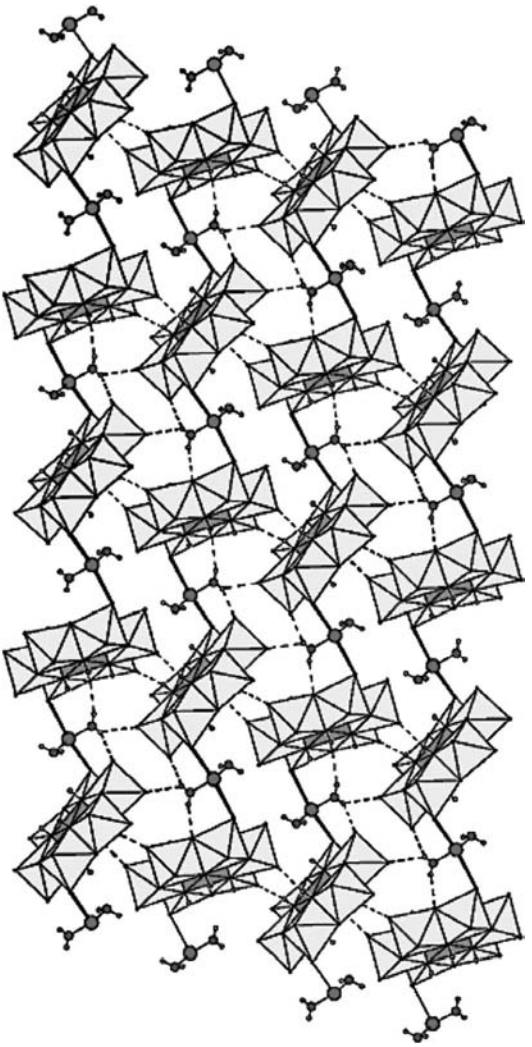

FIGURE 23. The extensive supramolecular network involving intrachain and interchain O–H · · · O hydrogen bonding in the compound $[Cu^{II}(2,2'\text{-bipy})(H_2O)_2Cl][Cu^{II}(2,2'\text{-bipy})(H_2O)_2Al(OH)_6Mo_6O_{18}] \cdot 4H_2O$. The Anderson anions are shown in polyhedral representation. *Color code:* Al, cyan; Mo, yellow; O, red; Cu, purple; H, white circle. The bipyridine ligands, coordinated to Cu(II) linkers, are not shown here for clarity (Reprinted with permission from ref. 45.)

(Eqs. (3) to (7)) for the formation of these compounds ($C_{12}H_8N_2$ = 1,10′-phenanthroline = phen) is proposed.

$$[MoO_4]^{2-} + M^{3+}(M = Al, Cr) + H^{1+} \rightarrow [M(OH)_6Mo_6O_{18}]^{3-} \qquad (3)$$

$$Cu^{2+} + \text{phen} + H_2O/\text{organic solvent} \rightarrow [Cu(\text{phen})(H_2O)_n(\text{organic solvent})_{4-n}]^{2+} \quad (4)$$

$$2[Cu(\text{phen})(H_2O)_n(\text{organic solvent})_{4-n}]^{2+} + [M(OH)_6Mo_6O_{18}]^{3-} \rightarrow [M(OH)_6Mo_6O_{18}\{Cu(\text{phen})(H_2O)_2\}_2]^{1+}(1c/2c) + 2H_2O/\text{organic solvent} \quad (5)$$

$$2[Cu(\text{phen})(H_2O)_n(\text{organicsolvent})_{4-n}]^{2+} + [M(OH)_6Mo_6O_{18}]^{3-} + 2Cl^{1-} \rightarrow [M(OH)_6Mo_6O_{18}\{Cu(\text{phen})(H_2O)Cl\}_2]^{1-}(1a/2a) + 3H_2O/\text{organic solvent} \quad (6)$$

$$[M(OH)_6Mo_6O_{18}\{Cu(\text{phen})(H_2O)_2\}_2]^{1+} + [M(OH)_6Mo_6O_{18}\{Cu(\text{phen})(H_2O)Cl\}_2]^{1-} + 5H_2O \rightarrow [M(OH)_6Mo_6O_{18}\{Cu(\text{phen})(H_2O)_2\}_2][M(OH)_6Mo_6O_{18}\{Cu(\text{phen})(H_2O)Cl\}_2] \cdot 5H_2O \quad (7)$$

We have used MCl_3 ($M = Al^{3+}$ and Cr^{3+}) in aqueous sodium molybdate solution to generate in situ the Anderson-type heteropolyanion, $[M(OH)_6Mo_6O_{18}]^{3-}$ (Eq. (3)). The isolated compounds contain monophenanthroline copper complexes; thereby, the formation of a solvated monophenanthroline copper complex is proposed (Eq. (4)). The reaction of the Anderson heteropolyanion with two equivalents of solvated monophenanthroline copper complex produces the cationic components **1c** and **2c** (Eq. (5)), and the reaction of the Anderson anion with the solvated monophenanthroline copper complex and chloride anion in a 1:2:2 ratio results in the formation of the anionic components **1a** and **2a** (Eq. (6)) of the ionpair complexes $[Al(OH)_6Mo_6O_{18}\{Cu(\text{phen})(H_2O)_2\}_2][Al(OH)_6Mo_6O_{18}\{Cu(\text{phen})(H_2O)Cl\}_2] \cdot 5H_2O$ and $[Cr(OH)_6Mo_6O_{18}\{Cu(\text{phen})(H_2O)_2\}_2][Cr(OH)_6Mo_6O_{18}\{Cu(\text{phen})(H_2O)Cl\}_2] \cdot 5H_2O$, respectively. In the final (ion pairing) step (Eq. (7), each of the ion pair compounds crystallizes with five water molecules. The crystal structure of $[Al(OH)_6Mo_6O_{18}\{Cu(\text{phen})(H_2O)_2\}_2][Al(OH)_6Mo_6O_{18}\{Cu(\text{phen})(H_2O)Cl\}_2] \cdot 5H_2O$ shows the abundance of a polyoxometalate-supported copper(II)-bis(aqua)-phenanthroline complex, $[Al(OH)_6Mo_6O_{18}\{Cu(\text{phen})(H_2O)_2\}_2]^{1+}$, as a cation and the same polyoxometalate-supported copper(II)-aqua-chloro-phenanthroline complex, $[Al(OH)_6Mo_6O_{18}Cu(\text{phen})(H_2O)C]\}_2]^{1-}$, as an anion (Fig. 24).

The cationic POM-supported copper complex is formed by an Anderson-type anion $[Al(OH)_6Mo_6O_{18}]^{3-}$ coordinated to two $[Cu(\text{phen})(H_2O)_2]^{2+}$ complexes through the terminal oxygen atoms of two nonadjacent MoO_6 octahedra. Similarly, the coordination of $[Al(OH)_6Mo_6O_{18}]^{3-}$ to two $[Cu(\text{phen})(H_2O)Cl]^{1+}$ results in the formation of the anion, $[Al(OH)_6Mo_6O_{18}Cu(\text{phen})(H_2O)Cl\}_2]^{1-}$. As in the structures of other Anderson anions, the present cluster anion $[Al(OH)_6Mo_6O_{18}]^{3-}$ has a B-type Anderson structure consisting of seven edge-shared

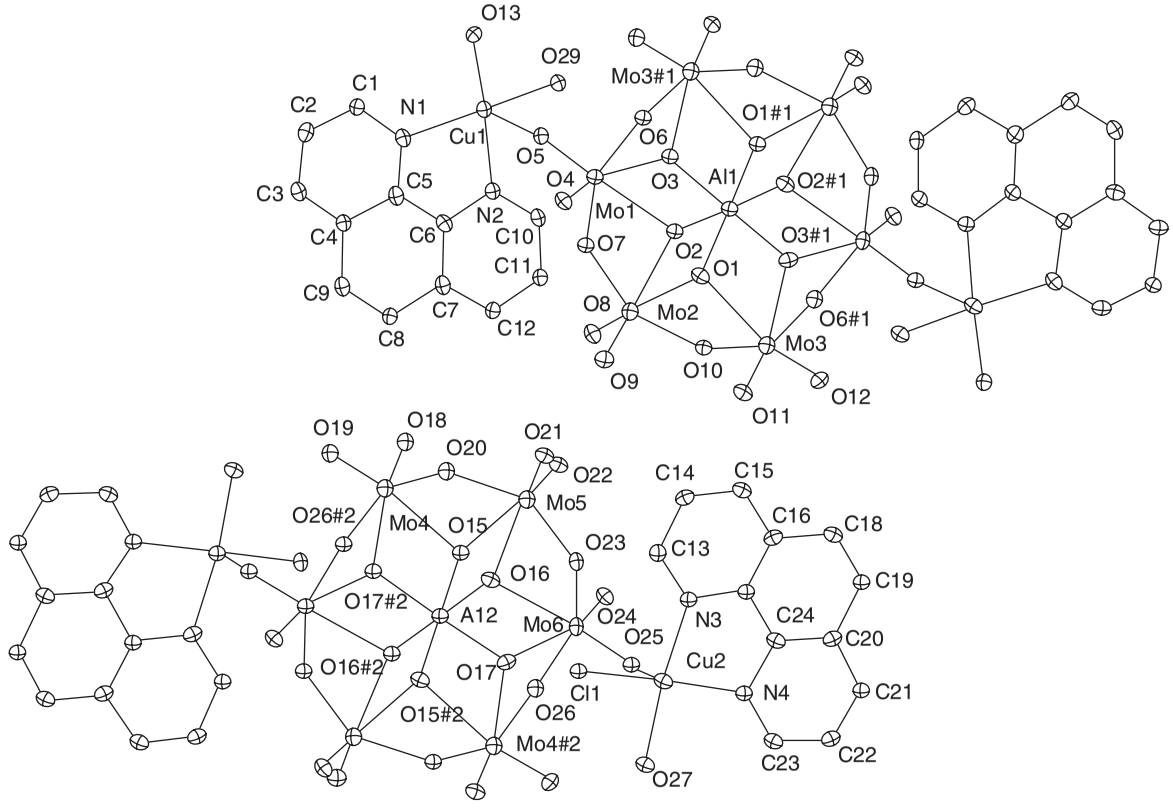

FIGURE 24. Thermal ellipsoidal plots: (a) the cation $[Al(OH)_6Mo_6O_{18}\{Cu(phen)(H_2O)_2\}_2]^{+}$, (b) the anion $[Al(OH)_6Mo_6O_{18}\{Cu(phen)(H_2O)Cl\}_2]^{1-}$. (Reprinted with permission from ref. 52.)

octahedra, six of which are Mo octahedra arranged hexagonally around the central Al^{3+} octahedron (Fig. 24). The hydrogen atoms of the hydroxyl groups around the Al^{3+} ions are located from difference Fourier maps, and their positions were refined.

In the complex cation $[Al(OH)_6Mo_6O_{18}\{Cu(phen)(H_2O)_2\}_2]^{1+}$, the copper is coordinated by two nitrogen atoms from phenanthroline ligand (Cu(1)-N(1) = 1.991(3) Å, Cu(1)-N(2) = 2.003(3) Å), two water molecules (Cu(1)-O(13) = 2.000(2) Å, Cu(1)-O(29) = 1.975(2) Å), and a terminal oxygen atom from the Anderson anion (Cu(1)-O(5) = 2.2490(19) Å) to complete a roughly square pyramidal geometry around the copper. Similarly, in the case of anion $[Al(OH)_6Mo_6O_{18}Cu(phen)(H_2O)Cl\}_2]^{1-}$, the copper square pyramid is defined by two nitrogen coordinations from the phenanthroline ligand (Cu(2)-N(3) = 2.001(3) Å, Cu(2)-N(4) = 2.002(2) Å), one water ligation (Cu(2)-O(27) = 1.983(2) Å), one chloride coordination (Cu(2)-Cl(1) = 2.2636(8) Å), and one terminal oxygen atom from the Anderson anion (Cu(2)-O(25) = 2.253(2) Å) (Fig. 24). In both cases, the terminal oxygen atom (from the Anderson anion) occupies the apical position. In the cation and anion, the copper ions are well separated with a Cu(1)$\cdots$Cu(1) distance of 12.51 Å in the cation and a Cu(2)$\cdots$Cu(2) distance of 11.28 Å in the anion. A relatively shorter distance (8.09 Å) between Cu(1) (of the cation) and Cu(2) (of the anion) manifests the intermolecular interactions, as shown in Figure 25. Indeed, Cu(1) (of the cation) and Cu(2) (of the anion) interact via hydrogen bonding interactions involving lattice waters and copper-coordinated water molecules, which results in a three-dimensional supramolecular network (Fig. 25).

The room-temperature ESR spectrum of $[Al(OH)_6Mo_6O_{18}\{Cu(phen)(H_2O)_2\}_2][Al(OH)_6Mo_6O_{18}\{Cu(phen)(H_2O)Cl\}_2]\cdot 5H_2O$ shows the axial feature (as expected for a square-pyramidal Cu^{2+} center) with $g\perp = 2.29$ and $g\perp = 2.08$. At liquid nitrogen temperature, the spectrum remains same. Even though two different copper complexes, $[Al(OH)_6Mo_6O_{18}\{Cu(phen)(H_2O)_2\}_2]^{1+}$ and $[Al(OH)_6Mo_6O_{18}Cu(phen)(H_2O)Cl\}_2]^{1-}$ (which differ in the chloride and water coordinations to the copper centers) are present in compound, $[Al(OH)_6Mo_6O_{18}\{Cu(phen)(H_2O)_2\}_2][Al(OH)_6Mo_6O_{18}\{Cu(phen)(H_2O)Cl\}_2]\cdot 5H_2O$, a single average ESR spectrum appears in its solid-state instead of a complex feature from two different complexes. This could be the result of the weak O–H$\cdots$O type hydrogen-bond interactions between two different copper centers (Cu(1) and Cu(2) (Fig. 25) from the cation and the anion, respectively, throughout the crystal lattice in its solid state.

Thus far, it has been demonstrated that Anderson-type POM anions can support "d-block" transition metal coordination complexes that result in both discrete entities and infinite chain-like arrangements and "f-block" complex cations form versatile one-dimensional chains. "S" block metal cation (e.g., Na^+) can also serve as a potential linker for assembling Anderson-type heteropolyanions, as described next.

A three-dimensional coordination polymer, $Na_3(H_2O)_6[Al(OH)_6Mo_6O_{18}]\cdot 2H_2O$, was isolated when we cooked an acidified aqueous solution of $AlCl_3$ with

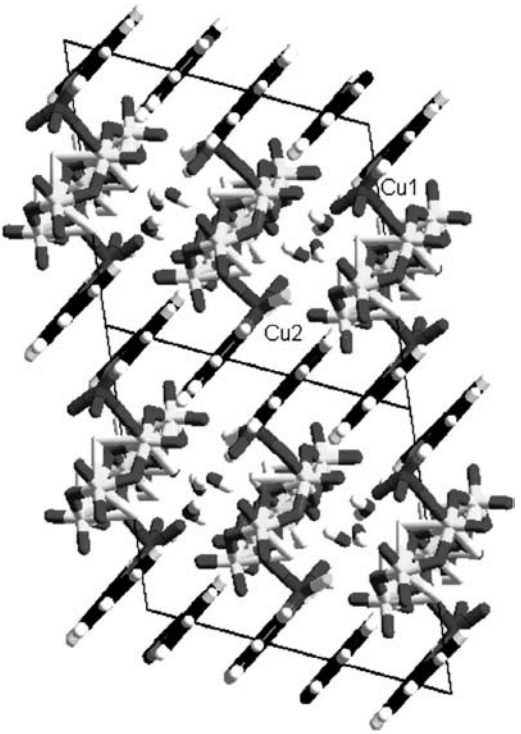

FIGURE 25. Packing diagram (wire-frame representation) of $[Al(OH)_6Mo_6O_{18}\{Cu(phen)(H_2O)_2\}_2][Al(OH)_6Mo_6O_{18}\{Cu(phen)(H_2O)Cl\}_2]\cdot 5H_2O$ (4×4 cells). Cu(1) is from the cation, and Cu(2) is from the anion. *Color code:* Al, cyan; Mo, yellow; O, red; Cu, blue; N, purple; Cl, green; C, dark gray; H, white (Represented with permission from ref. 52.)

sodium molybdate.[53,54] The relevant crystallographic unit cell contains 1.5 molecules as an asymmetric unit (Fig. 26). This shows the coordination environment of the Anderson anion $[Al(OH)_6Mo_6O_{18}]^{3-}$, which coordinates the sodium cation via the Mo = O terminal oxygen atoms.

The crystal structure of $Na_3(H_2O)_6[Al(OH)_6Mo_6O_{18}] \cdot 2H_2O$ shows a three-dimensional framework having "sinuous" channels (Fig. 27), which are constructed by Anderson-type anions as building blocks sharing sodium cations (Fig. 26). The three-dimensional framework is formed by a stacking of two-dimensional layers (Fig. 28a) that are linked laterally by sodium–water chains running in between these layers (Fig. 28b) through the coordination of Mo = O terminal oxygen atoms of Anderson anions. In the layer (Fig. 28a), each polyanion acts as a hexadentate ligand coordinating four Na ions around the anion through six terminal oxygen atoms of four $\{MoO_4(OH)_2\}$ octahedra. The coordination site of each Na ion in the layer (Fig. 28a) is a distorted octahedron formed by two terminal oxygen atoms in *trans* (axial) positions from

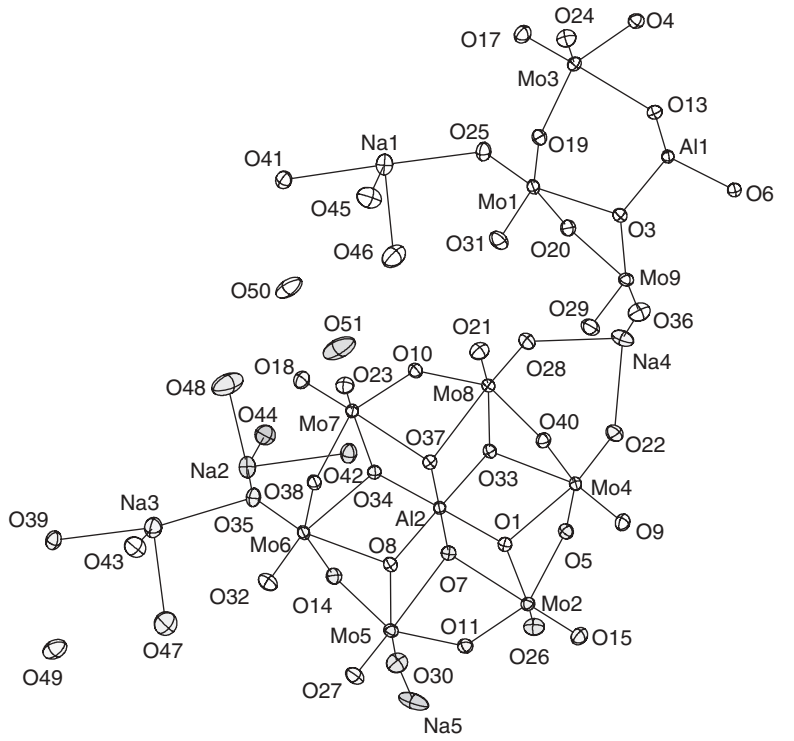

FIGURE 26. Asymmetric unit (as 1.5 molecules) in $Na_3(H_2O)_6[Al(OH)_6Mo_6O_{18}] \cdot 2H_2O$. Sodium coordination of the Anderson anion via terminal oxygen atoms on molybdenum is shown. Thermal ellipsoids at 50% probability. (Represented with permission from ref. 54.)

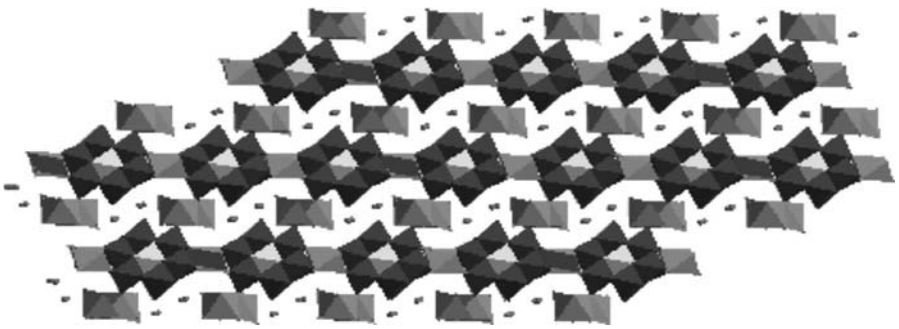

FIGURE 27. View of the ''sinuous'' channels occupied by the guest lattice water molecules in a three-dimensional polymer framework of $Na_3(H_2O)_6[Al(OH)_6Mo_6O_{18}] \cdot 2H_2O$.

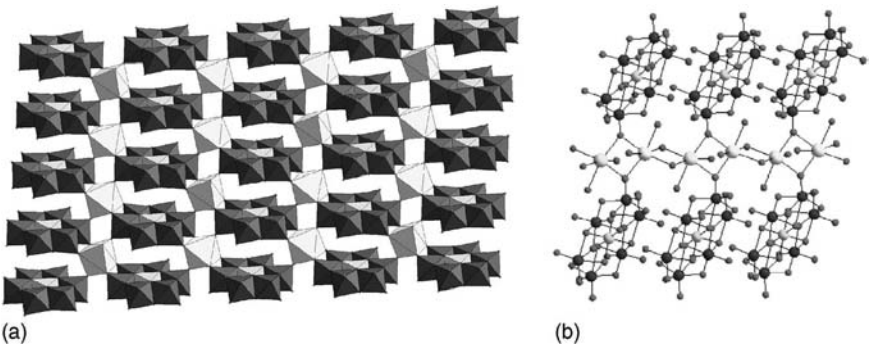

FIGURE 28. (a) Layer type of network formed by sodium octahedra and Anderson anions. (b) Sodium–water chain supported by the Anderson anions. (Represented with permission ref. 54.)

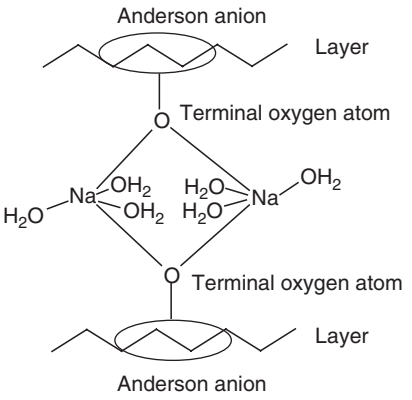

SCHEME 1

two Anderson anion units, and the equatorial positions of the octahedron are coordinated by four terminal oxygen atoms from the two different Anderson anions.

The sodium–water chain (Fig. 28b) can be thought to be formed as follows: two terminal oxygen atoms of two different Anderson anions from the respective layers bridge two sodium ions, each of which is additionally coordinated to three water molecules making them coordinately unsaturated (i.e., penta-coordinated sodium ions, Scheme **1**). The coordination saturation of each sodium ion is then achieved by interlinking of these dimers via a μ_2-type aqua bridge, thereby leading to a one-dimensional sodium chain, which runs between these layers (Scheme **2**). Along the chain, each sodium is octahedrally coordinated and shares two edges from two opposite sides (2O and $2H_2O$, respectively, Fig. 28b and Scheme **2**).

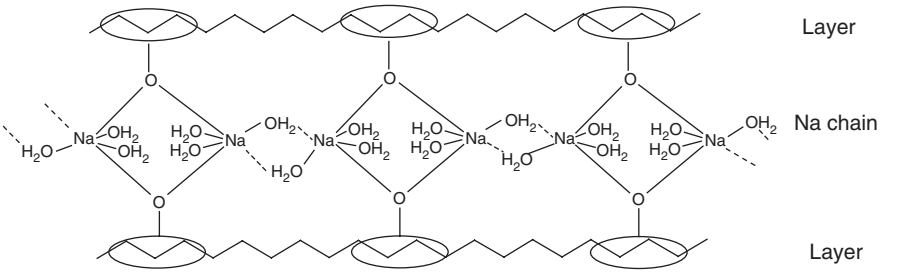

SCHEME 2

III. POLYOXOMETALATE CROWN ETHER COMPLEXES WITH SUPRAMOLECULAR CATIONS

Crown ethers have been extensively used in supramolecular chemistry because of their potential applications in molecular recognition, transportation, and catalysis.[55] The uniqueness of crown ethers lies in the fact that the hydrophilic cavity of a crown ether can selectively recognize an ion by electrostatic interaction based on the size compatibility between the guest ion and host cavity.[56–58] This selective recognition results in the formation of supramolecular cation structure. A simple example of such a supramolecular cation is NH_4^+([18]crown-6), which is formed by selective encapsulation of ammonium ion by the crown ether [18]crown-6 in which three crown ether oxygens form three N–H $\cdots$ O hydrogen bonds with three hydrogen atoms of the ammonium ion, thereby achieving a stable supramolecular cation.[22] The introduction of a POM anion into a matrix of such crown ether–based supramolecular cation has attracted special attention and opened a new field in the area of POM chemistry. The importance of this new area can be realized not only by the fact that the crown ethers, supported by POM cluster anions, can be used to separate specific metal ions (that depend on the cavity size of the concerned crown ether) from aqueous solutions by precipitation methods[59,60] but also that this represents an effective route for stabilizing unusual supramolecular structures that are otherwise not known.[61] One such unusual paradigm is a fivefold coordination of water molecules around copper(II) ion. The hydrated copper(II) complex was originally described as the octahedrally solvated Cu(II) ion, $[Cu(H_2O)_6]^{2+}$ from numerous spectroscopic investigations. However, this generally accepted picture became no longer true when Pasquarello and coworkers reported their combined experimental and theoretical investigation on the structure and dynamics of the hydrated copper(II) complex in aqueous solution.[62] They determined the structure of the hydrated copper(II) complex by both neutron diffraction and first-principles molecular dynamics, and their results favor a fivefold coordination around copper, $[Cu(H_2O)_5]^{2+}$.

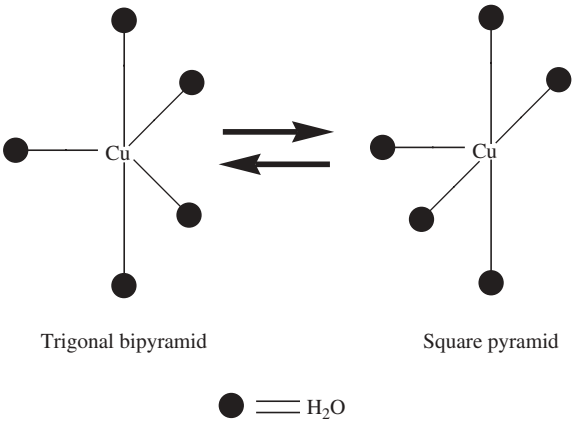

SCHEME 3

From the energy point of view, the solvated complex $[Cu(H_2O)_5]^{2+}$ undergoes frequent transformations between square pyramidal and trigonal bipyramidal (TBP) configurations by a Berry twists mechanism[63–65](Scheme **3**).

A fivefold coordination of water molecules around Cu^{2+} ion in a TBP geometry is one of the possible conformations according Pasquarello et al. However, a crystal structure evidence of a TBP-$[Cu(H_2O)_5]^{2+}$ was lacking for confirming its existence unambiguously until we reported the crystal structure of a "supramolecular sandwich," consisting of two crown ethers (18-crown-6), that stabilizes a TBP-$[Cu(H_2O)_5]^{2+}$ complex cation with a polyoxomolybdate anion $[Mo_6O_{19}]^{2-}$ in the compound $[Cu(H_2O)_5(C_{12}H_{24}O_6)_2][Mo_6O_{19}]$. The reaction of $[Bu_4N]_2[Mo_6O_{19}]$ with $C_{12}H_{24}O_6$ (crown ether) and $Cu(NO_3)_2 \cdot 3H_2O$ in MeCN/CH_3COOH results in the isolation of $[Cu(H_2O)_5(C_{12}H_{24}O_6)_2][Mo_6O_{19}]$ in good yield according to the following reaction:

$$Cu(NO_3)_2{\cdot}3H_2O + 2C_{12}H_{24}O_6 + [Bu_4N]_2[Mo_6O_{19}] + 2H_2O \rightarrow [Cu(H_2O)_5(C_{12}H_{24}O_6)_2][Mo_6O_{19}] + 2[Bu_4N]NO_3 \quad (8)$$

The crystal structure of $[Cu(H_2O)_5(C_{12}H_{24}O_6)_2][Mo_6O_{19}]$ consists of $[Cu(H_2O)_5(C_{12}H_{24}O_6)_2]^{2+}$ as a cation and $[Mo_6O_{19}]^{2-}$ as an anion, as shown in Figure 29. In the isopolyanion $[Mo_6^{VI}O_{19}]^{2-}$ (also known as Lindqvist type polyoxometalate anion), each Mo atom is surrounded by a distorted octahedron consisting of one central O_c, one terminal O_t and four bridging O_b atoms (Figure 29).

In the isopolyanion $[Mo_6^{VI}O_{19}]^{2-}$ (also known as a Lindqvist-type polyoxometalate anion), each Mo atom is surrounded by a distorted octahedron consisting of one central O_c, one terminal O_t, and four bridging O_b atoms (Fig. 29). In the crystal structure, the atypical trigonal bipyramidal TBP-$[Cu(H_2O)_5]^{2+}$ ion is

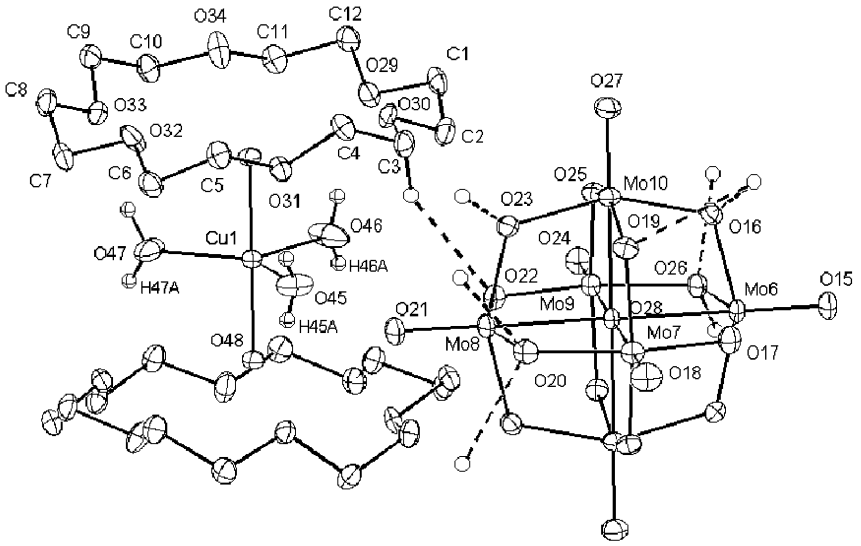

FIGURE 29. Thermal ellipsoidal plot of $[Cu(H_2O)_5(C_{12}H_{24}O_6)_2][Mo_6O_{19}]$. The crown ethers hydrogen atoms are not shown for clarity. The oxygen atoms (O(16), O(19), O(20), O(22) and O(26)) of the isopolyanion $[Mo_6O_{19}]^{2-}$, which are attached to the hydrogen atoms (white circles) of surrounding crown ethers (shown in dotted lines), are involved in C−H · · · O hydrogen bonding interactions (see also Scheme **4** and Fig. 30 in the context of molecular clipping). (Reprinted with permission from ref. 61.)

flawlessly sandwiched by two crown ether molecules via O−H · · · O hydrogen bonding interactions (Fig. 30). The exactness of the supramolecular sandwich is clearly manifested in its top/bottom view (one-to-one crown ethers) when viewed down to the crystallographic *b* axis, as shown in Figure 30c. The local molecular structure of $[Cu(H_2O)_5]^{2+}$ in the supramolecular sandwich species $[Cu(H_2O)_5(C_{12}H_{24}O_6)_2]^{2+}$ involves a five-coordinate CuO_5 chromophore with a trigonal bipyramidal geometry. The out-of-plane Cu(1)–O(48) distances (related by a symmetry operation) are identical (1.936 Å), and they are perfectly linear with O(48)–Cu(1)–O(48) = 179.7°. The in-plane Cu–O distances are not significantly different (average 2.012 Å) and longer than the out-of-plane Cu–O distances by 0.076 Å. The out-of-plane angle, which is perfectly 90° in the present study (Figs. 29 and 30), was rarely observed in previously reported copper trigonal bipyramidal complexes that showed the out-of-plane angular distortions of $90 \pm 10°$.[66] However, the in-plane angles show very significant deviations from the 120° necessary for a regular trigonal-bipyramidal geometry: O(45)–Cu(1)–O(46), 113.43(16)°, O(46)–Cu(1)–O(47), 112.86(18)°, and O(45)–Cu(1) –O(47), 133.72(16)° (Figs. 29 and 30).

The trigonal bipyramidal coordination geometry around the Cu^{2+} ion in $[Cu(H_2O)_5]^{2+}$species (Figs. 29 and 30) is decided by its participation in forming a supramolecular sandwich with two crown ethers that involves hydrogen

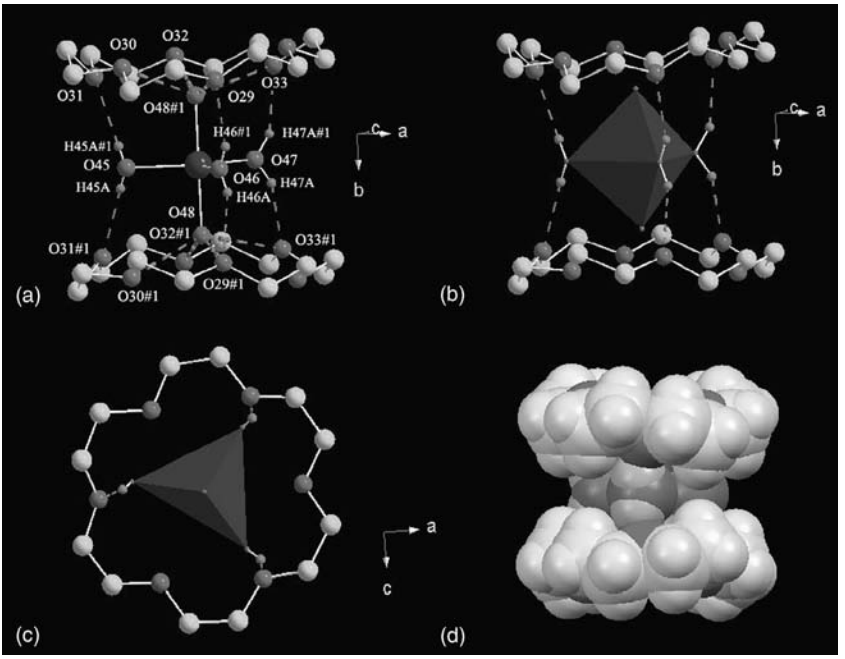

FIGURE 30. Supramolecular sandwich $[Cu(H_2O)_5(C_{12}H_{24}O_6)_2]^{2+}$ consisting of two crown ethers and a trigonal bipyramidal pentaaqua-copper(II) ion. (a) Ball-and-stick representation. (b) Polyhedral representation of $[Cu(H_2O)_5]^{2+}$ species. (c) View along crystallographic *b* axis showing the exactness of the sandwich (one-to-one crown ethers). *Color code:* Cu, blue; O, red; C, green; H, purple. Hydrogen bonds are shown in purple dashed lines. (d) Space-filling plot of the sandwich in different colors. The hydrogen bonding interactions between axial waters and crown ethers are shown in parelia only. (Reprinted with permission from ref. 61.)

bonding interactions of copper-coordinated waters with ethereal oxygen atoms of crown ethers. The formation of the sandwich can be justified by the fact that each of the equatorial waters of TBP-$[Cu(H_2O)_5]^{2+}$ species spans its two hydrogen atoms to form hydrogen bonds with both the upper and lower crown ethers, as if these waters brought both crown ethers closer in forming the sandwich. This accounts for the significant deviations of H–O–H angles (111.6°, 119° and 121.4°, respectively) in copper-coordinated equatorial water molecules from the ideal situation (109°). The Lindqvist-type POM anion $[Mo_6O_{19}]^{2-}$ plays an important role in ordering and/or arranging the crown ether molecules in the crystal of $[Cu(H_2O)_5(C_{12}H_{24}O_6)_2][Mo_6O_{19}]$. The coupling and/or pairing of two crown ethers in forming this sandwich is indeed facilitated by $[Mo_6O_{19}]^{2-}$ anions, which may be called, in the present context, sandwich "clippers" (Scheme **4**).

In the crystal structure of $[Cu(H_2O)_5(C_{12}H_{24}O_6)_2][Mo_6O_{19}]$, each sandwich is anchored (through C–H · · · O hydrogen bonding interactions; Fig. 29)

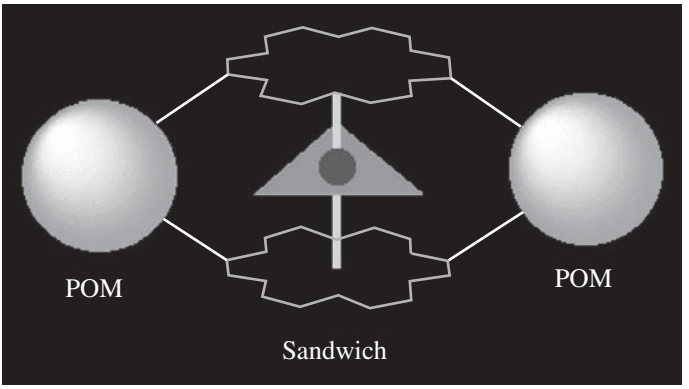

SCHEME 4

by four surrounding isopolyanions; similarly, each isopolyanion is hydrogen bonded to four surrounding sandwiches (Fig. 31). It is remarkable that each polyanion extends its four pairs of "C−H · · · O hydrogen bonding hands" toward four sandwiches in such way that each pair of hands uses one hand to attach the upper crown ether and the other hand is used to fasten the lower crown ether of the sandwich. This is equivalent to the situation that each sandwich is "clipped" by four surrounding isopolyanions. The clipping of the sandwich by two isopolyanions is presented in Scheme **4** (two out of four polyanions are shown for clear visualization).

The present TBP-$[Cu(H_2O)_5]^{2+}$ complex that is sandwiched by two crown ethers shows a tetragonal compression (vide supra) instead of tetragonal elongation toward the apical positions. The fact that TBP-$[Cu(H_2O)_5]^{2+}$ complex is sandwiched by two crown ethers, which in turn are supported by surrounding polyoxometalate anions, is seemingly the driving force for the formation of a compressed trigonal bipyramidal $[Cu(H_2O)_5]^{2+}$ complex cation. The existence of this compressed TBP-$[Cu(H_2O)_5]^{2+}$ complex is consistent with its ESR spectra, which exhibit an axially compressed trigonal geometry as characterized by a $\{d_z^2\}$ electronic ground state. Both room temperature and liquid nitrogen temperature powder ESR spectra of compound $[Cu(H_2O)_5(C_{12}H_{24}O_6)_2][Mo_6O_{19}]$ exhibit an "inverse" $g\perp > g_u > g_e$ pattern.

Polyoxometalates also play an important role in the selection of a metal ion for its complete encapsulation in the cavity of a crown ether to form an unusual supramolecular cation structure. For example, the crown ethers (macrocyclic polyethers), generally, do not readily form complexes with first-row transition metals in their low oxidation states because such metal ions provide only "soft" coordination (acceptor) sites and crown ethers have "hard" donor atoms. Naturally, only a few first-row transition metal–crown ether complexes had been structurally characterized in which a direct bond formation between a transition metal and the crown ether oxygen atoms became possible; rare examples of this kind are offered by the smaller ring crown ethers (e.g., 15-crown-5 and

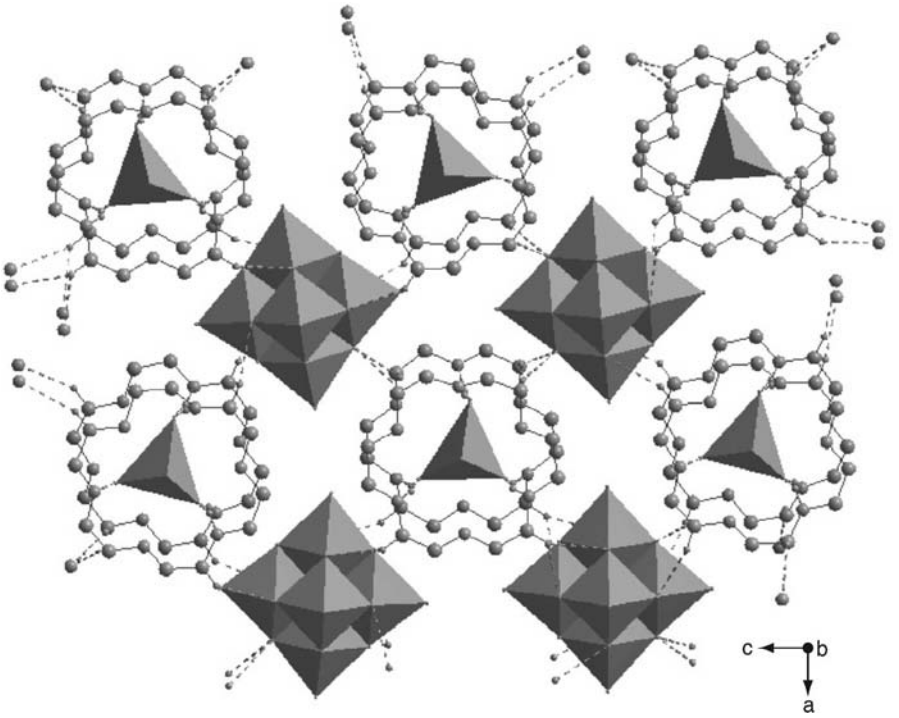

FIGURE 31. An assembly of $[Cu(H_2O)_5(C_{12}H_{24}O_6)_2]^{2+}$ sandwiches and polyoxometalate anions $[Mo_6O_{19}]^{2-}$ in the crystal structure of $[Cu(H_2O)_5(C_{12}H_{24}O_6)_2][Mo_6O_{19}]$, showing the molecular clipping of the sandwiches by polyoxometalate anions. (Reprinted with permission from ref. 61.)

12-crown-4 ethers).[67–69] We have shown the inclusion of a Cu^{2+} ion (a cation smaller than Na^+ ion) at the center of a "large-cavity crown ether," dibenzo-24-crown-8, via supramolecular hydrogen bonding interactions with an isopolyanion $[Mo_6O_{19}]^{2-}$ in the compound $[Cu^{II}(H_2O)_4$(dibenzo-24-crown-8$][Mo_6^{VI}O_{19}]$.[70] The structure of the supramolecular crown ether complex cation $[Cu^{II}(H_2O)_4$(dibenzo-24-crown-8$]^{2+}$ is shown in Figure 32.

As shown in Figures 32 and 33, the Cu^{2+} ion sits exactly at the center of an octagon consisting of crown ether oxygen atoms, which is nothing but the crystallographic inversion center. In $[Cu^{II}(H_2O)_4$(dibenzo-24-crown-8$]^{2+}$, the copper center is coordinated by two trans ethereal oxygen atoms (O(14)) of crown ether and four water molecules (two O(15) and two O(16) atoms) to give a distorted octahedral geometry around copper. The coordination of the crown ether–oxygen atoms at the apical sites of the copper ion (average axial Cu–O = 2.383(2) Å) is the geometrical constraint for a "large cavity crown ether," dibenzo-24-crown-8. Besides direct coordination of two crown ether–oxygen atoms to the copper ion, the linkage between the metal center and the

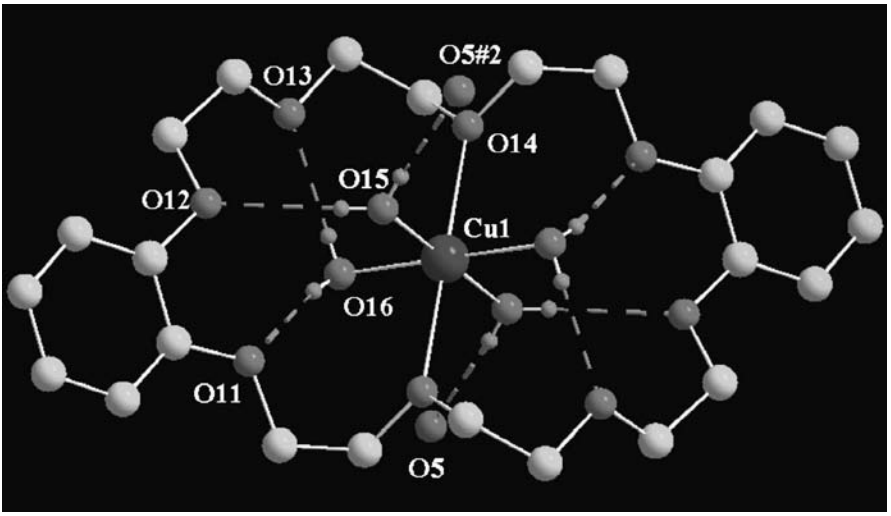

FIGURE 32. View of the $[Cu^{II}(H_2O)_4$(dibenzo-24-crown-8$]^{2+}$ cation, showing direct Cu–crown ether bonding and the interactivity hydrogen bonding as second sphere complexation *Color code*: Cu, blue; O, red; C, green; H, purple. Hydrogen bonds are shown as dashed purple lines. (Reprinted with permission from ref. 70.)

crown ether is additionally provided by one or more water molecules that are directly coordinated to the metal ion and hydrogen bonded to the oxygen atoms of the crown ether. Thus, in the present case, the crown ether also acts as second sphere ligand. The supramolecular cation $[Cu^{II}(H_2O)_4$(dibenzo-24-crown-8$]^{2+}$ is unique in the sense that, beside the inclusion of Cu^{2+} ion at the center of its cavity, all eight water hydrogen atoms and the crown ether–oxygen atoms are exclusively involved in supramolecular interactions (Fig. 32).

The planar conformation[71] of the 24-membered ring of the free ligand, dibenzo-24-crown-8, changes to a chair-like structure upon complex formation. This is consistent with the differences in torsion angles in the rings of free dibenzo-24-crown-8 and in complex $[Cu^{II}(H_2O$ $_{-4}$(dibenzo-24-crown-8$]^{2+}$. Six hydrogen atoms of four copper-coordinated water molecules get hydrogen bonded to the crown ether via ethereal oxygen atoms, and the remaining two hydrogen atoms, of the copper-coordinated water molecules are hydrogen bonded, to two bridging oxygen atoms (O(5)) of two neighboring polyoxometalate anions, $[Mo_6^{VI}O_{19}]^{2-}$. This results in the formation of a supramolecular chain-like arrangement along which the isopolyanion $[Mo_6^{VI}O_{19}]^{2-}$ is sandwiched by two copper-aqua-crown ether complex cations, $[Cu^{II}(H_2O)_4$(dibenzo-24-crown-8$]^{2+}$, and so on, as shown in Figure 34. We believe that the isopolyanion plays an important role in the encapsulation of the copper ion at the center of cavity of the larger ring crown ether. dibenzo-24-crown-8, by stabilizing a tetra-aqua-Cu(II) complex $[Cu(H_2O)_4]^{2+}$ and forming a sandwich like arrangement. Indeed, the O—H $\cdots$ O hydrogen bonds involving

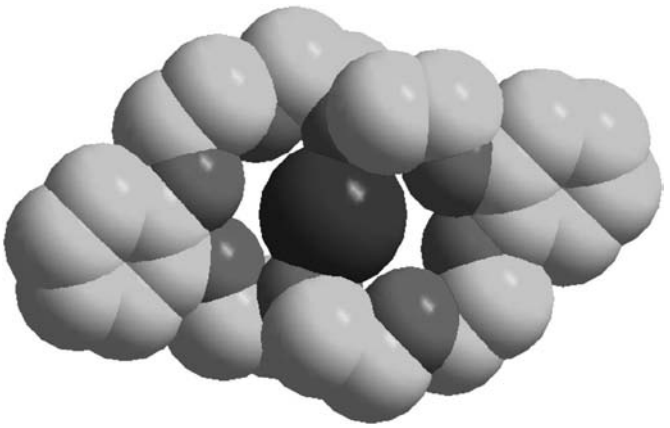

FIGURE 33. Space filling image of the crown ether, dibenzo-24-crown-8, that encapsulates the Cu^{2+} ion at the center of the cavity. Copper-coordinated waters and relevant hydrogen bonds are not shown. *Color code*: Cu, blue; O, red; C, green. (Reprinted with permission from ref. 70.)

isopolyanion $[Mo_6^{VI}O_{19}]^{2-}$ are the strongest among all eight hydrogen bonds, as far as ∠OHO angle is concerned.

When a relatively smaller crown ether, for example, dibenzo-18-crown-6 (DB18C6) is used in similar synthesis with same isopolyanion $[Mo_6^{VI}O_{19}]^{2-}$, a new type of three-dimensional supramolecular assembly consisting of sodium-dibenzo-18-crown-6(Na-DB18C6) supramolecular cation $[Na(C_{20}H_{24}O_6)(CH_3CN)_2]^{2+}$ and the isopolyanion $[Mo_6^{VI}O_{19}]^{2-}$ can be achieved.[8] This consists of two isostructural chains (designated as chains A and B) that are arranged nearly perpendicular to each other. One of these chains is shown in Figure 35. The chain is formed by C−H · · · O hydrogen bonding interaction in which the terminal oxygen (O1) of the Lindqvist isopolyanion is hydrogen bonded to C10 of the upper crown ether and C8 of the bottom crown ether and so on. In a similar manner chain B is formed. In the crystal structure, these chains pack in an AB · · · AB · · · AB fashion throughout the crystal forming a new type of two-dimensional arrangement, as shown in Figure 36.

The inter-layer C−H · · · O hydrogen bonding interactions result in the formation of a three-dimensional supramolecular network with one-dimensional sandglass type channels (Fig. 37) that have inner dimensions of 15.25 · 10.52 $Å^2$. Similar types of channels were obtained in the crystal structure of $[(DB18C6)Na(H_2O)_{1.5}]_2[Mo_6O_{19}] \cdot CH_3CN$ with the inner dimensions of 7.77 · 0.97 $Å^2$, as shown in Figure 38.[72] In this compound, the coordination number varies from seven to eight and acetonitrile molecules were found inside the channels, whereas in compound, $[Na(C_{20}H_{24}O_6)(CH_3CN)_2]_2[Mo_6O_{19}] \cdot 4CH_3CN$, the coordination number around sodium is eight, which includes six oxygen atoms from the crown ether and two nitrogen atoms from two coordinated aceonitrile molecules. The lattice/solvent acetonitrile molecules fill the channels.

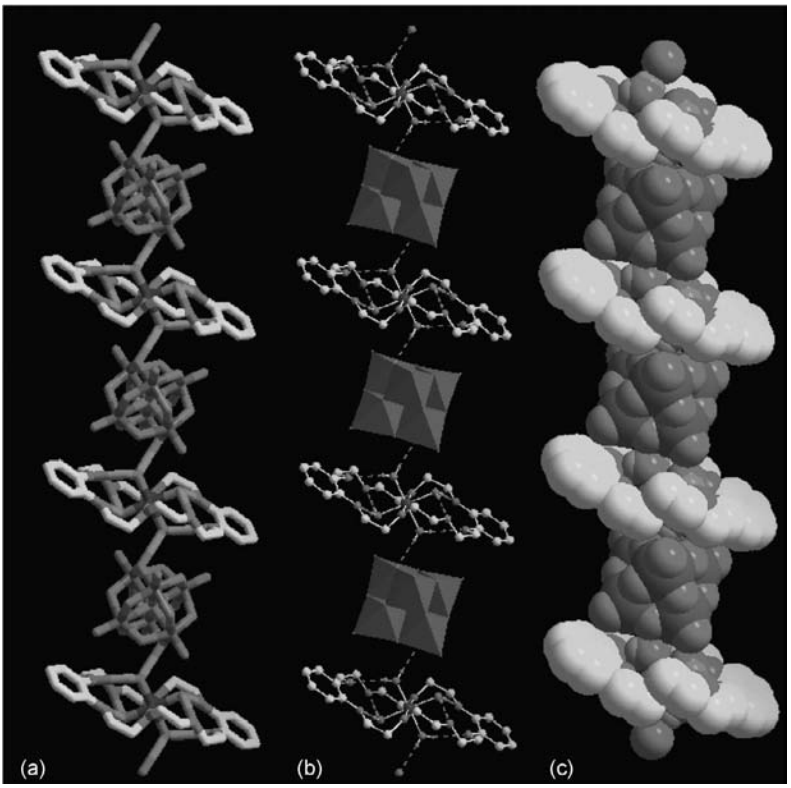

FIGURE 34. View illustrating intermolecular O–H · · · O hydrogen bonded interactions between $[Cu^{II}(H_2O)_4$(dibenzo-24-crown-8$]^{2+}$ and $[Mo_6^{VI}O_{19}]^{2-}$ which lead to the formation of a supramolecular sandwich-type chain-like arrangement: (a) polyhedral representation, (b) wire-frame, and (c) space-filling plot. *Color code:* Cu, blue; Mo, violet; O, red; C, green; H, purple. (Reprinted with permission from ref. 70.)

An unusual supramolecular alkali metal–crown ether POM structure has been shown to be formed in which the Keggin unit $[PMo_{12}O_{40}]^{3-}$ is coordinated to Na^+ cations through the three terminal oxygen atoms in a single M_3O_{13} triplet,[73] thereby forming a neutral and discrete molecule (Fig. 39). In this context, it is worth mentioning that in the crystal of two-electron-reduced $[K(18\text{-crown-}6)]_2$-$[N(PPh_3)_2][HPMo_{12}O_{40}]$ · 8MeCN · 18-crown-6, there is no coordinative interaction between K^+ ions and terminal oxygen atoms of the polyoxoanions.[74] It is interesting that, in the relevant crystal structure, the packing of the heteropolyanions form holes or voids that are filled by the supramolecular $[K(18\text{-crown-}6)]^+$ cations via electrostatic interactions.

According to soft and hard acid base (SHAB) principle, the hard oxygen donor of crown ethers prefer alkali metal ions and lanthanide cations because these are considered as hard acids. Thus it should not be difficult to obtain

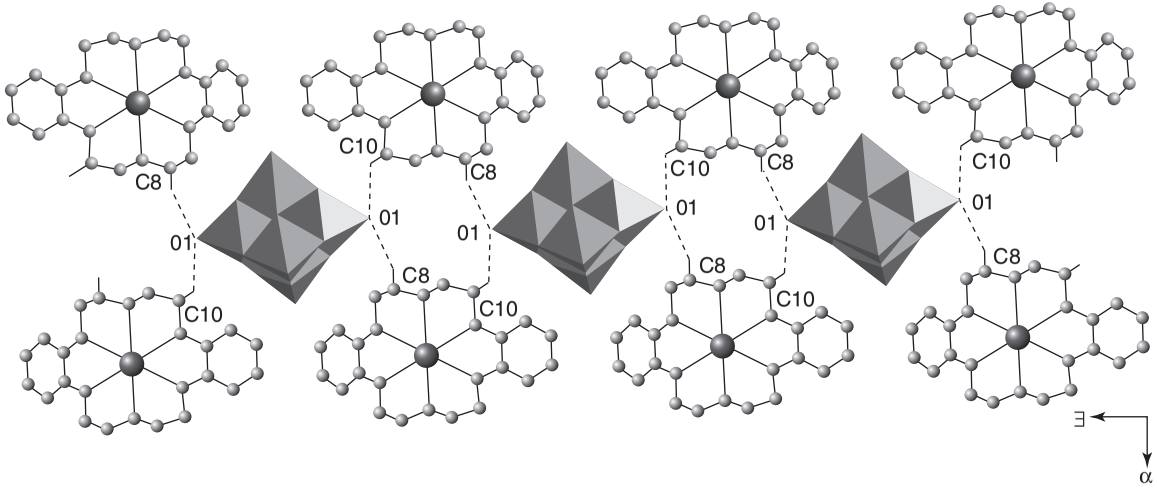

FIGURE 35. A one-dimensional chain showing that the terminal oxygen atoms of isopolyanion are hydrogen bonded to the ethereal carbon hydrogen atoms of the crown ether. Sodium coordinated and solvated acetonitrile molecules are omitted for clarity. (Reprinted with permission from ref. 8.)

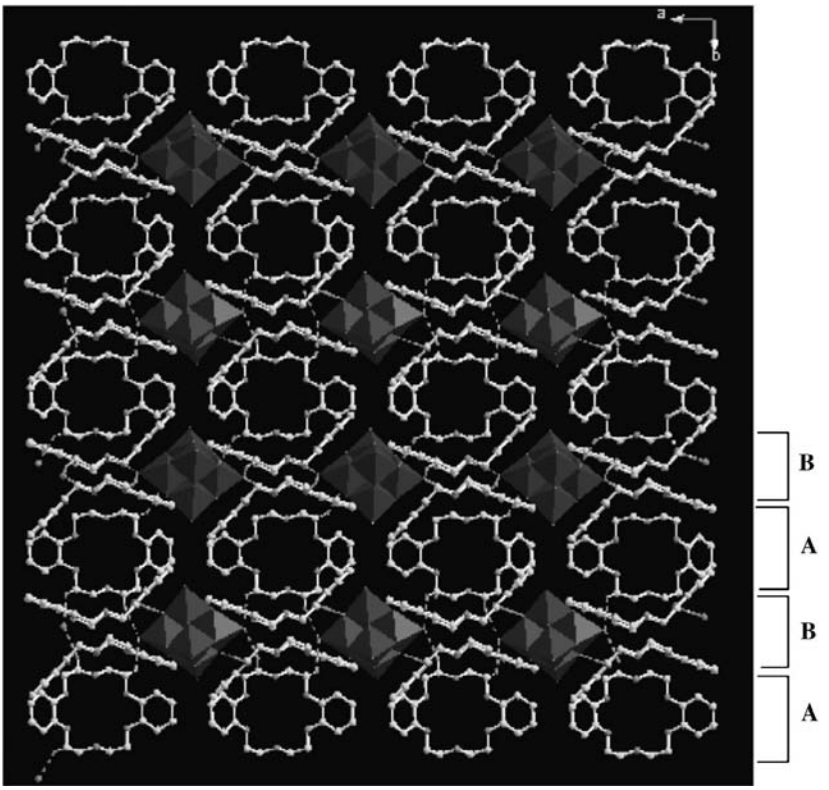

FIGURE 36. The alignment of ABAB isostructural chians along the crystallographic *b* axis. The encapsulated Na^{+} ion, and coordinated and solvated acetonitrile molecules are not shown for clarity. *Color code*: C, green; O, red. Isopolyanion is shown in violet polyhedral. Hydrogen bonding interactions are shown in purple.

supramolecular lanthanide-crown ether complexes that are stabilized with POM anions. Nogueiraa and co-workers have reported the europium(III)-benzo-15-crown-5-POM system in which Eu(III) is coordinated to eight solvent molecules ($6MeOH + 2H_2O$). The resulting complex is strongly hydrogen bonded to two moieties of crown ethers that undergo $C-H\cdots O$ type hydrogen bonding interactions toward the oxo groups of Keggin anions to form an extensive supramolecular network.[75] Crown ethers-POM supramolecular systems are not limited to metal ions that are generally encapsulated in the cavity of crown ethers but are also capable of encapsulating organic amine cations and oxonium cations. Nakamura, Akutagawa, and their group have reported the formation of a para-phenylenediamine-crown ether-Keggin supramolecular system that exhibits intra-molecular proton and electron transfers with the formation of reduced Keggin anion $[PMo_{12}O_{40}]^{4-}$[76]. They combined the phosphomolybdic acid ($H_3PMo_{12}O_{40}$) with supramolecular species of protonated phenylene diamines

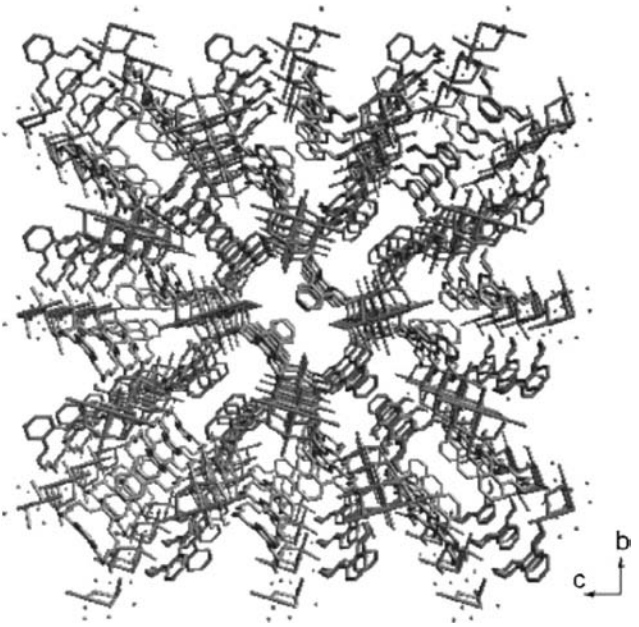

FIGURE 37. The perspective view of compound $[Na(C_{20}H_{24}O_6)(CH_3CN)_2]_2[Mo_6O_{19}] \cdot 4CH_3CN$ showing the 1D sandglass channels along the crystallographic *a*-axis. The solvent acetonitrile molecules, hydrogen atoms, and sodium ions are not shown for clarity. (Reprinted with permission from ref. 8.)

(PPDs) and crown ethers by changing the size of the crown ethers from [12]crown-4, to [15]crown-5, to [18]crown-6, which resulted in the formation of $(H_2PPD^{2+})_2([12]crown\text{-}4)_4[PMo_{12}O_{40}]^{4-}$, $(HPPD^{+})_4([15]crown\text{-}5)_4[PMo_{12}O_{40}]^{4-}$, and mixed-protonated $(HPPD^{+})_2(H_2PPD^{2+})([18]crown\text{-}6)_3[PMo_{12}O_{40}]^{4-}$, respectively (Scheme **5**).

The different protonated states of *para*-phenylene diamine (PPD) derivatives in these PPD-crown ether-POM complexes afforded interesting and distinct supramolecular structures. The oxonium ion has also been found to be encapsulated in the cavity of the crown ethers that are associated with POMs.[77–78] Wang and co-workers reported a supramolecular compound, $[C_{12}H_{24}O_6][H_3PMo_{12}O_{40}] \cdot 22H_2O$, that shows the existence of a supramolelcular cation, $[H_3O(C_{12}H_{24}O_6)]^+$, that stabilizes the H_3O^+ ion at the center of the crown ether through hydrogen bonding interactions with the crown ether oxygen atoms.[77] In another oxonium encapsulated compound, the hydrogen bonding interactions between the oxonium ion and the crown ether oxygen atoms are electrostatic in nature, and the oxonium encapsulated crown ether supramolecular cations in the relevant crystal pack alternatively in a parallel manner in the caves or voids that are formed by the supramolecular interactions among the $[PMo_{12}O_{40}]^{3-}$ POM anions.[78]

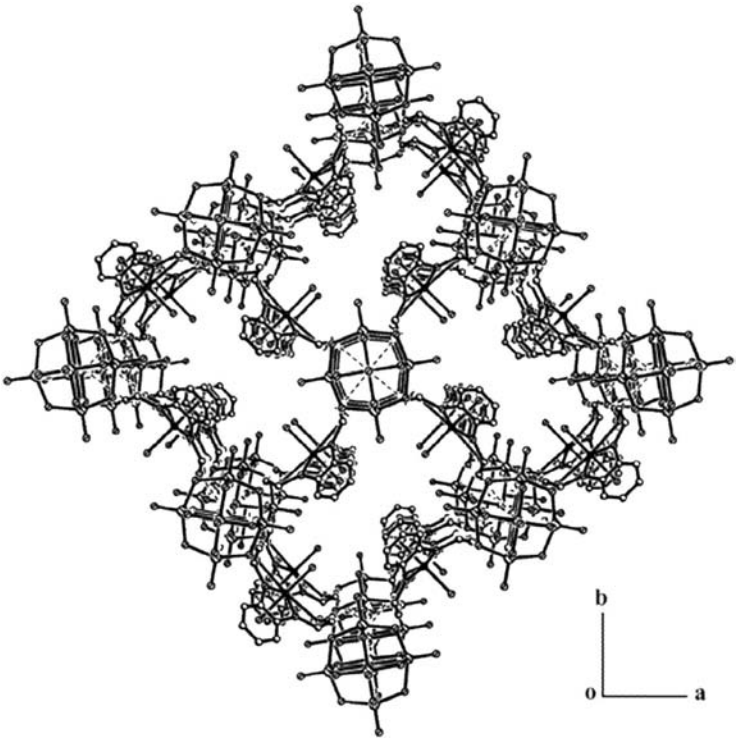

FIGURE 38. Three-dimensional network of $[(DB18C6)Na(H_2O)_{1.5}]_2[Mo_6O_{19}] \cdot CH_3CN$ with 1D sandglass-like channels along the *c* axis. The acetonitrile molecules are omitted for clarity. (Reprinted with permission from ref. 72.)

IV. SUPRAMOLECULAR WATER CLUSTERS ASSOCIATED WITH POLYOXOMETALATES

Water is a major constituent of planet earth and it plays an important role in many natural systems. Numerous biological systems depend on diverse noncovalent interactions in which water plays major role by stabilizing the native conformation of the respective biomolecules.[79–81] However, water is not a fully understood liquid due to its anomalous behavior. Thus numerous recent reports have appeared on extensive investigations of water structures. Studies on small water clusters and their noncovalent interactions are also significant because such clusters stabilize supramolecular systems both in solution and in the solid state. Therefore, there is a clear need to understand how such aggregates influence the overall structures of their surroundings.[82,83]

In many chemical systems, small water clusters are responsible for the aggregation or self-assembly of organic and inorganic molecules.[84] The study

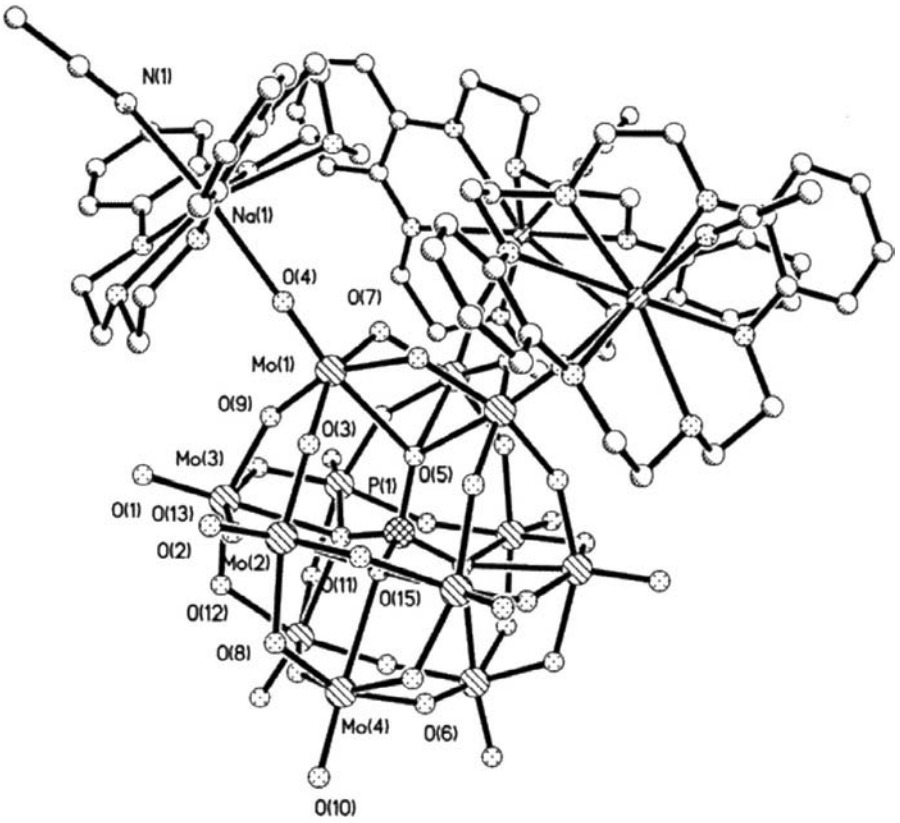

FIGURE 39. The molecular structure of [{Na(dibenzo-18-crown-6)(MeCN)}$_3$ {$PMo_{12}O_{40}$}] in which the Keggin unit supports three supramolecular sodium-crown ether complexes via three terminal oxygen atoms of a single {Mo_3O_{13}} unit of the Keggin anion. (Reprinted with permission from ref. 73.)

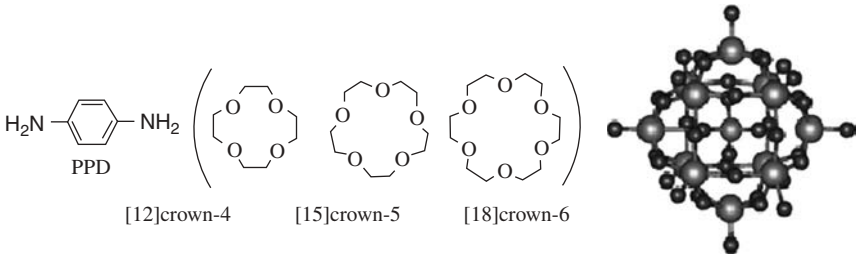

SCHEME 5

of small water clusters through crystallization is of fundamental importance as well in understanding the physical properties of liquid water and ice. However, the crystallization of a water cluster itself is difficult to study. Crystallographic investigations on molecular crystalline hydrates have shown that stabilization of small water clusters $(H_2O)_n$ is possible in a restricted environment—for example, in organic or organic-inorganic hybrid framework materials by hydrogen bonding interactions that occur between the host and the guest water molecules. A polyoxometalate matrix has recently been recognized in stabilizing water clusters ranging from the simple water dimer, $(H_2O)_2$, to complex $(H_2O)_{100}$ spherical cluster.[53,85] Infantes and Motherwell have reported the prototypes of water clusters within the Cambridge structural database (CSD), categorizing them as discrete rings and chains, infinite chains and tapes, and layered structures.[86] Later, Mascal et al. described water oligomers in crystalline hydrates by choosing 17 random recent publications that describe unprecedented assemblies of water molecules and compared these structures against those already in the CSD.[87] The present discussion on supramolecular water clusters is restricted to the crystallographic observation of water clusters that are stabilized in POM matrices, stressing the role of POM cluster anions in generating water clusters, the shape and size of which vary, depending on the particular type of supramolecular interactions in the concerned POM associated crystal.

The simplest and smallest water cluster is the water dimer. We have reported the crystallographic observation of water dimers in the channels of an inorganic framework material, $Na_{3n}(H_2O)_{6n}[Al(OH)_6Mo_6O_{18}]_n \cdot 2nH_2O$,[53] derived from the Anderson-type POM cluster anion $[Al(OH)_6Mo_6O_{18}]^{3-}$. The three-dimensional framework, which has "sinuous" channels accommodating water dimers, is constructed by the Anderson-type anions as building blocks that share sodium cations (Fig. 27, vide supra).[53] The supramolecular water dimer (as guest) is associated with the host by having hydrogen bonds in the channel, as shown in Figure 40.

The water dimer was realized in the vapor phase for the first time by Dyke and co-workers.[88,89] Their molecular beam resonance experiments showed that the lowest energy arrangement has a plane of symmetry containing the hydrogen donor molecule to the right and the symmetry axis of the molecule to the left (Scheme **6a**). The plane containing the hydrogen donor water molecule to the right bisects the water molecule to the left through the oxygen atom of the hydrogen acceptor molecule (Scheme **6a**). On the other hand, the water dimer, found in the channel of the isolated crystalline hydrate, $Na_{3n}(H_2O)_{6n}[Al(OH)_6Mo_6O_{18}]_n \cdot 2nH_2O$ (Fig. 40 and Scheme **6b**), is near linear, but it is not isosymmetrical with the theoretically predicted water dimer and/or the water dimer of the vapor phase (Scheme **6a**).[80,89] They differ by the position of one hydrogen atom (H49B in Scheme **6b**), which bisects the water molecule (O50 water) out of plane to the left. This is because the water dimer, which exists in the solid state, is hydrogen bonded to all of the possible sites that include the POM cluster anions and the sodium-coordinated water molecules (Fig. 40).

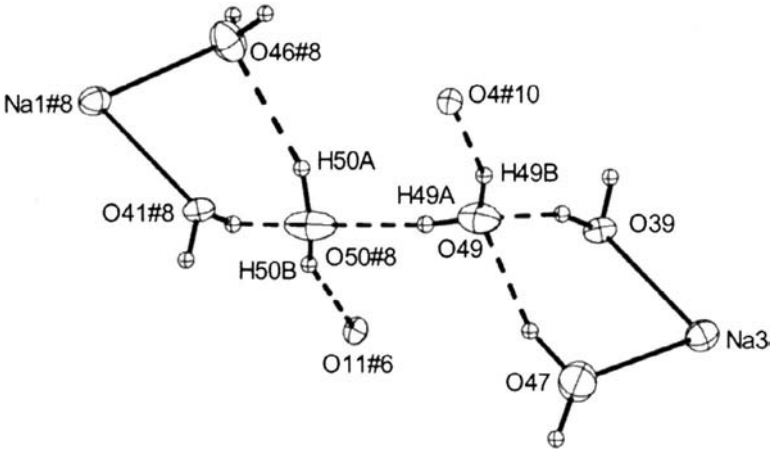

FIGURE 40. Representation of the supramolecular water dimer (guest) consisting of O(49) and O(50) water molecules and its immediate environment (host) as found in $Na_{3n}(H_2O)_{6n}[Al(OH)_6Mo_6O_{18}]_n \cdot 2nH_2O$ (50% thermal ellipsoids). Covalent chemical bonds are shown as solid lines (–) and H-bonds as dashed lines (- - -). O(4) is a bridging oxygen atom between two molybdenum atoms in an Anderson anion, and O(11) is a bridging oxygen atom of another Anderson anion.

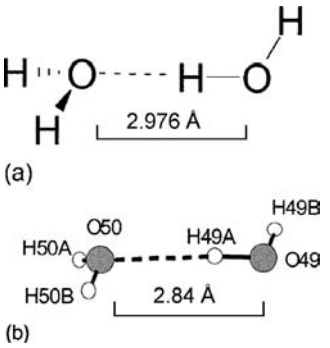

SCHEME 6

The resulting steric constraints decide the present conformation. It is interesting that both oxygen atoms of the water dimer (Fig. 40) have a "formal" coordination number of four (two hydrogen atoms of each oxygen of the dimer act as acceptors and the two lone pairs electrons on each oxygen act as donors), with approximately tetrahedral arrangement. It is thus possible to envision that the free water dimer (in the channel) is connected to the coordinated water molecules of the host framework through O–H · · · O hydrogen bonding.

However, it is reasonable to identify the pair of water molecules in the channel as a supramolecular water dimer because this pair is not at all involved in covalent interaction and is solely hydrogen bonded to its periphery. At this point, it is worth mentioning that, even though we have described this pair of water molecules as a water dimer, contributions from the peripheral hydrogen-bonding sites (POM cluster anion and sodium-coordinated waters) are unavoidably significant for the existence of this smallest water cluster. Thus the formation of supramolecular $(H_2O)_2$ in the channel appears to be facilitated by the peripheral hydrogen-bonding interactions POM cluster anions.

The next larger water cluster is the trimer. Theoretical calculations have established a six-membered minimum energy cyclic water trimer, which is chiral and undergoes two types of degenerate structural rearrangements. Not only has the cyclic supramolecular $(H_2O)_3$ cluster been identified (in liquid water) experimentally by various spectroscopic methods, including infrared vibration rotation tunneling (VRT) spectroscopy,[90,91] but also the ability of three water molecules to form a cyclic trimer has been observed crystallographically in the solid state of the complex hydrate, $\{[2,2,2]\text{cryptand-2H}\}[CoCl_4] \cdot 1.5H_2O$.[92] We have shown stabilization of an acyclic water trimer (Fig. 41) in crystal of a POM-supported transition-metal complex, $[Al(OH)_6Mo_6O_{18}\{Cu(phen)(H_2O)_2\}_2][Al(OH)_6Mo_6O_{18}\{Cu(phen)(H_2O)Cl\}_2] \cdot 5H_2O$.[52] This acyclic water trimer is, as such, energetically unfavorable, but its existence in the POM matrix can be justified by its supramolecular hydrogen bonding interactions with its surrounding, which includes the oxygen atoms (terminal and bridging) of the Anderson heteropolyanions and the copper-coordinated water molecules (Fig. 41b). As shown in Figure 41b, the water trimer is hydrogen bonded to all of its possible sites, and the resulting steric constraints determine the conformation of the present acyclic water trimer. More specifically, the surroundings of the water trimer, which stabilizes such a high-energy acyclic conformation, include four bridging oxygen atoms (O(1), O(2), O(3), and O(26)); three terminal oxygen atoms (O(8), O(19), and O(24)) of the Anderson polyanions; and three copper-coordinated water molecules (O(13), O(29), and O(27) (Fig. 41b). Contributions from the peripheral hydrogen-bonding sites (terminal and bridging oxygen atoms of the Anderson anions and copper-coordinated waters), which play an important role in the existence of this acyclic small water cluster $(H_2O)_3$, can be realized by the fact that some of the H-bond contacts to the peripheral surroundings of the water trimer are even shorter than those in the intrawater trimer (Fig. 41b). The water trimer and the other two lattice waters (O(30) and O(33)) in the crystal are extensively hydrogen bonded with their surrounding heteropolyanions, resulting in an intricate hydrogen bonding supramolecular network (Fig. 42).

Doedens and co-workers reported[93] a symmetrical cyclic water hexamer, $(H_2O)_6$, observed in the polyoxovanadate-based crystalline hydrate $Li_6[Ni_3V_{18}O_{42}(H_2O)_{12}(SO_4)] \cdot 24H_2O$, that forms a framework type structure in its crystalline state in which the building unit is the cage-like polyoxovanadate cluster

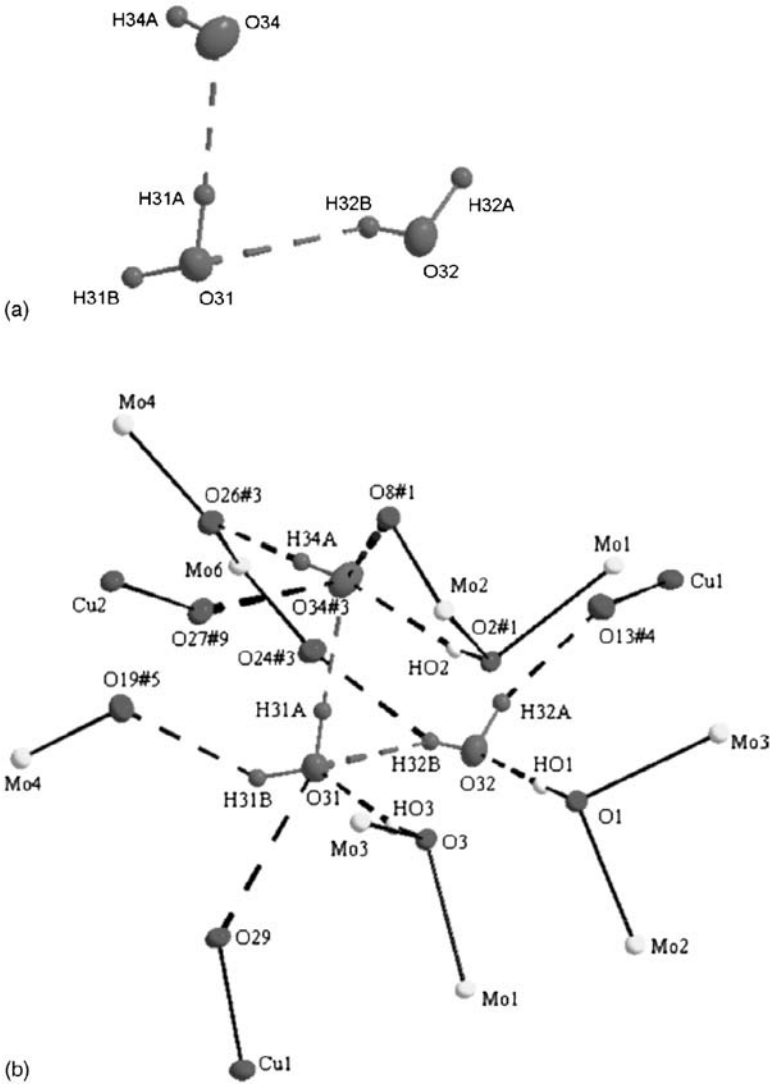

FIGURE 41. (a) Hydrogen-bonded water trimer (shown in violet). (b) Hydrogen bonding situation describing the water trimer (shown in violet) and its peripheral hydrogen bonding sites. *Color code*: Mo, yellow; O, red; Cu, blue; H, white. (Reprinted with permission from ref. 52.)

$\{V_{18}O_{42}(SO_4)\}$. The body-centered cubic unit cell of a relevant crystal contains eight equivalent hydrogen-bonded $(H_2O)_6$ clusters with a chair configuration as shown in Figure 43, which is an edge-on view of the unit cell in which four water hexamers can be observed. A view of the single water hexamer in this polyoxovanadate-based compound, $Li_6[Ni_3V_{18}O_{42}(H_2O)_{12}(SO_4)] \cdot 24H_2O$, is presented in

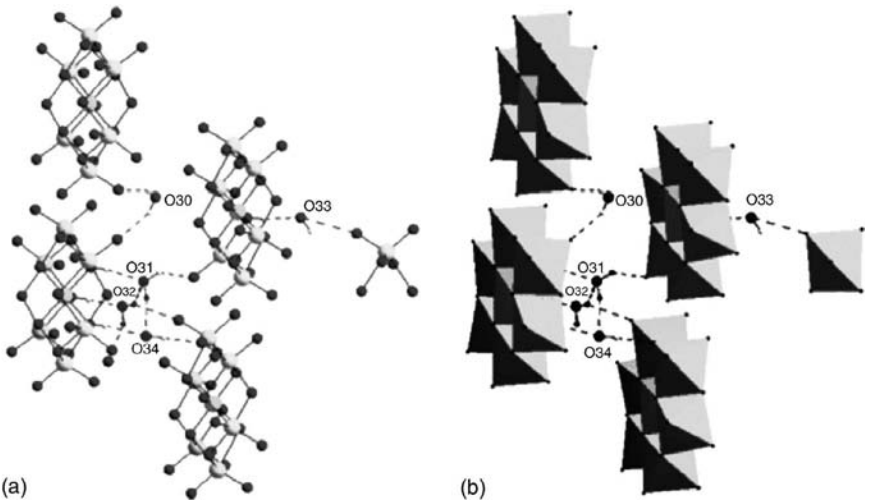

FIGURE 42. Linking the Anderson heteropolyanion via O-H · · · O hydrogen bonds that involve solvent waters including water trimer (shown in violet): (a) ball-and-stick representation and (b) polyhedral representation. *Color code*: Al, cyan; Mo, yellow; O, red; H, white. (Reprinted with permission from ref. 52.)

Figure 44. It must be mentioned in this case that the hydrogen atoms within the $(H_2O)_6$ ring show a twofold disorder and the axial hydrogen atom is hydrogen bonded to one of the terminal oxygen atoms of the polyoxovanadate cage $\{V_{18}O_{42}(SO_4)\}$. It has also been described that this chair conformation and the disordered hydrogen atoms of the $(H_2O)_6$ ring are found in hexagonal ice (I_h) as well as in the metastable cubic ice (I_c).[94]

A supramolecular water octamer, $(H_2O)_8$ has been crystallographically observed in the crystalline hydrate of an isopolyanion supported copper coordination complex, $[\{Cu(phen)(H_2O)_2\}_2(Mo_8O_{26})] \cdot 8H_2O$ (Fig. 4, vide supra).[31] Theoretical (ab initio) calculations, carried out on water octamers, $(H_2O)_8$, predicted that the octomers can exist in cyclic and cubic forms (Scheme **7**). The octamers with D_{2d} and S_4 conformations contain 12 hydrogen bonds and are energetically favorable, and the cyclic topologies possess fewer (8) H-bonds and thus are energetically disfavored.[95–100]. The $(H_2O)_8$ cluster found in the crystalline hydrate $[\{Cu(phen)(H_2O)_2\}_2(Mo_8O_{26})] \cdot 8H_2O$ is neither in the cubic form nor in the cyclic/bicyclic form. It is a new type of a discrete water octamer (Fig. 45) that is stabilized by its hydrogen bonding contacts with the POM cluster anion in the compound, $[\{Cu(phen)(H_2O)_2\}_2(Mo_8O_{26})] \cdot 8H_2O$. The water octamer can be described by a cyclic water tetramer (consisting of two O(14) and two O(17) water molecules), which further interacts with two water dimers, resulting in a water octamer. Thus the water octamer is formed from four copper-coordinated water molecules (i.e., two O(14) water molecules and two O(15) water molecules)

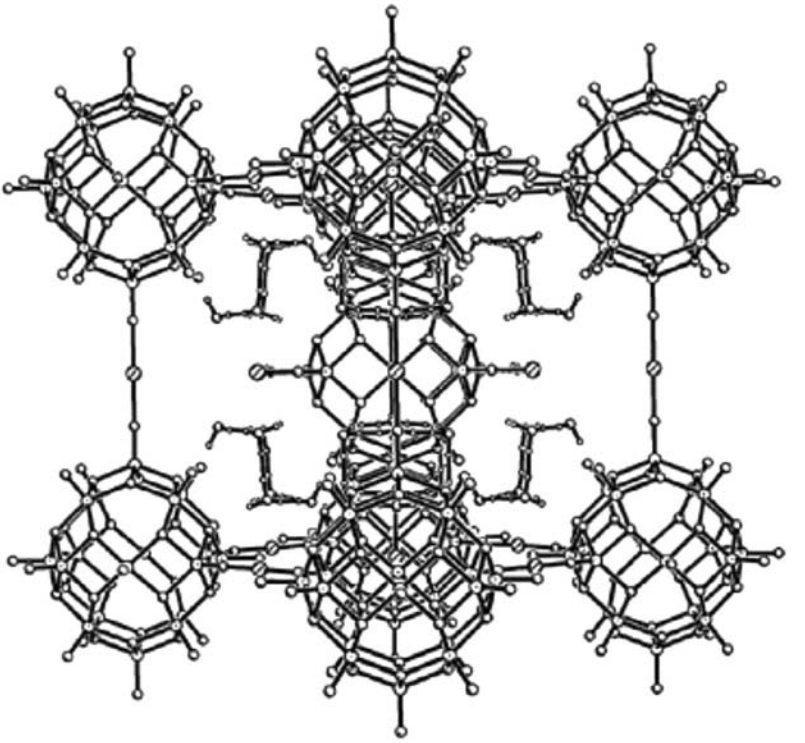

FIGURE 43. An edge-on view of the body-centered unit cell of $Li_6[Ni_3V_{18}O_{42}(H_2O)_{12}(SO_4)] \cdot 24H_2O$, showing the $\{V_{18}O_{42}(SO_4)\}$ cages, the Ni^{2+} ions linking them and the $(H_2O)_6$ clusters. For clarity, the encapsulated sulfate ions, the water molecules bound to the nickel ion, and the Li^+ ions have been omitted. Four of the eight water clusters are clearly visible; the others are obscured by the cages. (Reprinted with permission from ref. 93.)

and four lattice water molecules (two O(16) and two O(17) water molecules). The hydrogen bonding interactions between O(17) and O(16) water molecules cannot be described in terms of the proton donor/acceptor model, because the hydrogen atoms of the O(16) water molecule were not located in the crystal structure. The O(16) water molecule accepts a proton from the copper-coordinated water O(15), as shown in Figure 45.

The stabilization of such unusual and disfavored conformation of water octamer is thus achieved through supramolecular hydrogen bonding interactions with its surroundings, which include terminal oxygen atoms O(1) and O(5) attached to Mo(1) and Mo(5), respectively, of the isopolyanion. This situation is shown in Figure 46.

It has been demonstrated so far that polyoxometalates play an important role in stabilizing supramolecular water clusters by extending their surface oxo groups to form appropriate hydrogen bonds with water clusters. Now it will be

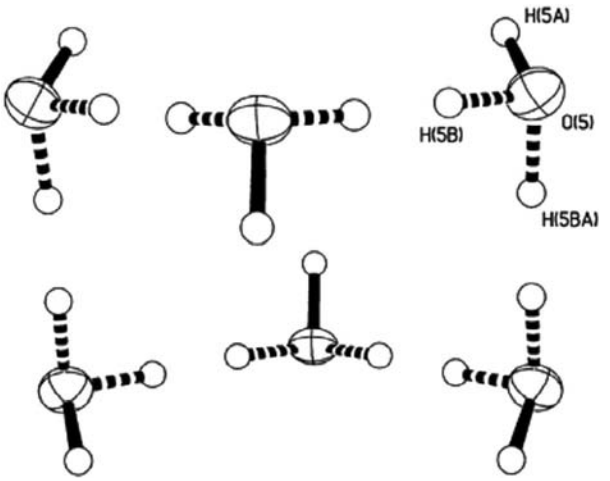

FIGURE 44. The cyclic water hexamer in $Li_6[Ni_3V_{18}O_{42}(H_2O)_{12}(SO_4)] \cdot 24H_2O$ showing the disorder of the equatorial hydrogen atoms. Each equatorial hydrogen atom is hydrogen bonded to the adjacent oxygen atom. (Reprinted with permission from ref. 93.)

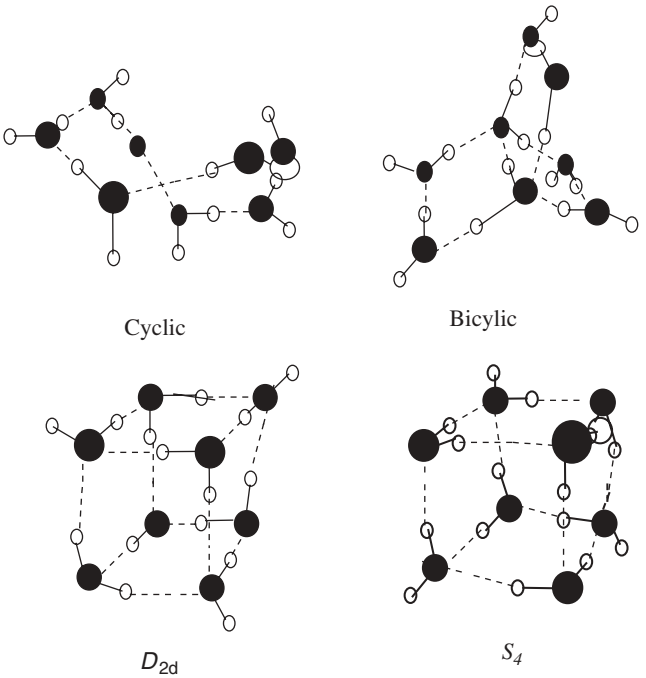

SCHEME 7

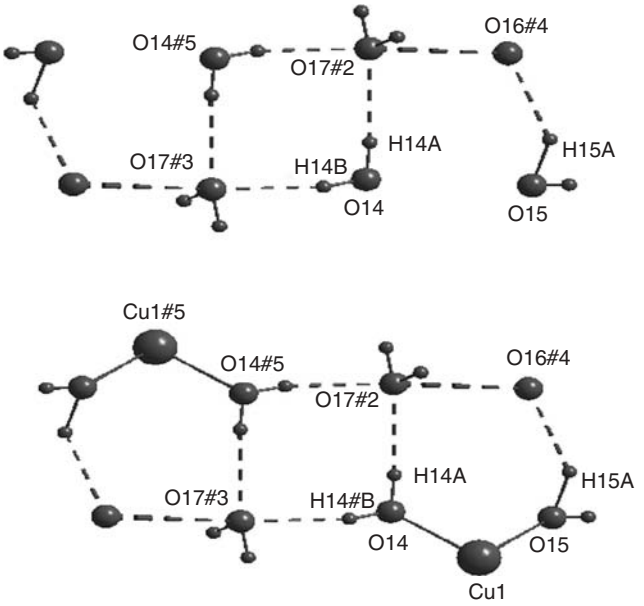

FIGURE 45. (a) Water octamer formed from the copper-coordinated waters and lattice waters. O(14) and O(15) are copper-coordinated water molecules. Cu ions are not shown. (b) Water octamer showing water coordination to the copper ions. (Reprinted with permission from ref. 31.)

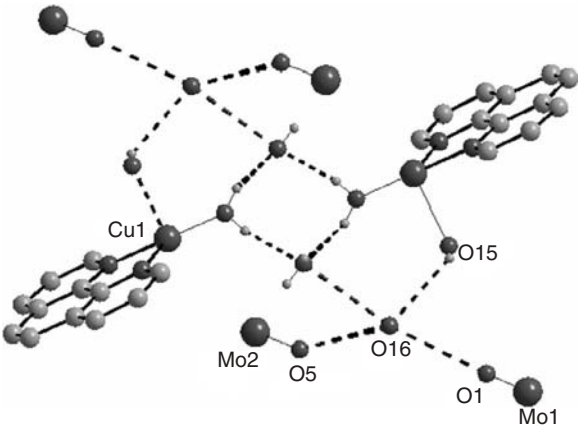

FIGURE 46. The immediate environment of the water octamers, $(H_2O)_8$, which includes the oxo groups of the POM anion. (Reprinted with permission from ref. 31.)

shown how a confined space, for example, the internal spherical cavity of a giant spherical/icosahedral POM cluster, influences the formation of giant icosahedral $(H_2O)_n$(n = 20, 40, 60, 80, 100) clusters inside the internal cavity. Müller and co-workers have established that several well-defined spherical water assemblies can

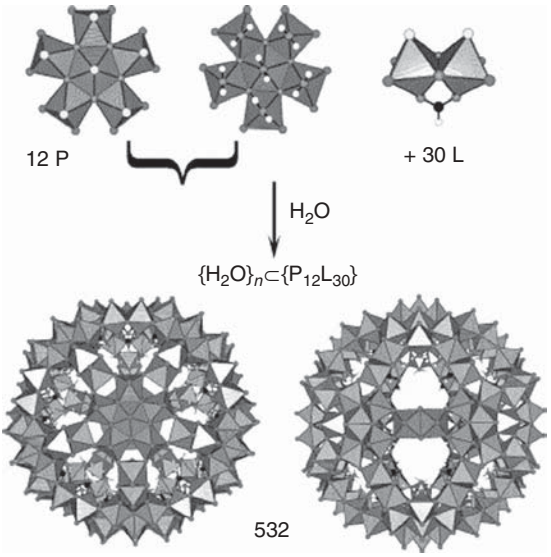

FIGURE 47. Polyhedral representation of nano-capsules that are formed by 12 pentagons (P) and 30 linkers.(L). P = $[(Mo)Mo_5O_{21}(H_2O)_6]^{6-}$ and in the present case L = $[Mo_2^{V}O_4(CH_3COO)]^{1+}$. (Reprinted with permission from ref. 101.)

be generated inside the cavities of a series of giant icosahedral clusters.[101] The fundamental skeleton of such icosahedral clusters can be described generally by $\{Pentagon\}_{12}\{Linker\}_{30}$ in which the pentagonal unit is the aggregation of six oxomolybdenum polyhedral, $[(Mo)Mo_5O_{21}(H_2O)_6]^{6-}$, that has a central $\{O=Mo^{VI}(H_2O)O_5\}$ bipyramid sharing the equatorial edges of five $\{O=Mo^{VI}(H_2O)O_4\}$ octahedra.[12] The linker can be a monomeric unit—for example, $\{O=Mo^{V}(H_2O)O_4\}$ unit (Mo-102 icosahedral cluster) or dinuclear fragments $[Mo_2^{V}O_4]^{2+}$, which are stabilized by coordinating ligands like $HCOO^-$, CH_3COO^-, SO_4^{2-}, and $H_2PO_2^-$. The formation of such nanocapsules is shown in Figure 47. The resulting metal-oxide based nanocapsule, which has 532 symmetry, has been characterized by 20 pores and channels with a nano-size central cavity.[12] Because these nano-size clusters are synthesized from an aqueous medium, there is no wonder that the internal spherical cavity of such nanocapsules would encapsulate a range of spherical water assemblies/clusters. The first nanocapsule of this series, which was discovered in 1999,[102] was generated with the dinuclear $\{Mo_2^{V}O_4(CH_3COO)\}^{1+}$ linker in compound $(NH_4)_{42}[\{Mo_2^{V}O_4(CH_3COO)\}_{30}\{(Mo)Mo_5O_{21}(H_2O)_6\}_{12}] \cdot 10\ CH_3COONH_4 \cdot$ ca. 300 H_2O. The inside cavity of the concerned nanocapsule was characterized by highly disordered water assemblies (amorphous water), and it was argued that the 30 methyl groups of 30 acetate anions that are ligated to dinuclear unit cover the internal surface and cause a disorder owing to their overall hydrophobic character. This strong disorder of the water assembly in the methyl groups

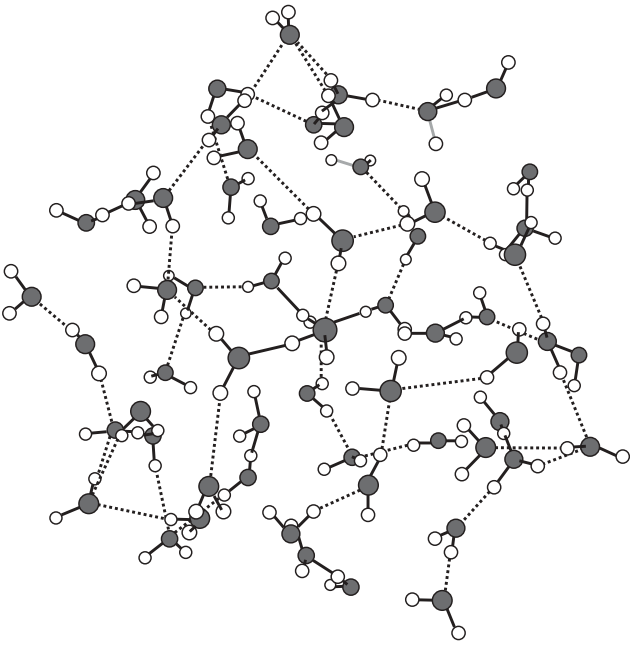

FIGURE 48. The disordered $\{H_2O\}_{59}$ water aggregate extracted from the electron density peaks found in the interior cavity of the nanocapsule in compound $(NH_4)_{42}[\{Mo_2^{V}O_4(HCOO)\}_{30}\{(Mo)Mo_5O_{21}(H_2O)_6\}_{12}] \cdot 30\ HCOONa \cdot$ ca. 250 H_2O. (Reprinted with permission from ref. 101.)

surrounding the cavity of the nanocapsule in $(NH_4)_{42}[\{Mo_2^{V}O_4(CH_3COO)\}_{30}\{(Mo)Mo_5O_{21}(H_2O)_6\}_{12}] \cdot 10\ CH_3COONH_4$ ca. 300 H_2O, can be slightly reduced when the acetate ligands of the 30 dinuclear units are replaced by 30 formate ligands, which result in the formation of a formate analog, $(NH_4)_{42}[\{Mo^{V}{}_2O_4(HCOO)\}_{30}\{(Mo)Mo_5O_{21}(H_2O)_6\}_{12}] \cdot 30\ HCOONa \cdot$ ca. 250 H_2O.[103]

The total water assembly in the interior cavity of the formate analog could not be observed crystallographically; however, a disordered aggregate of $\sim$59 H_2O molecules could be extracted from the total (real) assembly. The disordered $(H_2O)_{59}$ fragment is built up of reticulated chains of water molecules with no loops of ring (Fig. 48). Because of strong disorder, the entire water assembly could not observed crystallographically inside the cavity of both the acetate and the formate ligated nanocapsules. When the size of the spherical nanocapsule is reduced by sizing the linker—that is, by replacing the dinuclear unit with a mononuclear species like $\{Mo^{V}O(H2O)\}$, a relatively smaller nanocapsule can be obtained, (e.g., the nanocapsule in the compound $[\{Mo^{V}O(H_2O)\}_{30}\{(Mo)Mo_5O_{21}(H_2O)_4(CH_3COO)\}_{12}] \cdot$ ca. 150 H_2O).[104] It is interesting that, this shrunken nano-object encapsulates a highly organized water cluster $(H_2O)_{20}$, which has a shape of perfect pentagonal dodecahedron, in its central cavity. This capsule is surrounded by an another larger pentagonal

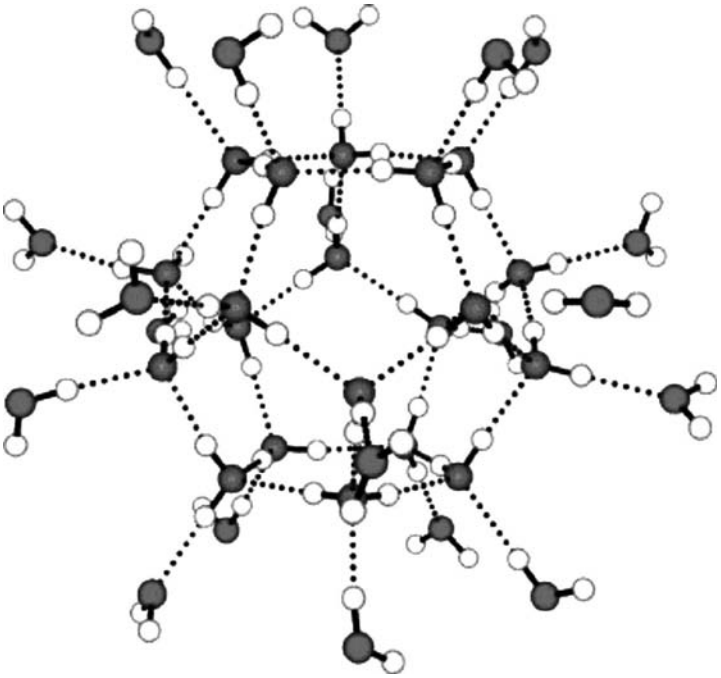

FIGURE 49. The $(H_2O)_{40}$ water assembly having two dodecahedra with the central *O*-atom-dodecahedron in blue and the second in red (central water molecule not given) found in the nanocapsule of the crystal structure of $[\{Mo^{V}O(H_2O)\}_{30}\{(Mo)Mo_5O_{21}(H_2O)_4(CH_3COO)\}_{12}] \cdot$ ca. 150 H_2O. (Reprinted with permission from ref. 101.)

$(H_2O)_{20}$ dodedecahedron through hydrogen bonds and result in a $(H_2O)_{40}$ nanowater droplet (Fig. 49), in contrast to the highly disordered water assembly found in the cavities of the relatively larger nanocapsules of acetate- and formate-ligated compounds (vide supra). It is remarkable that the central $(H_2O)_{20}$ dodecahedron clearly shows the pentagonal rings and the tetrahedral coordination of water molecules (Fig. 49). Even though this $(H_2O)_{20}$ dodecahedron with 30 hydrogen bonds is included inside the central cavity of a metal oxide-based nanocapsule, which is a single discrete entity, it is of fundamental importance because this is the basic unit of the crystalline clathrate hydrates in which it is embedded into a three-dimensional network of hydrogen bonds. Thus it has been shown that the reduction in size of the spherical nano-size POM clusters plays an important role in the ordering of the water molecules in a confined spherical space by exerting more stress on the organization of the encapsulated molecules.

It has already been mentioned that in the case of nanocapsules of compounds[102,103] $(NH_4)_{42}[\{Mo_2^{V}O_4(CH_3COO)\}_{30}\{(Mo)Mo_5O_{21}(H_2O)_6\}_{12}] \cdot 10$ $CH_3COONH_4 \cdot$ ca. 300 H_2O and $(NH_4)_{42}[\{Mo_2^{V}O_4(HCOO)\}_{30}\{(Mo)Mo_5O_{21}(H_2O)_6\}_{12}] \cdot 30$ $HCOONa \cdot$ ca. 250 H_2O, the organized water clusters could not

be identified in their internal cavities because the terminal parts of the ligands (e.g., methyl groups in the case of the acetate-ligated nanocapsule), which dangle from the internal wall, cover the confined spherical space inside the cavity, and the hydrophobic character of the methyl groups causes disordering of the encapsulated water molecules. Thus it is necessary to modify the wall of the internal surface to obtain ordered/organized water assemblies inside the cavity. This modification can be done simply by substituting the ligands of the dinuclear units. Thus treating the nanocapsules that contain acetate ligands with hypophosphite anions results in a complete substitution giving rise to the compound $(NH_4)_{42}[\{Mo_2^{V}O_4(H_2PO_2)\}_{30}\{(Mo)Mo_5O_{21}(H_2O)_6\}_{12}] \cdot$ ca. $300H_2O$.[105] The nanocapsule in this hyphophosphic compound is superior in terms of water organization in the central cavity due to the fact that there are 20 voids between 30×2 H atoms of $(O_2P)H_2$ ligands, which are not abundant in the acetate- or sulfate-ligated nanocapsules.[85] These 20 void spaces allow the inclusion of 20 water molecules that interact with the next $(H_2O)_{60}$ cluster shell, resulting in the formation of a spherical $(H_2O)_{80}$ cluster in the central cavity of the nanosphere of compound $(NH_4)_{42}[\{Mo_2^{V}O_4(H_2PO_2)\}_{30}\{(Mo)Mo_5O_{21}(H_2O)_6\}_{12}] \cdot$ ca. 300 H_2O (Fig. 50). The $(H_2O)_{80}$ cluster is characterized by the involvement of 120 hydrogen bonds. This spherical water cluster has a large and well-defined central

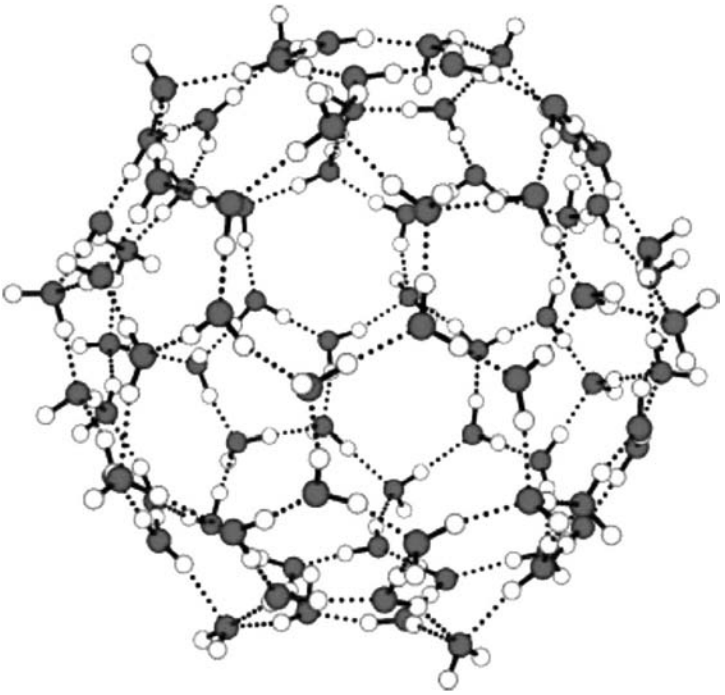

FIGURE 50. The $(H_2O)_{80}$ water assembly found in the central cavity of nanocapsule of $(NH_4)_{42}[\{Mo_2^{V}O_4(H_2PO_2)\}_{30}$-$\{(Mo)Mo_5O_{21}(H_2O)_6\}_{12}] \cdot$ ca. 300 H_2O. (Reprinted with permission from ref. 101.)

cavity (inscribed radius ~ 5.2 Å) and, accordingly, has been described as a nanobubble of water assembly in a confined space—namely, the internal central cavity of a spherical POM-based nanoobject. When 20 pores of the POM nanocapsule is closed by a guanidinium cation and the ligands of the dinulcear linkers are both hypophosphite and sulfate anions, 100 water molecules can be assembled into a $(H_2O)_{100}$ cluster. The structure of this assembly of 100 water molecules can be described by wrapping two centrally nested $(H_2O)_{20}$ dodecahedra by a strongly distorted $(H_2O)_{60}$ rhombicosidodecahedron. This can also be derived by intercalating a $(H_2O)_{20}$ dodecahedron into the two-shell $(H_2O)_{80}$ cluster.[101] Thus large water assemblies/clusters can be generated in a confined space of the giant spherical/icosahedral nanocapsules of the type $\{(Linker\}_{30}(Pentagon)_{12}\}$ POM clusters. These encapsulated water clusters may respond to physical influences, like the volume of the POM nanocapsules, chemical modifications of the internal capsule surface, and closing of the nanocapsule pores.

Thus far, discrete water clusters have been discussed that are associated with POM cluster anions. Polyoxometalates may also influence the stabilization of the water polymer. We have described the crystallographic observation of a new type of waterpipe (a water polymer) identified in supramolecular channels that are formed in the polyoxometalate POM-based inorganic–organic hybrid compound $[Cu_2(phen)_2(CH_3COO)(CH_3COOH)(H_2O)_2][Al(OH)_6Mo_6O_{18}]\cdot 28H_2O$.[106] This compound consists of an Anderson-type POM anion, $[Al(OH)_6Mo_6O_{18}]^{3-}$; a dimeric copper complex cation, $[Cu_2(phen)_2(CH_3COO)(CH_3COOH)(H_2O)_2]^{3+}$; and 28 lattice water molecules. It is interesting that 13 lattice water molecules (out of 14 water molecules in the asymmetric unit) are involved in forming a supramolecular $(H_2O)_{13}$ cluster, as shown in Figure 51.

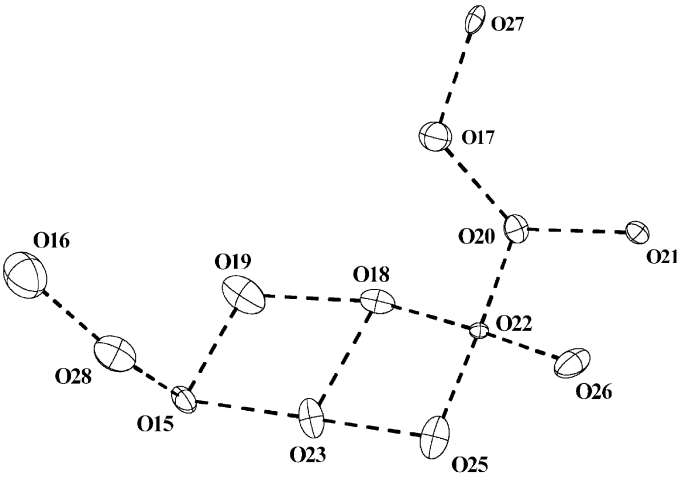

FIGURE 51. Hydrogen bonding interactions among lattice water molecules, O(15)–O(28) resulting in the formation of a $(H_2O)_{13}$ cluster. (Reprinted with permission from ref. 106.)

FIGURE 52. The generation of a waterpipe formed by the repetition of a $(H_2O)_{13}$ cluster (as shown in Fig. 51). (Reprinted with permission from ref. 106.)

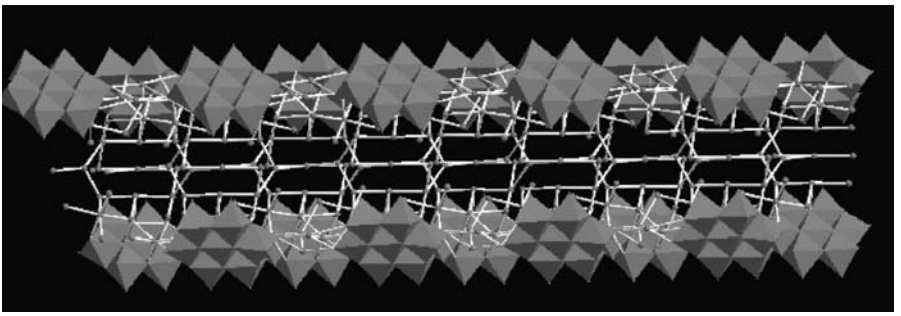

FIGURE 53. The side view of the water tube (white sticks) in between the Anderson heteropolyanions (polyhedral representation, red color). The copper dimeric complex cation is not shown for clarity.

The repeating arrangement of the $(H_2O)_{13}$ cluster leads to the construction of a new type of waterpipe, as shown in Figure 52. The inner diameter dimensions of the water tube were found to be 8.527×8.061 Å^2. The existence of such unstable pipe (vide supra) has been made possible by interactions with its surroundings, including an Anderson heteropolyanion and a dimeric copper complex cation.

There are extensive hydrogen bonding interactions between surface oxygen atoms of the Anderson anion (terminal, bridging and μ_3-O oxygen atoms) and the water tube oxygen atoms. Figure 53 shows the importance of the POM cluster anion in stabilizing such a waterpipe.

V. CONCLUDING REMARKS

Transition-metal coordination complexes that are susceptible to showing facile electron transfer through red-ox reactions are generally good catalysts for organic transformations of industrial importance. However, the major drawback in using these coordination complexes as catalysts is the loss of catalyst in each run because the soluble metal coordination complex (catalyst) cannot be

recovered from the homogeneous reaction mixture. POMs, which have available coordination sites (oxo donors), can easily support coordination complexes on their surface and thereafter can be used as a heterogeneous catalyst because the POM-supported transition-metal complexes are not generally soluble in the catalysis reaction mixture. In the first part of this chapter, both heteropolyanion- and isopolyanion-supported metal coordination complexes were described. It was shown that a particular type of heteropolyanion—namely the Anderson-type anion $[Al(OH)_6Mo_6O_{18}]^{3-}$—can be used as a potential building block to obtain a new class of one-dimensional coordination polymer using lanthanide ions as linkers. When this lanthanide linker is replaced by a transition-metal (copper) coordination complex, a spiral type chain is obtained in which the copper phenanthroline complex is the linker. Finally, if we choose an "s" block metal ion (e.g., sodium ion) as a linker in the same system of Anderson heteropolyanion, we end up with a three-dimensional coordination polymer with a framework type structure that has well-defined channels. Thus a POM cluster anion can be used as a versatile building block to achieve new metal oxide–based materials of diverse dimensions. The POM cluster anions in these POM-supported transition-metal complexes undergo a variety of hydrogen bonding interactions and generate remarkable supramolecular structures.

The second part of the chapter dealt with crown ether encapsulated- or associated-metal ions or organic cations known as supramolecular cations, which are coupled with POM anions. It was demonstrated that POM cluster anions play an important role in identifying a new type of supramolecular sandwich consisting of two crown ethers and an unusual penta-aqua copper(II) ion. The formation of such a unique sandwich is otherwise not known. It has also been shown that a soft metal ion can be included in the hard donor center of a large-cavity crown ether through its supramolecular interactions with the POM cluster anion. The important structural feature of POM clusters is the presence of a bare nucleophilic surface, which acts as a hydrogen bond acceptor. It was shown that the projection of hydrogen bond donors (e.g., organic ligands, crown ethers, and water) toward the POM cluster surface can lead to remarkable supramolecular structures.

In the last part of this chapter, the importance of POM cluster anions in generating a diverse range of water clusters was described. The role of giant icosahedral/spherical nanocapsules on the water assembly that is trapped within the central cavity of the nanocapsules was emphasized.

VI. ACKNOWLEDGEMENTS

I am grateful for important contributions to our own work in this research area from my co-workers. I thank Department of Science and Technology, Government of India, for financial support (Project No. SR/SI/

IC-23/2007). The National X-Ray Diffractometer facility at the University of Hyderabad by the Department of Science and Technology, Government of India, is gratefully acknowledged. I am grateful to UGC, New Delhi, for providing the infrastructure facility at University of Hyderabad under a UPE grant.

VII. REFERENCES

1. M. T. Pope, *Heteropoly and Isopoly Oxometalates*, Springer Verlag, New York, **1983**.
2. J. J. Borrás-Almenar, E. Coronado, A. Müller, and M. Pope, *Polyoxometalate Molecular Science*, Kluwer Academic, Dordrecht, **2003**.
3. E. Coronado, and J. Gómez-García, *Chem. Rev*., **1998**, *98*, 273.
4. C. L. Hill, *Chem. Rev.,* **1998**, *98*, 1.
5. J. T. Rhuie, C. L. Hill, D. A. Judd, and R. F. Schinazi, *Chem. Rev*., **1998**, *98*, 327.
6. J. M. Lehn, *Angew. Chem*. **1989**, *27*, 89.
7. Z. Han, Y. Zhao, J. Peng, A. Tian, Y. Feng, and Q. Liu, *J. Solid State Chem*., **2005**, *178*, 1386.
8. V. Shivaiah, *Inorg. Chem. Commun*., **2006**, *9*, 1191.
9. G. R. Desiraju, *Angew. Chem., Int., Ed*, **1995**, *34*, 2311.
10. J. C. MacDonald, and G. M. Whitesides, *Chem. Rev*., **1994**, *94*, 2383.
11. A. Müller and C. Serain. *Acc. Chem. Res*., **2000**, *33*, 2.
12. A. Müller, P. Kögerler, and C. Kuhlmann, *Chem. Commun*., **1999**, 1347.
13. L. Cronin, P. Kögerler, and A. Müller. *J. Solid State Chem*, **2000**, *152*, 57.
14. A. Müller, P. Kögerler, and H. Bögge. *Struct. Bond. (Berlin)*, **2000**, *96*, 203.
15. A. Müller, F. Peters, M. T. Pope, and D. Gatteschi. *Chem. Rev*., **1998**, *98*, 239.
16. D.-L. Long, E. Burkholder, and L. Cronin, *Chem. Soc. Rev*., **2007**, *36*, 105.
17. M. Pope and A. Müller, Eds., *Polyoxometalate Chemistry from Topology via Self-Assembly to Applications*, Kluwer Academic, London, **2001**.
18. T. Yamase and M. Pope, Eds., *Polyoxometalate Chemistry for Nano-Composite Design,* Kluwer Academic, New York, **2002**.
19. L. Cronin, *Compr. Coord. Chem. II*, **2004**, *7*, 1.
20. A. Müller, P. Kögerler, and A. W. M. Dress, *Coord. Chem. Rev*., **2001**, *222*, 193.
21. A. Müller and S. Roy, *Coord. Chem. Rev*., **2003**, *245*, 153.
22. T. Akutagawa, D. Endob, S.-I. Nora, L. Cronin, and T. Nakamura, *Coord. Chem. Rev*., **2007**, *251*, 2547.
23. P. J. Hagraman, D. Hagraman, and J. Zubieta, *Angew. Chem., Int. Ed*., **1999**, *38*, 2638.
24. H. Zeng, G. R. Newkome, and C. L. Hill, *Angew. Chem., Int. Ed*., **2000**, *39*, 1771.
25. A. Mueller, W. Plass, E. Krickemeyer, S. Dillinger, H. Bögge, A. Armatage, A. Proust, C. Beugholt, and U. Bergmann, *Angew. Chem., Int. Ed. Engl*., **1994**, *33*, 849.
26. P. Gouzerh and A. Proust, *Chem. Rev*., **1998**, *98*, 77.
27. M. Yaun, Y. Li, E. Wang, C. Tian, L. Wang, N. Hu, and H. Jia, *Inorg. Chem*., **2003**, *42*, 3670.
28. M.-X. Li, J. Du, J.-P. Wang, and J.-Y. Niu, *Inorg. Chem. Commun*., **2007**, *10*, 1391.
29. Y. Xu, J.-Q. Xu, K.-L Zhang, Y. Zhang, and X.-Z. You, *Chem. Commun*., **2000**, 153.

30. D. G. Allis, E. Burkholder, and J. Zubieta, *Polyhedron*, **2004**, *23,* 1145.
31. V. Shivaiah, T. Chatterjee, and S. K. Das, *Synthesis and Reactivity in Inorganic, Metal-Organic, and Nano-Metal Chemistry*, **2008**, *38*, 12.
32. J. Luo, M. Hong, R. Wang, Q. Shi, R. Cao, J. Weng, R. Sun, and H. Zhang, *Inorg. Chem. Commun*., **2003**, *6*, 702.
33. P. J. Hagraman and J. Zubieta, *Inorg. Chem*., **1999**, *38*, 4480.
34. C.-D. Wu, C.-Z. Lu, H.-H. Zhuang, and J.-S. Huang, *Inorg. Chem*., **2002**, *41*, 5636.
35. A. M. Khenkin, L. J. W. Shimon, and R. Neumann, *Inorg. Chem*., **2003**, *42*, 3331.
36. H. T. Evans, B. Gatehouse, and P. Leverett, *J. Chem. Soc., Dalton Trans*., **1975**, 505.
37. T. Li, J. Lu, S. Gao, and R. Cao, *Inorg. Chem. Commun*., **2007**, *10*, 1342.
38. D.-L. Long, P. Kögerler, L. J. Farrugia, and L. Cronin, *Angew. Chem., Int. Ed*., **2003**, *42*, 4180.
39. D.-L. Long, P. Kögerler, L. J. Farrugia, and L. Cronin, *J. Chem. Soc., Dalton Trans*., **2005**, 1372.
40. T. Arumuganathan, A. Srinivasarao, T. Vijay Kumar, and S. K. Das, *J. Chem. Sci*. **2008**, *120*, 95.
41. V. Shivaiah, T. Arumuganathan, and S. K. Das, *Inorg. Chem. Commun*., **2004**, *7*, 367.
42. Y. Lu, Jian Lü, E. Wang, Y. Guo, X. Xu, L. Xu, *J. Molecular Structure*, **2005**, *740*, 159.
43. V. Shivaiah, P. V. N. Reddy, L. Cronin, and S. K. Das, *J. Chem. Soc. Dalton Trans*., **2002**, 3781.
44. D. Drewes, E. M. Limanski, and B. Krebs, *J. Chem. Soc., Dalton Trans*, **2004**, 2087.
45. V. Shivaiah, M. Nagaraju, and S. K. Das, *Inorg. Chem*., **2003**, *42*, 6604.
46. P. Mialane, A. Dolbecq, L. Lisnard, A. Mallard, J. Marrot, and F. Sécheresse, *Angew. Chem., Int. Ed*., **2002**, *41*, 2398.
47. M. I. Khan, S. Tabassum, and R. J. Doedens, *Chem. Commun*., **2003**, 532.
48. F.-X. Liu, C. Marchal-Roch, P. Bouchard, J. Marrot, J-.P. Simonato, G. Herve, and F. Sécheresse, *Inorg. Chem*., **2004**, *43*, 2240.
49. W. Yang, C. Lu, X. Zhan, and H. Zhuang, *Inorg. Chem*. **2002**, *41*, 4621.
50. C.-De. Wu, C.-Z. Lu, X. Lin, H.-H. Zhuang, and J.-S. Huang, *Inorg. Chem. Commun*., **2002**, *5*, 664.
51. C.-M. Liu, J.-L. Luo, D.-Q. Zhang, N.-L. Wang, Z.-J Chen, and D.-B. Zhu, *Eur. J. Inorg. Chem*., **2004**, 4774.
52. V. Shivaiah and S. K. Das, *Inorg. Chem*., **2005**, *44*, 8846.
53. S. Manikumari, V. Shivaiah, and S. K. Das, *Inorg. Chem*. **2002**, *41*, 6953.
54. V. Shivaiah and S. K. Das, *J. Chem. Sci*., **2005**, *117*, 227.
55. J.-M. Lehn, *Angew. Chem., Int. Ed. Engl*., **1988**, *27*, 89.
56. C. J. Pederson, *J. Am. Chem. Soc*., **1967**, *89*, 7017.
57. C. J. Pederson, *J. Am. Chem. Soc*., **1970**, *92*, 391.
58. C. J. Pederson, *J. Am. Chem. Soc*., **1970**, *92*, 386.
59. V. Svec, V. Mikulaj, and R. J. Hanzel, *J. Radioanal. Nucl. Chem*., **1996**, *208*, 487.
60. S. Sheem and Shiu, *Analyst*., **1992**, *117*, 1691.
61. V. Shivaiah and S. K. Das, *Angew. Chem. Int. Ed. Engl*., **2006**, *45*, 245.
62. A. Pasquarello, I. Petri, P. S. Salmon, O. Parisel, R. Car, E. Toth, D. H. Powell, H. E. Fischer, L. Helm, and A. E. Merbach, *Science*, **2001**, *291*, 856.
63. B. J. Hathaway, in *Comprehensive Coordination Chemistry*, vol. 5, Ed., G. Wilkinson, Pergamon, Oxford, **1987**, p. 533.
64. J. E. Huheey, E. A. Keiter, and R. L. Keiter, *Inorganic Chemistry*, 4th ed., Pearson Education, Singapore, **2000**.

65. N. N. Greenwood and A. Earnshaw, *Chemistry of the Elements*, Pergamon, Oxford, **1989**.
66. W. D. Harrison and B. J. Hathaway, *Acta Crystallogr. Sect. B.*, **1980**, *36*, 1069.
67. V. K. Belsky, N. R. Streltsova, B. M. Bulychev, P. A. Storozhenko, L. V. Ivankina, and A. I. Gorbunov, *Inorg. Chim. Acta.*, **1989**, *164*, 211.
68. T. Sakuraa, K. Kobayashi, S. Tsuboyama, Y. Kohno, and K. Ishizu, *Acta Crystallogr.*, **1983**, *C39*, 206.
69. F. P. Van Remoorte, F. P. Boer, and E. C. Steiner, *Acta Crystallogr.*, **1975**, *31*, 1420.
70. V. Shivaiah and S. K. Das, *Inorg. Chem.*, **2005**, *44*, 7313.
71. I. R. Hanson, D. L. Hughes, and M. R. Truter, *J. Chem. Soc., Perkin Trans.*, **1976**, *2*, 972.
72. Y. Li, N. Hao, E. Wang, M. Yuan, C. Hu, N. Hu, and H. Jia, *Inorg. Chem.*, **2003**, *42*, 2729.
73. W. You, E. Wang, Y. Xu, Y. Li, L. Xu, and C. Hu, *Inorg. Chem.*, **2001**, *40*, 5468.
74. R. Neier, C. Trojanowski, and R. J. Mattes, *Chem. Soc., Dalton Trans.*, **1995**, 2521.
75. F. L. Sousaa, F. A. A. Pazb, P. C. R. Soares-Santosa, A. M. V. Cavaleiroa, H. I. S. Nogueiraa, J. Klinowskib, and T. Trindade, *J. Molecular Structure*, **2004**, *689*, 61.
76. T. Akutagawa, D. Endo, H. Imai, S.-I. Noro, L. Cronin, and T. Nakamura, *Inorg. Chem.*, **2006**, *45*, 8628.
77. W. You, E. Wang, Q. He, L. Xu, Y. Xing, and H. Jia, *J. Molecular Structure*, **2000**, *524*, 133.
78. W. You, E. Wang, H. Zhang, L. Xu, and Y. Wang, *J. Molecular Structure* **2000**, *554*, 141.
79. L. E. Cheruzel, M. S. Pomentum, M. R. Cecil, M. S. Mashuta, R. J. Wittebort, and R. M. Buchanan, *Angew. Chem. Int. Ed.*, **2003**, *42*, 5452.
80. R. Ludwig, *Angew. Chem. Int. Ed.*, **2001**, *40*, 1809.
81. P. R. ten Wolde and D. Frankel, *Science*, **1997**, *277*, 1975.
82. S. D. Colson and T. H. Dunning, *Science*, **1994**, *265*, 43.
83. K. Liu, J. D. Cruzan, and R. S. Saykally, *Science*, **1996**, *271*, 929.
84. F. N. Keutsch and R. J. Saykally, *Proc. Natl. Acad. Sci. U. S. A.*, **2001**, *98*, 10533.
85. A. Müller, E. Krickemeyer, H. Bögge, M. Schmidtmann, B. Botar, and M. O. Talismanova, *Angew. Chem. Int. Ed.*, **2003**, *42*, 2085.
86. L. Infantes and S. Motherwell, *CrystEngComm.*, **2002**, *4*, 454.
87. M. Mascal, L. Infantes, and J. Chisholm, *Angew. Chem. Int. Ed.*, **2006**, *45*, 32.
88. T. R. Dyke, K. M. Mack and J. S. Muenter, *J. Chem. Phys.*, **1977**, *66*, 498.
89. J. A. Odutola and T. R. Dyke, *J. Chem. Phys.*, **1980**, *72*, 5062.
90. K. Liu, J. G. Loeser, M. J. Elrod, B. C. Host, J. A. Rzepiela, N. Pugliano, and R. J. Saykally, *J. Am. Chem. Soc.*, **1994**, *116*, 3507.
91. N. Pulgliano, and R. J. Saykally, *Science*, **1992**, *257*, 1937.
92. L. R. MacGillivray and J. L. Atwood, *J. Am. Chem. Soc.*, **1997**, *119*, 2592.
93. R. J. Doedens, E. Yohannes, and M. I. Khan *Chem. Commun.*, **2002**, 62.
94. D. Eisenberg and W. Kauzmann, *The Structure and Properties of Water*, Oxford University Press, Oxford, **1969**.
95. C. J. Gruenloh, J. L. Carney, C. A. Arrington, T. S. Zwier, S. Y. Fredericks, and K. D. Jordan, *Science*, **1997**, *276*, 1678.
96. C. J. Tsai and K. D. Jordan, *J. Chem. Phys.*, **1991**, *95*, 3850.
97. C. J. Tsai and K. D. Jordan, *J. Chem. Phys.*, **1993**, *99*, 6957.
98. K. Kim, and T. S. Zwier, *J. Am. Chem. Soc.*, **1994**, *116*, 11568.

99. F. Weinhold, *J. Chem. Phys.*, **1998**, *109*, 367.
100. F. Weinhold, *J. Chem. Phys.*, **1998**, *109*, 373.
101. M. Henry, H. Bögge, E. Diemannb, and Achim Müller, *J. Mol. Liquids*, **2005**, *118*, 155.
102. A. Müller, E. Krickemeyer, H. Bögge, M. Schmidtmann, and F. Peters, *Angew. Chem. Int. Ed.*, **1999**, *38*, 3360.
103. A. Müller, V. P. Fedin, C. Kuhlmann, H. Bögge, and M. Schmidtmann, *J. Chem. Soc. Chem. Commun.*, **1999**, 927.
104. A. Müller, S. Q. N. Shah, H. Bögge, M. Schmidtmann, P. Kögerler, B. Hauptfleisch, S. Leiding, and K. Wittler, *Angew. Chem. Int. Ed.*, **2000**, *39*, 1614.
105. A. Müller, S. Polarz, S. K. Das, E. Krickemeyer, H. Bögge, M. Schmidtmann, and B. Hauptfleisch, *Angew. Chem. Int. Ed.*, **1999**, *38*, 3241.
106. V. Shivaiah, T. Chatterjee, K. Srinivasu, and S. K. Das, *Eur. J. Inorg. Chem.*, **2007**, 231.

CHAPTER 4

Supramolecular Coordination Networks Employing Sulfonate and Phosphonate Linkers: From Layers to Open Structures

George K. H. Shimizu, Jared M. Taylor, and Ramanathan Vaidhyanathan

Department of Chemistry, University of Calgary, Calgary, Alberta T2N 1N4, Canada

CONTENTS

Macromolecules Containing Metal and Metal-Like Elements,
Volume 9: Supramolecular and Self-Assembled Metal-Containing Materials,
Edited by Alaa S. Abd-El Aziz, Charles E. Carraher Jr., Charles U. Pittman Jr., and Martel Zeldin.

I. INTRODUCTION

Metal organic frameworks (MOFs) or porous coordination polymers (PCPs) represent an immense and still growing field of research.[1] These materials represent hybrids of inorganic and organic components and, as such, their structural properties span a wide range. One could look at these materials as analogous to metal oxides where the anion can be replaced by a virtually limitless number of organic ligands. This conceptual substitution, even if maintaining the same topology, likely necessitates the formation of pores in the solid. This is a key distinction between MOFs/PCPs and traditional coordination polymers and one that is not always well defined; the formation and retention of an open structure is a paramount synthetic challenge for these solids.

Conventional and correct thinking would dictate that a porous architecture requires sufficiently strong bonding between components to sustain the void being formed, such as the Al-O and Si-O bonds in zeolites.[2] Coordinate covalent bonding does not, on an individual bond basis, provide comparable strength to bonds in zeolites. However, several authors have definitively shown that, by elegant strategies employing cooperative bonding effects, permanent porosity is attainable in coordination solids.[3] Porosity can be to differing degrees but with the common basis that the interior of the solid is accessible to a fluid phase. The highest degree requires a rigid architecture and the observation of a reversible gas sorption isotherm; this is now regularly attainable for coordination solids.[4] Another level of porosity is observed in coordination solids where a structural change accompanies removal of the solvent that occupies the pores. If this process is reversible and a fluid phase can again access the solid's interior, this also represents a form of porosity.[5] The porosity of coordination solids has been classified into three generations by Kitagawa: the first being solids that include solvent but that collapse irreversibly on guest removal (hence not truly porous), the second being those that sustain pores giving a reversible gas sorption isotherm, and the third being those materials that shift structure yet reversibly resorb removed guest molecules.[6] Much effort is ongoing to develop new design strategies to enable porous solids from coordination building blocks. Two interrelated challenges facing the preparation of any porous coordination solid are the use of bonding interactions strong enough to allow the formation of a porous solid and the retention of a crystalline architecture.[7] These two aspects can be conflicting as very strong interactions between building units can lead to rapid precipitation of less ordered solids.

With a focus on design, a logical avenue of thought is to pursue building units with regular and predictable bonding tendencies. Balancing this with the bond strength requirements mentioned earlier has translated to the large majority of coordination network research focusing on polytopic carboxylate[8] and pyridine-like ligands[9] as the organic linkers. Correspondingly, metal ions

with regular geometrical preferences have also been the focus, largely transition-metal ions. Metal phosphonates have been studied primarily as layered networks.[10] They are prototypical "hybrid inorganic–organic" solids, in which inorganic layers alternate with organic interlayer regions. In these materials, the pendant organic groups pack in a manner to preclude any interlayer porosity. Even with densely packed interlayer regions, these solids have demonstrated function in solid catalysis,[11] optical devices,[12] and film precursors.[13] More discussion on efforts to generate porous solids from these materials will follow later in this chapter, however, at this point, the key illustration is simply that the inorganic backbone provides a rigid and regular scaffolding from which a wide range of organic groups can be appended while maintaining the same core structure. Metal sulfonates have been examined with transition metals as potential analogs of metal phosphonates.[14] Under hydrous conditions, with transition metals and most hard metal ions, the most frequent observation is the formation of ion pairs between fully hydrated metal cations and sulfonate anions—that is, no true network is formed.[15]

There are numerous groups that have made very significant contributions in the areas of sulfonate networks, as referenced throughout this chapter, and our contribution to the phosphonate field has been modest. With acknowledgment of these works, the invitation for this chapter was a focus on our own efforts and so the focus will be on the work of the Shimizu group since 1999. With respect to the design of functional coordination solids, our group has taken an alternative approach to that of the pairing of components with regular coordination tendencies outlined earlier. Rather than focusing on building units with rigidly defined (and constrained) bonding preferences, we have chosen to study units that have more pliant bonding tendencies with a range of possible structural motifs within a narrow energetic window.[16] This approach will be clarified and expanded in this chapter, but, essentially, we view our approach as enabling the formation of not necessarily less-defined structures but more adaptable ones. In particular, we will discuss the chemistry of network solids formed by metal-sulfonate (RSO_3)[17] and metal phosphonate (RPO_3^{2-}) building blocks.

II. THE SULFONATE GROUP AS A LIGAND

The sulfonate group in coordination chemistry is generally regarded as a poor ligand.[18] The use, therefore, of such a functional group in the formation of robust networks may seem counterintuitive. Two important clarifications must be made in the chemistry of the sulfonate group and its preconception as a weakly coordinating ligand. The first is that, while an O donor group, owing to the delocalization of the valence electrons, the group can be considered a soft Pearson base. In most cases, in which it is observed to be weakly coordinating,

harder transition-metal complexes are the systems under study. This is corroborated by the fact that, with transition-metal ions in aqueous solutions, sulfonate ions typically fail to displace water from the primary coordination sphere.[15] Softer metal ions should be favored for coordination by sulfonates. The second key point is that the bonding tendencies of any functional group in solution, either in molecular complexes or in discrete assemblies, do not transfer linearly to its coordinative tendencies in network solids. A network solid represents the extreme case of cooperative bonding interactions between components, so-called matrix effects, and so what may be a weak interaction in a discrete system in solution can have its stability augmented dramatically in an infinite solid.

With respect to metal ions that sulfonate groups coordinate well to, as a soft base, the best partners are metal ions with polarizable coordination spheres. We have found very good success with Ag^+ and heavier alkaline earth ions, in particular, Ba^{2+}. The ensuing sections discuss metal sulfonates initially as more classical hybrid inorganic–organic solids with layered structures and then proceed to pillared layered motifs and finally nonlayered structures. Scheme **1** shows the ligands discussed in this chapter.

III. LAYERED METAL SULFONATES

The structure of a prototypical hybrid inorganic–organic solid is that of continuous inorganic layers with pendant organic groups. The inorganic layers have a rigid structure and serve to provide a scaffolding of regular anchor points for the organic groups. In 1998, two groups reported the structure of silver *p*-toluenesulfonate, AgL1, **1**.[19] The structure fits that of the classic inorganic–organic hybrid, as shown in Figure 1a. The silver ion had an irregular geometry with a coordination sphere of five oxygen atoms. Rather surprisingly, for all the complexations and reactions in which this compound must have been employed over the years, the X-ray structure had never been reported. Likely, this fact stems from the difficulty in growing sufficiently thick single crystals, as the solid is predisposed to forming very thin plates, coupled with the lack of accessibility to CCD X-ray diffraction technology before to the mid-1990s.

The single crystal structure of a closely related material to **1** was obtained, that of silver benzenesulfonate, AgL2, **2**.[20] The side-on view of **2** (Fig. 2a), appears to resemble that of **1**. Although the organic groups orient differently, the structure of **2** is still that of an inorganic–organic hybrid. A closer look at the layer structure (Fig. 2b) shows that not only are the aryl groups oriented differently but they are anchored to the layer at different points. That is, the silver coordination and the layer structure were fundamentally different in **2** than in **1**.

In **2**, the silver (I) ion adopted a six-coordinate geometry and the SO_3 groups each bridged six different silver centers (i.e., a saturated μ^6 mode).

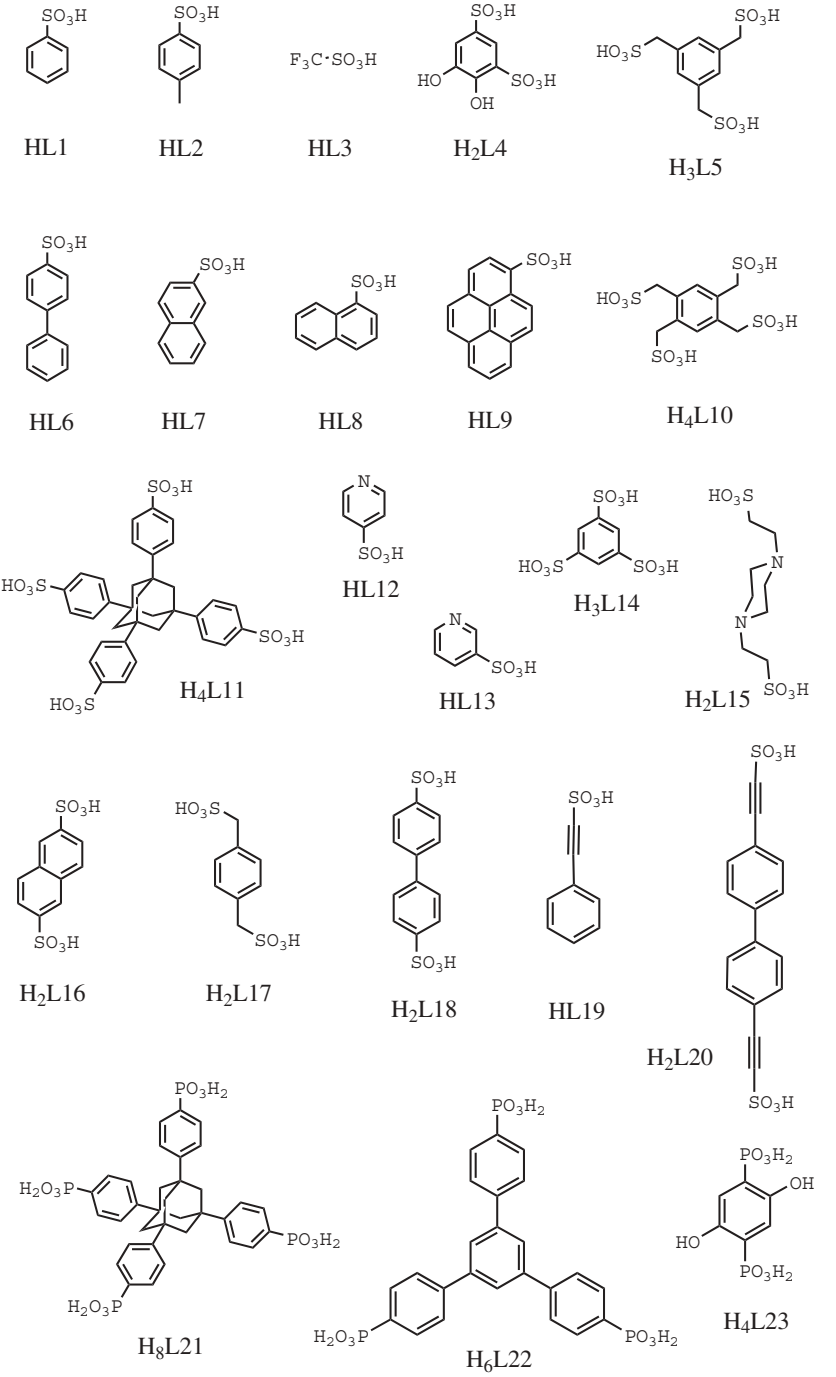

SCHEME 1. Sulfonate and phosphonate ligands with their numbering.

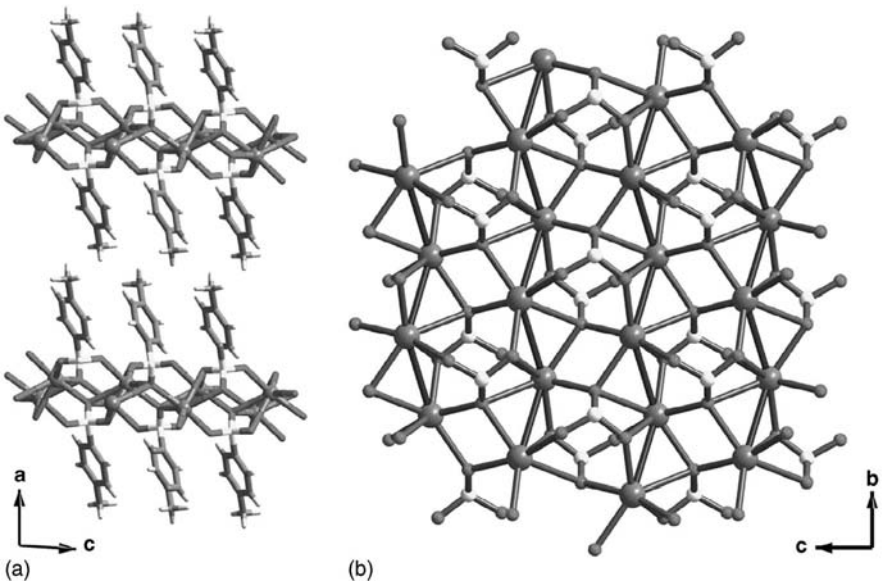

FIGURE 1. (a) The inorganic–organic hybrid structure of the silver *p*-toluenesulfonate, AgL1, **1**. Sulfonate-Ag connectivities form the infinite lamellar structure, while the toluene groups directed into the interlayer region impart significant hydrophobic character to these spaces. (b) View down onto a single layer of AgL1, **1**, with the toluene groups omitted for clarity, showing the fivefold donacity of the SO_3 groups and the seven-atom coordination about each silver. Ag, dark large spheres; S, light medium spheres; O, dark small spheres.

In both **1** and **2**, there is no water ligated to any of the silver(I) centers, although the crystals were obtainable from aqueous solutions. A key observation to extract from these two examples, which diverges from the pattern observed for metal phosphonates, is that the inorganic backbone does not provide an inflexible skeleton on which the organic groups are merely pendant. In **1** and **2**, the organic groups play a structural affecting role, if not necessarily a structure-determining one. The differences in the two-layered solids arose simply from the presence of the methyl group in the 4-position of the phenyl ring in **1**. The larger inference of this small observation was that packing and aryl-aryl interactions in the interlayer could affect the coordination modes of both the silver ions and the SO_3 groups in the layer itself, a direct deviation from the chemistry of metal phosphonates. This point was the origin of the concept of metal sulfonates as adaptable solids. A later section discusses the dependence of the layered motif with variation of organic group.

The formation of a metal sulfonate solid with a two-dimensional structure reminiscent of more robust metal phosphonates was an intriguing result. However, a more important illustration would be that metal sulfonates were not simply structurally similar to metal phosphonates but that they could

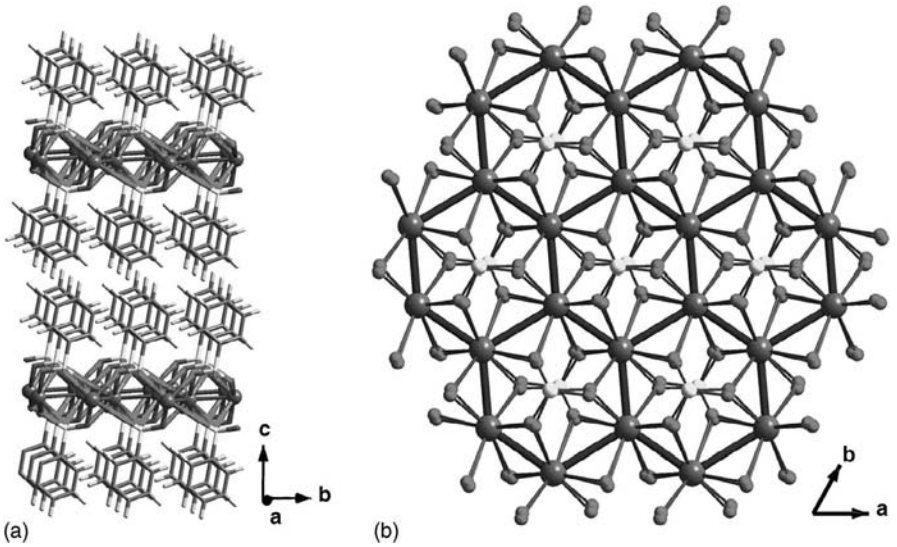

FIGURE 2. (a) Structure of silver benzenesulfonate, AgL2, **2,** showing the overall lamellar network with phenyl groups protruding into the interlayer region. The grid-like arrangement of the silver atoms in the *ab* plane is shown in brown lines. Disorder has been removed for clarity. (b) View down onto a single lamella of the structure of silver benzenesulfonate, AgL2, **2**, with phenyl rings and disordered oxygen atoms removed for clarity. Note the hexagonal arrangement of the silver(i) centers, the nonavalent coordination mode, and the μ_6-sulfonate groups.

behave in a similar manner chemically. For solids that are strongly bonded in two-dimensions, such as graphite,[21] metal sulfides,[22] and clays,[23] a fundamental physical observation is that the layers can be separated and other molecular species intercalated between the layers. A preliminary study was performed on **1** with nonylamine and monitored by powder X-ray diffraction (PXRD).[19a] After treatment of **1** with nonylamine and heating to 70°C, indexing the sample gave a unit cell that showed intercalation. The indexing result showed that two axes, those in the plane of the $AgSO_3$ layer, were closely related if not identical, whereas the third axis increased markedly. These data were consistent with retention of the inorganic layers, albeit with minor rearrangement, and the expected swelling of the structure. We reported a more detailed study on the intercalation of alcohols into Ag triflate, AgL3, **3a**, another layered material that corroborated these findings.[24] In this case, single crystal X-ray structural data of an actual intercalate complex was obtained. Figure 3 shows the structure of AgL3$(EtOH)_{0.5}$, **3b**, which shows that the ethanol solvate forms a coordinative intercalate. A series of alcohols of varying chain length were examined and, by PXRD and thermogravimetric analysis (TGA), it was confirmed that the entire series was structurally related, with the guest alcohols adopting an identical coordination mode to the layer as in **3b** (Figure 4).

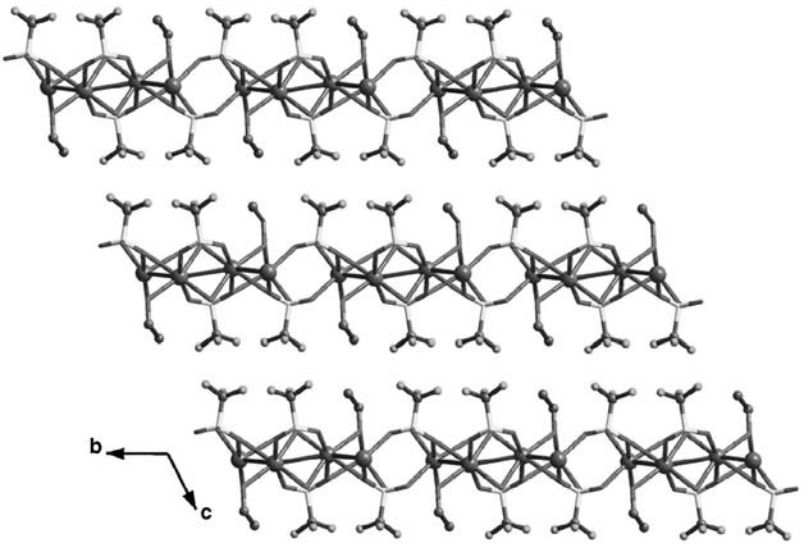

FIGURE 3. The lamellar network formed by $AgL3(EtOH)_{0.5}$, **3a**, showing the CF_3 and EtOH groups directed into the interlayer region. Ag, dark large spheres; F, light small spheres; C, dark small spheres. Hydrogens have not been shown for clarity.

Thus the intercalation was topotactic. From progressive swelling of the layers, the tilt angles of the alcohols were obtained. Another observation made in both these intercalation studies was that the silver salts showed no photodecomposition as is often observed with silver(I) salts. The principal conclusion to these intercalation studies was that, although flexible and sustained by $M\text{-}SO_3$ interactions, the Ag sulfonate inorganic layers were sufficiently robust to display intercalation, a phenomenon more associated with strongly bonded solids. As mentioned, heavier alkaline earth ions also coordinate well with sulfonate ions. For simpler monosulfonate ions, it would be expected that a layered motif would also result. In fact, barium sulfonates have been employed as lubricants, owing to the regularity of their two-dimensional motif,[25] this despite a paucity of single crystal X-ray data on barium sulfonates. To form a layered sulfonate with an open pillared layered structure, we examined the tironate anion, 1,3-disulfo-4,6-dihydroxybenzene, L4.[26] The SO_3 groups on this ligand do not orient at 180°, and so it was anticipated that some interlayer porosity would be created. The structure of the barium tironate complex, **4**, is (Fig. 5).

Indeed, the bent conformation of the pillar resulted in micropores in the interlayer. The stability of this structure was augmented by chelation of the hydroxyl groups to the Ba centers in addition to the SO_3 ligation. The pores in **4** were occupied by water molecules, which was to be expected. Unexpectedly, the hydrogen atoms of the intrachannel water molecules were readily observed in the difference map during the single crystal X-ray structure

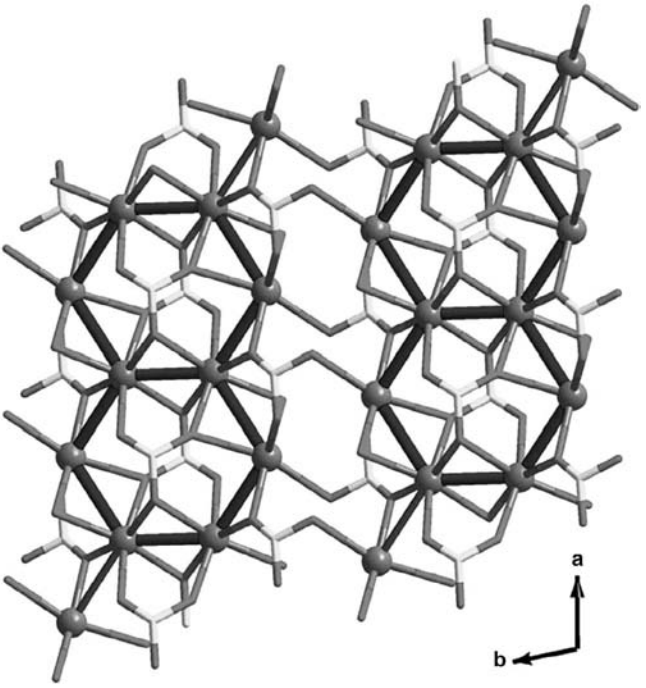

FIGURE 4. View down onto a single layer of compound AgL3$(EtOH)_{0.5}$, **3a**. Note the rows of edge-sharing Ag hexagons (blue trace) and the two types (μ_4 and μ_5) of bridging sulfonate groups.

determination. This indicated that the water guest molecules were held in a regular orientation and that the pore was well suited to the shape of H_2O molecules. Given this, a more interesting and structurally related guest molecule, that being H_2S, was examined as a potential guest. The subtle nature of intercalation in these pores was evidenced by this system. Heating a bulk sample of **4** to 110°C on the TGA selectively removed only the water molecules in the channels without altering the structure, as confirmed by PXRD analysis. This left empty channels imprinted with the shape of the guest water molecules. When the flow gas was changed to H_2S, 0.93 equivalent of H_2S, with respect to 1 equivalent of displaced H_2O, was observed. The network, **4**, with empty channels was also selective, as other small molecules such as H_2, O_2, Cl_2, SO_2, CO_2, Ar, MeOH, and CH_4 were not absorbed. This reversible and selective H_2S uptake constituted the first illustration of functional porosity in a layered metal sulfonate. More generally, it showed that permanent pores could exist in a metal sulfonate material. In this solid, the structural integrity (TGA showed stability to >400°C) was augmented by a chelating catechol moiety in the tironate ligand. A later example, compound **6**, illustrates that a homoleptic barium sulfonate could be sufficiently robust to allow for interlayer chemistry.

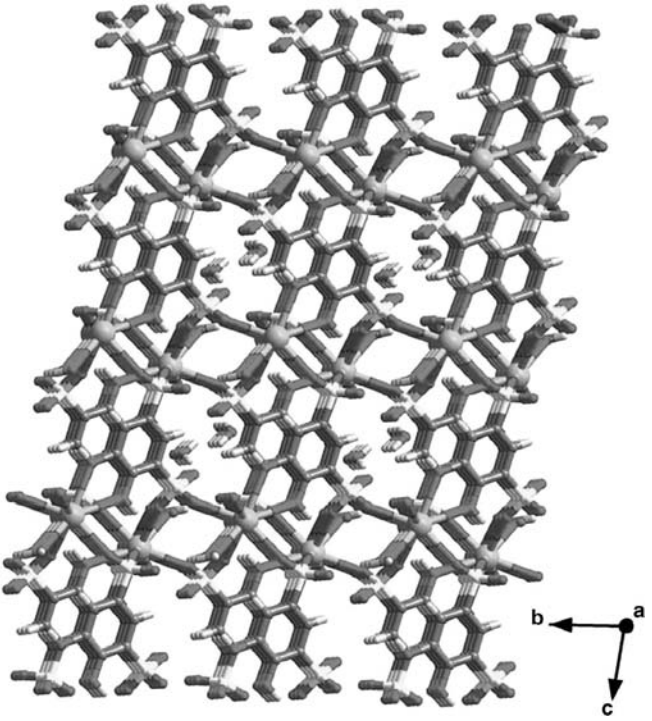

FIGURE 5. Structure of Ba Tironate Complex, **4**, viewed down the *a* axis. Ba, large spheres, S, light small spheres; O, dark small spheres. Note the channels and the water molecules occupying them.

The silver(I) complex of the pseudo-trigonally symmetric trisulfonate ligand 1,3,5-*tris*(sulfonomethyl)-benzene, $\{[Ag_6(L5)_2(H_2O)_5]\cdot 2H_2O\}_\infty$, **5**, formed a pillared layered solid, as shown in Figure 6.[27] The overall structure is a pillared layered motif, in which sheets of SO_3-bridged Ag ions are separated by mesitylene units. Each molecule of L5 has one sulfonate group coordinating to one layer and two sulfonate groups ligating to an adjacent layer. Alternating ligand molecules have their orientations flipped. Notably, the pillars were not densely packed, which resulted in the creation of interlayer void space in which water molecules were included. The channels had dimensions of 8.50(5) Å by 4.25(5) Å and are occupied by two crystallographically unique water molecules. TGA showed that this network was stable to 320°C after desolvation.

The stability of pillared layered networks with polysulfonate ligands will be discussed later; however, at this point, it is worth noting that the layered $AgSO_3$ structure was retained even with the creation of void space with the mesitylene pillar. An indication of the favorability of the network structure of compound **5**, beyond the stability over 300°C, came from the $BaCl_2$ complex of the same ligand, compound **6**.[28] Despite the increased charge on the cation, a

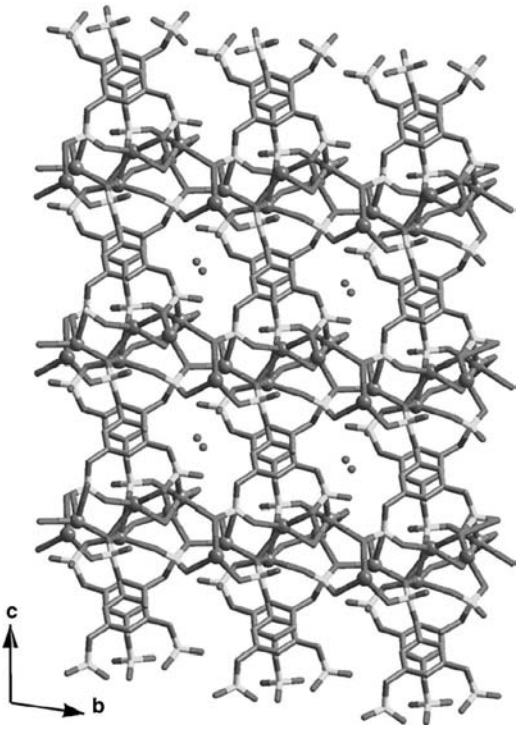

FIGURE 6. Structure of $\{[Ag_6(L5)_2(H_2O)_5] \cdot 2H_2O\}_\infty$, **5**, viewed down the *a* axis. Note the alternating pattern of mesitylene cores and the one-dimensional channels occupied by water molecules.

similar pillared layered network structure was formed, which then necessitated secondary ions in the pores.

The $BaCl_2$ complex of 1,3,5-*tris*(sulfonomethyl)-benzene (L5), also formed a pillared layered solid, as shown in Figure 7. The formula for **6** was $\{Ba_2[(L5)(H_2O)_5]Cl\}$. The chloride ion was not ligated to the barium ion in this solid; rather it was situated in pores between the layers. The dimensions of the channels were $\sim$9.1 by 7.9 Å, which translates to 6.7 by 5.1 Å, when van der Waals radii are considered (van der Waals radius of Cl = 1.75 Å). Water molecules in the structure were coordinated to Ba^{2+} and formed long hydrogen bonds with the Cl^- ions. TGA analysis showed that after dehydration, **6** was stable to 420°C. Given this stability and the "free" nature of the chloride ion, an anion exchange experiment was conducted. Before this, the anion dependence of the structure was examined.

As a general comment, it is not typical that any of the metal sulfonate structures we have studied form as bulk solids with mixed anions. Without exception, the few that do form with mixed ions have a very stable three-dimensional cationic metal sulfonate skeleton, which requires additional charge

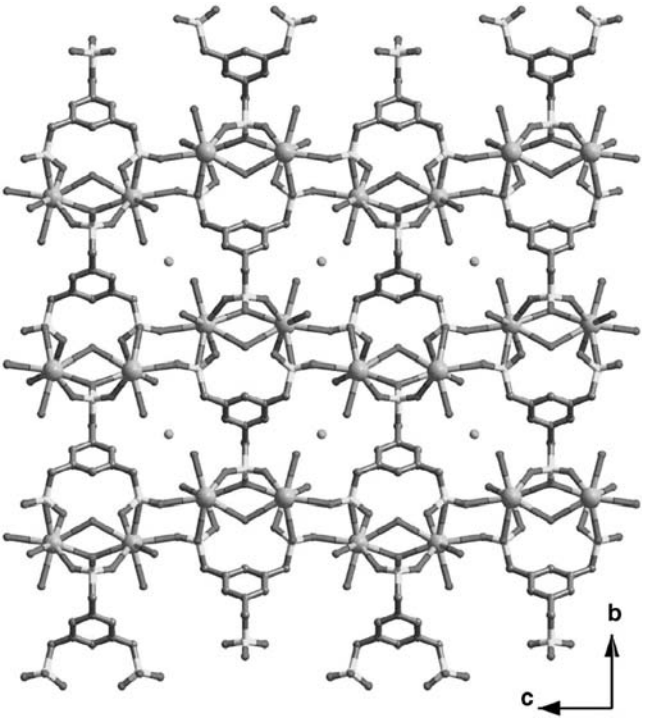

FIGURE 7. Structure of $\{Ba_2[(L5)(H_2O)_5]Cl\}$, **6**, viewed down the *a* axis. Note the alternating pattern of mesitylene cores and the spaces occupied by the charge compensating chloride moieties.

compensation. With L5, we studied the halide series of anions because $BaCl_2$ gave the interesting structure, **6**. With BaF_2, the only solid isolable was BaF_2 itself. With $BaBr_2$, an isomorphous material to **6** was obtained: {Ba2[(L5)(-H2O)5]Br}, **7**. Iodide was estimated to be too large for the cationic pillared layered structure formed by Ba^{2+} and $L5^{3-}$, and a different phase, which was not able to be determined, was obtained. It is interesting that when the triacid form of L5 was complexed with $Ba(OH)_2$, so that no secondary ion was present, the mixture remained very soluble in water, indicating that an extended network was not forming.

Attempts to exchange Br^- for Cl^- in **6** were unsuccessful; however, F^- could be efficiently exchanged. This selectivity is contrary to that typically observed for ion exchange materials.[29] In the presence of 1 equivalent of fluoride ion, a 75–80 % exchange of the chloride ions was observed in 3h. This was confirmed by AgCl gravimetric analysis, PXRD;[19] F NMR spectroscopy; and C, H, Cl, and F elemental microanalysis, which also discounted the potential formation of BaF_2. Anion exchange in coordination networks is rare and generally occurs only if a large excess of the new anion is present.[30]

Upon standing **6** in F^- for a week, there is complete exchange of Cl^- to obtain $\{Ba_2[(L5)(H_2O)_5]F\}$, **8**. To our knowledge the exchange in **6** is still the most facile exchange reported in a coordination network to date. We also proposed a model for the exchange because the channel is sufficiently large to permit two-way passage of halide ions (Fig. 8) provided intrachannel solvents were mobile. This was confirmed by NMR experiments in D_2O.

A final noteworthy comment concerning the F^- ion exchange is that whereas **8** can be prepared by ion exchange from **6** it cannot be prepared directly from BaF_2. This is perhaps the strongest evidence for a heterogeneous exchange mechanism with retention of framework integrity.

IV. NONLAYERED METAL SULFONATES

Building further on the concept of a solid being adaptable, we sought to probe whether a silver sulfonate could be directed to form a motif other than simple $AgSO_3$ layers. Two general routes to this were explored. The first involved employing organic R groups on the sulfonate, which would sterically disfavor the two-dimensional $AgSO_3$ motif. The second involved incorporating other ligating units into the sulfonate to alter the stoichiometry of silver ions available to coordinate with the SO_3 groups.

The first approach, that of varying the organic spacer, was pursued using both monosulfonate and polysulfonate ligands. With monosulfonates, it was clear that only a certain size of R group on the sulfonate could be tolerated while retaining a two-dimensional motif, and so this was varied

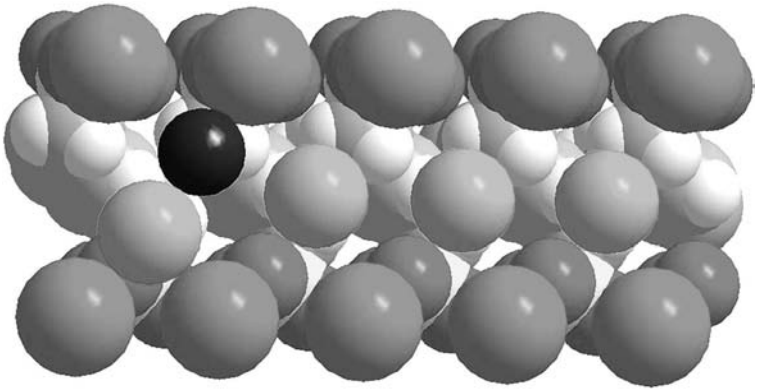

FIGURE 8. Representation of the cross-section of a channel in $\{Ba_2[(L5)(H_2O)_5]Cl\}$, **6**. Atoms are depicted at vdW radii distances and show passage of Cl^- (green) and F^- (purple) in the channel. Passage of ions required mobile solvent, which was confirmed by NMR spectroscopy. Important to note as well is the fact that the ions are not rigid spheres.

systematically.[31] To determine this structural tolerance, it was first necessary to define an ideal framework as a reference point. For this purpose, AgL2, **2**,[20] was chosen. This structure shows a nearly perfect hexagonal arrangement of Ag centers, with each face of a hexagon being capped by a SO_3 group in a μ^6 coordination mode. The parameters of the unit cell for this compound traced onto the inorganic layer are a 5.160 by 5.198 Å rhombus (Fig. 9); this corresponds to an area of 23.45 $Å^2$. This was viewed as the area in a plane required for a sulfonate group to coordinate to silver(I) ions in a simple layered motif. The sulfonate group itself has a breadth of 3.66 Å, which is sufficient for accommodating the thickness of an aryl ring. Thus with respect to the aryl group, there must exist a critical lateral breadth that, if exceeded, would preclude the formation of a simple SO_3-bridged layered solid.

Using the area in a plane defined by the reference compound, **2**, of 23.45 Å and dividing this value by 3.66 Å would allow an aryl group with a lateral breadth of 6.41 Å to be accommodated while maintaining the lamellar structure. This prediction was tested with four different monosulfonate aromatic R groups and silver(I). Figure 10 shows the four sulfonate ligands employed and their respective lateral breadth parallel to the layer. Five silver complexes were obtained: [Ag(4-biphenylsulfonate)]$_\infty$, AgL6, **9**; [Ag(2-naphthalenesulfonate)]$_\infty$, AgL7, **10**; [Ag (H_2O)0.5(1-naphthalenesulfonate)]$_\infty$, Ag(H2O)0.5L8, **11a**; and [Ag(1-naphthalenesulfonate)]$_\infty$, AgL8, **11b**; and [Ag(1-pyrenesulfonate)]$_\infty$, AgL9, **12**.

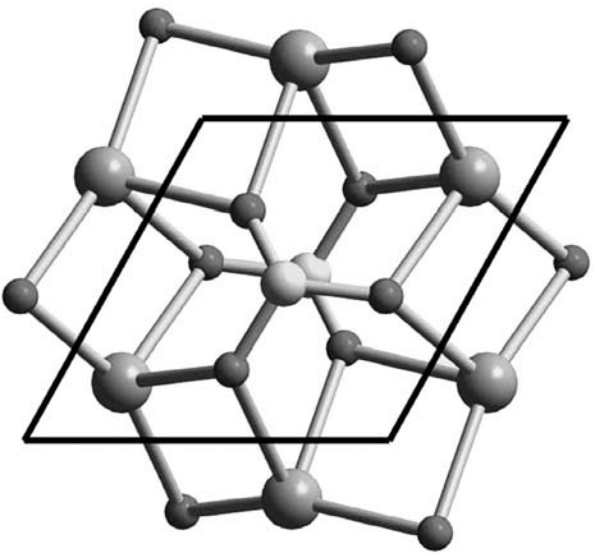

FIGURE 9. The view onto a single layer of Ag benzenesulfonate, **2**. The rhombus represents the trace of the unit cell onto the layer (5.160 by 5.198 Å) with an area of 23.45 $Å^2$. This is taken as an approximation of the minimum area required to accommodate an $AgSO_3$ building unit in the construction of a simple layered solid.

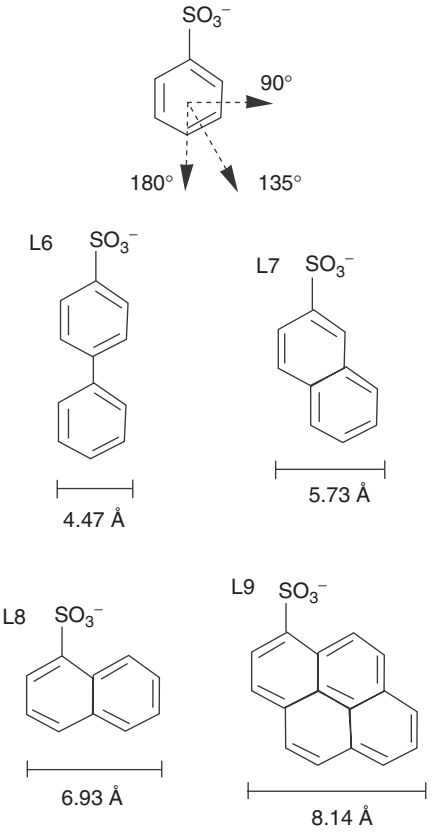

FIGURE 10. Lateral breadths of a series of monosulfonate ligands employed to gauge the resilience of the layered motif in silver sulfonates.

For compounds **9–12**, whose lateral breadths are given in Figure 10, the approximation held as accurate. Only compounds **9** and **10**, with biphenyl and 2-naphthyl appendages, respectively, had lateral breadths below the calculated threshold, and both formed simple layered solids. For the 1-naphthyl appendage used in compounds **11a** and **11b**, which exceeded the threshold by a relatively small amount (6.93 Å versus 6.41 Å), the Ag sulfonate backbone was displaced to allow the incorporation of a water molecule or, under anhydrous conditions, shifted to allow the formation of Ag-π interactions with half of the naphthyl groups. For compound **12**, the 1-pyrene appendage significantly exceeded the estimated critical breadth to allow a continuum of SO_3-bridged Ag ions (8.14 Å versus 6.41 Å). In this case, the structure adapted to a greater extent by forming cation-π interactions between silver(I) centers and *all* the aromatic moieties. Structural details for all compounds are given in the caption to Figure 11.

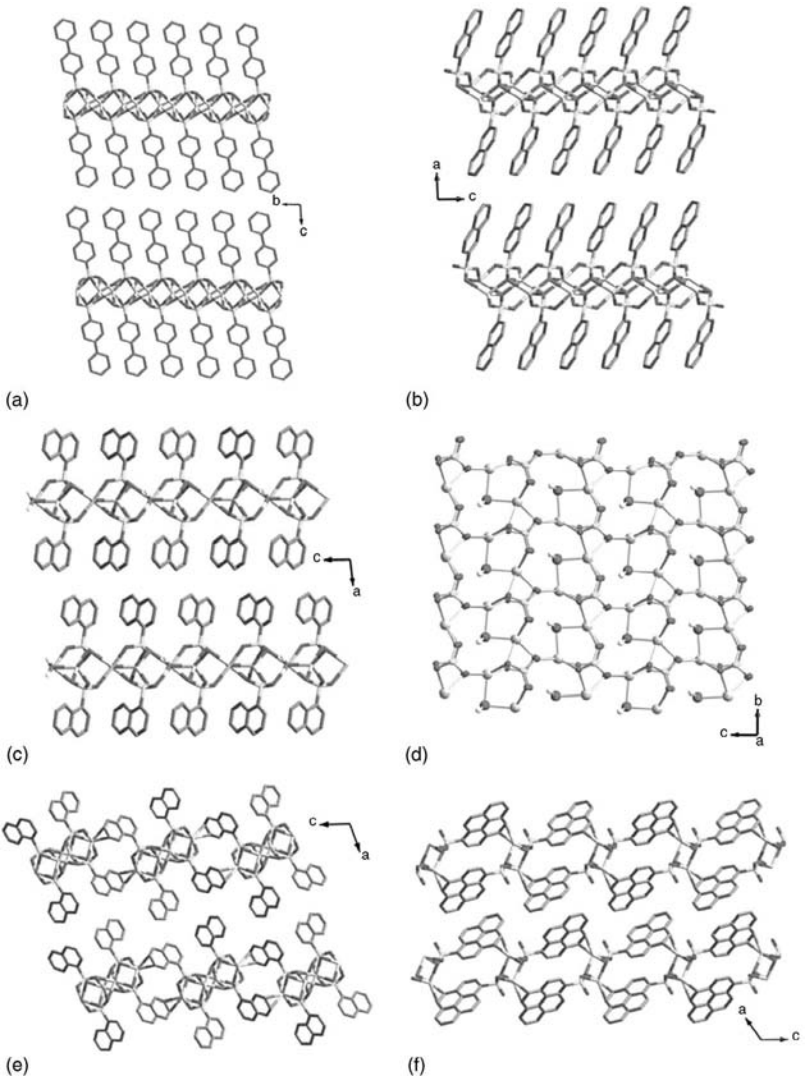

FIGURE 11. (a) [Ag(4-biphenylsulfonate)]∞, AgL6, **9**, with a simple layered structure. The breadth of the ligand is below the threshold value (6.41Å). (b) [Ag(2-naphthalenesulfonate)]∞, AgL7, **10**, also with a simple layered structure. (c) [Ag(1-naphthalenesulfonate)]∞, AgL8, **11a.** The breadth of the ligand exceeded the threshold by a relatively small amount (6.93 Å versus 6.41 Å); the Ag sulfonate backbone was displaced to allow the incorporation of a water molecule under hydrous conditions. (d) The layer view of **11a** showing the ligated water molecule and more diffuse structure. (e) [Ag(1-naphthalenesulfonate)]∞, AgL8, **11b**, under anhydrous conditions. The structure shifted to allow the formation of Ag-π interactions with half of the naphthyl groups. (f) Structure of [Ag(1-pyrenesulfonate)]∞, AgL9, **12**. In this compound, the 1pyrene appendage significantly exceeded the estimated critical breadth to allow a continuum of SO_3-bridged Ag ions (8.14 Å versus 6.41 Å), so the structure adapted to a greater extent by forming cation-π interactions between silver(I) centers and *all* the aromatic moieties.

The formation of π interactions with the appended arene and the silver ion necessitated the conversion of two-dimensional (2D) $AgSO_3$ layers into one-dimensional (1D) columns. Based on the structural prediction and the obtained results, we proposed a classification for silver sulfonates into three families, referred to as type 1, type 2, and type 3. Type 1 structures are those sustained exclusively by bonding between Ag ions and sulfonate oxygen atoms. Type 2 structures involve a continuum of interactions between Ag ions and sulfonate oxygen atoms but with ancillary ligation by additional simple Lewis bases. Type 3 networks involve coordination between Ag ions and sulfonate oxygen atoms but with additional coordination of Ag by the π system of the appended arene. Beyond providing a predictive reference for the design of silver sulfonates, this work affirmed the structural role of the organic groups in these networks. In the case of **10**, the 2-naphthyl rings were observed to form a herringbone pattern that very closely resembled that seen in naphthalene itself. Clearly, the final structure represented a balance of both optimized coordinative and aryl-aryl interactions.

The publication in which compound **5** was reported concerned variation of organic cores as a route that disrupts the $AgSO_3$ layered structure and potentially forms open framework materials.[27] In addition to the mesitylene core already mentioned, silver(I) networks were reported with α,α′,α″,α‴-durenetetrasulfonate (L10), to form $\{[Ag_4(L10)(H_2O)_2]\}_\infty$, **13**, and 1,3,5,7-tetra(4,4′-sulfonophenyl) adamantane (L11), to form $\{[Ag_4(L11)(H_2O)_2]\cdot 1.3H_2O\}_\infty$, **14.** Compound **13**, based on the durene core, formed a three-dimensional structure (Fig. 12) but not that of a pillared layered type.

With the durene core, formation of a layered (type 1) solid was not possible. Rather, the layers were disrupted and 1D inorganic columns resulted. Adjacent sulfonate groups ligated to the layers in meta-orientations off the ring. Given that in the mesitylene analog, **5** also has two methylsulfonate groups ligated in a 1,3-arrangment (unavoidable for this ligand), it was not surprising that the 1D columns defined by the durene cores did not define very large pores. The distance between columns was 9.929(2) Å between column midpoints but, factoring the breadth of the column, the columns were realistically separated by only a Ag-coordinated water molecule. From TGA, all the water molecules were lost by 125°C from which point no further changes were observed until decomposition at 325°C. Going to the much larger tetrasulfonate ligand based on the tetraphenyladamantane core, L11, was expected to give much larger pores.

The structure of the silver(I) complex of 1,3,5,7-tetra(4,4′-sulfonophenyl)-adamantane, **14**, (Fig. 13) clearly showed that the structure was composed of 1D columns of Ag-SO_3 aggregates that were cross-linked in two dimensions by L11. Two types of channel were defined by the adamantane cores of the ligand. The first was primarily occupied by coordinated water molecules with approximate dimensions 7.4 by 5.9 Å. The second was occupied by disordered water molecules and had dimensions of 8.3 by 6.0 Å. The distances between adjacent columns were 11.46(1) Å and 12.49(1) Å. In this structure, guest and

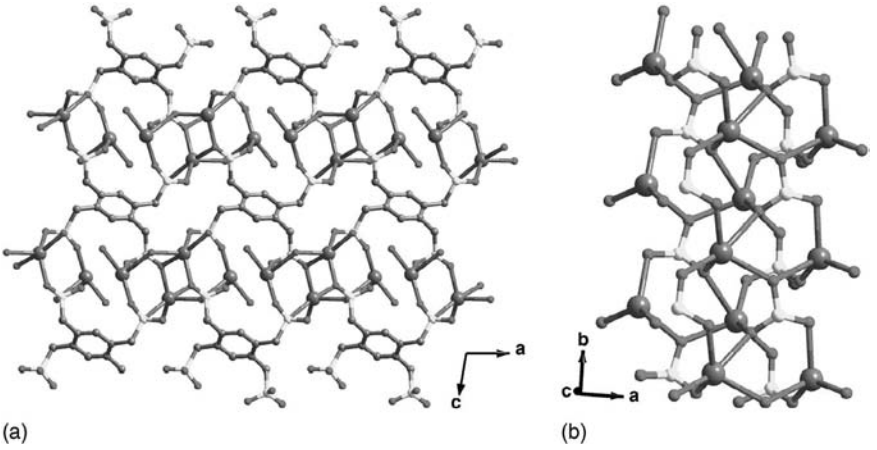

FIGURE 12. (a) Structure of $\{[Ag_4(L10)(H_2O)_2]\}_\infty$, **13,** where L10 = α,α′,α″,α‴-durenetetrasulfonate. The one-dimensional columns point out of the page and each durene core links four different columns. The three-dimensional framework is entirely different from the prototype pillared-layer structures, owing to the increased orientational flexibility of the sulfonate groups assisted by the methylene moieties linking them to the benzene core. (b) The isolated inorganic columns observed in $\{[Ag_4(L10)(H_2O)_2]\}\infty$, **13,** when periodically along the *a* axis.

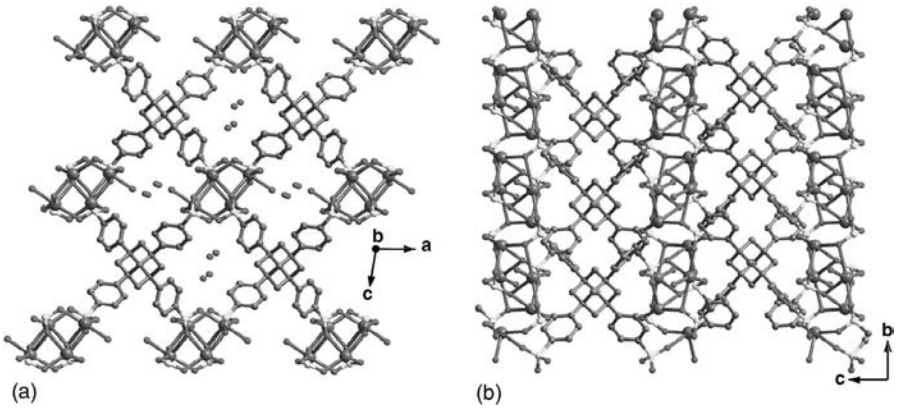

FIGURE 13. (a) The structure of $\{[Ag_4(L11)(H_2O)2]\cdot 1.3H_2O\}_\infty$, **14,** where L11 = 1,3,5,7-tetra(4,4′-sulfophenyl)adamantane. The cross-linking of inorganic columns are directed out of the page by the tetraphenyladamantane units. One-dimensional voids are shown between the organic linkers. Note the presence of guest water molecules in the channels. (b) Shown is the columnar structure of $\{[Ag_4(L11)(H_2O)_2]\cdot 1.3H_2O\}_\infty$, **14,** highlighting the cross-linking role of the tetraphenyladamantane units. Although, there are one-dimensional channels along both the *b*- and the *c*-axes, none propagates along the *a* axis.

coordinated water molecules could be removed and resorbed but the structure did not persist in the absence of the guest molecules. Compound **14** lost water molecules, both channel and coordinated, from 25° to 275°C and was then stable to 375°C.

To extract some design principles from the structures of **13** and **14**, the approach of defining an ideal reference structure was again employed. As with the monosulfonate study, Ag benzenesulfonate, **2**,[20] was employed as a reference and treated as an ideal 2D silver sulfonate. The most pertinent parameter for structural comparison was determined to be the distance between sulfonate S atoms in the structures because they represented the anchor points to the layers/aggregates and did not vary greatly with the identity or orientation of the organic moiety to which they were linked. This distance in Ag benzenesulfonate is $\sim$ 5.2 Å. It should be noted that this sulfur–sulfur distance is somewhat flexible. For example, Ag 2-naphthalenesulfonate, **10**, maintains a layered motif by the Ag sulfonate layer, rearranging to 4.53(1) and 6.01(1) Å to accommodate the broader pendant group. However, these two values are still centered roughly on the 5.2 Å value.

Compound **13**, with its durene core, was viewed as having two sets of meta-xylyl spacers constraining the structure. Only half of each ligand was crystallographically unique, and so there were only two independent sulfonate groups. The meta sulfur-sulfur distance in L10 is 5.835(2) Å, considerably above the ideal 5.2 Å distance defined earlier. This results in the observed one-dimensional structure rather than a two-dimensional network typical for silver sulfonates. For comparison, with the mesitylene analog **5**, only one side of the ligand was constrained by the meta-orientation of the sulfonate groups, so the third SO_3 group could effectively function as a "filler" to permit the formation of continuous layers. With compound **14**, the tetraphenyladamantane derivative, sulfonate sulfur atoms were situated at a distance of 12.65 Å apart, well beyond that required to preclude a simple layered solid.

The design principles that evolved from this work were that, for silver sulfonate networks, any spacer that would rigidly position sulfonate groups farther than 5.2 Å apart should disfavor a layered solid and likely form one-dimensional columns. Going a step further, one could say that a ligand, which imposed such the same constraint in two dimensions, could dictate the formation of zero-dimensional (0D) clusters. The Ba complex of L11, **15**, illustrates this potential.[32] With each Ba ion carrying double the charge of a silver ion, half the metal centers are available to cross-link the tetrasulfophenyladamantane ligands. Thus, **15** (Fig. 14) showed the first observation of 0D clusters in metal sulfonate chemistry.

The second approach that was pursued to direct the formation of silver sulfonates without layered structures was to attempt to alter not the Ag/SO_3 ratio, as that would entail additional counteranions, but the number of silver ions that were available to interact with the sulfonate ions. This was accomplished by choosing pyridylsulfonate ligands because pyridine regularly forms linear 2:1 complexes with silver(I).[33] The rationale was therefore that if a 2:1

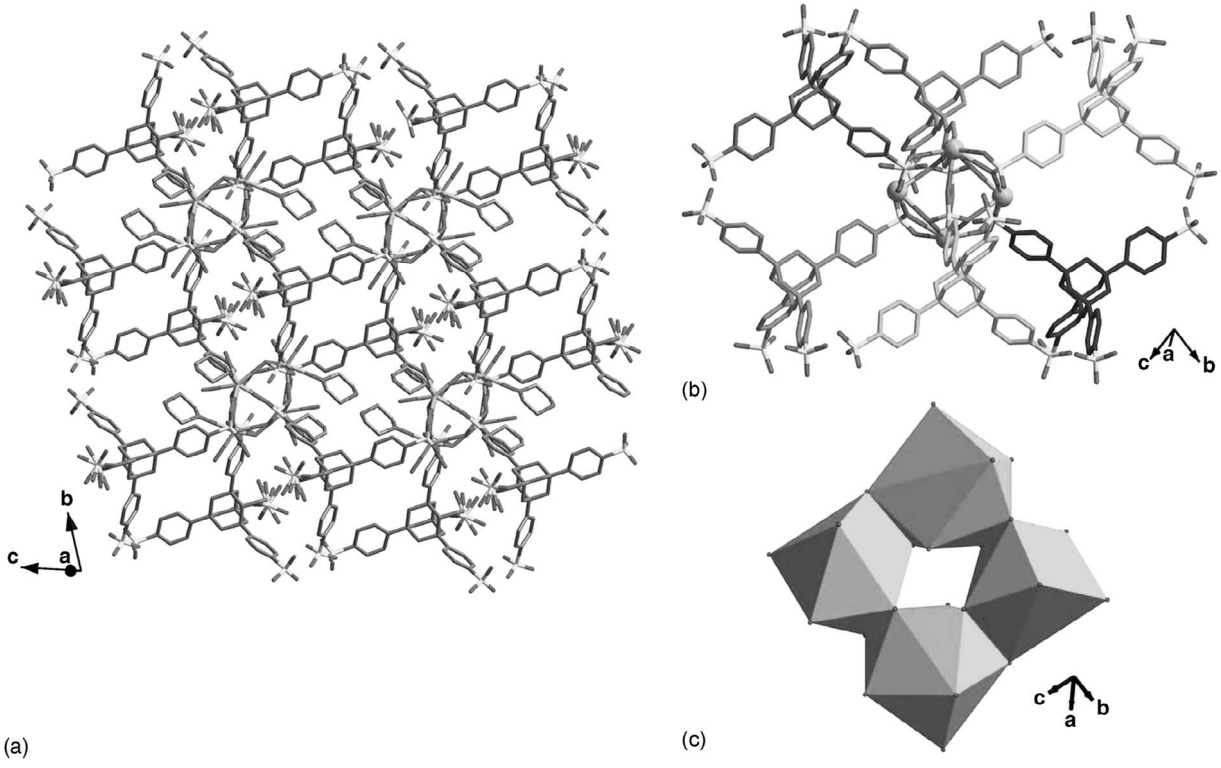

FIGURE 14. (a) Layered structure of the Ba^{2+} complex of L11, **15**. Note the presence of tetra-nuclear metal clusters cross-linked by the organic moiety. (b and c) Two different representations of the tetra-nuclear Ba clusters present in the compound **15**. Each cluster is connected to six different ligands, and if the cluster is considered as one entity and each ligand as a single unit, the coordination around the cluster is octahedral. Alternatively, the cluster is formed by the edge sharing ammy the four BaO_8 units, with a mono-capped pentagonal bipyramidal coordination environment. The resemblance of the cluster to the SBU-4 type of building units is noteworthy.

pyridylsulfonate:Ag linear complex was formed as a building block employing the stronger Ag-pyridine bonds, there would necessarily only be a single silver(I) center left to interact with the two sulfonate groups. This was examined with 4-pyridinesulfonate, L12, and 3-pyridinesulfonate, L13.

With L12, the structure-directing role of the 2:1 ligand:silver coordination is readily borne out in the structure of AgL12, **16**, shown in Figure 15.[34] The strongest individual linking interaction in the system was the silver-pyridine bonds (Ag1–N1 = 2.163(3) Å versus Ag2–O = 2.359(3), 2.410(3) Å to the sulfonate O atoms) to form linear monoanionic bricks. Thus, according to the design, there would be only one silver cation to cross-link the two free

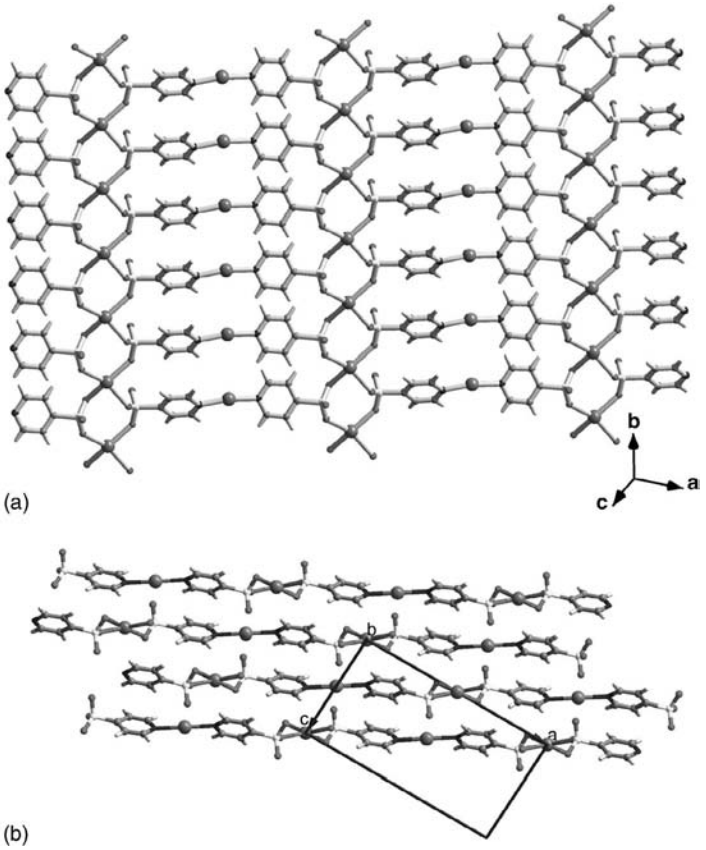

FIGURE 15. (a) Structure of the AgL12 (where L12 = 4-pyridine sulfonate), **16,** showing a single layer. Note the presence of two distinct Ag centers as well as the continuous layer structure. (b) View of AgL12, **16**, looking in the plane of the layers showing the relative orientations of four adjacent sheets. The Ag-S bonds are the only strong interactions in the entire structure, and there are no strong interactions between the layers.

sulfonate groups. The silver sulfonate aggregate that formed was a 1D column rather than the typical layered $AgSO_3$ motif formed, not surprising as there were half the number of silver ions available. The cross-linking of the linear bricks by the 1D columns ultimately still resulted in the formation of layers, but layers that were, in a sense, a compromise between those of layered coordination solids and typical hybrid inorganic–organic solids. Unlike hybrid inorganic–organic solids, these layers incorporated the R group rather than it being pendant to the layers; however, like these solids, the layers formed continuous sheets. Like most layered coordination solids, **16** incorporated the R group of the sulfonate into the layer, but unlike them, in **16** an open-grid layer structure was not formed. Given the continuous layer structure of **16**, intercalation experiments were carried out.

The primary amines, octyl, decyl, dodecyl, and tetradecylamine, were individually dissolved in ether and added to a suspension of **16** also in ether in a 1:1 amine/L ratio. Upon treatment with the amines, the texture of **16** became waxy, but the solid was still air and light stable. Figure 16 shows the PXRD of these complexes along with host **16**. The PXRD patterns of all complexes indicated layered solids, with the most intense reflections arising from an equally spaced Bragg family of planes {0 0 *n*}. The value for the lowest angle (0 0 1) Bragg reflection for each of the intercalates increased linearly, from 27.88(2) Å for **16**· octylamine to 39.22(2) Å for **16**· tetradecylamine, proportionally to the number of carbon atoms in the amine. These values were also consistent with formation of, a bilayer arrangement of the guests rather than an interdigitated structure. The slope of a plot of length of amine molecule (or the number of C atoms in the amine) versus the increase in *d*-spacing shows that the intercalated amines are tilted at an angle of 49° from the perpendicular.

To determine if the intercalation was selective, the sorption experiments were repeated using guests containing other functional groups. In the presence of straight-chain alkanes, nitriles, alcohols, aldehydes, benzene, toluene, and mesitylene, no guest uptake was observed by gas chromatographic analysis of the contact solution. PXRD analysis showed no change in the host diffraction patterns. Selectivity was also examined in the amine series by studying $(n\text{-Bu})NH_2$, $(n\text{-Bu})_2NH$, and $(n\text{-Bu})_3N$, in competitive experiments with one another. Compound **16** was treated with each amine individually and an equimolar mixture of all three amines and again monitored by PXRD, while the contact solution was monitored by GC analysis. The tertiary amine was never adsorbed, but 70% of the secondary amine was removed from solution in 3 h. The primary amine was almost completely removed from solution (96 %) in 3 h. Both results showed the expected changes in the PXRD patterns of the host consistent with layer swelling. In the presence of the primary amine, neither $(n\text{-Bu})_2NH$ nor $(n\text{-Bu})_3N$ were intercalated at all.

The next example, AgL13, **17**, was introduced earlier because it employs the same strategy as used in **16**, that of shifting the Ag/SO_3 aggregate stoichiometry, to direct the $AgSO_3$ structure away from simple layers. It could

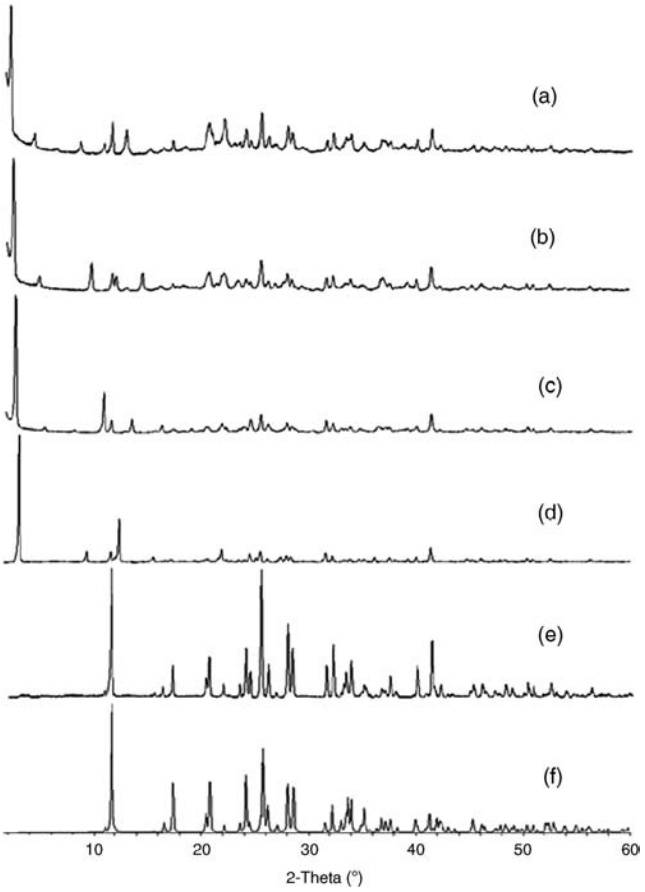

FIGURE 16. PXRD patterns for (a) **16** · tetradecylamine, (b) **16** · dodecylamine, (c) **16** · decylamine, (d) **16** · octylamine, (e) bulk **16**, and (f) **16** simulated from single crystal data.

be presented here, but for the purposes of this chapter it is better classified with the dynamic crystalline materials.

A. Dynamic and Crystalline Metal Sulfonate Frameworks

Through the course of our studies, it has become apparent that a possible, though not essential, feature of metal sulfonate networks is a predisposition to dynamic behavior in the solid state. There are two key contributing factors to this tendency. The first is the fact that, individually, each M-O (sulfonate) bond is not strong. The second factor is the coupling of the spherical ligating ability offered by the SO_3 group (through all three O atoms) with a metal center

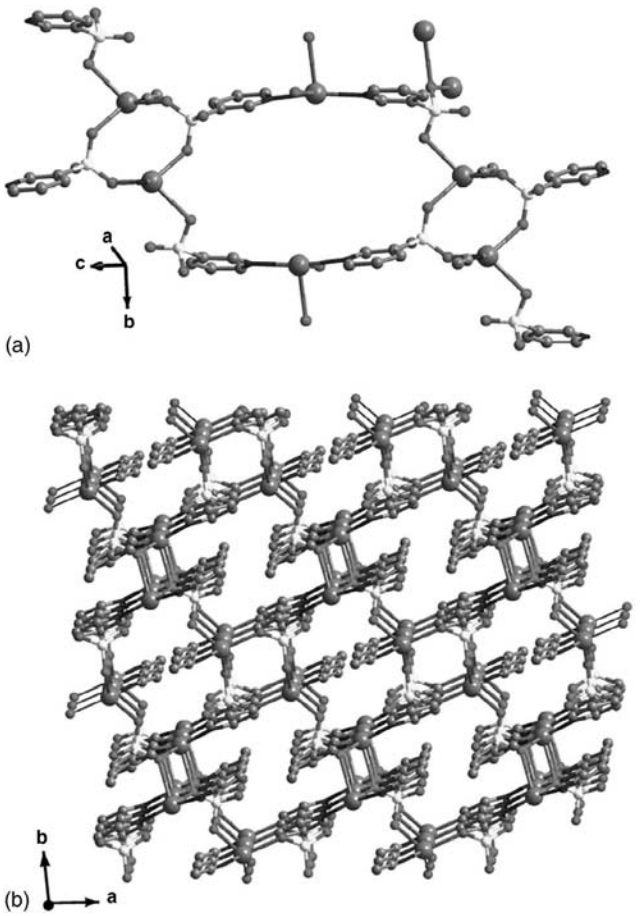

FIGURE 17. (a) The 24-membered rings of structure $[Ag(L13)(MeCN)_{0.5}]$ (where L13 = 3-pyridyl sulfonate), **17a,** linking to the eight-membered rings. (b) View of the extended structure of **17a** down the *c*-axis, showing the linking of the 24-membered MeCN-filled channels by the eight-membered rings.

and an equally pliant coordination sphere. This results in multiple metal–ligand coordination scenarios within a small energetic range.

With L13, in MeCN, the network $[Ag(L13)(MeCN)_{0.5}]$, **17a**, was formed.[35] This compound showed the expected linear coordination of silver ions by the pyridyl moieties. The remaining silver ion interacted with the sulfonate groups to form 24-membered rings (Fig. 17).

The coordination sphere of the SO_3-ligated Ag center was a distorted tetrahedron containing three oxygen atoms, from three different sulfonate groups that cross-link adjacent 24-membered rings, and a molecule of MeCN. The rings pack along the crystallographic *c*-axis in an eclipsed fashion to give

channels containing the MeCN guests. The channel dimensions are 7.9(1) high by 14.6(1) Å wide, as defined by the transannular Ag–Ag distances of the rings. Heating to remove the MeCN in this structure was attempted in the hope of forming a pore in the material. Instead, as observed by PXRD, a phase change was observed to a more dense phase, as is often the case with coordination solids. However, treatment of this phase with MeCN liquid or vapor brought about a reversion to the nascent structure. At the time this work was published, there were very few examples of such pliant networks,[36]although they are now much more common and their structural transformations accepted as occurring in the solid state.[37]

The crystal structure of the dense phase, compound **17b**, which had trigonal symmetry, showed a three-dimensional (3D) solid containing 1D ribbons of silver ions (Fig. 18). Knowledge of this structure allowed an

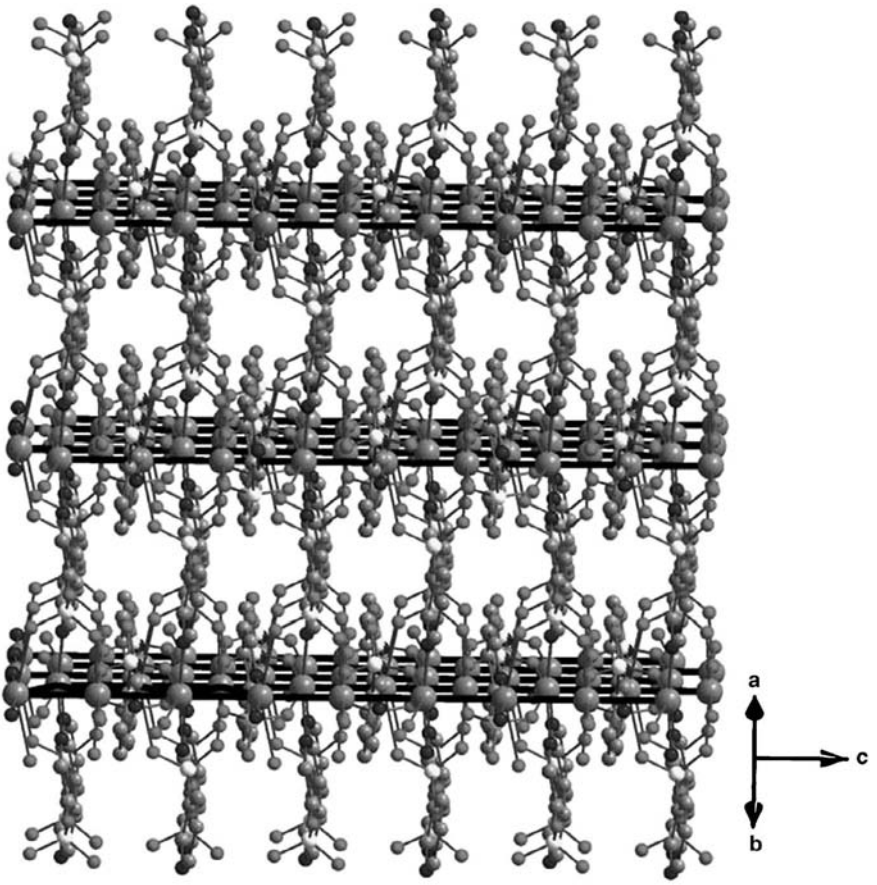

FIGURE 18. Three-dimensional structure of the dense phase, [Ag(L13)], **17b.** The parallel ribbons of Ag ions permeating the structure are shown in black lines.

examination into the possible mechanism of how the structure changed between the open and closed forms. In **17b**, only one silver ion was contained in the asymmetric unit of [Ag(L13)]≡ but was distributed over three partially occupied *sites* in a 2:1:1 ratio, with only one unique molecule of L13 present. Ag1 occupied 50% of the silver sites and was the only silver center to bond to the N atoms of pyridyl rings. It had two longer contacts to sulfonate oxygen atoms and two even longer contacts to two adjacent silver centers, Ag2 and symmetry related Ag1′. Ag1 and Ag2 formed the ribbons of silver ions permeating through this structure, repeating in a Ag1-Ag2-Ag1 unit, with distances shorter (2.988–3.015 Å) than the sum of van der Waals radii (3.44 Å). Ag3 was coordinated by 4 equivalents of sulfonate oxygen atoms.

The mechanism of interconversion of the open and dense forms of **17** (Fig. 19) can be viewed akin to the folding of a cardboard box, where the pyridyl-ligated Ag units form the top and the sulfonate ligated silver ions form the sides. The network would respond to removal of the guest MeCN molecules by filling the void by swinging one side of the box ($AgSO_3$ unit) into the void.

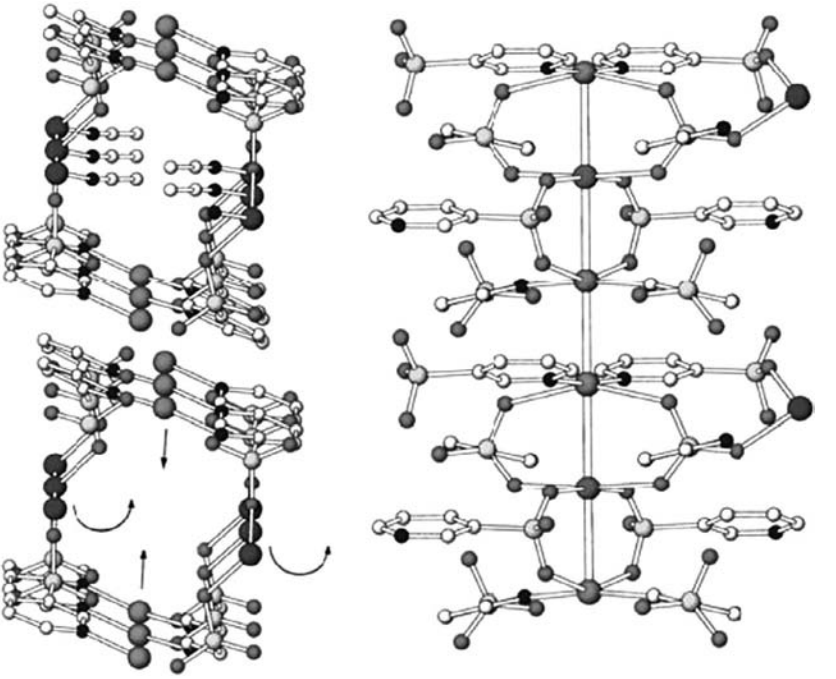

FIGURE 19. Representation of the mechanism of conversion between solvated [Ag(L13)(MeCN)], **17a**(shown at left with MeCN molecules removed from the lower channel) and the dense phase [Ag(L13)], **17b.** The three crystallographic types of Ag ions, which exist in a 2:1:1 ratio in **17b**, are depicted as light, medium, and dark shades, respectively.

This silver ion now becomes proximal to the pyridine bound silver atoms. This motion requires the second, originally equivalent, sulfonate-ligated silver ions to shift in the same direction but out of the square. Looking at the silver centers in **17b**, the dense phase, this is consistent with pyridine-ligated silver ions, SO_3-ligated silver ions in proximity to the py-ligated silvers, and other SO_3-ligated silver ions in a ratio of 2:1:1. This was exactly what was observed crystallographically. It is important that this mechanism did not require the cleavage of any of the stronger Ag-pyridine bonds, only reorientation of the SO_3 groups. Undoubtedly, the d^{10} coordination sphere of silver(I) played an important role as a partner in enabling these structural dynamics.[38] This type of behavior led to the analogy of the ligating ability of a sulfonate group with a "ball of Velcro."

Beyond the reversible MeCN sorption observed for this system, selectivity with other structurally similar molecules was examined. Treatment of **17b** with other nitriles, even propionitrile, MeOH, EtOH, and THF, yielded no change in the observed PXRD, indicating selectivity for MeCN. This observation was corroborated by heterogeneous extraction experiments of MeCN from a mix of four nitriles suspended in tetradecane. In this experiment, which was designed to confirm both selectivity and heterogeneity, some uptake of propionitrile was observed. While initially viewed as somewhat of a negative, the fact that propionitrile was absorbed only in the presence of MeCN, actually further corroborated the heterogeneity of this process. If a dissolution/recrystallization process had been occurring, a pure MeCN phase would have resulted, as the fit for MeCN was ideal. In a heterogeneous scenario, given the connectivity of the framework, many channels would have opened simultaneously in the presence of MeCN and under this circumstance; propionitrile was able to be included.

As mentioned, dynamic coordination solids are now much more frequently reported, although efficiently reversible transformations involving changes in the metal ion's coordination sphere are still not common.[39] The next example concerns our best example to date of an "adaptable" solid. It is the Ba complex of 1,3,5-trisulfonobenzene, $Ba_3(L14)_2$, **18**.[40] Although in compound **6**, the versatility of the Ba ion enabled a very stable ion exchange material to form, in this case, the irregular and easily varied coordination sphere is key to enabling facile structural dynamics.

Compound **18** existed as a fully hydrated (orthorhombic) form, **18a**, which was 17.5 % water by weight. The structure of this compound is shown in Figure 20a. Water is contained both in 1D channels as well as coordinated to the Ba centers. Considerable difficulty was experienced in collecting the single crystal structure of this compound because dehydration, accompanied by a change in crystal symmetry, was observed to occur immediately upon removal of the crystal from solution. Ultimately, the crystal was selected and mounted under a flow of blow-off from liquid N_2 to give the orthorhombic phase. Loss of water from this sample occurred but, at virtually any stage of dehydration, the crystal could be frozen and a unit cell collected. However, at most intervals, the full X-ray crystallographic data set collected would fail to yield a satisfactory structure

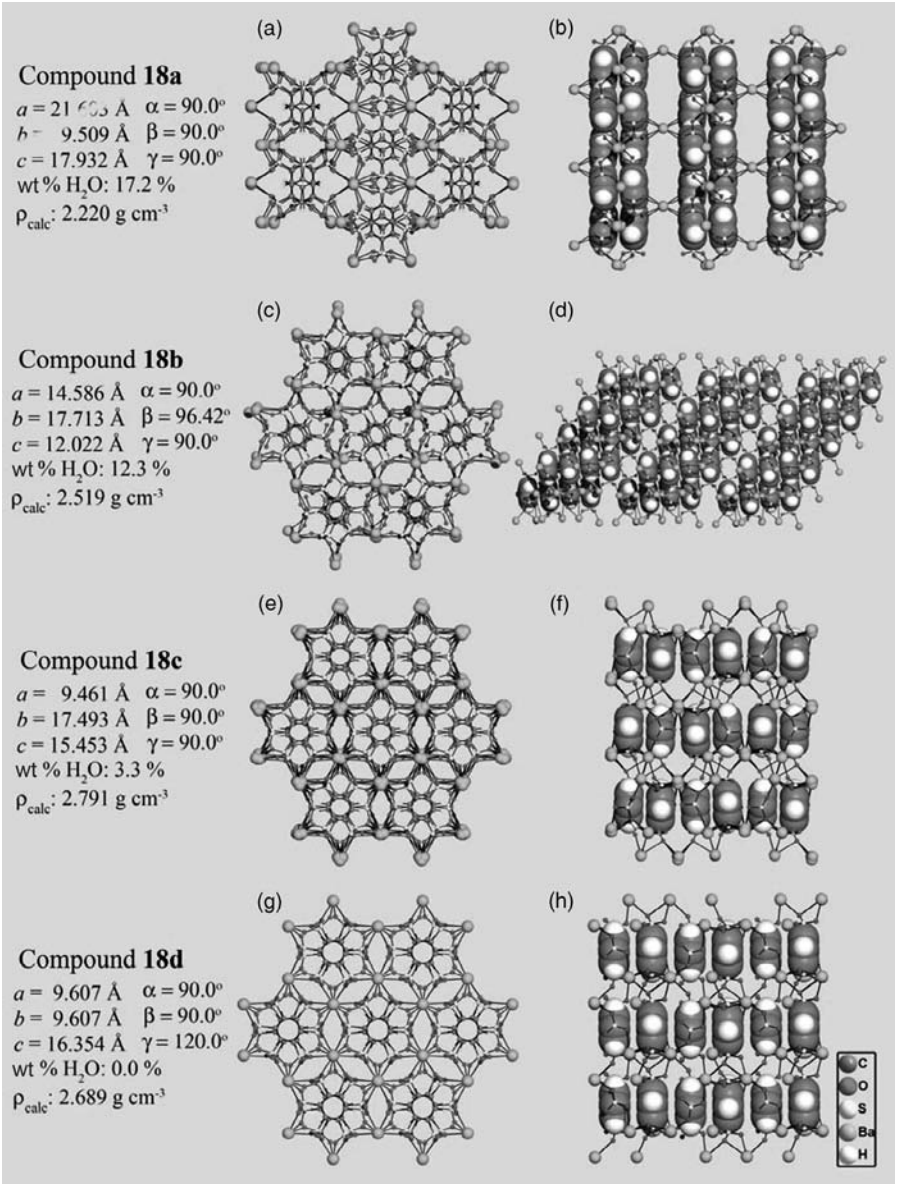

FIGURE 20. Crystal structures of the four isolated phases (1, 2a, 3, and 4) of compound **18**. Key features to note are the closing of pores between molecules of L14 with dehydration and then, at the final stages of dehydration, the slight reopening of pores.

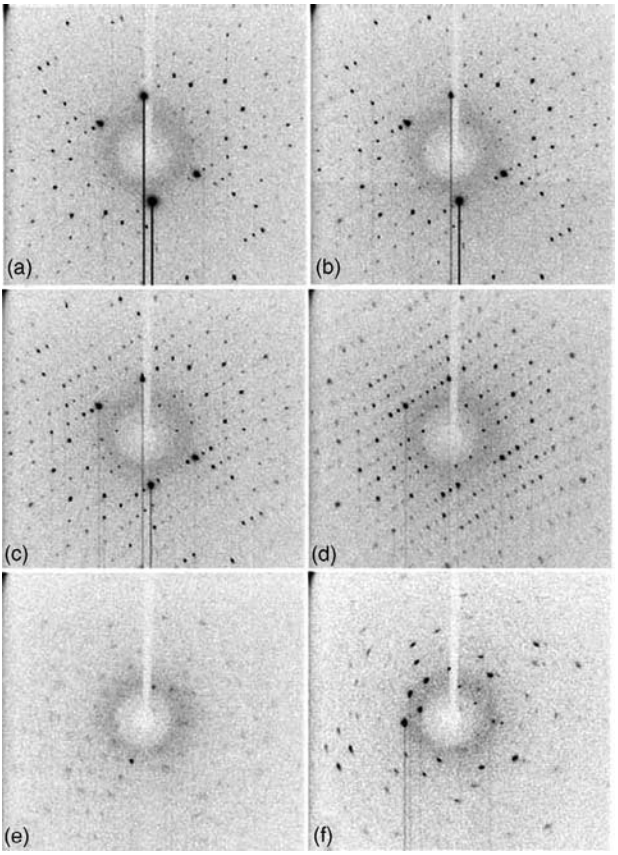

FIGURE 21. X-ray diffraction images of a single crystal of **18a** undergoing heating while on the diffractometer: (a) 192 K; (b) 253K; (c) 263K; (d) 283K; (e) 333K; (f) 393K. The image in panel a represents **18a** and that in panel f represents **18d**. Images in panels b–d shows spots for both **18b** and **18c**. Panel e represents a stage of rapid heating en route to conversion to **18d**.

solution. Figure 21 shows the diffracted X-ray patterns obtained by slowly dehydrating single crystals of **18a** with heating on the CCD diffractometer.

Upon aggressive heating, the fully dehydrated (trigonal) phase, **18d**, could be formed and also structurally characterized. The fully dehydrated phase, **18d**, can be viewed as forming by the channels in **18a** twisting to pinch off discrete cages. Upon immersion of dehydrated **18d** in Paratone oil to mount the single crystal, an unusual observation was made, in that bubbles of gas were observed to escape the crystal. Based on such an odd observation, insights into the intermediate phases were desirable and, ultimately, through careful heating and patient analysis, two plateaus at intermediate stages of dehydration—**18b** (12% water) (Fig. 20b) and **18c** (3% water) (Fig. 20c)—could be characterized crystallographically by X-ray diffraction.

The structures at the intermediate stages showed an unexpected observation for a dehydration process in the coordination solid. Desolvation in such systems is typically accompanied by a densification of the solid. In the case of **18**, the solid became more dense, forming an efficiently packed material at 3% hydration with no pores between the arene rings. However, at the ultimate stages of dehydration, the pores were observed to reopen slightly to form a gap between arene rings of L14. With the size of Ba, six cations are able to bridge sulfonate groups and effectively form a continuous belt about two cofacial L14 molecules. The L14 molecules and six Ba ions then frame a cavity in which gases may be trapped. The dehydrated **18d** was stable to in excess of 500°C, a tremendously high value for a metal-organic material.

The bubbling observed from **18d** was an exceptionally odd phenomenon[41] and merited closer examination. Varying the atmosphere (CO_2, O_2, N_2, CH_4, Ar, NH_3) during heating yielded a dry solid, which released gas on rehydration. The gas trapping could be reconciled by considering the intermediate stages of dehydration of **18** that showed that the structure initially closed and then reopened. The conclusion was that any gas composing the external atmosphere during the dehydration of **18** was captured and stored in the material.

To verify this, several experiments were considered to characterize the gas inside the closed pores of **18d** as distinct from the surrounding atmosphere. Ultimately, a simple colorimetric experiment was performed (Fig. 22). Crystals of **18a** were dehydrated to **18d** in an atmosphere of NH_3(g) and then heated under vacuum to liberate externally adsorbed NH_3. The dried crystals were then placed in an aqueous $Co(NO_3)_2$ solution. The Co^{2+} ions readily adsorbed to the crystal's surface to give a pink color. This coincided with release of gas from the crystal as water rehydrated the Ba ions and opened the closed pores. In $\sim$ 2 min, the crystals changed color from pink to a deep green characteristic of hexaammine Co(II). As any externally absorbed gases would have been removed in the desorption cycle, the only source for NH_3(g) would be the interior of the solid, confirming that the external atmosphere was trapped during dehydration. Figure 22b shows spots of green, indicating where NH_3 was escaping the crystal.

With respect to structural dynamics, we have specifically chosen the Ba/organosulfonate couple owing to the diffuse ionic nature of the intermolecular interactions and the adaptable coordination preferences of both metal and ligand components. To illustrate this contrast note that in **18a** there are two crystallographic types of Ba centers, both 8-coordinate but one with two ligated water molecules and the other with four ligated water molecules; the remaining sites are occupied by sulfonate O atoms. In **18d**, the Ba center is also 8-coordinate but ligated exclusively by sulfonate O atoms. Loss of water from the coordination sphere could be compensated for by simple rotation of the SO_3 group to provide a low-energy continuum of ligation to the Ba centers.

The main illustrations from this particular work are that a solid can be truly adaptable, leading to facile transformations between different structures. The second, more practical illustration concerns the gas storage. The vast majority of molecular materials for storing gases rely on either physisorption or

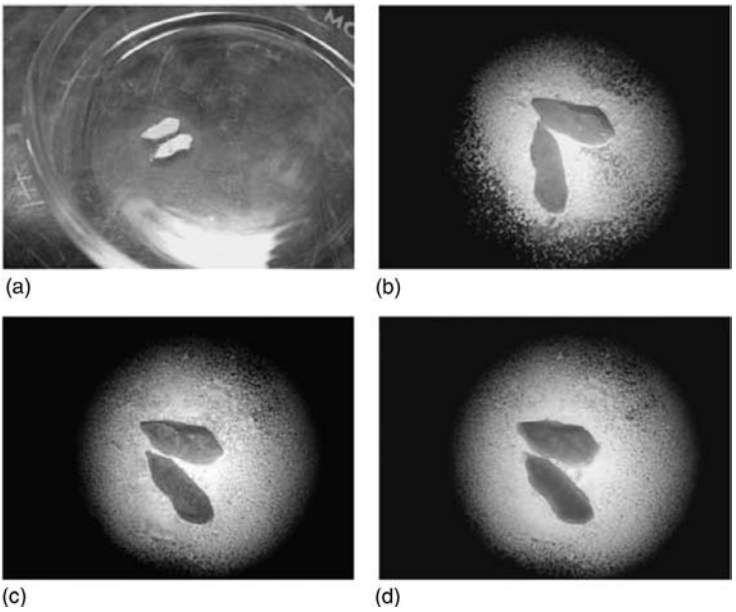

FIGURE 22. Release of NH_3 from **18d** upon rehydration. Single crystals of **18a** were dehydrated in an atmosphere of anhydrous NH_3 (30 psi). This sample was then further heated under vacuum (150°C, 10^{-4} torr) for 2 h to liberate externally adsorbed NH_3 on the crystals (a) This crystal was placed in a crystallizing dish containing aqueous $Co(NO_3)_2 \cdot 6H_2O$. (b) The pink coloration due to Co^{2+} adsorption is observed immediately. (c) Within 10–15 s a color change to green, characteristic of hexammine Co^{2+}, is apparent. (d) Within 2 min, the crystal forms small fractures as dissolution begins, resulting in a pronounced color change to a more intense green. The main illustration of this experiment is not to show the mechanism of release but rather to demonstrate that the external atmosphere was trapped in the solid.

chemisorption of gases as their means of storage. A dichotomy in the storage problem is that materials that store gases efficiently typically do not release them rapidly, and conversely, rapid release is correlated with ineffective storage at temperatures > 100°C (or even ambient conditions). Some organic container molecules have been observed to contain gases in their networks via van der Waals interactions.[41] Compound **18** presents a solid able to absorb the ambient atmosphere and store it to 150°C while providing instantaneous release of the gas at room temperature simply by the addition of water to the solid. The material is robust and highly recyclable.

B. Hydrogen Bonded Second Sphere Coordination Networks

Through discrete structures obtained with the mesitylene ligand, L5, it was found not only that L5 itself had very high complementarity with the triangular faces of hexaaquo metal ions (compound **19,** $[Fe(H_2O)_6L5]$, Fig. 23)

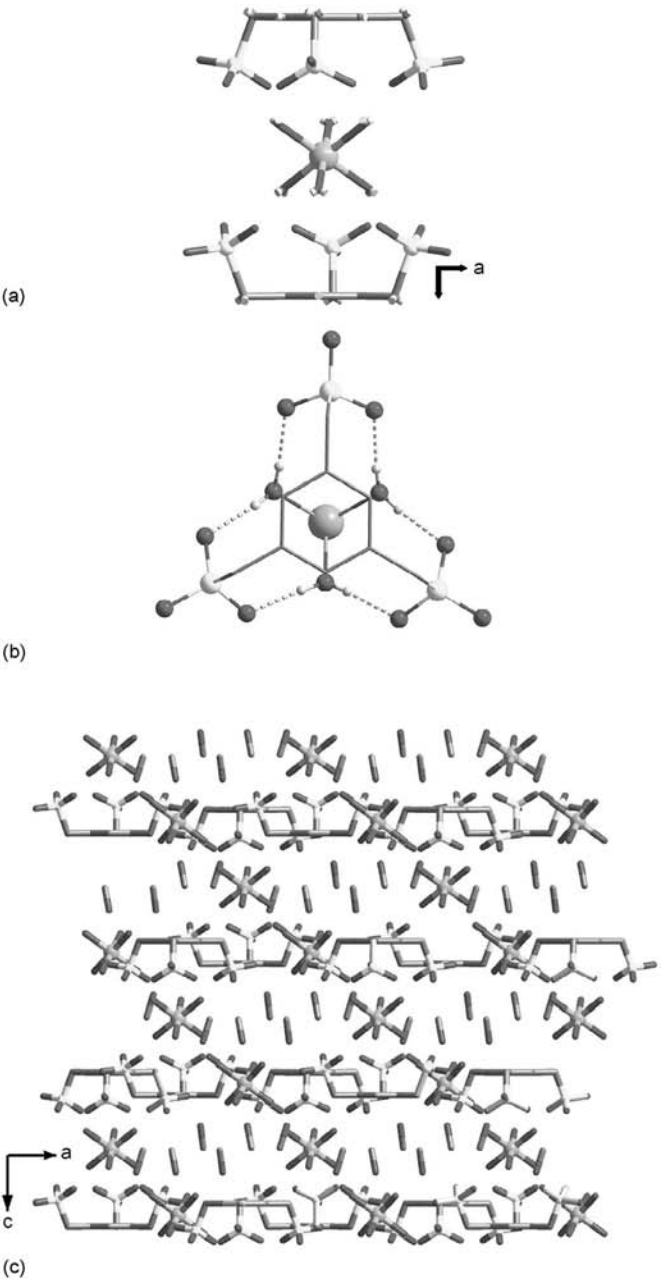

FIGURE 23. Views of the trianionic second sphere moiety of complex FeL5, **19**. (a) The doubly capping mode of L with $[Fe(H_2O)_6]^{3+}$. (b) The six hydrogen bonds formed between L and the triangular triaquo faces of $Fe(H_2O)_6]^{3+}$. The offset column arrangement along the *c*-axis and the placement of the MeOH molecules. Note the up-down alternation of the anionic organic moieties along the *a*-axis enabling the efficient packing and strong h-bond interactions with the cationic units.

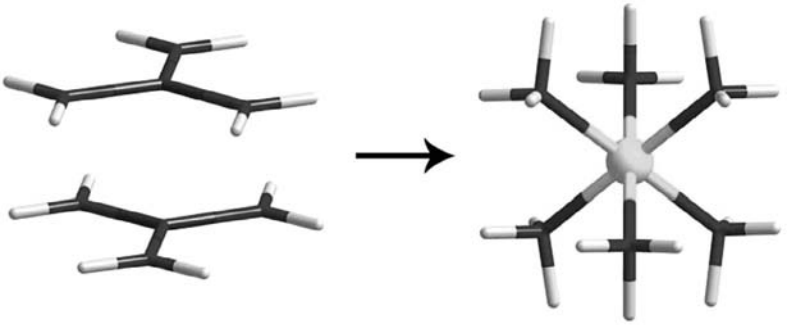

FIGURE 24. Structural relationship, with respect to hydrogen-bond donor ability between two guanidinium (G) cations and an octahedral hexammine complex oriented along its C_3 axis.

but that two oxygen atoms of a sulfonate group were highly complementary with two water molecules ligated in a cis orientation to a metal center.[42] Aquo ligands were not stable enough to form robust H-bonded networks, but it raised the question as to whether an inert hexammine complex could be employed as a H-bond donor to form networks. The precedent for this approach existed in the literature in the form of the guanidinium sulfonate inclusion family.[43] These solids are composed of H-bonded layers formed by perfectly complementary trigonal H-bonding between guanidinium donors and sulfonate acceptors. The vast array of inclusion phenomena observed for this family of compounds ($>$ 350 structures) owes to the ability of the GS framework to adjust to different guests via puckering of the layers and "turnstile-like" rotation of the pillars. Looking at Figure 24, one can see that the H-bond donation properties of a guanidinium cation could be mimicked by the triangular face of a metal hexammine octahedron. Thus, with a divalent complex, two guanidinium cations could be replaced in a network with metal complex. This would serve to enhance the stability of the structure because adjacent layers in a bilayer structure would be cross-linked.

Owing to the inertness and availability of $[Co(NH_3)_6]^{3+}$, despite its trivalent nature, initial studies with this complex were pursued.[44] It is important to keep in mind that, while the use of an octahedral metal has some advantages, the octahedron, beyond the desired C_3 orientation, can also lay along C_2 or C_4 axes. The bulk of our results on this system showed that, with many combinations of pillaring disulfonate and guest molecules, the overriding trend was that the components would arrange in a manner that would minimize porosity.[45]

Two general cases were observed in which some interlayer porosity could be created.[46] The first were situations in which secondary anions were included (e.g., Cl^-). This served two functions, the first being to form effectively a divalent metal center as the Cl^- would typically "nest" atop on the triangular

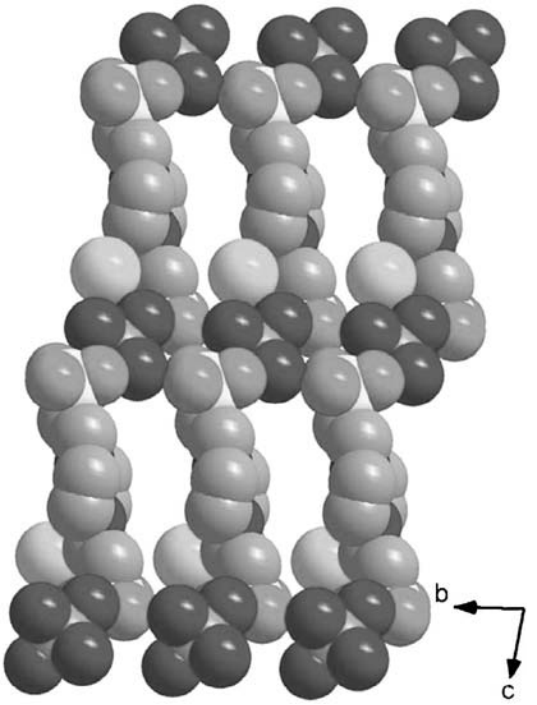

FIGURE 25. Structure of $\{[Co(NH_3)_6Cl](L15)(H_2O)_6\}_\infty$ **20**, where L15 = 1,4-piperazine-bis(ethanesulfonate): space-filling representation, perpendicular to the layers showing the spatial arrangement of the pillars and the "nesting" of the Cl^- ions (large light spheres).

triamine faces, bringing about the desired C_3 orientation. The second function was to reduce by 33% the required number of sulfonate pillars required. The second general case in which porosity could be generated in the interlayer was in situations in which the breadth of the sulfonate pillar prevented efficient interlayer packing. One example of each of these cases was reported in our initial report on these systems, $\{[Co(NH_3)_6Cl](L15)(H_2O)_6\}_\infty$, **20**, where L15 = 1, 4-piperazine-bis(ethanesulfonate), and $\{[Co(NH_3)_6](L16)_{1.5}(H_2O)_2$ (dioxane)$\}_\infty$, **21**, where L16 = 2,6-naphthalenedisulfonate. The structures of these compounds are shown in Figures 25 and 26.

Porosity, in the form of guest exchange, in weakly bonded solids had been observed in the absence of permanent pores.[47] This type of behavior would be more expected for solids in which the interlayer was not porous but, at the same time, was not efficiently packed and so could potentially reorient to accommodate a suitable guest species. A library of structural data on members of this family was screened and $[Co(NH_3)_6](L17)_{1.5}(H_2O)_2\}$, **22a**, where L17 = α,α′-*p*-xylenedisulfonate, was identified as a prospective nonporous host.[48] Figure 27 shows the structure of **22a** along with the inefficient packing of xylyl groups in the interlayer.

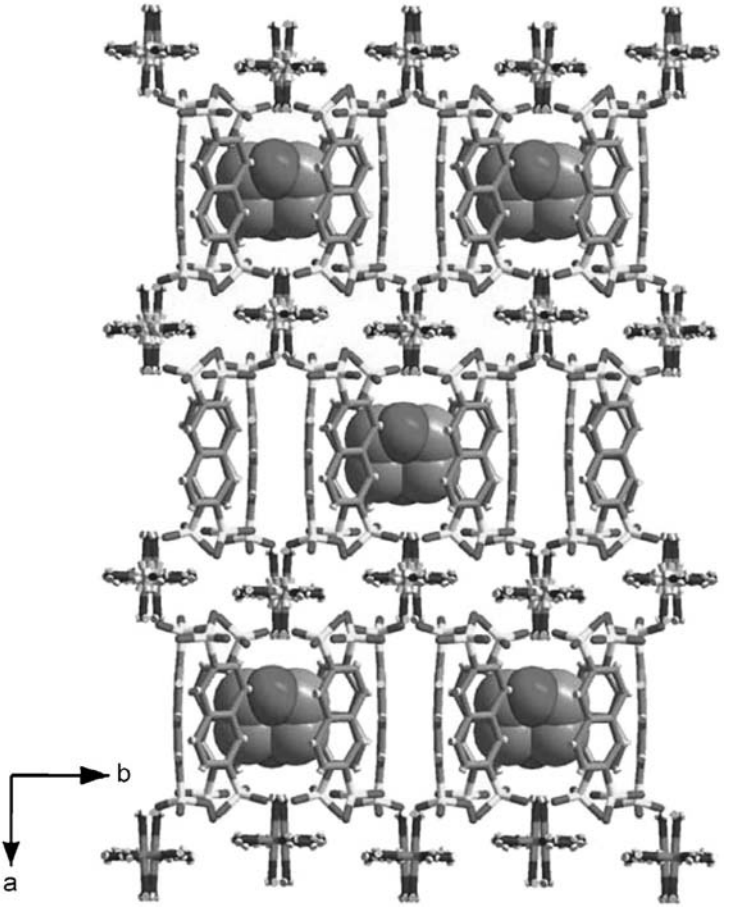

FIGURE 26. Structure of $\{[Co(NH_3)_6](L16)_{1.5}(H_2O)_2(dioxane)\}_\infty$**21**, where L16 = 2,6-naphthalenedisulfonate: the view perpendicular to the layers showing the 2,6-naphthyl pillars and, in space-filling representation, the included dioxane molecules.

The overall structure represented a compromise between the H-bonded layers and the interactions between aryl groups in the interlayer. The hydrogen-bonded sheets appeared to dominate the structure, as strong π-stacking interactions between aryl rings did not exist. There are two unique rings that arrange in a repeating *ABA* fashion. Within each trimer, there is slight overlap of single edges of adjacent rings at a mean distance of 3.52(1) Å. Between trimeric units, the shortest contact was between C6 vertices of *A* rings at 3.780(7) Å. Although this was not an efficiently stacked interlayer, it would certainly not be deemed porous.

Despite not having a porous interlayer, compound **22a** was observed to selectively absorb aniline as a guest molecule. Upon treatment of **22a** with

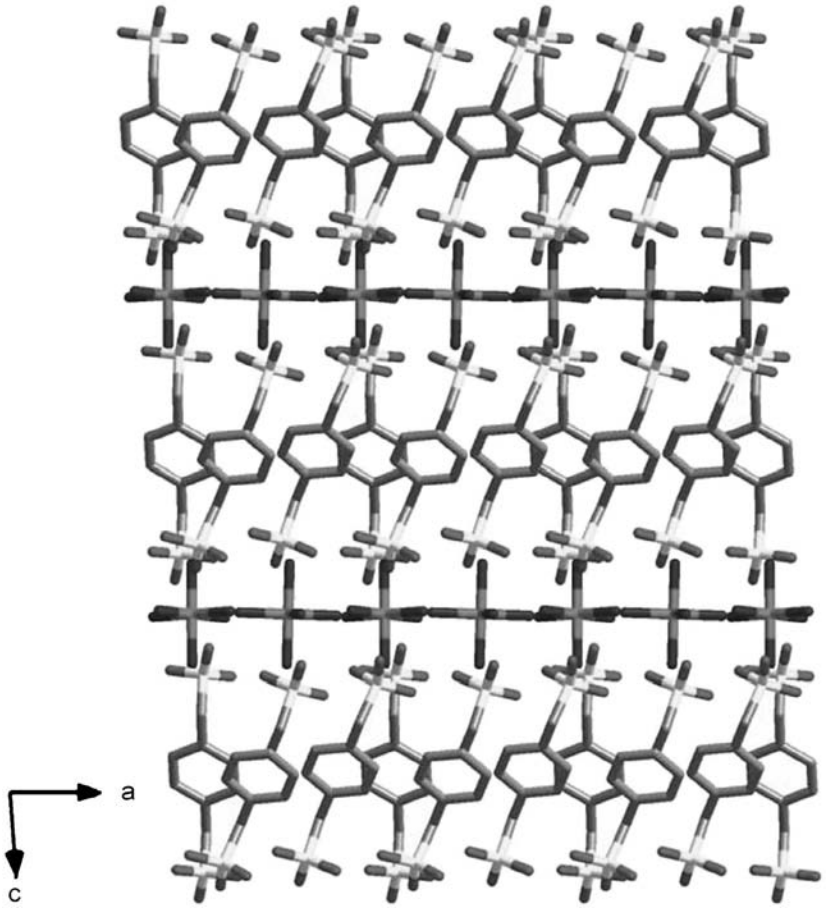

FIGURE 27. Structure of $[Co(NH_3)_6](L17)_{1.5}(H_2O)_2\}$, **22a**, where L17 = α,α′-*p*-xylenedisulfonate, showing the inefficient packing of the organic ligands in intercationic spaces.

aniline and water (either as liquid or vapor phase), conversion to $\{[Co(NH_3)_6](L17)_{1.5}(aniline)(H_2O)_3\}$, **22b**, was observed, as shown in Figure 28. Compound **22b** was also a pillared layered solid but with aniline molecules incorporated between the *p*-xylene units at a stoichiometry of one aniline molecule for every three *p*-xylyl pillars. The pillars adopt a more vertical alignment, and this was reflected in an increase in the perpendicular layer spacing to 13.55(1) Å (*cf.* 12.74 Å).

There was increased hydration in the hydrophilic layers as three molecules of water were incorporated for each Co center. The interlayer region was more densely packed in **22b** than **22a,** as would be expected with the incorporation of aniline guests. All aryl units in the interlayer region aligned

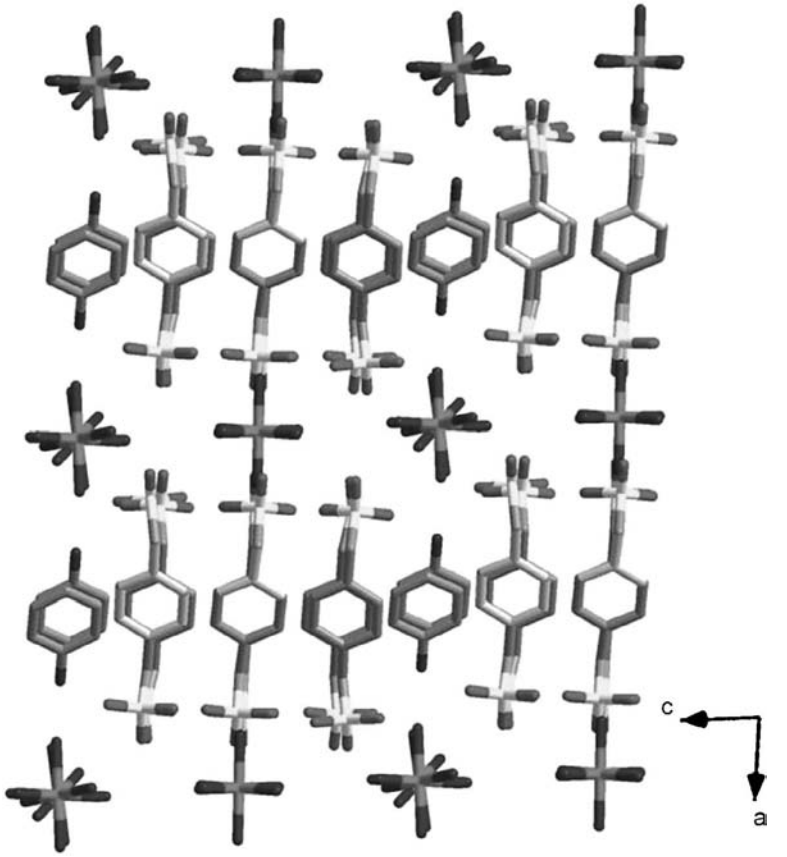

FIGURE 28. Structure of $\{[Co(NH_3)_6](L17)_{1.5}(aniline)(H_2O)_3\}$, **22b**, viewed parallel to the layers. The aniline guests appear above and below some Co centers and alternate in their orientation. Water molecules residing above and below each aniline moiety have not been shown. Note the relatively vertical arrangement of the L17 units. The subsequent accommodation of the aniline molecules make the interlayer spaces much denser than those in **22a**.

in rows such that half of each aryl face overlapped with each adjacent row of aryl rings. For each aniline guest, this resulted in four π-interactions with neighboring xylyl groups (C—C = 3.371(9) –3.436(9) Å). The aniline amino group also formed two hydrogen bonds with sulfonate O atoms (N—O = 2.958(6), 3.284(7) Å), which further augmented the π stacking interactions. Given the exactness of the fit of the guest aniline molecules in **22b**, the selectivity of uptake of other guests was examined using direct treatment of the fully desolvated $\{[Co(NH_3)_6](L17)_{1.5}\}$, **22c**, with guests in the presence and absence of water vapor. Simple aromatic guests, such as benzene and toluene, as well as the functionalized rings, chlorobenzene, benzonitrile, nitrobenzene,

and benzyl chloride, were not included. In fact, based on PXRD experiments, only amines were absorbed by the host. The PXRD of the complex of 1,4-phenylenediamine closely matched that of **22b**. There was a steric dependence to the selectivity because, while 3-methylaniline was taken up, giving a PXRD similar to **22b**, 3,5-dimethylaniline was excluded. The water was required along with the amine guest because interlayer guest inclusion was accompanied by layer dispersion, requiring additional hydrophilic guests to fill the layers. While the guest inclusion in this system was clear, the system did not demonstrate a reversible gas sorption isotherm; more strongly interacting guests were required to bring about a structural rearrangement.

In the field of crystal engineering, the use of coordination bonds to sustain permanently porous materials has been studied only for the past decade. The weaker the sustaining interactions become, the less likely it is that a porous structure will result. Employing H-bonds, as shown by compounds **19–22**, the formation of even an open structure presents a formidable challenge. In keeping with the design strategy of forming an open pillared layered solid by using an octahedral metal complex analogously to two guanidinium cations, it became apparent that needed a key design shift was the stabilization of an divalent metal complex that offered a trigonal H-bond donor set. To meet this requirement, the ligand, *tris*(aminomethyl)ethane (tame), was employed and used to form the divalent complex $[Ni(tame)_2]^{2+}$.[49] It was anticipated that the self-assembly of this divalent metal complex, which offered two trigonal triamine H-bond donor sets with a pillaring disulfonate, would yield the desired structural motif. Figure 29 shows the outcome with 4,4′-biphenyldisulfonate (L18) to form $[Ni(tame)_2](L18)$, compound **23**.[45]

This was clearly not the desired result. Rather than a structure dictated by N–H · · · O–S H-bonds, the dominant interaction in the structure was N–H π-interactions. This was a surprising and disappointing result. An idealized model of **23** with the desired N–H · · · O–S bonds optimized showed that three of the disulfonate pillars could indeed surround a $[Ni(tame)_2]$ cation. However, when the construction of the complete layered array was attempted, it became apparent that there was some steric congestion between the H atoms on the methylene bridges of the tame ligands and the α-H atoms on the aryl rings bonded to the SO_3 groups. This subtlety (Fig. 30) was sufficient to prevent formation of the desired structure, and so a pillaring group without α-H atoms was sought.

To address the steric congestion caused by the α-H atoms, the monosulfonate compound 2-phenylethynesulfonate (L19) was prepared. This was self-assembled with the $[Ni(tame)_2]$ dication to form compound **24**.[50] Figure 31 shows the structure of **24**. The self-assembly had occurred exactly as predicted to form a hexagonal H-bonded motif between SO_3 groups and the NH_2 groups of the tame molecules (Fig. 31a). The lateral view of the layers (Fig. 31b) shows the expected alternating polar/nonpolar stacking arrangement resulting from H-bonded sheets and pendant aromatic groups. The structure of **24** was not porous, but it was not expected to be because a simple monosulfonate anion

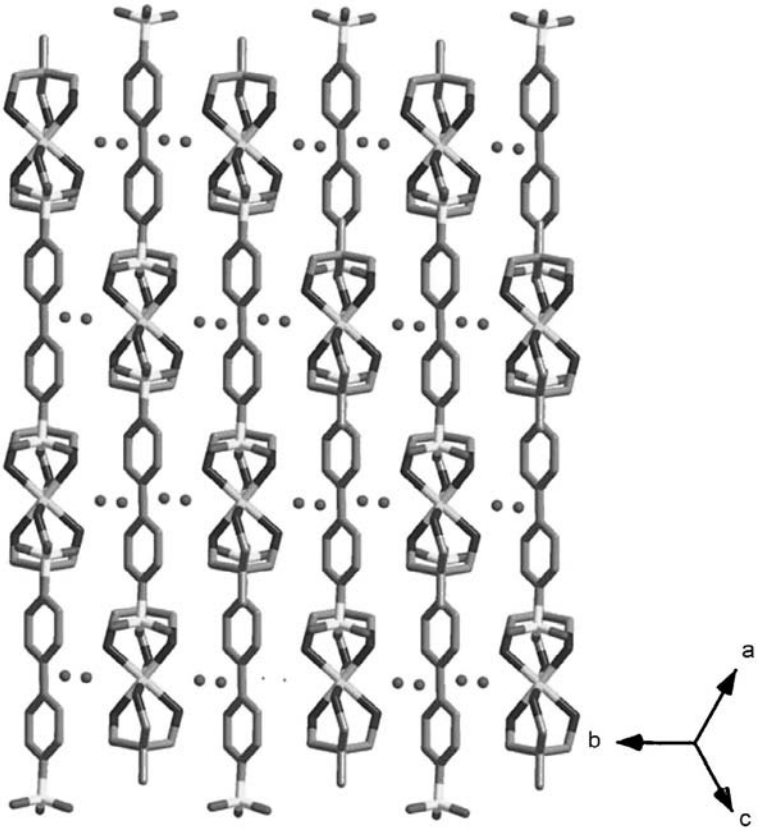

FIGURE 29. The extended second sphere network derived from hydrogen-bonding interactions is depicted in $[Ni(tame)_2](L18)$, where L18 = 4,4′-biphenyldisulfonate. Note that the strongest interactions are of the N–H · · · π-type.

was used; a pillaring ligand would be required to form a porous structure. Figure 31b shows that the phenylethyne units interdigitated in the interlayer to form a dense material.

Based on the promising result of **24**, a pillaring disulfonate ligand was prepared, 4,4′-bis(sulfoethynyl)biphenyl (L20). Complexation of L20 with the $[Ni(tame)_2]$ dication yielded an immediate precipitate, formulated as $[Ni(tame)_2]$L20, **25a**, with somewhat broadened powder X-ray diffraction pattern not reminiscent of a layered solid (Fig. 32a). To order the solid, refluxing of this powder in water was attempted, and indeed, a phase change was observed. This second phase, **25b**, formulated as a monohydrate, also did not yield a PXRD pattern resembling a layered material. Upon desolvation of **25b**, no change in the PXRD pattern was observed. Gas sorption analyses showed a surface area of 70 m^2/g. Although a modest result, the solid was shown to be robust. This phase was designated as **25c**.

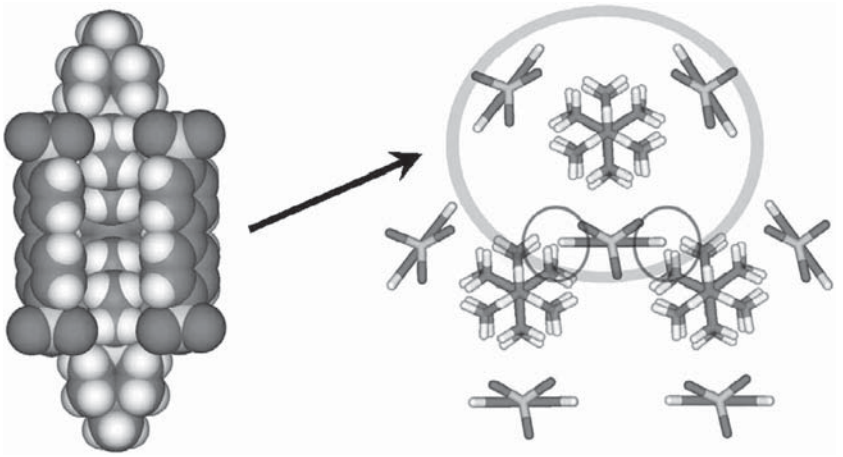

FIGURE 30. An artificially idealized model of the $Ni(Tame)_2$(L18) hydrogen-bonded assembly showing (a) three L18 molecules around a $Ni(tame)_2$ complex and (b) the steric congestion between α-hydrogens of the aryl rings and the tame methylene H-atoms.

In a further attempt to direct the self-assembly of the Ni(tame) dication with L20, benzene was added to the reflux mixture. The rationale for this addition was simply that, in the targeted structure, the aryl groups of L20 would be situated ~ 7.0 Å apart. This was well suited for aryl-stacking interactions given an aromatic guest was present. Upon refluxing **25a** in a water/benzene solution, a second phase change was observed giving a PXRD that did resemble a layered material, compound **25d**. To extract structural data on **25d**, the PXRD pattern was indexed giving a monoclinic unit cell (a' = 13.865, b' = 7.794, c' = 19.379 Å, β' = 100.63°). Because the $Ni(tame)_2$-sulfonate layers should have been identical in **24** and **25d**, a comparison of the unit cell parameters was made.

Figure 33 shows the hexagonal $Ni(tame)_2$-sulfonate layer observed in **24**, with the trace of its unit cell in purple. A second very plausible unit cell for this sheet (in green) has parameters a' = 13.86 Å and b' = 8.00 Å, γ' = 90°. This is in excellent accord with the refined unit cell obtained from the indexing of **25d** (a' = 13.865 Å, b' = 7.794 Å, γ' = 90°). The fact that the cell axes in **25d** are actually shorter indicates stronger H-bonds within the layer; an observation that was quite feasible given the layer structure in **24** would be balanced with the interlayer aryl contacts. This was strong support that the ideal H-bonded array had formed. Further evidence supporting this point came from the match of the calculated and expected perpendicular axis for **25d**. With a hexagonal H-bonded layer and the orthogonal disulfonate pillars, c' is predicted as 19.151 Å.[15] The indexed c' axis for **25d** was 19.379 Å. Ultimately, a model of the proposed structure was built on the indexed unit cell, which showed a good correlation

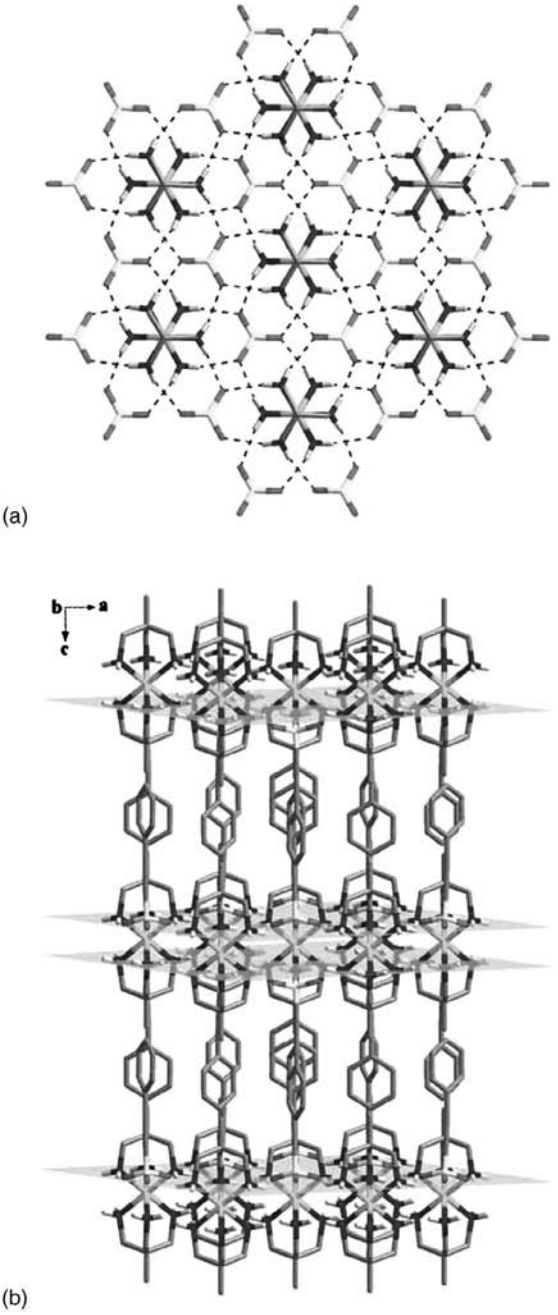

FIGURE 31. The single crystal X-ray structure of [Ni(tame)$_2$ 2-phenylethynesulfonate] L19), **24**. (a) The hexangonal H-bonded double layer to each trigonal face of the C_3 oriented octahedral metal complex. (b) View perpendicular to the layers showing the pendant phenylethynyl rings.

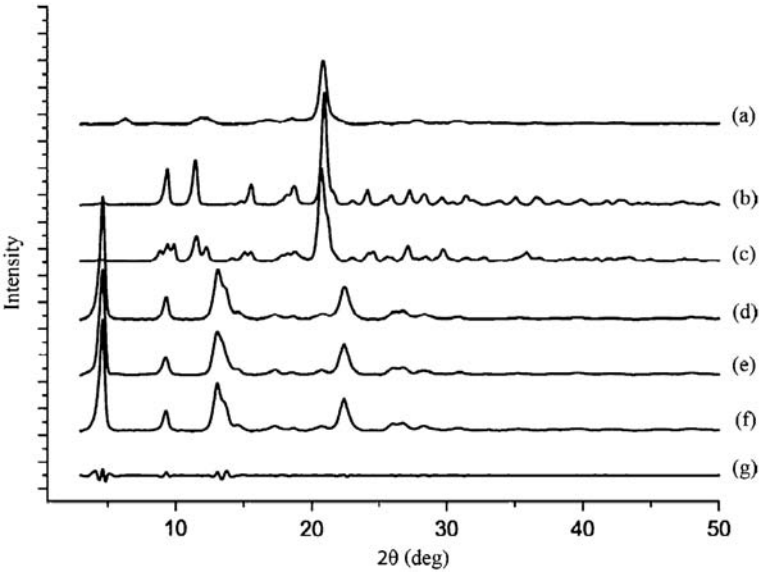

FIGURE 32. PXRD patterns for the Ni(tame)2(L20), compound **25** phases. (a) Bulk precipitate, **25a.** (b) Structure **25b** formed by refluxing **25a** in water. (c) Structure **25c**, formed by dehydrating **25b.** (d) Structure **25d**, formed by refluxing **25a** in water/benzene. (e) Structure **25e**, formed by desolvating **25d.** (f) Pawley fitting for the indexed unit cell of **25e.** (g) Difference plot between the observed (e) and refined (f) profiles.

with the observed PXRD. The modeled cell was built in P1 symmetry so extra peaks were observed; however, all peaks observed in the experimental pattern were present. Based on this evidence, we proposed **25d** as having the desired and designed structure of GS-like H-bonded sheets pillared by L20 (Fig. 34).

Powder XRD on a heated sample of **25d** showed no change in the observed pattern. This would infer a robust architecture, but given the proposed structure, void space would necessarily have to be generated in this desolvated solid, **25e**. To further confirm the proposed structure of **25d** and definitively illustrate the porosity of this system, CO_2 and N_2 sorption isotherms were performed on **25e** (Fig. 35). Both yielded type 1 isotherms characteristic of microporous solids. For CO_2, surface areas of 326, 373, and 380 m^2/g for BET, Langmuir, and Dubinin-Radushkevich (DR) models, respectively, were obtained.

The isotherm did not reach saturation, and no hysteresis was present. With N_2, surface areas of 392, 565, and 561 m^2/g were obtained for BET, Langmuir, and DR models, respectively. The use of charge-assisted H-bonds resulted in several key observations. First, the weaker interactions allowed the solid to optimize its structure in the presence of the aromatic guests, a key illustration of a more supramolecular approach. Second, the solid that resulted was permanently porous. To the best of our knowledge, **25e** was the only example of a permanently porous solid sustained exclusively by charge-assisted

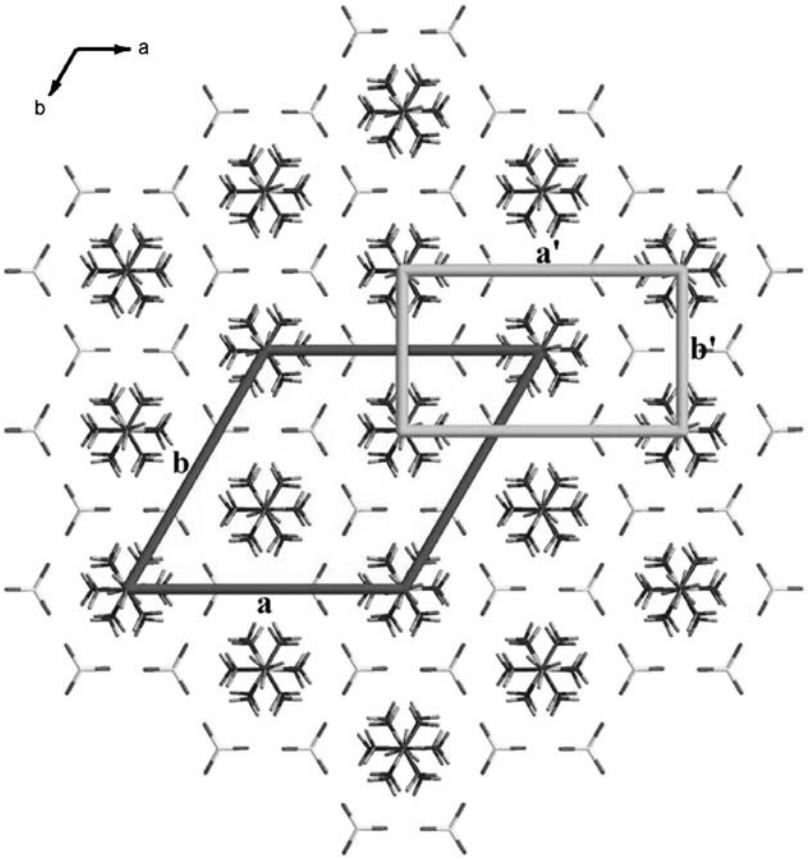

FIGURE 33. Structure of a H-bonded layer of **24**. The crystallographic *a*- and *b*-axes are shown as a dark rhombus. A plausible unit cell for **25e**, with parameters, $a' = 13.86$ Å and $b' = 8.00$ Å, is outlined as the lighter rectangle.

hydrogen bonds. Third, this was not an example in which porosity was obtained because the material simply could not pack efficiently, as two other more dense phases, **25a** and **25b**, were formed before to the most porous phase, **25e**. This was an illustration of the use of complementarity between weak interactions to yield a highly robust material.

V. METAL PHOSPHONATES

There is an obvious structural analogy between sulfonates and phosphonates; however, the two groups vary greatly in the strength of their bonding interactions with metal cations. That said, there are parallels with

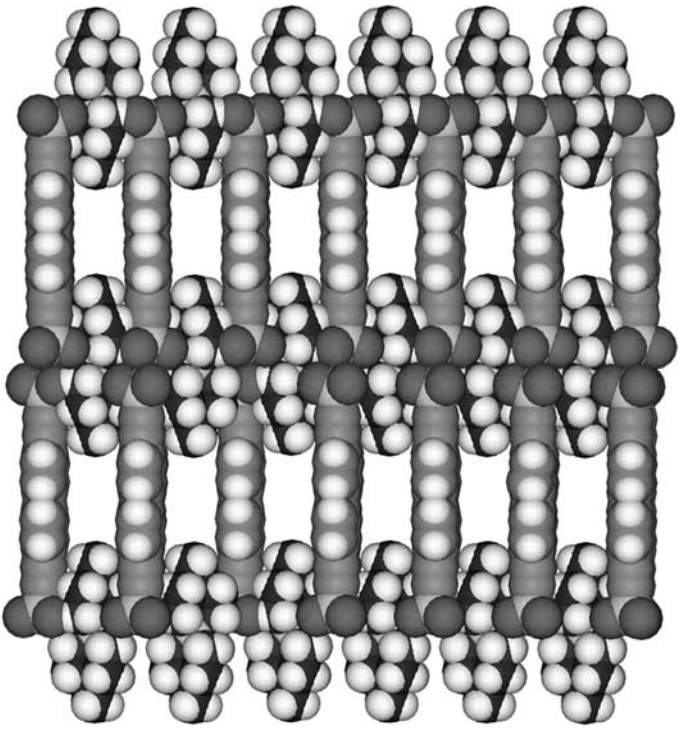

FIGURE 34. Proposed structure **25e** built on the indexed unit cell from PXRD data showing the pillared layered structure and resulting interlayer void space.

respect to the design of open frameworks, beginning with the predisposition of each group to form layered solids.[10,14] This tendency to form nonporous two-dimensional structures is more prominent with phosphonate groups, and so different approaches to generate porosity in a metal-phosphonate system have been studied. First, within the layered structures, one can replace some phosphonates in the layer with a nonpillaring group to create some space. For example, one can add phosphate, phosphite, or a small monophosphonate in the inorganic layer to create void space.[51] The problem with this approach is that substitution is random, so even though a porous phosphonate is typically formed, structural characterization and tunability is a challenge. Second, phosphonates with small R groups, such as methylphosphonic acid, can be employed to direct the structure away from the layered motif simply because of inefficient packing.[52] These 3D hexagonal structures contain small 1D channels. Structural variation by this approach is quite limited, because a small phosphonate is essential. A third approach involves adding a second functional group to the ligand to chelate the metal ion and direct the structure again away from simple layers. This can result in an open phosphonate framework, though often these are heteroleptic structures, with the second

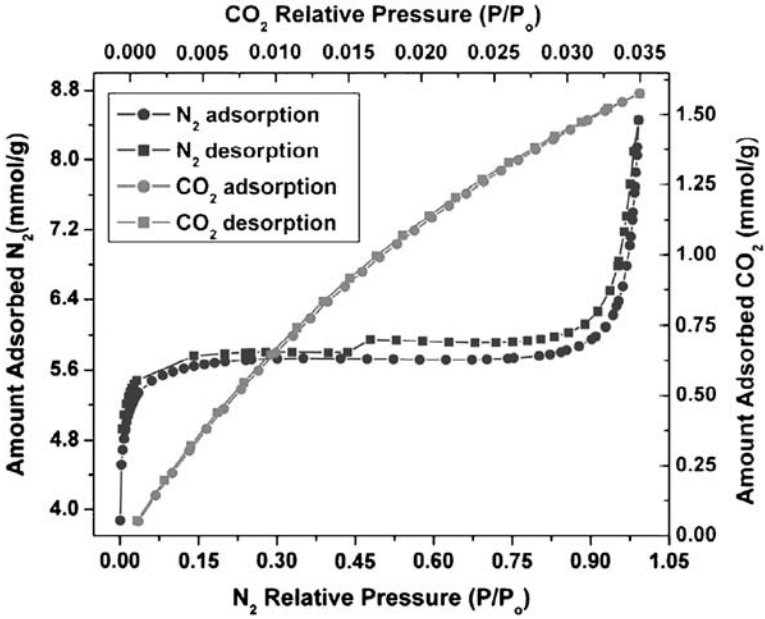

FIGURE 35. Gas sorption isotherms with CO_2 (light trace) and N_2 (dark trace) for **25e**. Both show reversible type 1 isotherms characteristic of a microporous solid.

ligating group dictating the framework formed.[53] Last, one can design a polyphosphonate ligand that itself cannot form a layered structure simply based on its geometry, akin to the metal sulfonate examples studied earlier. Lin et al. have used this successfully in the formation of binaphthyl-based lanthanide bis(phosphonates).[54]

Based on the previous sulfonate work in the group, an adamantane-based tetraphosphonate was synthesized in four steps from 1-bromoadamantane. This ligand, 1,3,5,7-tetrakis (4-phenyl phosphonic acid)-adamantane (L21), consisted of four phosphonic acid moieties spaced by rigid phenyl groups from an adamantane core. L21 by design could not adopt the pillared layered motif typical for bis(phosphonates) because it was locked into a tetrahedral geometry. Because L21 was tetrahedral, it was believed that coordination frameworks synthesized using this ligand would adopt a diamondoid topology. This deviated from other phosphonate work in that the tetrahedral ligand geometry controlled the topology of the networks formed, and not the phosphonate group or the metal used, a so-called inorganic aggregate director.

Originally the crystal structure of $H_8L21 \cdot 4H_2O \cdot 2CHCl_3$ was solved after crystals of the acid form of the ligand were grown from 0.5M $HCl_{(aq)}$ with diffusing $CHCl_3$.[55] This fourfold interpenetrated network had a diamondoid topology in which the second tetrahedral vertices consisted of hydrogen bonded water-phosphonic acid clusters, as shown in Figure 36. This result showed the

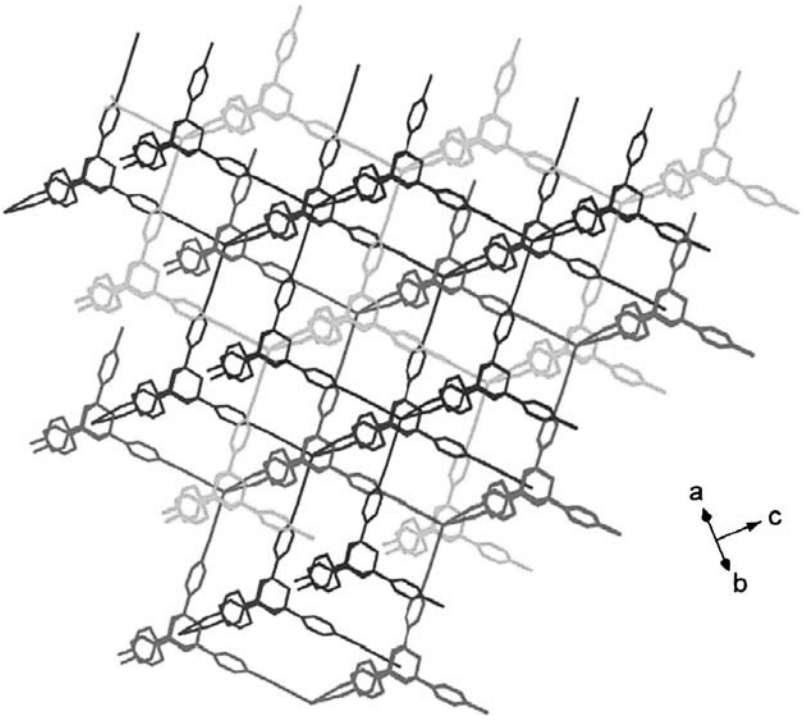

FIGURE 36. Fourfold interpenetrating diamondoid topology of H8L21 is observed in the crystal structure of $H_8L21 \cdot 4H_2O \cdot 2CHCl_3$. The second set of nodes in this structure is formed from tetrahedral water/phosphonic acid clusters.

propensity of the ligand to form diamondoid networks and the diamondoid networks to interpenetrate.

Between our report of the crystal structure of the ligand and our publishing the ensuing work, the group of Neumann reported two papers concerning open framework, but less ordered phosphonate systems with Ti^{4+} [56] and V^{3+} [57] and L21. No crystal structures were obtained, but the catalytic activity of the V framework for aerobic oxidation was studied. Given the rigid geometry of L21, to facilitate ordering of the solid, metals with pliant coordination spheres were used. In particular, the d^9 Cu^{2+} was used to form a network, which was structurally characterized by single crystal X-ray diffraction.[58] Small blue octahedral crystals of $[Cu_3(H_3L21)(OH)(H_2O)_3] \cdot H_2O \cdot MeOH$, compound **26**, were grown phase pure from a methanolic solution of L21 and $Cu(ClO_4)_2 \cdot 6H_2O$ through diffusion of hexanes. Structure **26** consisted of trigonal trinuclear copper clusters, in which the copper centers were in a distorted square pyramidal geometry, coordinated by three separate phosphonate groups and capped by a fourth phosphonate group to create a pseudo-tetrahedral arrangement of phosphonates around the cluster

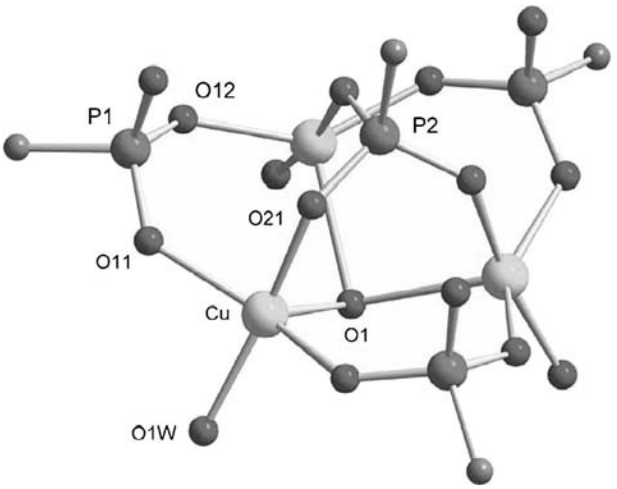

FIGURE 37. Crystal structure of the tricopper cluster in $[Cu_3(H_3L21)(OH)(H_2O)_3]\cdot H_2O\cdot MeOH$, **26**. The cluster is composed of three Cu^{2+} centers, three H_2O molecules, doubly-bridging RPO_3H^- (P1), and triply bridging OH^- ion (O1), RPO_3^{2-} (P2) groups.

(Fig. 37) The other side of the cluster contained a μ^3-hydroxyl group to charge balance. Because the copper clusters were in a pseudo-tetrahedral geometry, coupled with the tetrahedral ligand, the framework did have diamondoid geometry. Structure **26** was also twofold interpenetrated to fill some of the void space generated (Fig. 38).

Even though **26** was twofold interpenetrated, there was still a large amount of void space in the crystal structure. The bulky copper clusters prevented efficient interpenetration, and voids filled with H_2O/MeOH remained. The internal surface area of the sample was modeled from the crystal structure using the MS modeling studio, and the program gave a predicted internal surface area, assuming full desolvation with a N_2 adsorbent, of $2800 m^2 g^{-1}$. The modeled result led to real gas sorption analysis of **26** using a CO_2 adsorbent. Structure **26** was heated to 120°C under vacuum to activate it, and a BET surface area of only $200 m^2 g^{-1}$ was obtained.

Due to the large discrepancy between the modeled and the real values for internal surface area, it was believed that the framework was collapsing to some extent. To characterize this, variable temperature powder X-ray diffraction was performed on **26**. Compound **26** was heated from 30 to 280°C, and a scan was taken every 50°C. The PXRD showed that even at 30°C there was some loss in crystallinity, based on the broadening of the peaks and by 280°C, there was a significant loss in crystallinity. This result indicated that there was some destabilization of the structure on desolvation, causing collapse and the significant decrease in internal surface area from the solvated to

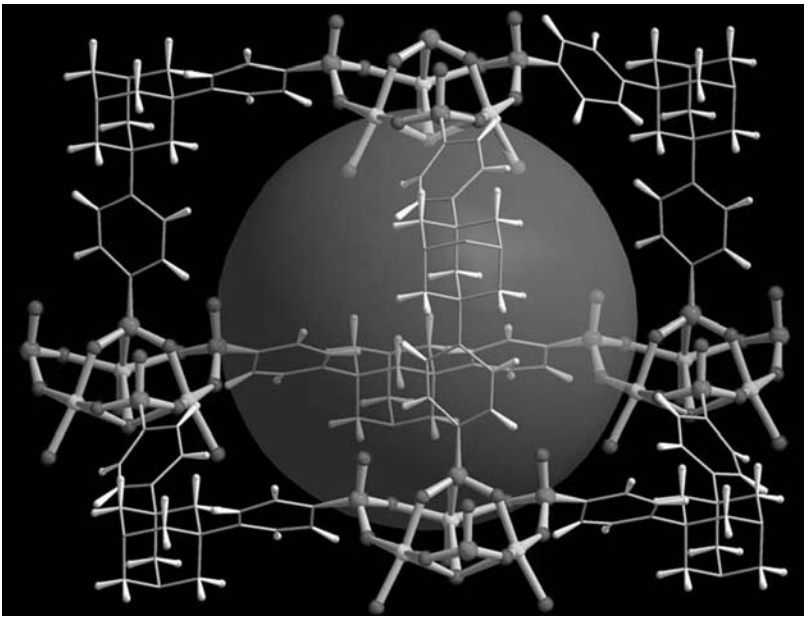

FIGURE 38. Crystal structure of $[Cu_3(H_3L21)(OH)(H_2O)_3] \cdot H_2O \cdot MeOH$, **26**, showing a single diamondoid net (inorganic clusters: balls and sticks; organic linkers: wireframe). For clarity, the ligands, L, are truncated and the disordered phenyl rings are shown in the major orientation.

desolvated product. Despite the loss of internal surface area on desolvation, **26** still remained permanently porous. This shows that inorganic aggregate director approach to this work was a valid one. The metal clusters formed were novel and generated as a direct result of the ligand geometry, creating a porous diamondoid framework.

Another inorganic aggregate director approach was taken using the ligand 1,3,5-tris(4-phosphonophenyl)benzene (L22), a triphosphonate with a rigid D_{3h} geometry.[59] Again this ligand was designed to deviate from the pillared-layered phosphonate motif because the trigonal nature of the ligand will not allow layers to bridge. Upon hydrothermal reaction with $Sr(OH)_2$ in the presence of MeOH, L22 formed a twofold interpenetrated, 3D crystalline solid with the formula $Sr_2(H_2L22)(CH_3OH)(H_2O)_4$, compound **27** (Fig. 39).

Compound **27** contained 1D SrO chains linked together by the trigonal L22. The chain was composed of face-sharing SrO_8 monocapped pentagonal biprisms, in which the two crystallographically independent Sr centers were coordinated by a μ2-bridging methoxy oxygen, five phosphonate oxygen atom, and two water molecules. Each L22 binds to three different chains and vice-versa, so a three-dimensional framework with large 1D channels along the *a*-axis resulted. In a single column, the organic groups were separated by

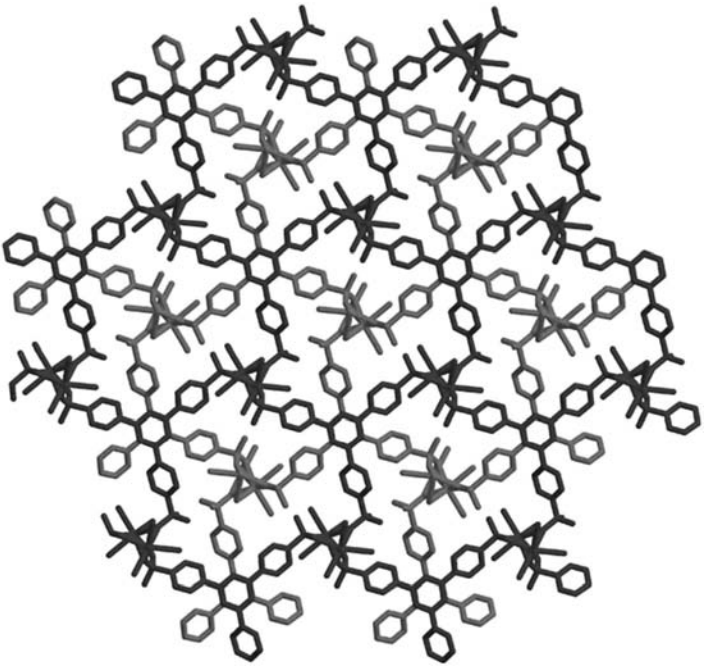

FIGURE 39. Crystal structure of $Sr_2(H_2L22)(CH_3OH)(H_2O)_4$, **27**. The structure is composed of one-dimensional Sr phosphonate columns cross-linked by the trigonal L22 molecules into a pseudo-hexagonal assembly. Two such structures interpenetrate (light and dark) and come into contact via π-stacking interactions between central aryl rings of L22 molecules.

6.92(1) Å along the *a*-axis, a distance suitable for inclusion of another aromatic system; this is where the interpenetration arose. The one-dimensional inorganic chains from one network filled the channels of the other network to form the interpenetrated structure. The pendant organic groups from the second network sat at a 60° offset from the first network, creating efficiently packed π-stacked columns of aryl rings (centroid-centroid distance = 3.52(1) Å). Though **27** was interpenetrated, clefts remained between the three peripheral aryl rings.

Thermogravimetric analysis was performed on **27** to test its stability. Structure **27** had a two-step weight loss of 13.54% between 65°C and 400°C, corresponding to a loss of four water molecules and the methoxy group. Gas sorption isotherms of **27** using CO_2 indicated that this material is porous, with a BET surface area of $146 m^2/g$. When left standing, it was observed that **27** took up CO_2 from the air, as was evidenced by IR spectroscopic measurements. To test this, **27** was desolvated at 100°C and placed under a CO_2 atmosphere for 2 h at RT. A 2% weight gain, corresponding to 0.4 mol of CO_2/formula unit was observed. Over three sorption/desorption cycles in the temperature range of 25–300°C, a 2.5–3% CO_2 uptake was observed.

Compound **27** is stabilized by both the 1D inorganic chains and the organic π-stacked structure, with a microporous network arising. This topology has design implications, where the most obvious means of increasing porosity would be to add additional phenyl spacers to L22. This network would retain the stability of both the π-stacked aromatic system and the 1D inorganic chain, but increase the internal surface area because the phenyl spacers would inadequately fill the space and a third interpenetrating network would not be possible.

Another method of introducing porosity into a metal-phosphonate system is through small modification of a simple linear ligand. For example, 1,4-benzenediphosphonic acid readily forms layered structures with most metals,[60] as this allows both robust inorganic layers and close packing of the interlayer phenyl rings. Through the addition of two hydroxyl groups in the *ortho* positions from each phosphonate, the structure is directed such that a layered structure is no longer the favorable motif.[61] This ligand, 1,4-dihydroxy-2,5-benzenediphosphonic acid (L23) was prepared in three steps from hydroquinone.

Upon reaction of L23 with $Zn(ClO_4)_2 \cdot 6H_2O$ in dimethylformamide (DMF), crystals of the formula $Zn(H_2L23)(DMF)_2$, compound **28**, were formed as a pure phase. Each of the zinc centers in **28** was in a distorted tetrahedral arrangement, fully coordinated by four oxygen atoms, each from four separate phosphonate groups. Each phosphonate bridged two zinc atoms, ultimately creating a 1D chain, in which the zinc coordination was homoleptic with respect to phosphonate oxygen atoms, as shown in Figure 40a. The phenyl rings on each ligand sat orthogonal from each other, which served to bridge each chain, ultimately creating a 3D porous network, with 1D chains running down the *c*-axis and bridges occurring in the *a* and *b* directions (Fig. 40b). Even though **28** was grown from an aqueous solution, no water was coordinated to the zinc centers. The OH groups on each ligand remained protonated and uncoordinated.

Through PXRD and TGA measurements, it was determined that **28** was stable to loss of ~80% of the included DMF molecules, which inferred porosity. CO_2 and N_2 gas sorption analysis gave BET surface areas of 216 m^2/g and 209 m^2/g, respectively. Upon complete loss of DMF, a loss of order was observed by PXRD, but order was regained upon resolvation. The addition of two hydroxyl groups *ortho* to the phosphonate groups provided sufficient steric effects to disrupt the formation of the layered motif and form an open structure in **28**. Stability in this structure is sustained by the 1D chains of phosphonate-bridged tetrahedral Zn ions, with no solvent molecules coordinating Zn. Stability is evidenced by the permanent porosity of **28**.

The slight modification of phosphonate ligands through the addition of the *ortho* hydroxyl group represented a new method of forming open framework phosphonates. The free hydroxyl group in **28** also represented a reactive site within the pores and may be a means to tune channel functionality.

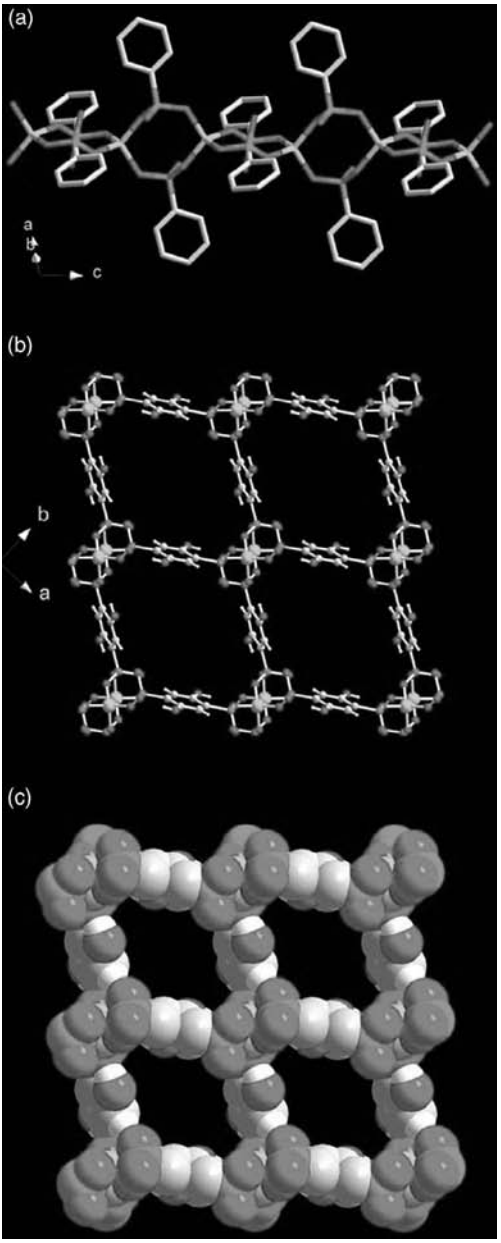

FIGURE 40. Single crystal X-ray structure of **28**. (a) A single RPO_3-bridged Zn chain. (b) View perpendicular to that in panel a showing the network of pores. (c) A space-filling depiction of the porous network.

VI. CONCLUSION

This work has presented a review of some of the research conducted in the Shimizu group since 1998 concerning metal sulfonates and metal phosphonates. The presentation has been largely chronological, beginning with the idea that metal sulfonates and phosphonates were almost exclusively two-dimensional materials. This was well known for phosphonates and it was equally well known that these solids possessed functionality stemming from the robust layered architecture. Subtleties in X-ray structures showed that, for metal sulfonates, the layered structures are predominant but that their intralayer bond connectivity is not as fixed as with metal phosphonates. A number of examples were presented to illustrate that intercalation phenomena are observable for metal sulfonates despite the layers being sustained by weaker interactions. Two studies to parameterize the tolerance of the layered motif to the size of the R group were discussed. Pillaring of layers was presented, and with alkaline earth sulfonates, it was shown that reversible gas sorption and anion exchange can occur within the interlayer region. Finally, design strategies to disrupt the layered motif and form open frameworks were presented. With metal sulfonates, these open frameworks predominantly show sponge-like sorption behavior rather than rigid open structures. This is truly the unique aspect of metal sulfonate networks because they are predisposed to not only dynamic behavior but also dynamic behavior with the retention of crystallinity. These efficient structure-shifting solids offer a broad range of new solids with switchable properties, an example of which was illustrated by a gas capture and release material. Beyond sorption phenomena, coupling these features with metal-based properties such as magnetism, color, or metal-based reactivity opens the door to new classes of sensors and reaction vessels.

These same strategies employed with the sulfonates, such as the choice of large polyvalent organic cores, when employed with metal phosphonates, result in the formation of permanently porous open structures with reversible gas sorption isotherms. The fact 0D and 1D phosphonate aggregates can be stabilized, as opposed to the default layered structure, and by altering the organic linker is an important result. Not only does this offer prospects for systems with 1D and 3D pore structures it offers opportunities for new inorganic aggregates with different properties. That is, the ligand would direct the inorganic structure rather than the opposite typically observed for metal phosphonates. Again, this offers a broad prospectus for new porous solids in which the design of the organic linker plays a key role.

Finally, we have shown that, with appropriate design, even (charge-assisted) H-bonds can sustain permanent pores. In this case, the complementarity between sulfonate anions and metal ammine complexes was exploited. Work on such systems with phosphonate ligands is under study, but the expectation is clear that such materials should also sustain permanent pores.

VII. REFERENCES

1. (a) S. Kitagawa, R. Kitaura, and S. Noro, *Angew. Chem. Int. Ed.*, **2004**, *43*, 2334. (b) C. Janiak, *Dalton Trans.*, **2003**, 2781. (c) U. Mueller, M. Schubert, F. Teich, H. Puetter, K. Schierle-Arndt, and J. Pastre, *J. Mater. Chem.*, **2006**, *16*, 626.
2. (a) D. W. Breck, *Zeolite and Molecular Sieves: Structure, Chemistry and Use*, Wiley, New York, **1974**. (b) P. Sozzani, A. Comotti, R. Simonutti, T. Messmann, and J. W. Logan., *Angew. Chem. Int. Ed.*, **2000**, *39*, 2695.
3. (a) O. M. Yaghi, M. O'Keeffe, N. W. Ockwig, H. K. Chae, M. Eddaoudi, and J. Kim, *Nature*, **2003**, *423*, 705. (b) M. J. Rosseinsky, *Micropor. Mesopor. Mater.* **2004**, *73*, 15. (c) G. Férey, C. Mellot-Draznieks, C. Serre, and F. Millange, *Acc. Chem. Res.*, **2005**, *38*, 217. (d) D. Tanaka and S. Kitagawa, *Chem. Mater.*, **2008**, *20*, 922.
4. (a) M. Eddaoudi, J. Kim, N. Rosi, D. Vodak, J. Wachter, M. O'Keeffe, and O. M. Yaghi, *Science*, **2002**, *295*, 469. (b) G. Férey, *Chem. Soc. Rev.*, **2008**, *37*, 191. (c) S. S. Y. Chui, S. M. F. Lo, J. P. H. Charmant, A. G. Orpen, and I. D. Williams, *Science*, **1999**, *283*, 1148.
5. (a) K. Uemura, R. Matsuda, and S. Kitagawa, *J. Solid State Chem.*, **2005**, *178*, 2420. (b) T. K. Maji, R. Matsuda, and S. Kitagawa, *Nature-Mater.*, **2007**, *6*, 142. (c) D. V. Soldatov, J. A. Ripmeester, S. I. Shergina, I. E. Sokolov, A. S. Zanina, S. A. Gromilov, and Y. A., Dyadin, *J. Am. Chem. Soc.*, **1999**, *121*, 4179. (d) D. N. Dybtsev, H. Chun, K. Kim, *Angew. Chem. Int. Ed.*, **2004**, *43*, 5033 (e) S. Kitagawa and K. Uemura, *Chem. Soc. Rev.*, **2005**, *34*, 109. (f) G. J. Halder and C. J. Kepert, *Aus. J. Chem.*, **2006**, *59*, 597.
6. S. Kitagawa and M. Kondo, *Bull. Chem. Soc. Jpn.*, **1998**, *71*, 1739.
7. H. Li, M. Eddaoudi, M. O'Keeffe, and O. M. Yaghi, *Nature*, **1999**, *402*, 276.
8. (a) C. N. R. Rao, S. Natarajan, and R. Vaidhyanathan, *Angew. Chem. Int. Ed.*, **2004**, *43*, 1466. (b) G. Férey, C. Mellot-Draznieks, C., Serre, F. Millange, J. Dutour, S. Surble, and I. Margiolaki, *Science*, **2005**, *309*, 2040. (c) W. Mori and S. Takamizawa, *J. Solid State Chem.*, **2000**, *152*, 120.
9. (a) X. Zhao, B. Xiao, A. J. Fletcher, K. M. Thomas, D. Bradshaw, and M. J. Rosseinsky, *Science*, **2004**, *306*, 1012. (b) G. H. Halder, C. J. Kepert, B. Moubaraki, K. S. Murray, and J.D. Cashion, *Science*, **2002**, *298*, 1762. (c) K. Takaoka, M. Kawano, M. Tominaga, and M. Fujita, *Angew. Chem. Int. Ed.*, **2005**, *44*, 2151.
10. (a) A. Clearfield, *Prog. Inorg. Chem.*, **1998**, *47*, 371. (b) G. Alberti and U. Costantino, in *Comprehensive Supramolecular Chemistry*, vol. *7*, ed. J. L. Atwood, J. E. D. Davies, D. D. MacNicol, and F. Vögtle, Elsevier Science, New York, **1996**. (c) K. Maeda, *Micropor. Mesopor. Mater.*, **2004**, *73*, 47.
11. (a) T. Bein, *Chem. Mater.*, **1996**, *8*, 1636. (b) P. M. Forster and A. K. Cheetham. *Topics., Catal.*, **2003**, *24*, 79.
12. M. E. Thompson, *Chem. Mater.*, **1994**, *6*, 1169.
13. J.-C. Grenier, J.-M Bassat, J.-P. Doumerc, J. Etourneau, Z. Fang, L. Fournes, S. Petit, M. Pouchard, and A. Wattiaux, *J. Mater. Chem.*, **1999**, *9*, 25.
14. (a) G. Bernardinelli, E. A. C. Lucken, and M. Z. Costines, *Kristallogr.*, **1991**, *195*, 145. (b) B. J. Gunderman and P. J. Squattrito, *Inorg. Chem.*, **1995**, *34*, 2399. (c) B. J. Gunderman and P. J. Squattrito, *Inorg. Chem.*, **1994**, *33*, 2924. (d) J. S. Haynes, J. R. Sams, and R. C. Thompson, *Can. J. Chem.*, **1981**, *59*, 669. (e) A. L. Arduini, M. Garnett, R. C. Thompson, and T. C. T. Wong, *Can. J. Chem.*, **1975**, *53*, 3812. (f) J. Cai, C.-H. Chen, C.-Z. Liao, J.-H. Yao, X.-P. Hu, X.-M. Chen, *J. Chem. Soc. Dalton Trans.*, **2001**, 1137. (g) A. J. Shubnell, E. J. Kosnic, and P. J. Squattrito, *Inorg. Chim. Acta.*, **1994**, *216*, 101. (h) M. A. Leopard, P. J. Squattrito, and S. N. Dubey, *Acta. Cryst. C*, **1999**, *C55*, 35.
15. (a) E. J. Kosnic, E. L. McClymont, R. A. Hodder, and P. J. Squattrito, *Inorg. Chim. Acta.*, **1992**, *201*, 143. (b) S. A. Dalrymple, M. Parvez, and G. K. H. Shimizu, *Chem. Commun.*, **2001**, 2672. (c) S. A. Dalrymple and G. K. H. Shimizu, *Supramol. Chem.*, **2003**, *15*, 591.
16. G. K. H. Shimizu, *J. Solid State Chem.*, **2005**, *178*, 2519.

17. (a) A. P. Côté and G. K. H. Shimizu, *Coord. Chem. Rev.*, **2003**, *245*, 49. (b) J. W. Cai, *Coord. Chem. Rev.*, **2004**, *248*, 1061. (c) J. L. Atwood, L. J. Barbour, M. J. Hardie, and C. L. Raston, *Coord. Chem. Rev.*, **2001**, *222*, 3.
18. G. A. Lawrence, *Chem. Rev.*, **1986**, *86*, 17.
19. G. K. H. Shimizu, G. D. Enright, C. I. Ratcliffe, G. S. Rego, J. L. Reid, and J. A. Ripmeester, *Chem. Mater.*, **1998**, *10*, 3282. (b) G. Smith, B. A. Cloutt, D. E. Lynch, K. A. Byriel, and C. H. L. Kennard, *Inorg. Chem.*, **1998**, *37*, 3236.
20. G. K. H. Shimizu, G. D. Enright, C. I. Ratcliffe, K. F. Preston, J. L. Reid, and J. A. Ripmeester, *Chem. Commun.*, **1999**, 1485.
21. (a) S. A. Solin, *Adv. Chem. Phys.*, **1982**, *49*, 455. (b) M. S. Dresselhaus and G. Dresselhaus, *Adv. Phys.* **1981**, *30*, 139.
22. M. S. Whittingham, *Prog. Solid State Chem.*, **1978**, *12*, 41.
23. (a) J. T. Kloprogge, *J. Porous Mater.*, **1998**, *5*, 5. (b) A. Vaccari, *Catal. Today*, **1998**, *41*, 51.
24. A. P. Côté, M. J. Ferguson, K. A. Kahn, G. D. Enright, A. D. Kulynych, S. A. Dalrymple, and G. K. H. Shimizu, *Inorg. Chem.*, **2002**, *41*, 287.
25. S. K. Sharma, C. E. Snyder Jr, and L. J. Gschwender, *Lubr. Eng.*, **1999**, *55*, 27.
26. (a) A. P. Côté and G. K. H. Shimizu, *Chem. Commun.*, **2001**, 251. (b) A. P. Côté and G. K. H. Shimizu, *Chem. Eur. J.*, **2003**, *9*, 5361.
27. D. J. Hoffart, S. A. Dalrymple, G. K. H. Shimizu, *Inorg. Chem.*, **2005**, *44*, 8868.
28. S. A. Dalrymple and G. K. H. Shimizu, *Chem. Eur. J.*, **2002**, *8*, 3010.
29. (a) R. Custelcean and B. A. Moyer, *Eur. J. Inorg. Chem.*, **2007**, *10*, 1321. (b) R. Custelcean, T. J. Haverlock, and B. A. Moyer, *Inorg. Chem.*, **2006**, *45*, 6446.
30. (a) K. S. Min and M. P. Suh, *J. Am. Chem. Soc.*, **2000**, *122*, 6834. (b) O. M. Yaghi and H. Li, *J. Am. Chem. Soc.*, **1996**, *118*, 295. (c) B. Sui, J. Fan, T. Okamura, W.-Y. Sun, and N. Ueyama, *New J. Chem.*, **2001**, *25*, 1379. (d) O.-S. Jung, Y. J. Kim, Y.-A. Lee, H. K. Chae, H. G. Jang, and J. Hong, *Inorg. Chem.*, **2001**, *40*, 2105.
31. A. P. Côté and G. K. H. Shimizu, *Inorg. Chem.* **2004**, *43*, 6663.
32. D. J. Hoffart, A. P. Côté, and G. K. H. Shimizu, *Inorg. Chem.*, **2003**, *42*, 8603.
33. (a) S. Kitagawa, S. Matsuyama, M. Munakata, and T. Emori, *J. Chem. Soc. Dalton Trans.*, **1991**, 2869. (b) L. M. Englehardt, C. Pakawatchai, A. H. White, and P. C. Healy, *J. Chem. Soc. Dalton Trans.*, **1985**, 117. (c) H. Adams, N. A. Bailey, D. W. Bruce, S. C. Davis, D. A. Dunmur, P. D. Hempstead, S. A. Hudson, and S. Thorpe, *J. Mater. Chem.*, **1992**, *2*, 395. (d) T. Suzuki, H. Kotsuki, K. Isobe, N. Moriya, Y. Nakagawa, and M. Ochi, *Inorg. Chem.*, **1995**, *34*, 530. (e) F. Jaber, F. Charbonnier, R. Faure, and M. Petit-Ramel, *Z. Kristallogr.*, **1994**, *209*, 536.
34. L. J. May and G. K. H. Shimizu, *Chem. Mater.*, **2005**, *17*, 217.
35. S. K. Makinen, N. J. Melcer, M. Parvez, and G. K. H. Shimizu, *Chem. Eur. J.*, **2001**, *7*, 5176.
36. (a) L. Carlucci, G. Ciani, M. Moret, D. E. Proserpio, and S. Rizzato, *Angew. Chem. Int Ed.*, **2000**, *39*, 1506. (b) K. Kasai, M. Aoyagi, and M. Fujita, *J. Am. Chem. Soc.*, **2000**, *122*, 2140. (c) L. Carlucci, G. Ciani, P. Macchi, D. E. Proserpio, and S. Rizzato, *Chem. Eur. J.* **1999**, *5*, 237.
37. (a) A. J. Fletcher, K. M. Thomas, and M. J. Rosseinsky, *J. Solid State Chem.*, **2005**, *178*, 2491. (b) K. Uemura. R. Matsuda, and S. Kitagawa, *J. Solid State Chem.* **2005**, *178*, 2420. (c) T. K. Maji, R. Matsuda, and S. Kitagawa, *Nanopor. Mater. IV*, **2005**, *156*, 497. (d) D. V. Soldatov, *J. Chem. Crystallogr.*, **2006**, *36*, 747. (e) L. J. May and G. K. H. Shimizu, *Z. Kristallogr.*, **2005**, *220*, 364.
38. D. Venkataraman, Y. Du, S. R. Wilson, P. Zhang, K. Hirsch, and J. S. Moore, *J. Chem. Ed.*, **1997**, *74*, 915.
39. (a) E. Cariati, X. Bu, and P. C. Ford, *Chem. Mater.*, **2000**, *12*, 3385. (b) L. G. Beauvais, M. P. Shores, and J. R. Long, *J. Am. Chem. Soc.*, **2000**, *122*, 2763. (c) L. Carlucci,

G. Ciani, D. W. v. Gudenberg, and D. M. Proserpio, *New J. Chem.*, **1999**, *23*, 397. (d) D. V. Soldatov and J. A. Ripmeester, *Chem. Mater.*, **2000**, *12*, 1827.

40. B. D. Chandler, G. D. Enright, S. Pawsey, J. A. Ripmeester, D. T. Cramb, and G. K. H. Shimizu, *Nature-Mater.*, **2008**, *7*, 229.
41. (a) G. D. Enright, K. A. Udachin, I. L. Moudrakovski, and J. A. Ripmeester, *J. Am. Chem. Soc.*, **2003**, *125*, 9896. (b) J. L. Atwood, L. J. Barbour, A. Jerga, and B. L. Schottel, *Science* **2002**, *298*, 1000.
42. S. A. Dalrymple and G. K. H. Shimizu, *Chem. Commun.*, **2002**, 2224.
43. (a) K. T. Holman and M. D. Ward, *Angew. Chem. Int. Ed.*, **2000**, *39*, 1653. (b) V. A. Russell, C. C. Evans, W. Li, and M. D. Ward, *Science*, **1997**, *276*, 575. (c) J. A. Swift, A. M. Pivovar, A. M. Reynolds, and M. D. Ward, *J. Am. Chem. Soc.*, **1999**, *121*, 5887. (d) V. A. Russell, M. C. Etter, and M. D. Ward, *J. Am. Chem. Soc.*, **1994**, *116*, 1941.
44. (a) R. Bala, R. P. Sharma, and A. D. Bond, *J. Mol. Struct.*, **2007**, *830*, 198. (b) X. Y. Wang, R. Justice, and S. C. Sevov, *Inorg. Chem.*, **2007**, *46*, 4626.
45. S. A. Dalrymple and G. K. H. Shimizu, *J. Mol. Struct.*, **2006**, *796*, 96.
46. D. S. Reddy, S. Duncan, and G. K. H. Shimizu, *Angew. Chem. Int. Ed.*, **2003**, *42*, 1360.
47. (a) K. Endo, T. Sawaki, M. Koyanagi, K. Kobayashi, H. Masuda, and Y. Aoyama, *J. Am. Chem. Soc.*, **1995**, *117*, 8341. (b) N. Malek, T. Maris, M. Simard, and J. D. Wuest, *J. Am. Chem. Soc.*, **2005**, *127*, 5910. (c) C. J. Kepert, D. Hesek, P. D. Beer, and M. J. Rosseinsky, *Angew. Chem. Int. Ed.* **1998**, *37*, 3158.
48. S. A. Dalrymple and G. K. H. Shimizu, *Chem. Commun.*, **2006**, 956.
49. J. G. Geue and G. H. Searle, *Aust. J. Chem.*, **1983**, *36*, 927.
50. S. A. Dalrymple and G. K. H. Shimizu, *J. Am. Chem. Soc.*, **2007**, *129*, 12114.
51. (a) G. Alberti, U. Costantino, F. Marmottini, R. Vivani, and P. Zappelli, *Angew. Chem. Int. Ed.*, **1993**, *32*, 1357. (b) G. Alberti, F. Marmottini, S. Murcia-Mascarós, and R. Vivani, *Angew. Chem. Int. Ed.*, **1994**, *33*, 1594. (c) N. J. Clayden, *J. Chem. Soc. Dalton Trans.* **1987**, 1877. (d) M. D. M. Gómez-Alcántara, A. Cabeza, L. Moreno-Real, M. A. G. Aranda, and A. Clearfield, *Micropor. Mesopor. Mater.,* **2006**, *88*, 293.
52. (a) J. Le Bideau, C. Payen, P. Palvadeau, B. Bujoli, *Inorg. Chem.*, **1994**, *33*, 4885. (b) K. Maeda, J. Akimoto, Y. Kiyozumi, and F. Mizukami, *Angew. Chem. Int. Ed.*, **1994**, *33*, 2335.
53. (a) N. Stock, G. D. Stucky, and A. K. Cheetham, *Chem. Commun.*, **2000**, 2277. (b) A. Distler and S. Sevov, *Chem. Commun.*, **1998**, 959. (c) M. Riou-Cavallec, M. Sanselme, N. Guillou, and G. Férey, *Inorg. Chem.*, **2001**, *40*, 733. (d) P. Rabu, P. Janvier, and B. Bujoli, *J. Mater. Chem.* **1999**, *9*, 1323. (e) A. Cabeza, M. A. G. Aranda, and S. Bruque, *J. Mater. Chem.,* **1998**, *8*, 2479.
54. (a) O. R. Evans, H. L. Ngo, and W. Lin, *J. Am. Chem. Soc.,* **2001**, *123*, 10395. (b) H. L. Ngo and W. Lin, *J. Am. Chem. Soc.* **2002**, *124*, 14298.
55. K. M. E. Jones, A. H. Mahmoudkhani, B. D. Chandler, and G. K. H. Shimizu, *CrystEngComm*, **2006**, *8*, 303.
56. M. V. Vasylyev, E. J. Wachtel, R. Popovitz-Biro, R. Neumann, *Chem. Eur. J.*, **2006**, *12*, 3507.
57. M. Vasylyev and R. Neumann, *Chem. Mater.*, **2006**, *18*, 2781.
58. J. M. Taylor, A. M. Mahmoudkhani, and G. K. H. Shimizu, *Angew. Chem. Int. Ed.*, **2007**, *46*, 795.
59. R. Vaidhyanathan, A. M. Mahmoudkhani, and G. K. H. Shimizu, *Can. J. Chem.* **2009**, *87*, 247.
60. D. M. Poojary, B. Zhang, P. Bellinghausen, and A. Clearfield, *Inorg. Chem.* **1996**, *35*, 5254.
61. J. Liang and G. K. H. Shimizu, *Inorg. Chem.*, **2007**, *46*, 10449.

CHAPTER 5

Transition-Metal-Based Linear Chain Compounds

Moumita Majumdar and Jitendra K. Bera

Department of Chemistry, Indian Institute of Technology Kanpur, Kanpur 208016, India

CONTENTS

Macromolecules Containing Metal and Metal-Like Elements,
Volume 9: Supramolecular and Self-Assembled Metal-Containing Materials,
Edited by Alaa S. Abd-El Aziz, Charles E. Carraher Jr., Charles U. Pittman Jr., and Martel Zeldin.

I. INTRODUCTION

The possibility of an organic superconductor, as proposed by Little in 1964[1] and the discovery of the extraordinary electrical conductivity in the organic charge transfer salt tetrathiofulvalene (TTF) tetracyanoquinodimethane (TCNQ) by Heeger in 1973,[2] fueled much interest among physicists and chemists in the field of low-dimensional materials. The quest for high-temperature superconductors motivated numerous studies involving one-dimensional compounds.[3] The emphasis, however, has currently shifted toward the characterization of unusual properties that are typically associated with nanoscale systems.[4] The electrical, magnetic, and photochemical bistability exhibited by low-dimensional nanostructures make them attractive candidates for developing nanodevices.[5]

A considerable surge of interest is presently noted in linear chain compounds involving transition-metal backbones. Two distinct approaches have been followed in their synthesis. In one method, the metal atoms are placed in linear arrays by employing carefully designed ligands. The number of donor sites determines the nuclearity of the chain compound. By employing this ''ligand-driven approach,'' linear chain compounds containing three to nine metal atoms have been reported (Figure **1**).

A different approach, appropriately termed the ''metal-driven approach'' relies on metal–metal bonds (Figure **1**). The largest class of one-dimensional inorganic compounds is square-planar d^8 complexes, which form columnar stacks in the solid state. Metal–metal bonds formed by the overlap of their d_{z^2} orbitals stabilize the stack. Oxidative doping of such one-dimensional compounds results in conducting materials as exemplified by partially oxidized tetracyanoplatinate salts $K_2[Pt(CN)_4]X_{0.3}.(H_2O)_n$ (X = C1, Br), commonly referred as Krogmann salts. Platinum has an average oxidation state of approximately +2.3, and compounds exhibit metallic luster and high conductivity.[6] The metal-driven approach also uses metal–metal bonded dimetal

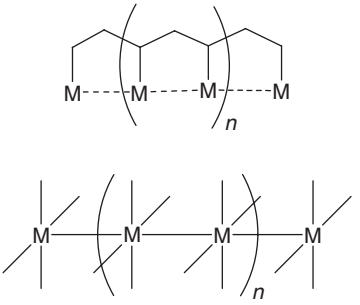

FIGURE 1

precursors. Condensation of dimetal precursors resulted in numerous oligomeric and polymeric linear metal chain compounds.

In this chapter, we describe linear metal chain compounds, consisting of at least three metal ions, supported by ligand systems. Extended metal atom chains (EMACs) of Cr, Co, Ni, and Cu, supported by polypyridylamide ligands, are discussed.[7] This is followed by linear and bent Pd chains sandwiched by unsaturated hydrocarbons. Unsupported linear metal chain compounds are discussed in subsequent sections. Because synthetic protocols and the bonding schemes are different for different metals, our discussion is classified according to metal ions.

II. LIGAND-SUPPORTED METAL CHAINS

A. Linear Chains of Chromium

The trichromium $Cr_3(dpa)_4Cl_2$ was obtained in high yield from the reaction between 3 equivalents of $CrCl_2$ and 4 equivalents of Lidpa in THF.[8] Initially, the reaction produces a red dinuclear complex $Cr_2(dpa)_4$, which converts to a green product $Cr_3(dpa)_4Cl_2$ on refluxing, as shown in Scheme **1**.[9] An identical synthetic method is employed in the preparation of trichromium complexes of the ligands dPhIP (di(phenylimino)piperidinate)[10] and bPAP (2,6-bisphenylaminopyridinate),[11] as shown in Scheme **2**.

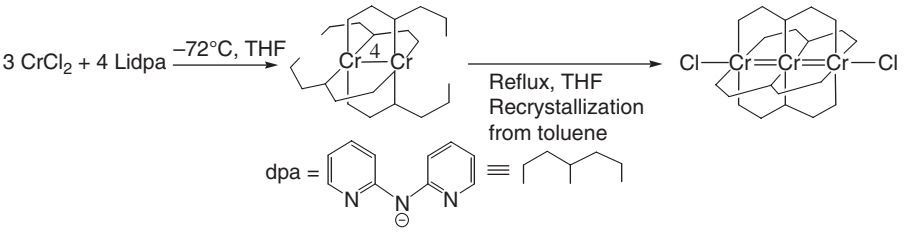

SCHEME 1

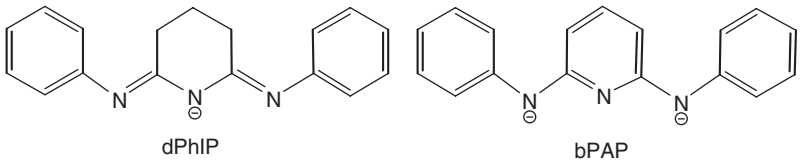

SCHEME 2

Partial or complete substitution of axial chlorine atoms in the parent $Cr_3(dpa)_4Cl_2$ by BF_4^-, PF_6^-, and $PhC{\equiv}C^-$ has been reported with varied degree of difficulties (Scheme **3**).[8] Use of 2 equivalents of $AgBF_4$ results in a redox reaction to produce crystals of $[Cr_3(dpa)_4F(BF_4)](BF_4)$.[12] Although it was possible to substitute two chlorides by acetylides, crystallization invariably produced a mixture of the starting material and the diacetylide product. Many attempts to obtain analytically pure samples were unsuccessful.[8b,9a] However, recently, $Cr_3(dpa)_4(CCPh)_2$ has been prepared in good yields and purity by using $[Cr_3(dpa)_4(MeCN)_2][PF_6]_2$ as the starting material.[13]

The structure of $Cr_3(dpa)_4Cl_2$ consists of a linear Cr_3 chain ligated by a spiral set of four dipyridylamides, and each terminal Cr atom is bonded to a Cl, as shown in Figure **2**.

The metal–metal separations in these compounds fall in two categories: symmetrical (D_4) and unsymmetrical (C_4) (Scheme **4**). For $Cr_3(dpa)_4Cl_2$, all known structures possess unsymmetrical metal–metal distances. Replacement of chlorides by cyanides results in a symmetrical chain.[14] The presence of two different terminal ligands clearly favors an unsymmetrical arrangement. For $Cr_3(dpa)_4(X)(Y)$, the Cr-Cr distances are so different that the Cr_3^{6+} chain could

$$Cr_3(dpa)_4Cl_2 + (2-n)X^- \longrightarrow Cr_3(dpa)_4Cl_nX_{2-n} + (2-n)Cl^-$$
$$n = 0, 1$$

SCHEME 3

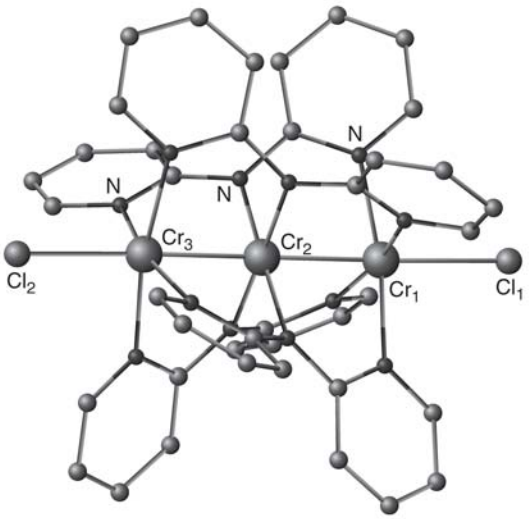

FIGURE 2

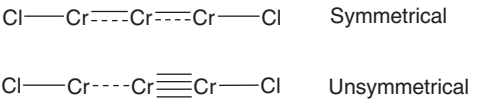

SCHEME 4

be described as consisting of a diamagnetic $[Cr_2]^{4+}$ quadruple bond (2.0 Å) and a high-spin Cr^{II} ion at a nonbonding distance (2.59 to 2.74 Å).[15] It has been shown that very weak σ donors such as nitrates and tetrafluoroborates give rise to unsymmetrical complexes with short Cr-Cr quadruple bonds and an isolated Cr atom, the latter forms a strong bond to the axial ligand. Moderately strong anionic ligands (Cl, NCS, NCO) give rise to medium-length Cr-Cr bonds. The exceptionally strong axial ligands such as cyanides and phenylacetylides stabilize symmetrical trichromium chains with equivalent Cr-Cr bond distances. The symmetric state is described in terms of a 3-center-3-electron (3c-3e) bond consisting of a filled 3-center σ-bonding orbital and a half-filled σ nonbonding orbital. The remaining metal-based nine electrons are localized on the three Cr atoms in orbitals of π and δ symmetry. Strong axial σ-donors destabilize the σ bond component of the Cr-Cr quadruple bond and raise the energy of the d_z^2 orbital of the isolated Cr^{II} ion as well. The localized Cr-Cr quadruple bond is destroyed, and the molecule responds to this by employing 3c-bonding. The axial ligands do not destabilize the delocalized 3c-3e bonding to the same degree as the localized Cr-Cr bond.[16]

Another major factor affecting the occurrence of a symmetrical versus unsymmetrical structure is the basicity of the bridging ligands. More basic bridging ligands appear to favour symmetrical Cr_3^{6+} chains, whereas less basic ligands favour unsymmetrical compounds.

All of the known trichromium compounds are paramagnetic. Variable temperature magnetic susceptibility data for both symmetrical and unsymmetrical $[Cr_3]^{6+}$ compounds follow the Curie-Weiss law with μ_{eff} = 4.6-5.1 μ_B, corresponding to four unpaired electrons.[8b] Therefore, it is not possible to distinguish between symmetrical and unsymmetrical compounds by magnetic susceptibility data alone. For the unsymmetrical Cr_3^{6+} compounds, four unpaired electrons are localized on the isolated high spin Cr^{2+} ion. In the case of the symmetrical Cr_3^{6+} species, four unpaired electrons are delocalized over the Cr_3 chain.

The tetranuclear Cr chain $[Cr_4(dpyf)_4Cl_2]Cl_2$, (dpyf = bis(2-pyridyl)formamidinato) has been reported (Scheme **5**). In the tetranuclear ion $[Cr_4(dpyf)_4Cl_2]^{2+}$, the Cr atoms pair up to form two isolated Cr_2^{4+} quadruply bonded units (ave. Cr-Cr = 2.01 Å) with a distance of 2.73 Å separating them.[17] The pentanuclear $Cr_5(tpda)_4Cl_2$ (tpda = di-anion of tripyridyldiamine) (Scheme **6**) and $Cr_5(tpda)_4(NCS)_2$ have been reported.[18] Oxidation of $Cr_5(tpda)_4Cl_2$ with 2 equivalents of $AgBF_4$ and AgOTf lead to the formation of oxidized products $[Cr^{III}Cr_4^{II}(\mu_5\text{-tpda})_4F_2][BF_4]$ and $[Cr^{III}Cr_4^{II}(\mu_5\text{-tpda})_4$

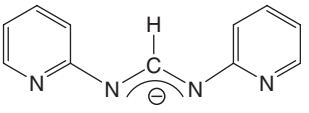

dpyf

SCHEME 5

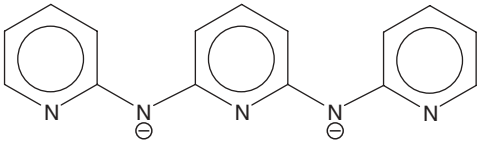

tpda

SCHEME 6

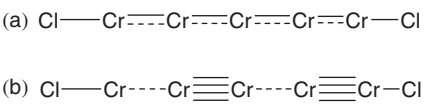

SCHEME 7

$F(CF_3SO_3)][CF_3SO_3]$, respectively. The origin of F^- ions in these complexes is from the dissociation of BF_4^- and $SO_3CF_3^-$ anions in THF.[19] The parent $Cr_5(tpda)_4Cl_2$ may exists in two possible structures: (a) a highly delocalized one and (b) one with localized quadruple bonds as shown in Scheme **7**. The type of structure found for $Cr_5(tpda)_4Cl_2$ is (b). Distances in the essentially linear chain, Cl-Cr-Cr≡Cr-Cr≡Cr-Cl are from left to right: 2.499(6), 2.578(7), 1.901(6), 2.587(6), 2.031(6), and 2.604(5) Å.[20]

Crystallographic disorder in the positions of the metal atoms is an important issue in deciding whether a localized/delocalized model is applicable. The pentanuclear $Cr_5(tpda)_4(NCS)_2$ and the heptanuclear $Cr_7(teptra)_4Cl_2$ (teptra = tri-anion of tetrapyridyltriamine)[21] (Scheme **8**) have been reported as being consistent with the delocalized model, though the elongated thermal ellipsoids for the Cr atoms in the crystal structures suggest that localized model is probably a better description.

By employing pyrazine-modulated pentapyridyltetraamine (H_4-mpz = *N*^{2},*N*^{6}-bis-[6-(pyridine-2-ylamino)-pyridin-2-yl]pyrazine-2,6-diamine) (Scheme **9**), Peng successfully synthesized linear nona-chromium (II) complex $Cr_9(\mu_9\text{-mpz})_4Cl_2$ (Figure **3**), which is the highest nuclearity Cr^{II} chain to date.[22] The length of the whole molecule is 23–25 Å. Four ligands wrapped around the

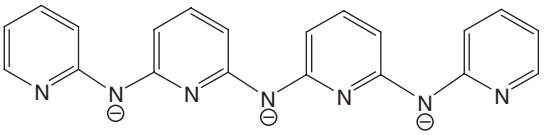

teptra

SCHEME 8

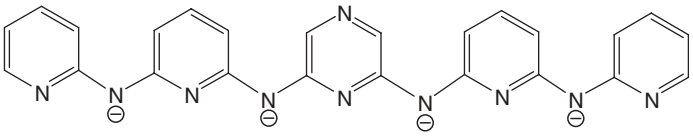

mpz

SCHEME 9

metal string in *syn-syn* form as a nonadentate anion helix. The Cr-Cr bond distances fall into two categories, the shorter one is in the range 1.973–2.097 Å, which is consistent with Cr-Cr quadruple bonds. The longer Cr-Cr distances range from 2.397 to 2.497 Å. Thus the Cr_9 chain is composed of four quadruple Cr-Cr bonds and a single terminal Cr^{II} atom coordinated in a pyramidal Cl-Cr-N_4 unit, in the same style as trichromium and pentachromium chains.

B. Linear Metal Chains of Cobalt

$Co_3(dpa)_4Cl_2$ was prepared in high yields following the reaction of anhydrous $CoCl_2$ with Lidpa in refluxing THF, as shown in Scheme **10**.[23] $Co_3(dpa)_4Cl_2$, dissolved in CH_2Cl_2 and layered on top with hexane at ambient temperature provided the symmetrical *s*-$Co_3(dpa)_4Cl_2.CH_2Cl_2$. In addition, an unsymmetrical *u*-$Co_3(dpa)_4Cl_2.2CH_2Cl_2$ was also isolated in 15% of the total amount. The structure of $[Co_3(dpa)_4Cl_2]$ is shown in Figure **4**. The three Co^{II} ions and two chloride ions are collinear.[24] The *syn-syn* conformation of the four dipyridylamido ligands allows each nitrogen atom to coordinate with a separate Co^{II} ion. The *s*-$Co_3(dpa)_4Cl_2$ has a symmetrical Co-Co-Co chain with a separation of 2.3178(9) Å between pairs of Co atoms and a distance of 2.520(2) Å for each of the two axial Co-Cl bonds. The metal–metal bonding in this symmetrical compound is delocalized along the linear tricobalt unit with a three-center metal–metal bond order of 0.75. The *s*-$Co_3(dpa)_4Cl_2.CH_2Cl_2$ molecule is symmetrical in the temperature range 298 to 168 K and crystallizes in the orthorhombic space group. Between 168 and 109 K, the symmetric structure undergoes a phase transition from the orthorhombic form to a monoclinic form. This breaks the crystallographically imposed

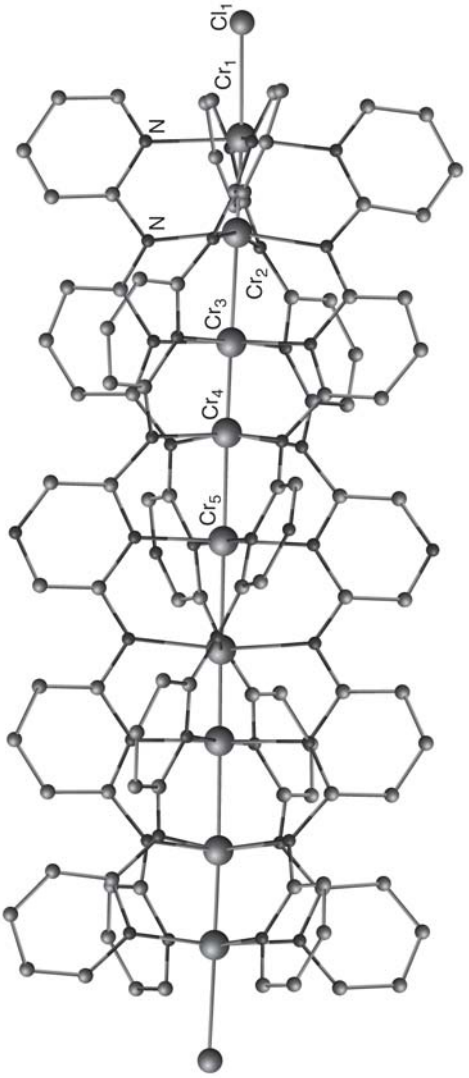

FIGURE 3

$$3\ CoCl_2 + 4\ Lidpa \longrightarrow Co_3(dpa)_4Cl_2 + 4\ LiCl$$

SCHEME 10

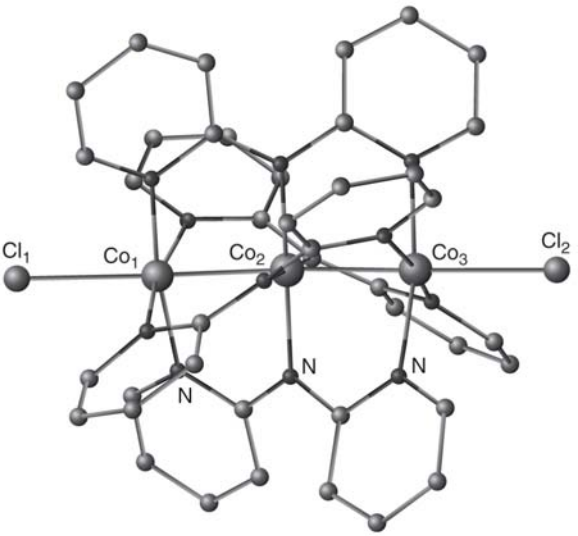

FIGURE 4

equivalences of the Co-Co distances, though the compound remains symmetrical within experimental error [Co-Co distances of 2.3224(8) and 2.3214(8) Å at 109 K].

The *u*-$Co_3(dpa)_4Cl_2.2CH_2Cl_2$ crystallizes in the tetragonal $I\bar{4}$ space group. At room temperature, the Co-Co distances are 2.290(3) and 2.472(3) Å; however, they become more symmetrical as the temperature is lowered, reaching 2.3035(7) Å and 2.3847(8) Å. The *u*-$Co_3(dpa)_4Cl_2$ trimer could be described as a diamagnetic dimer Cl-$Co^{II}N_4$-$Co^{II}N_4$ chromophore and a spin crossover $Co^{II}N_4$-Cl chromophore. The dimer chromophore exhibits a short Co^{II}-Co^{II} distance [2.290(3) Å] and a long Co-Cl bond [2.432(4) Å] and short Co-N bonds [1.96, 1.90 Å], consistent with full pairing of the electrons in a $\sigma^2\pi^4\delta^2\delta^{*2}\pi^{*4}$ molecular orbital. In the spin crossover square-pyramidal $Co^{II}N_4Cl$ chromophore, the mean Co-N distance, 2.121 Å, and the Co-Cl distance, 2.361(4) Å, are consistent with those normally found in a square-based pyramidal Co^{II} compounds. The Co $\cdots$ Co distance between the Co-Co dimer and the third Co atom is 2.472(3) Å.

A powder diffraction pattern from a typical preparation of $Co_3(dpa)_4Cl_2$ shows that both tetragonal and orthorhombic forms are present, with the former making up 10–20%. Both forms when dissolved in CH_2Cl_2 give the same

^{1}H NMR spectrum. The two forms of the molecule, being energetically similar, crystallize out simultaneously from CH_2Cl_2 solution.[25]

The magnetic moment of $Co_3(dpa)_4Cl_2$ was measured in CH_2Cl_2 solution by the Evans method in the temperature range 193–308 K.[26] The μ_{eff} changes from 2.78 to 4.48 μ_B as temperature increases. The increase in magnetic moments with increase in temperature is attributed to the spin transition. Calculations show that the three Co^{II} atoms contribute a total of 21 electrons, which occupy 12 MOs; 16 electrons occupy the bonding and nonbonding orbitals, and five electrons occupy antibonding orbitals, so that two such orbitals are doubly occupied and one electron is left unpaired in an antibonding orbital, as shown in Scheme **11**. The SOMO is the σ_{nb}, which has Co-Co nonbonding character and Co-C1 antibonding character.

The ground state for three linearly and symmetrically distributed Co^{2+} ions is doublet (S = 1/2), which is supported by a frozen-glass EPR measurement. As temperature increases, the lowest quartet state is attained by the promotion of a nonbonding or a weakly antibonding electron to the remaining unoccupied orbital, the bonding is weakened and the bond order drops to 0.5. However, the measured magnetic moment of 4.48 μ_B at 308 K is larger than the spin-only value for an S = 3/2 state but smaller than that for a high-spin S = 5/2 state. It indicates that the thermally populated high-spin state could possibly be either 3/2 or 5/2.

More basic ligands such as Hdepa (di(4-ethyl-2-pyridyl)amide) has been used to make Co_3 chains.[27] The line drawing of the ligand is shown in Scheme **12**.

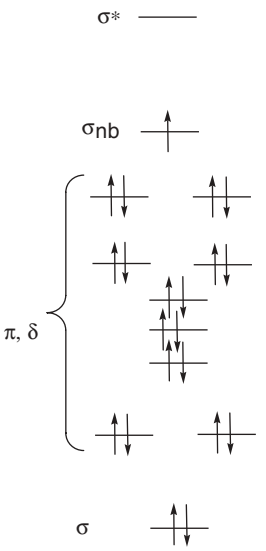

SCHEME 11

Introduction of eight ethyl groups into the tricobalt entity improves solubility and makes oxidation easier. The plot of magnetic susceptibility of $Co_3(depa)_4Cl_2$ as a function of temperature clearly indicates complete spin-crossover process and that the upper state is S = 3/2. However, $Co_3(depa)_4(CN)_2$ exhibits different magnetic susceptibility data. The S = 3/2 state for $Co_3(depa)_4Cl_2$ is 90% occupied at 350 K, whereas $Co_3(depa)_4(CN)_2$ is only 29% populated at room temperature. The spin crossover process involves removing an electron from a filled orbital of lower energy (π^*) and placing it in the σ^*orbital, resulting in observed quartet state. A larger energy gap between the filled orbitals and the σ^* orbitals would disfavor spin crossover. Thus as the σ^* orbital moves higher in energy with increasing axial donor strength (e.g., CN^-), the spin crossover becomes less favorable.

The reaction of $Co_3(dpa)_4Cl_2$ with $NOBF_4$ yields the one-electron oxidized form $[Co_3(dpa)_4Cl_2][BF_4]$ (Scheme **13**).[28] The crystal structure of $[Co_3(dpa)_4Cl_2][BF_4]$ shows that the Co-Co-Co unit is linear and essentially symmetrical. Two independent Co-Co distances are 2.3168 (8) and 2.3289 (8) Å. The terminal Co-Cl and Co-N distances are shorter as compared to the neutral species. The factor contributing to a decrease in metal-ligand distances is the removal of one electron from the antibonding orbital of the neutral molecule.

Cyclic voltammogram of $Co_3(dpa)_4Cl_2$ displays two reversible one-electron waves at $E_{1/2}$ $(ox)_1$ = +0.32 V, $E_{1/2}$ $(ox)_2$ = +1.24 V. However, chemical oxidation with $NOBF_4$ in CH_2Cl_2 solution resulted the singly oxidized species $[Co_3(dpa)_4Cl_2][BF_4]$. Electronic absorption spectra for parent and singly oxidized species are clearly different. The singly oxidized species $[Co_3(dpa)_4Cl_2][BF_4]$ is EPR silent at low temperature (4.2 K). An investigation of magnetic properties of the oxidized species in solution by NMR spectroscopy and in solid state by magnetic susceptibility measurements revealed spin crossover behavior that occurs in two gradual steps. The plot of effective magnetic moment (μ_{eff}) vs. temperature (T) for $[Co_3(dpa)_4Cl_2][BF_4]$ in a solid

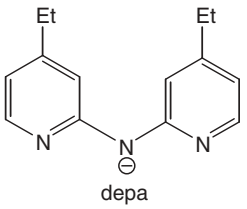

SCHEME 12

$$Co_3(dpa)_4Cl_2 + NOBF_4 \longrightarrow [Co_3(dpa)_4Cl_2][BF_4] + NO(g)$$

SCHEME 13

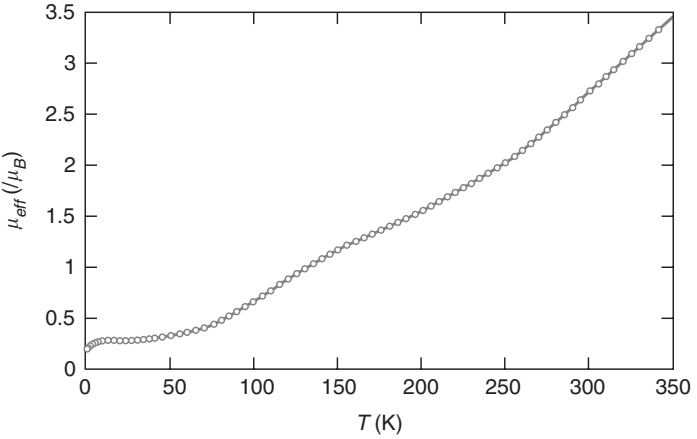

FIGURE 5

state is shown in Figure **5** (Reprinted with permission from J. Am. Chem. Soc. 2000, 122(10), 2272). Between 1.8 K and 50 K, the compound is essentially diamagnetic. The gradual nature of the curve, which is devoid of an intermediate plateau, implies a noncooperative spin crossover. This is confirmed by the lack of thermal hysteresis. The effective moment gradually increases reaching a value of 3.45 μ_B at 350 K. The absence of saturation is the evidence for an incomplete spin-crossover. A similar trend is observed in solution, though the characteristic temperature is lower compared to that of the solid state.

Electronic structure calculations suggest that the neutral molecule $Co_3(dpa)_4Cl_2$ possess a $b_2^2e^4a_2^1$ ground state.[29] The unpaired electron occupies the a_2 orbital, which is of metal nonbonding and metal-chloride antibonding character. One-electron oxidation leads to diamagnetic $b_2^2e^4$ ground state. The small energy difference between the a_2 (LUMO) and e (HOMO) orbitals leads to a thermally accessible low-lying excited state, leading to S = 1 excited state. At higher temperature, the higher lying orbitals (metal-centered antibonding orbital a_1, the ligand antibonding orbitals, or a combination of both) can be populated to give an S = 2 species (Scheme **14**).

The reaction of $Co_3(dpa)_4Cl_2$ with $AgPF_6$ in acetonitrile solution yields $[Co_3(dpa)_4(CH_3CN)_2][PF_6]_2$ in which the axially coordinated halide atoms are replaced by acetonitrile molecules, charge being compensated by PF_6^- anions (Scheme **15**).[30] The compound crystallizes from the same solution as two different solvates—namely, a chiral $P2_1$ form, $[Co_3(dpa)_4(CH_3CN)_2][PF_6]_2.CH_3CN.2Et_2O$, and a centrosymmetric $P\bar{1}$ form, $[Co_3(dpa)_4(CH_3CN)_2][PF_6]_2.3CH_3CN$. Chiral crystals in the monoclinic form were isolated in either Λ or $\triangle$ configuration, and their absolute structures were determined by X-ray crystallography. Crystals with different absolute configurations exhibit circular dichroism spectra of essentially

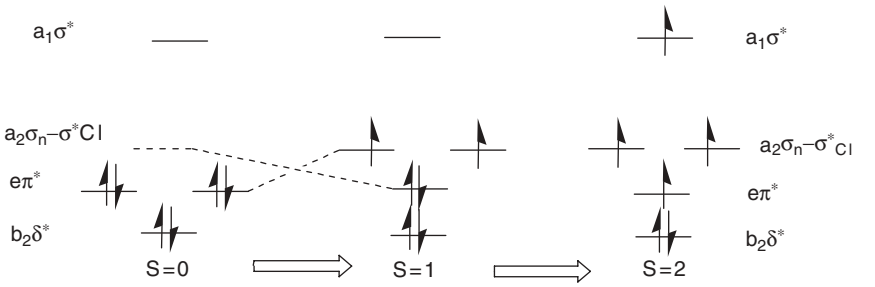

SCHEME 14

$$Co_3(dpa)_4Cl_2 + 2\ AgPF_6 + 2CH_3CN = [Co_3(dpa)_4(CH_3CN)_2][PF_6]_2 + 2\ AgCl$$

SCHEME 15

same intensity but opposite signs that indicate that the two enantiomers do not interconvert in solution. In the centrosymmetric $P\bar{1}$ form, the compound was found as a racemate, with an equal amount of Λ and Δ isomers.

$Co_3(dpa)_4X_2$ (X = NCS^-, CN^-, $(N(CN)_2)^-$) were synthesized from $Co_3(dpa)_4(BF_4)_2$.[31] The compound $Co_3(dpa)_4(NCS)_2$ was obtained in three solvated crystalline forms, $Co_3(dpa)_4(NCS)_2$. $1.5CH_2Cl_2$, $Co_3(dpa)_4(NCS)_2$. 5THF, and $Co_3(dpa)_4(NCS)_2$. 2toluene. In all three structures, the Co_3 chain is symmetrical—that is, either two Co-Co distances are identical by crystallographic symmetry, or they are almost identical even though there is no crystallographic constraint. The molecule $Co_3(dpa)_4(CN)_2$ and $Co_3(dpa)_4(NCNCN)_2$ are also symmetrical. Thus it appears that only the $Co_3(dpa)_4(X)_2$ compounds with X = Cl and Br[32] have a tendency to display unsymmetrical Co_3 chains. The magnetic behavior for all three compounds is quite similar, the effective magnetic moment increases gradually from 1.8 to 400 K without reaching saturation, indicating a spin-crossover process observed in analogous compounds.

Synthesis, structural characterization, and magnetic studies of $[Co_2Pd(dpa)_4Cl_2]$ have been reported.[33] The electronic ground state of the mixed-metal compound is different from the tricobalt homologue. The accommodation of additional electrons provided by the central Pd^{II} offsets the advantage of a delocalized bond along the metal chain. It is of interest that the inclusion of a hetero atom tunes the magnetic and conducting properties of the metal chain.

Penta-cobalt chain was stabilized using tpda ligand (Scheme **6**).[34] The synthesis of the ligand and the pentanuclear cobalt complexes, including both neutral and one-electron oxidation products, is outlined in Scheme **16.**

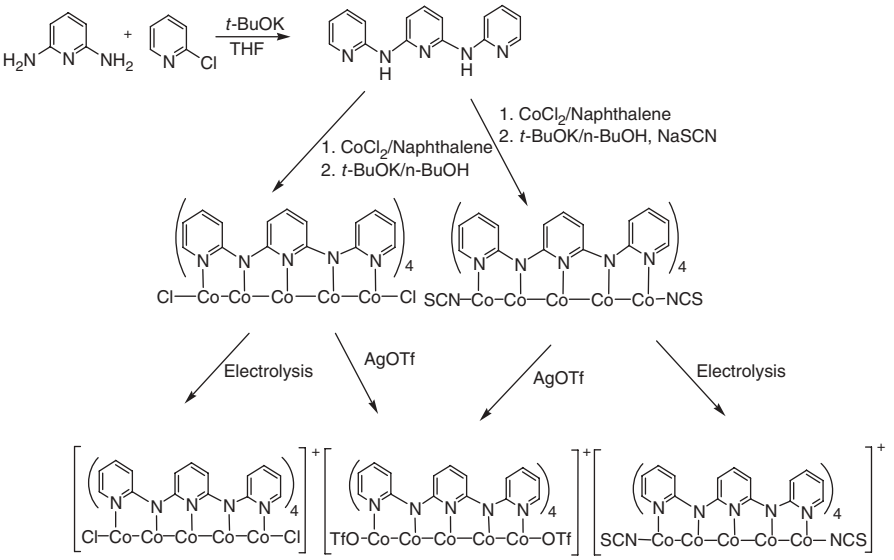

SCHEME 16

In all cases, the pentacobalt chain is helically wrapped by four tpda ligands and is linear and symmetrical. Two types of Co-Co bond distances are observed. The average internal Co-Co bond lengths fall into the range 2.22–2.24 Å, whereas external bonds range from 2.27 to 2.29 Å. All of the Co-N distances lie in the range 1.90–1.96 Å. The identity of the axial ligands influence the Co-Co and Co-N bond distances; the weaker axial ligands result in shorter Co-Co and Co-N bond distances as compared to complexes with strong axial ligands.

Compounds $Co_5(tpda)_5X_2$ show two reversible redox couples at about + 0.35 and + 0.85 V (vs. Ag/AgCl). The first oxidation is metal centered, and the product has been structurally characterized. The second oxidation product is stable on the timescale of spectroelectrochemistry but undergoes reduction to form the corresponding one electron oxidation product under crystallization conditions.

One electron oxidation products were obtained either by reacting the neutral complexes with silver salts or by bulk electrolysis at + 0.55 V, a value that is more positive than the formal potential for the first oxidation. Molecular structures of one-electron oxidized compounds are similar to those of the neutral analogs, except for the presence of a counteranion to compensate the positive charge on the Co_5 core. The average Co-Cl bond distance in one electron oxidized species is 0.15 Å shorter than that for the neutral analog. This is due to the removal of one electron from the singly occupied HOMO, which has Co-Co nonbonding and Co-Cl antibonding characters as suggested by theoretical calculations. However, the decrease is not significant because the electron is

removed from the nonbonding δ orbital to form a paramagnetic complex with S = 1. This phenomenon is supported by magnetic measurement studies. Unlike $[Co_3(dpa)_4Cl_2]$, the Co_5 chains do not undergo spin crossover at temperatures <300 K. The effective magnetic moment indicates that the singly oxidized complex is paramagnetic and that there are two unpaired electrons in the molecule (S = 1), in which both the nonbonding σ and nonbonding δ orbitals are singly occupied. The broadened peaks and large chemical shifts for the ^1H NMR resonance signal for both the neutral and one-electron oxidized Co_5 complexes are consistent with their paramagnetism.

Naphthyridine-based ligands H_2bpyany (2,7-bis (α- pyridylamino)-1,8-naphthyridine) has been employed in the synthesis of linear metal chain compounds. The line drawing of bpyany ligand is shown in Scheme **17** and the diagram of the cationic unit of the hexa-cobalt product $[Co_6(\mu_6\text{-bpyany})_4(NCS)_2](PF_6)$ is shown in Figure **6**.[35] One-electron oxidation with $[Cp_2Fe](PF_6)$ in a mixture of CH_2Cl_2 and MeOH leads to the formation of $[Co_6(\mu_6\text{-bpyany})_4(NCS)_2](PF_6)_2$. Axial ligands were exchanged with triflates to

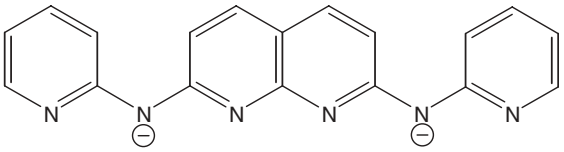

SCHEME 17 Bpyany.

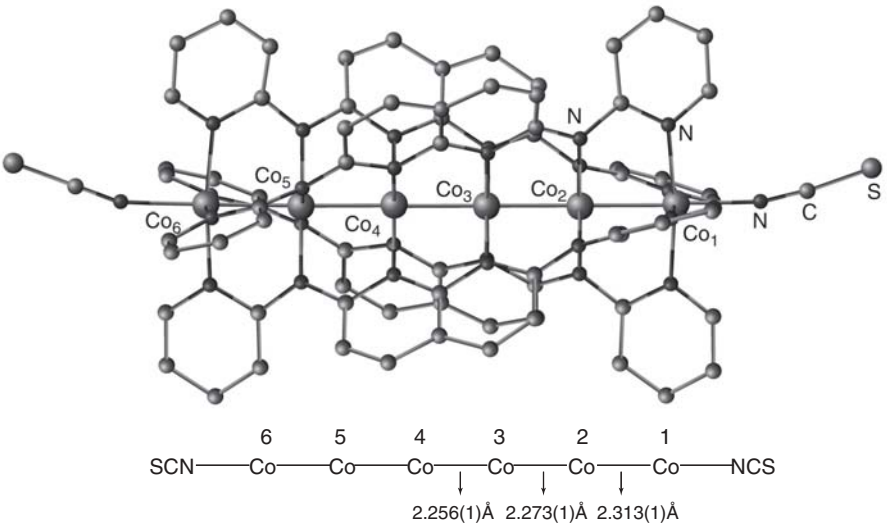

FIGURE 6

form $[Co_6(\mu_6\text{-bpyany})_4(OTf)_2](OTf)_2$, which was subsequently reduced with hydrazine to form $[Co_6(\mu_6\text{-bpyany})_4(OTf)_2](OTf)$. Crystal structures of these compounds are similar and all have roughly D_4 symmetry without considering axial ligands. The outer Co-Co distances are slightly longer than the inner three Co-Co distances due to square pyramidal environment for Co(1) and Co(6) (Figure **6**).

The use of pyrazine modulated oligo-α-pyridylamine resulted in linear heptanuclear cobalt compounds.[36] The ligands employed are shown in Scheme **18.** In $Co_7(pzpz)_4Cl_2$, the seven Co^{II} ions are collinear with Co-Co-Co angles in the range 177.4–179.9°. The heptacobalt chain is helically wrapped by four deprotonated ligands, all *syn*-coordinated. The Co-Co distances in Co_7 follow the order: $(Co\text{-}Co)_{terminal} > (Co\text{-}Co)_{intermediate} > (Co\text{-}Co)_{innermost}$, as illustrated in Figure **7**.

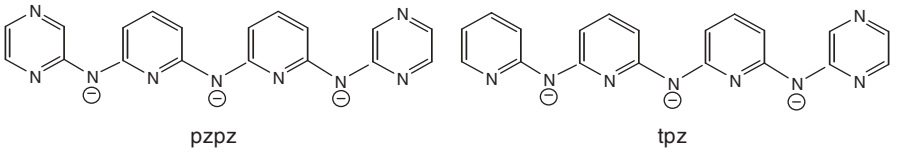

SCHEME 18

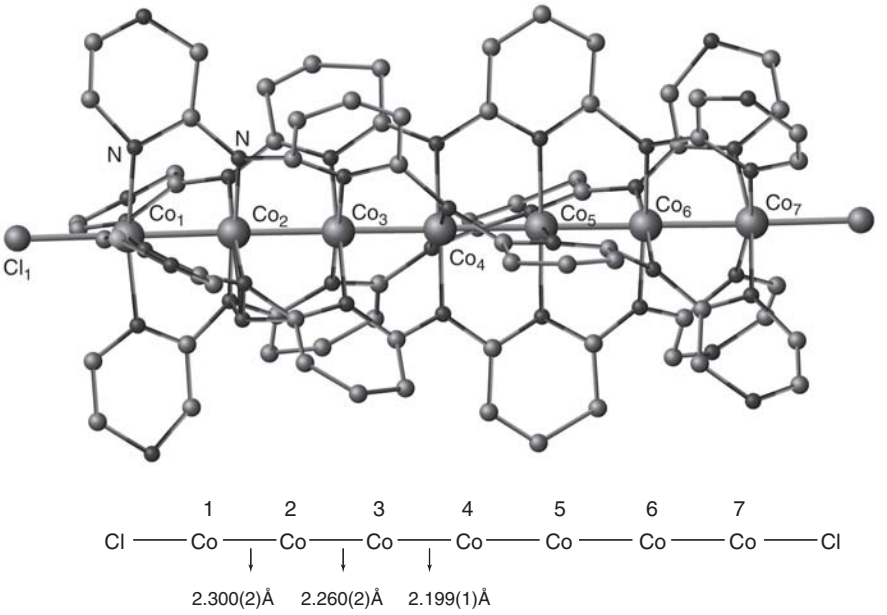

FIGURE 7

Magnetic measurements revealed anomalous magnetic behavior with intermediate magnetic moment values between quartet and doublet states. From MO theory, the larger a molecule is and more metal atoms it contains and the lower the energy gap between the HOMO and LUMO. Consequently, the higher spin state is more accessible. The Co_7 chain has spin admixed state from S = 1/2 to S = 7/2.

It is interesting that the μ_{eff} values of complexes incorporating two-pyrazine-based (pzpz) ligands are much lower than those of one-prazine-based ligands (tpz). This suggests that the electron configuration of linear metal chain is adjusted by the ligands. The equitorial and axial ligands dictate the energy gap between HOMO and LUMO and thus play an important role in determining the electronic structures.

C. Linear Chains of Copper

The trinuclear copper compound $Cu_3(dpa)_4Cl_2$ (dpa = di(2-pyridyl)amido) has been synthesized following the equation, as shown in Scheme **19**. The structure of $[Cu_3(dpa)_4Cl_2]$ (Figure **8**) shows three linear Cu^{II} ions and two chlorides.[37] The molecule has a crystallographic twofold symmetry. The Cu · · · Cu distance is

$$4\ \text{Lidpa} + 3\ CuCl_2 \longrightarrow Cu_3(dpa)_4Cl_2 + 4\ LiCl$$

SCHEME 19

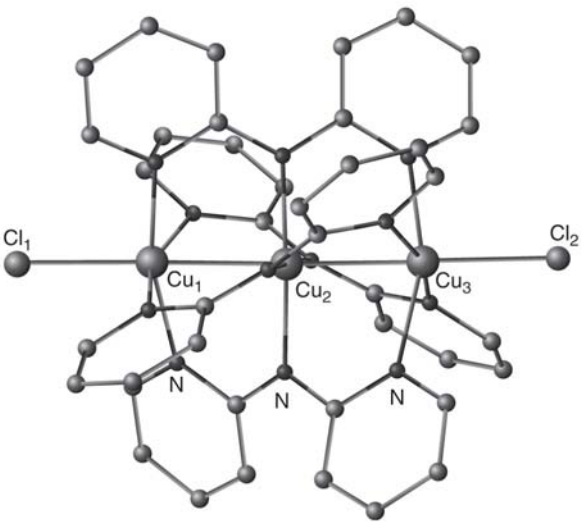

FIGURE 8

2.4712(4) Å. Magnetic studies of this complex reveals a ground state of S = 1/2, which is separated by 560 cm^{-1} from a higher quartet state. A localized picture, in which three nonbonded Cu^{II} ions are spin coupled to give a doublet or a quartet state, has been proposed to explain the magnetism.[38]

Oxidation of $Cu_3(dpa)_4Cl_2$ involves removal of electrons from the highest energy orbital, which displays a major contribution on the central copper and its equitorial coordinating nitrogens. The oxidized $[Cu_3(dpa)_4Cl_2][SbCl_6]$ has Cu · · · Cu separations of 2.51 to 2.52 Å.[16b] The modest increase of 0.05 Å in the Cu · · · Cu distances upon oxidation is the result of increased electrostatic repulsion between the more positively charged Cu atoms than in the neutral species. The central Cu atom with shorter Cu-N distances (1.89 Å, as compared to the outer Cu-N distances of 2.06 Å) is due to oxidized Cu^{III}. This is consistent with the localized picture, the central square planar Cu atom is the one oxidized to a d^8 Cu^{III} species and the outer Cu-N_4 moieties are antiferromagnetically coupled.

Linear Cu_3 chain compounds $[Cu_3(pdf)_4](CF_3SO_3)_2$, $[Cu_3(pmf)_4](CF_3SO_3)_2$, and $[Cu_3(mpdf)_4](CF_3SO_3)_2$ have been synthesized. The line drawing of the ligands are shown in Scheme **20**. X-ray structure of the cationic unit of $[Cu_3(pdf)_4](CF_3SO_3)_2$ is given in Figure **9**. Three Cu^{II} ions are surrounded by four ligand molecules in a propeller mode, each of which being tetracoordinating to the three Cu^{II} atoms.[39] The central Cu atom is distorted square planar and the outer Cu atoms are six coordinated with distorted square-based geometry. The Cu · · · Cu distances are in the range of 2.67 Å. Magnetic measurements reveal strong antiferromagnetic interaction between Cu^{II} ions with S = 1/2 ground state below temperature of 120 K.

A linear trimeric Cu^{I} complex incorporating tspa (tspa = *N, N*′-bis-(*p*-tolylsulphonyl)-pyridine-2,6-diaminato) ligands has been reported (Scheme **21**).[40] The structure of consists of a triethylammonium cation and the tri-copper(I) complex anion. The structure of the anion is shown in Figure **10**. The Cu · · · Cu distances are 2.466(1) and 2.468(1) Å. Reaction of $[Cu^{I}(CH_3CN)_4][ClO_4]$ with 7-diphenyl phosphino-2,4-dimethyl-1,8-naphthyridine (dpnapy) (Scheme **22**) in CH_3CN afforded $[Cu_3(\mu\text{-dpnapy})_3(CH_3CN)][ClO_4]_3$.[41]

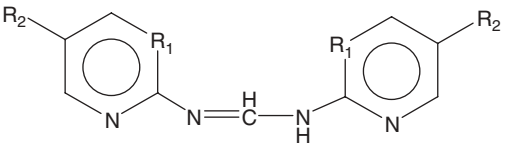

N,N′-bis(pyridine-2-yl)formamidine (Hpdf) R_1 = CH, R_2 = H
N,N′-bis(pyrimidine-2-yl)formamidine (Hpmf) R_1 = N, R_2 = H
N,N′-bis(5-methylpyridine-2-yl)formamidine (Hmpdf) R_1 = CH, R_2 = CH_3

SCHEME 20

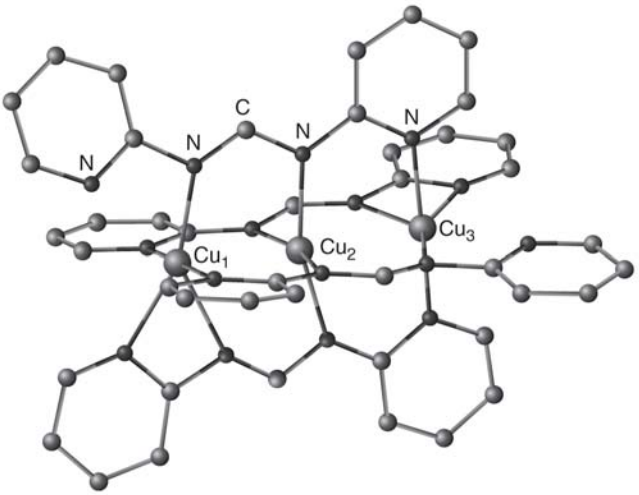

FIGURE 9

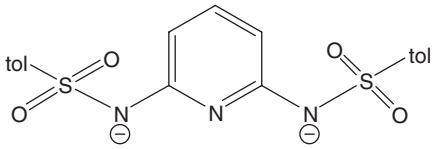

SCHEME 21

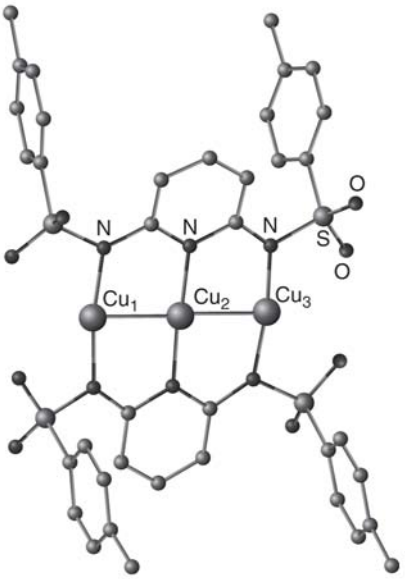

FIGURE 10

The crystal structure reveals a linear Cu···Cu···Cu array with both trigonal and tetrahedral coordination modes for the Cu atoms. The tetrahedral geometry is due to acetonitrile coordination. The intramolecular Cu···Cu distances are 2.449(2) and 2.721(2) Å. Besides bridging ligands, attractive $Cu^{I}\cdots Cu^{I}$ interactions are predicted to be the driving force for the formation of linear tricopper array.

$[Cu_3(dPhIP)_2](CuCl_2)_2$ [dPhIP = anion of 2,6-diphenyliminopiperidine] was obtained by reacting CuCl with Li(dPhIP) in 2:1 ratio (Scheme **23**).[42] X-ray structure shows that the central Cu atom is linearly coordinated by two pyridyl nitrogens, while terminal Cu atoms are 3-coordinated with bonds to two N atoms from two dPhIP ligands and a Cl atom from the nearest $[CuCl_2^-]$ unit, as shown in Figure **11**. Each cation has weak interactions with two adjacent $CuCl_2$ anions, and each anion interacts with two neighboring $[Cu_3(dPhIP)_2]^+$ cations, forming an infinite zigzag chain of Cu^{I} atoms.

A tetranuclear mixed-valence copper chain $[Cu^{I}Cu^{II}_2Cu^{I}(dPhIP)_4][CuCl_2]$ was isolated from the reaction of $CuCl_2$, CuCl and Li(dPhIP) in 1:2:2 ratio (Scheme **24**). The $[Cu_4(dPhIP)_4]^{2+}$ cation consists of two inner divalent Cu atoms with square planar coordination environments, and two terminal Cu atoms are monovalent with a typical linear ligand arrangement. In spite of the diamagnetic nature of the compound, molecular orbital calculations indicate that no direct Cu···Cu bonds are present; instead the bridging ligands affect a strong coupling of the spins (Figure **12**).

D. Linear Chains of Nickel

The earliest known polypyridylamido complex, $Ni_3(dpa)_4Cl_2$ was synthesized in 1968 by high-temperature reaction of $NiCl_2(Hdpa)_2$ with ^{n}BuOK in molten naphthalene. An interesting structure, as shown in Scheme **25**, was proposed based on spectroscopic and magnetic measurements.[43]

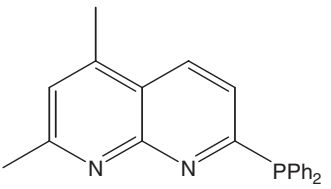

SCHEME 22

$$4CuCl + 2\ Li(dPhIP) \longrightarrow [Cu_3(dPhIP)_2](CuCl_2) + 2\ LiCl$$

SCHEME 23

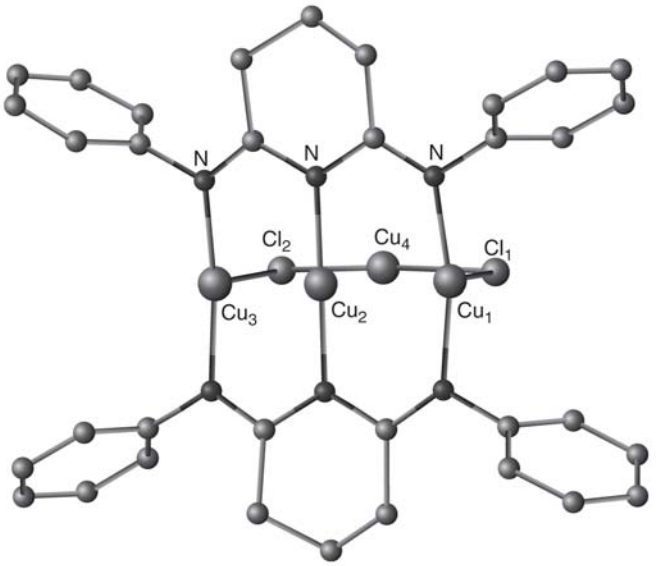

FIGURE 11

$$2\ CuCl_2 + 4\ CuCl + 4\ Li(dPhIP) \longrightarrow [Cu_4(dPhIP)_4](CuCl_2)_2 + 4\ LiCl$$

SCHEME 24

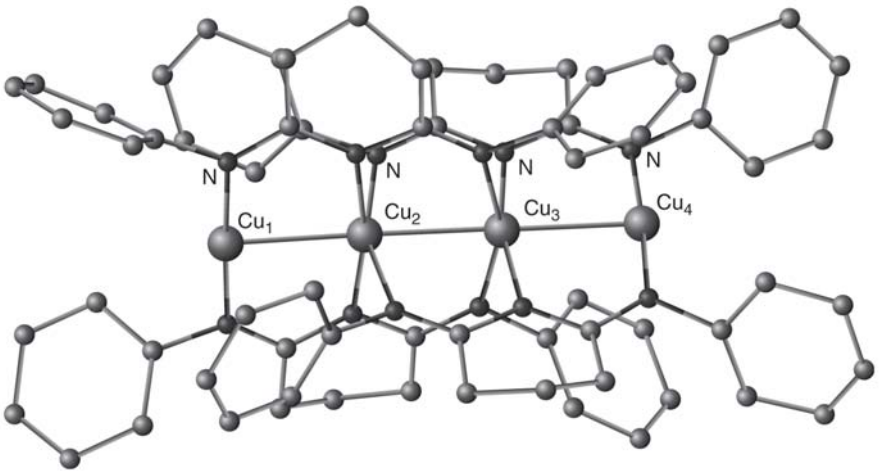

FIGURE 12

About 20 years later, X-ray crystallographic study showed that the compound possesses a linear structure.[44] The structure is very similar to analogous Co, Cr, and Cu compounds consisting of a nearly linear Ni_3 unit, with a Ni · · · Ni distance of ~2.44 Å. The central Ni atom is coordinated to four amido-nitrogens of the ligands and the two terminal Ni atoms involve a square-pyramidal (NiN_4Cl) geometry involving four pyridine nitrogen atoms of the ligands and an axial Cl atom (Figure **13**). The compound $Ni_3(dpa)_4Cl_2$ crystallizes out in two forms: $Ni_3(dpa)_4Cl_2.2CH_2Cl_2$ and $Ni_3(dpa)_4Cl_2.THF$.[45] In both the forms, a symmetric chain of nickel atoms is observed. Replacement of axial chlorides in $Ni_3(dpa)_4Cl_2$ by cyanides and acetylides have been accomplished resulting $Ni_3(dpa)_4(CN)_2$ and $Ni_3(dpa)_4(CCPh)_2$.[46]

In a typical $Ni_3(dpa)_4X_2$ complex, each terminal Ni atom has two unpaired electrons, while the central one is typical of diamagnetic square-planar Ni^{II}. Magnetic properties reveal antiferromagnetic coupling between

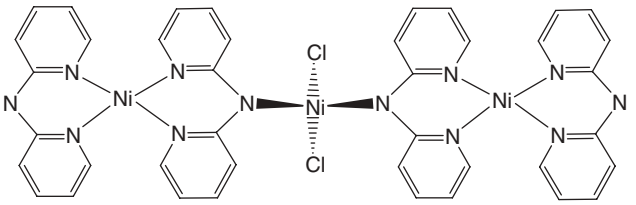

SCHEME 25

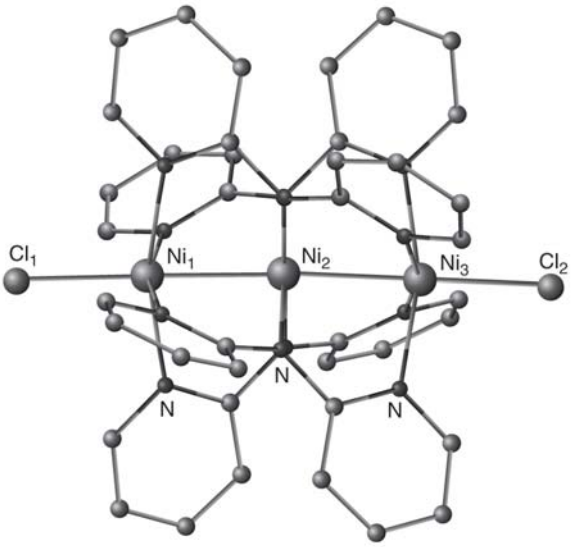

FIGURE 13

terminal Ni^{II} ions. A possible pathway for the intramolecular exchange coupling involves the central Ni atom.[47] The d_z^2 orbital of the central Ni atom contains an electron pair that is polarized by interactions with unpaired spins in the d_z^2 orbitals of the terminal Ni atoms (Scheme **26**). This spin polarization leads to antiferromagnetic coupling of the electrons in d_{z^2} orbitals. The other unpaired electrons on the $d_{x^2-y^2}$ orbitals of each Ni atom couple in similar manner.[46] A series of linear trinickel complexes supported by two kinds of ligands have been synthesized. Structures of mixed-ligand compounds, including the combinations 2:2 dpa and Lpts (Lpts = *N,N′*-bis(*p*-toluenesulfonyl)pyridyldiamido); 2:2 dpa and Lms (Lms = *N,N′*-bis(4-methylsulfonyl)-pyridyldiamido); 2:1 Lpts and peptea (peptea = pentapyridyldiamidodiamine); and 2:2 dpa and LAc (LAc = *N, N′*- biacetyl-pyridyldiamido[48] are shown in Scheme **27**.

Magnetic studies and DFT calculations indicate that the relative basicities of the donor atoms of the equatorial ligands are sufficient to influence the ground state of the metal framework.[49] Further, in the absence of axial coordination, a chain of Ni^{II}atoms simply consists of stacked square, diamagnetic NiN_4 units.

Oxidation of $Ni_3(dpa)_4Cl_2$ with 3 equivalents of $AgPF_6$ resulted $Ni_3(dpa)_4(PF_6)_3$ in high yield.[50] X-ray structure determination shows that two PF_6^- anions occupy axial positions having weak Ni · · · F interactions. The Ni · · · Ni distance is remarkably short 2.283 (1) Å compared to 2.44 Å in the parent compound. It clearly indicates the formation of a partial Ni-Ni bond. This result is in contrast to what was observed for Cu. The lengthening in Cu · · · Cu distances from $[Cu_3(dpa)_4Cl_2]^{2+}$ (2.47 Å) to $[Cu_3(dpa)_4Cl_2]^{3+}$ (2.51 Å) has been rationalized by the assumption that, upon oxidation, an electron is removed formally from the central Cu atom with the formation of d^8 Cu^{III} square planar species. The terminal Cu^{II} ions are electrostatically repelled by the central Cu^{III}, resulting in longer Cu · · · Cu distances. In the case of Ni_3, significant metal-metal attraction is present in the oxidized species, which is consistent with a 3-center Ni-Ni bonding.[16b]

Linear trinickel chain compounds $Ni_3(PhPyF)_4Cl_2$[51] and $Ni_3(dpza)_4Cl_2$[52] have been reported having structures similar to the dpa analog. The line drawings of the ligands are shown in Scheme **28**. A long polydentate ligand H_4peptea (pentapyridyltetraamine) reacts with $NiCl_2$ to form a protective

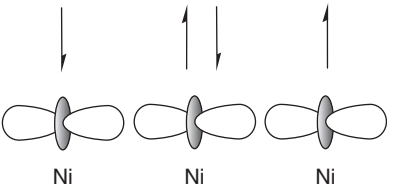

SCHEME 26

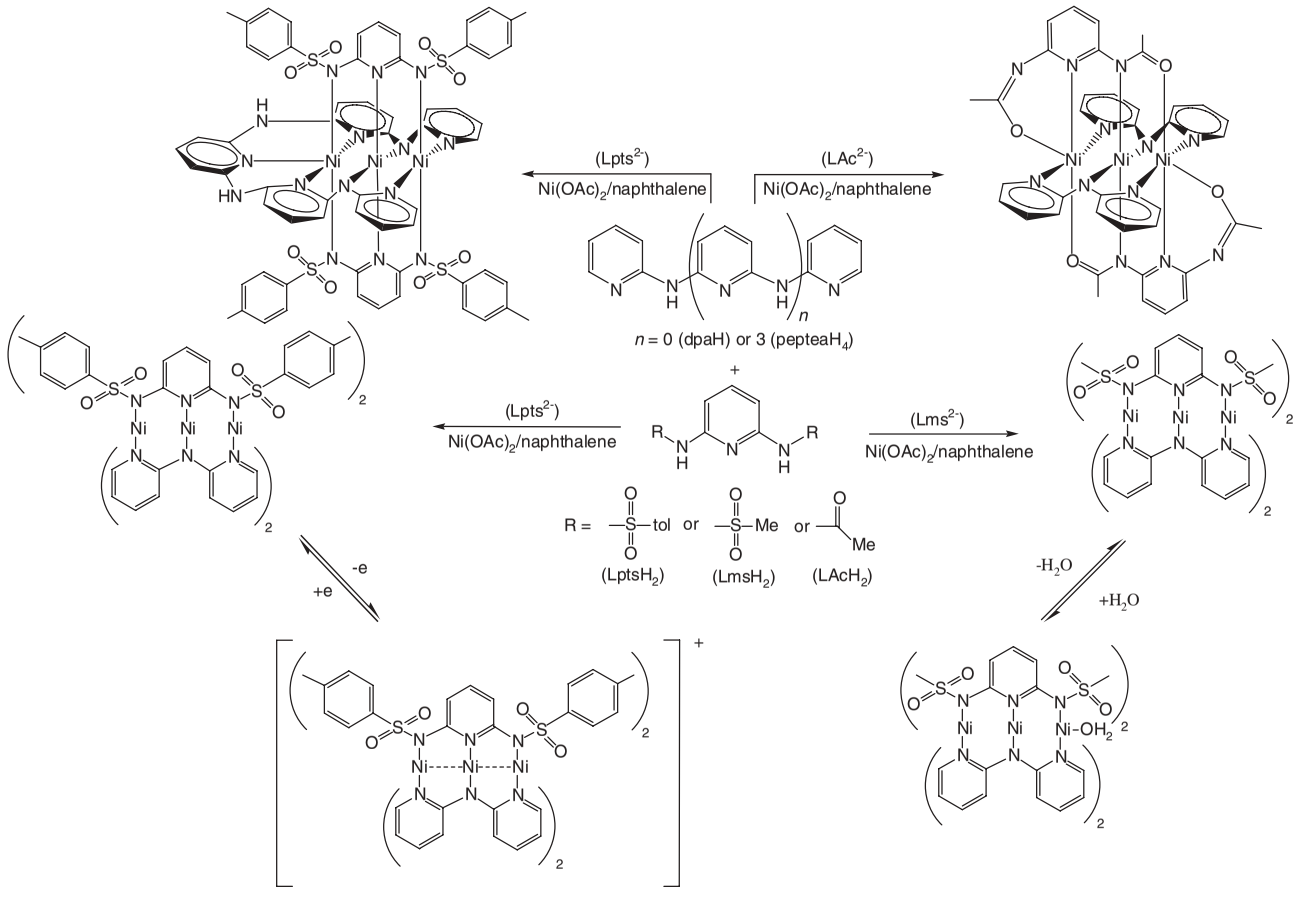
(Lpts2-)
Ni(OAc)2/naphthalene
(LAc2-)
Ni(OAc)2/naphthalene
n = 0 (dpaH) or 3 (pepteaH4)
(Lpts2-)
Ni(OAc)2/naphthalene
(Lms2-)
Ni(OAc)2/naphthalene
R = tol or Me or Me
(LptsH2)
(LmsH2)
(LAcH2)
-e
+e
-H2O
+H2O

SCHEME 27

cocoon around a Ni_3 chain in $Ni_3(H_2pepta)_2Cl_2$.[53] The large polydentate ligand runs up one side and down the other locking in donor atoms at the axial positions of the Ni_3 chain as shown in Scheme **29**.

An assortment of ligands has been employed to stabilize linear tetranuclear Ni chains. The isolated compounds are $[Ni_4(\mu_4\text{-phdpda})_4]$ (H_2phdpda = *N*-phenyldipyridyldiamine),[54] $[Ni_4(\mu_4\text{-Tsdpda})_4(H_2O)_2]$ (H_2Tsdpda = *N*-(*p*-toluenesulfonyl)dipyridyldiamine),[55] $[Ni_4(\mu_4\text{-DAniDANy})_4]$ (H_2DAniDANy = *N, N′*-bis-p-anisyl-2,7-diamino-1,8-naphthyridine) (Scheme **30**).

DFT calculations reveal that the spin state of nickel ions in the tetranuclear chain depends on the interplay between axial and equitorial

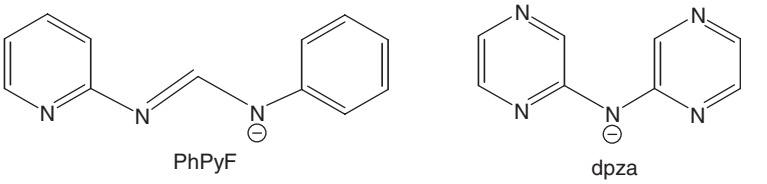

SCHEME 28

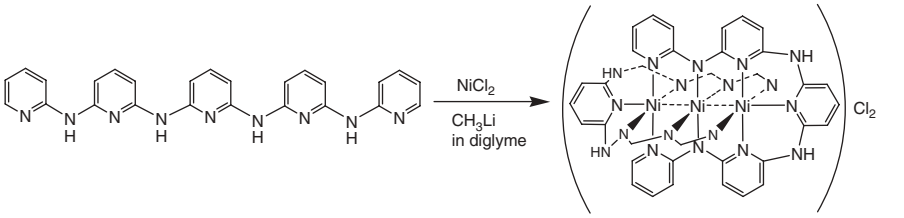

SCHEME 29

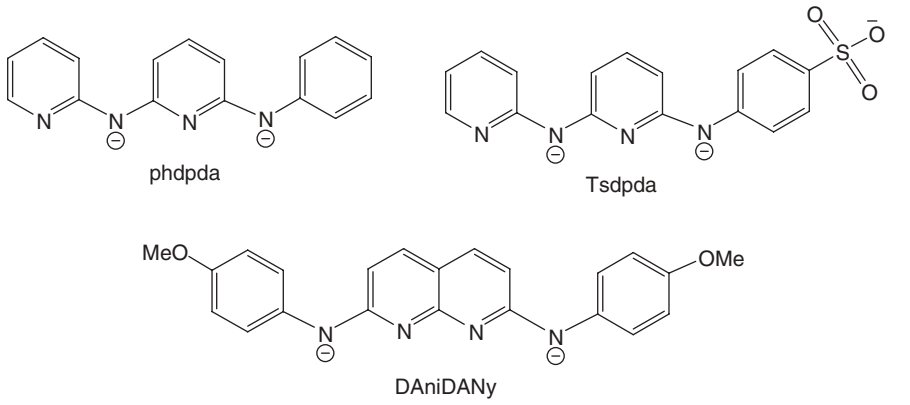

SCHEME 30

coordination. For $[Ni_4(\mu_4\text{-phdpda})_4]$ and $[Ni_4(\mu_4\text{-DAniDANy})_4]$ complexes lacking axial ligands, the inner Ni ions are high-spin, and the terminal Ni ions are diamagnetic. On the contrary, the $[Ni_4(\mu_4\text{-Tsdpda})_4(H_2O)_2]$ exhibits axial coordination and restores the antiferromagnetic coupling between terminal Ni atoms. The electron-withdrawing ability of the sulfonyl substituent possibly tunes the basicity of the terminal amido ligands and restores the antiferromagnetic coupling between terminal atoms.

A Ni_5 chain has been stabilized by employing tpda (Scheme **6**).[56] The ligands are in all-*syn* arrangements and five nickel atoms and two chlorides are collinear. Two unique Ni···Ni distances Ni1-Ni2 2.385(2) and Ni2-Ni3 2.306(2) Å are noted in the X-ray structure of $Ni_5(tpda)_4Cl_2$ (Scheme **31**).

The $[Ni_5(tpda)_4]^{2+}$ fragments for $[Ni_5(tpda)_4X_2]$ [X = Cl, CN, N_3, CH_3CN, NCS] are isostructural with a variation of terminal Ni···Ni distances 2.340–2.400 Å.[57] Molecular orbital calculations reveal that there are no net bondings between the metals. Magnetic susceptibility and *X*-ray near-edge absorption spectrum confirm the existence of two unpaired electrons located at each of the two terminal Ni^{II} ions and all inner Ni^{II} ions are diamagnetic with paired electrons. The terminal high-spin Ni atoms are strongly antiferromagnetically coupled.

The introduction of ethyl groups in tpda increases the solubility of the compounds and makes oxidation easier, likewise the Ni_3 chain.[58] Oxidation of $[Ni_5(etpda)_4Cl_2]$ (H_2etpda = *N, N*′-bis(4-ethylpyridyl)-2,6-diaminopyridine) (Scheme **32**) led to shorter Ni···Ni distances.[59] 2,7-Bis(α-pyridylamino)-1,

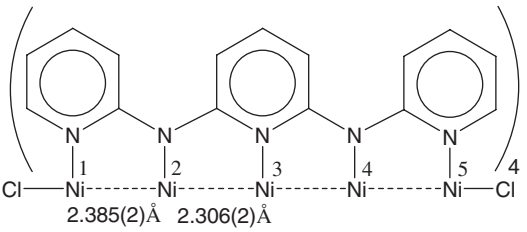

SCHEME 31

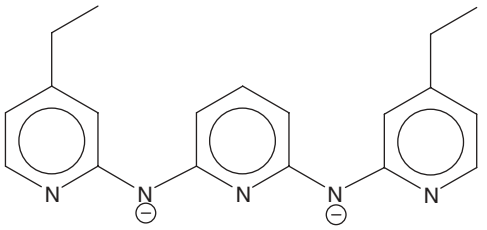

SCHEME 32

8-naphthyridine (H_2bpany) ligand has been used to synthesize hexanuclear Ni^{II} complexes (Scheme **33**).[60] The inclusion of a naphthyridine unit allows the reduction of these species. An analogous hexa-nickel string complex $[Ni_6(\mu_6\text{-bpmany})_4X_2][BF_4]_2$[61] (bpmany = 2, 7-bis(α-pyrimidylamino)-1,8-naphthyridine) (X = Cl, NCS) (Scheme **34**) has been synthesized. The structural details and magnetic behaviors are similar to that reported for $[Ni_6(\mu_6\text{-bpany})_4X_2][PF_6]_2$.

One electron reduction product $[Ni_6(\mu_6\text{-bpmany})_4X_2]^+$ was obtained by reaction of $[Ni_6(\mu_6\text{-bpmany})_4X_2][BF_4]_2$ with $N_2H_4.H_2O$ in CH_2Cl_2. According to the structural analysis of the reduced species, the one electron reduction occurs at central Ni(3)-Ni(4) unit. The Ni(3)-$N(3)_{av}$ bond shows a significant increase of 0.106 (13) Å from Ni_6^{12+} to Ni_6^{11+} compounds. Most likely, in the Ni_6^{11+} compounds the extra electron occupies a δ bond, mainly constructed from Ni(3) and Ni(4) $d_{x^2-y^2}$ orbitals. This δ bond also has M-L σ* antibonding character. This is consistent with the shortened Ni(3)-Ni(4) distance and the elongated Ni(3)-$N(3)_{av}$ distance. The Ni_6^{12+} complexes reveal weak antiferromagnetic coupling of $J = -5\ cm^{-1}$ between two terminal Ni^{II} ions, consistent with other multinickel complexes. The corresponding coupling values of about $-60\ cm^{-1}$ are measured for Ni_6^{11+} compounds.

Linear array of eight nickel atoms supported by four deprotonated tnda (tris naphthyridyldiamine) (Scheme **35**) has been reported.[62]

The $[Ni_8(tnda)_4X_2]^{3+}$ ion (X = Cl, NCS) and the corresponding oxidized ions $[Ni_8(tnda)_4X_2]^{4+}$ and $[Ni_8(tnda)_4X_2]^{5+}$ have been synthesized following Scheme **36**. The $[Ni_8]$ core exhibits interesting redox properties. In complex $[Ni_8(tnda)_4(NCS)_2]^{4+}$, the Ni2 and Ni7 are in +1 state, the inner Ni^{II} ions have low-spin character (S = 0), and the terminal Ni^{II} are in high-spin state (S = 1). In the reduced $[Ni_8(tnda)_4Cl_2]^{3+}$, the extra electron is delocalized between Ni4 and Ni5. One electron oxidation of $[Ni_8(tnda)_4Cl_2]^{3+}$ removes an electron from Ni4 and Ni5 ions, and the second oxidation occurs on either Ni2 or Ni7 with equal probability, resulting the Ni next to the terminal atom to have an average charge of +1.5.

Single-molecule conductance of linear metal strings $[M_nL_4(NCS)_2]$, (M_n = Co_3, Cr_3, Ni_3, Cr_5, Co_5, Ni_5 and Cr_7; L = oligo-α-pyridylamine), isolated within an *n*-alkylthiol matrix, were measured quantitatively by a scanning tunneling microscopy (STM) break junction method.[63,64] In a typical experiment, the isothiocyanate axial ligands at the termini of the metal string was placed between a gold STM tip and the gold electrode completing a molecular junction. At a fixed bias voltage across the electrodes, the STM tip is pulled away from the substrate, which results in current and conductance of the metal string complex to decrease in quantized steps.

Although metal chains have identical ligands, similar crystallographic structures, and physical dimensions, the resistance varies with the identity of the metal. For example, the resistance values of penta-chromium, penta-cobalt, and penta-nickel strings are 3.2 MΩ, 10.0 MΩ, and 24.0 MΩ, respectively. The discrepancy is linked to the extent of coupling of *d*-orbital electrons between

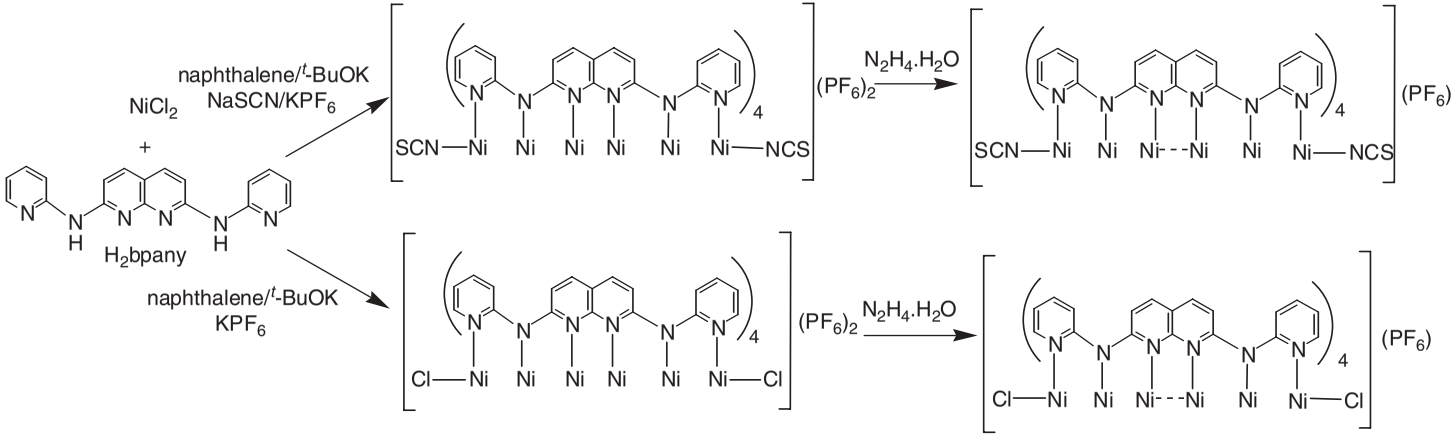
naphthalene/t-BuOK
NaSCN/KPF6
NiCl2
+
H2bpany
naphthalene/t-BuOK
KPF6
(PF6)2
N2H4.H2O
(PF6)
SCN—Ni
Cl—Ni
Ni—NCS
Ni—Cl
Ni--Ni
4

SCHEME 33

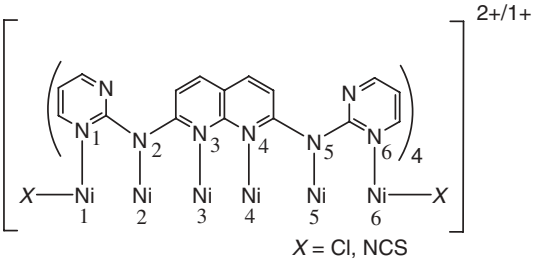

SCHEME 34

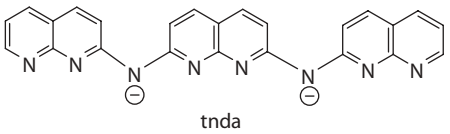

SCHEME 35

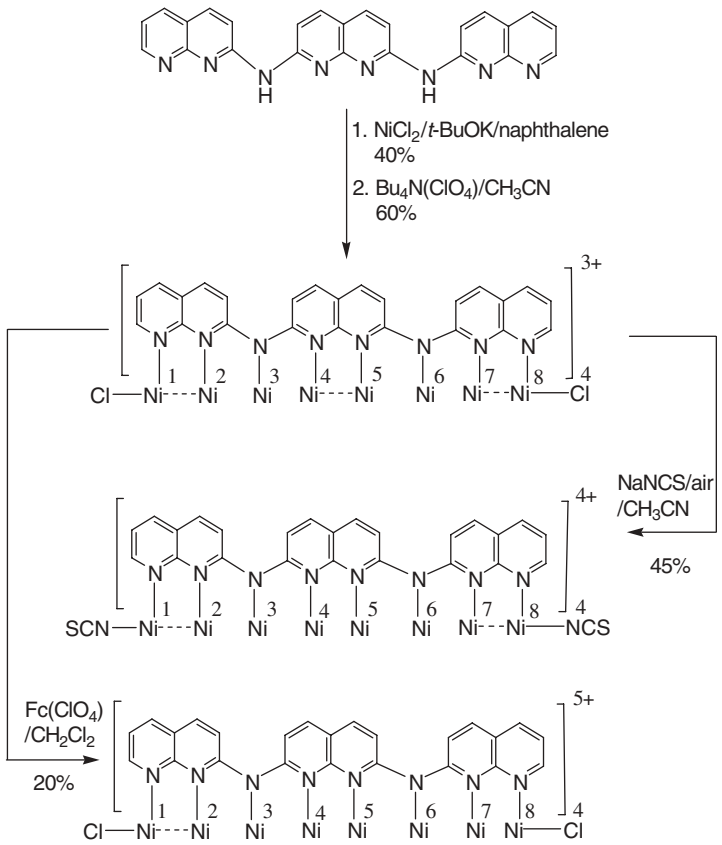

SCHEME 36

the adjacent metal atoms. Extended Hückel calculations for Ni_5, Co_5, and Cr_5 revealed the metal-metal bond orders 0.0, 0.5, and 1.5, respectively. Conductance in metal-string complexes correlates well with the metal-metal bond order. The stronger the degree of electron delocalization, the more the magnitude of electrons conducting through the metal chains increases. Further, electric on/off switching of each penta and hepta chromium strings was observed. This phenomenon is ascribed to conformations of delocalized (symmetric) and alternating (asymmetric) bond lengths.[65] Electrons in the asymmetric string are localized, thus resulting in a molecular conductance inferior to that of the delocalized conformation (Scheme **37**).

Continuous efforts are being made to extend the chain length further. Sophisticated tools of organic chemistry allow fabrication of ligands with repetitive pyridylamine units. However, the major challenge of progressively adding binding units to the ligand is the problem of eventual insolubility. The ligand extended up to 12 pyridylamine units has been made. Complexes up to nona-nickel (Ni_9) have been characterized crystallographically. Purification and crystallization become increasingly difficult for longer oligomers. From the MALDI-MS spectrum, it has been shown that a string of 17 nickel (Ni_{17}) is obtainable. Chemical decoration of the ligand with appropriate groups increases the solubility and the basicity of the ligand as well. It is hoped that the next generation ligands would provide metal-chain compounds suitable for nano-scale electronic applications.

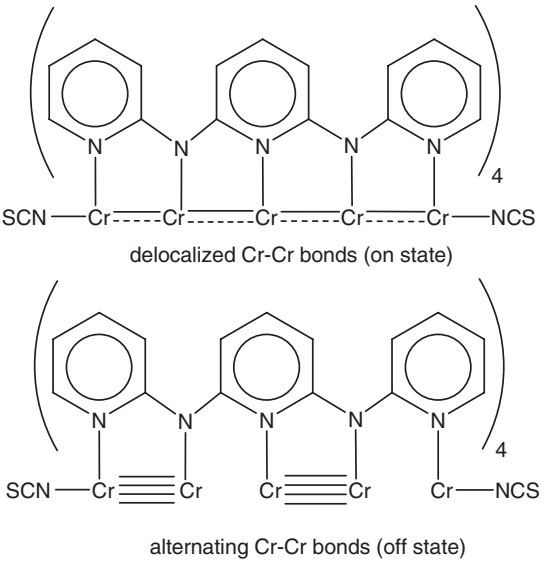

SCHEME 37

E. Linear Chains of Palladium

Conjugated polyenes have been used effectively in the construction of linear palladium array. The combination of two low-dimensional extended molecules threaded by chemical bond offer intriguing prospect toward new functional molecular organization. A linear Pd-Pd-Pd core sandwiched by triphenyl phosphine ligands in μ-η^1:η^2:η^2 mode has been reported (Scheme **38**).[66]

Multipalladium assemblies sandwiched by unsaturated hydrocarbon ligands have been developed by Kurosawa and Murahashi. A general synthetic scheme involves the reaction of 2 equivalents of Pd^I and $(n-2)$ equivalents of Pd^0, with two linear polyenes having $(n+1)$ {C=C} bonds to construct a linear Pd_n skeleton (Scheme **39**).[67] A homoleptic solvated Pd^I dimer $[Pd_2(CH_3CN)_6]^{2+}$ has been employed as a monovalent palladium precursor.[68] The polyene ligand coordinate to the Pd_n chain in η^3:η^2: $\cdots$:η^2: η^3 fashion. For polyene with n {C=C} bonds, one {C=C} bond of the terminal phenyl ring participates in coordination to the Pd_n chain as shown in Scheme **40**.

Linear dicationic Pd_n chains for n = 3, 4, and 5 have been synthesized.[69] X-ray structure of the $[Pd_4\{\eta^3{:}\eta^2{:}\eta^2{:}\eta^3\text{-Ph-}(C{=}C)_4\text{-Ph}\}_2]^{2+}$ ion (Figure **14**) reveals that the Pd metal skeleton is highly linear (178.25(4)°) and each Pd-Pd distance (2.7322(8) Å, 2.654(1) Å and 2.7322(8) Å) is normal and consistent with four-centered six-electron bond of the Pd_4 core.

In solution, facile slippage of the polyene ligand along the Pd_4 chain is observed based on ^{1}H NMR study that exhibits averaged 4 vinyl proton signals even down to −90°C (Scheme **41**). If the motion is not rapid enough on the

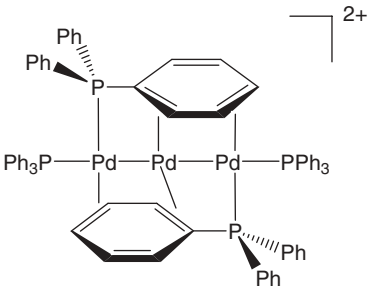

SCHEME 38

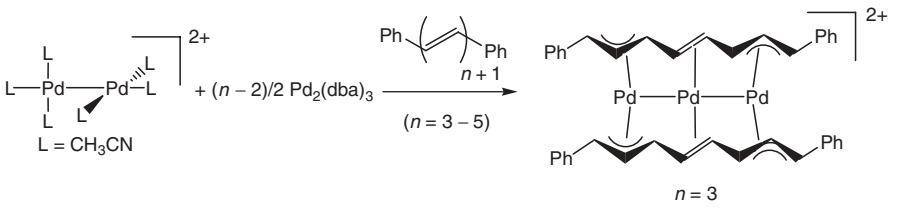

SCHEME 39

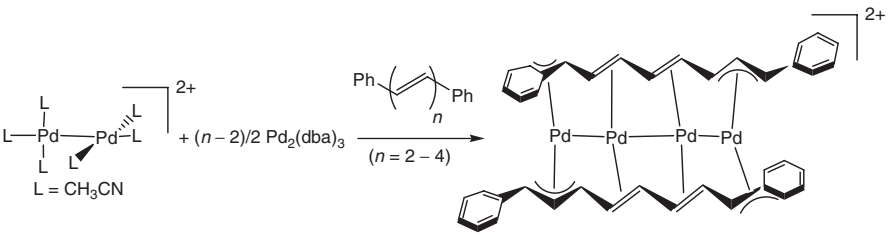

SCHEME 40

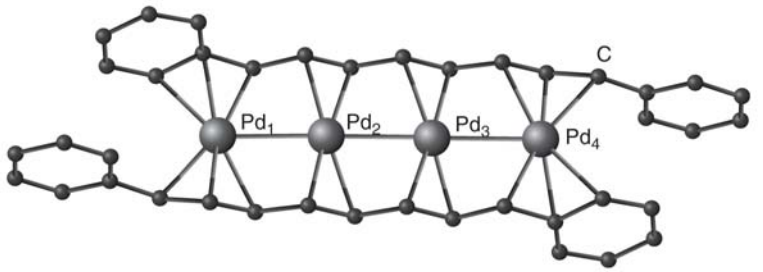

FIGURE 14

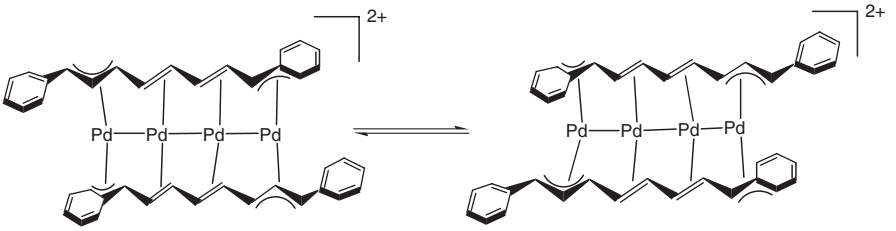

SCHEME 41

NMR time scale, 8 vinyl signals should have been observed. A proposed intermediate between two $\eta^3{:}\eta^2{:}\eta^2{:}\eta^3$ complexes is a symmetrical $\eta^2{:}\eta^2{:}\eta^2{:}\eta^2$ species. Use of coordinating solvent pyridine helps in arresting this symmetric mode and the structure of $[Pd_4\{\eta^2{:}\eta^2{:}\eta^2{:}\eta^2\text{-Ph-}(C{=}C)_4\text{-Ph})_2\}]^{2+}$ has been determined (Scheme **42**).

Movements of mononuclear and dinuclear Pd moieties have been observed along the π-conjugated five-carbon chain with subsequent bonding rearrangement providing cumelenyl-type compounds.[70]

Although linear Pd_n ($n = 3$–5) chains sandwiched by sp^2 carbon frameworks are isolated in the solid state and only lateral slippage of the ligands are evident in solution, dynamic interconversion between sandwiched and half-sandwiched species is reported for Pd_2-triene system as shown in Scheme **43**.[71]

The stepwise growth of a Pd chain of up to four metals has been achieved within the sandwich polyene framework.[72] Dipalladium(I) compound sandwiched by 1,4-diphenyl-1,3-butadiene (dpbd) is obtained from the reaction of

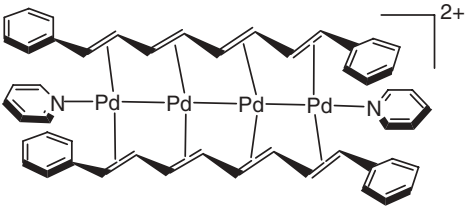

SCHEME 42

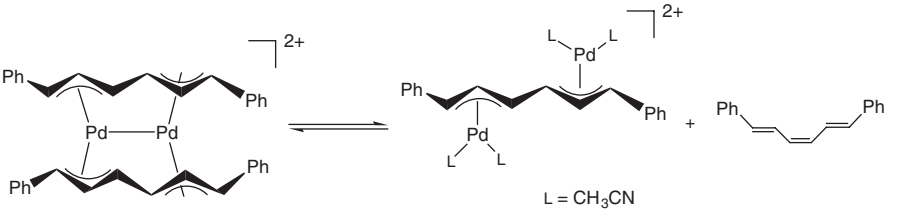

SCHEME 43

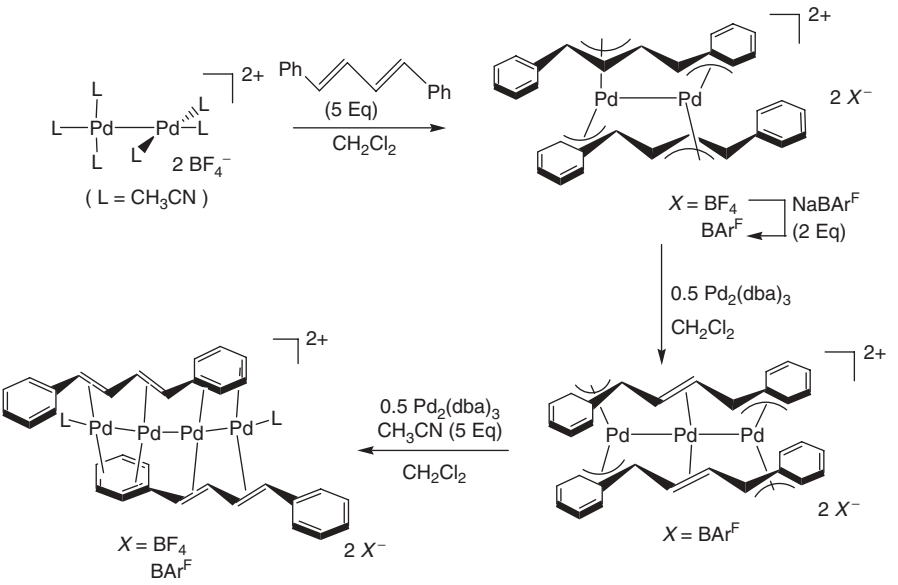

SCHEME 44

$[Pd_2(CH_3CN)_6]^{2+}$ with 5 equivalents of the corresponding ligand in CH_2Cl_2. The addition of one Pd^0 in the form of $Pd_2(dba)_3$ to $[Pd_2(\mu_2\text{-}\eta^3{:}\eta^3\text{-}Ph\text{-}(C{=}C)_2{=}Ph)]^{2+}$ provides the trinuclear Pd chain (Scheme **44**). The linear Pd-Pd-Pd chain is held in the π-corridor of 1,4-diphenyl-1,3-butadiene (dpbd). X-ray structure reveals deviations of the phenyl rings from the parallel stacking position to make a direct contact between the terminal Pd atoms and one of

the ortho-C atoms. The coordination mode of the ligand is μ_3-η^3:η^2:η^3. The subsequent addition of Pd^0 results in a Pd_4 chain held by the same ligands through μ_4-η^2:η^2:η^2:η^2 coordination and is capped by acetonitrile ligands. Stepwise incorporation of metal has tremendous implication in the construction of a metal chain of a specific length in an organometallic framework. It is also revealing that the dpbd ligand effectively changes its coordination modes according to the stepwise growth of the Pd chain.

Photo-irradiation of $[Pd_3\{Ar(CH=CH)_4Ar\}_2][BAr^F]_2$ results in an unusual photochemical face inversion of the multihapto-coordinated μ-olefin ligands on a metal–metal chain. This process originates from the unique electronic structure of the polyene sandwich compounds as well as from the π-stacking of the pπ-conjugated ligands (Scheme **45**).[73]

Reduction of the $[Pd_4]^{2+}$ complex $[Pd_4(\mu_4\text{-}\eta^2\text{:}\eta^2\text{:}\eta^2\text{:}\eta^2\text{-}^t\text{Bu-DPOT})_2(py)_2][B(Ar^F)_4]_2$ (^{t}Bu-DPOT = 1,8-bis(3,5-di-*t*-Bu)phenyl-1,3,5,7-octatetraene) with Cp_2Co in CH_3CN gave a $[Pd_4]^0$ chain (Scheme **46**).[74] Oxidation of $[Pd_4]^0$with 2 equivalents of $[Cp_2Fe][B(Ar^F)_4]$ in the presence of pyridine gave back $[Pd_4(\mu_4\text{-}\eta^2\text{:}\eta^2\text{:}\eta^2\text{:}\eta^2\text{-}^t\text{Bu-DPOT})_2(py)_2][B(Ar^F)_4]_2$ quantitatively. Molecular structure of the $[Pd_4]^0$ complex was determined by X-ray crystallography. The Pd-Pd distances (Pd1-Pd2 = 2.6272(8) Å, Pd2-Pd3 = 2.6048(7) Å, Pd3-Pd4 = 2.6662(8) Å) (Scheme **46**) are shorter than the Pd-Pd distance in bulk Pd metal (2.76 Å) or in $[Pd_4]^{2+}$ complexes. In the dicationic complexes, both 1,8-diaryltetraene ligands bind a $[Pd_4]^{2+}$ chain in identical modes: μ_4-η^3:η^2:η^2:η^3, binding in the absence of capping ligands at the Pd chain ends, or μ_4 η^2:η^2:η^2:η^2, in the presence of capping ligands. In contrast, the ligands in a $[Pd_4]^0$ complex coordinate to the chain in two different coordination modes, one in μ_4-η^3:η^2:η^2:η^3 mode and the other one in μ_4-η^2:η^2:η^2:η^2 mode. $[Pd_4]^0$ reacts with dibenzylideneacetone or allyl chloride immediately to form $Pd_2(dba)_3$ or $[Pd(\eta^3\text{-allyl})Cl]_2$, thus emphasizing the zero-valent character of the palladium chain. Quantum calculations bring out the fact that the wide range of charge capacities for the π-conjugated polyenes from negative to positive values plays an important part in stabilizing Pd chains in different oxidation states.

Four consecutive C=C units embedded in polycyclic aromatic ligand (PAL) is demonstrated to stabilize a Pd_4 chain.[75] The Pd-Pd-Pd-Pd chain is sandwiched by two perylene ligands (Scheme **47**) in η^2:η^2:η^2:η^2 coordination modes. Most remarkable aspect of the X-ray structure is that the tetra-palladium

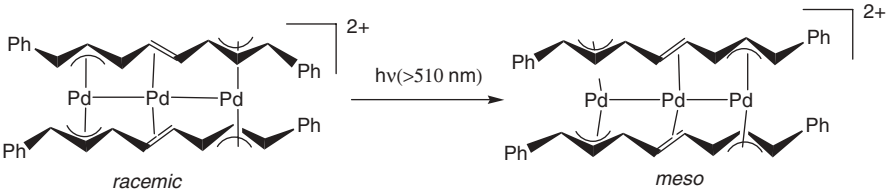

SCHEME 45

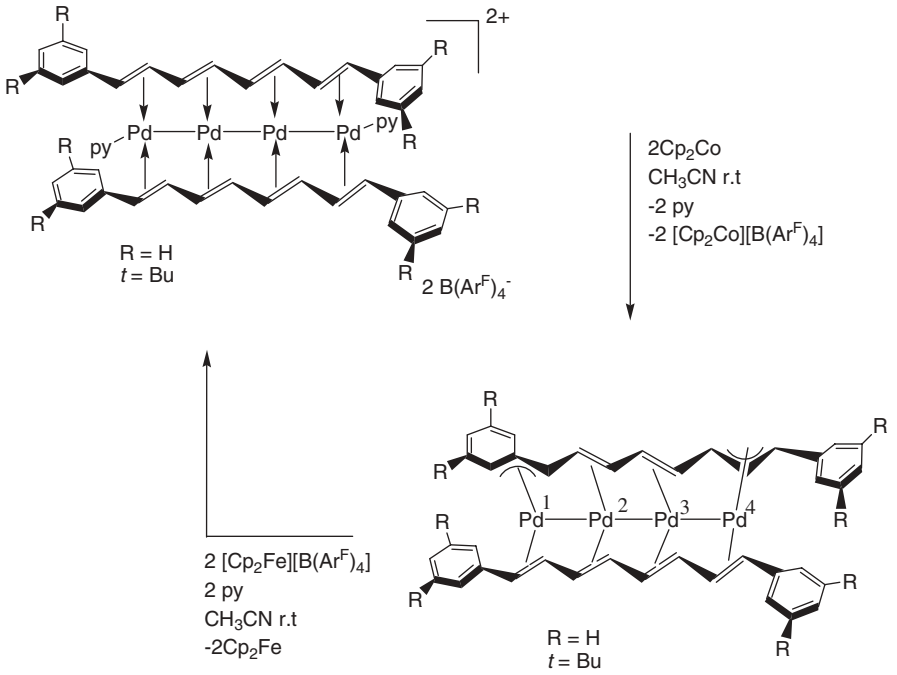

SCHEME 46

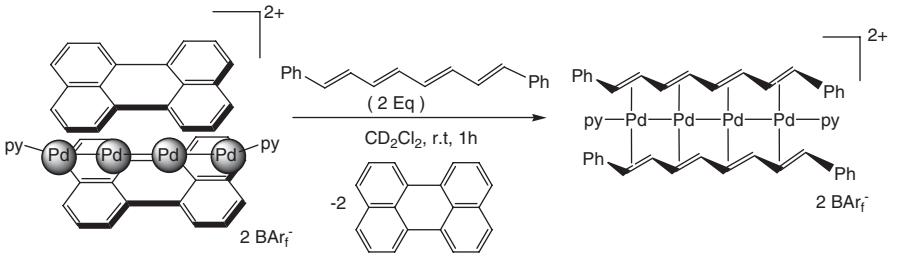

SCHEME 47

unit in chain form is placed in the C_8 carbon array in one of the edge positions. Two acetonitrile or pyridine molecules cap the end sites. Further, two perylene planes are stacked in an eclipsed position to each other, leaving void space between two planes at the other side with respect to the Pd_4 chain. The diphenyl tetraene readily displaces the perylenes from the Pd_4 chain, revealing weak interaction of PAL with the metal chain (Scheme **47**).

Different conjugation geometries of pπ-conjugated ligands from the linear ones have been reported accommodating multinuclear metal moiety. Treatment of bis(perylene)tetrapalladium complex $[Pd_4(perylene)_2L_2][BAr^F]_2$ with 1,2-bis(4-phenyl-1,3-butadienyl)benzene (*o*-bpbb) results in the quantitative formation of tetra-palladium complex $[Pd_4(o\text{-}bpbb)_2][BAr^F]_2$ (Scheme **48**).

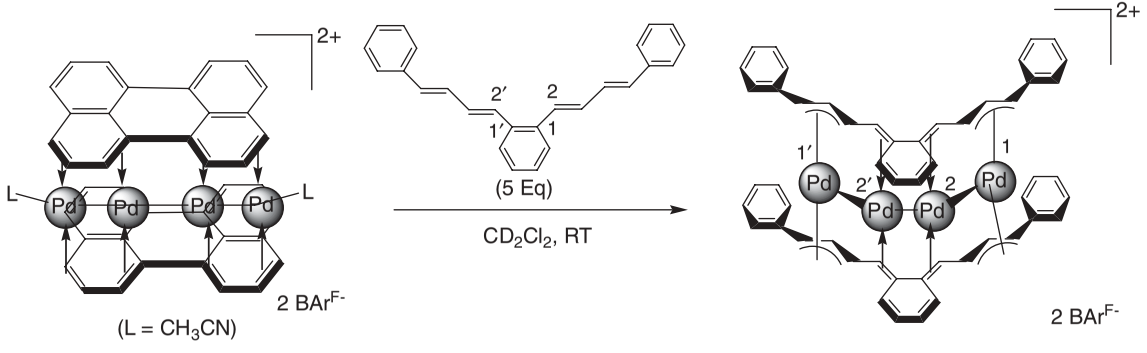
2+
L
Pd
Pd
Pd
Pd
L
2 BAr^F-
(L = CH3CN)
2′
2
1′
1
(5 Eq)
CD2Cl2, RT
2+
1′
1
Pd
2′
2
Pd
Pd
Pd
2 BAr^F-

SCHEME 48

The same compound was isolated in 69% yield by applying 2 equivalents of Pd^1 and 2 equivalents of Pd^0 in the form of $[Pd_2(CH_3CN)_6][BF_4]_2$ and $Pd_2(dba)_3$, respectively, with *o*-dpbb and a subsequent anion exchange of BF_4 with BAr^F.

X-ray structure revealed a Pd_4 arch-shaped geometry sandwiched between two *o*-bpbb ligands (Figure **15**).[76] The coordination mode is μ_4-η^3:η^2:η^2:η^3. The Pd_4 chain is bent at Pd2 and Pd2′ along the *cisoid* pπ-conjugation framework of C2-C1-C1′-C2′. The internal Pd2-Pd2′ bond of 2.584(1) Å is shorter than terminal Pd1-Pd2 and Pd1′-Pd2′ distances (2.701(1) Å). The CH(*o*-C_6H_4)CH unit of the *o*-bpbb ligand is described as an *o*-xylylene moiety in view of the η^2(C2-C1): η^2(C2′-C1′) coordination mode and the single bond character of the C1-C1′ bond length of 1.51(1) Å (Scheme **48**).

Reaction of *p*-bpbb (1,4-bis(4-phenyl-1,3-butadienyl)benzene) with $[Pd_4(perylene)_2][BAr^F]_2$ gives a Pd_4 chain $[Pd_4(p\text{-}bpbb)_2][BAr^F]_2$, which was identified by a combination of NMR techniques (Scheme **49**). It transforms spontaneously into bis(*p*-bpbb)pentapalladium complex $[Pd_5(p\text{-}bpbb)_2][BAr^F]_2$ in a 1:1 v/v mixture of CD_2Cl_2 and CD_3CN with a yield of 41% after 2 days. It is suggested that the partial decomposition of $[Pd_4(p\text{-}bpbb)_2][BAr^F]_2$ generates Pd(0) species, a part of which is trapped by the remaining Pd_4 complex to form the Pd_5 complex. It is interesting that the addition of 1 equivalent of Pd(0) does not improve the yield. The penta-palladium complex $[Pd_5(p\text{-}bpbb)_2][BAr^F]_2$ is stable in solution over 1 week, as revealed from NMR spectra.

The X-ray structure of $[Pd_5(p\text{-}bpbb)_2][BAr^F]_2$ reveals a V-shaped Pd_5 chain sandwiched between two *p*-bpbb ligands via the μ_5-η^3:η^2:η^2:η^2:η^3 mode. The Pd_5 chain is bent at the central Pd3 atom (Pd2-Pd3-Pd4 121.81(4)°), which is coordinated to the *p*-phenylene moieties. A formal quinoid character of the CH(*p*-C_6H_4)CH moiety of the *p*-bpbb ligand is suggested by examination of coordination modes and by the alteration in C-C bond lengths.

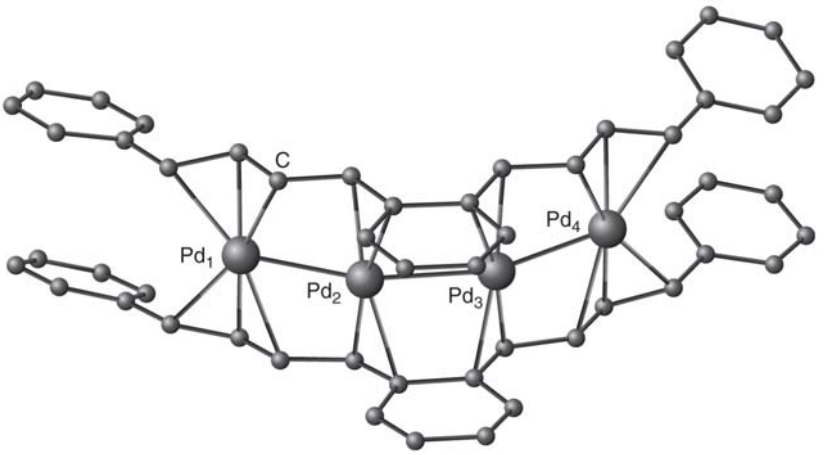

FIGURE 15

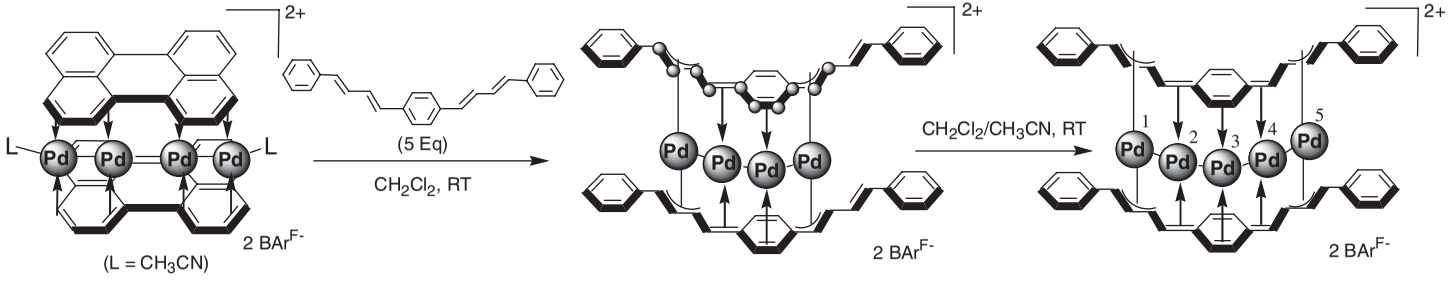
2+
L
Pd
Pd
Pd
Pd
L
2 BAr^F-
(L = CH3CN)
(5 Eq)
CH2Cl2, RT
2+
Pd
Pd
Pd
Pd
2 BAr^F-
CH2Cl2/CH3CN, RT
2+
1
2
3
4
5
Pd
Pd
Pd
Pd
Pd
2 BAr^F-

SCHEME 49

The bending of the $[Pd_4(o\text{-bpbb})_2][BAr^F]_2$ and $[Pd_5(p\text{-bpbb})_2][BAr^F]_2$ chains occur along the *cisoid* C_4 moieties at the phenylene units of the ligands. The bending angles of Pd_4 chain (149.93(3)°) and Pd_5 chain (121.81(4)°) reflect the angles of the pπ-conjugated skeleton (150° in *o*-bpbb and 120° in *p*-bpbb). This work suggests the potential utility of carbon π templates in controlling the shape of the metal assembly.

Rearrangement of a Pd_4 skeleton from a one-dimensional (1D) chain to a two-dimensional (2D) sheet on the face of polycyclic aromatic hydrocarbon perylene or fluoranthene has been described.[77] One of the perylene ligand in $[Pd_4(perylene)_2L_2][BAr^F]_2$ is readily replaced by 1,3,5,7-cyclooctatetraene (cot) to form a mixed sandwich complex $[Pd_4(perylene)(cot)L_2][BAr^F]_2$ (L = CH_3CN or pyridine) (Scheme **50**). X-ray crystallographic analysis reveals a rhombic Pd_4 sheet between cot and perylene ligands. The rhombic Pd_4 sheet is held by 10 carbon atoms of the perylene ligand through a μ_4-η^2:η^3:η^2:η^3 coordination mode and 8 carbon atoms of the cot ligand by μ_4-η^2:η^2:η^2:η^2 coordination mode. The Pd-Pd distances are as follows: Pd1-Pd2 2.749(1) Å, Pd2-Pd3 2.711(1) Å, Pd3-Pd4 2.757(1) Å, Pd4-Pd1 2.715(1) Å, and Pd2-Pd4 2.874(1) Å (Scheme **50**). A similar chain to sheet transformation of a Pd_4 moiety was observed on the face of fluoranthene. However, a chain of Pd_4 can be regenerated by employing tetraene, which substitutes both ligands from mixed-ligand complex.

A sandwich complex $[PPh_4][Pd_3(C_7H_7)_2Cl_3]$ (Scheme **51**), where three palladium centers form a planar triangular array capped by chlorides, sandwitched between two planar cycloheptatrienyl ligands, has been synthesized and structurally characterized.[78] The Pd-Pd bonds (2.745 to 2.789 Å) are within the range of normal Pd-Pd bond lengths and the two cycloheptatrienyl rings are slightly deviated from the mutually eclipsed position.

A pentapalladium sheet adopting an edge-sharing triangle-trapezoid skeleton between two naphthacene rings, $[Pd_5(naphthacene)_2(toluene)][B(Ar^F)_4]_2$ (Scheme **52**), has been synthesized, and characterized by X-ray crystallography and NMR spectroscopy. The two naphthacene ligands coordinate to the pentapalladium sheet through 12 carbons via μ_5-η^2:η^2:η^2:η^3:η^3-coordination mode. The Pd-Pd distances in the edge-sharing triangle-trapezoid metal skeleton are Pd1-Pd2 (2.687(2) Å), Pd2-Pd3 (2.770(2) Å), Pd2-Pd4 (2.779(2) Å), Pd3-Pd5 (2.781(2) Å), Pd1-Pd3 (2.700(2) Å), and Pd4-Pd5 (2.916 Å), indicating that the Pd4-Pd5 distance is relatively long.

DFT calculations on Pd_n chain compounds reveal that the driving force to the complex organization is a strong donation interaction from the π system of hydrocarbons to an orbital with appropriate phase and composition, delocalized over the metal chain and depopulated by the double oxidation process. No net bonding interaction can be characterized along the metal string, and the metal-metal distances are mainly governed by the hapticities of adjacent atoms. The Pd chain is stabilized by the large delocalization of positive charge transferred to the hydrocarbon backbones.[79]

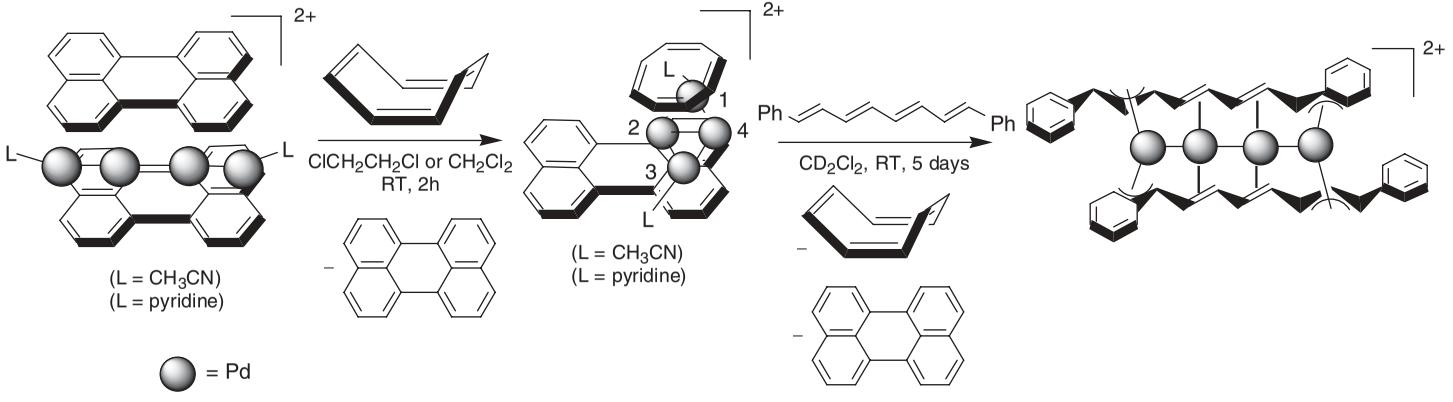
2+
L
L
(L = CH3CN)
(L = pyridine)
= Pd
ClCH2CH2Cl or CH2Cl2
RT, 2h
2+
L
1
2
4
3
L
(L = CH3CN)
(L = pyridine)
Ph
Ph
CD2Cl2, RT, 5 days
2+

SCHEME 50

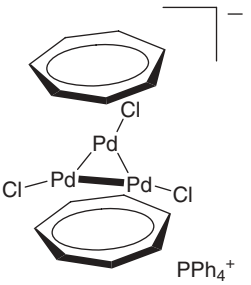

SCHEME 51

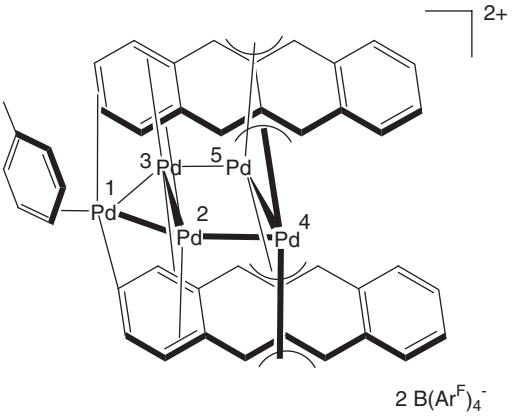

SCHEME 52

III. UNSUPPORTED METAL CHAINS

A. Linear Chain Compounds of Rhodium

The self-association of planar d^8 transition-metal complexes with the formation of weak metal-metal bonds is prominently featured for Rh^I. Discrete oligomers to infinite stacks have been isolated in the solid state. As discussed in the following sections, the stability of these 1D Rh^I chain molecules has been attributed to weak metal–metal interactions. Vacancy in the Rh^I *d*-band results mixed-valent chain compound of rhodium. The ligand-ligand interactions have been invoked to rationalize the stability of chain compounds as well.

Cationic rhodium(I) isocyanide complexes of the type $[(RNC)Rh^I]^+$ self associate to the limit of dimers and trimers (Scheme **53**).[80] Salts of dirhodium dications $[(PhNC)_8Rh^I_2][BPh_4]_2$ (3.193(1) Å),[81] $[(p\text{-}F\text{-}C_6H_4NC)_8Rh^I_2]Cl_2$[82] (3.207(2) Å), $[(p\text{-}O_2N\text{-}C_6H_4NC)_8Rh^I_2]Cl_2$ (3.25(1) Å),[82] and $[(C_6H_{11}NC)_8Rh^I_2]$

$$2[(RNC)_4Rh^{I}]^{+} \rightleftharpoons [(RNC)_8Rh^{I}_2]^{2+}$$

$$3[(RNC)_4Rh^{I}]^{+} \rightleftharpoons [(RNC)_{12}Rh^{I}_3]^{3+}$$

SCHEME 53

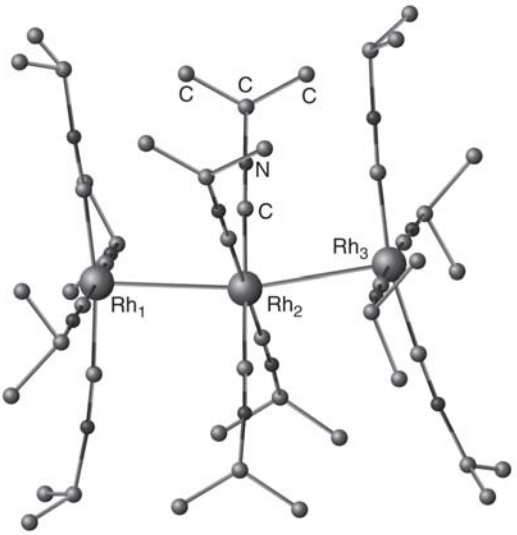

FIGURE 16

Cl_2[83] (3.287(2) Å) have been reported. The values in parenthesis are the corresponding Rh · · · Rh separations.

A trimeric structure is reported for $[(i\text{-PrNC})_{12}Rh^{I}_3]Cl_3$.[83] The trimer is situated on a crystallographic mirror plane involving all three rhodium ions (Figure **16**). The Rh1-Rh2 and Rh2-Rh3 distances are 3.101(1) and 3.074(1) Å, respectively. Both these distances are significantly shorter than the Rh · · · Rh distances found in dimers. The Rh1 · · · Rh2 · · · Rh3 angle (168.05(2)°) deviates from linearity. The terminal Rh atoms are displaced by 0.110 Å and 0.124 Å, respectively, from the plane of the surrounding four carbon atoms toward the central Rh2. In contrast, Rh2 is only 0.002 Å away from its C_4 plane.

Monomeric cations have been isolated by employing large R group in RNC and/or through the use of bulky anions. Examples are $[(2,6\text{-}Me_2C_6H_3NC)_4Rh^{I}][BPh_4]$,[84] $[(C_6H_{11}NC)_4Rh^{I}][BPh_4]$, and $[(i\text{-prNC})_4Rh^{I}][BPh_4]$.[85] Relative solubilities of different salts, the degree of solvation, and the rate of nucleation under crystallization conditions are a few factors that determine the nuclearity of the isolated salts. Different anions allow crystallization of different forms of $[(RNC)_4Rh^{I}]^{+}$ salt, but the process is not anion specific. The tetraphenyl borate produces monomers, whereas chlorides yield dimers and trimers as well.

Monomeric, dimeric and trimeric Rh^{I} compounds are distinguished by their UV-Vis spectra. Yellow crystals of $[(C_6H_{11}NC)_4Rh^{I}](BPh_4)$, dispersed in

KBr, exhibit a lowest-energy absorption at λ_{max} 384 nm, while red-colored $[(C_6H_{11}NC)_8Rh^I{}_2]Cl_2$ shows its lowest-energy absorption at λ_{max} 464 nm, green crystals of $[(i\text{-}PrNC)_{12}Rh^I_3]Cl_3$ is identified by the corresponding lowest energy absorption at λ_{max} 684 nm. The degree of association of Rh^I compounds in solution is reflected in their absorption spectrum.

Binuclear Rh^I complex $[Rh_2(bridge)_2]^{2+}$ (bridge = 1,3-diisocyanopropane) forms $[Rh_2(bridge)_4Cl]_2^{4+}$ in 12 M HCl and $[Rh_2(bridge)_4]_2^{6+}$ in 1 N H_2SO_4. These tetranuclear compounds are believed to be the photoactive species in the production of hydrogen upon irradiation. A similar tetranuclear species $[Rh_4(bridge)_8Cl]^{5+}$ was structurally characterized by Mann, and co-workers. The salt $H_3[Rh_4(bridge)_8Cl][CoCl_4]_4 \cdot nH_2O$ was crystallized on addition of $CoCl_2.6H_2O$ to the photoactive solution of $[Rh_2(bridge)_4][BF_4]_2$ in 12 M HCl.

The tetranuclear $[Rh_4]^{6+}$ core is made up of two binuclear $[Rh_2(bridge)_4]^{3+}$ units linked by a Rh-Rh bond. The chloride bridges $[Rh_4(bridge)_8]^{6+}$ units to form a linear infinite chain of repeat unit Rh_4Cl (Figure **17**).[86] The Rh-Rh bond distance between binuclear units [Rh2-Rh3] is 2.775(4) Å, whereas the Rh-Rh distances [Rh1-Rh2; Rh3-Rh4] within the binuclear units are 2.932(4) Å and 2.923(3) Å, respectively. This is consistent with a Rh^I-Rh^{II}-Rh^{II}-Rh^I formulation. The binuclear units $[Rh_2(bridge)_4]^{3+}$ have approximately eclipsed ligand system but are nearly perfectly staggered with respect to each other. The presence of hydronium ion $[H^+ \cdot nH_2O]$ within the crystal structure precluded an unambiguous assignment of charge to the tetranuclear cation. In a subsequent publication, the oxidation level was confirmed by redox titrations.[87] The formation of hexanuclear, octanuclear, and dodecanuclear rhodium-isocyanide oligomers on incomplete reduction of $[Rh_4]^{6+}$ have also been indicated.

Highly conjugated molecules offer prospect in the formation of a 1D stack through π-π interactions. Cofacial linear oligomers of rhodium have been

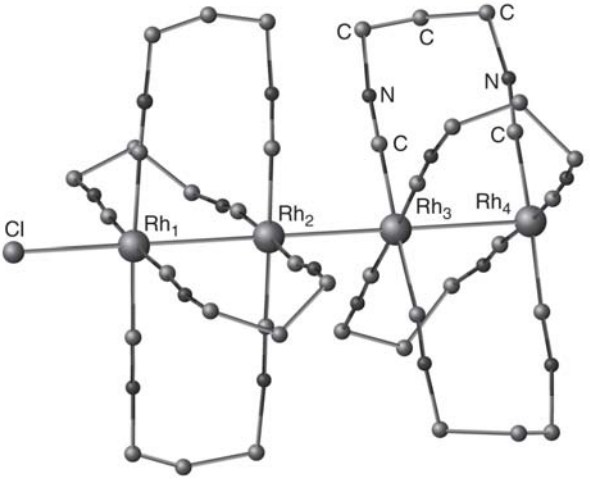

FIGURE 17

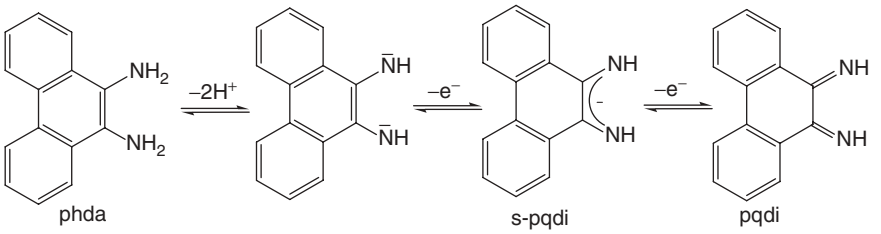

SCHEME 54

synthesized involving ligands derived from 9,10-diamino-phenanthrene (phda).[88] Redox-active ligand phda exists in different forms, as shown in Scheme **54**. A d^8-d^8 dimer $[(s\text{-pqdi})Rh^I(CO)_2]_2$ (*s*-pqdi = 9,10-phenanthrose-miquinonediimine) was obtained in the reaction of phda with $[RhCl(CO)_2]_2$ in acetonitrile followed by oxidation in air (Figure **18**). A similar dimer $[Rh^I(\text{s-disn})(CO)_2]_2$ (s-disn = semi-diiminosuccinonitrile) has been reported.[89]

Substitutions of CO from $[(\text{s-pqdi})Rh^I(CO)_2]_2$ by phda in dmf and subsequent oxidation of the ligand followed by dimerization led to the formation of Rh^I tetramer $[(\text{s-pqdi})_2(\text{pqdi})_4Rh^I_4(CO)_4]Cl_2$ (Figure **18**). The molecular structure of the cationic unit consists of discrete near-linear tetra-nuclear Rh^I chain with the center of inversion located between Rh2 and Rh2′ atoms. The Rh1-Rh2 and Rh2-Rh2′ distances are 2.848 (1) and 2.858(1) Å, respectively, and Rh1-Rh2-Rh2′ angle is 160.2(4)°. The Rh1 atom is displaced 0.194(5) Å from the plane formed by four coordinating atoms (N_2C_2) toward Rh2, and Rh2 is displaced 0.070(4) Å from the plane formed by four coordinating N atoms toward Rh2′ atom.

Further substitution of CO from $[(\text{s-pqdi})_2(\text{pqdi})_4Rh^I_4(CO)_4]Cl_2$ by phda followed by oxidation resulted in the trimeric $[Rh^{II}_2Rh^I(\text{s-pqdi})_4(\text{pqdi})_2]Cl$ (Figure **18**). The linear trinuclear chain involves a $[Rh_3]^{5+}$ core with Rh1-Rh2 distance 2.754(2) Å, which is intermediate between that of a Rh^{II}-Rh^{II} single bond distance 2.624(1) Å in $[Rh_2(CH_3CN)_{10}]^{4+}$ and a $Rh^I \cdots Rh^I$ distance 2.833(2) Å in $[Rh(\text{s-disn})(CO)_2]_2$, 2.923(1) Å in $[(\text{s-pqdi})Rh^I(CO)_2]_2$ and 2.853(2) Å in $[(\text{s-pqdi})_2(\text{pqdi})_4Rh^I_4(CO)_4]Cl_2$.

The metal–metal bond in $[Rh^{II}_2Rh^I(\text{s-pqdi})_4(\text{pqdi})_2]Cl$ is assigned as three-centered 6-electron σ-bonds. The pqdi and s-pqdi ligands in compounds $[(\text{s-pqdi})Rh^I(CO)_2]_2$, $[(\text{s-pqdi})_2(\text{pqdi})_4Rh^I_4(CO)_4]Cl_2$ and $[Rh^{II}_2Rh^I(\text{s-pqdi})_4(\text{pqdi})_2]Cl$ are arranged in eclipsed conformation. The concept of δ-type bonding between cofacial ligands has been invoked to rationalize the eclipsed arrangement of the ligands.[90]

Redox active dioxolene derivatives exist as different isomers of benzo-quinone, semiquinonate and catecholate by two-step one-electron transfer (Scheme **55**). A linear chain structure with direct a $Rh^I \cdots Rh^I$ bond was reported with 3,6-di-*tert*-butyl-1,2- benzosemiquinonate (3,6-DBSQ) radical anion in $[Rh^I(CO)_2(\text{3,6-DBSQ})]$.[91] It was originally synthesized by the reaction of Tl(3,6-DBSQ)

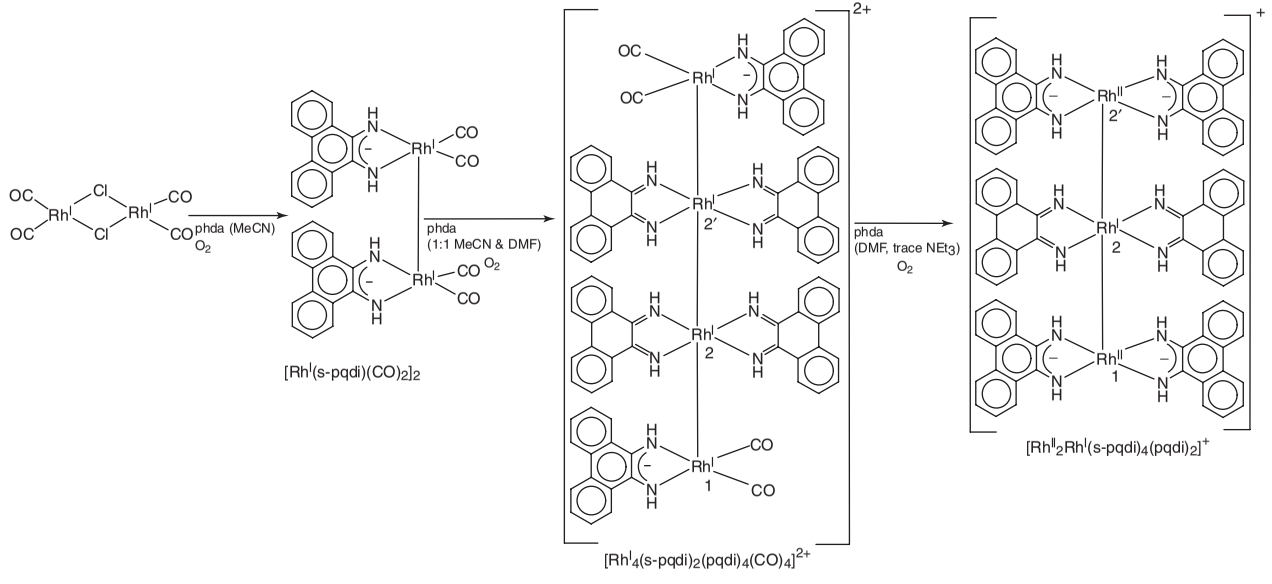
phda (MeCN)
O2
phda
(1:1 MeCN & DMF)
O2
phda
(DMF, trace NEt3)
O2
[RhI(s-pqdi)(CO)2]2
[RhI4(s-pqdi)2(pqdi)4(CO)4]2+
[RhII2RhI(s-pqdi)4(pqdi)2]+

FIGURE 18

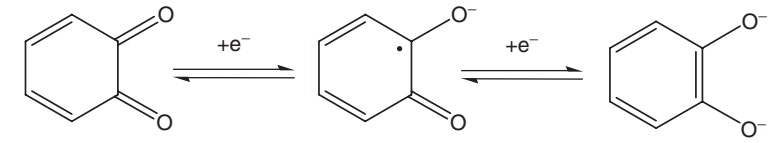

SCHEME 55

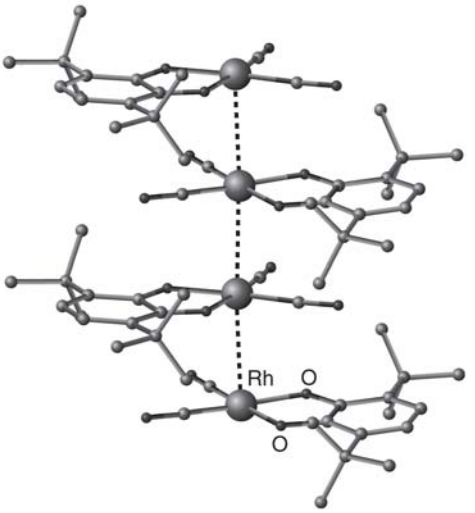

FIGURE 19

with $[RhCl(CO)_2]_2$ in toluene.[92] A redox reaction of $Rh_4(CO)_{12}$ with *o*-benzoquinone provided an identical rhodium(I)-semiquinonato complex. Crystal structure reveals that Rh atoms that form the core of the stacked column are near-perfectly aligned atop one another with angles between Rh-Rh vectors and complex planes ranging from 86.6° to 88.8° (Figure **19**). Two unique Rh^I-Rh^I distances were noted: 3.252(4) Å and 3.304(5) Å, values which are similar to Rh-Rh separations for other stacked Rh^I dimers and oligomers.[93]

Radical semiquinonate ligands are the paramagnetic centers of the individual complex units in the molecular chain. Magnetic measurements of $[Rh(CO)_2(3,6\text{-DBSQ})]$ reveal marked temperature dependence with both ferromagnetic and antiferromagnetic interactions. The temperature dependence of susceptibility from 330 K to ~105 K was fitted to Curie-Weiss plot with a θ value of +20.7 K, indicating the presence of a ferromagnetic interaction. At low temperature, the susceptibility quenched and was fitted to a Curie-Weiss plot with a value of θ−11.7 K and with a drop in magnetic moment to 0.63 μ_B at 5 K. The complicated magnetic behavior in the solid state indicates the presence of at least three types of intermolecular interactions within and, possibly, between chains of molecules. Direct interaction between radical ligands separated by >7 Å along

the column presumed to be weak, indicating magnetic coupling between radical ligands (3,6-DBSQ) propagated through Rh-Rh interactions along the column.

UV-Vis-NIR spectra of the $[Rh(CO)_2(3,6\text{-DBSQ})]$, recorded in pentane over the temperature range, show evidence for oligomer formation. Dramatic color change occurs from orange-brown at room temperature to dark green at lower temperature. Strong transition that appears in the NIR region (1500 nm) at low temperature resembles the solid-state spectrum at room temperature. The temperature and concentration dependence of the solution spectra credits to molecular assembly, yielding stacked oligomers. The degree of stacking of the Rh^I monomer in solution can be estimated from the low-energy transition.[80,94]

Linear chain compounds $[Rh(PhenSQ)(CO)_2]$ (PhenSQ = 9,10-phenanthrasemiquinonato) and $[Rh(2,6\text{-DBPhenSQ})(CO)_2]$ (2,6-DBPhenSQ = 2,6-di-*tert*-butyl-9,10-phenanthrasemiquinonato) have been synthesized via redox reaction of $Rh_4(CO)_{12}$ with the corresponding ligands in THF and *n*-pentane, respectively. Four crystallographically independent one-dimensional chain, of $[Rh^I(PhenSQ)(CO)_2]$ were noted in the unit cell.[95] In each one-dimensional chain, two types of intermolecular distances between central six-membered rings of PhenSQ ligands (3.14(9)–3.25(6) Å and 3.51(6)–3.56(9) Å) were noted, indicating that the ligands have dimerized structures (Figure **20**). Intradimer Rh-Rh distances are 3.117(1)–3.335(2) Å, whereas interdimer Rh-Rh distances

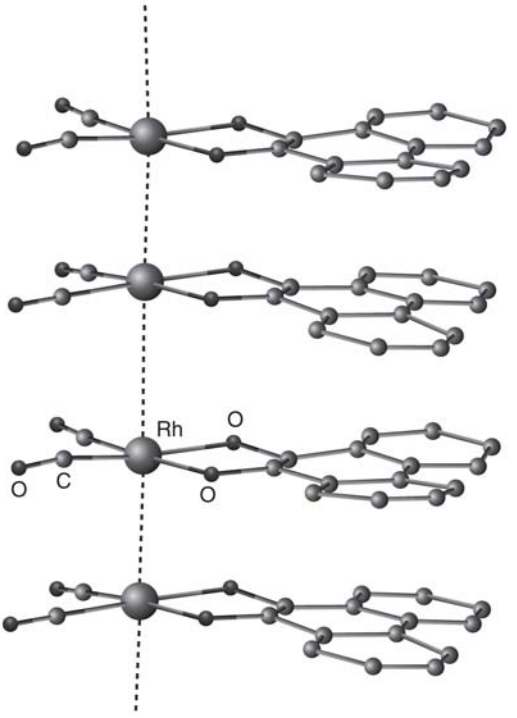

FIGURE 20

are 3.741(2)–3.963(1) Å. The one-dimensional columnar stack with eclipsed conformation is considered to be formed by the overlap of π-orbitals of ligands because interdimer Rh-Rh distances are longer than the corresponding interplanar distances between the ligands.

$[Rh^{I}(2,6\text{-DBPhenSQ})(CO)_2]$ forms a zigzag chain structure of dimer molecules stacked in staggered conformation (Figure **21**). The Rh1-Rh1-Rh1 angle is 147.97(2)°. The intradimer Rh-Rh distance is 3.1233(8) Å, whereas the interdimer Rh-Rh distance is 3.6414(8) Å. The complex molecules are overlapped so as to avoid steric hindrance between *tert*-butyl groups and to increase the overlap between the central six-membered rings of 2,6-DBPhenSQ. Magnetic susceptibility measurements of these two compounds indicate that the spin on each semiquinonato ligand is strongly coupled antiferromagnetically, although the impurity spin and thermally excited spin were measured at high temperature.

It is argued if the frontier orbitals of the metal *d* and ligand π-orbitals could be adjusted to the same or closely related energy levels by chemical modification, mixed-valence or partially oxidized metal chain would be achieved by intramolecular electron transfer between metals and ligands.[96] Metal-dioxolene compounds have very close energy levels between the frontier orbitals of metal *d* and the dioxolene ligands π-orbitals, and intramolecular electron transfer between the metal and the ligand is a possibility in a thermal

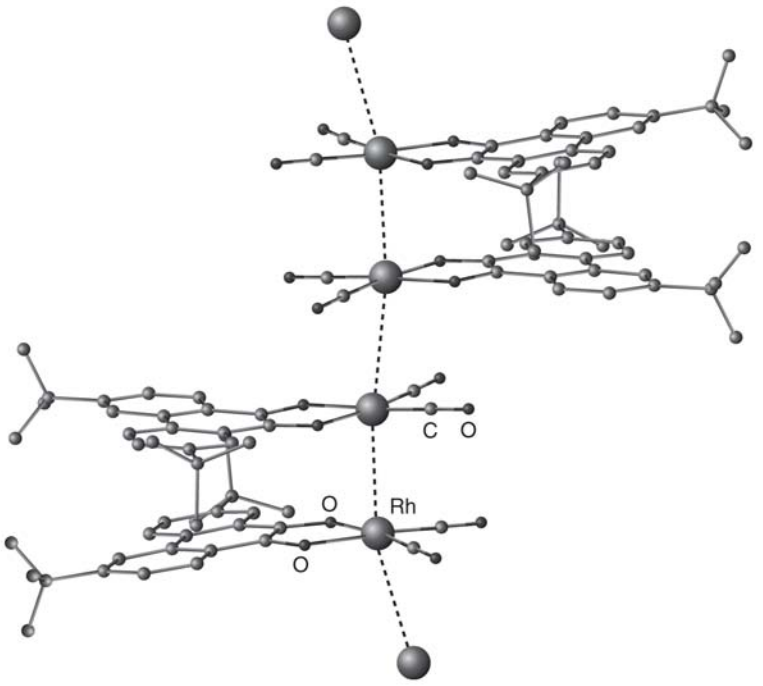

FIGURE 21

equilibrium known as "valence tautomerism".[96] In rhodium(I) semiquinonato complex $[Rh(3,6\text{-DBSQ})(CO)_2]_\infty$, although the energy levels of the electron-rich Rh(I) core and electron-deficient semiquinonato ligands are considered to be relatively close, valence tautomerism was not observed.

By introducing two chlorine atoms at the 4 and 5 positions of the 3,6-DBSQ ligand, the energy of the ligand π^* was adjusted to be close to or the same as the energy of one-dimensional Rh *d* band, made up of metal d_z^2 orbitals. The first example of a neutral mixed-valence rhodium(I,II) semiquinonato/catecholato complex $[Rh(3,6\text{-dbdiox-4,5-Cl}_2)(CO)_2]_\infty$, in which the 3,6-dbdiox-4,5-Cl_2 indicates 3,6-di-*tert*-butyl-4,5-dichloro-1,2-benzosemiquinonate (3,6-dbsq-4,5-$Cl_2^{\bullet -}$) or 3,6-di-*tert*-butyl-4,5-dichlorocatcholate (3,6-dbcat-4,5-Cl_2^{2-}) state, is reported.[97] The X-ray photoelectron spectrum (XPS) of $[Rh(3,6\text{-dbdiox-4,5-Cl}_2)(CO)_2]_\infty$ revealed a mixed-valence state composed of Rh^I and Rh^{II} on the rapid XPS time scale. The ratio of $Rh^I \cdots Rh^{II}$ was determined to be nearly 2:1. This is in contrast to the XPS data of Rh^I complex $[Rh(3,6\text{-DBSQ})(CO)_2]_\infty$ which exhibits the formal oxidation state of rhodium as +1. A comparative scheme of the stacking of $Rh^I.SQ^-$ in $[Rh(3,6\text{-dbsq})(CO)_2]_\infty$ and mixed stack of $\{Rh^I.SQ^{\bullet -}\}$ and $\{Rh^{II}.\ Cat^{2-}\}$ is shown in Figure **22**.

The X-ray structure of $[Rh(3,6\text{-dbdiox-4,5-Cl}_2)(CO)_2]_\infty$ was determined at 302 and 56 K with synchrotron radiation. Crystal structure reveals neutral linear chains of $[Rh(3,6\text{-dbdiox-4,5-Cl}_2)(CO)_2]$ molecules, which form trimeric units in the linear chain at 302 K. The Rh-Rh distances in the trimer are 2.8685(2) and 2.8629(2) Å, shorter than the Rh-Rh distances between trimers (2.8942(3) and 2.8984(3) Å) (Figure **23**a). The formation of the trimer is consistent with the formal oxidation state of $Rh^{1.33+}$ estimated from the XPS

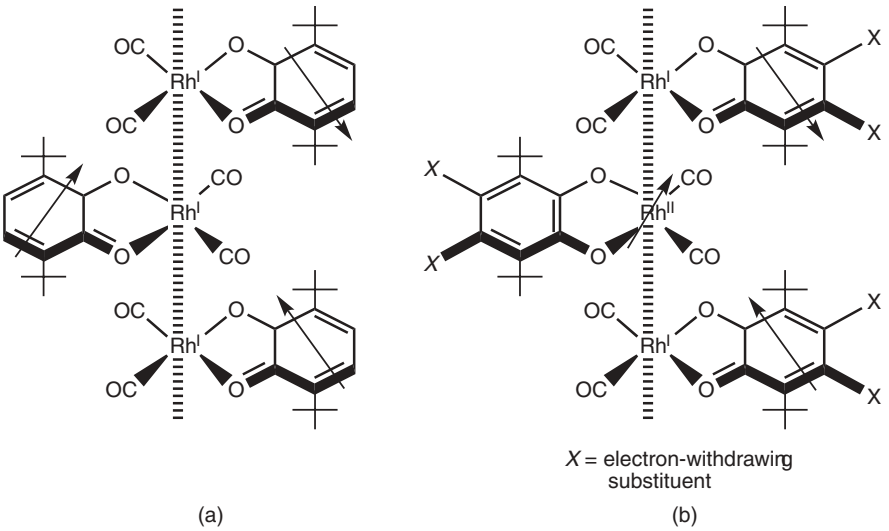

FIGURE 22

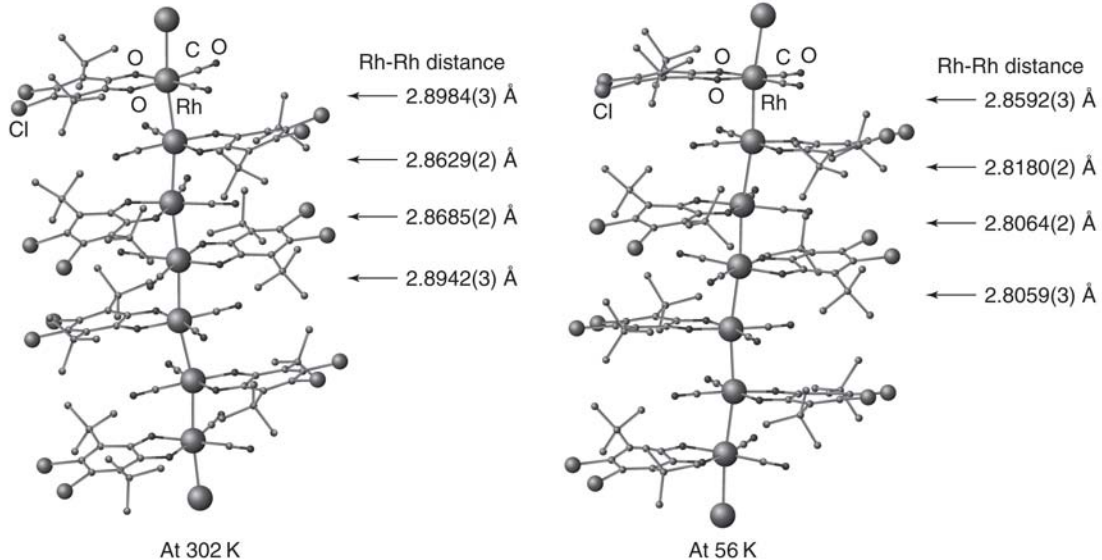
Cl
O
O
C O
Rh
Rh-Rh distance
2.8984(3) Å
2.8629(2) Å
2.8685(2) Å
2.8942(3) Å
At 302 K
(a)
Cl
O
O
C O
Rh
Rh-Rh distance
2.8592(3) Å
2.8180(2) Å
2.8064(2) Å
2.8059(3) Å
At 56 K
(b)

FIGURE 23

spectrum. At 56 K, the trimers in the linear chain are dimerized to form hexameric units. The Rh-Rh distances in the hexamer are in the range 2.8059(3)–2.8180(2) Å, while the Rh-Rh distance between hexamers is 2.8592(3) Å (Figure **23**b). The observed dimerization of trimers in the 1D chain originates from Pierels distortion associated with the pairing of unpaired electrons in the d_z^2 orbitals of Rh^{2+} ions.

The C-C and C-O bond lengths of each dioxolene ligand are in the boundary region of the semiquinonate and catecholate forms. These structural features indicate that the dioxolene ligands are either charge-localized but structurally disordered or charge-delocalized. Therefore, it is not possible to determine the oxidation state of each ligand from the C-C and C-O bond lengths.

Compound $[Rh(3,6\text{-dbdiox-}4,5\text{-}Cl_2)(CO)_2]_\infty$ exhibits an intense, broad absorption band that extends from 15,000 cm^{-1} to IR regions in the solid state. In contrast, $[Rh(3,6\text{-DBSQ})(CO)_2]_\infty$ shows an absorption at 6700 cm^{-1} in the solid state, which is assigned to the absorption associated with the band structure formed by d_z^2 orbitals along the linear chain.[91] The lower energy absorption band in the IR region probably consists of several overlapping bands, including the intervalence charge-transfer transitions of $Rh^{2+} \leftarrow Rh^{+}$ and/or $\pi(SQ^{\bullet-}) \leftarrow \pi^*(Cat^{2-})$[98] along with the absorption associated with band structure formed by d_z^2 orbitals. The absorption spectrum of a solution of $[Rh(3,6\text{-dbdiox-}4,5\text{-}Cl_2)(CO)_2]_\infty$ in CH_2Cl_2 is quite similar to that observed for $[Rh(3,6\text{-DBSQ})(CO)_2]_\infty$ in the same solvent, and this indicates that $[Rh(3,6\text{-dbdiox-}4,5\text{-}Cl_2)(CO)_2]_\infty$ exists as a discrete rhodium(I)-semiquinonato complex in CH_2Cl_2 solution.

Single-crystal electrical resistivity (ρ) of $[Rh(3,6\text{-dbdiox-}4,5\text{-}Cl_2)(CO)_2]_\infty$ along the one-demensional chain direction was measured in the temperature range 80–300 K by a four-probe technique. Compound $[Rh(3,6\text{-dbdiox-}4,5\text{-}Cl_2)(CO)_2]_\infty$ exhibits high electrical conductivity (σ = 17-34 $S.cm^{-1}$) at room temperature in spite of its being a neutral molecule, demonstrating that the rhodium atoms in $[Rh(3,6\text{-dbdiox-}4,5\text{-}Cl_2)(CO)_2]_\infty$ are in the mixed-valence state. The electrical conductivity varies with temperature, confirming semiconducting behavior, and the activation energies in high- and low-temperature regions are 114 meV (300–179 K) and 64.4 meV (154–80 K), respectively. The increase in resistivity with decreasing temperature is attributable to dimerization of the trimers.

It is remarkable that the mixed-valence state is realized in rhodium(I,II) semiquinonato/catecholato complex by electron transfer between metal *d* and semiquinonate π^* orbitals. Tuning of the energy levels between the metal *d* and ligand π orbitals would be expected to facilitate the control of electron transfer between metal and ligand by external factors, such as light, heat, and/or pressure. Therefore, this research offers scope for the development of novel neutral conducting polymers based on metal complexes in which the solid-state properties could be changed by metal-ligand electron transfer induced by external fields. Precise control of the frontier orbitals is essential in achieving such compounds.

The most fascinating compound in this series is the novel 1D rhodium chain, $[\{Rh(CH_3CN)_4\}(BF_4)_{1.5}]_\infty$, obtained by the slow reduction of $[Rh_2(CH_3CN)_{10}][BF_4]_4$ at a Pt electrode.[99] The infinite chain results from radical polymerization of the unstable $\{Rh^IRh^{II}\}$ dinuclear cation (Figure **24**). It represents the first example in which a discrete metal–metal singly bonded $\{Rh_2(CH_3CN)_{10}\}^{4+}$ dimer has been used as precursor for one-dimensional mixed-valent metal chain.[100] Further, nitriles offer prospects to chemically modify the chain. Two unique Rh-Rh distances, 2.9277(8) and 2.8442(8) Å are observed. The MeCN ligands on Rh(1) and Rh(1B), which define the shorter Rh-Rh distances, are twisted by 44.8°, whereas the ligands on Rh(1) and Rh(1A) adopt a torsional angle of 15.3°. In the parent molecule $\{Rh_2(CH_3CN)_{10}\}^{4+}$, average ligand torsional angle is close to 45°. Charge transfer experiments suggested the chain compound as a semiconductor.

The mixed-valent, square-planar cation $[Rh^I(CO)_2(CH_3CN)_2]^+$ was reported to form one-dimensional stack in the solid state. The chain is composed of the repeat unit $[\{Rh_2^{I,I}(O_2CCF_3)_2(CO)_4\}\{Rh_2^{II,II}(O_2CCF_3)_4\}\{Rh_2^{I,I}(O_2CCF_3)_2(CO)_4\}]_n$, in which an $\{Rh^{II},Rh^{II}\}$ unit is connected with two dimeric $\{Rh^I,Rh^I\}$ units.[101] A linear chain composed of dirhodium units is not limited to acetonitriles and carbonyls. Metal chains of the type $[\{Rh_2(OAc)_2(LL)_2\}(BF_4)]_n$ (LL = 1,10-phenanthroline; 2,2′-bipyridyl) have been prepared by one-electron reduction of the corresponding dirhodium(II,II) precursors $[Rh_2(OAc)_2(LL)_2]^{2+}$ in aqueous ethanol.[102] For the phen compound, three different Rh-Rh separations are noted in the Rh chain. The carboxylate bridged Rh-Rh distance is 2.652 Å; the unsupported interdimer Rh-Rh distance is 2.739 Å; and the resultant tetranuclear fragments are linked into an infinite chain by Rh-Rh

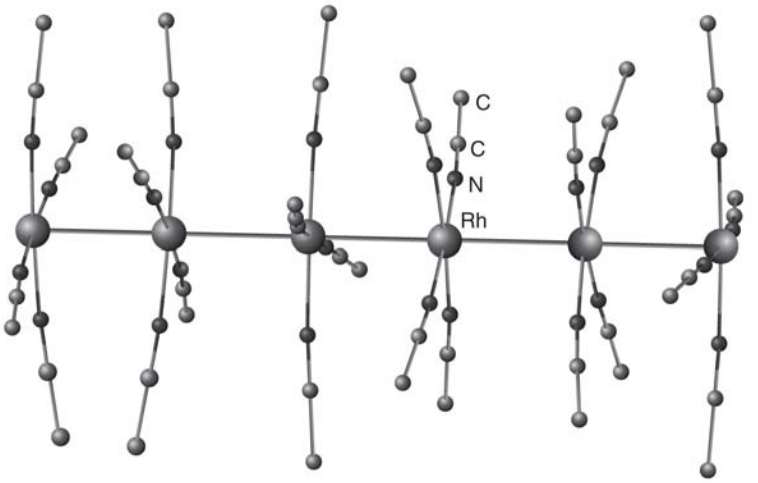

FIGURE 24

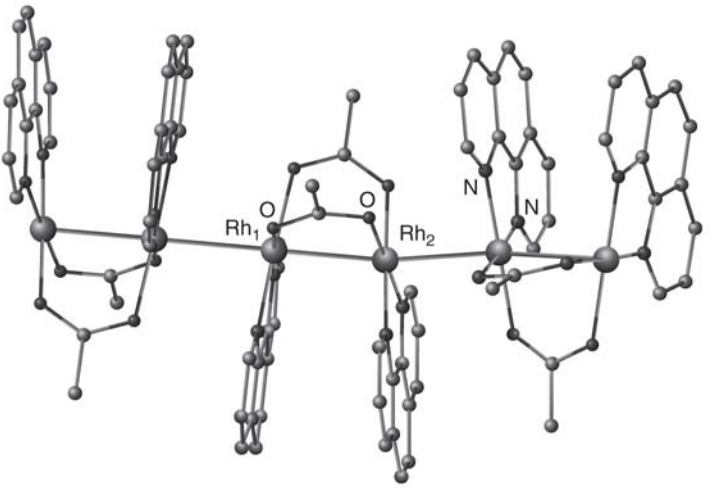

FIGURE 25

separation 2.832 Å (Figure **25**). The corresponding Rh-Rh distances are 2.678, 2.793, and 2.921 Å for the bpy analog [{$Rh_2(OAc)_2(bpy)$}(BF_4)]. Electrochemical fabrication of thin films of [{$Rh_2(OAc)_2(phen)$}]$^+$ chain by electron reduction of $Rh_2(OAc)_2(phen)_2(BF_4)_2$ has been reported.[103]

B. Linear Chain of Iridium

Linear chain of four and six iridium atoms have been synthesized by Oro and co workers. The approach involves oxidation of a diiridium(I) core with iodine resulting in the condensation of n molecules to produce I-[Ir-Ir]$_n$-I displaying a chain of $2n$ Ir atoms. The value of n has been limited to 3, conditioned by the stoichiometry of the iodine supply. The diiridium(I) precursor used is [$Ir_2(\mu\text{-Opy})_2(CO)_4$] (Opy = 2-pyridonate), which was isolated by bubbling CO through a solution of [$Ir_2(\mu\text{-Opy})_2(cod)_2$] (cod = 1,5-cyclooctadiene) in toluene.[104] The X-ray structure of [$Ir_2(\mu\text{-Opy})_2(CO)_4$] reveals a head-to-head (HH or A) configuration for the bridging ligands, which hold the metals in close proximity (Ir$\cdots$Ir = 2.8693(5) Å), generating two different types of iridium centers, *O,O* and *N,N* coordinated. Two such dinuclear units form a ″dimer of dimers″ in which two A isomers are connected by a weak and unsupported Ir$\cdots$Ir interaction (2.9808(6) Å) (Scheme **56**). The interdimer Ir$\cdots$Ir interaction occurs between the less hindered faces, that is, *O,O*-coordinated iridium atoms link to form the dimer. The NMR spectrum of the complex in benzene or toluene shows a 1:1 mixture of HH and HT isomers, from which two HH isomers crystallize as the AA dimer.

Oxidation of [$Ir_2(\mu\text{-Opy})_2(CO)_4$] in toluene with diiodine in a 1:0.5 ratio provides the mixed-valence tetrametallic compound HH,HH-[$Ir_2(\mu\text{-Opy})_2$(I)

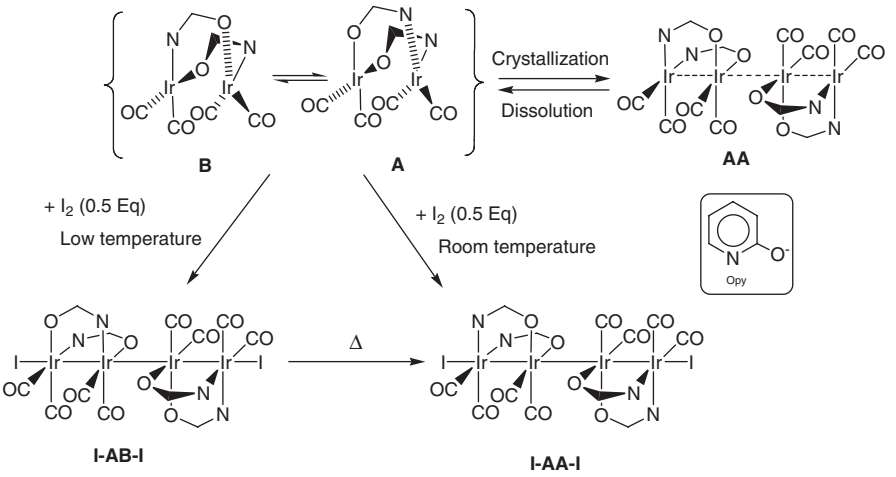

SCHEME 56

$(CO)_4]_2$ or I-AA-I (Scheme **56**).[105] The pure HH,HT-$[Ir_2(\mu\text{-Opy})_2(I)(CO)_4]_2$ or I-AB-I was isolated when the reaction was carried out in toluene at 0°C. For the I-AA-I isomer, two A isomers are joined by an unsupported Ir-Ir bond between the O,O-O,O coordinated Ir atoms, whereas for I–AB-I isomer, the corresponding iridium atoms are O,O-N,O coordinated. In both compounds, two diiridium units, which are linked through an unsupported Ir-Ir bond, are arranged in an almost *transoid* conformation. The ligand bridged Ir-Ir distances (2.7015 (15) Å for I-AA-I isomer and 2.6915(11), 2.7114(11) Å for I-AB-I isomer) are shorter than the central unsupported Ir-Ir bonds (2.750(2) Å for I-AA-I isomer and 2.7793(11) Å for I-AB-I isomer). The three metal-metal bonds are nearly linear (within a deviation of 15° from linearity), and the iodine atoms are linearly disposed with respect to the metal–metal bonds. The structure of $[Ir_2(\mu\text{-Opy})_2(I)(CO)_4]_2$ is shown in Figure **26**.

Remarkably, both I-AA-I and I-AB-I are stable in solution. The equivalence of the four 2-pyridonate ligands observed in the ^1H NMR spectrum of the complex I-AA-I indicates an averaged C_{2h} symmetry of the molecule in solution. The I-AB-I exhibits four nonequivalent signals for bridging ligands, reflecting the absence of any symmetry element (C_1 chiral). The green complex I-AB-I was found to evolve into the blue isomer I-AA-I on heating at 60°C in < 5 min. This transformation, quantitative by ^1H NMR spectroscopy, also occurred at room temperature but more slowly. The preparation and isolation of pure I-AB-I was possible only at low temperature, avoiding the isomerization of I-AB-I to I-AA-I. It is concluded that I-AA-I is the thermodynamic product, whereas I-AB-I corresponds to the kinetic product from the reaction of the mixture of A and B, in equilibrium at a 1:1 ratio, with iodine (Scheme **56**).

The addition of solid iodine to a solution of A and B isomers of $[Ir_2(\mu\text{-}Opy)_2(CO)_4]$ in toluene at 0°C in 1:3 molar ratio provided HH,HT,HH-$\{[Ir_2(\mu\text{-}Opy)_2(CO)_4]_3I_2\}$ (I-ABA-I), containing a linear chain made of six iridium atoms in a formal oxidation number of +1.33 (Scheme **57**).[106]

X-ray structure revealed the hexametallic chain formed by an almost linear array in which two A isomers sandwich a B isomer (Figure **27**). The six iridium atoms are linked by metal-metal bonds, two of which are unsupported. The unsupported Ir-Ir distances are (range 2.7757(14) – 2.7929(14) Å) longer than the ligand bridged Ir-Ir distances (range 2.6849(14) – 2.7096(14) Å). The hexametallic chain was found to be thermally stable in the solid state and under 0°C in solution. The observation of resonance signals corresponding to three inequivalent ligands in the ^{1}H NMR spectrum indicates C_2 symmetry of the species in solution. The hexametallic chain can be broken stepwise maintaining the configuration of the individual link. Addition of diiodine to I-ABA-I produced I-AB-I along with I-A-I. Further reaction of I-AB-I with diiodine provided an equimolar mixture of I-A-I and I-B-I (Scheme **58**). Likewise, I-AA-I produces 2 equivalents of I-A-I on oxidation with iodine.

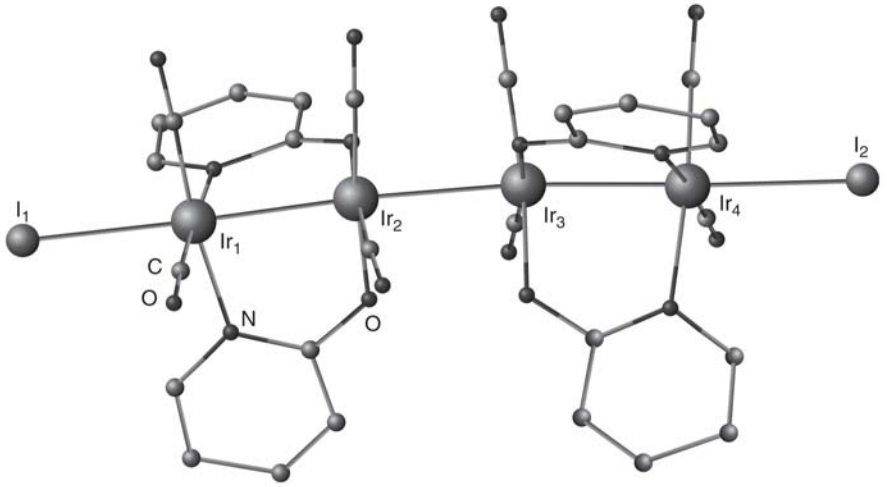

FIGURE 26

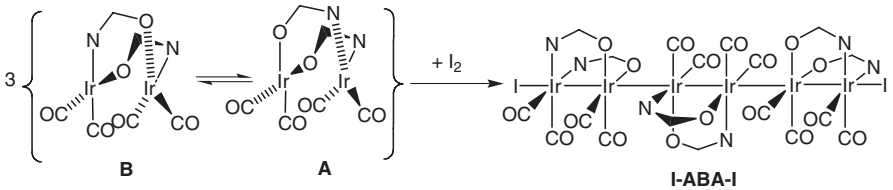

SCHEME 57

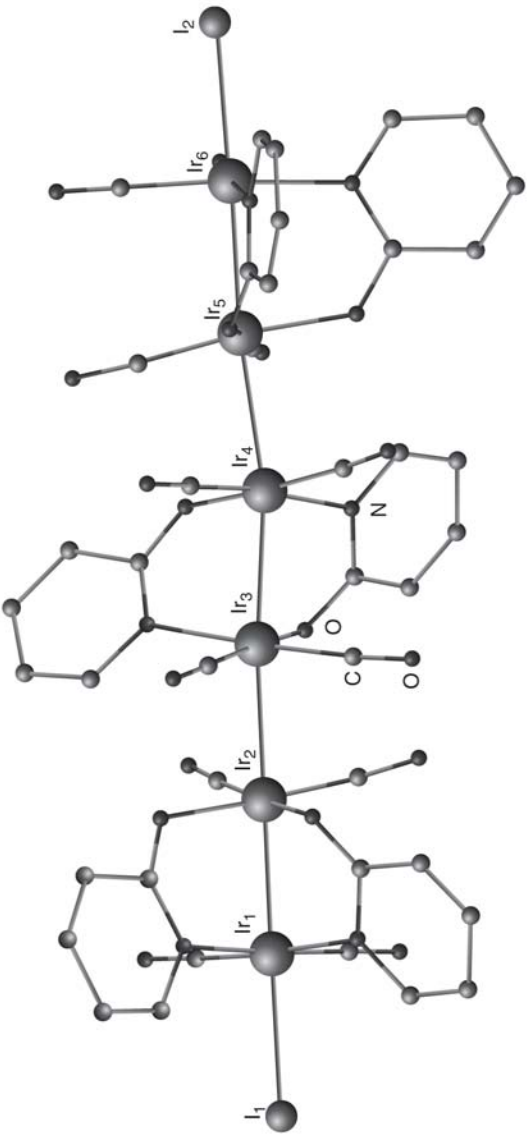

FIGURE 27

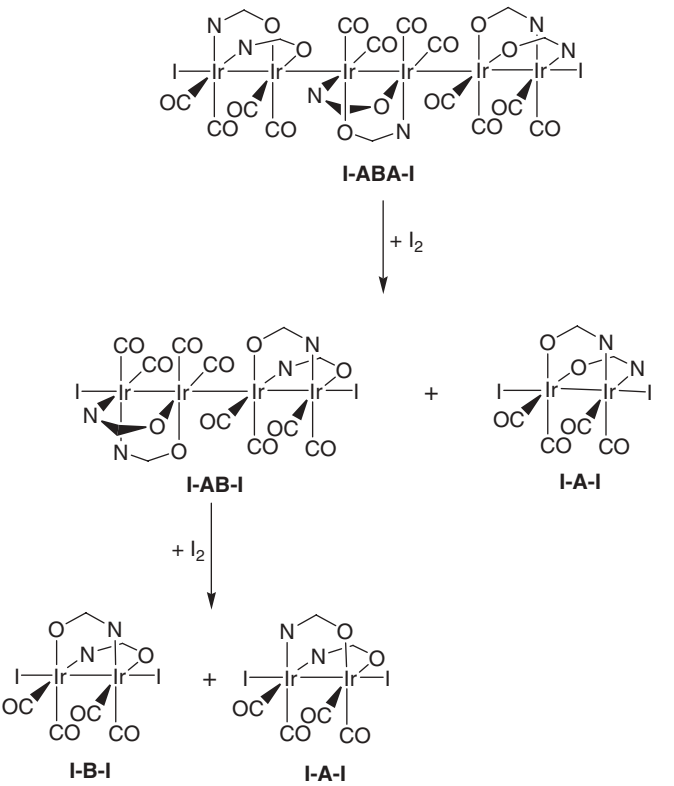

SCHEME 58

Linear Ir_4 chains are also accessible with different bridges. The first linear Ir_4 cluster $[Ir_4(\mu\text{-}C_7H_4NS_2)_4(I)_2(CO)_8]$ ($C_7H_4NS_2$ = benzothiazole-2-thiolate) was isolated and characterized as an intermediate in transannular oxidative-addition reactions.[107] By introducing pyrazolate bridges, a tetrairidium species $[\{(CN^tBu)_2(I)Ir(\mu\text{-}pz)_2Ir(CN^tBu)_2\}_2]$ has been synthesized by iodine oxidation of the dimer $[\{Ir(\mu\text{-}pz)(CN^tBu)_2\}_2]$.[108] The question posed by this work: Is it possible to assemble diiridium precursors beyond n = 3? Calculations show that the exothermic balance of the oxidation of the diiridium precursor sharply decreases from 40 kcal.mol^{-1} to 12.5 for $n = 2$ and 9.8 for $n = 3$ chain. The assembly of four precursor units would require an additional unsupported Ir-Ir bond. In the absence of a hypothetical chain of eight iridium atoms, it was proposed that I-ABAA-I would be the most stable based on steric considerations. Calculated exothermicity of 1.7 kcal.mol^{-1} with respect to I-ABA-I and A makes its synthesis and characterization a challenging task.[109]

A bonding scheme for iridium wire composed of n dimeric units I-[Ir-Ir]$_n$-I has been analyzed. The formal positive charge of the metal backbone is $2n + 2$, which corresponds to a total of $16n-2$ metal electrons. All MOs belonging to

the t_{2g} sets are doubly occupied, keeping $4n-2$ electrons to be accommodated on the σ MOs. Qualitative fragment MO diagrams involving d_z^2 orbitals (σ) for iridium chain for $n = 1-3$ are given in Scheme **59**. The energy of these MOs increases with the number of nodes along the chain. All levels are doubly filled, except the highest one. Close inspection of the LUMO indicates antibonding character between every pair of adjacent metal atoms. The vacancy of this highest-energy σ MO is therefore responsible for fully delocalized 2-electron/2*n*-center bond. The delocalized bonding that firmly holds the dimeric units together originates from the 2-electron oxidation of the complex by diiodine. For a count of $4n$ electrons, all σ MOs are filled. In that case, the chain either breaks apart or experience considerable stretching of the Ir-Ir bond due to the vanishing of the delocalized bond.

In addition to the delocalized bonding, another source of metal-metal bonding is metallophilic interaction between metal atoms in closed-shell electronic configurations.[110] The participation of $6s$ and $6p_z$ orbitals to the M-M ($d_z^2 + d_z^2$) orbital effectively reduces the antibonding character and contributes to the stability of the metal chain. The $5d \rightarrow 6s/p_z$ density transfer is maximal for the Ir^I precursor. Metallophilic interactions are therefore expected to partly counterbalance the decline of the delocalized 2-electron/2*n*-center bond strength as *n* increases. As the fractional oxidation state of iridium, equal to $1 + 1/n$, comes closer to 1, the strength of the delocalized 2-electron/2*n*-center bond diminishes among the pair of metal atoms. In the case of Ir^I complexes, corresponding to a full occupancy of the metal σ MOs, two extreme cases are possible, the Ir^Idimer and a linear chain of $Ir^I$with infinite chain length. Linear infinite stacks of Ir^I stabilized solely by the metallophilic d^8-d^8 interactions are not encountered in iridium chemistry.[111] A tetrairidium (dimer of dimers) $[Ir_2(\mu\text{-Opy})_2(CO)_4]$ has been characterized in solid state.[109]

Dihalodicarbonyl iridium compounds constitute an important class of chain compounds. These compounds are synthesized by treating K_2IrX_6 with CO under pressure[112] or heating in formic acid.[113] Single crystal study of $[Ir(CO)_2Cl_2]^{0.6-}$ revealed a chain structure. Alkali metal counterions compensate the charge. The fractional oxidation states of iridium in this series vary in the small range of $+1.39$ to $+1.44$.[114] These compounds exhibit metallic copper luster and metal-like conductivity.

Electro-crystallization has been successfully employed for the fabrication of numerous low-dimensional electronic materials.[115] Notably, the well-known Krogmann's salts $K_2Pt(CN)_4X_{0.3} \cdot 3H_2O$ (X = Cl, Br) were electrochemically prepared.[116] Organometallic charge-transfer compound $[(C_5Me_5)_2Fe]_2[TCNQ]_2$[117] and related compounds, the Magnus's green salts $Pt(NH_3)_4 \cdot PtCl_4$, $Pt(NH_3)_4 \cdot PtCl_6$,[118] and the mixed-valence $[Pt(en)_2][PtCl_2(en)_2](ClO_4)_4$[119] were obtained by the electro-crystallization process. Balch and co-workers carried out electro-oxidation of $(Ph_4As)[IrCl_2(CO)_2]$ on gold electrodes and reported three distinctly different forms of materials, depending on the conditions used.[120] Electro-oxidation of $(Ph_4As)[IrCl_2(CO)_2]$ in the presence of tetra(alkyl)ammonium salts resulted in conducting iridium

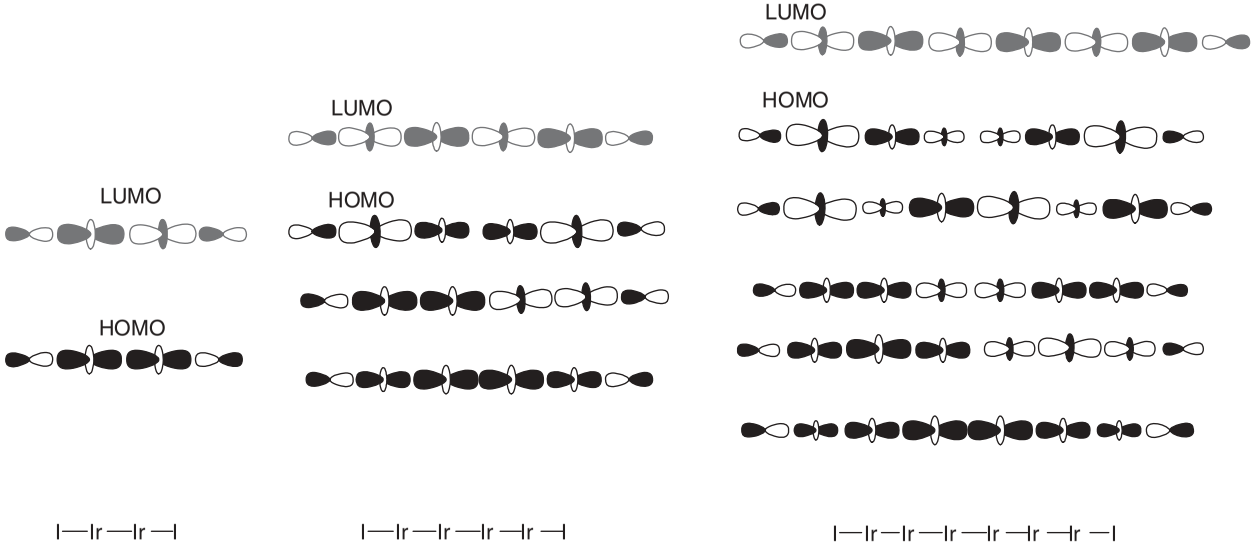
LUMO
HOMO
LUMO
HOMO
LUMO
HOMO
I—Ir—Ir—I
I—Ir—Ir—Ir—Ir—I
I—Ir—Ir—Ir—Ir—Ir—Ir—I

SCHEME 59

complexes $(TAA)_x[IrCl_2(CO)_2]$ [$x = 0.55$ for tetra-(*n*-hexyl)-ammonium and tetra-(ethyl)-ammonium cation; $x = 0.62$ for tetra-(*n*-butyl)-ammonium cation] in dichloromethane and 1,2-dichloroethane. Constant potential electrolysis at 200 mV revealed randomly oriented long needles on the electrode surface. The composition of the electrochemically generated material was found to be similar to that of chemically synthesized compounds. Sharp increase of current at the electrode covered with needle-like materials indicates that the deposit is conductive.[121] One-dimensional growth, as revealed in the SEM images, reflects the anisotropic behavior. The efficiency of electrodeposition depends on the nature of the cations used, because it affects the solubility of the deposit formed. Solvents do affect the morphology of the oxidized products. In strongly polar solvents such as DMF or DMSO, the irreversible oxidation of $[IrCl_2(CO)_2]^-$ does not produce any deposit at the electrode surface. Needle-like crystals are formed in chlorinated solvents, whereas unstructured film is deposited in acetonitrile. Electro-oxidation of $[IrCl_2(CO)_2]^-$ at higher potential (600 mV) results in structural changes of the initial needle-like deposit to spherical black particles and finally desorption from the electrode surface and diffusion into the bulk of the solution.

Recently, an unsupported Ir^{II} dimer $[IrCl_2(CO)_2]_2$ has been reported. This compound provides the opportunity to make linear mixed-valent Ir chains by electro-reduction.[122] Linear polymeric 1D chains incorporating d^8 Ru^0 and Os^0 have been reported.[123] Electro-reductions of $[M^{II}(L)(CO)_2Cl_2]$ (L = 2,2′-bipyridine or 1,10-phenanthroline) produce linear chains $[M(L)(CO)_2]_n$, obtained as adherent crystalline thin films on conductive supports. Polymerization occurs by an electrochemical propagation process (Scheme **60**). The first step involves the reduction to an unstable radical anion that concurrently loses one Cl^-ligand and transforms to a coordinatively unsaturated species. The reactive $17e^-$ transient species rapidly forms dimer. Subsequent reduction of the dimer at the applied potential promotes further chain extension, leading to oligomers and polymers (Scheme **61**).

The polymeric $[Ru(L)(CO)_2]_n$ chain that has been determined by XRPD methods packs pseudohexagonally in the *ab* plane and grows along *c*, with Ru-Ru distances close to 3.0 Å and a total chain length of 60 Å. The flat $Ru(L)(CO)_2$ monomers are staggered by 45° or 135° rotations but stack in random sequence along the chain.

In case of Os, the radical anion $[Os^{II}(bpy^{\bullet-})(CO)_2Cl_2]^-$ has been characterized spectroscopically at low temperature. The *in situ* formation of

$$n[M^{II}(L)(CO)_2Cl_2] + 2ne^- \longrightarrow [M^0(L)(CO)_2]_n + 2nCl^-$$

M = Ru, Os
L = 2,2′-bipyridine

SCHEME 60

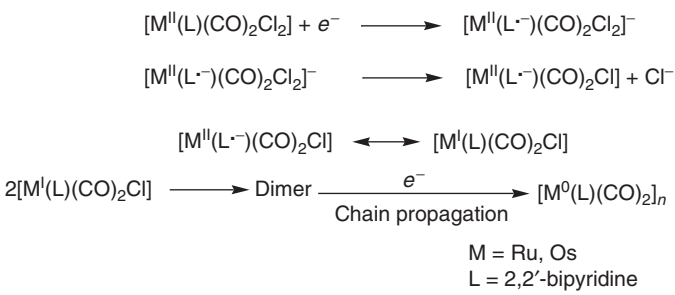

SCHEME 61

$[Os^0(bpy)(CO)_2]_n$ polymer has been characterized by IR, UV-Vis and EPR spectroelectrochemistry. The polymer species is an electron-rich electrocatalyst for CO_2 reduction and its fair solubility in polar organic solvents is important for potential use.

C. The Platinum Blues

The first platinum blue compound was reported in 1908. It was obtained when the yellow complex *cis*-$Pt^{II}Cl_2(CH_3CN)_2$ was reacted with Ag_2SO_4 in water.[124] The resultant dark blue compound, referred as "platinblau" was formulated as the platinum(II) complex $Pt(CH_3CONH)_2(H_2O)$. Further examples of Pt-amide blues were followed in subsequent years, but their geometric and electronic structures were unknown and were subject of controversies.[125] Studies by Rosenberg's group on the interaction of the anticancer drug *cis*-$Pt^{II}(NH_3)_2\ Cl_2$ with pyrimidines, such as thymine and uracil, resulted a new set of blue compounds, which were also anticancer active.[126] This led to a renewed effort to gain a better structural characterization of platinum blues.

By using 2-pyridone, Lippard and co-workers were able to characterize a tetranuclear structure, which is now being recognized as common structural feature for platinum blues. A combination of structural and spectroscopic measurements and theoretical calculations revealed the paramagnetic complex *cis*-$[Pt_4(2\text{-pyridonato})_4(NH_3)_8(NO_3)_2](NO_3)_3 \cdot H_2O$.[127] The ethylenediamine analog, $[Pt_4(2\text{-pyridonato})_4(en)_4(NO_3)_2](NO_3)_3 \cdot H_2O$, has been synthesized and structurally characterized.[128] The choice of 2-pyridonate as bridge is critical because it provides the discrete tetramer, unlike the long-chain oligomers that result in the case of pyrimidines. The tetranuclear chain is formed through an unsupported metal-metal bond between two diplatinum complexes, which display a face-to-face structure bridged by two ligands in a head-to-head (HH) position. It has two different types of platinum centers, *O,O* and *N,N* coordinated, and the unsupported metal-metal bond is formed

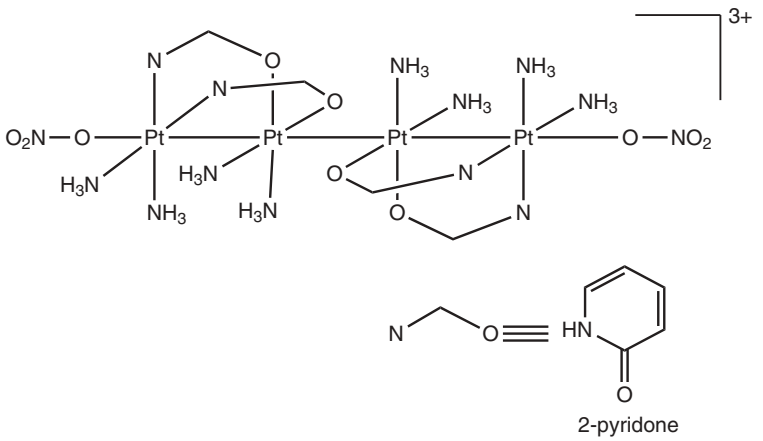

FIGURE 28

between the less-hindered Pt centers, that is, the *O,O*-coordinated Pt atoms. The average charge on the metal is +2.25. The Pt-Pt distances are 2.774(1) Å for the outer Pt pairs, connected by an unsupported Pt-Pt bond 2.877(1) Å (Figure **28**).

The 2-pyridone platinum blue and other related tetranuclear compounds bear a close structural relationship with $[\{Rh_2(\mu\text{-pz})(CN^tBu)_2\}_4]^{2+}$, $[\{Ir_2(\mu\text{-pz})_2(I)(CN^tBu)\}_2]$, (pz = pyrazolates) and $[\{Ir_2(\mu\text{-bztzt})_2(I)(CO)_4\}_2]$ (bztzt = benzothiazol-2-thiolate); $[Rh_4Cl(bridge)_8]^{5+}$ (bridge = 1,3-diisocyanopropane), termed rhodium and iridium blues.[129, 130]

DFT calculations on platinum blue compounds provide insight on their electronic structures. The four $d_z^2(\sigma)$ orbitals of metals form four nondegenerate σ MOs. The HOMO is singly occupied. The blue color of the compound is the consequence of the excitation from one of the three filled molecular orbitals into the half-filled σ* orbital. Further, it illustrates that a one-electron oxidation from the HOMO should lead to a strengthening of the Pt-Pt bonds.

Matsumoto's group has carried out complete characterization of $[\{cis\text{-}Pt_2(pyrr)_2\}_m]^{n+}$ (pyrr = 2-pyrrolidonate) compounds. The "α-pyrrolidone green"[131] and "α-pyrrolidone violet"[132] have been characterized as $[Pt_4(pyrr)_4(NH_3)_8](NO_3)_{5.48}]$ α $3H_2O$ and $[Pt_4(pyrr)_4(NH_3)_8](PF_6)_2(NO_3)_{2.56}] \cdot 5H_2O$, respectively. The nonstoichiometric composition of these compounds is attributed to the mixed-valency.

The X-ray structure of "2-pyrrolidone tan" reveals a tetranuclear structure similar to that of "2-pyridone blue," except that the axial nitrates are missing in the former. The Pt-Pt distances are 2.702(6) Å, 2.710(5) Å, and

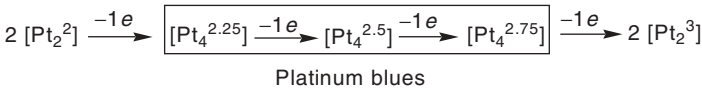

SCHEME 62

2.706(6) Å, which are shorter than that found in pyridone blue.[133] It indicates that the average oxidation state is higher in pyrrolidone analog. This pyrrolidone tan disproportionates into $[Pt_2^{III}(NH_3)_4(pyrr)_2]^{4+}$ and $[Pt_2^{II}(NH_3)_4(pyrr)_2]^{2+}$.[133] Chemical oxidation of $[Pt_4(pyrr)_4(NH_3)_8](NO_3)_6.3H_2O$ by $[S_2O_8]^{2-}$ in strongly acidic medium lead to $[Pt_4^{III}(pyrr)_4(NH_3)_8](SO_4)_2(ClO_4)_4 \cdot 6H_2O$[134]. This tetranuclear Pt^{III} compound exhibits excellent affinity to oxidize water into molecular oxygen.[135] Although initially termed as 2-pyrrolidine-platinum tan owing to its dark red color, subsequent studies show that it belongs to platinum blue category.

The oxidation state and nuclearity relationship in platinum blues are summarized in Scheme **62**.

Platinum-acetamide-blue and platinum-uracil-blue compounds have been reported. The tetranuclear uracil blue $[Pt_4(1\text{-MeU})_4(NH_3)_8](NO_3)_5 \cdot H_2O$, where 1-MeU is the mono-anion of 1-methyluracil, has structure and properties resembling 2-pyridone-blues. Platinum blue compounds with uridine, isonicotinamide, malonamide, and biuret have been described.[136]

Lippert and Neugebauer have reported the blue cation $[\{Pt_2(\mu\text{-}C_5H_5N_2O_2)_2(NH_3)_4\}_2]^{5+}$ and the pentanuclear Pt_2AgPt_2 species $[(NH_3)_4Pt_2(\mu\text{-}C_5H_5N_2O_2)_2\text{-}Ag\text{-}(\mu\text{-}C_5H_5N_2O_2)_2Pt_2(NH_3)_4]^{5+}$.[137] A remarkable octanuclear chain of Pt was reported by Matsumoto and co-workers. The average oxidation state of Pt in diamagnetic $[Pt_8(NHCOCH_3)_8(NH_3)_{16}](NO_3)_{10} \cdot 4H_2O$ is +2.25. Four alternate supported and unsupported Pt-Pt bond distances in this centrosymmetric structure are 2.880(2) Å, 2.900(1) Å, 2.778(1) Å, and 2.934(1) Å (Figure **29**).[138]

A series of partially oxidized 1D platinum chain compounds consisting of carboxylate-bridged *cis*-diammineplatinum dimers have been reported.[139] The Pt-dimers are characterized as $[Pt_2(acetato)_2(NH_3)_4](NO_3)_{2.4} \cdot 2H_2O$ and $[Pt_2(propionato)_2(NH_3)_4](NO_3)_2(ClO_4)_{0.4} \cdot 2H_2O$. In both compounds, the bridged Pt-Pt distances range from 2.81 to 2.85 Å while the interdimer distances are around 3.0 Å. From the solid-state structures it has been shown that the dimer associations are stabilized by four hydrogen bonds formed between the amino groups and the carboxylate anions. Employing pivalamidate bridge, the $[Pt_2^{II}(PVM)_2(NH_3)_4](PF_6)_2 \cdot H_2O$ and the oxidized dark green product $[Pt_4(PVM)_4(NH_3)_8](PF_6)_4(ClO_4) \cdot 2H_2O$ have been synthesized recently. X-ray structure of both compounds reveals tetranuclear structures. However, the Pt-Pt bond distances are very different (Scheme **63**).[140]

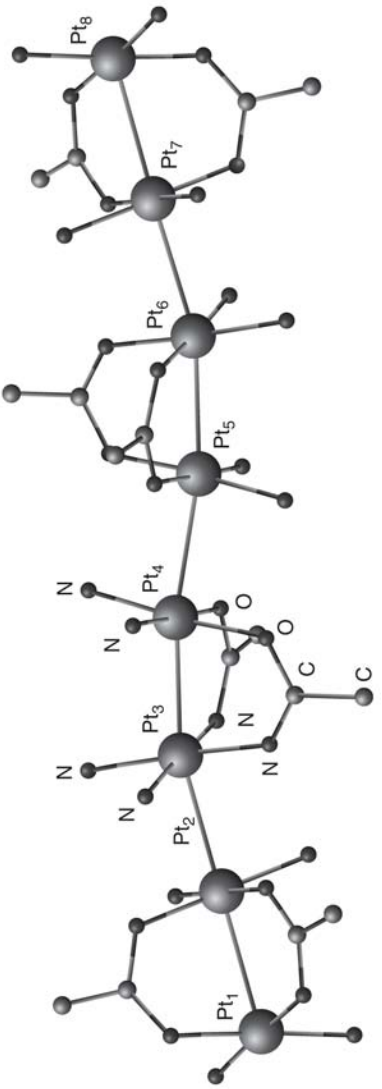

FIGURE 29

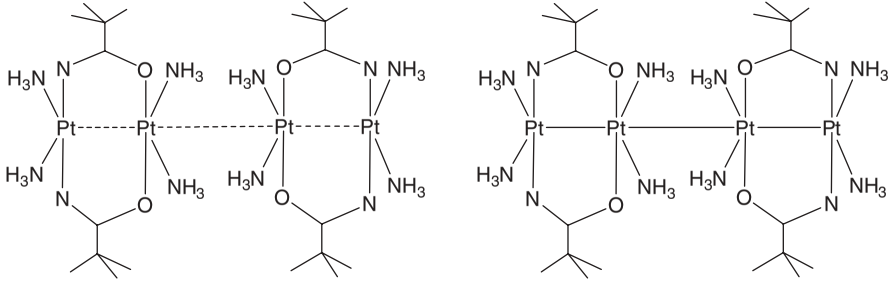

$[Pt_2(PVM)_2(NH_3)_4]^{2+}$ $[Pt_4(PVM)_4(NH_3)_8]^{4+}$

SCHEME 63

—Pt^{3+}—Cl—Pt^{3+}—$Rh^{2.5+}$—Pt^{2+}—Pt^{2+}—Pt^{2+}—Pt^{2+}—$Rh^{2.5+}$—Pt^{3+}—Cl—Pt^{3+}—

2.5959(6) 2.5959(6) 2.5987(11) 2.7337(11) 2.8450(7) 3.0634(10) 2.8450(7) 2.7337(11) 2.5987(11) 2.5959(6) 2.5959(6)

SCHEME 64

A novel infinite chain of Pt_6Rh_2 units bridged by Cl^- ions has been synthesized from the reaction of Pt^{II} dimer $[Pt_2(PVM)_2(NH_3)_4](PF_6)_2 \cdot H_2O$ and mixed-metal dimer $[PtRh(PVM)_2(NH_3)_2Cl_3]$. X-ray structure reveals that the complex cation of $\{PtRh(PVM)_2(NH_3)_2Cl_{2.5}]_2[Pt_2(PVM)_2(NH_3)_4]_2(PF_6)_6 \cdot 2MeOH \cdot 2H_2O\}_n$, is an infinite repetition of the octameric segment of "Pt_6Rh_2" units bridged by Cl^-ions. The formal oxidation state of the metal ions and metal-metal distances are summarized in Scheme **64**.[140] Single-crystal electrical conductivity of this chain molecule exhibits semiconducting behavior in the temperature range 267–295 K and the activation energy was estimated to be 1.0 eV.

Linear chain Pt-Pd complexes $\{[Pt_2(NH_3)_2X_2(\mu\text{-}PVM)_2(CH_2COCH_3)]_2[PdX_4]\}$ [X = Cl, Br] have been reported. The pentanuclear mixed-metal chain is composed of a monomeric Pd^{II} unit sandwiched by two amidato-bridged dimeric Pt^{III} units. Both ends of the chain are capped by acetonyl groups.[141] Linear trinuclear chain Pt-Tl complexes $[\{PtX(RNH_2)_2(NHCO^tBu)_2\}_2Tl]^+$ [X = NO_3, Cl, OTf] have been synthesized and structurally characterized by Chen, and co-workers.[142] Mixed-metal compounds $[\{PtX(NH_3)_2(NHCO^tBu)_2\}_2Tl]X$ (X = ClO_4, NO_3) adopt an extended zigzag chain structure consisting of repeatedly stacked $[\{PtX(NH_3)_2(NHCO^tBu)_2\}_2Tl]^+$ units; however, a helical chain was reported for X = PF_6 anion. Similar Pt^{II}-Tl^{I} coordination polymers assembled via metallophilic interaction have been reported with 1,2-diaminocyclohexane ligands.[143]

IV. CONCLUDING REMARKS

Studies on oligomeric and polymeric linear chain compounds with transition-metal backbones have been the subject of contemporary interest. A variety of metal ions possessing 3d, 4d, and 5d valence electrons are incorporated in the chain structures. Two general schemes have been employed. In one approach, metal ions are linearly placed via coordination with multidentate ligands. The neighboring metal ions in ligand-supported chains interact, exhibiting interesting conducting and magnetic properties. Covalent and noncovalent metal-metal bonding results in unsupported metal chain compounds. It has been shown that metal-metal bonded dimetal complexes are excellent precursors in the construction of metal chains, consisting of

alternate supported and unsupported metal pairs. Recent advances in the microscopy experiments allow the measurement of electrical conductivity of a single oligomeric chain. It is believed that further studies on metal chain compounds would provide materials suitable for nanoscale device applications.

V. REFERENCES

1. W. A. Little, *Phys. A., Rev.* **1964**, *134*, 1416.
2. L. B. Coleman, M. J. Cohen, D. J. Sandman, F. G. Yamagishi, A. J. Garito, and A. Heeger, *Solid State Commun.*, **1973**, *12*, 1125.
3. (a) J. S. Miller, ed; *Extended Linear Chain Compounds*, Plenum, Vols. *1–3*; New York, **1982**. (b) J.M. Williams, and A. Schultz, in *Molecular Metal*, ed. W. E Hatfield, New York, **1979**; p. 337. (c) J. S. Miller and A. J. Epstein, *Progress in Inorganic Chemistry*, ed. S. J. Lippard, Wiley, New York, **1976**, chap. 1. (d) S. Roth, *One-Dimensional Metals*, VCH, New York, **1995**.
4. J. K. Bera and K. R. Dunbar, *Angew. Chem. Int. Ed.* **2002**, *41*, 4453.
5. (a) J. M. Lehn and C. W. Rees, eds.; *Molecular Semiconductors*, Springer-Verlag, New York, **1982**. (b) F. Carter, ed.; *Molecular Electronic Devices*; Marcel Dekker, New York, **1982**.
6. (a) K. Krogmann, *Angew. Chem. Int. Ed. Engl.,* **1969**, *8*, 35. (b) J. M. Williams, *Adv. Inorg. Chem. Radiochem.,* **1983**, *26*, 235. (c) J. R. Ferraro and J. M. Williams, *Introduction to Synthetic Electrical Conductors*, Academic Press, San Diego, California, **1987**, chap. 4.
7. J. F. Berry, in *Multiple Bonds Between Metal Atoms*, 3rd ed., F. A. Cotton, C. A. Murillo, and R. A. Walton, Springer Science and Buisness Media, New York, **2005**, chap. 15.
8. (a) F. A. Cotton, L. M. Daniels, C. A. Murillo, and I. Pascual, *J. Am. Chem. Soc.,* **1997**, *119*, 10223. (b) R. Clerac, F. A. Cotton, L. M. Daniels, K. R. Dunbar, C. A. Murillo, and I. Pascual, *Inorg., Chem.*, **2000**, *39*, 748.
9. (a) F. A. Cotton, L. M. Daniels, C. A. Murillo, and I. Pascual, *Inorg. Chem. Commun.* **1998**, *1*, 1. (b) R. Clerac, F. A. Cotton, S. P. Jeffery, C. A. Murillo, and X. Wang, *Dalton Trans.,* **2003**, 3022.
10. R. Clerac, F. A. Cotton, L. M. Daniels, K. R. Dunbar, C. A. Murillo, and H.-C. Zhou, *Inorg., Chem.,* **2000**, *39*, 3414.
11. F. A. Cotton, L. M. Daniels, P. Lei, C. A. Murillo, and X. Wang, *Inorg. Chem.,* **2001**, 2778.
12. R. Clerac, F. A. Cotton, L. M. Daniels, K. R. Dunbar, C. A. Murillo, and I. Pascual, *Inorg. Chem.,* **2000**, *39*, 752.
13. J. F. Berry, F. A. Cotton, C. A. Murillo, and B. K. Roberts, *Inorg. Chem.,* **2004**, *43*, 2277.
14. J. F. Berry, F. A. Cotton, T. Lu, C. A. Murillo, B. K. Roberts, and X. Wang, *J. Am. Chem., Soc.,* **2004**, *126*, 7082.
15. M. -M. Rohmer, and M. Benard, *J. Cluster Sci.,* **2002**, *13*, 333.
16. (a) N. Benbellat, M. -M. Rohmer, and M. Benard, *Chem. Commun.,* **2001**, 2368. (b) J. F. Berry, F. A. Cotton, L. M. Daniels, C. A. Murillo, and X. Wang, *Inorg. Chem.,* **2003**, *42*, 2418.

17. (a) F. A. Cotton, L. M. Daniels, C. A. Murillo, and L. S. Wang, *Chem. Commun.,* **1998**, 39. (b) F. A. Cotton, P. Lei, C. A. Murillo, and L. -S. Wang, *Inorg. Chim. Acta*, **2003**, *349*, 165. (c) F. A. Cotton, P. Lei, and C. A. Murillo, *Inorg. Chim. Acta*, **2003**, *349*, 173.
18. F. A. Cotton, L. M. Daniels, T. Lu, C. A. Murillo, and X. J. Wang, *Chem. Soc., Dalton Trans.* **1999**, 517.
19. H. -C. Chang, J. -T. Li, C. -C. Wang, T. -W. Lin, H. -C. Lee, G. -H. Lee, and S. -M. Peng, *Eur. J. Inorg. Chem.,* **1999**, 1243.
20. F. A. Cotton, L. M. Daniels, C. A. Murillo, and X. Wang, *Chem. Commun.,* **1999**, 2461.
21. Y. -H. Chen, C. -C. Lee, C. -C. Wang, G. -H. Lee, S. -Y. Lai, F. -Y. Li, C. -Y. Mou, and S. -M. Peng, *Chem. Commun.,* **1999**, 1667.
22. R. H. Ismayilov, W. -Z. Wang, R. -R. Wang, C. -Y. Yeh, G. -H. Lee, and S. -M. Peng, *Chem. Commun.,* **2007**, 1121.
23. (a) E. -C. Yang, M. -C. Cheng, M. -S. Tsai, and S. -M. Peng, *J. Chem. Soc., Chem. Commun.,* **1994**, 2377. (b) F. A. Cotton, L. M. Daniels, and G. T. Jordon, *Chem. Commun.,* **1997**, 421.
24. (a) F. A. Cotton, L. M. Daniels, G. T. Jordan IV, and C. A. Murillo, *J. Am. Chem. Soc.* **1997**, *119*, 10377. (b) M. -M. Rohmer, and M. Benard, *J. Am. Chem. Soc.,* **1998**, *120*, 9372. (c) F. A. Cotton, C. A. Murillo, and X. Wang, *J. Chem. Soc., Dalton Trans.* **1999**, 3327.
25. M. -M. Rohmer, and M. Bénard, *J. Am. Chem. Soc.,* **1998**, *120*, 9372.
26. (a) F. A. Cotton, C. A. Murillo, and X. Wang, *Inorg. Chem.* **1999**, *38*, 6294. (b) R. Clerac, F. A. Cotton, L. M. Daniels, K. R. Dunbar, C. A. Murillo, and X. Wang, *Inorg. Chem.*, **2001**, *40*, 1256.
27. J. F. Berry, F. A. Cotton, T. Lu, and C. A. Murillo, *Inorg. Chem.,* **2003**, *42*, 4425.
28. R. Clerac, F. A. Cotton, K. R. Dunbar, T. Lu, C. A. Murillo, and X. Wang, *J. Am. Chem. Soc.*, **2000**, *122*, 2272.
29. D. A. Pantazis, and J. E. McGrady, *J. Am. Chem. Soc.*, **2006**, *128*, 4128.
30. R. Clerac, F. A. Cotton, K. R. Dunbar, T. Lu, C. A. Murillo, and X. Wang, *Inorg. Chem.,* **2000**, *39*, 3065.
31. R. Clerac, F. A. Cotton, S. P. Jeffery, C. A. Murillo, and X. Wang, *Inorg. Chem.,* **2001**, *40*, 1265.
32. R. Clerac, F. A. Cotton, L. M. Daniels, K. R. Dunbar, C. A. Murillo, and X. Wang, *J. Chem. Soc. Dalton Trans.,* **2001**, 386.
33. M. -M. Rohmer, I. -P. C. Liu, J. -C. Lin, M. -J. Chiu, C. -H. Lee, G. -H. Lee, M. Bénard, X. López, and S. -M. Peng, *Angew. Chem. Int. Ed.,* **2007**, *46*, 3533.
34. C. -Y. Yeh, C. -H. Chou, K. -C. Pan, C. -C. Wang, G. -H. Lee, Y. -O. Su, and S. -M. J. Peng, *Chem. Soc. Dalton Trans.* **2002**, 2670.
35. C. -H. Chien, J. C. Chang, C. -Y. Yeh, G. -H. Lee, J. -M. Fang, and S. -M. Peng, *Dalton Trans.,* **2006**, 2106.
36. W. -Z. Wang, R. H. Ismayilov, G. -H. Lee, I. P. -C. Liu, C. -Y. Yeh, and S. -M. Peng, *Dalton Trans.* **2007**, 830.
37. (a) L. -P. Wu, P. Field, T. Morrissey, C. Murphy, P. Nagle, B. Hathaway, C. Simmons, and P. Thornton, *J. Chem. Soc., Dalton Trans.* **1990**, 3835. (b) G. J. Pyrka, MO. El-Mekki, and A. A. Pinkerton, *J. Chem. Soc., Chem. Commun.* **1991**, 84.
38. (a) J. F. Berry, F. A. Cotton, P. Lei, and C. A. Murillo, *Inorg. Chem.* **2003**, *42*, 377. (b) M. Benard, J. F. Berry, F. A. Cotton, C. Gaudin, X. Lopez, C. A. Murillo, and M. M. Rohmer, *Inorg. Chem.* **2006**, *45*, 3932.

39. (a) G. A. Albada, I. Mutikainen, U. Turpeinen, J. Reedijk, *Eur. J. Inorg. Chem.* **1998**, 547. (b) G. A. Albada, J. Koningsbruggen, I. Mutikainen, U. Turpeinen, and J. Reedijk, *Eur. J. Inorg. Chem.,* **1999**, 2269.
40. M. -S. Tsai, and S. -M. Peng, *J. Chem. Soc., Chem. Commun.,* **1991**, 514.
41. W. -H. Chan, S. -M. Peng, and C. -M. Che, *J. Chem. Soc. Dalton Trans.,* **1998**, 2867.
42. R. Clerac, F. A. Cotton, L. M. Daniels, J. Gu, C. A. Murillo, and H. -C Zhou,. *Inorg. Chem.,* **2000**, *39*, 4488.
43. T. J. Hurley, and M. A. Robinson, *Inorg. Chem.* **1968**, *7*, 33.
44. S. Aduldecha, and B. Hathaway, *J. Chem. Soc. Dalton Trans.*, **1991**, 993.
45. R. Clerac, F. A. Cotton, K. R. Dunbar, C. A. Murillo, I. Pascual, and X. Wang, *Inorg. Chem.* **1999**, *38*, 2655.
46. J. F. Berry, F. A. Cotton, and C. A. Murillo, *Dalton Trans.,* **2003**, 3015.
47. P. Kiehl, M. -M. Rohmer, M. Benard, *Inorg. Chem.,* **2004**, *43*, 3151.
48. M. -Y. Huang, C. -Y. Yeh, S. -M. Peng, *Dalton Trans.,* **2006**, 5683.
49. X. Lopez, M. Benard, and M. M. Rohmer, *Inorg., Chem.* **2007**, *46*, 5.
50. J. F. Berry, F. A. Cotton, L. M. Daniels. and C. A. Murillo, *J. Am. Chem. Soc.,* **2002**, *124*, 3212.
51. F. A. Cotton, P. Lei, C. A. Murillo, *Inorg. Chim. Acta,* **2003**, *351*, 183.
52. R. H. Ismayilov, W. -Z. Wang, G. -H. Lee, R. -R. Wang, I. P. -C. Liu, C. -Y. Yeh, and S. M. Peng, *Dalton Trans.,* **2007**, 2898.
53. F. A. Cotton, H. Chao, C. A. Murillo, and Q. Wang, *Dalton Trans.,* **2006**, 5416.
54. S. -Y. Lai, T. -W. Lin, Y. -H. Chen, C. -C. Wang, G. -H. Lee, M. Yang, M. Leung, and S. -M. Peng, *J. Am. Chem. Soc.,* **1999**, *121*, 250.
55. X. Lopez, M. -Y. Huang, G. -C. Huang, S. -M. Peng, F. -Y. Li, M. Benard, and M. M. Rohmer, *Inorg. Chem.* **2006**, *45*, 9075.
56. (a) S. -J. Shieh, C. -C. Chou, G. -H. Lee, C. -C. Wang, and S. -M. Peng, *Angew. Chem. Int. Ed. Engl.,* **1997**, *36*, 56. (b) C. -Y. Yeh, Y. -L. Chiang, G. -H. Lee, and S. -M. Peng, *Inorg. Chem.* **2002**, *41*, 4096.
57. C. -C. Wang, W. -C. Lo, C. -C. Chou, G. -H. Lee, J. -M. Chen, and S. -M. Peng, *Inorg. Chem.* **1998**, *37*, 4059.
58. J. F. Berry, F. A. Cotton, T. Lu, C. A. Murillo, and X. Wang, *Inorg. Chem.,* **2003**, *42*, 3595.
59. J. F. Berry, F. A. Cotton, P. Lei, T. Lu, and C. A. Murillo, *Inorg. Chem.,* **2003**, *42*, 3534.
60. C. -H. Chien, J. -C. Chang, C. -Y. Yeh, G. -H. Lee, J. -M. Fang, Y. Song, and S. M. Peng, *Dalton Trans.,* **2006**, 3249.
61. T. -B. Tsao, S. -S. Lo, C. -Y. Yeh, G. -H. Lee, and S. -M. Peng, *Polyhedron*, **2007**, *26*, 3833.
62. H. Hasan, U. -K. Tan, G. -H. Lee, and S. -M. Peng, *Inorg. Chem. Commun.,* **2007**, *10*, 983.
63. I. -W. P. Chen, M. -D. Fu, W. -H. Tseng, J. -Y. Yu, S. -H. Wu, C. -J. Ku, C. H. Chen, and S. M. Peng, *Angew. Chem. Int. Ed.,* **2006**, *45*, 5814.
64. S. -Y. Lin, I-W. P. Chen, C. -H. Chen, M. -H. Hsieh, C. -Y. Yeh, T. -W. Lin, Y. -H. Chen, and S. -M. Peng, *J. Phys. Chem. B* **2004**, *108*, 959.
65. D. -H. Chae, J. F. Berry, S. Jung, F. A. Cotton, C. A. Murillo, and Z. Yao, *Nano Lett.* **2006**, *6*, 165.

66. (a) T. Murahashi, and H. Kurosawa, *Coord. Chem. Rev.,* **2002**, *231*, 207. (b) S. Kannan, A. J. James, and P. R. Sharp, *J. Am. Chem. Soc.,* **1998**, *120*, 215.
67. H. J. Kurosawa, *Orgmet. Chem.* **2004**, *689*, 4511.
68. T. Murahashi, T. Nagai, T. Okuno, T. Matsutani, and H. Kurosawa, *Chem. Commun.*, 2000, 1689.
69. T. Murahashi, E. Mochizuki, Y. Kai, and H. Kurosawa, *J. Am. Chem. Soc.,* **1999**, *121*, 10660.
70. Y. Takahashi, K. Tsutsumi, Y. Nakagai, T. Morimoto, K. Kakiuchi, S. Ogoshi, and H. Kurosawa, *Organometallics*, **2008**, *27*, 276.
71. T. Murahashi, T. Nagai, Y. Mino, E. Mochizuki, Y. Kai, and H. Kurosawa, *J. Am. Chem. Soc.*, **2001**, *123*, 6927.
72. Y. Tatsumi, T. Naga, H. Nakashima, T. Murahashi, and H. Kurosawa, *Chem. Commun.*, **2004**, 1430.
73. T. Murahashi, Y. Higuchi, T. Katoh, and H. Kurosawa, *J. Am. Chem. Soc.,* **2002**, *124*, 14288.
74. Y. Tatsumi, T. Murahashi, M. Okada, S. Ogoshi, and H. Kurosawa, *Chem. Commun.,* **2008**, 477.
75. T. Murahashi, T. Uemura, and H. Kurosawa, *J. Am. Chem. Soc.,* **2003**, *125*, 8436.
76. Y. Tatsumi, K. Shirato, T. Murahashi, S. Ogoshi, and H. Kurosawa, *Angew. Chem. Int. Ed.,* **2006**, *45*, 5799.
77. T. Murahashi, N. Kato, T. Uemura, and H. Kurosawa, *Angew. Chem. Int. Ed.,* **2007**, *46*, 3509.
78. T. Murahashi, M. Fujimoto, M. Oka, Y. Hashimoto, T. Uemura, Y. Tatsumi, Y. Nakao, A. Ikeda, S. Sakaki, and H. Kurosawa, *Science*, **2006**, *313*, 1104.
79. P. Labeguerie, M. Bénard, and M. Róhmer, M. *Inorg. Chem.,* **2007**, *46*, 5283.
80. K. R. Mann, J. G. Gordon II, and H. B. Gray, *J. Am. Chem. Soc.*, **1975**, *97*, 3553.
81. K. R. Mann, N. S. Lewis, R. M. Williams, H. B. Gray, and J. G. Gordon II,. *Inorg. Chem.*, **1978**, *17*, 828.
82. H. Endres, N. Gottstein, H. J. Keller, R. Martin, W. Rodemer, and W. Z. Steiger, and *Naturforsch, B: Anorg. Chem. Org. Chem.*, **1979**, *34*, 827.
83. N. T. Tran, J. R. Stork, D. Pham, M. M. Olmstead, J. C. Fettinger, and A. L. Balch, *Chem. Commun.*, **2006**, 1130.
84. T. V. Ashworth, D. C. Liles, H. E. Oosthuizen, and E. Singleton, *Acta crystallogr., Sect. C: Cryst. Struct. Commun.*, **1984**, *40*, 1169.
85. J. W. Dart, M. K. Lloyd, R. Mason, and J. A. McCleverty, *J. Chem. Soc. Dalton Trans.*, **1973**, 2039.
86. K. R. Mann, M. J. DiPierro, and T. P. Gill, *J. Am. Chem. Soc.*, **1980**, *102*, 3965.
87. I. S. Sigal, K. R. Mann, and H. B. Gray,, *J. Am. Chem. Soc.*, **1980**, *102*, 7252.
88. S. S. Chern, G. H. Lee, and S. M. Peng, *J. Chem. Soc., Chem. Commun.*, **1994**, 1645.
89. S. S. Chern, M. C. Liaw, and S. M. Peng, *J. Chem. Soc., Chem. Commun.*, **1993**, 359.
90. S. M. Peng, D. S. Liaw, Y. Wang, and A. Simon, *Angew. Chem. Int. Ed. Engl.*, **1985**, *24*, 210.
91. C. W. Lange, M. Foldeaki, V. I. Nevodchikov, V. K. Cherkasov, G. A. Abakumov, and C. G. Pierpont, *J. Am. Chem. Soc.*, **1992**, *114*, 4220.
92. V. I. Nevodchikov, G. A. Abakumov, V. K. Cherkasov, and G. A. Razuvaev, *J. Organomet. Chem.*, **1981**, *214*, 119.
93. (a) L. N. Zakarov, Y. T. Struchkov, G. A. Abakumov, and V. I. Nevodchikov, *Koord. Khim.*, **1990**, *16*, 1101. (b) G. C. Gordon, P. W. DeHaven, M. C. Weiss, V. L. Goedken,

J. Am. Chem. Soc., **1978**, *100*, 1003. (c) A. Takenaka, Y, Sasada, T. Omura, H. Ogoshi, and Z. I Yoshida,. *J. Chem. Soc., Chem. Commun.*, **1973**, 792. (d) N. A. Bailey, E. Coates, G. B. Robertson, F. Bonati, and R. Ugo, *J. Chem. Soc. Chem. Commun.*, **1967**, 1041.

94. N. S. Lewis, K. R. Mann, J. G. Gordon II, and H. B. Gray, *J. Am. Chem. Soc.*, **1976**, *98*, 7461.
95. M. Mitsumi, S. Umebayashi, Y. Ozawa, M. Tadokoro, H. Kawamura, and K. Torumi, *Chem. Lett.*, **2004**, *33*, 970.
96. C. G. Pierpont, *Coord. Chem. Rev.*, **2001**, *99*, 216.
97. M. Mitsumi, H. Goto, S. Umebayashi, Y. Ozawa, M. Kobayashi, T. Yokoyama, H. Tanaka, S. Kuroda, and K. Toriumi, *Angew. Chem. Int. Ed.*, **2005**, *44*, 4164.
98. H. C. Chang, K. Mochizuki, and S. Kitagawa, *Inorg. Chem.,* **2002**, *41*, 4444.
99. G. M. Finniss, E. Canadell, C. Campana, and K. R. Dunbar, *Angew. Chem. Int. Ed.*, **1996**, *35*, 2772.
100. (a) K. R. Dunbar, *J. Am. Chem. Soc.,* **1988**, *110*, 8247. (b) M. E. Prater, L. E. Pence, R. Clerac, G. M. Finniss, C. Campana, P. Auban-Senzier, D. Jerome, E. Canadell, and K. R. Dunbar, *J. Am. Chem. Soc.*, **1999**, *121*, 8005.
101. (a) F. A. Cotton, E. V. Dikarev, and M. A. Petrukhina, *J. Organomet. Chem.*, **2000**, *596*, 130. (b) F. A. Cotton, E. V. Dikarev, and M. A. Petrukhina, *J. Chem. Soc. Dalton Trans.*, **2000**, 4241.
102. (a) F. P. Pruchnik, P. Jakimowicz, Z. Ciunik, K. Stanislawek, L. A. Oro, C. Tejel, and M. A. Ciriano, *Inorg. Chem. Commun.,* **2001**, *4*, 19. (b) F. P. Pruchnik, P. Jakimowicz, and Z. Ciunik, *Inorg. Chem. Commun.,* **2001**, *4*, 726.
103. F. Lafolet, S. Chardon-Noblat, C. Duboc, A. Deronzier, F. P. Pruchnik, and M. Rak, *Dalton Trans.*, **2008**, 2149.
104. (a) M. A. Ciriano, B. E. Villarroya, L. A. Oro, M. C. Apreda, C. Foces-Foces, and F. H. Cano, *J. Organomet. Chem.*, **1989**, *366*, 377. (b) G. S. Rodean, and K. R. Mann, *Inorg. Chem.*, **1988**, *27*, 3388.
105. C. Tejel, M. A. Ciriano, B. E. Villarroya, R. Gelpi, J. A. Lopez, F. J. Lahoz, and L. A. Oro, *Angew. Chem., Int. Ed.,* **2001**, *40*, 4084.
106. C. Tejel, M. A. Ciriano, B. E. Villarroya, J. A. Lopez, F. J. Lahoz, and L. A. Oro, *Angew. Chem., Int. Ed.,* **2003**, *42*, 530.
107. (a) M. A. Ciriano, S. Sebastian, L. A. Oro, A. Tiripicchio, M. T. Camellini, and F. J. Lahoz, *Angew. Chem., Int. Ed.,* **1988**, *27*, 402. (b) C. Tejel, M. A. Ciriano, and L. A. Oro, *Chem. Eur. J.* **1999**, *5*, 1131.
108. C. Tejel, M. A. Ciriano, J. A. Lopez, F. J. Lahoz, and L. A. Oro, *Angew. Chem., Int. Ed.,* **1998**, *37*, 1542.
109. B. E. Villarroya, C. Tejel, M. Rohmer, L. A. Oro, M. A. Ciriano, and M. Benard, *Inorg. Chem.,* **2005**, *44*, 6536.
110. (a) F. Scherbaum, A. Grohmann, B. Huber, C. Kruger, and H. Schmidbaur, *Angew. Chem. Int. Ed. Engl.,* **1988**, *27*, 1544. (b) P. Pyykko, J. Li, and N. Runeberg, *Chem. Phys. Lett.*, **1994**, *218*, 133. (c) P. Pyykko, *Angew. Chem., Int. Ed.*, **2004**, *43*, 4412.
111. J.C. Vickery, M. M. Olmstead, E. Y. Fung, and A. L. Balch, A. *Angew. Chem. Int. Ed.,* **1997**, *36*, 1179.
112. (a) L. Malatesta, and M. Angoletta, *J. Inorg. Nucl. Chem.,* **1958**, *8*, 273. (b) L. Malatesta, and F. Canjiani, *J. Inorg. Nucl. Chem.* **1961**, *19*, 81.
113. M. J. Cleare, and W. P. Griffith, *J. Chem. Soc., A* **1970**, 2788.
114. (a) L. N. Buravov, R. N. Stepanova, M. L. Khidekel, and I. F. Shchegolev, *Dokl. Akad. Nauk SSSR*, **1972**, *203*, 819. (b) A. P. Ginsberg, J. W. Koepke, J. J. Hauser,

K. W. West, F. J. DiSalvo, C. R. Sprinkle, and R. L. Cohen, *Inorg. Chem.,* **1976**, *15*, 514.

115. (a) H. Awano, S. Sakai, T. Kuriyama, Y Ohba. *Bull. Chem. Soc. Jpn.* **1994**, *67*, 1737. (b) P. Batail, K. Boubekeyr, M. Fourmigue, and J. -C. Gabriel, *Chem. Mater.*, **1998**, *10*, 3005.
116. (a) J. S. Miller. *Science*, **1976**, *194*, 189. (b) J. M. Williams, D. P. Gerrity, A. J. Schultz, *J. Am. Chem. Soc.*, **1977**, *99*, 1668.
117. Y. Orihashi, H. Ohno, E. Tsuchida, H. Matsuda, H. Nakanishi, and M. Kato, *Chem. Lett.*, **1987**, 601.
118. H. Awano, T. Kumazawa, and K. Kasuya, *Electrochim. Acta* **1997**, *42*, 483.
119. J. Pei and X. Li, *J. Solid State Electrochem.*, **2000**, *4*, 131.
120. M. Wysocka, K. Winkler, J. R. Stork, and A. L. Balch, *Chem. Mater.*, **2004**, *16*, 771.
121. D. C. Loveday, A. R. Hillman, A. G. Orpen, P. G. Pringle, and M. Hepel, *J. Mater. Chem.* **1996**, *6*, 993.
122. S. K. Patra, S. M. W. Rahaman, M. Majumdar, A. Sinha, and J. K. Bera, *Chem. Commun.*, **2008**, 2511.
123. (a) N. Masciocchi, A. Sironi, S Chardon-Noblat, and A. Deronzier, *Organometallics* **2002**, *21*, 4009. (b) F. Hartl, T. Mahabiersing, S. Chardon-Noblat, P. Da Costa, and A. Deronzier, *Inorg. Chem.*, **2004**, *43*, 7250.
124. K. A. Hofmann, and G. Bugge, *Ber. Dtch. Chem. Ges.*, **1908**, *41*, 312.
125. R. D. Gillard, and G. Wilkinson, *J. Chem. Soc.*, **1964**, 2835.
126. (a) J. P. Davidson, P. J. Faber, R. G. Fischer, S. Mansy, Jr. H. J. Peresie, B. Rosenberg, and L. V. Camp, *Cancer Chemother. Rep. Part 1*, **1975**, *59*, 287. (b) B. Rosenberg, *Cancer Chemother. Rep. Part 1*, **1975**, *59*, 589. (c) J. K. Barton, H. N. Rabinowitz, D. J. Szalda, and S. J. Lippard, *J. Am. Chem. Soc.*, **1977**, *99*, 2827.
127. (a) J. K. Barton, D. J. Szalda, H. N. Rabinowitz, J. V. Waszczak, and S. J. Lippard, *J. Am. Chem. Soc.*, **1979**, *101*, 1434. (b) A. P. Ginsberg, T. V. O'Halloran, P. E. Fanwick, L. S. Hollis, S. J. Lippard, *J. Am. Chem. Soc.*, **1984**, *106*, 5430.
128. (a) T. V. O'Halloran, M. M. Roberts, and S. J. Lippard, *J. Am. Chem. Soc.*, **1984**, *106*, 6427. (b) T. V. O'Halloran, P. K. Mascharak, P. K. Williams, P. K. Roberts, and S. J. Lippard, *Inorg. Chem.*, **1987**, *26*, 1261.
129. C. Tejel, C. Ciriano, and L. A. Oro, *Chem. Eur. J.*, **1999**, *5*, 1131.
130. C. A. Murillo, *in Multiple Bonds Between Metal Atoms*, 3rd Ed. F. A. Cotton, C. A. Murillo, and R. A. Walton, Springer Science and Buisness Media, New York, **2005**; chap. 14.
131. K. Matsumoto, H. Takahashi, and K. Fuwa, *J. Am. Chem. Soc.*, **1984**, *106*, 2049.
132. K. Matsumoto. *Bull. Chem. Soc. Jpn.*, **1985**, *58*, 651.
133. (a) K. Matsumoto, and K. Fuwa, *J. Am. Chem. Soc.*, **1982**, *104*, 897. (b) K. Matsumoto, H. Takahashi, and K. Fuwa, *Inorg. Chem.*, **1983**, *22*, 4086.
134. K. Sakai, T. Tsubomura, and K. Matsumoto, *Inorg. Chim. Acta*, **1993**, *213*, 11.
135. K. Matsumoto, and T. Watanabe, *J. Am. Chem. Soc.*, **1986**, *108*, 1308.
136. (a) P. K. Mascharak, I. D. Williams, and S. J. Lippard, *J. Am. Chem. Soc.*, **1984**, *106*, 6428. (b) B. Lippert, H. Schollhorn, and U. Thewalt, *Inorg. Chem.*, **1987**, *26*, 1736.
137. B. Lippert, and D. Neugebauer, *Inorg. Chem.*, **1982**, *21*, 451.
138. K. Sakai, and K. Matsumoto, *J. Am. Chem. Soc.*, **1989**, *111*, 3074.
139. K. Sakai, E. Ishigami, Y. Konno, T. Kajiwara, and T. Ito, *J. Am. Chem. Soc.*, **2002**, *124*, 12088.

140. K. Uemura, K. Fukui, H. Nishikawa, S. Arai, K. Matsumoto, and H. Oshio, *Angew. Chem. Int. Ed.*, **2005**, *44*, 5459.

141. S. Arai, M. Ochiai, K. Ishihara, and K. Matsumoto, *Eur. J. Inorg. Chem.*, **2007**, 2031.

142. W. Chen, F. Liu, K. Matsumoto, J. Autschbach, B. L. Guennic, F. Ziegler, M. Maliarik, and J. Glaser, *Inorg. Chem.*, **2006**, *45*, 4526.

143. W. Chen, F. Liu, D. Xu, K. Matsumoto, S. Kishi, and M. Kato, *Inorg. Chem.*, **2006**, *45*, 5552.

CHAPTER 6

Boronate-Linked Materials: Ranging from Amorphous Assemblies to Highly Structured Networks

Brett M. Rambo, R. William Tilford, Laura M. Lanni, Jie Liu, and John J. Lavigne

Department of Chemistry and Biochemistry, University of South Carolina

CONTENTS

Macromolecules Containing Metal and Metal-Like Elements,
Volume 9: Supramolecular and Self-Assembled Metal-Containing Materials,
Edited by Alaa S. Abd-El Aziz, Charles E. Carraher Jr., Charles U. Pittman Jr., and Martel Zeldin.

I. INTRODUCTION AND SCOPE

Since their discovery nearly two centuries ago,[1] boronic acids have developed a rich history, though it has been only in the past few decades that the breadth and use of this functional group has truly emerged. Specifically, boronic acids are boron-containing organic compounds that possess one alkyl or aryl substituent and two hydroxyl groups (Fig. 1). The resulting sp^2 hybridization around the boron confers a trigonal planar geometry to the boron center and is structurally analogous to a carboxylic acid.[2] In a manner similar to carboxylic acids, boronic acids can undergo substitution reactions to replace the $-$OH groups with $-$OR groups to generate boronate esters. Uniquely though, both hydroxyl moieties can be replaced to afford diesters. The cyclic versions, which arise from 1,2- and 1,3-diols tend to be more stable than their acyclic analogs (Fig. 1).[3] These esters form in aqueous media at elevated pH or, if an internal Lewis base can coordinate to the boron, complexation occurs at neutral pH.[4] In nonaqueous media, ester formation is facile with the removal of water. The principal interest and utility found in this boronate ester formation resides in the stable covalent bonds formed with alcohols (bonding energies of $\sim$536 kJ/mol for B–OR) that also display reversibility based on nucleophilic displacement that is more facile than the

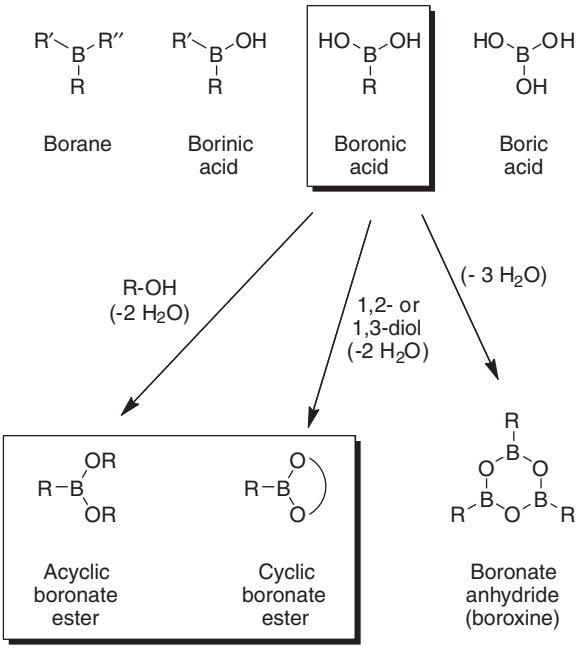

FIGURE 1. Boron-containing functional groups. Boronic acids undergo dehydration reactions on their own (anhydrides) and with alcohols to form acyclic and cyclic diesters.

more conventional carboxylic esters.[5] This covalent yet reversible nature forms the basis of the utility of boronate ester formation in many diverse applications.

From a historical perspective, boronic acids/esters have perhaps found their widest applicability as building blocks in organic synthesis, most notably as reactive intermediates in Suzuki cross-coupling reactions (conversion of boronic acids to their cyclic esters typically enhances solubility of these synthons).[6] Subsequently, boronic acids/esters have found use as components in numerous other synthetic transformations. While not within the scope of this review, more detailed descriptions of these facilities have been outlined in numerous other resources.[7] Furthermore, the boronic acid–ester equilibrium has proven to be a useful recognition motif for the creation of molecular sensors targeting diol-containing analytes, such as sugars. Numerous reviews can be found for the reader seeking more information on this topic.[8]

Boron-containing polymers in which the boron is not integral in the main chain (such as side-chain functionalized polyolefins and conjugated polymer sensors) or other organoboron polymers that do not include boronate esters (such as polyboranes) are beyond the scope of this review. The interested reader is referred to more general references on boron-containing polymers.[9] Similarly, boronate anhydride–containing analogs, although closely related to boronate esters, will not be discussed within the context of this review, though references will be provided when relevant. The scope of this chapter focuses on macromolecular and polymeric materials development based on the boronate ester functionality.

As an outline for this review, various supramolecular and macromolecular architectures have recently been developed that rely on boronate ester formation to define their structure and function. For instance, small molecule diesters have displayed supramolecular self-assembly in the solid state based on a unique, noncovalent phenyl-boron-phenyl sandwich motif. Subsequently, these small oligomers have been coordinately linked together to generate macrocycles and other polymers relying on ester formation to obtain the desired products. In progression, covalently linked poly(boronate ester) macrocyclic and linear structures have also been formed, demonstrating self-repair capabilities as well as leading to a new class of wide band-gap semiconducting materials. Finally, through the incorporation of polyvalent boronates, covalent organic frameworks (COFs) have been generated, taking advantage of the covalent-reversible nature of the boronate ester linkage to create highly crystalline, porous network materials.

II. SUPRAMOLECULAR BORONATE ASSEMBLIES

There is abundant information available on supramolecular assemblies that incorporate boronic acids. The vast majority of these ensembles have been observed primarily in the solid state, though several are stable in solution. This section begins with a brief discussion of hydrogen bonded assemblies, followed

by discussion of a relatively novel assembly strategy based on the formation of a phenyl-boron-phenyl sandwich. More conventional macrocyclic and linear assemblies ensue based on coordination phenomena. Here, the most common strategy relies on coordination between a Lewis basic amine and some electron deficient atom. The Lewis acid component can either be a cationic metal or the empty *p*-orbital on boron.

A. "Traditional" Hydrogen Bonded Supramolecular Assemblies

Given the focus of this review on boronate ester–containing materials, it perhaps seems odd to begin with a brief discussion of hydrogen bonded assemblies. However, such a large portion of the supramolecular chemistry that involves boronate derivative containing building blocks relies on this motif, thereby warranting mention.

Even simple monoboronic acids, such as phenyl boronic acid, are known to hydrogen bond into supramolecular architectures.[10] Much like carboxylic acids, boronic acids also tend to dimerize (Fig. 2a). However, given the additional hydrogen compared to their carbon analogs, boronic acid dimers often associate through additional lateral hydrogen bonds with adjacent dimers into ribbon structures (Fig. 2b).[11] Similar motifs have been observed for certain amides.[12] Diboronic acids, such as phenylene-1,4-diboronic acid, form linear chains from linking these ditopic compounds end to end and subsequently tying these ribbon structures together into sheets (Fig. 2c).[13] In a predictable manner, addition of a compound that can disrupt this lateral hydrogen bonding, such as THF, can basically unweave the sheets to produce linear threads (Fig. 2d).[11] Difunctional ethers such as 1,4-dioxane again link these chains together into sheets; however, these assemblies are now less dense than the original, solely hydrogen bonded networks (Fig. 2e).[11]

Maintaining this theme of using boronic acids as co-crystallizing agents capable of forming heteromeric structures, numerous other assemblies have been observed. For example, bipyridine and amino-pyridine hydrogen bond acceptors have been used with simple monoboronic and diboronic acids to create macromolecular boxes, ladders, and infinite chains and sheets (Fig. 3a).[14] Alcohol-containing monomers such as 1,2,4,5-tetrahydroxybenzene have also been assembled with diboronic acids in which both the boronic acid and bis-diol building blocks serve as hydrogen bond donors and acceptors (Fig. 3b).[15] This complex bonding motif forms infinite two-dimensional (2D) corrugated sheets that negate boronic acid dimer formation. Still other heterodimeric structures have been reported involving boronic acids with carboxylic acids and carboxylate anions.[16]

B. "Novel" Phenyl-Boron-Phenyl Sandwich Supramolecular Assembly

Boronate ester formation precludes the involvement of the boron containing moiety serving as a hydrogen bond donor in hydrogen bonding interactions,

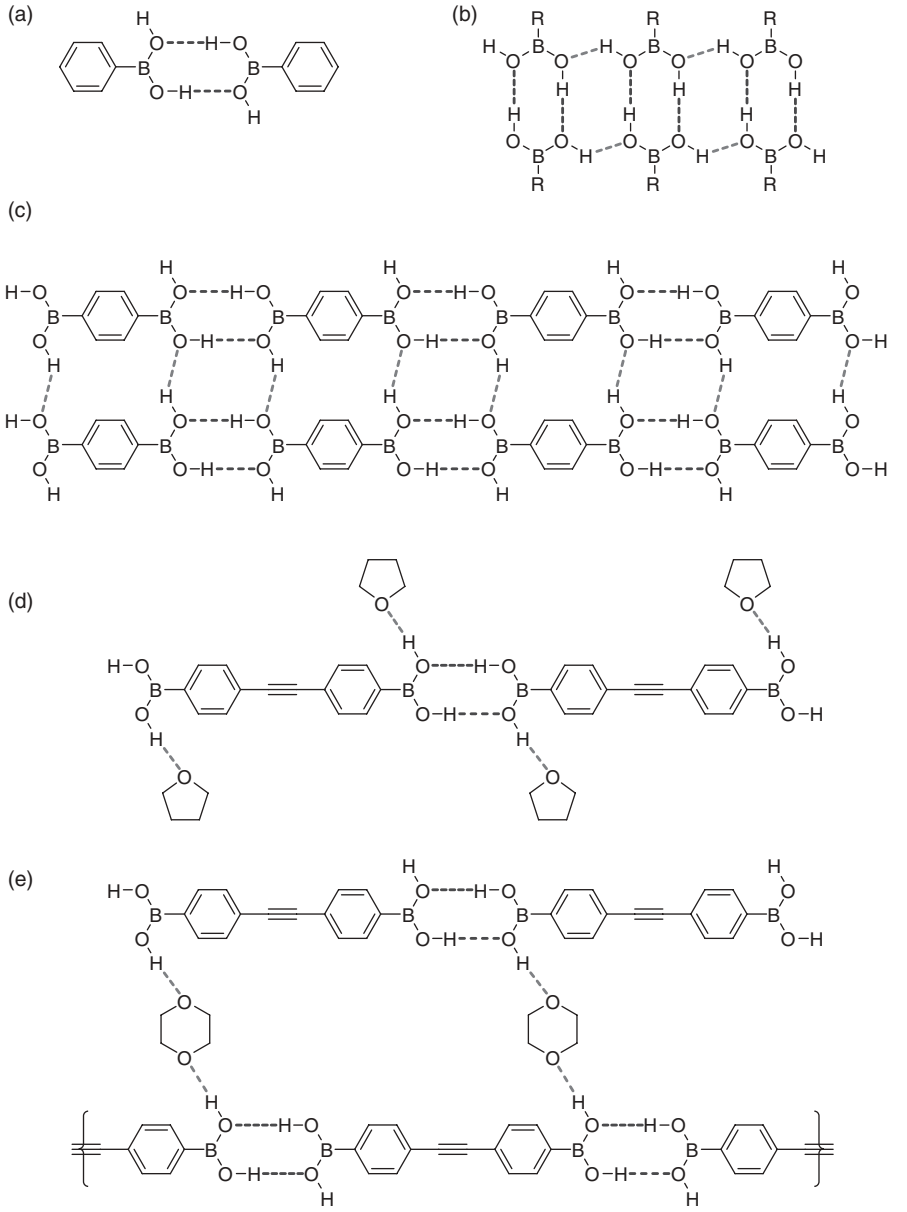

FIGURE 2. Hydrogen bonding motifs found from boronic acids. Simple diesters (a) link together via lateral hydrogen bonds to form ribbons (b) Diboronic acids form chains (c) that are linked into sheets by lateral hydrogen bonds (d). Alternate structures can be obtained by interrupting lateral bonding with monoethers (d) and diethers (e).

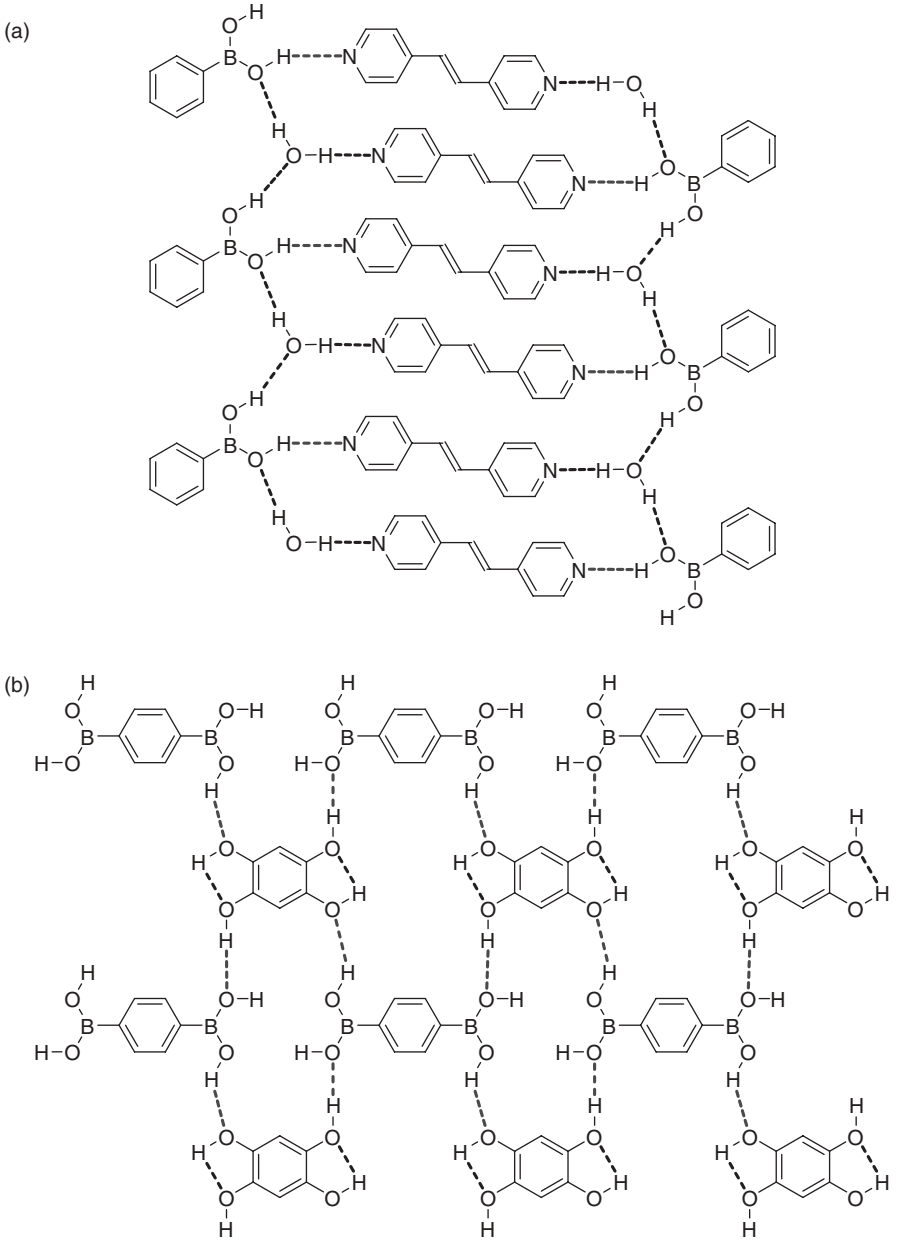

FIGURE 3. Boronic acids form hetero-dimeric hydrogen bonded complexes with (a) hydrogen bond accepting bipyridines and (b) hydrogen bond donating and accepting bis-diols.

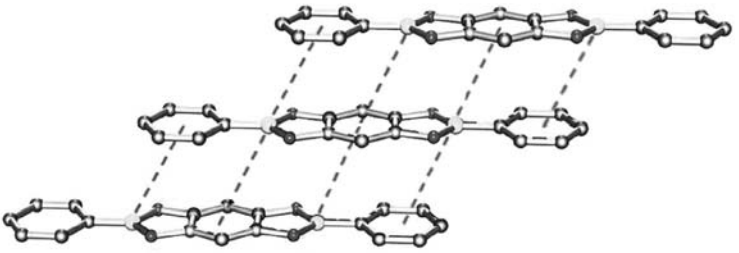

FIGURE 4. Electron-deficient boron atoms (yellow) in aromatic boronate esters tend to stack in supramolecular assemblies between electron-rich π-clouds, forming a phenyl-boron-phenyl sandwich.

and thus different intermolecular forces dictate the assembly of this functionality. Solid-state studies have shown that substituents on the boronate esters often direct the overall three-dimensional assembly of these compounds.[17] However, regardless of the variations in the solid-state assembly previously observed, these compounds consistently display a strong stacking preference wherein the empty *p*-orbital of the sp^2-hybridized, trigonal planar boron atom is sandwiched between the electron-rich π-clouds of adjacent phenyl rings.[18,17] This phenyl-boron-phenyl sandwich motif is particularly notable for mono and bis(dioxaborole)s (planar, 5-membered boronate esters) stemming from both diboronic acid and bis-diol central ester bridges (Fig. 4).[17,18b] The resulting offset π-stacked arrangements form columnar supramolecular structures that have been denoted in a number of solid-state analyses but have yet to be quantified in solution. With the perpendicular distance between adjacent parallel molecules ranging from 3.3 to 3.6 Å in the solid state, there is precedence on how to control this stacking. Such distinctions in intermolecular spacing between π-stacked layers can be important in tuning the conductive properties in electronic materials.[19]

C. Coordination-Based Macrocyclic Assemblies

The directional bonding afforded by boronate ester formation, allows selection of the desired geometric outcome by careful design of the constituent building blocks. Taking advantage of this paradigm, the structure and bonding in macrocycles and cages containing boron has received great attention and has been recently reviewed.[20] The diversity found in these structures is vast. While supramolecular structures incorporating three- and four-coordinate boron atoms, based on boranes, borinic acids, boronic acids, and boric acid all exist, this discussion focuses on tricoordinate and tetracoordinate boronate ester derivatives.

Of those cycles that incorporate boronate esters as an integral linkage, many involve some coordinative event between Lewis acidic and Lewis

basic moieties found in the building blocks. One approach is to use coordinating moieties, most often amines, as part of the boronate component that combines with metal centers in other monomers to enforce cyclization. Alternatively, the Lewis base may be used to coordinate to the empty *p*-orbital on the boron, forming an anionic tetra-coordinate center. In this situation, the boron is integral for forming not only the ester but also serving as the point of coordination, leading to cyclic, thermodynamically stable products. It is interesting to note that the amine coordination is stronger with the ester than with the acid, while at the same time coordination of the Lewis base with the acid kinetically enhances ester formation.

Conceptually, this was first demonstrated using a metallated porphyrin that was functionalized with 2 diols (zinc dicatechol porphyrin) (Fig. 5).[21] After addition of 3-pyridylboronic acid, absorption spectroscopy indicated that the pyridyl moiety was coordinated to the Zn-porphyrin. The observed affinity constant for this interaction, however, was more than 30 times what was expected for a simple pyridyl-Zn-porphyrin complex. It was, therefore, reasoned that the diols reacted with the boronic acids to afford the esters that would result in a cyclic structure (Fig. 5). Indeed, vapor phase osmometry (VPO) confirmed the 2:2 dimeric nature of the complex. Here the ester served as the key covalent linkage, though associated coordination was required between the metal and pyridine to create the cyclic structure.

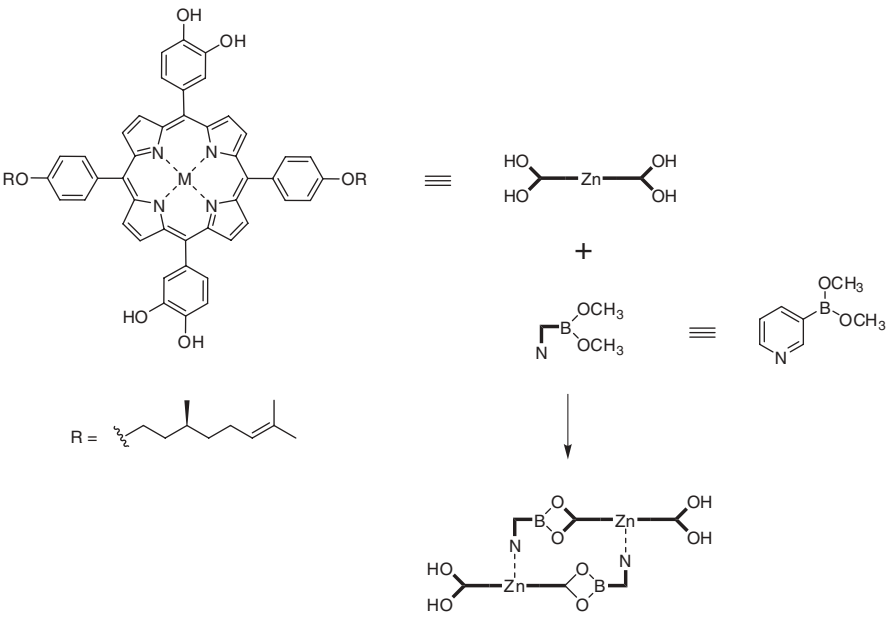

FIGURE 5. Bis-diol functionalized porphyrins assemble into macrocycles based on boronate ester formation coupled with metal ligation to a Lewis basic pyridine.

Alternatively, the metal binding and diol binding functionality could be incorporated into the same molecule. For example, sugars have been used to cyclize boronic acid appended 2,2′-bipyridine[22] and phenanthroline-based[23,24] metal complexes. The order of addition plays a substantial role in defining the type of structures that are obtained through this tandem assembly process. For example, if metallation occurs first, the boronic acids are organized in a manner to bind only one sugar, resulting in a simple cycle (in a 1:2:1 ratio of metal: boronic acid: sugar) (Fig. 6a).[22,24] CD was used to show that, depending on the chirality of the sugar, different helical structures were obtained (D-glucose produced a P-form helicate, whereas L-glucose resulted in an M-form structure).[24] Subsequently, initial ester formation produces two distant metal binding sites such that addition of metal now produces helical complexes involving two metal centers, four phenanthroline units, and two saccharides (2:4:2 adduct) (Fig. 6b).[23] Formation of these dimeric, dinuclear helicates was confirmed by MS. These assemblies also displayed saccharide-specific helical chirality.

One might then expect that using diboronic acid–appended metal binders would result in oligomeric structures. However, polymeric materials were not observed, rather, depending on the nature of the bridging saccharide used in the assembly, helicates and catenates were formed.[25] Metallation before boronate ester formation resulted in the expected 2:1 complex, and those tetraboronic acids bind two discrete sugars (such as glucose, maltose, and maltahexaose). Again, the helical twist was defined by the stereogenicity of the sugar. It was found that short monosaccharides and disaccharides formed helicates, whereas longer oligosaccharides formed catenates. This results from how the sugars interact with the boronic acids of the phenanthroline-metal complex. Using modeling and CD spectroscopic analysis, it was found that short saccharides bind to boronic acids on the different ligands because they are closer in space to form helicates (Fig. 7). Alternately, longer sugars produce catenates because they bind with boronic acids on the same ligand (Fig. 7), again based on length arguments. It is important that both boronate ester formation and metal ligation are again required for cyclization.

It has further been shown that cobaloximes display reactivity similar to cis-diols toward boronic acids.[26] It then follows that reaction of methylaquacobaloxime with 3-pyridylboronic acid would produce a 2 + 2 adduct as described earlier (Fig. 8a).[27,28] Indeed, X-ray diffraction has confirmed that this combination results in a cyclic dimer with coplanar pyridyl moieties. It is interesting that if 4-pyridylboronic acid is used instead, a similar dimeric structure is formed, but the pyridyl rings are now parallel (Fig. 8b).[28–30] This self-assembly is reversible, dependening on pH. Subsequently, cycles that are formed near a pH of 7 can be disassembled by lowering the pH < 4 or raising it > 9. These dimers reform when the pH is returned to near neutral. An analogous trimer is generated when this cobaloxime is combined with 3-aminophenylboronic acid (Fig. 8c).[30,31] It is interesting that even in methanol, the cobaloxime-boronate ester maintains its tetracoordinate hydroxy-ligand, which is involved in hydrogen bonding within the cycle to the adjacent cobalt-coordinated anilino-nitrogen.

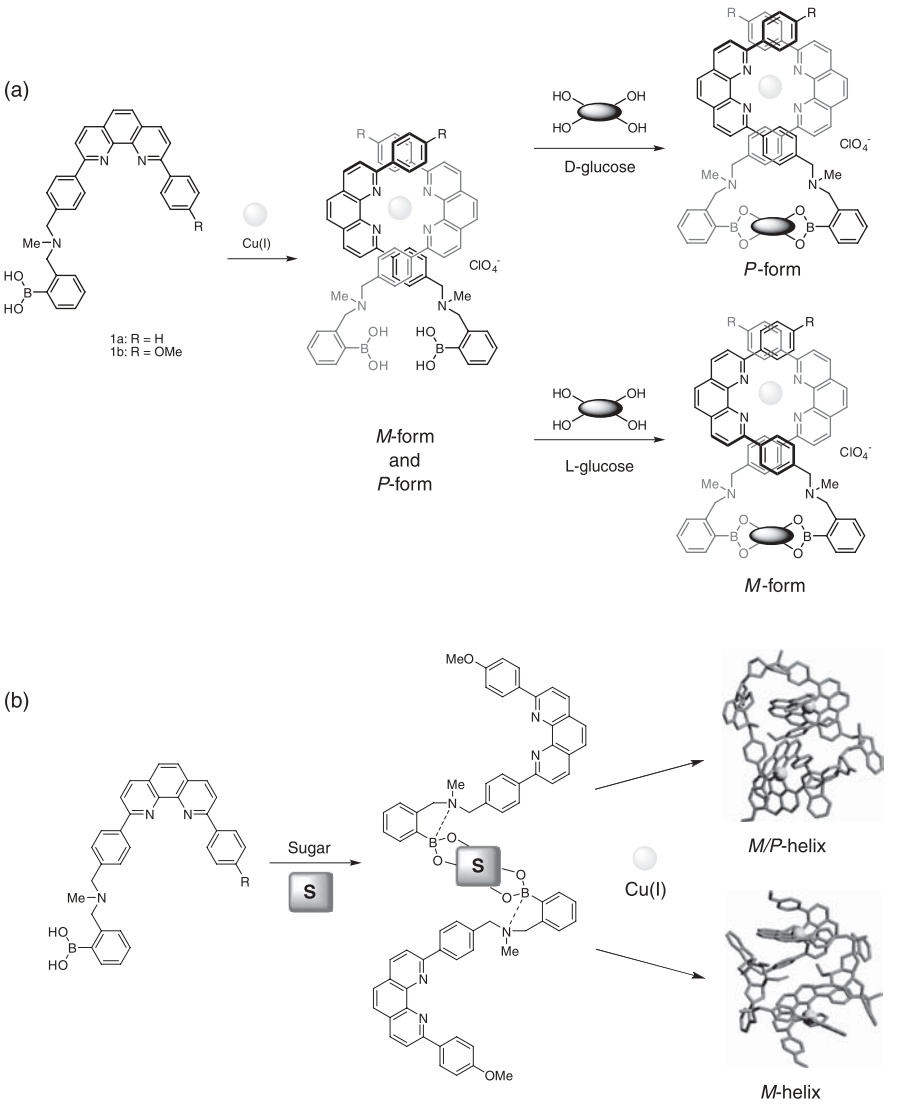

FIGURE 6. The resulting structures formed from boronic acid–appended phenanthroline depends on the order of construction. (a) Metallation forms duplexes that bind one sugar, producing helices in which the stereochemical outcome depends on the nature of the sugar. (b) Forming the ester before metallation results in larger helical bimetallic complexes (Reprinted with permission from Ref. 23. Copyright 2000 Elsevier.)

Maintaining approximate C_3 symmetry, this hydrogen bond helps essentially "freeze" the cycle and limit most conformational freedom.

Unlike the examples given, the boronate ester can be involved in both the covalent and coordinative tethers involved in completing the macrocyclization

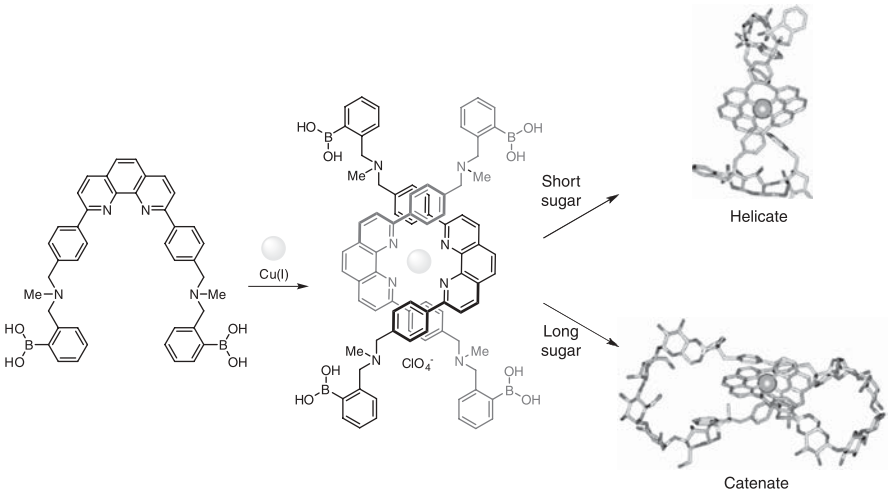

FIGURE 7. Phenanthroline diboronic acids complex one metal and two saccharides. Helicates form with short sugars, whereas catenates form with longer sugars (Reprinted with permission from Ref. 25. Copyright 2002 Elsevier.)

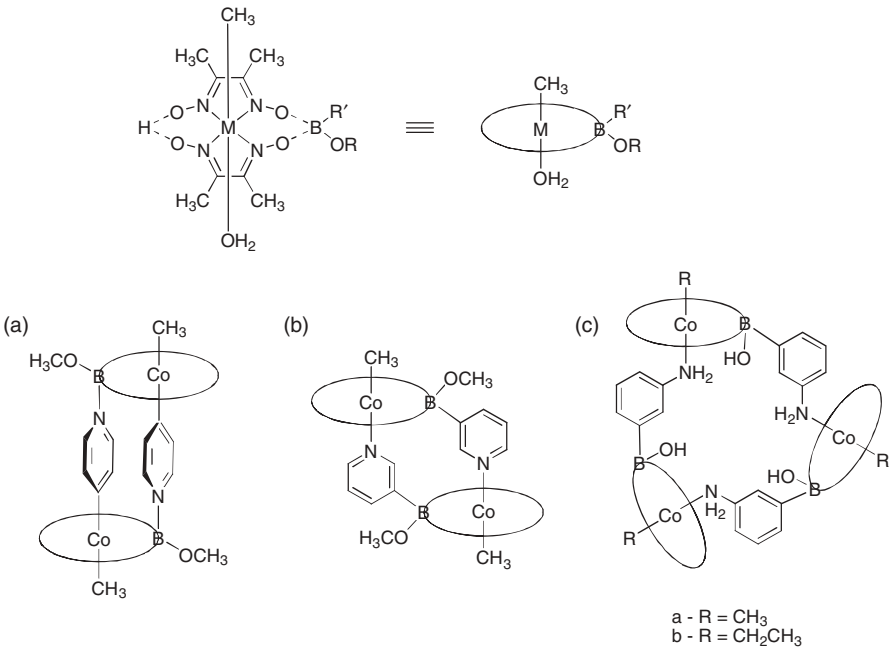

FIGURE 8. Cobaloximes have been shown to form boronate esters with pyridyl boronic acids to produce (a) a dimeric "molecular box," (b) a "molecular parallelogram," and (c) trimeric assemblies

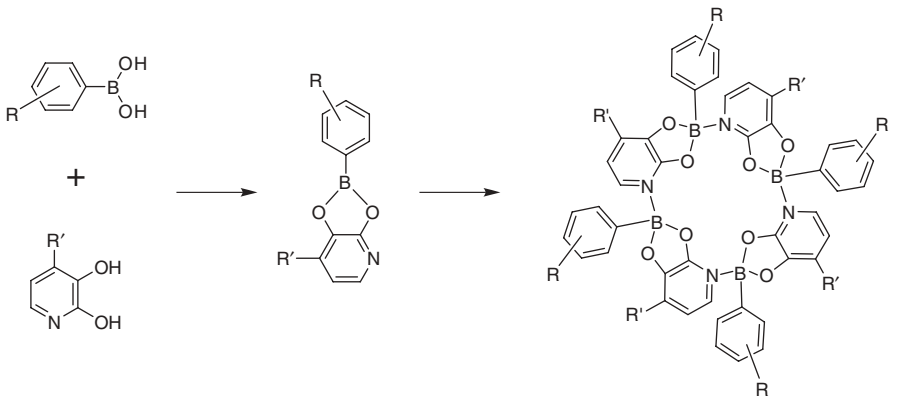

FIGURE 9. Boronate esters, formed from aryl boronic acids and 2,3-dihydroxypyridine, serve as Lewis acidic coordination sites, leading to the formation of a tetrameric macrocycle.

process. Here, instead of having the Lewis base ligated to some metal center, the cycle is formed by the creation of a dative B-N bond.[32] Cyclization was observed on condensation of 2,3-dihydroxypyridine with phenylboronic acids to form highly symmetrical complexes (Fig. 9)[33] as indicated by NMR spectroscopies. Single crystal X-ray diffraction confirmed that the boronic acid had undergone dehydration with the aromatic diol to form the five-membered cyclic boronate ester, and subsequent complexation between the ester and an intermolecular pyridyl amine resulted in a tetrameric assembly with perfect S_4 symmetry. It is interesting that the B-N bond length is relatively short in these complexes compared to other relevant tetrahedral boronates with N-donor ligands[32d,34] suggesting enhanced thermodynamic stability. The kinetic stability of the cycles was demonstrated by performing scrambling experiments, in which two differently substituted tetramers were mixed in chloroform. Even after 24 h, no mixed species were apparent by ^{1}H NMR.

Subsequent studies with the isomeric diol, 3,4-dihydroxypyridine, provided pentameric assemblies when reacted with aryl and alkyl boronic acids (Fig. 10).[35] In contrast to the tetrameric assemblies formed with 2,3-dihydroxypyridine ligands, the stereogenicity of the five boron centers in these later cycles all have the same configuration. However, much like the tetrameric analogs, enhanced thermodynamic and kinetic stability were also observed for these pentamers. Through NMR and X-ray diffraction studies it was also determined that these pentameric macrocycles display guest inclusion properties. In particular, benzene was found to fit within the macrocyclic pore cavity, though the binding affinity was quite low.

Further exploitation of this synthetic methodology was able to take advantage of not only ester formation and B-N interactions but also the condensation of aldehydes with primary amines. The flexibility of this methodology was demonstrated in the construction of dendritic nanostructures, in a single step,

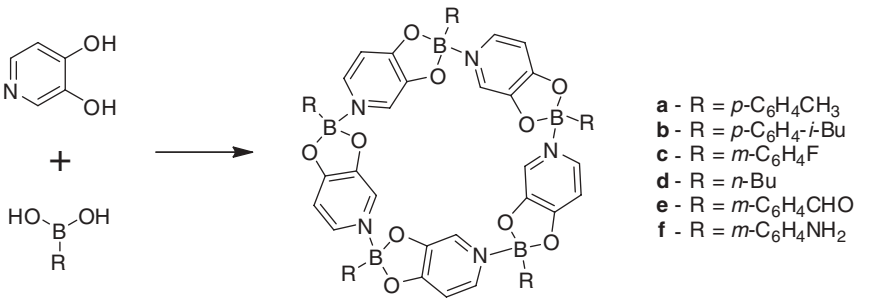

FIGURE 10. Aryl boronic acids interact with 3,4-dihydroxypyridine to form pentameric macrocycles, with the boronate ester serving as a coordination site for pyridine.

based on these cyclic boronate cores.[35] Several tetrameric and pentameric products were synthesized. The most impressive of these is akin to a third-generation dendrimer, in which each generation is connected by a different chemistry—that is, boronate macrocyclic core, imine branching points, and an ether branch layer (Fig. 11). Analogous structures have been reported based on boronate anhydride formation, including branched polyacetylenes[36] and simple boroxines as nonlinear optical materials.[37]

D. Coordination-Based Linear Assemblies

Through simple modification of the building blocks, different polymeric architectures can be obtained. This may take advantage of the directionality afforded through boronate ester formation or be based on the coordination geometry of an incorporated metal. From some of the metal-coordinated macrocycle examples discussed earlier, it is possible to change the assembly geometry by simply altering the metal components. For example, in contrast to the five-coordinate zinc used to assemble porphyrin macrocycles (Fig. 5), switching to a six-coordinate magnesium center in the metallated porphyrin allows two pyridine binding sites, resulting in a linear, ladder-type polymer (Fig. 12a).[21] In this analysis, VPO was not useful for obtaining molecular weight due to low solubility. However, light scattering measurements indicated a molecular weight approaching 1 billion, clearly not a simple discrete cycle. Similarly, cobaloximes have been shown to serve as bifunctional linkers to generate dimeric and trimeric macrocycles. However, if rhodoximes are used instead in conjunction with 3-aminophenylboronic acid in alcohol solvents, the linear polymer (Fig. 12b) precipitates from solution.[31] In aqueous media, no ester product is observed, suggesting that this polymerization may be reversible in response to water.

Assemblies relying on the dative B-N interaction in conjunction with boronate ester formation to form linear polymers have also been identified. Unlike the stepwise phenanthroline-boronate assembly, esterification coupled with ligation occurs simultaneously. In fact, it is likely that coordination

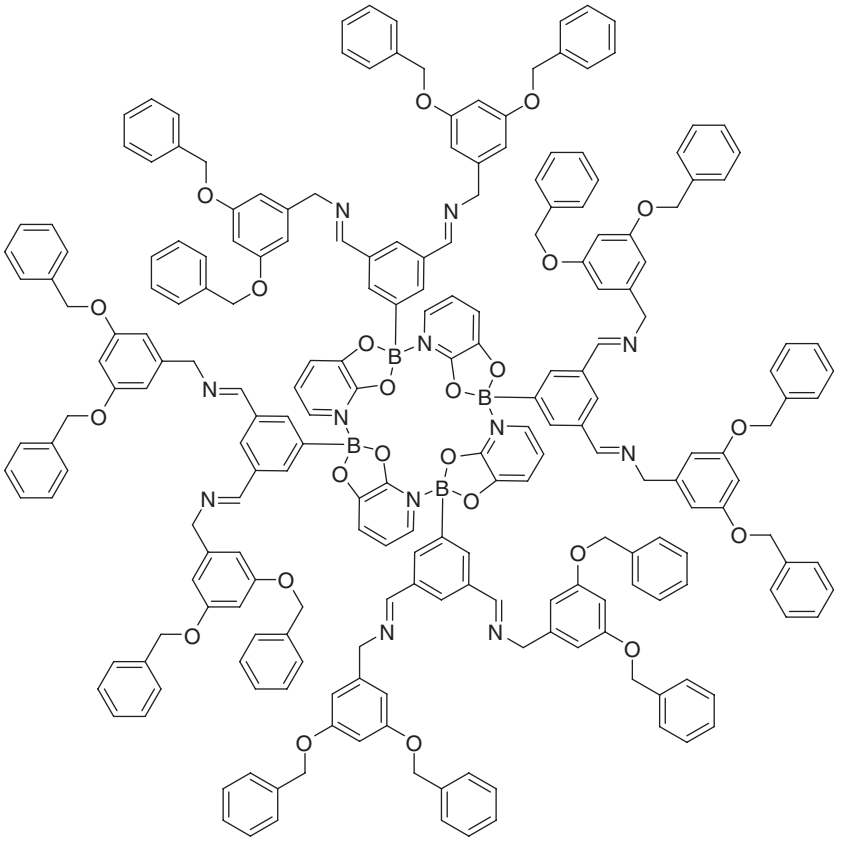

FIGURE 11. The synthesis of dendrimers based on a coordinatively assembled pyridine-boronate ester macrocyles combine ester formation, B-N interaction, and imine formation in one step.

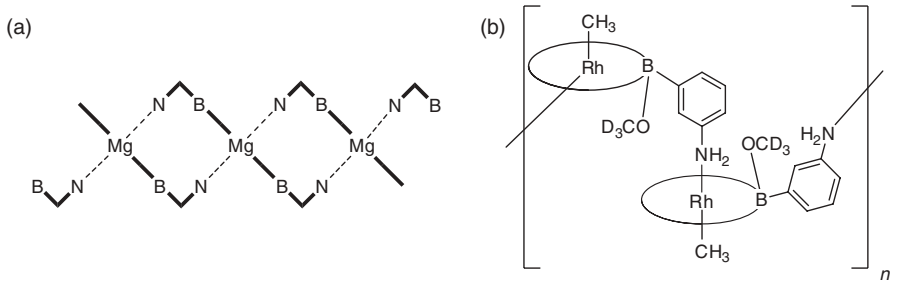

FIGURE 12. Coordinative linear polymers based on boronate ester formation result from (a) ditopic coordination of pyridyl boronic acids to bis-diol functionalized porphyrins and (b) through coordinative interactions between rhodoximes and 3-aminoboronic acid.

of the Lewis base by the boronic acid actually facilitates ester formation. To facilitate polymer formation, diesters were formed based on 1,2,4,5-tetrahydroxybenzene and coordinated with ditopic *N*-donor ligands (e.g., 4,4′-bipyridine and 1,2-di(4-pyridyl)ethylene) (Fig. 13a).[38] Modularity was demonstrated by not only varying the *N*-donor ligands but also using a series of alkyl and aryl boronic acids. Crystallographic analyses showed that the polymer strands have a zigzag geometry (Fig. 13b). These polymers display low solubility in most organic solvents; however, they are soluble in warm chloroform. It is interesting that the solid polymers were a dark purple color, but in solution, the material was light yellow. The authors argue that the strong purple color of the polymers is due to efficient intrastrand charge transfer from the tetraoxobenzene to the dipyridyl linker. Dissolution breaks the weak B-N interactions, which negates this charge transfer, thereby eliminating the low

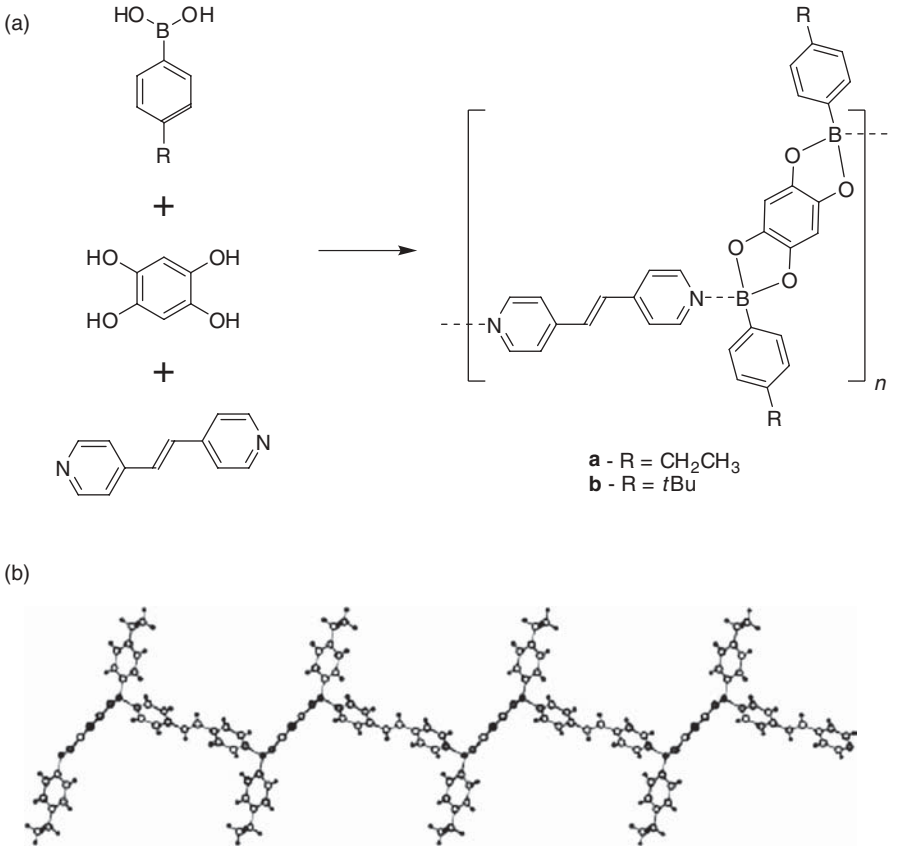

FIGURE 13. Di-boronate esters based on 1,2,4,5-tetrahydroxybenzene coodinatively interact with bipyridyl systems to form zigzag linear polymers (Reprinted with permission from Ref. 38. Copyright 2007 Wiley-VCH Verlag GmbH & Co. KGaA.)

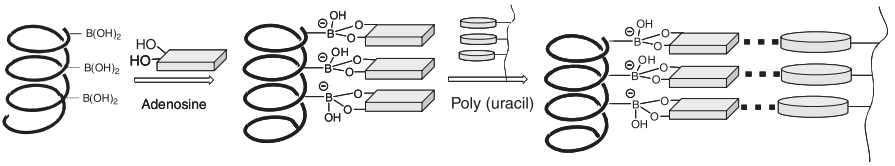

FIGURE 14. Boronate ester formation produces poly(adenosine) RNA mimics that coordinate with poly(uracil) to produce organized duplex RNA motifs.

energy visible transition. The process is reversible, where upon cooling, a dark precipitate re-forms.

Boronate ester formation coupled with coordinative events have also been used to assemble polymeric structures into superstructure architectures. A novel RNA mimic has been developed in which adenosine was attached to a boronic acid functionalized poly(lysine) backbone through boronate ester formation (Fig. 14).[39] Ester formation was carried out at elevated pH to afford a one-dimensional display of nucleic bases along an anionic backbone (analogous to conventional RNA). CD was used to determine that sugar binding affinity and the secondary structure adopted by the boronate-tethered, adenylated poly(lysine) could be modified as a function of pH. CD was further useful for demonstrating that a complementary strand of poly(uracil) bound to this ensemble (Fig. 14). On the contrary, no significant binding was noted for a strand of noncomplimentary poly(cytosine). Likewise, individual adenosine units without the boronated poly(lysine) showed no significant affinity for the poly(uracil). Given the pH sensitivity of this assembly paradigm, these RNA mimics can be constructed reversibly, taking advantage of boronate ester formation to assemble nucleic acids into a one-dimensional motif that could be used to form a noncovalent chiral duplex structure with a complimentary poly(phosphate)-based RNA strand.

III. COVALENTLY LINKED BORONATE ASSEMBLIES

Beyond the coordinative interactions described, boronate ester formation by itself has been shown to facilitate the generation of macromolecular and polymeric structures. Taking advantage of the covalent yet reversible nature of boronate ester formation has allowed for the formation of thermodynamically stable assemblies. Of course, simple monoesters, diesters, and triesters have been readily synthesized and characterized.[40] Numerous reports have taken advantage of the formation of cyclic diesters as a means to define selectivity for molecular sensors,[7] but these small cycles will not be discussed here. Attempts to synthesize and characterize macrocyclic, polymeric and extended covalently

linked frameworks relying on boronate ester formation have been the focus of more recent advances, and as such will be the focus of this discussion.

A. Covalently Linked Macrocyclic and Cage Assemblies

Covalent macrocycle synthesis is traditionally quite challenging. Therefore, the ability to generate cycles that self-assemble, via boronate ester formation, provides a more amenable approach to stable covalently linked compounds. One might assume that the most straightforward approach to generate cyclic boronate-based structures would be to use a simple diboronic acid and bis diol of the appropriate geometry to form macrocyles linked with tricoordinate boron. However, there are limited examples based on this seemingly simple design, and most have only recently been realized. In contrast, the most prevalent design uses an intramolecular Lewis basic amine/imine to form a tetracoordinate boronate system that displays enhanced stability toward hydrolytic degradation.

It is well established that 1,2- and 1,3 diols form cyclic boronate esters,[40a] whereas 1,4- and 1,5-alkane diols principally give rise to dimeric macrocycles.[41] While the crude product is a mixture of various size cycles and oligomeric materials, distillation, which likely shifts this dynamic equilibrium toward the compounds with higher volatility, can be used to isolate the 2:2 complex (Fig. 15a). Analogously if dithioboronate esters are heated with bisphenols, cyclic dimeric diboronates are isolated (Fig. 15b).[42]

Taking advantage of the more traditional cyclic ester formation between boronic acids and 1,2- and 1,3-diols can also lead to macrocyclic structures. It has been shown by NMR, FTIR, and size exclusion chromatography (SEC) that reaction between phenylene-1,3-diboronic acid and pentaerythritol principally produces 6:6, hexameric cycles (Fig. 16a).[43] As before, the crude reaction mixture was a dynamic mixture of cyclic and oligomeric products, but the

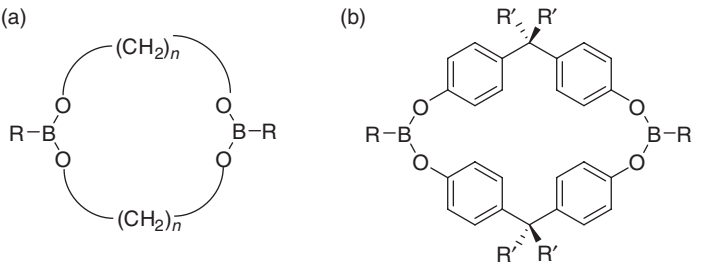

a - $n = 4$, R = Et
b - $n = 5$, R = Et

a - R = *n*Bu, R′ = Me
b - R = Ph, R′ = Me

FIGURE 15. (a) Long-chain α, ω-alkane diols form acyclic, 2:2 boronate ester macrocycles. (b) Bisphenols also form macrocycles based on acyclic diester formation.

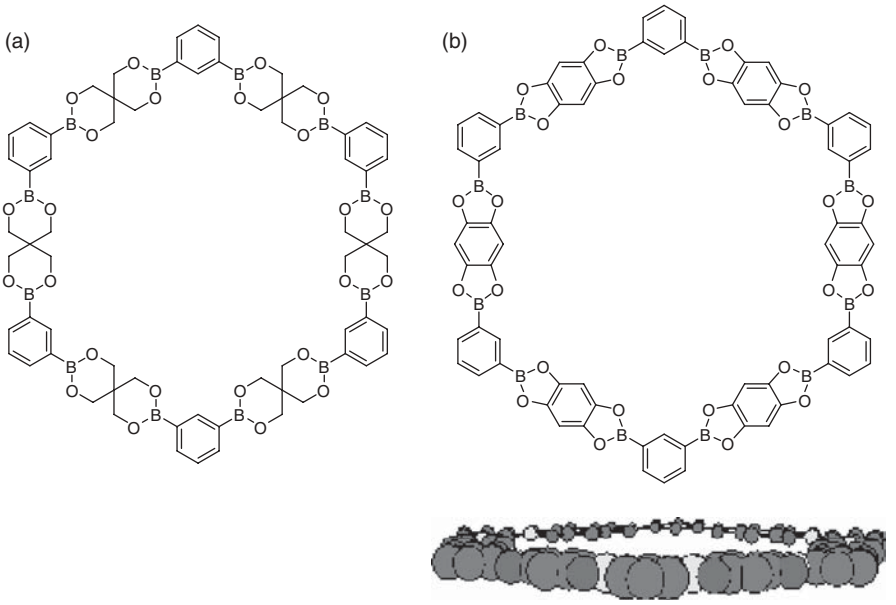

FIGURE 16. (a) When phenylene-1,3-diboronic acid was coupled with the bis-1,3-diol, pentaerythritol, traditional cyclic boronate ester formation resulted in macrocyclic structures. (b) The bis-1,2-diol 1,2,4,5-tetrahydroxybenzene forms similar structures.

hexamer precipitates from solution making isolation facile. Demonstrating the dynamic nature observed for tri-coordinate boron, dissolution of this isolated product with gentle warming quickly returns this pure compound to a mixture of cyclic and oligomeric boronates. The spiro-tetrol can be replaced with the planar bis-diol, 1,2,4,5-tetrahydroxybenzene, to afford what molecular modeling predicts to be planar cyclic structures (Fig. 16b). These later cycles suffer from poor solubility, though solid-state analyses (NMR and FTIR, no structure was determined) have shown that ester formation does in fact proceed.

Phenylene-1,4-diboronic acid has also been assembled into macrocycles using a racemic bis diol.[44] Again, the dynamic nature afforded with tri-coordinate boron produces a mixture of products. It is interesting that this dynamic self-assembly can be directed via templation. For example, when toluene/methanol was used as a solvent, the 2:2 adduct was isolated with toluene serving as a guest within the cavity (Fig. 17a). Even more interesting, when benzene/methanol was used as the solvent, the 3:3 assembly product was obtained with two molecules of benzene trapped within the macrocycle cavity (Fig. 17b). These assemblies could be interconverted by switching to the complementary methanol/solvent mixture. However, if methanol was not present, only guest exchange occurred and the cycles did not interconvert. The authors refer to this "freeze or free" conversion as a switch based on the presence of protic media. It has further been shown that in the absence of benzene and/or

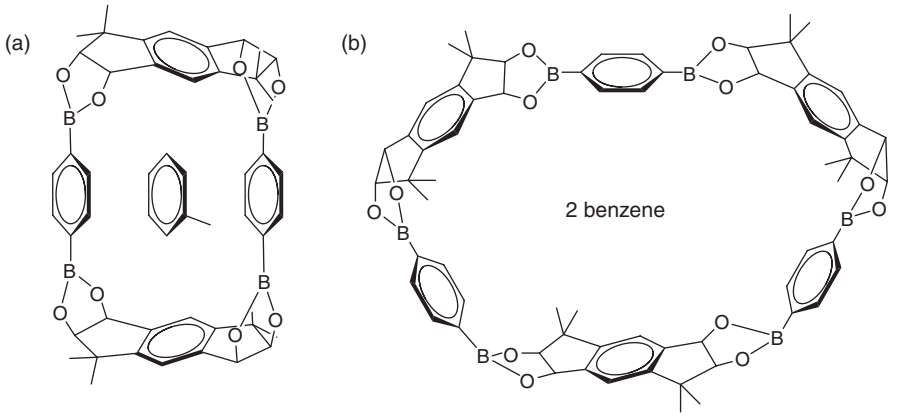

FIGURE 17. Solvent can form templates of (a) 2:2 and (b) 3:3 cyclic adducts from phenylene-1,4-diboronic acid with a racemic bis-diol.

toluene, other guest molecules, such as naphthalene and triphenylene, can serve as templates for macrocycle formation (2:2 and 3:3, respectively).

Again, forming the boronate diester using hydroxy-containing components from different molecules (i.e., not a traditional cyclic ester) allows for the formation of cage-like materials. Akin to the coordination-based cycles seen previously, each of three metal ligands are covalently tethered through a boron-oxygen bond forming a covalent, tripodal chelator.[45] The aryl boronic acid acts as a hub from which three dimethylglyoxime branches coordinate to one technetium (Fig. 18a). This coordination forms a relatively small cage-like complex that contains an isothiocyanate for facile conjugation to biologicals, which can serve as a radiotracer/radiotherapeutic. While this small cage clearly has utility, it may not qualify to a broad audience as a "macrocyclic" entity. Therefore, let us move on to larger cage structures that include silicon. Perhaps the most well known boron-containing hybrid materials are borosilicate glasses. However, discrete borosilicate cycles and cages have also been established (Fig. 18b,c).[46] The synthesis of these compounds was targeted primarily as a means to access various three-dimensional structures that could be reacted further to produce new molecular scaffolds in a controlled manner. To this end, coordination assemblies have been achieved using pyridyl amines and diamines to investigate higher-ordered structures (Fig. 18d).[47]

Incorporation of this coordinative amine ligand within the cycle structure is an alternative approach for generating stable macrocycles. In this regard, alkyl bridged bis(2-hydroxyphenylmethyl) amines have been reacted with 4,4′-biphenyldiboronic acid (Fig. 19a).[48] Esterification proceeds with concomitant coordination of the amine to the resulting ester. The paraquat dication is complexed by this assembly in a 1:1 manner (Fig. 19b) through ionic interactions (anionic boronate with pyridyl cation), attractive π-π interactions (between biphenyl components) and C—H—O hydrogen bonds (paraquat

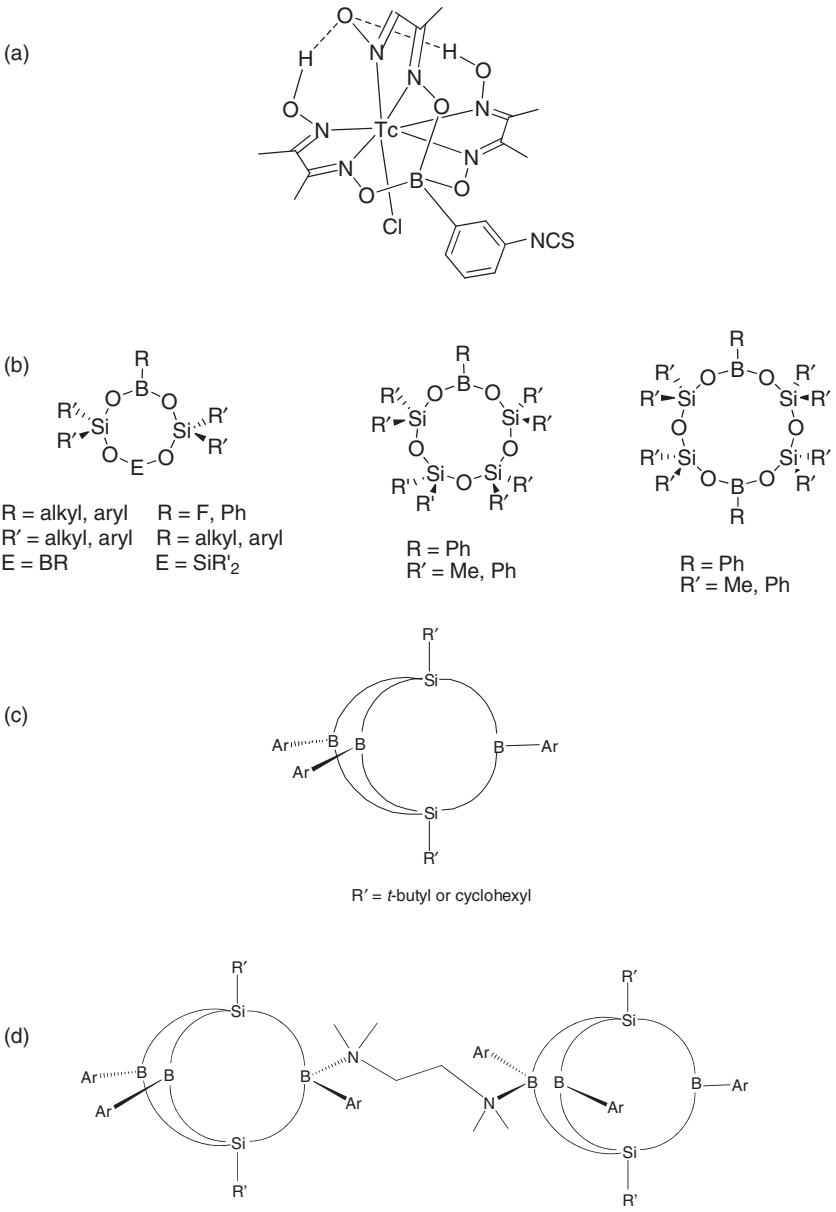

FIGURE 18. (a) A tripodal technetium chelator is based on three oxime ligands tethered through an acyclic boronate triester. (b) Borosilicate macrocycles and (c) cages have been formed as building blocks and (d) assembled via coordinative ditopic Lewis bases.

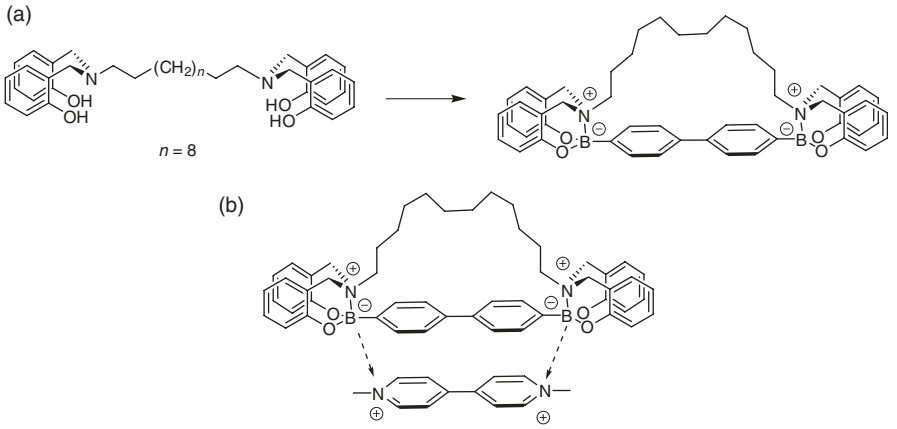

FIGURE 19. (a) Acyclic boronate diesters form macrocyclic assemblies with coordinate amines for added stability. (b) These macrocyles bind paraquat in a 1:1 manner.

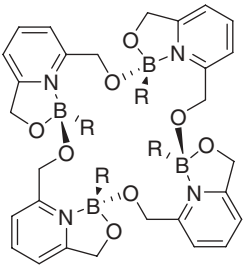

a - R = Ph
b - R = *m*-$C_6H_4NO_2$

FIGURE 20. 2,6-Pyridinedimethanol binds in a unique bidentate manner with aryl boronic acids to form tetrameric macrocycles, involving acyclic ester formation and B-N coordination.

methyl groups and boronate oxygens). The Coulombic attraction between the boronate dianion and the paraquat dication is integral in this recognition process, thereby highlighting the importance of the amine coordination.

Using 2,6-pyridinedimethanol and aryl boronic acids, other covalently linked macrocyclic structures have been obtained that take advantage of theB-N coordination to stabilize the ester linkage. The resulting tetrameric assemblies show approximate S_4 symmetry (Fig. 20).[49] The unsymmetric coordination of the 2,6-pyridinedimethanol to the boronic acid was confirmed by NMR spectroscopic techniques. It may seem surprising that acyclic esters are formed because 2,6-pyridinedimethanol typically acts as a tridentate, monochelating ligand with metal ions.[50] In the case of boron, however, the small covalent radius

and tetrahedral geometry are not sufficient for coordination of all three sites to one boron atom as it would be for a trigonal-bipyramidal or an octahedral metal center. The X-ray structure further confirms this bonding motif, showing the tetrahedral geometry for the boron and the planarity for the ligands.

An alternate approach, and one of the more common designs that leads to tetra-coordinate boronate linked macrocycles, derives from salicylideneamino alcohols condensed with aromatic boronic acids (Fig. 21a–d).[49,51] Salicylideneamino alcohols are easily prepared ligands that react readily with arylboronic acids to form the corresponding monomeric or dimeric esters. This assembly motif again relies on the "open" diester form of the boronate ester, where these ligands are constructed in a way that the boron atom is chelated by only two of the three functional groups of the same ligand. The accompanying amine coordination this time stems from an imine resulting from the condensation between salicylaldehyde and a hydroxy-substituted amine (aryl, benzyl and aliphatic). The structural assignments were made based on NMR and crystallographic data. A large series of differentially substituted dimers have been generated and studies have shown that electronic and steric factors play a small role in the formation of these cyclic products. Semianhydride, oxo-bridged macrocycles have also been isolated based on this imine coordination scheme to form Salen-supported compounds (Fig. 21e).[52]

Larger macrocycles have also been generated based on altering the functional group inclusion, such that the amine functionality is combined in the same molecule with the boronic acid, thereby serving in both the imine and boronate ester linkages. Subsequently, trimeric and tetrameric cycles have been generated from *o*-hydroxybenzenecarbonyl systems with 3-aminophenylboronic acid (Fig. 22).[53] Unlike the previous design, in which steric influences were minimal, here substitution of the carbonyl component defines the ultimate ring size. Specifically, aldehydes produce tetrameric assemblies whereas ketones result in trimeric products. The difference in ring size is due to steric hindrance between the substituent at the imine group (alkyl for the ketone) and the aromatic moiety of the boronic acid.

It has further been shown that substitution on the aromatic ring of the salicylaldehyde units can cause "puckering" of the cycle to produce trimeric calixarene-like compounds. Smaller substituents such as halogen and hydroxyl tend to produce mixtures of *cone-cone* and *cone-partial cone* conformers,[54] whereas larger di-*t*-butyl groups tend to enforce a single *cone-cone* structure (Fig. 23).[55] All of these compounds exhibit C_3 symmetry and are stable against moisture and air. From variable temperature NMR studies of the di-*t*-butyl substituted calix[3]arene, it was demonstrated that the fast dynamic equilibrium between conformers typically observed for this class of compounds does not exist. The "locked" conformation was reasoned to result from the rigidity of the six-membered dative/ester rings that link the aromatic groups, thereby suppressing rotation. These added substituents enhance solubility over their unsubstituted analogs such that host-guest properties can be studied in solution for these novel macrocycles. Beyond simple solvent guests that are dynamically

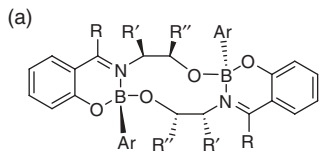

a R = H, R′ = H, R″ = H
b R = H, R′ = H, R″ = Me
c R = H, R′ = H, R″ = Ph
d R = H, R′ = Me, R″ = Ph
e R = Me, R′ = H, R″ = H

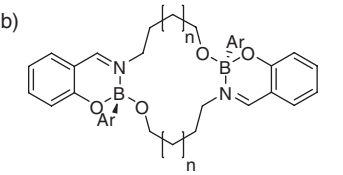

a *n* = 2
b *n* = 3
c *n* = 4

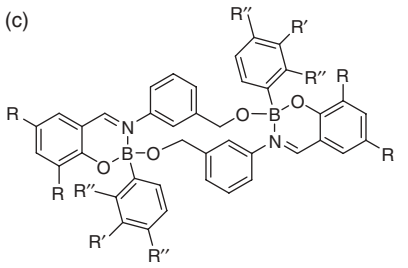

a R = H, R′ = H, R″ = H
b R = *t*-Bu, R′ = H, R″ = H
c R = H, R′ = H, R″ = F
d R = H, R′ = NO_2, R″ = H

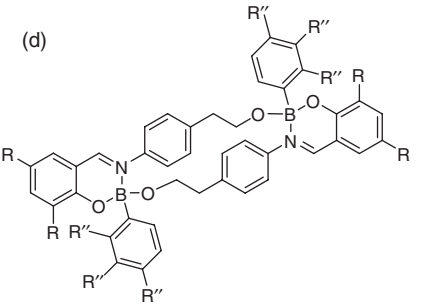

a R = H, R′ = H, R″ = H
b R = *t*-Bu, R′ = H, R″ = H
c R = H, R′ = H, R″ = F
d R = H, R′ = NO_2, R″ = H

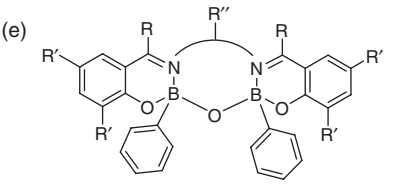

a R = H, R′ = H, R″ = $CH_2(CHCH_3)$
b R = H, R′ = *t*-Bu, R″ = CH_2CH_2
c R = H, R′ = H, R″ = $CH_2CH(OH)CH_2$
d R = H, R′ = *t*-Bu, R″ = $CH_2CH_2CH_2$
e R = Me, R′ = H, R″ = $CH_2CH_2CH_2$

FIGURE 21. Numerous macrocycles based on salicylideneamino alcohols, arising from (a and b) aliphatic and (c and d) aromatic amines, interacting with aryl boronic acids have been identified. (e) Analogous semianhydride bridged structures have also been observed.

exchanged, alkyl-ammonium cations have been shown to bind within the cavity.[54,55]

It then follows that these calix[3]arenes could be assembled into carcerand- or hemicarcerand-type molecules. However, rather than linking existing

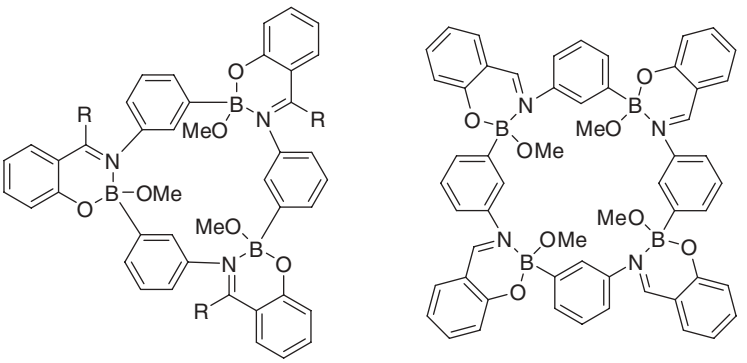

1: R = Me, 2: R = Ph

FIGURE 22. Trimeric and tetrameric macrocycles result from *o*-hydroxybenzenecarbonyl systems binding with 3-aminophenylboronic acid. Trimers result from ketone starting materials, whereas aldehydes produced tetramers.

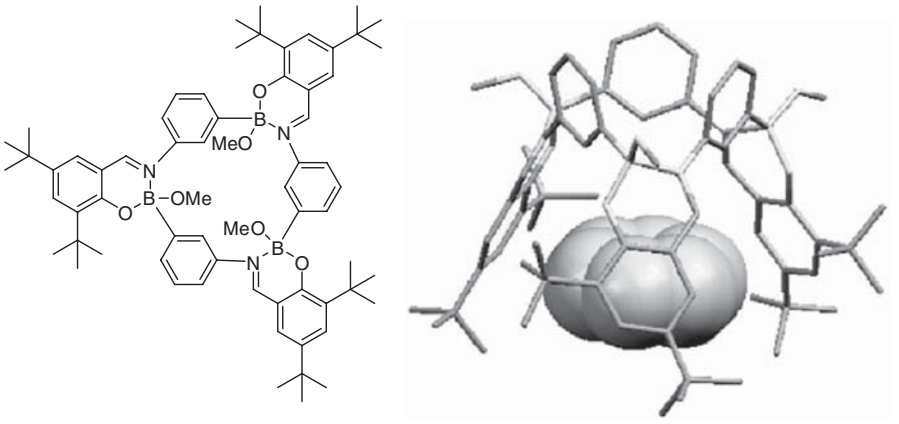

FIGURE 23. Steric bulk (di-*t*-butyl groups) added to the phenyl ring of trimeric *o*-hydroxybenzenecarbonyl-boronic acid based macrocycles causes puckering, resulting in *cone-cone* calix[3]arenes that are capable of guest inclusion (Reprinted with permission from Ref. 55. Copyright 2004 Royal Society of Chemistry.)

calixarenes, it has been shown that the same chemistry can be employed based on bis(salicylaldehyde)s to create cage-like targets.[56] By simply tying two salicylaldehyde units together with a methylene spacer, polymacrocyclic structures were obtained (Fig. 24). NMR and X-ray analyses have shown that two double-cone fragments are connected by three methylene bridges, possessing pseudo-D_3 symmetry. It is interesting that the synthesis was diastereoselective with all six boron atoms within any given assembly having the same stereochemical configuration, as defined by the B-N interaction. The resulting cavity

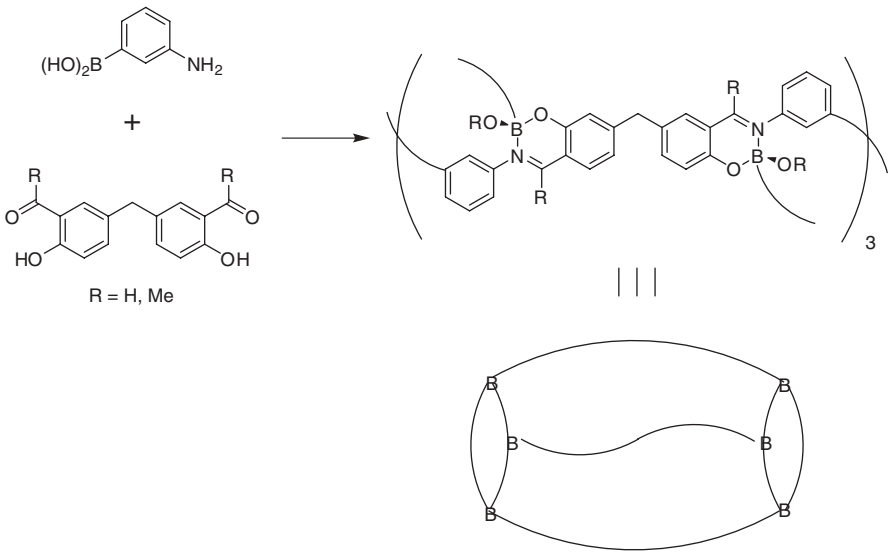

FIGURE 24. Bis(salicylaldehyde)s reacted with 3-aminophenylboronic acid produce methylene-bridged hemicarcerands with threefold symmetry.

is ~1.5 nm in diameter and upon formation includes two benzene molecules stacked within the pore. These solvents are not efficiently trapped and escape under ambient conditions to produce a porous, though less crystalline, material. Analogous *o*-hydroxyketones can also be used to obtain similar calixarenes, though the yields are greatly reduced.[56]

Simultaneous, multiple ester formation was employed to assemble larger multitopic assemblies. For example, self-assembled molecular capsules via boronate esterification have been demonstrated. Two calix[3]arenes, one having the upper rim functionalized with diols, the other functionalized with boronic acids, were combined in the presence of a templating agent to form the heterodimeric capsule (Fig. 25).[57] Extensive NMR analysis was performed to show that the two calixarenes in solution by themselves do not interact. It is only when tetramethyl ammonium acetate is added that the capsule forms. NMR diffusion studies have further demonstrated that the ammonium cation is included within the cavity. In addition, reversible decomposition-reconstruction of the capsule was observed in response to pH.

B. Covalently Linked Linear Assemblies

Boron-linked polymers are not rare. The most obvious include borosilicate glasses and "slime."[58] However, these common materials rely primarily on borate as the key linking element and not boronic acids. Poly(boronate)s can be found in the literature as far back as the 1960s,[59] and then, after a long drought, most progress has been made in the last decade. As seen with coordination

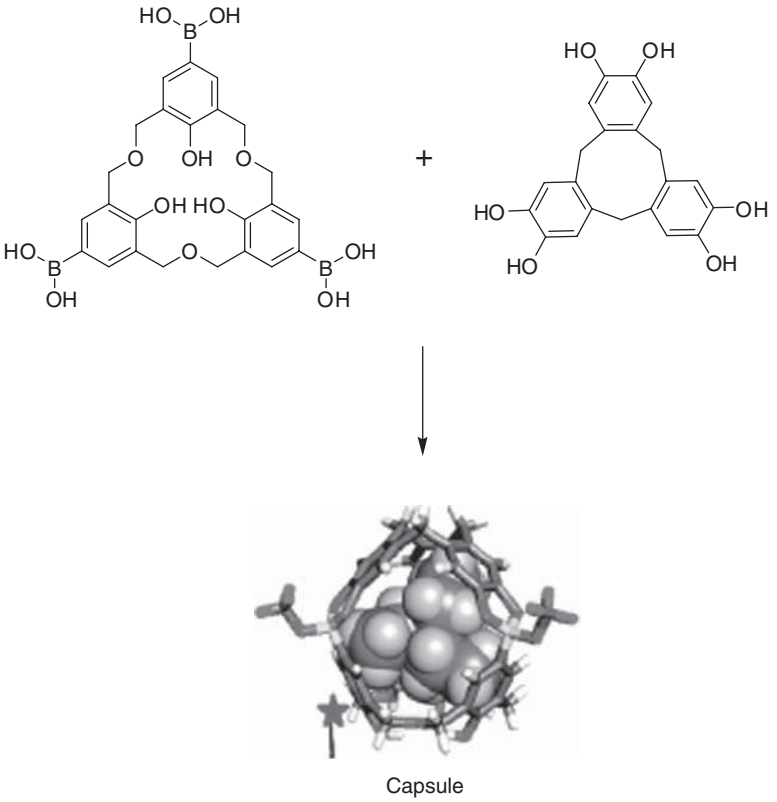

FIGURE 25. Heterodimeric capsules form upon the templated assembly of tris-diol and triboronic acid calixarenes (Reprinted with permission from Ref. 57. Copyright 2007 American Chemical Society.)

polymers, the directionality of the boronate ester formation is integral in defining the subsequent geometric outcomes found in the resulting materials. Linear polymers often arise from the combination of linear diboronic acids and bis diols. Polymers have also been obtained if flexible building components were employed or if the product was kinetically trapped. Boronate ester formation provides a covalent alternative to traditional polymer synthesis though typically offering a more facile synthetic route, without the need for added catalyst or exhaustively dry and anaerobic conditions. Alternatively, compared to their noncovalent equivalents, poly(boronate)s are more stable and can be readily processed. As seen before, polymers exist with tri-coordinate boron in the backbone and result in self-repairing materials and novel conjugated polymers. Similarly, tetra-coordinate boron can be found in the polymer backbone of poly(boronate)s and have afforded pH responsive gels.

The earliest recorded poly(boronate)s were tri-coordinate systems based on phenylene-1,4-diboronic acid. Some of the first materials were not in fact esters

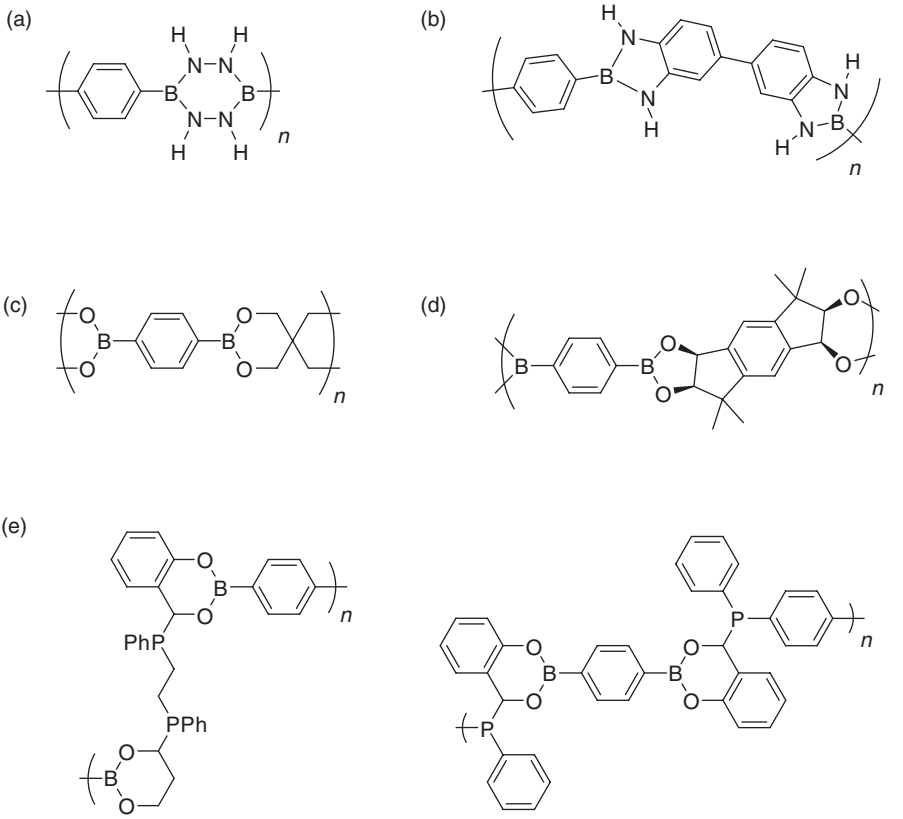

FIGURE 26. Covalent poly(boronate)s were first identified as (a) the borono-hydrazone analogs before (b–e) ester linked materials were identified. (d and e) Phosphino-integrated poly(boronate)s display reactivity and structural motifs similar to the monomeric precursors.

but rather their diamino-analogs, such as diazaboroles (also known as borazoles and boronate amides) (Fig. 26a)[60] and borono-hydrazones (Fig. 26b).[61] Ester-linked materials formed by the dehydration of phenylene-1,4-diboronic acid with pentaerythritol soon followed (Fig. 26c).[62] Neither of these novel polymers were investigated in great detail due to their low solubility. The noteworthy result recorded for both polymers was their particularly high thermal stability, 200–460°C and ~400°C in vacuo, respectively. More recently, the same group that generated the guest-included macrocycles described earlier, have also reported linear polymers based on phenylene-1,4-diboronic acid.[44] When combined with racemic bis diol in methanol a precipitate formed immediately (Fig. 26d). The isolated product was insoluble in all solvents examined, but the elemental analysis was consistent with the expected linear polymeric product. Still others have used phenylene-1,4-diboronic acid to generate poly(boronate)s, which

included phosphine and phosphinate functionality in the main chain to probe the influence of valency on the structure and reactivity of the phosphorus containing component (Fig. 26e).[63] The structures of these soluble polymers were confirmed using NMR and IR while ebullioscopy was used to assess molecular weights (MW $\sim$ 8000, 12–15 repeat units). These materials underwent facile hydrolysis of the boronate ester, yet the phosphorus could be oxidized and sulfonated without disrupting the boronate backbone. Ultimately, it was determined that the unique steric structures and reactivity for these oligomers mirrored that of the monocyclic precursors.

More soluble analogs have been generated based on the condensation of pentaerythritol and 9,9-dihexylfluorene-2,7-diboronic acid (Fig. 27a).[64] It was shown that the molecular weights of these polymers could be controlled by varying reaction time and/or monomer ratio though the synthetic route described was much less sensitive to monomer ratios compared to traditional condensation polymers, providing a more hardy synthetic approach. Molecular weights of soluble polymers approaching 80,000 were measured using NMR end-group analysis as well as gel permeation chromatography (GPC). Furthermore, the molecular weight of the material could be controlled/modified post-polymerization. If desired, the polymer was stable in solution; however, upon addition of protic solvents, such as water and alcohols, the polymer decomposed over time. It is interesting that if the polymer was stored as a solid under reduced pressure, the molecular weight continued to increase by a transesterification process that also occurred at elevated temperatures. Taking advantage of this decomposition/growth process, hydrolytically damaged polymer was repaired without the addition of catalyst or reintroduction to the original synthetic conditions. The sp^2 hybridized boron of the aryl boronate ester undergoes substitution more readily than tetrahedral boron, allowing for more facile repair.[65]

Analogous polymers incorporating aromatic bis-diols have defined a new class of conjugated, wide band-gap, semiconducting polymers (Fig. 27b).[66] Pi-delocalization arises from overlap between the lone pair of electrons on the oxygen and the empty *p*-orbital on boron.[67] Absorption spectroscopy of these polymers combined with molecular modeling (polarizability calculations and electronic spectral predictions) and crystallographic investigations of model compounds provided evidence for the extended π-conjugation. The dependence

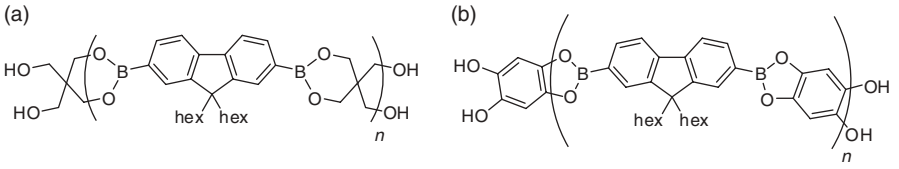

FIGURE 27. Poly(boronate)s using fluorene-diboronic acids with pentaerythritol (a) and 1,2,4,5-tetrahydroxybenzene (b) have shown to act as self-repairing materials (a and b) and as a new class of wide band-gap semiconductor (b).

of the absorption properties of these polymers on molecular weight was used to estimate that delocalization extended over three to five bridging ester units (6–10 phenyl rings).

The polymers previously discussed represent discrete structures formed in noncoordinating organic solvents that did not exhibit significant inter-chain interactions or boronate transesterification (under ambient conditions). Other more structurally involved glucuronamide-based diboronic acids have been used with alkyl appended α,ω-di-saccharides as the bis-diol building blocks to generate pH dependent, reversible dynamic polymers in aqueous solution (Fig. 28).[68] These materials form at elevated pH (> 10) as monitored using ^{11}B NMR. Molecular weight was determined based on MALLS measurements to be ~2 million with a polydispersity near 11. When the pH was lowered to ~3, complete dissociation of the polymer was obtained. As the pH was raised, polymeric structures were again observed.

As was seen, coordinating amines can be built into the monomer structure to enhance the stability of the ester linkage by generating tetra-coordinate boron. Polymers based on this design have been created using amino-substituted biphenyl-4,4′-diboronic acid interacting with saccharides (Fig. 29).[69] The biphenyl moiety was incorporated to provide a spectroscopic handle to probe

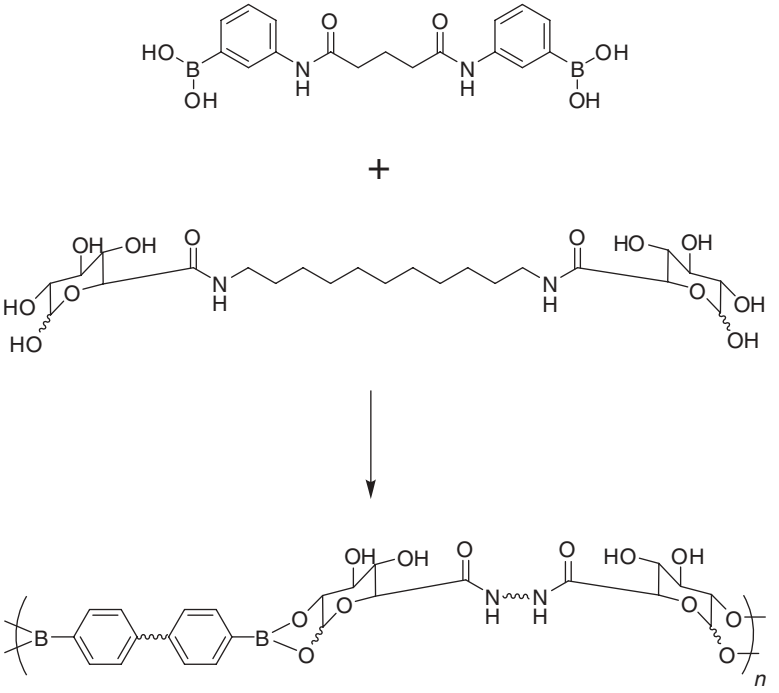

FIGURE 28. Diboronic acid bola-amphiphiles combined with alkyl tethered disaccharides form pH responsive poly(boronate)s in aqueous media.

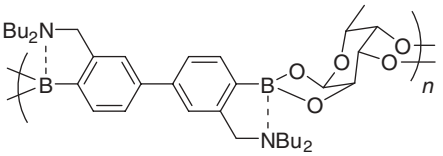

FIGURE 29. Ester formation coupled with intramolecular dative B-N bond formation has been used to create tetra-coordinate poly(boronate)s upon introduction of saccharides.

chirality induced upon sugar binding. Di-butyl substituents were added to the amine ligands to enhance solubility in organic solvents. Molecular weights, assessed using light scattering, were on the order of 50,000 to 100,000. Chirality in the assemblies was measured using CD, and as observed in coordinative polymers,[24] the sign of the signal for the polymer depended on the chirality of the saccharide incorporated into the polymer backbone.

As with coordination events associated with boronate appended polymers, covalent cross-linking can occur to define secondary super-structure architectures within traditional polymer based materials. The same poly(lysine) polymer that was coordinatively assembled into duplex structures[39] was used with poly-functional saccharides to define the secondary structure of the polymer.[70] Upon addition of fructose, the helical content of the poly(lysine) increased (determined by CD) and the pH at which this maximum was reached dropped (10.3 to 7.9). Given the distance the sugar is removed from the polymer backbone, it was reasoned that hydrogen bonding interactions between saccharides (Fig. 30) and a decrease in the boronic acid pK_a were responsible for these changes. Similarly, when glucose was added to this boronic acid appended poly(lysine), a higher helical content was observed (85%) at a lower pH (8.7). It was noted that the CD sign inverted at high pH, as would be consistent for glucose binding with two boronic acids to form intrastrand cross-links, therefore resulting in the formation of β-turn structures (Fig. 30). Thus the hierarchical organization of this boronic acid appended polymer was controlled by the simple addition of different saccharides.

C. Covalently Linked Network Assemblies

Growing from simple polymeric assemblies, more complex structures arise from the interactions between polyvalent boronic acids interacting with poly-functional diols. These products may be dynamic, highly cross-linked polymer networks, analogous to slime. Alternatively, these assemblies have taken the form of highly ordered frameworks with persistent pores. Regardless of the degree of order inherent in these systems, the key assembly motif still relies on boronate ester formation.

As discussed earlier, linear assemblies can cause gelation via boronate ester formation.[68] Multidimensional or network systems have also been

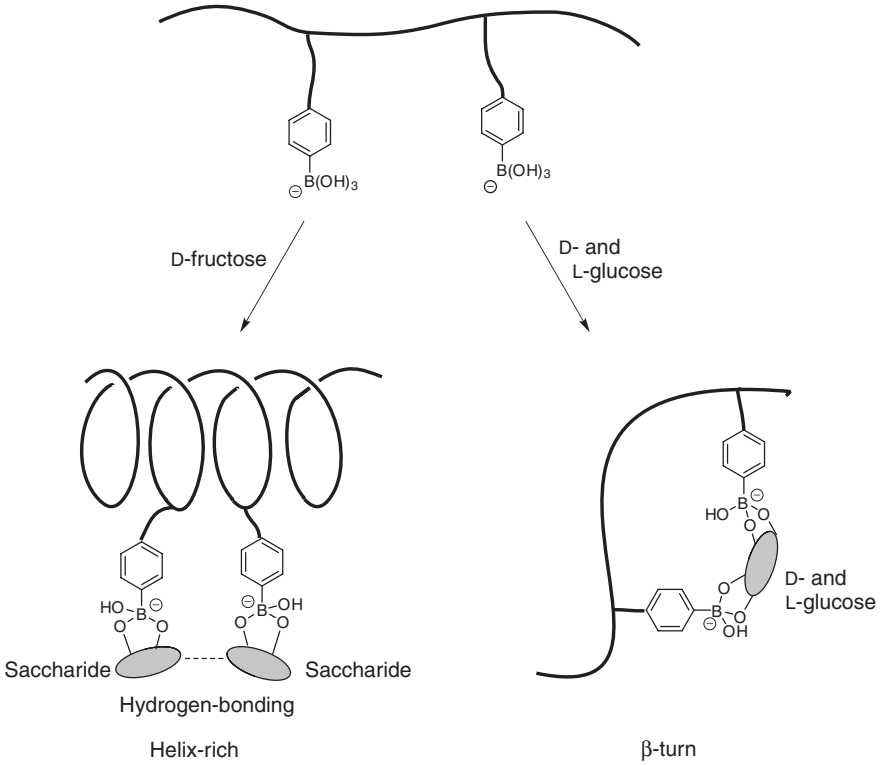

FIGURE 30. (a) Poly(lysine) appended boronic acids interact with fructose to form helix-rich super-structure architectures. (b) Alternatively "ditopic" glucose intramolecularly cross-links to the polymer to introduce β-turns.

described—for example, boronate functionalized polysaccharides have been used as gelators (Fig. 31a).[71] Essentially, a boronate ester version of slime, which is capable of forming in aqueous environments, is used as a viscosifying fluid to access subterranean oil deposits. Alternatively, it has been shown that layered assemblies can be made based on boronate ester formation using a simple layer-by-layer deposition technique.[72] Specifically, multilayered structures were obtained using boronic acid functionalized poly(aniline) along with RNA (Fig. 31b). Spectroscopic measurements support ester formation as well as coordinative B-N interactions. Incorporation of the redox-active conjugated polymer into these layered assemblies provided for the potential-induced release of RNA from the multilayer.

One of the unique architectural motifs that truly relies on the covalent yet reversible nature of boronate ester formation is the creation of complex hierarchical structures referred to as COFs. If boronate ester formation can be used to obtain discrete macrocyclic structures, it is then reasonable to expect that linked macrocyclic networks may be generated. These networks assemble

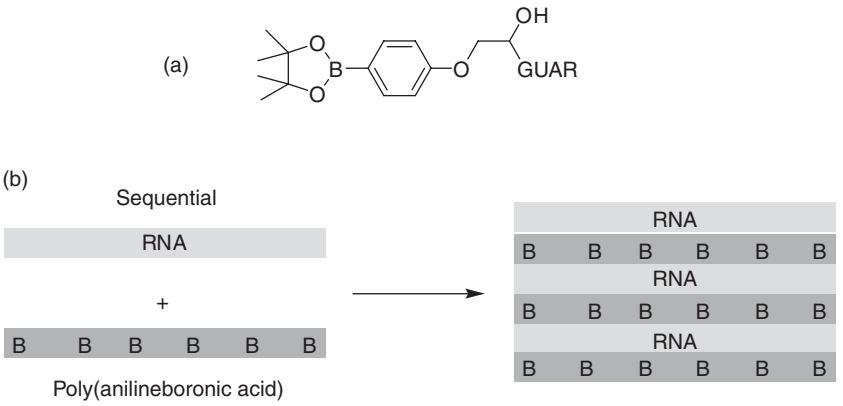

FIGURE 31. Amorphous assemblies form from boronate functionalized polysaccharides as well as in layer-by-layer assemblies between boronic acid functionalized poly(aniline) and RNA.

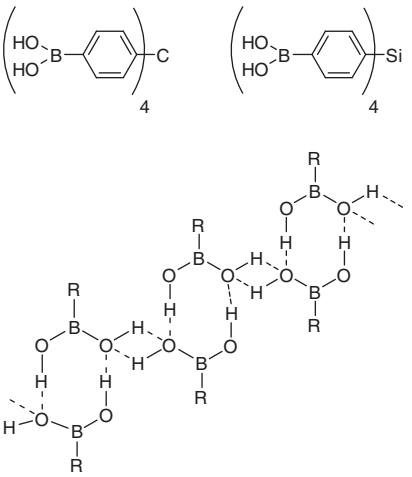

FIGURE 32. Highly interpenetrated hydrogen bonded networks form porous materials that serve as precursors to covalent organic frameworks.

to form a thermodynamically favored product, as highly crystalline assemblies. However, before discussing these novel assemblies, a brief discussion is warranted of a precursor porous material, based on the hydrogen bonded assembly of tetra-boronic acids. Specifically, a highly interpenetrated network resulted from 16 independent hydrogen bonds formed between tetraphenylmethane (silane) based tetra-boronic acid monomers (Fig. 32).[73] Despite five-fold interpenetration, ~60% free volume was maintained for inclusion of guests. The afforded channels were highly interconnected such that diffusion

within the crystal was available through multiple redundant pathways. Guest exchange, within the geometric constraints of the system, took place without significantly altering the ordered network. However, complete removal of the guests leads to loss of crystallinity.

Growing from these noncovalent assemblies, covalently linked poly(boronate) frameworks have proven to be robust porous materials. The enhanced stability of these assemblies was manifested by the ability to remove guests included in the crystal while still retaining porosity and maintaining crystallinity. To date, there are 10 COFs that have been reported relying on boronate ester formation as the integral assembly motif (three other networks exist that were assembled based on boronate anhydride formation). Pore dimensions range from 7 to 32 Å. These ester-linked networks have been assembled to form hexagonal two-dimensional sheets resembling graphite or boron nitride as well as three-dimensional cubic structures.

The first reported boronate-linked COF was COF-5 (Fig. 33a).[74] This materials derives from the dehydration between phenylene-1,4-diboronic acid and 2,3,6,7,10,11-hexahydroxytriphenylene. COF-5 assembles into a hexagonal structure (P6/mmm symmetry) similar to that of boron nitride with the boronate-linked sheets aligned in an eclipsed fashion along the *c*-axis. The resulting hexagonal pores were $\sim$27 Å in diameter with an apparent surface area of 1590 m^2/g, as calculated using the BET model. A second, highly analogous COF, COF-18 Å, stems from the reaction between phenylene-1,3,5-triboronic acid and 1,2,4,5-tetrahydroxybenzene (Fig. 33b).[75] Falling into the same space group as COF-5, this planar COF was synthesized in higher yields using a more facile synthetic method. As indicated by the name, the hexagonal pore diameter is 18 Å. Based on the BET model, the apparent surface area was 1260 m^2/g with a pore volume of 0.29 cm^3/g. A series of three more 2D COFs have also been reported, COF-6, COF-8, COF-10, with surface areas determined (fit to a Langmuir model) to be 980, 1400, and 2080 m^2/g, respectively.[76] All of these COFs exhibit rigid, thermally stable pores (to 500°C) with high surface areas. Detailed NMR and FTIR analyses have confirmed ester formation to be the determining factor in COF formation.

Using structurally diverse monomers, the porosity (i.e., size and surface area) of these frameworks can be tailored. An alternate approach, similar to the studies described earlier and analogous to salicylideneamino alcohol-based macrocycles,[49,51d] is to use the same fundamental building blocks but alter the substituents on those monomers to investigate how this influences the fidelity of the assembly process as well as the porosity of the resulting materials. In this regard, frameworks based on the structural paradigm presented in COF-18 Å (phenylene-1,3,5-triboronic acid and 1,2,4,5-tetrahydroxybenzene) were synthesized using dialkyl substituted bis-diols (methyl, COF-16Å; ethyl, COF-14 Å; propyl, COF-11 Å) (Fig. 34).[77] These substitutions alter the pore dimensions (16 Å, 14 Å, and 11 Å, respectively), but they do not alter the geometry around the boronate ester or the network geometry as confirmed by MAS NMR, FTIR, and PXRD. It is noteworthy that solvent (THF) was trapped in the two larger

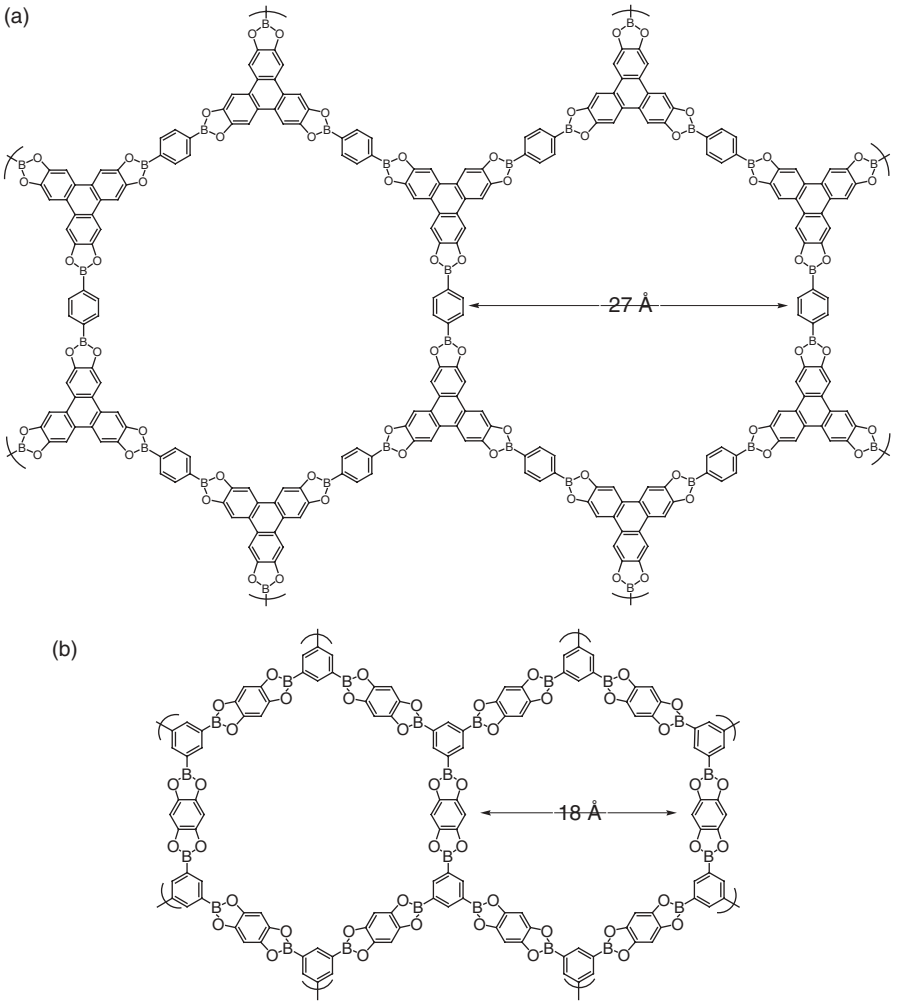

FIGURE 33. Planar, hexagonal COFs based on boronate ester formation produces porous networks with varying pore dimensions.

pore systems during synthesis but were absent in the smaller pores of COF-14 Å and COF-11 Å, thereby illustrating that insertion of the hydrocarbon chains along the pore walls fills the pores, reducing the diameter such that the host environment of the pore was altered. Gas adsorption with nitrogen confirmed that the pores are indeed smaller (COF-16 Å: 753; COF-14 Å: 805; COF-11 Å: 105 m^2/g). It is interesting that gas adsorption with hydrogen produced a much different result. Whereas nitrogen uptake was diminished 10-fold from COF-18 Å to COF-11 Å, hydrogen uptake was only attenuated 20%. The smaller gas molecules can access corner pore cavities that are too small to include nitrogen,

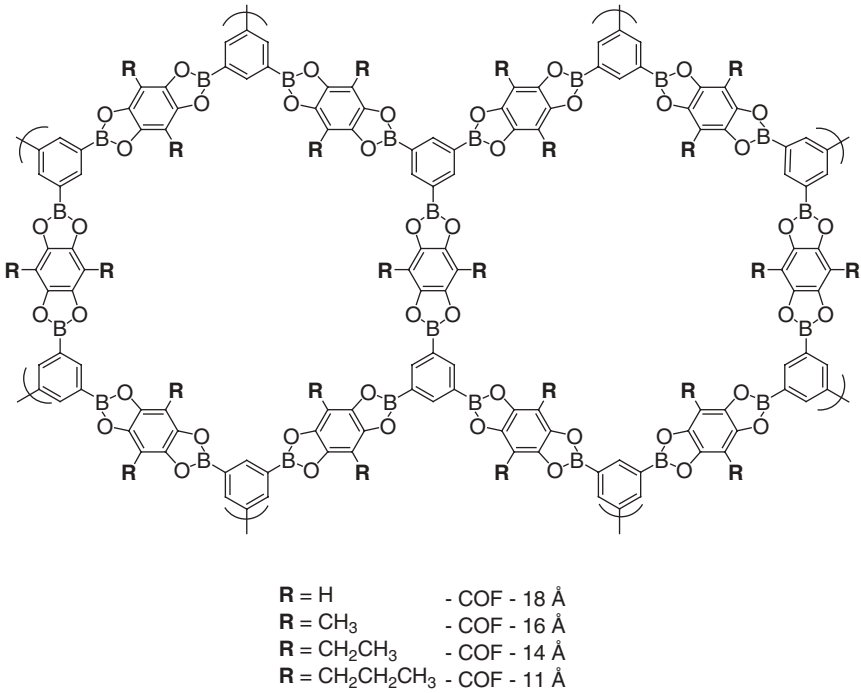

FIGURE 34. Alkyl functionalization within the pores of COFs provides a method for probing the formation and porous properties of highly analogous materials.

and in reality, more hydrogen was taken up on a per pore basis with increasing alkyl bulk.

Beyond planar sheet assemblies, three-dimensional COFs have also been synthesized. The tetrahedral boronic acids used to create porous, hydrogen bonded networks were condensed with 2,3,6,7,10,11-hexahydroxytriphenylene to produce COF-105 and COF-108 (Fig. 35).[78] The resulting materials have a cubic structure with an open pore system. It is interesting that these two COFs do not have identical structures, even though they differ only in that COF-105 has a carbon tetrahedral center and COF-108 has a silicon atom at the tetrahedral centers. While no surface area measurements were reported for these boronate COFs, they were reported as low-density crystals with densities of 0.17 to 0.18 g/cm^3.

IV. SUMMARY AND OUTLOOK

Though the earliest references associated with boronate-linked materials date back to the 1950s, it has only been in the last 10–20 years that great strides have been made using these covalent-reversible boronic acid-diol interactions.

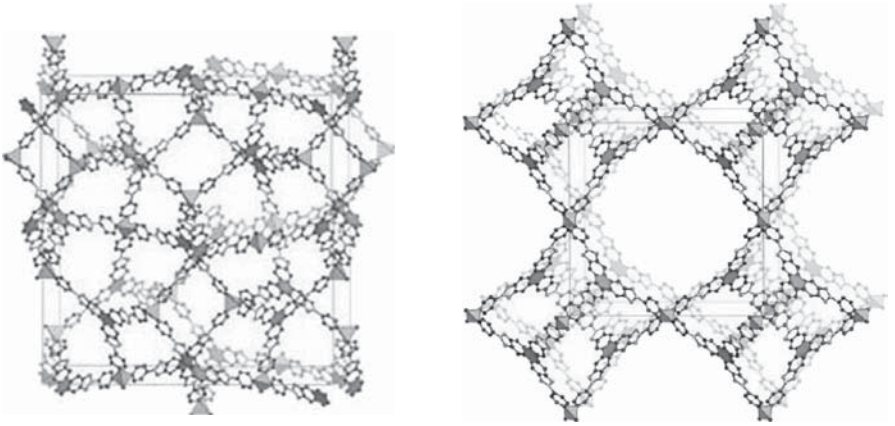

FIGURE 35. Three-dimensional COFs produce low-density crystalline networks with redundant pore connectivity (Reprinted with permission from Ref. 78. Copyright 2007 American Association for the Advancement of Science.)

Boronate ester formation has proven to be a facile alternative to traditional polymer assembly, given the ease of synthesis and dynamic reversibility to afford error-checking mechanisms during synthesis. Compared to conventional supramolecular polymers, boronate-linked materials display enhanced stability. It is argued that boronate ester formation takes the best from both worlds.

As demonstrated by examples, these relatively novel assemblies hold promise in a number of different venues. The simple phenyl-boron-phenyl binding motif provides a unique supramolecular assembly strategy for researchers to take advantage of. Macrocyclic assemblies have been shown to serve as host molecules for molecular recognition events. Linear polymers have shown self-repair capabilities as well as serving as wide band-gap semiconductors. And porous COFs provide stable network geometries for the inclusion of guests.

Each of these properties can and will be investigated and combined by researchers looking to advance the field. The guest inclusion properties hold promise as storage and separation media for gases and small molecules. The cavities formed in macrocyclic and COF materials will likely be used as is or functionalized to afford new catalysts, both homogeneous and heterogeneous. The reversibility of this assembly mechanism is expected to allow for the creation of self-healing materials and highly crystalline polymers. The π-delocalization observed in poly(boronate)s has already been taken advantage of to generate blue emissive materials and continued efforts will likely produce more highly conjugated materials as well. Investigation into the utility of boronate-linked materials is still in its infancy, and already numerous varied and promising leads have been identified.

V. REFERENCES

1. E. Frankland, *J. Chem. Soc*., **1862**, *15*, 363.
2. D. G. Hall, in *Boronic Acids*, ed. D. G. Hall, Wiley-VCH, New York, **2005**, Chap. 1.
3. H. G. Kuivila, A. H Keough, and E. J. Soboczenzki, *J. Org. Chem*., **1959**, *24*, 780.
4. G. Wulff, *Pure & Appl. Chem*., **1982**, *54*, 2093.
5. (a) T. Charnley, H. A. Skinner, and N. B. Smith, *J. Chem. Soc*., **1952**, 2288. (b) T. L. Cottrell, *The Strengths of Chemical Bonds*., 2nd ed., Butterworths, London, **1958**.
6. (a) A. Suzuki, in *Modern Arene Chemistry*, ed. D. Astruc, Wiley-VCH, Weinheim, **2002**, p. 53. (b) A. Suzuki, in *Boronic Acids*, ed. D. G. Hall, Wiley-VCH, New York, **2005**, chap. 3.
7. (a) D. G. Hall, ed, *Boronic Acids*, Wiley-VCH, New York, **2005**, chaps. 2–11. (b) M. Vaultier and B. Carboni, in *Comprehensive Organometallic Chemistry II*, vol. *II*, E.V. Able and G. Wilkinson, Pergamon Press, Oxford, **1995**, chap. 9. (c) N. Miyaura and A. Suzuki, *Chem. Rev*, **1995**, *95*, 2457. (d) A. Pelter, K. Smith, and H. C. Brown, *Borane Reagents*, Academic Press, New York, **1988**. (e) B. M. Mikhailov and Y. N. Bubnov, *Organoboron Compounds in Organic Synthesis*, Harwood Academics, Glasgow, **1984**. (f) A. Suzuki, *Acc. Chem. Res*., **1982**, *15*, 178.
8. (a) T. D. James, M. D. Phillips, and S. Shinkai, in *Boronic Acids in Saccharide Recognition*; ed. J. F. Stoddard, RCS Publishing, Cambridge, **2006**. (b) D. G. Hall, ed., *Boronic Acids*, Wiley-VCH, New York, **2005**, chaps. 12–13. (c) W. Wang, X. Gao, and B. Wang, *Curr. Org. Chem*, **2002**, *6*, 1285. (d) T. D. James and S. Shinkai, *Top. Curr. Chem*., **2002**, *218*, 159. (e) T. D. James, K. R. A. S. Samankumara, and S. Shinkai, *Angew. Chem., Int. Ed. Engl*., **1996**, *35*, 1911. (f) J. J. Lavigne and E. V. Anslyn, *Angew. Chem. Int. Ed*., **1999**, *38*, 3666. (g) M. Yamamoto, M. Takeuchi, and S. Shinkai, *Tetrahedron*, **1998**, *54*, 3125.
9. (a) F. Jäkle, *Coord. Chem. Rev*., **2006**, *250*, 1107. (b) D. Gabel, in *Science of Synthesis: Houben–Weyl Methods of Molecular Transformations*, vol. *8*, ed. D. Kaufmann and D. S. Matteson, Georg Thieme Verlag, Stuttgart, **2005**, pp. 1277.
10. (a) S. J. Rettig and J. Trotter, *Can. J. Chem*., **1977**, *55*, 3071. (b) J. S. O. Santos, J.-C. Lancelot, A. Bouillon, and S. Rault, *Acta Crystallogr*., **2003**, *C59*, o111.
11. For example see: K. E. Maly, M. Thierry, and J. D. Wuest, *CrystEngComm*, **2006**, *8*, 33.
12. A. T Hagler and S. Lifson, *J. Am. Chem. Soc*., **1974**, *96*, 5327–5335.
13. P. Rodrìguez-Cuamatzi, G. Vargas-Dìaz, T. Maris, J. D. Wuest, and H. Höpfl, *Acta Crystallogr*., **2004**, *E60*, o1316.
14. V. R. Pedireddi and N. Seetha Lekshmi, *Tetrahedron Lett*., **2004**, *44*, 1903.
15. B. M. Rambo, *Self-Assembly of Boronate Based Materials: Dynamic Macromolecular Systems Based on Covalent Reversible Interactions*, Ph.D. dissertation, University of South Carolina, Columbia, **2008**.
16. P. Rodriguez-Cuamatzi, O. I. Arillo-Flores, M. L. Bernal-Uruchurtu, and H. Höpfl, *Cryst. Growth Des*., **2005**, *5*(1), 167.
17. W. Niu, B. M. Rambo, M. D. Smith, and J. J. Lavigne, *Chem. Commun*., **2005**, 5166.
18. (a) V.F. Zettler, H. D. Hausen, and H. Hess, *Acta Crystallogr., Sect. B*, **1974**, *30*, 1876. (b) W. Niu, M. D. Smith, and J. J. Lavigne, *Cryst. Growth Des*., **2006**, *6*, 1274.
19. (a) Q. Miao, X. Chi, S. Xiao, R. Zeis, M. Lefenfeld, T. Siegrist, M.L. Steigerwald, and C. Nuckolls, *J. Am. Chem. Soc.,* **2006**, *128*, 1340. (b) G. S. Tulevski, Q. Miao, A. Afzali, T. O. Graham, C. R. Kagan, and C. Nuckolls, *J. Am. Chem. Soc*., **2006**, *128*, 1788. (c) M. D. Curtis, J. Cao, and J. W. Kampf, *J. Am. Chem. Soc*., **2004**, *126*, 4318. (d) M. Ling, and Z. Bao, *Chem. Mater*., **2004**, *16*, 4824. (e) J. E. Anthony, J. S. Brooks, D. L. Eaton, and S. R. Parkin, *J. Am. Chem. Soc*., **2001**, *123*, 9482. (f) J. Roncali, *Acc. Chem. Res*., **2000**, *33*, 147.
20. (a) H. Höpfl, *Struct. Bonding*, **2002**, *103*, 1. (b) K. Ma, M. Scheibitz, S. Scholz, and M. Wagner, *J. Organomet. Chem*., **2002**, *652*, 11.

21. L. D. Sarson, K. Ueda, M. Takeuchi, and S. Shinkai, *Chem. Commun*., **1996**, 619.
22. G. Nuding, K. Nakashima, R. Iguchi, T. Ishi-i, and S. Shinkai, *Tetrahedron Lett*., **1998**, *39*, 9473.
23. M. Yamamoto, M. Takeuchi, and S. Shinkai, *Tetrahedron Lett*., **2000**, *41*, 3137.
24. M. Yamamoto, M. Takeuchi, S. Shinkai, F. Tani, and Y. Naruta, *J. Chem. Soc., Perkin Trans. 2*, **2000**, 9.
25. M. Yamamoto, M. Takeuchi, and S. Shinkai, *Tetrahedron*, **2002**, *58*, 7251.
26. R. Dreos, G. Tauzher, S. Vuano, F. Asaro, G. Pellizer, G. Nardin, L. Randaccio, and S. Geremia, *J. Organomet. Chem*., **1995**, *505*, 135.
27. R. Dreos, G. Nardin, L. Randaccio, G. Tauzher, and S. Vuano, *Inorg. Chem*., **1997**, *36*, 2463.
28. R. Dreos, P. Siega, S. Scagliola, L. Randaccio, G. Nardin, C. Tavagnacco, and M. Bevilacqua, *Eur. J. Inorg. Chem*., **2005**, 3936.
29. R. Dreos, G. Nardin, L. Randaccio, P. Siega, G. Tauzher, and V. Vrdoljak, *Inorg. Chem*., **2001**, *40*, 5336.
30. R. Dreos, G. Nardin, L. Randaccio, P. Siega, S. Scagliola, and G. Tauzher, *Eur. J. Inorg. Chem*., **2004**, 4266.
31. R. Dreos, G. Nardin, L. Randaccio, P. Siega, and G. Tauzher *Eur. J. Inorg. Chem*., **2002**, 2885.
32. (a) L. Zhu, S. H. Shabbir, M. Gray, V. M. Lynch, S. Sorey, and E. V. Anslyn, *J. Am. Chem. Soc*., **2006**, *128*, 1222. (b) H. A. LeTourneau, R. E. Birsch, G. Korbeck, and J. L. Radkiewicz-Poutsma, *J. Phys. Chem. A*, **2005**, *109*, 12014. (c) L. Fisher, and T. Holme, *J. Comp. Chem*., **2001**, *22*, 913. (d) H. Höpfl, *J. Organomet. Chem*., **1999**, *581*, 129. (e) M. A. Dvorak, R. S. Ford, R. D. Suenram, F. J. Lovas, and K. R. Leopold, *J. Am. Chem. Soc*., **1992**, *114*, 108. (f) R. C. Taylor, and C. L. Cluff, *Nature*, **1958**, *182*, 390.
33. N. Christent, R. Scopelliti, and K. Severin, *Chem. Commun*., **2004**, 1158.
34. W. Clegg, A. J. Scott, F. E. S. Souza, and T. B. Marder, *Acta Crystallogr. Sect. C*, **1999**, *55*, 1885.
35. N. Christinat, R. Scopelliti, and K. Severin, *J. Org. Chem*., **2007**, *72*, 2192.
36. E. K. Perttu, M. Arnold, and P. M Iovine, *Tetrahedron Lett*., **2005**, 8753.
37. G. Alcaraz, L. Euzenat, O. Mongin, C. Katan, I. Ledoux, J. Zyss, M. Blanchard-Desce, and M. Vaultier, *Chem. Commun*., **2003**, 2766.
38. N. Christinat, E. Croisier, R. Scopelliti, M. Cascella, U. Röthlisberger, and K. Severin, *Eur. J. Inorg. Chem*., **2007**, 5177.
39. H. Kobayashi, M. Amaike, K. Koumoto, and S. Shinkai, *Bull. Chem. Soc. Jpn*., **2001**, *74*, 1311.
40. (a) J. P. Lorand, and J. O. Edwards, *J. Org. Chem*., **1959**, *24*, 769. (b) G. Kaupp, M. R. Naimi-Jamal, and V. Stepanenko, *Chem. Eur. J*., **2003**, *9*, 4156.
41. (a) W. V. Dahlhoff, and R. Köster, *Liebigs Ann. Chem*., **1975**, 1625. (b) U. W. Z. Gerwarth, *Naturforsch*, **1977**, *B32*, 1408.
42. B. M. Mikhailov, and T. K. Kozminskaya, *Izv. Akad. Nauk. SSSR, Ser. Khim (Russ)*, **1965**, 439.
43. J. J. Lavigne, B. M. Rambo, and W. Niu, *Polym. Mater. Sci. Eng*., **2004**, *90*, 816.
44. N. Iwasawa, and H. Takahagi, *J. Am. Chem. Soc*., **2007**, *129*, 7754.
45. K. E. Linder, M. D. Wen, D. P. Nowotnik, K. Ramalingam, R. M. Sharkey, F. Yost, R. K. Narra, A. D. Nunn, and W. C. Eckelman, *Bioconjugate Chem*., **1991**, *2*, 407.
46. (a) T. R. Spalding, B. O. O'Leary, L. Neville, and G. Ferguson, in *Contemporary Boron Chemistry*, Special Publication No. 253, ed. M. Davidson, A. K. Hughes, T. B. Marder, and K. Wade, Royal Society of Chemistry, London, **2000**, p. 92. (b) L. A. Neville, T. R. Spalding, and G. Ferguson, *Angew. Chem., Int. Ed*., **2000**, *39*, 3598. (c) A. G. Avent,

S. E. Lawrence, M. M. Meehan, T. G. Russell, and T. R. Spalding, *Collect. Czech. Chem. Commun.*, **2002**, *67*, 1051.

47. G. Ferguson, S. E. Lawrence, L. A. Neville, B. J. O'Leary, and T. R. Spalding, *Polyhedron*, **2007**, *26*, 2482.
48. J. T. Bien, M. J. Eschner, and B. D. Smith, *J. Org. Chem.*, **1995**, *60*, 4525.
49. N. Farfan, H. Höpfl, V. Barba, M. E. Ochoa, R. Santillan, E. Gomez, and A. Gutierrez. *J. Organomet. Chem.*, **1999**, *581*, 70.
50. For example see J. M. Berg, and R. H. Holm, *Inorg. Chem.*, **1983**, *22*, 1768. (b) M. Gielen, M. Boualam, M. Biesemans, B. Mahieu, and R. Willem, *Heterocycles*, **1992**, *34*, 549. (c) H. Höpfl, and N. Farfan, *Heteroat. Chem.*, **1998**, *9*, 377.
51. (a) H. Höpfl, and N. Farfan, *J. Organomet. Chem.*, **1997**, *547*, 71. (b) H. Höpfl, M. Sánchez, V. Barba, N. Farfan, S. Rojas, and R. Santillan, *Inorg. Chem.*, **1998**, *37*, 1679. (c) V. Barba, G. Vargas, E. Gómez, and N. Farfan, *Inorg. Chem. Acta*, **2000**, *311*, 133. (d) M. Sanchez, H. Höpfl, M. E. Ochoa, N. Farfan, R. Santillan, and S. Rojas-Lima, *Chem. Eur. J.*, **2002**, *8*, 612.
52. M. Sánchez, T. S. Keizer, S. Parkin, H. Höpfl, and D. A. Atwood, *J. Organomet. Chem.*, **2002**, *654*, 36.
53. V. Barba, E. Gallegos, R. Santillan, and N. Farfan, *J. Organomet. Chem.*, **2001**, *622*, 259.
54. V. Barba, R. Villamil, R. Luna, C. Godoy-Alcántar, H. Höpfl, H. I. Beltran, L. S. Zamudio-Rivera, R. Santillan, and N. Farfan, *Inorg. Chem.*, **2006**, *45*, 2553–2561.
55. V. Barba, H. Höpfl, N. Farfan, R. Santillan, H. I. Beltranc, and L. S. Zamudio-Riverac, *Chem. Commun.*, **2004**, 2834
56. V. Barba, and I. Betanzos, *J. Organomet. Chem.*, **2007**, *692*, 4903.
57. K. Kataoka, T. D. James, and Y. J. Kubo, *J. Am. Chem. Soc.*, **2007**, *129*, 15126.
58. (a) E. T. Wise, and S. G. Weber, *Macromolecules*, **1995**, *28*, 8321. (b) E. Z. Casassa, A. M. Sarquis, and C. H. Van Dyke, *J. Chem. Ed.*, **1986**, *63*, 57. (c) V. F. Fischer, S. Lochner, *J. Prakt. Chem.*, **1964**, *23*, 119.
59. A. L. McCloskey, in *Inorganic Polymers*, ed. F. G. A. Stone, and W. A. G. Graham, Academic Press, New York, **1962**, p. 159.
60. J. E. Mulvaney, J. J. Bloomfield, and C. S. Marvel, *J. Polym. Sci.*, **1962**, *62*, 59.
61. C. Ungurenesu, S. Cihodaru, and I. Popescu, *Tetrahedron Lett.*, **1969**, *18*, 1435.
62. I. G. C. Coutts, H. R. Goldschmid, and O. C. Musgrave, *J. Chem. Soc. C*, **1970**, 488.
63. E. I. Musina, I. A. Livinov, A. S. Balueva, and G. N. Nikonov, *Russ. J. Gen. Chem.*, **1999**, *69*, 413.
64. W. Niu, C. O'Sullivan, B. M. Rambo, M. D. Smith, and J. J. Lavigne, *Chem. Commun.*, **2005**, 4342.
65. K. L. Bhat, S. Hayik, and C. W. Bock, *J. Mol. Struct. (Theochem)*, **2003**, *638*, 107.
66. W. Niu, M. D. Smith, and J. J. Lavigne, *J. Am. Chem. Soc.*, **2006**, *128*, 16466.
67. (a) L. W. Hall, J. D. Odom, and P. D. Ellis, *J. Am. Chem. Soc.*, **1975**, *97*, 4527. (b) V. Bachler, N. Metzler-Nolte, *Eur. J. Inorg. Chem.*, **1998**, 733.
68. I. Nakazawa, S. Suda, M. Masuda, M. Asai, and T. Shimizu, *Chem. Commun.*, **2000**, 881.
69. (a) M. Mikami, and S. Shinkai, *J. Chem. Soc., Chem. Commun.*, **1995**, 153. (b) M. Mikami, and S. Shinkai, *Chem. Lett.*, **1995,** 603.
70. H. Kobayashi, K. Nakashima, E. Ohshima, Y. Hisaeda, I. Hamachi, A. Shinkai, *J. Chem. Soc., Perkin Trans. 2*, **2000**, 997.
71. R. E. Hanes, J. D. Weaver, B. F. Slabaugh, Boronic Acid Networking Agents and Associated Methods. U.S. Pat. 0089265A1, Apr. 27, **2006**.
72. L. Recksiedler, B. A. Deore, and M. S. Freund, *Langmuir*, **2006,** *22*, 2811.
73. J.-H. Fournier, T. Maris, J. D. Wuest, W. Guo, and E. Galoppini, *J. Am. Chem. Soc.*, **2003,** *12*, 1002.

74. A. P. Côté, A. I. Benin, N. W. Ockwig, M. O'Keeffe, A. J. Matzger, and O. M. Yaghi, *Science*, **2005**, *310*, 1166.
75. R. W. Tilford, W. R. Gemmill, H.-C. zur Loye, and J. J. Lavigne, *Chem. Mater.*, **2006,** *18*, 5296.
76. A. P. Côté, H. M. El-Kaderi, H. Furukawa, J. R. Hunt, and O. M. Yaghi, *J. Am. Chem. Soc.*, **2007**, *129*, 12914.
77. R. W. Tilford, S. J. Mugavero, P. J. Pellechia, J. J. Tailoring, Microporosity in Covalent Organic Frameworks (COFs). *Adv. Mater.* **2008**, *20*, 2741.
78. H. M. El-Kaderi, J. R. Hunt, J. L. Mendoza-Cortés, A. P. Côté, R. E. Taylor, M. O. Keeffe, O. M. Yaghi, *Science*, **2007**, *316*, 268.

CHAPTER 7

Mixed-Metal Supramolecular Complexes Coupling Polyazine Light Absorbers and Reactive Metal Centers

Shamindri M. Arachchige Ph.D. and Prof. Karen J. Brewer Ph.D.

Department of Chemistry, Virginia Polytechnic Institute and State University, Blacksburg, VA 24061-0212

CONTENTS

Macromolecules Containing Metal and Metal-Like Elements, Volume 9: Supramolecular and Self-Assembled Metal-Containing Materials,
Edited by Alaa S. Abd-El Aziz, Charles E. Carraher Jr., Charles U. Pittman Jr., and Martel Zeldin.

I. INTRODUCTION

This chapter focuses on the coupling of light-absorbing metal centers to reactive Rh(III), Pt(II), and Pd(II) centers. It is intended to highlight recent progress in this field and basic methods used to study these complexes. While the study of supramolecular complexes bridged with polyazine ligands is an active field, the coupling of reactive metals is far less studied. The coupling of ruthenium and osmium light absorbers to reactive metals has broad application in diverse areas such as light to energy conversion, sensing, and photodynamic therapy. Illustrative examples of different structural motifs are provided. Focus is on the more available basic chemical and photophysical properties of reactive metal-containing assemblies. Studies are limited in the arena of application of these promising assemblies to problems of current interest, with highlights of these initial exciting studies presented herein. The understanding of the basic ground and excited state properties of mixed-metal supramolecular complexes is critically important to their future application in a wide arena of light-activated chemistry. The studies to date show the promise of this class of molecules in solar energy conversion, emission-based sensing, spectroscopic probes of biomolecules, DNA modification, DNA photocleavage agents, anticancer drug development, and photodynamic therapy.

Considerable attention has been focused toward the development of polymetallic supramolecular complexes capable of light and/or redox-induced processes.[1] These systems consist of molecular components with definite and individual functions combined within the supramolecular architecture to perform unique and complex functions. Bridging ligands are used to hold the metal centers together within the polymetallic architecture as well as provide low lying acceptor orbitals. The structure of the bridging ligand plays an important role in the functioning of these systems. Since the discovery of $[Ru(bpy)_3]^{2+}$ (bpy = 2,2′-bipyridine) and its favorable photophysical and redox properties, ruthenium(II) complexes of polyazine type and related chromophores have been widely used as building blocks for synthesizing redox-active and luminescent supramolecular metal complexes.[1–3] Intermolecular light and/or redox-induced processes using $[Ru(bpy)_3]^{2+}$ type chromophores is limited by the need for molecular collision before relaxation of the metal-to-ligand charge-transfer (^{3}MLCT) excited state.[1,2] One class of complexes with potential to use intramolecular processes for harvesting energy couples polyazine chromophores to reactive metals. Balzani et al. provide a comprehensive review on polynuclear luminescent compounds.[1] This chapter focuses on a class of ruthenium and/or osmium polyazine chromophores that couple Rh, Pt, or Pd. The electrochemical, photochemical, and photophysical properties of these molecules are discussed, probing how component substitution modulates properties of these assemblies. Applications of these mixed-metal complexes with reactive metal centers to solar energy conversion and light activated DNA interactions will be summarized.

A. Light Absorption

A chromophore/light absorber molecule (LA) absorbs a photon of light to afford an electronically excited state (*LA), which has distinctive properties compared to the ground state system, Eq. (1).

$$\mathrm{LA} + h\nu \xrightarrow{I_a} {}^{*}\mathrm{LA} \tag{1}$$

Once excited, relaxation of the *LA to the ground state can occur in a nonradiative fashion, through heat loss, Eq. (2), or in a radiative fashion by emitting light, Eq. (3).

$${}^{*}\mathrm{LA} \xrightarrow{k_{nr}} \mathrm{LA} + \mathrm{heat} \tag{2}$$

$${}^{*}\mathrm{LA} \xrightarrow{k_{r}} \mathrm{LA} + h\nu' \tag{3}$$

Relaxation of the *LA to the ground state can also occur through electron or energy transfer to a quencher molecule (Q), Eqs. (4)–(6). The excited state light absorber (LA) is both a better oxidizing and reducing agent than the ground state. Electron transfer can occur oxidatively in the presence of a quencher molecule that is an electron acceptor (EA), Eq. (5), or reductively in the presence of quencher molecule that is an electron donor (ED), Eq. (6).

$${}^{*}\mathrm{LA} + \mathrm{Q} \xrightarrow{k_{en}} \mathrm{LA} + {}^{*}\mathrm{Q} \tag{4}$$

$${}^{*}\mathrm{LA} + \mathrm{EA} \xrightarrow{k_{et}} \mathrm{LA}^{+} + \mathrm{EA}^{-} \tag{5}$$

$${}^{*}\mathrm{LA} + \mathrm{EA} \xrightarrow{k'_{et}} \mathrm{LA}^{-} + \mathrm{EA}^{+} \tag{6}$$

The driving forces, (E_{redox}^{red} or E_{redox}^{oxd}), for these reactions depends on the excited state reduction potential of the LA, $E(^{*}LA^{n+}/LA^{(n-1)+})$ and the ground state oxidation potential of the ED, $(E(ED^{0/+}))$ or the excited state oxidation potential of the LA, $E(^{*}LA^{n+}/LA^{(n+1)+})$ and the ground state reduction potential of the EA, $(E(EA^{0/-}))$, Eqs. (7)–(10), where $E^{0\text{-}0}$ is the energy gap between the ground vibronic state of the electronic ground and excited state.

$$E_{redox}^{red} = E(^{*}LA^{n+}/LA^{(n-1)+}) - E(ED^{0/+}) \tag{7}$$

$$E_{redox}^{oxd} = E(^{*}LA^{n+}/LA^{(n+1)+}) - E(EA^{0/-}) \tag{8}$$

$$E(^{*}LA^{n+}/LA^{(n+1)+}) = E(LA^{n+}/LA^{(n+1)+}) - E^{0-0} \tag{9}$$

$$E(^{*}LA^{n+}/LA^{(n-1)+}) = E(LA^{n+}/LA^{(n-1)+}) + E^{0-0} \tag{10}$$

i. Molecular Photovoltaics

A major research area has been the design and development of complex molecular architectures capable of photoinduced charge separation. Photoinduced charge separation is a key component in many schemes for conversion of solar energy to chemical energy and entails absorption of light by a LA followed by intramolecular electron transfer. In applying charge transfer states, extension of the excited state lifetime of the charge-separated state is important for efficient chemical energy transformations. A simple device for photoinitiated charge separation would consist of a LA, ED, and EA. In such a system, absorption of light by a LA would create an excited state of the LA, which would be reductively quenched by the ED, eliminating the decay of the LA to the ground state. The excited electron can be transferred to an EA, affording a spatially separated charge-separated state that consists of a positively charged ED and a negatively charged EA (Fig. 1). The coupling of two photovoltaics replacing the electron acceptor with an electron collector (EC) provides a device for photoinitiated electron collection, ED-LA-EC-LA-ED.

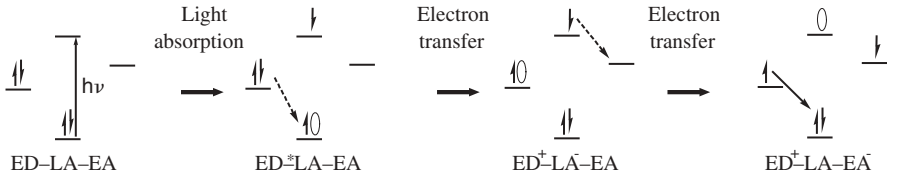

FIGURE 1. Photo-induced charge separation in a ED-LA-EA molecular device (ED = electron donor, LA = light absorber, EA = electron acceptor).

ii. Ruthenium Charge Transfer Light Absorbers

Ruthenium and osmium polyazine complexes have been widely used as light absorbers. The complex $[Ru(bpy)_3]^{2+}$ (Fig. 2) is a well studied LA with high extinction coefficients in the ultraviolet and visible regions of the spectrum.[1–5] This complex shows intense absorptions in the UV region that are intraligand $\pi \rightarrow \pi^*$ (IL) and in the visible region that are MLCT transitions. Upon optical excitation at 450 nm, population of the $Ru(d\pi) \rightarrow bpy(\pi^*)$ ^{1}MLCT occurs.

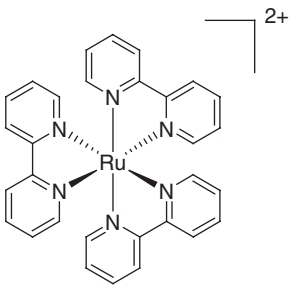

FIGURE 2. Representation of $[Ru(bpy)_3]^{2+}$ (bpy = 2,2′-bipyridine).

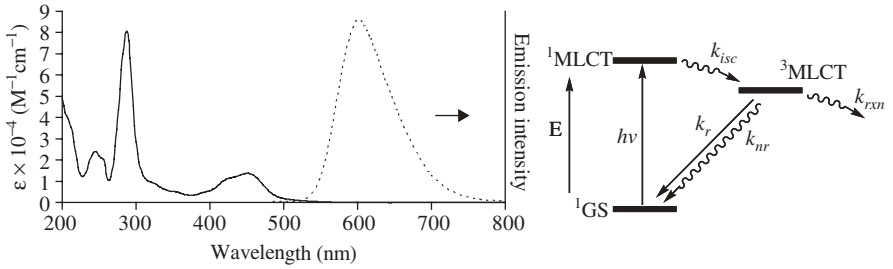

FIGURE 3. The electronic absorption and RT emission data for $[Ru(bpy)_3](PF_6)_2$ in acetonitrile (left) and a Jablonski diagram for $[Ru(bpy)_3]^{2+}$ (right) (bpy = 2,2′-bipyridine; GS = ground state; MLCT = metal-to-ligand charge-transfer; k_r = rate constant for radiative decay; k_{nr} = rate constant for non-radiative decay; k_{isc} = rate constant for intersystem crossing, k_{rxn} = rate constant for rate of reaction).

A MLCT state promotes an electron from a formally metal-based orbital to a ligand-based orbital, providing a formally oxidized metal center and reduced acceptor ligand. The ^{1}MLCT excited state undergoes a intersystem crossing to populate the ^{3}MLCT state with unit efficiency (Fig. 3). The ^{3}MLCT state can undergo electron or energy-transfer quenching and/or radiatively (k_r) or non-radiatively (k_{nr}) decay to the ground state. The ^{3}MLCT state of $[Ru(bpy)_3]^{2+}$ is relatively long lived and emissive (λ_{max}^{em} = 605 nm, excited-state lifetime of the ^{3}MLCT state, τ = 860 ns in room temperature (RT) acetonitrile solution) (Fig. 3).[4] The excited state lifetime is defined as the inverse of the sum of all the rate constants for deactivation of the excited state in the absence of a quencher. For $[Ru(bpy)_3]^{2+}$, τ is given by Eq. (1):

$$\tau = \frac{1}{k_r + k_{nr}} \tag{11}$$

The quantum yield, Φ, for an excited state process is given by the ratio of the rate constants for the process of interest, divided by the sum of all the rate constants for the deactivation of a state for a directly populated state. For an indirectly populated state, this ratio is multiplied by the fraction of light that populates this state, Eq. (12). For emission from the ^{3}MLCT state of $[Ru(bpy)_3]^{2+}$ in the absence of a quencher, Φ^{em} is:

$$\Phi^{em} = \Phi_{^3MLCT} \frac{k_r}{k_r + k_{nr}} \tag{12}$$

where $\Phi_{^3MLCT}$ is the quantum efficiency for generation of the ^{3}MLCT state. The $\Phi_{^3MLCT}$ for $[Ru(bpy)_3]^{2+}$ and most Ru(II) polyazine light absorbers is 1. The emissive excited state of $[Ru(bpy)_3]^{2+}$ provides a probe to study excited state dynamics.

The use of the tridentate ligand, 2,2′:6′,2″-terpyridine (tpy), in place of bpy in $[Ru(bpy)_3]^{2+}$, affords $[Ru(tpy)_2]^{2+}$ (Fig. 4), whose excited state reactivity is

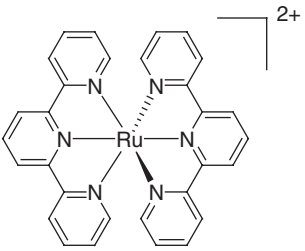

FIGURE 4. Representation of $[Ru(tpy)_2]^{2+}$ (tpy = 2,2′:6′,2″-terpyridine).

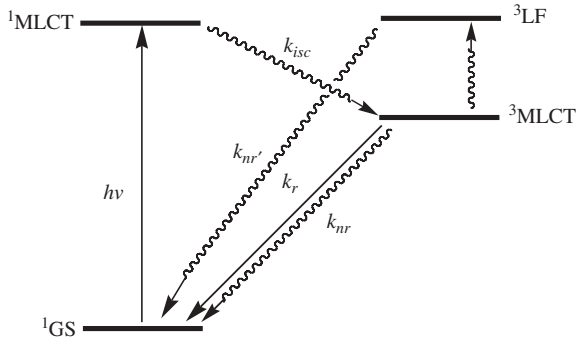

FIGURE 5. Jablonski diagram for $[Ru(tpy)_2]^{2+}$ (tpy = 2,2′:6′,2″-terpyridine; GS = ground state; MLCT = metal-to-ligand charge-transfer; k_r = rate constant for radiative decay; k_{nr} = rate constant for non-radiative decay; k_{isc} = rate constant for intersystem crossing).

relatively less explored. The complex $[Ru(tpy)_2]^{2+}$ shows no detectable emission in fluid solution at RT and possesses a short ^{3}MLCT excited state lifetime of 0.25 ns in aqueous solutions.[6] The short excited state lifetime for $[Ru(tpy)_2]^{2+}$ limits the application in intermolecular electron or energy transfer schemes.[6] The short excited state lifetime of the ^{3}MLCT state is attributed to the presence of low-lying ligand field (LF) states that are thermally accessible at room temperature (Fig. 5). The low-energy LF states are a result of the poor bite angle of the tpy ligand. LF excited states rapidly decay nonradiatively, k_{nr}, to the ground state.

iii. Osmium Charge Transfer Light Absorbers

The use of osmium in place of ruthenium within the coordination architectures leads to changes in the properties of the LAs. Osmium possesses higher-energy dπ orbitals that lead to stabilization of the MLCT states and complexes with red-shifted absorptions and emissions relative to their ruthenium analogs. The higher degree of spin orbit coupling of osmium relative to ruthenium also modulates system properties. The Os(dπ)→bpy(π*) ^{1}MLCT transition of $[Os(bpy)_3]^{2+}$ occurs red shifted relative to $[Ru(bpy)_3]^{2+}$ at 640 nm.[7] The Os(dπ)→bpy(π*) ^{3}MLCT state emits at 746 nm in acetonitrile with τ = 60 ns.[7] The considerably shortened excited state lifetime relative to $[Ru(bpy)_3]^{2+}$ is

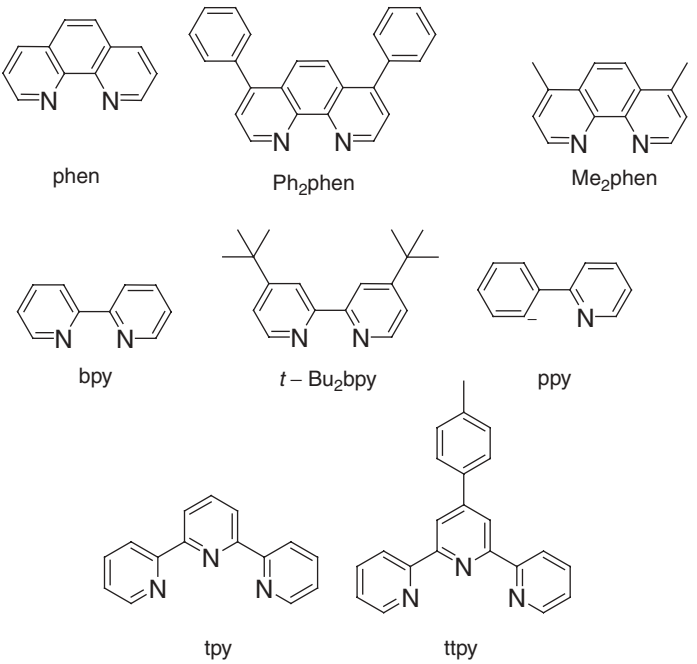

FIGURE 6. Representative polyazine terminal ligands.

consistent with the stabilization of the ^{3}MLCT state of $[Os(bpy)_3]^{2+}$ and the energy gap law. The complex $[Os(tpy)_2]^{2+}$ displays an intense ^{1}MLCT absorption at 477 nm and an intense ^{3}MLCT absorption at 657 nm. The ^{3}MLCT excited state emits at 718 nm with $\Phi^{em} = 0.014$ and $\tau = 269$ ns in acetonitrile.[8] The longer excited state lifetime of the osmium complex relative to $[Ru(tpy)_2]^{2+}$ is very unusual and is attributed to the stabilization of the ^{3}MLCT state and the destabilization of the ^{3}LF state, which limits the thermal population of the ^{3}LF state for the osmium complex. The ability to control the photophysical properties by variation of the metal and/or the ligands within the light absorber is a very attractive feature in the construction of molecular architectures for energy- or electron-transfer schemes. Figure 6 illustrates some common terminal ligands (TL) used in the construction of ruthenium and osmium polyazine charge transfer LAs.

B. Solar Water Splitting

One application of ruthenium and osmium charge transfer LAs is the harvesting of solar energy. Solar water splitting uses energy from the sun to split water into hydrogen and oxygen. The splitting of water is an energetically uphill process. The overall reaction for water splitting is a multielectron process and can be represented as Eq. (13):

$$H_2O_{(l)} \rightarrow H_{2(g)} + \frac{1}{2}O_{2(g)} \tag{13}$$

Splitting into the relevant reduction and oxidation half reactions gives Eqs. (14) and (15):

$$2H^+{}_{(aq)} + 2e^- \rightarrow H_{2(g)} \tag{14}$$

$$H_2O_{(l)} \rightarrow \frac{1}{2}O_{2(g)} + 2e^- + 2H^+{}_{(aq)} \tag{15}$$

The free energy change for reaction (13) corresponds to 1.23 V per electron (vs NHE).[9] This energy is smaller than for water splitting via a single electron mechanism, which corresponds to 5 V per electron (vs NHE).[10] Solar light in the visible and ultraviolet regions possessing energy > 1.23 V (Fig. 7) is capable of driving the water-splitting reaction via a multielectron process. Water does not absorb in the visible region, thus photochemical agents that do absorb in the visible region are necessary for water splitting. The complex $[Ru(bpy)_3]^{2+}$ and other light-absorbing analogs possess ^{3}MLCT states of sufficient energy to split water into hydrogen and oxygen, yet direct photocatalysis does not occur. The need for multielectron reactions to drive water splitting at 1.23 V makes this an ideal forum to apply mixed-metal polymetallic complexes of the type described herein.

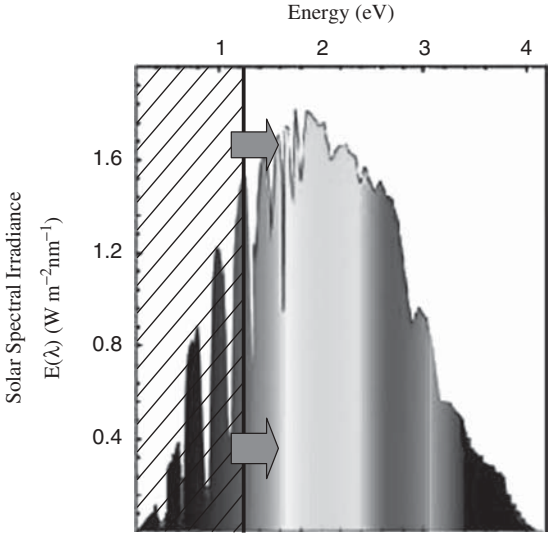

FIGURE 7. Solar spectrum. (Adopted with permission from www.lbl.gov/Science-Articles/Archive/MSD-full-spectrum-solar-cell.html.)

Complicated multicomponent systems incorporating light-absorbing units (LA), electron relays, and redox catalysts are necessary for solar energy conversion schemes. A multi-component system that can photochemically produce hydrogen from water employing $[Ru(bpy)_3]^{2+}$ as the LA, $[Rh(bpy)_3]^{3+}$ as the electron acceptor, and metallic platinum as the catalyst has been reported.[11] In this system, $[Rh(bpy)_3]^{3+}$ acts as an electron relay. Energy and electron-transfer efficiency using $[Ru(bpy)_3]^{2+}$ LA and related analogs is limited by the necessity for collisional contact with the other components during the excited state of the LA. Such limitations have stimulated interest in the design of polymetallic multicomponent systems capable of multielectron photocatalysis.

C. Metal Complexes as DNA Targeting Agents

The *cis*-$Pt^{II}Cl_2$ moiety is known to covalently bind to DNA and is the reactive subunit in the well-studied anticancer drug cisplatin, *cis*-$[Pt(NH_3)_2Cl_2]$.[12,13] Rhodium and ruthenium complexes have been shown to photocleave DNA. Ruthenium and osmium polyazine complexes with emissive ^{3}MLCT states are studied as DNA light switches. Rh(III) complexes intercalated into DNA serve as electron acceptors for excited ruthenium chromophores via long-range electron transfer.[14,15] One class of supramolecular complexes couple ruthenium or osmium polyazine LAs to biologically significant reactive metals that interact with DNA. These assemblies exploit intramolecular electron and energy transfer processes. Coupling of the ruthenium and osmium charge transfer LAs to reactive metals would unite the intense, visible light-absorbing properties of the chromophore with the favorable reactive properties of the biologically significant reactive metal center.

D. Supramolecular Charge Transfer Complexes

Supramolecular complexes as described herein are composed of an assembly of individual inorganic and organic components that act together to provide an overall function to the molecule. Such systems have been also proposed as photochemical molecular devices by Balzani.[16] The overall function of the supramolecular complex can be modulated by careful selection of the individual components. Because the individual components within the supramolecular complex are chemically bonded, bimolecular reaction for energy or electron transfer is eliminated, increasing the efficiency of the photochemical processes. The covalent coupling of subunits provides significant perturbation of the component's basic properties.

In the construction of polymetallic charge transfer complexes, bridging ligands (BLs) are used to chemically bond the individual components within the supramolecular assembly. A wide range of BLs have been used for this purpose.[1] Some common BLs consist of simple ligands such as CN^- and polyazine-type BLs separated by rigid and nonrigid spacers (Fig. 8).[1,17–23] Polyazine type BLs

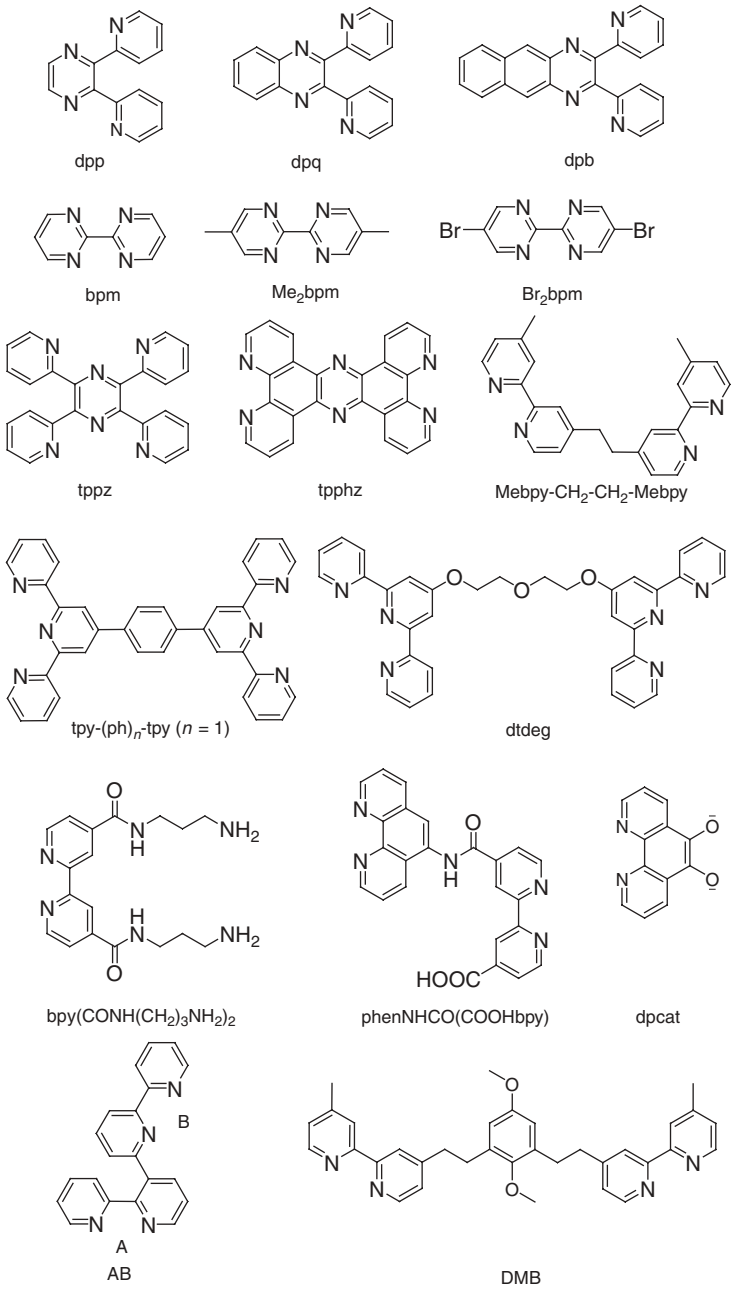

FIGURE 8. Representative polyazine bridging ligands.

separated by short rigid spacers are generally preferred, since directional electron or energy transfer occurs more efficiently in these systems.[1] While polyazine bridging ligands could be used to prepare a wide assortment of supramolecular complexes, the greater part of this work has focused on the coupling of similar metal centers with similar coordination environments. By contrast, many applications desired for supramolecular complexes containing polyazine LAs can be efficiently achieved by structurally diverse systems built of varied building blocks, each bringing its own unique set of properties to the supramolecular architecture. In this vein, coupling polyazine LAs to reactive metals such as Rh, Pt, or Pd may impart unique and potentially useful properties to the supramolecular assembly. The study of the basic chemical properties of such systems is important for understanding the perturbations introduced by the coupling of these varied components into the complex supramolecular assemblies. The knowledge gained in these studies should provide for future design of appropriate assemblies for optimized functioning.

E. Cyclic Voltammetry of Charge Transfer Light Absorbers

Electrochemistry is an analytical tool that can be used to determine redox potentials of an analyte as well as the fate of a molecule upon addition or removal of electrons. Of particular importance to photochemists is the highest occupied molecular orbital (HOMO) and the lowest unoccupied molecular orbital (LUMO). Cyclic voltammetry is one of the most commonly used electrochemical techniques and is based on the change in potential as a linear function of time. An electrochemical reaction is reversible if $i_p^a/i_p^c = 1$ and $\Delta E_p = 59/n$ mV, where i_p^a is the anodic peak current, i_p^c is the cathodic peak current, and ΔE_p ($\Delta E_p = \Delta E_p^a - E_p^c$) is the potential peak separation for the anodic (E_p^a) and cathodic (E_p^c) peaks. The oxidation or reduction potential for a reversible electrochemical process is given by $E_{1/2} = (E_p^a + E_p^c)/2$ and is recorded vs. a reference electrode. All electrochemical data provided herein are converted to V vs. saturated calomel electrode (SCE) to make the comparison more facile. A reversible redox couple implies that the complex undergoes facile electron transfer with the electrode and that no chemical reaction follows the electrochemical step.

If a chemical reaction follows an electrochemical step, the cyclic voltammogram is typically irreversible and $i_p^a/i_p^c \neq 1$ and/or $\Delta E_p \neq 59/n$ mV. Cyclic voltammetry can be used to estimate the relative energy of the frontier orbitals of a series of complexes for each coordination site. A cyclic voltammogram for $[Os(bpy)_3]^{2+}$ shows a reversible oxidation with $E_{1/2} = 0.81$ V and three reversible reductions starting at -1.29 V.[7] The oxidation is representative of $Os^{II/III}$, while the reduction represents sequential $bpy^{0/-}$ for each coordinated ligand. The electrochemistry shows that frontier orbitals of $[Os(bpy)_3]^{2+}$ involve an osmium-based HOMO and a bpy-based LUMO. This is consistent with the photochemical properties of $[Os(bpy)_3]^{2+}$ in which the lowest energy

spectroscopic transition is Os(dπ)→bpy(π*) MLCT in character and the lowest lying excited state is ^{3}MLCT in nature.

II. SUPRAMOLECULAR COMPLEXES COUPLING Ru(II) OR Os(II) POLYAZINE LIGHT ABSORBERS AND Rh(III) REACTIVE METAL CENTERS

The electrochemical and photophysical properties of a variety of mixed-metal supramolecular complexes incorporating Ru(II)/Os(II)-polyazine LAs to reactive Rh(III) systems have been investigated. The coupling of Rh(III) to ruthenium and osmium chromophores has been explored in some detail due to the known energy and electron transfer quenching of ^{3}MLCT states of ruthenium and osmium by Rh(III) complexes in bimolecular processes.[1] The systems studied to date most frequently included tris(bidentate) or bis(tridentate) coordination on Rh(III). While these studies provide considerable insight into the intramolecular excited state dynamics, these coordination environments typically prevent reactivity at the rhodium site.

A. The Complexes $[(bpy)_2Ru(BL)RhH_2(PPh_3)_2]^{3+}$

Petersen et al. reported the electrochemical, photochemical, and photophysical properties of $[(bpy)_2Ru(BL)RhH_2(PPh_3)_2]^{3+}$, where the ruthenium and rhodium metals were bridged through the BL = bpm, dpp, or dpq (bpm = 2,2-bipyrimidine, dpp = 2,3-bis(2-pyridyl)pyrazine, and dpq = 2,3-bis(2-pyridyl)-quinoxaline) (Fig. 9).[24]

These systems use BLs that provide intercomponent coupling and a photoreactive rhodium dihydride system. The authors demonstrated that these complexes undergo photoinduced reductive elimination of hydrogen when irradiated at wavelengths $\leq$ 436 nm (Fig. 10).[24]

i. Redox Properties of $[(bpy)_2Ru(BL)RhH_2(PPh_3)_2]^{3+}$

Electrochemistry is used to determine the frontier orbitals involved in electron transfer. The electrochemistry of $[(bpy)_2Ru(BL)RhH_2(PPh_3)_2]^{3+}$ (BL = bpm, dpp, or dpq) shows two oxidations during an anodic scan and four reductions during a cathodic scan (Table 1).[24] In the anodic scan for $[(bpy)_2Ru(BL)RhH_2(PPh_3)_2]^{3+}$ (BL = dpp or dpq) the two oxidations appear at 1.70 and 1.56 V representing a $Ru^{II/III}$ and $Rh^{III/IV}$ oxidation, respectively, with only the $Ru^{II/III}$ oxidation being reversible. For $[(bpy)_2Ru(bpm)RhH_2(PPh_3)_2]^{3+}$, an overlapping anodic wave is observed at 1.65 V for $Ru^{II/III}$ and $Rh^{III/IV}$ oxidations. The reductive scans for all three complexes show a series of four reversible reductions that are BL- and bpy-based with only the first two BL-based reductions behaving in a Nernstian manner (Table 1).[24] The first reduction is

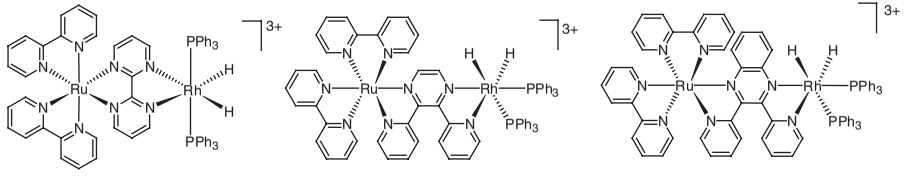

FIGURE 9. Representations of $[(bpy)_2Ru(BL)RhH_2(PPh_3)_2]^{3+}$ (BL = bpm (left), dpp (center), dpq (right)). (bpy = 2,2′-bipyridine, bpm = 2,2-bipyrimidine, dpp = 2,3-bis(2-pyridyl)pyrazine, dpq = 2,3-bis(2-pyridyl)quinoxaline).

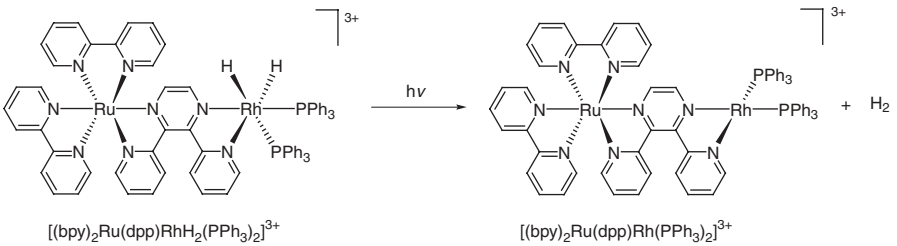

FIGURE 10. Representation of photoinduced reductive elimination of hydrogen by $[(bpy)_2Ru(dpp)RhH_2(PPh_3)_2]^{3+}$ (bpy = 2,2′-bipyridine, dpp = 2,3-bis(2-pyridyl)pyrazine).

attributed to the $BL^{0/-}$ couple, followed by the $BL^{-/2-}$ and two $bpy^{0/-}$ couples. The $BL^{0/-}$ reduction potential varies considerably, occurring at the most positive potential in $[(bpy)_2Ru(dpq)RhH_2(PPh_3)_2]^{3+}$, −0.44 V. Such a positive shift in the reduction potential of the BL is consistent with the lower energy π* orbitals of dpq relative to dpp and the bpm π* orbitals. The occurrence of the $BL^{-/2-}$ couple before $bpy^{0/-}$ reduction indicates bridged complexes, in which the BL(π*) orbitals are stabilized on bridging two electropositive metals. The electrochemistry predicts the Rh(dπ) nature of the HOMO and the BL(π*) nature of the LUMO of these complexes.

ii. Spectroscopic Properties of $[(bpy)_2Ru(BL)RhH_2(PPh_3)_2]^{3+}$

The electronic absorption spectra for $[(bpy)_2Ru(BL)RhH_2(PPh_3)_2]^{3+}$ (BL = bpm, dpp, or dpq) are consistent with typical ruthenium polyazine LAs with absorptions in the UV and visible regions. The visible regions for $[(bpy)_2Ru(BL)RhH_2(PPh_3)_2]^{3+}$ (BL = dpp, dpq, or bpm) are dominated by two major transitions (488 and 425 nm for $[(bpy)_2Ru(dpp)RhH_2(PPh_3)_2]^{3+}$, 572 and 397 nm for $[(bpy)_2Ru(dpq)RhH_2(PPh_3)_2]^{3+}$, and 551 and 413 nm for $[(bpy)_2Ru(bpm)RhH_2(PPh_3)_2]^{3+}$) (Table 2).[24] The lower-energy bands appearing in the visible region are attributed to an overlap of two MLCT transitions, one due to charge transfer from a ruthenium dπ orbital to a π* orbital of a BL (Ru→BL MLCT) and the other due to charge transfer from a rhodium dπ orbital to a π* orbital of a BL (Rh→BL MLCT), with the Rh→BL MLCT transition occurring as low energy shoulders (Table 2). This observation is consistent with the observed electrochemistry, in which the first oxidation is rhodium-based and the first reduction is BL-based. The higher-energy transitions at 425, 397, and 413 nm for $[(bpy)_2Ru(dpp)RhH_2(PPh_3)_2]^{3-}$, $[(bpy)_2Ru(dpq)RhH_2(PPh_3)_2]^{3+}$, and $[(bpy)_2Ru(bpm)RhH_2(PPh_3)_2]^{3+}$, respectively, are attributed to Ru→bpy MLCT transitions.

iii. Photophysical and Photochemical Properties of $[(bpy)_2Ru(BL)RhH_2(PPh_3)_2]^{3+}$

The complexes $[(bpy)_2Ru(dpp)RhH_2(PPh_3)_2]^{3+}$ and $[(bpy)_2Ru(bpm)RhH_2(PPh_3)_2]^{3+}$ display emissions from the Ru→BL ^{3}MLCT

state with the λ_{max}^{em} centered around 770 nm. The $\Phi^{em} = 9.2 \times 10^{-3}$ and $\tau = 106$ ns for $[(bpy)_2Ru(dpp)RhH_2(PPh_3)_2]^{3+}$, while the $\Phi^{em} = 1.9 \times 10^{-3}$ and $\tau = 41$ ns for $[(bpy)_2Ru(bpm)RhH_2(PPh_3)_2]^{3+}$ (Table 2).[24] The smaller τ for the weakly emissive $[(bpy)_2Ru(bpm)RhH_2(PPh_3)_2]^{3+}$ is consistent with the energy gap law[25] and typical of bpm-bridged complexes. The smaller excited state lifetime for $[(bpy)_2Ru(bpm)RhH_2(PPh_3)_2]^{3+}$ relative to $[(bpy)_2Ru(dpp)RhH_2(PPh_3)_2]^{3+}$ is attributed to the ability of the bpm ligand to couple the ruthenium and rhodium metal centers to a greater extent relative to dpp, allowing the rhodium center to facilitate the deactivation of the Ru→BL ^{3}MLCT state.[24] The complex $[(bpy)_2Ru(dpq)RhH_2(PPh_3)_2]^{3+}$ did not display an observable emission, consistent with the lower energy of the dpq(π^*) orbitals, relative to dpp(π^*) and bpm(π^*) orbitals making this emission outside the detection limit of their instrument. These complexes are of interest as models for possible rhodium hydrides in solar energy conversion schemes.

B. Cyanide-Bridged Ru(II)-Rh(III) Complexes

Endicott et al. examined the redox properties for a series of complexes, including the Ru(II)-Rh(III) complexes, $[(bpy)_2(CN)Ru(CN)Rh(NH_3)_5]^{3+}$, $[(bpy)_2Ru\{(CN)Rh(NH_3)_5\}_2]^{6+}$, $[(bpy)_2(CN)Ru(CN)Rh(NH_3)_4I)]^{2+}$, $[(bpy)_2(CN)Ru(CN)Rh(NH_3)_4Br)]^{2+}$, and $[(bpy)_2(CN)Ru(CN)Rh(NH_3)_4CN)]^{2+}$ (Fig. 11).[26] Using cyanide as the BL provides a means to electronically couple the bridged metal centers.

i. Redox Properties of Cyanide-Bridged Ru(II)-Rh(III) Complexes

Electrochemistry can be used to understand the frontier orbitals associated with electron transfer processes. The oxidative electrochemistry of the $[(bpy)_2Ru(CN)_2]$ subunit shows a $Ru^{II/III}$-based oxidation at 1.00, 1.18, and 0.92 V (in acetonitrile using a 0.1 M Et_4NClO_4 supporting electrolyte) for $[(bpy)_2(CN)Ru(CN)Rh(NH_3)_5]^{3+}$, $[(bpy)_2Ru\{(CN)Rh(NH_3)_5\}_2]^{6+}$, and $[(bpy)_2(CN)Ru(CN)Rh(NH_3)_4I)]^{2+}$, respectively (Table 1).[26] Coordination of a second Rh(III) shifts the $Ru^{II/III}$ oxidation to a more positive potential in

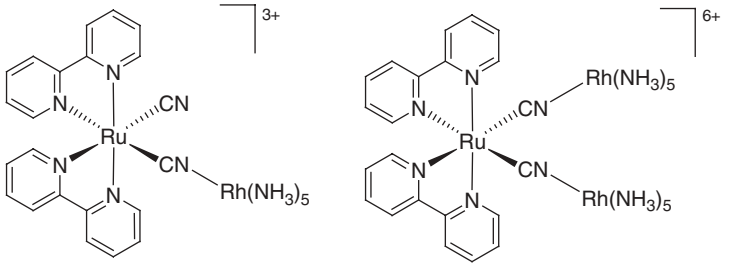

FIGURE 11. Representations of $[(bpy)_2(CN)Ru(CN)Rh(NH_3)_5]^{3+}$ (left) and $[(bpy)_2Ru\{(CN)Rh(NH_3)_5\}_2]^{6+}$ (right) (bpy = 2,2′-bipyridine).

$[(bpy)_2Ru\{(CN)Rh(NH_3)_5\}_2]^{6+}$ relative to $[(bpy)_2(CN)Ru(CN)Rh(NH_3)_5]^{3+}$. The reductive electrochemistry of $[(bpy)_2(CN)Ru(CN)Rh(NH_3)_5]^{3+}$ and $[(bpy)_2Ru\{(CN)Rh(NH_3)_5\}_2]^{6+}$ reveals two $bpy^{0/-}$ based reductions at -1.70 and -1.94 V in acetonitrile. The electrochemistry predicts a Ru(dπ)-based HOMO and a bpy(π*)-based LUMO in these complexes.

ii. Spectroscopic Properties of Cyanide-Bridged Ru(II)-Rh(III) Complexes

The Ru(II)-Rh(III) cyanide-bridged complexes show absorptions that are characteristic for ruthenium and rhodium polyazine complexes. The electronic absorption spectra of a series of cyanide-bridged Ru(II)-Rh(III) complexes recorded in DMSO-H_2O solutions correlate well with the electrochemical properties. Coordination of a second Rh(III) shifts the lowest energy transition, which is Ru→bpy MLCT in nature, to higher energy in $[(bpy)_2Ru\{(CN)Rh(NH_3)_5\}_2]^{6+}$ relative to $[(bpy)_2(CN)Ru(CN)Rh(NH_3)_5]^{3+}$. This positive shift is consistent with the stabilization of the Ru(dπ) orbitals of $[(bpy)_2Ru\{(CN)Rh(NH_3)_5\}_2]^{6+}$ and correlates well with the electrochemistry where the $Ru^{II/III}$ oxidation moves to more positive potential with Rh(III) addition.[26] The λ_{max}^{abs} of the Ru→bpy MLCT transitions for $[(bpy)_2(CN)Ru(CN)Rh(NH_3)_5]^{3+}$and $[(bpy)_2Ru\{(CN)Rh(NH_3)_5\}_2]^{6+}$ are 430 and 413 nm, while the corresponding λ_{max}^{abs} for the monometallic precursor, $[Ru(bpy)_2(CN)_2]$, occurs at 457 nm.[26]

iii. Photophysical and Photochemical Properties of Cyanide-Bridged Ru(II)-Rh(III) Complexes

Emission spectroscopy is used to study the excited state dynamics of the Ru(II)-Rh(III) cyanide-bridged complexes. The cyanide-bridged Ru(II)-Rh(III) complexes exhibit emissions from the Ru→bpy ^{3}MLCT states.[26] The emission maxima shifts to higher energy with each successive Rh(III) metallation. For example, λ_{max}^{em} at 298 K in DMSO-H_2O solution for $[(bpy)_2(CN)Ru(CN)Rh(NH_3)_5]^{3+}$ and $[(bpy)_2Ru\{(CN)Rh(NH_3)_5\}_2]^{6+}$are 604 and 576 nm, respectively, with excited state lifetimes of 0.31 and 0.04 μs. For comparison, the corresponding λ_{max}^{em} for the monometallic precursor, $[Ru(bpy)_2(CN)_2]$, occurs at 634 nm with an excited state lifetime of 0.43 μs at 298 K. At 77 K, the λ_{max}^{em} occur at 556 and 543 nm for $[(bpy)_2(CN)Ru(CN)Rh(NH_3)_5]^{3+}$ and $[(bpy)_2Ru\{(CN)Rh(NH_3)_5\}_2]^{6+}$, with concomitant enhancements in the excited state lifetimes of 5.7 and 8.4 μs, respectively (Table 2). For comparison, at 77 K, the monometallic precursor, $[Ru(bpy)_2(CN)_2]$, has an excited state lifetime of 4.3 μs. The excited state emission and lifetime determinations were reported to be complicated for $[(bpy)_2(CN)Ru(CN)Rh(NH_3)_4I)]^{2+}$ and $[(bpy)_2(CN)Ru(CN)Rh(NH_3)_4Br)]^{2+}$ due to photodecomposition and interference from the strongly emitting $[Ru(bpy)_2(CN)_2]$ impurities. This interesting study provides insight into the coupling of LAs and reactive metals with the small cyanide bridging ligands and highlights that complexes with reasonable ^{3}MLCT lifetimes can be produced which can be exploited in light activated processes.

C. Polyazine-Bridged $[(bpy)_2Ru(dpp)Rh(bpy)_2]^{5+}$

Kalyanasundaram et al. investigated the photophysical properties and the excited state intramolecular interactions in $[(bpy)_2Ru(dpp)Rh(bpy)_2]^{5+}$ (Fig. 12).[27] The dpp BL is a widely studied polyazine system that provides electronic coupling of the bridged metals. The tris(bidentate) coordination of the rhodium center prevents reactivity at this metal site. This early study of a bridged complex with a reactive metal highlights the complicated excited state dynamics in systems with only two metal centers.

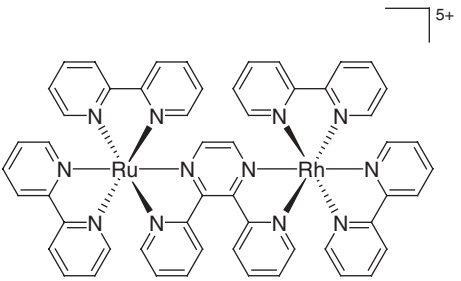

FIGURE 12. Representation of $[(bpy)_2Ru(dpp)Rh(bpy)_2]^{5+}$ (bpy = 2,2′-bipyridine, dpp = 2,3-bis(2-pyridyl)pyrazine).

i. Redox Properties of $[(bpy)_2Ru(dpp)Rh(bpy)_2]^{5+}$

The electrochemical properties of the dpp-bridged Ru(II)-Rh(III) complex provides insight into the orbital energetics. The reductive electrochemistry of $[(bpy)_2Ru(dpp)Rh(bpy)_2]^{5+}$ shows an irreversible reduction at −0.65 V (Table 1).[27] DeArmond has shown that reductive electrochemistry of $[Rh(bpy)_3]^{3+}$ consists of a quasi-reversible reduction at ca. −0.80 V in acetonitrile attributed to $Rh^{III/II/I}$ reduction. The irreversible nature of this $Rh^{III/II/I}$ reduction is due to bpy loss to form $[Rh^{I}(bpy)_2]^{+}$.[28] In the homobimetallic complex, $[(bpy)_2Ru(dpp)Ru(bpy)_2]^{4+}$, the first reduction is dpp(π*)-based and occurs at ca. −0.70 V. Thus the dpp(π*) orbitals and the Rh(dσ*) orbitals in $[(bpy)_2Ru(dpp)Rh(bpy)_2]^{5+}$ are very close in energy. The electrochemistry of $[(bpy)_2Ru(dpp)Rh(bpy)_2]^{5+}$ predicts a low-lying metal-to-metal charge-transfer excited state (MMCT) due to the Ru(dπ) nature of the HOMO and Rh(dσ*)-based LUMO.

ii. Spectroscopic Properties of $[(bpy)_2Ru(dpp)Rh(bpy)_2]^{5+}$

The dpp-bridged Ru(II)-Rh(III) complex displays typical absorptions for ruthenium and rhodium polyazine complexes in the UV and visible regions.[27] The UV region in the electronic absorption spectrum of $[(bpy)_2Ru(dpp)Rh(bpy)_2]^{5+}$ in acetonitrile reveals two bands at λ_{max}^{abs} = 312 and 295 nm characteristic of Rh(III)-based transitions and ligand-based $\pi \rightarrow \pi^*$

transitions, respectively. The visible region is dominated by Ru→dpp MLCT transitions at λ_{max}^{abs} = 514 and 351 nm (Table 2). Consistent with the greater stabilization of the dpp(π*) orbital upon metallation, the Ru→dpp MLCT transition of $[(bpy)_2Ru(dpp)Rh(bpy)_2]^{5+}$ is considerably red shifted compared to the corresponding transition in the monometallic precursor $[(bpy)_2Ru(dpp)]^{2+}$ occurring at 468 nm.

iii. Photophysical and Photochemical Properties of $[(bpy)_2Ru(dpp)Rh(bpy)_2]^{5+}$

Emission spectroscopy is used to understand the excited state properties of the dpp-bridged Ru(II)-Rh(III) complex. The complex $[(bpy)_2Ru(dpp)Rh(bpy)_2]^{5+}$ displays a weak emission at λ_{max}^{em} = 778 nm with τ = 37 ns in acetonitrile at RT from the Ru→dpp ^{3}MLCT state (Table 2).[27] Both the λ_{max}^{abs} and λ_{max}^{em} for $[(bpy)_2Ru(dpp)Rh(bpy)_2]^{5+}$ are red shifted with respect to $[(bpy)_2Ru(dpp)]^{2+}$ (λ_{max}^{abs} = 468, λ_{max}^{em} = 682 nm) with a blue shifted absorbance with respect to $[(bpy)_2Ru(dpp)Ru(bpy)_2]^{4+}$ (λ_{max}^{abs} = 526, λ_{max}^{em} = 790 nm). The luminescence intensity of Ru→dpp ^{3}MLCT of $[(bpy)_2Ru(dpp)Rh(bpy)_2]^{5+}$ is considerably reduced with respect to the homobimetallic, $[(bpy)_2Ru(dpp)Ru(bpy)_2]^{4+}$, with a concurrent reduction in the excited state lifetime (τ = 37 and 140 ns for $[(bpy)_2Ru(dpp)Rh(bpy)_2]^{5+}$and $[(bpy)_2Ru(dpp)Ru(bpy)_2]^{4+}$, respectively). At 77 K, the λ_{max}^{em} of $[(bpy)_2Ru(dpp)Rh(bpy)_2]^{5+}$is red shifted with a concurrent increase in τ to 1.71 μs. The τ of $[(bpy)_2Ru(dpp)Rh(bpy)_2]^{5+}$ at 77 K is similar to the τ = 2.38 μs of $[(bpy)_2Ru(dpp)Ru(bpy)_2]^{4+}$, suggesting that additional intramolecular quenching processes occurring at room temperature due to the Rh(III)-polypyridyl unit of $[(bpy)_2Ru(dpp)Rh(bpy)_2]^{5+}$ are prohibited at 77 K. The electrochemical and photophysical data suggest that photoexcitation in the Ru→dpp MLCT state may lead to transfer of the promoted electron to Rh(III) to create a MMCT (metal-to-metal charge-transfer) state, which can decay to the ground state, quenching the ^{3}MLCT emission at RT. This study demonstrated that intramolecular electron transfer plays a significant role in the excited state dynamics of $[(bpy)_2Ru(dpp)Rh(bpy)_2]^{5+}$, leading to weaker luminescence and short excited state lifetime for the Ru→dpp ^{3}MLCT state compared to $[(bpy)_2Ru(dpp)Ru(bpy)_2]^{4+}$.[27]

D. Tridentate-Bridged Complexes: $[(ttpy)Ru(tpy\text{-}(Ph)_n\text{-}tpy)Rh(ttpy)]^{5+}$ (n = 0 – 2)

Indelli et al. investigated the electrochemical and photophysical properties of Ru(II)-Rh(III) complexes of the form $[(ttpy)Ru(tpy\text{-}(Ph)_n\text{-}tpy)Rh(ttpy)]^{5+}$ (Fig. 13), to understand the photoinduced electron and energy transfer processes (n = 0 – 2; ttpy = 4′-*p*-tolyl-2,2′:6,2″-terpyridine, tpy-(ph)$_n$-tpy = 2,2′:6′,2″-terpyridine units are either directly linked together (n = 0) or connected through one or two (n = 1 or 2) phenyl spacers in the 4′-position).[29] The use of the tridentate coordination provides stereochemically defined systems, but the tpy type ligands

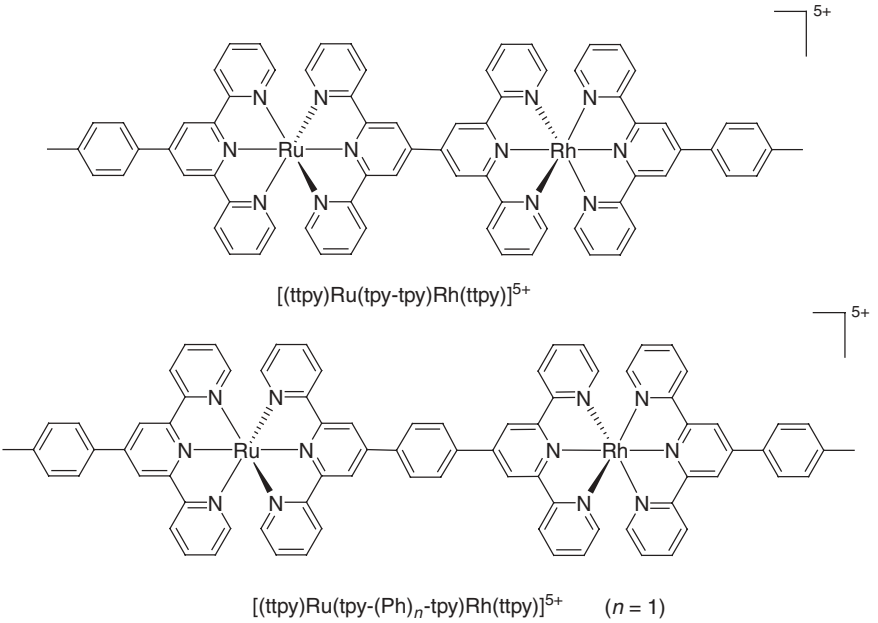

FIGURE 13. Representations of $[(ttpy)Ru(tpy\text{-}(Ph)_n\text{-}tpy)Rh(ttpy)]^{5+}$ ($n = 0$ (top), $n = 1$ (bottom)) (ttpy = 4′-*p*-tolyl-2,2′:6,2″-terpyridine).

display significantly shorter lived ^{3}MLCT excited states. The bis(tridentate) coordination of the rhodium center prevents reactivity at this site. The variation of the link is employed to probe the role of linker and inter-chromophore distance on the observed properties.

i. Redox Properties of $[(ttpy)Ru(tpy\text{-}(Ph)_n\text{-}tpy)Rh(ttpy)]^{5+}$

Electrochemistry of the Ru(II)-Rh(III) systems provides a means to understand the orbital energetics within the supramolecular architecture. The $Ru^{II/III}$ couple of $[(ttpy)Ru(tpy\text{-}(Ph)_n\text{-}tpy)Rh(ttpy)]^{5+}$ ($n = 0$, 1, or 2) appears at 1.31, 1.29, or 1.27 V, respectively, (in CH_3CN solution using 0.1 M Bu_4NBF_4 as the supporting electrolyte) (Table 1).[29] A positive shift is observed in the $Ru^{II/III}$ oxidation with decreasing Ru-Rh distance. This positive shift in the $Ru^{II/III}$ oxidation suggests a ruthenium center with a more stabilized dπ orbital in $[(ttpy)Ru(tpy\text{-}(Ph)_n\text{-}tpy)Rh(ttpy)]^{5+}$ ($n = 0$) relative to $[(ttpy)Ru(tpy\text{-}(Ph)_n\text{-}tpy)Rh(ttpy)]^{5+}$ ($n = 1$ or 2). The $Ru^{II/III}$ oxidation for $[(ttpy)Ru(tpy\text{-}(Ph)_n\text{-}tpy)Rh(ttpy)]^{5+}$ ($n = 0$) occurs at a significantly more positive potential than for the corresponding $Ru^{II/III}$ oxidation of $[Ru(ttpy)_2]^{2+}$ (1.25 V)[30] and at the same potential as the homobimetallic analog $[(ttpy)Ru(tpy\text{-}(Ph)_n\text{-}tpy)Ru(ttpy)]^{4+}$ ($n = 0$).[30] The reductive electrochemistry shows an irreversible $Rh^{III/II/I}$ reduction at −0.54 V for $[(ttpy)Ru(tpy\text{-}(Ph)_n\text{-}tpy)Rh(ttpy)]^{5+}$ ($n = 0$) and at

-0.56 V for $[(ttpy)Ru(tpy\text{-}(Ph)_n\text{-}tpy)Rh(ttpy)]^{5+}$ ($n = 1$ or 2). The $Rh^{III/II/I}$ reductions are followed by two reversible $ttpy^{0/-}$ reductions at −1.22 and −1.44 V, −1.18 and −1.41 V, and −1.20 and −1.37 V for $[(ttpy)Ru(tpy\text{-}(Ph)_n\text{-}tpy)Rh(ttpy)]^{5+}$ ($n = 0$), $[(ttpy)Ru(tpy\text{-}(Ph)\text{-}tpy)Rh(ttpy)]^{5+}$, and $[(ttpy)Ru(tpy\text{-}(Ph)_2\text{-}tpy)Rh(ttpy)]^{5+}$, respectively (Table 1). The electrochemistry predicts a Ru(dπ)-based HOMO and a Rh(dπ*)-based LUMO in these structural motifs, with the Ru(dπ) orbitals of $[(ttpy)Ru(tpy\text{-}(Ph)_n\text{-}tpy)Rh(ttpy)]^{5+}$ ($n = 0$) being the most stabilized.

ii. Spectroscopic Properties of $[(ttpy)Ru(tpy\text{-}(Ph)_n\text{-}tpy)Rh(ttpy)]^{5+}$

The heterobimetallic Ru(II)-Rh(III) complexes absorb in much of the UV and visible regions of the spectrum. The λ_{max}^{abs} of the MLCT transitions $[(ttpy)Ru(tpy\text{-}(Ph)_n\text{-}tpy)Rh(ttpy)]^{5+}$ ($n = 1$ or 2) coincide with the λ_{max}^{abs} of $[Ru(ttpy)_2]^{2+}$ at 490 nm in acetonitrile (Table 2).[30] By contrast, the λ_{max}^{abs} of the MLCT transition is considerably red shifted in $[(ttpy)Ru(tpy\text{-}(Ph)_n\text{-}tpy)Rh(ttpy)]^{5+}$ ($n = 0$) and occurs at the same position as the λ_{max}^{abs} of the MLCT transition of $[(ttpy)Ru(tpy\text{-}(Ph)_n\text{-}tpy)Ru(ttpy)]^{4+}$ ($n = 0$) at ~520 nm.[30] The UV regions of the electronic absorption spectra are dominated by Ru(II) and Rh(III) coordinated $\pi \rightarrow \pi^*$ IL transitions, with the shoulders at 360 and 330 nm attributed to the Rh(III) component. The absorptions in this region shift to lower energies with increasing number of spacers.

For $[(ttpy)Ru(tpy\text{-}(Ph)_n\text{-}tpy)Rh(ttpy)]^{5+}$ ($n = 1$ or 2), the electrochemistry correlates well with the monometallic $[Ru(ttpy)_2]^{2+}$ and $[Rh(ttpy)_2]^{3+}$ molecular components and the λ_{max}^{abs} of the MLCT transitions coincide with the corresponding transition for $[Ru(ttpy)_2]^{2+}$. This suggests electronic isolation between the ruthenium and rhodium components. By contrast, the oxidative electrochemistry shifts to a more positive potential in $[(ttpy)Ru(tpy\text{-}(Ph)_n\text{-}tpy)Rh(ttpy)]^{5+}$ ($n = 0$) compared to $[Ru(ttpy)_2]^{2+}$, while a red shift is observed in the λ_{max}^{abs}. These shifts in the electrochemical and spectroscopic data of $[(ttpy)Ru(tpy\text{-}(Ph)_n\text{-}tpy)Rh(ttpy)]^{5+}$ ($n = 0$) suggest the possibility of perturbation of the redox and light absorption properties of the Ru(II) by the electron-withdrawing Rh(III). The authors suggest that the identical shifts observed for the homobimetallic complex $[(ttpy)Ru(tpy\text{-}(Ph)_n\text{-}tpy)Ru(ttpy)]^{4+}$ ($n = 0$) rule out the possibility of perturbations in the redox and spectroscopic properties by Rh(III) in $[(ttpy)Ru(tpy\text{-}(Ph)_n\text{-}tpy)Rh(ttpy)]^{5+}$ ($n = 0$) and indicate that these perturbations arise due to the lower-energy π* orbitals of the tpy-$(Ph)_n$-tpy ($n = 0$) ligand compared to tpy-$(Ph)_n$-tpy ($n = 1$ or 2).

iii. Photophysical and Photochemical Properties of $[(ttpy)Ru(tpy\text{-}(Ph)_n\text{-}tpy)Rh(ttpy)]^{5+}$

Emission spectroscopy provides a probe to study the excited state properties of the $[(ttpy)Ru(tpy\text{-}(Ph)_n\text{-}tpy)Rh(ttpy)]^{5+}$ systems. The photophysical properties of the complexes were investigated at 300, 150, and 77 K.[29] At 150 K in fluid aerated 4:1 ethanol/methanol solutions, the Ru(II)-Rh(III) complexes

exhibit emissions from the Ru-based excited states. At 150 K, the λ_{max}^{em} for $[(ttpy)Ru(tpy\text{-}(Ph)_n\text{-}tpy)Rh(ttpy)]^{5+}$ (n = 1 or 2) occur at 655 and 648 nm, respectively (Table 2), similar to $[Ru(ttpy)_2]^{2+}$ (λ_{max}^{em} = 645 nm) with similar intensity in absorbance matched samples. This indicates that no quenching of the Ru-based emission occurs at this temperature. Consistent with this, at 150 K, the τ of the Ru-based excited states are similar and are 3.0, 3.5, and 3.2 μs for $[(ttpy)Ru(tpy\text{-}(Ph)_n\text{-}tpy)Rh(ttpy)]^{5+}$ (n = 1 or 2) and $[Ru(ttpy)_2]^{2+}$, respectively (Table 2). The λ_{max}^{em} for $[(ttpy)Ru(tpy\text{-}(Ph)_n\text{-}tpy)Rh(ttpy)]^{5+}$($n$ = 0) occurs considerably red shifted at 720 nm and occurs at a similar energy to that of $[(ttpy)Ru(tpy\text{-}(Ph)_n\text{-}tpy)Ru(ttpy)]^{4+}$ (n = 0, λ_{max}^{em} = 708 nm). The emission from the Ru-based excited state of $[(ttpy)Ru(tpy\text{-}(Ph)_n\text{-}tpy)Rh(ttpy)]^{5+}$ (n = 0) is efficiently quenched with a concurrent reduction in the excited state lifetime (τ = < 0.1 μs) with respect to the corresponding emission of $[(ttpy)Ru(tpy\text{-}(Ph)_n\text{-}tpy)Ru(ttpy)]^{4+}$ (n = 0, τ = 3.5 μs). The excitation spectra matched closely to the absorption spectra for $[(ttpy)Ru(tpy\text{-}(Ph)_n\text{-}tpy)Rh(ttpy)]^{5+}$ (n = 1 or 2) at RT. A precise excitation spectrum was not obtained for $[(ttpy)Ru(tpy\text{-}(Ph)_n\text{-}tpy)Rh(ttpy)]^{5+}$ (n = 0). No quenching of the emission from the Ru-based excited state was observed at 77 K. For example, at 77 K in a solid matrix of 4:1 ethanol/methanol, the emission intensities and the excited state lifetimes for $[(ttpy)Ru(tpy\text{-}(Ph)_n\text{-}tpy)Rh(ttpy)]^{5+}$ (n = 1 or 2) were similar to $[Ru(ttpy)_2]^{2+}$ (τ = 13.0, 13.2, and 13.5 μs, respectively, for $[(ttpy)Ru(tpy\text{-}(Ph)_n\text{-}tpy)Rh(ttpy)]^{5+}$ (n = 1 or 2) and $[Ru(ttpy)_2]^{2+}$), while emission intensities and the excited state lifetimes for $[(ttpy)Ru(tpy\text{-}(Ph)_n\text{-}tpy)Rh(ttpy)]^{5+}$ (n = 0) were similar to $[(ttpy)Ru(tpy\text{-}(Ph)_n\text{-}tpy)Ru(ttpy)]^{4+}$($n$ = 0) (τ = 12.5 and 12.9 μs, respectively, for $[(ttpy)Ru(tpy\text{-}(Ph)_n\text{-}tpy)Rh(ttpy)]^{5+}$ (n = 0) and $[(ttpy)Ru(tpy\text{-}(Ph)_n\text{-}tpy)Ru(ttpy)]^{4+}$ (n = 0) Table 2.[29]

An energy state diagram that illustrates the orbital energetics and the electron and energy transfer processes of the Ru(II)-Rh(III) complexes is illustrated in Figure 14, which also summarizes excited state dynamics of the Ru(II)-Rh(III) heterobimetallics. The electrochemical and the photophysical properties suggest (a) electron transfer from Ru(II) to Rh(III) (k_{et}), (b) electron transfer from Ru(II) to excited Rh(III) (k_{et}'), (c) energy transfer from excited Rh(III) to Ru(II) (k_{en}), and (d) charge recombination (k_{nr}'). These studies demonstrated that at 77 K and 150 K, energy transfer occurs from Rh(III) to Ru(II) in all complexes, while electron transfer occurs from Ru(II) to Rh(III) only in $[(ttpy)Ru(tpy\text{-}(Ph)_n\text{-}tpy)Rh(ttpy)]^{5+}$ (n = 0) at 150 K. The different behavior for the n = 0 species is rationalized in terms of better electronic coupling and smaller reorganizational energies for this complex. At low temperature in a frozen matrix, electron transfer quenching is not observed, while energy transfer is postulated to occur. The freezing of electron transfer quenching but not of energy transfer in rigid glasses reflects the different reorganizational energies involved in the two processes. The study of these complicated excited state dynamics in a stereochemically defined system keenly highlights the factors impacting intercomponent interactions within a mixed-metal assembly.

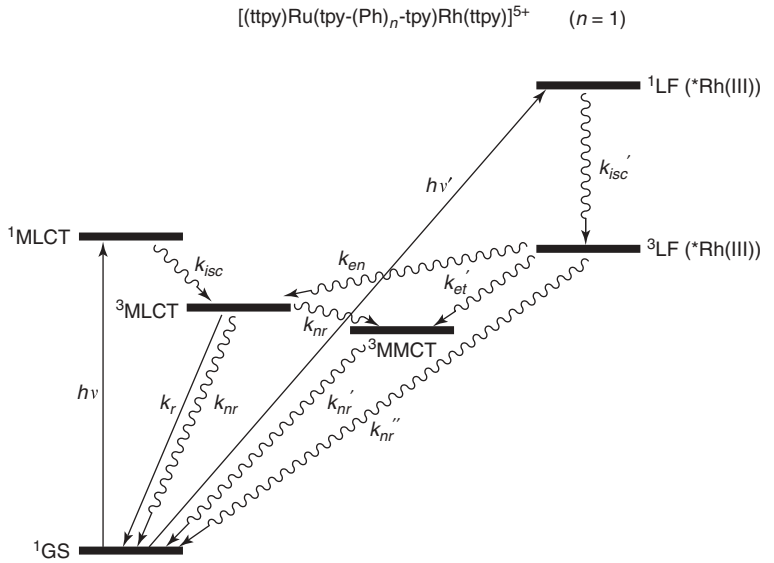

FIGURE 14. Energy level diagram for $[(ttpy)Ru(tpy\text{-}(Ph)_n\text{-}tpy)Rh(ttpy)]^{5+}$ (n = 0, 1, or 2). GS = ground state; MLCT = metal-to-ligand charge-transfer; MMCT = metal-to-metal charge-transfer; k_r = rate constant for radiative decay; k_{nr} = rate constant for non-radiative decay; k_{isc} = rate constant for intersystem crossing; k_{et} = rate constant for electron transfer; k_{en} = rate constant for energy transfer.

E. Ru(II)-Rh(III) Complexes Bridged with a Flexible Spacer: $[(Me_2phen)_2Ru(Mebpy\text{-}CH_2\text{-}CH_2\text{-}Mebpy)Rh(Me_2bpy)_2]^{5+}$

Indelli et al. reported a study of the intercomponent electron and energy transfer processes of the Ru(II)-Rh(III) complex $[(Me_2phen)_2Ru(Mebpy\text{-}CH_2\text{-}CH_2\text{-}Mebpy)Rh(Me_2bpy)_2]^{5+}$ (Fig. 15) (Me_2phen = 4,7-dimethyl-1,10-phenanthroline, Mebpy = 4-methyl-2,2′-bipyridine, Me_2bpy = 4,4′-dimethyl-2,2′-bipyridine) by studying the electrochemical, photochemical, and photophysical properties of this complex and its mono-metallic synthons $[(Me_2bpy)_2Rh(Mebpy\text{-}CH_2\text{-}CH_2\text{-}Mebpy)](ClO_4)_3$ and $[(Me_2phen)_2Ru(Mebpy\text{-}CH_2\text{-}CH_2\text{-}Mebpy)](PF_6)_2$.[31] The BL used in this study typically provides for electronic isolation of the metals due to the saturated aliphatic linker.

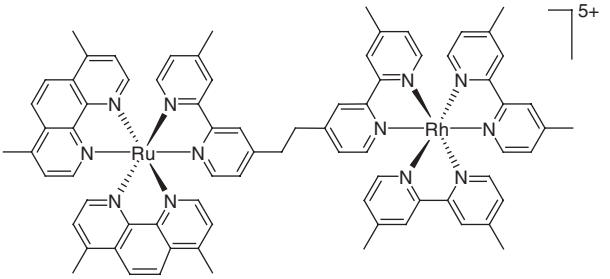

FIGURE 15. Representation of $[(Me_2phen)_2Ru(Mebpy\text{-}CH_2\text{-}CH_2\text{-}Mebpy)Rh(Me_2bpy)_2]^{5+}$ (Me_2phen = 4,7-dimethyl-1,10-phenanthroline, Mebpy = 4-methyl-2,2′-bipyridine, Me_2bpy = 4,4′-dimethy-2,2′-bipyridine).

i. Redox Properties of $[(Me_2phen)_2Ru(Mebpy\text{-}CH_2\text{-}CH_2\text{-}Mebpy)Rh(Me_2bpy)_2]^{5+}$

Electrochemistry predicts the relative energy of the frontier orbitals in the Ru(II)-Rh(III)-bridged systems. The electrochemistry of the Ru(II)-Rh(III) complex coincides well with the monometallic synthons and the oxidative and reductive electrochemical waves were assigned by comparison with the electrochemistry of the monometallic synthons. The oxidative electrochemistry shows a reversible $Ru^{II/III}$oxidation at 1.13 V (in acetonitrile using 0.1 M Bu_4NPF_6 as the supporting electrolyte) (Table 1).[31] The reductive electrochemistry shows two reversible reductions corresponding to the reduction of the polypyridine ligands at −1.45 and −1.66 V and a quasireversible reduction at -0.92 V due to $Rh^{III/II/I}$ reduction (Table 1).[31] The electrochemistry predicts a Ru(dπ) HOMO and Rh(dπ*) LUMO.

ii. Spectroscopic Properties of $[(Me_2phen)_2Ru(Mebpy\text{-}CH_2\text{-}CH_2\text{-}Mebpy)Rh(Me_2bpy)_2]^{5+}$

The Ru(II)-Rh(III)-bridged complexes show absorptions that are typical for ruthenium and rhodium polyazine complexes. The electronic absorption spectrum of $[(Me_2phen)_2Ru(Mebpy\text{-}CH_2\text{-}CH_2\text{-}Mebpy)Rh(Me_2bpy)_2]^{5+}$ in acetonitrile coincides with the additive absorption spectra of the monometallic synthons.[31] The visible region of $[(Me_2phen)_2Ru(Mebpy\text{-}CH_2\text{-}CH_2\text{-}Mebpy)Rh(Me_2bpy)_2]^{5+}$ is dominated by Ru→polypyridine based MLCT transitions, with energies of the Ru→ Me_2phen and Ru→Mebpy-CH_2-CH_2-Mebpy MLCT excited states being almost identical. The UV region is dominated by ligand-based π→π* transitions with the bands centered at 280 and 295 nm, corresponding to ligand-based transitions of the Ru(II) component; those at 302 and 313 nm correspond to ligand-based transitions of the Rh(III) component. The Rh(III) component does not display any observable transitions in the visible region of the spectrum. The similar electrochemical and photochemical properties of the Ru(II)-Rh(III) system with respect to the monometallic synthons suggest weak intercomponent interaction of the components in this Ru(II)-Rh(III) system consistent with the unsaturated nature of the BL.

iii. Photochemical and Photophysical Properties of $[(Me_2phen)_2Ru(Mebpy\text{-}CH_2\text{-}CH_2\text{-}Mebpy)Rh(Me_2bpy)_2]^{5+}$

Emission spectroscopy was used to probe the excited state properties of $[(Me_2phen)_2Ru(Mebpy\text{-}CH_2\text{-}CH_2\text{-}Mebpy)Rh(Me_2bpy)_2]^{5+}$. This complex exhibits a weak emission from the Ru→polypyridine based ^{3}MLCT state ($\lambda_{max}^{em} \approx$ 610 nm, $\Phi_{RuRh}^{em} \approx 1.0 \times 10^{-3}$) (Table 2).[31] The emission profile is identical to the corresponding Ru→polypyridine based ^{3}MLCT emission of $[(Me_2phen)_2Ru(Mebpy\text{-}CH_2\text{-}CH_2\text{-}Mebpy)](PF_6)_2$ ($\lambda_{max}^{em} = 610$ nm, $\Phi_{Ru}^{em} = 0.11$, $\tau = 1.8$ μs) in deaerated acetonitrile at RT. The intensity of the emission is reduced considerably for the Ru(II)-Rh(III) complex with respect to $[(Me_2phen)_2Ru(Mebpy\text{-}CH_2\text{-}CH_2\text{-}Mebpy)](PF_6)_2$ ($\Phi_{Ru}^{em}/\Phi_{RuRh}^{em} = 90$, Φ_{RuRh}^{em} and Φ_{Ru}^{em} are quantum yields of emission of $[(Me_2phen)_2Ru(Mebpy\text{-}CH_2\text{-}CH_2\text{-}Mebpy)Rh(Me_2bpy)_2]^{5+}$ and $[(Me_2phen)_2Ru(Mebpy\text{-}CH_2\text{-}CH_2\text{-}Mebpy)](PF_6)_2$, respectively). The emission lifetime of $[(Me_2phen)_2Ru(Mebpy\text{-}CH_2\text{-}CH_2\text{-}Mebpy)Rh(Me_2bpy)_2]^{5+}$displays a short-lived component (6 ns) and long lived component ($\geq$ 30 ns) at RT in acetonitrile.[31] The excitation spectrum of $[(Me_2phen)_2Ru(Mebpy\text{-}CH_2\text{-}CH_2\text{-}Mebpy)Rh(Me_2bpy)_2]^{5+}$ differs from the absorption spectrum at RT. At 77 K, in a 4/1 ethanol/methanol matrix, the Ru(II)-based emission is not significantly quenched with $\tau = 6.8$ μs, similar to $[(Me_2phen)_2Ru(Mebpy\text{-}CH_2\text{-}CH_2\text{-}Mebpy)](PF_6)_2$. At 77 K, the excitation spectrum of the Ru(II)-Rh(III) complex is similar to the absorption spectrum. The energy level diagram for $[(Me_2phen)_2Ru(Mebpy\text{-}CH_2\text{-}CH_2\text{-}Mebpy)Rh(Me_2bpy)_2]^{5+}$ is represented in Fig. 16 and is similar to the $[(ttpy)Ru(tpy\text{-}(Ph)_n\text{-}tpy)Rh(ttpy)]^{5+}$ system discussed above. The electrochemical, photochemical, and photophysical properties of $[(Me_2phen)_2Ru(Mebpy\text{-}CH_2\text{-}CH_2\text{-}Mebpy)Rh(Me_2bpy)_2]^{5+}$ demonstrate intercomponent electron and energy transfer processes in this system, including electron transfer from excited Ru(II) MLCT states to Rh(III), electron transfer from Ru(II) to excited Rh(III), charge recombination from Rh(II) to Ru(III), and energy transfer from excited Rh(III) to Ru(II). This early study of the coupling of Ru(II) to Rh(III) with nonconjugated linkers shows the promise of this structural motif to provide systems with unexpectedly efficient quenching of the chromophore's ^{3}MLCT state.

F. Dendrimeric Ru(II)/Os(II)-Rh(III) Complexes: $[M\{(dpp)Rh(ppy)_2\}_3](PF_6)_5$

Balzani et al. have reported the electrochemical, photochemical, and photophysical properties of many dpp-bridged complexes.[1,2,16] The Ru(II)/Os(II)-Rh(III) complexes, $[Ru\{(dpp)Rh(ppy)_2\}_3](PF_6)_5$ and $[Os\{dpp)Rh(ppy)_2\}_3](PF_6)_5$ (Fig. 17) (ppy = phenylpyridine anion), reported by Balzani et al. incorporate the dpp BL and a C-N type cyclometallating terminal ligand (TL) in the construction of complex molecular architectures.[32] The dpp BL provides electronic coupling of the bridged metals. The tris(bidentate) coordination environments of rhodium inhibit reactivity at this site.

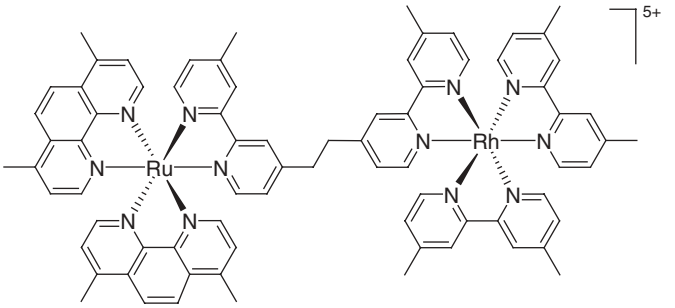

$[(Me_2phen)_2Ru(Mebpy\text{-}CH_2\text{-}CH_2\text{-}Mebpy)Rh(Me_2bpy)_2]^{5+}$

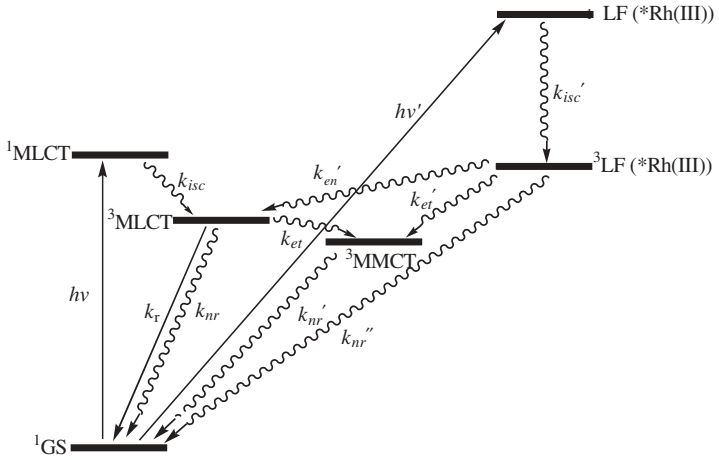

FIGURE 16. State diagram for $[(Me_2phen)_2Ru(Mebpy\text{-}CH_2\text{-}CH_2\text{-}Mebpy)Rh(Me_2bpy)_2]^{5+}$. GS = ground state, MLCT = metal-to-ligand charge-transfer, MMCT = metal-to-metal charge-transfer, k_r = rate constant for radiative decay, k_{nr} = rate constant for non-radiative decay, k_{isc} = rate constant for intersystem crossing, k_{et} = rate constant for electron transfer, k_{en} = rate constant for energy transfer.

i. Redox Properties of $[M\{(dpp)Rh(ppy)_2\}_3](PF_6)_5$

Electrochemistry is useful to estimate the relative energies of the frontier orbitals upon variation of the subunit in supramolecular assemblies. The oxidative electrochemistry for $[Ru\{(dpp)Rh(ppy)_2\}_3](PF_6)_5$ (in dichloromethane using Bu_4NClO_4 as the supporting electrolyte) shows an irreversible one electron oxidation at 1.25 V due to the $Ru^{II/III}$ couple (Table 1).[32] An irreversible one electron oxidation of the osmium core in $[Os\{dpp)Rh(ppy)_2\}_3](PF_6)_5$ occurs at a less positive potential of 0.75 V consistent with the higher energy $d\pi$ orbitals on osmium (Table 1). The irreversible multielectron oxidation process, which follows the oxidation of the central osmium core at 1.50 V, is attributed to the simultaneous one electron oxidation of the three independent peripheral rhodium-based units indicative of electronic isolation of these metal centers. The reductive electrochemistry of $[Ru\{(dpp)Rh(ppy)_2\}_3](PF_6)_5$ displays three

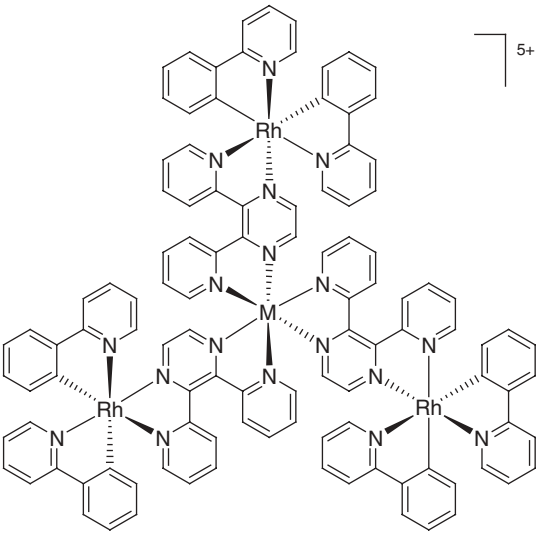

FIGURE 17. Representation of $[M\{dpp)Rh(ppy)_2\}_3]^{5+}$ (M = Ru or Os) (bpy = 2,2′-bipyridine, dpp = 2,3-bis(2-pyridyl)pyrazine, ppy = phenylpyridine anion).

reversible reduction processes at −0.48, −0.60, and −0.70 V, corresponding to the three sequential $dpp^{0/-}$ reductions (Table 1). The reductions at −1.19, −1.37, and −1.60 V correspond to the successive second reduction of each BL, $dpp^{-/2-}$. The reductive electrochemistry of $[Os\{dpp)Rh(ppy)_2\}_3](PF_6)_5$ displays three similar processes that are quasireversible. The electrochemistry predicts a Ru(dπ)- or Os(dπ)-based HOMO and dpp(π*) LUMO.

ii. Spectroscopic Properties of $[M\{(dpp)Rh(ppy)_2\}_3](PF_6)_5$

The dendrimeric Ru(II)/Os(II)-Rh(III) complex shows characteristic absorptions that are typical for polyazine LAs. The complexes $[Ru\{(dpp)Rh(ppy)_2\}_3](PF_6)_5$ and $[Os\{dpp)Rh(ppy)_2\}_3](PF_6)_5$ display dpp-based π→π* transitions in the UV region and M(dπ)→dpp(π*) (M = Ru or Os) MLCT transitions in the visible at λ_{max}^{abs} = 471 and 515 nm, respectively, in dichloromethane (Table 2).[32] The red shift in the λ_{max}^{abs} of the osmium complex is consistent with the higher energy dπ orbitals of osmium. The osmium complex also possesses significant intensity in the lower energy tail of the Os(dπ)→dpp(π*) CT transitions at > 600 nm representing direct population of the ^{3}MLCT state, gaining intensity by the significant spin-orbit coupling in osmium.

iii. Photophysical and Photochemical Properties of $[M\{(dpp)Rh(ppy)_2\}_3](PF_6)_5$

Emission spectroscopy is useful for understanding the excited state properties of the dendrimeric Ru(II)/Os(II)-Rh(III) complexes. The complexes $[Ru\{(dpp)Rh(ppy)_2\}_3](PF_6)_5$ and $[Os\{dpp)Rh(ppy)_2\}_3](PF_6)_5$ display emissions from the M(dπ)→dpp(π*) (M = Ru or Os) ^{3}MLCT states at RT at 681 and 821 nm with τ = 330 and 55 ns and Φ = 0.018 and 0.0058 for M = Ru and Os,

respectively (Table 2).[32] The differences in the photophysical properties rule out the involvement of the peripheral rhodium components in the luminescence of these complexes and strongly suggest that these difference are due to the ruthenium or osmium polypyridine core. At 77 K, an increase in the lifetime of $[Os\{dpp)Rh(ppy)_2\}_3](PF_6)_5$ is observed (τ = 0.62 μs) with the expected shift in the $\lambda_{max}{}^{em}$ to higher energy. A biexponential decay (τ = 1.05 and 3.40 μs) is observed for $[Ru\{(dpp)Rh(ppy)_2\}_3](PF_6)_5$, suggesting that two different emitting states, Ru→dpp MLCT and a Rh→dpp MLCT, may be responsible for the dual exponential emission at 77 K. This study demonstrated how the redox properties change with component modification and how the combination of N-N type polyazine BLs and C-N (cyclometallating type) chelating sites allow the expansion of the molecular architecture to extend the number and the type of metals and/or ligands that can be incorporated in multinuclear luminescent and redox-active complexes. The use of cyclometallating ligands provides a means to tune over large ranges the orbital energetics of the Rh(III) site.

G. Extended Supramolecular Architectures with Fe(II)/Ru(II)/Rh(III)

Petersen et al. reported the synthesis, characterization, and the photoinduced processes in a series of trimetallic complexes containing Fe(II), Ru(II), and Rh(III) of the form $[(CN)_4Fe(BL)Ru(bpy)(BL)Rh(tpy)(MQ^+)](PF_6)_4$ (BL = dpp or bpm; MQ^+ = *N*-methyl-4,4′-bipyridinium) (Fig. 18).[33] The trimetallic complexes consist of three molecular components: (a) the tetracyanoferrate unit, which is the ED; (b) the Ru(II) polyazine unit, which acts as the LA; and (c) the Rh(III) polyazine unit, which contains the ligands tpy and MQ^+, which is the electron acceptor. The electrochemical and photophysical properties demonstrated that the trimetallic complexes display good communication between the ED and LA metal centers.

Time-resolved experiments conducted on $[(CN)_4Fe(BL)Ru(bpy)(BL)Rh(tpy)(MQ^+)](PF_6)_4$ (BL = dpp or bpm) and the redox properties (bridging ligands are more easily reduced than Rh(III) and MQ^+) suggested the formation of a transient Fe^{III}/Ru^{II} intermediate of the form $[Fe^{III}\text{-}Ru^{II}\text{-}L^{-\cdot}\text{-}Rh^{III}]$ with a $\tau \leq 70$ ns. Component modification on the Rh(III) center to have a more negative $Rh^{III/II/I}$ redox potential has been suggested as a means of designing species with a more spatially-separated charge-separated state. Tables 1 and 2 show some electrochemical and spectroscopic data of the Fe(II)/Ru/(II)/Rh(III) complexes.

H. Stereochemically Defined Tridentate-Bridged Ru(II)-Rh(III) Complex

Brewer et al. reported the synthesis and characterization of $[(tpy)Ru(tppz)RhCl_3](PF_6)_2$ (Fig. 19), which couples a ruthenium light absorber

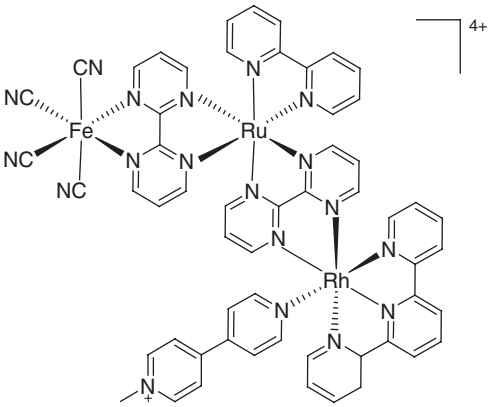

FIGURE 18. Representation of $[(CN)_4Fe(bpm)Ru(bpy)(bpm)Rh(tpy)(MQ^+)]^{4+}$ (bpy = 2,2′-bipyridine, bpm = 2,2-bipyrimidine, tpy = 2,2′:6′,2″-terpyridine, MQ^+ = *N*-methyl-4,4′-bipyridinium).

to a rhodium electron acceptor to create the first tppz-bridged light-absorber-electron-acceptor dyad.[34] The bimetallic system, $[(tpy)Ru(tppz)RhCl_3](PF_6)_2$ (tppz = 2,3,5,6-tetrakis(2-pyridyl)pyrazine), consists of a Ru(II) LA component and a Rh(III) reactive metal covalently attached through a tppz BL to afford a stereochemically defined LA-BL-EA system.

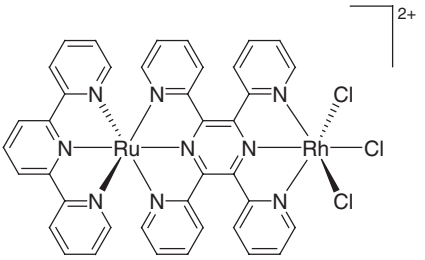

FIGURE 19. Representation of $[(tpy)Ru(tppz)RhCl_3]^{2+}$ (bpy = 2,2′-bipyridine, tppz = 2,3,5,6-tetrakis(2-pyridyl)pyrazine)..

i. Redox Properties of [(tpy)Ru(tppz)RhCl₃](PF₆)₂

Electrochemistry provides the relative energies of the frontier orbitals in Ru(II)-Rh(III) dyads. The cyclic voltammogram of $[(tpy)Ru(tppz)RhCl_3](PF_6)_2$ (in acetonitrile using Bu_4NPF_6 as supporting electrolyte) displayed a reversible oxidation at 1.55 V, a quasi-reversible reduction at -0.28 V, followed by three reversible reductions at −0.65, −1.03, and −1.45 V (Table 1).[34] The oxidation at 1.55 V is attributed to the $Ru^{II/III}$ couple. The quasi-reversible reduction at −0.28 V, which becomes irreversible with decreasing scan rate, is attributed

to $Rh^{III/II/I}$ reduction. Similar to systems of the type $[Rh(LL)_2Cl_2]^+$(LL = bpy or dpp),[28] the rhodium reduction is followed by loss of the two chloride ligands to form a square-planar Rh^I species. The reductions at −0.65, −1.03, and −1.45 V are attributed to $tppz^{-/0}$, $tppz^{-/2-}$, and $tpy^{0/-}$, respectively. These electrochemical data indicate that this mixed-metal system possesses a ruthenium-based HOMO and a rhodium-based LUMO, predicting a lowest lying $Ru(d\pi) \rightarrow Rh(d\sigma^*)$ ^{3}MMCT excited state.

ii. Spectroscopic Properties of [(tpy)Ru(tppz)RhCl$_3$](PF$_6$)$_2$

The electronic absorption spectra of the Ru(II)-Rh(III) complexes display transitions characteristic for ruthenium polyazine complexes. The tppz and tpy $\pi \rightarrow \pi^*$ absorptions appear in the UV region.[34] The lowest energy absorption at 516 nm is due to the $Ru(d\pi) \rightarrow tppz(\pi^*)$ MLCT transition (Table 2). This MLCT transition is blue shifted with respect to the corresponding absorption of the homobimetallic system $[(tpy)Ru(tppz)Ru(tppz)](PF_6)_4$, which occurs at 548 nm. This blue shift is attributed to the presence of the chlorides making the Rh(III) more electron rich.

iii. Photophysical and Photochemical Properties of [(tpy)Ru(tppz)RhCl$_3$](PF$_6$)$_2$

Emission spectroscopy was used to study the excited state dynamics of $[(tpy)Ru(tppz)RhCl_3](PF_6)_2$. The $Ru(d\pi) \rightarrow tppz(\pi^*)$ MLCT state once optically populated is known to undergo intersystem crossing to populate the often emissive ^{3}MLCT state. The $Rh(d\sigma^*)$ LUMO provides for facile intramolecular electron transfer to produce the $Ru(d\pi) \rightarrow Rh(d\sigma^*)$ ^{3}MMCT state (Fig. 20). This electron transfer leads to a quenching of the emission normally observed from the $Ru(d\pi) \rightarrow tppz(\pi^*)$ ^{3}MLCT excited states. For example, $[(tpy)Ru(tppz)RhCl_3](PF_6)_2$ displays a weak emission at RT in deoxygenated acetonitrile solution from the $Ru(d\pi) \rightarrow tppz(\pi^*)$ ^{3}MLCT state, λ_{max}^{em} = 830 nm, $\Phi^{em} = 2.0 \times 10^{-4}$, τ = 22 ns (Table 2).[34] Compared to $[(tpy)Ru(tppz)Ru(tppz)](PF_6)_4$, which lacks a rhodium electron acceptor, λ_{max}^{em} = 830 nm, $\Phi^{em} = 1.10 \times 10^{-3}$, τ = 100 ns, the emission from the $Ru(d\pi) \rightarrow tppz(\pi^*)$ ^{3}MLCT state of $[(tpy)Ru(tppz)RhCl_3](PF_6)_2$ is reduced by 80% due to intramolecular electron transfer leading to the population of the lower lying $Ru(d\pi) \rightarrow Rh(d\sigma^*)$ ^{3}MMCT state (Fig. 20). Emission quenching for $[(tpy)Ru(tppz)RhCl_3](PF_6)_2$ via electron transfer is efficient with a k_{et} of 3.5×10^7 s^{-1}.

Energy-transfer quenching of the emissive ^{3}MLCT excited state by the Rh(III) is unlikely in this system due to the lower energy of the ^{3}MLCT excited state, which will shift it below the energy typically expected for the rhodium ^{3}LF state. At 77 K, an intense structured emission is observed in an ethanol/methanol glassy solvent with a concomitant increase in the excited state lifetime (τ = 330 ns) (Table 2).[34] This excited state lifetime is comparable to the reported excited state lifetime of $[(tpy)Ru(tppz)Ru(tppz)](PF_6)_4$ at 77 K (τ = 360 ns). Similar excited state lifetimes for $[(tpy)Ru(tppz)RhCl_3](PF_6)_2$ and

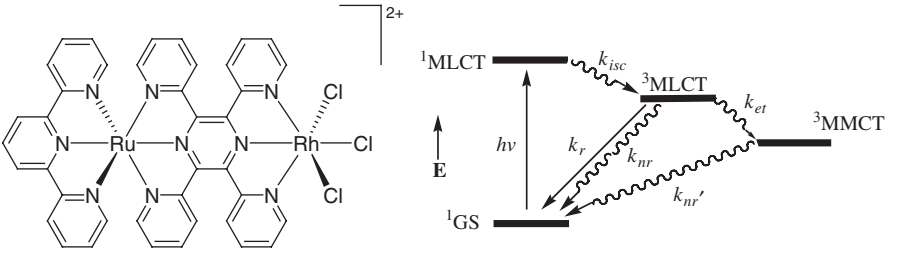

FIGURE 20. State diagram for $[(tpy)Ru(tppz)RhCl_3](PF_6)_2$. GS = ground state, MLCT = metal-to-ligand charge-transfer, MMCT = metal-to-metal charge-transfer, k_r = rate constant for radiative decay, k_{nr} = rate constant for non-radiative decay, k_{isc} = rate constant for intersystem crossing, k_{et} = rate constant for electron transfer.

$[(tpy)Ru(tppz)Ru(tppz)](PF_6)_4$ are expected, if intramolecular electron transfer, prohibited in the frozen matrix, is responsible for the decrease in ^{3}MLCT emission at RT.

I. Photoinitiated Electron Collection

The coupling of two LAs to a single rhodium-based electron collector (EC) should afford photoinitiated electron collection. Photoinitiated electron collection is a process by which light energy is used to collect reducing equivalents. Photoinitiated electron collection has been of long-term interest, although elusive due to the complexity of multielectron photochemistry. The development of supramolecular assemblies that function as photoinitiated electron collectors allows for the development of solar hydrogen production schemes using these complexes.[1-3,16] The first functioning photoinitiated electron collector in a molecular system was reported by Brewer.[35] The supramolecular assembly couples two ruthenium LA units to a central iridium that functions to electronically isolate the two LA subunits. The $[\{(bpy)_2Ru(dpb)\}_2IrCl_2](PF_6)_5$ system when excited with visible light in the presence of the electron donor, *N*,*N*-dimethylaniline (DMA), photochemically reduces by two electrons to form $[\{(bpy)_2Ru(dpb^-)\}_2IrCl_2]^{3+}$. MacDonnell and Campagna[36] reported two Ru-Ru bimetallic complexes of the molecular architecture $[(phen)_2Ru(BL)Ru(phen)_2]^{4+}$ (BL = phenanthroline-pyrazine-benzene-pyrazine-phenanthroline (tatpp) or phenanthroline-pyrazine-quinone-pyrazine-phenanthroline (tatpq)), that photochemically collect up to four electrons on the bridging ligand (BL) in the presence of triethylamine (TEA). These systems couple two ruthenium LA units through an extended aromatic BL. Bocarsly has studied a series of Pt(IV) centered trimetallic complexes of the form $[(NC)_5M^{II}(CN)Pt^{IV}(NH_3)_4(NC)M^{II}(CN)_5]^{4-}$ (M = Fe, Ru, or Os) that undergoes photoinitiated electron collection on metal centers using two Fe, Ru, or Os LAs.[37] Nocera has made significant contributions to the field of multielectron photochemistry. Nocera[38] designed a dirhodium photocatalyst,

$[Rh_2^{0,0}(dfpma)_3(PPh_3)(CO)]$ (dfpma = $MeN(PF_2)_2$), that undergoes photochemical multielectron chemistry.

i. LA-BL-Rh-BL-LA Supramolecular Assemblies

Brewer et al. have designed trimetallic supramolecular assemblies that combine two Ru(II)/Os(II) LAs to a single Rh(III) acceptor through polyazine BLs.[39–47] A wide array of such complexes have been studied, which provides considerable insight into the perturbations of subunit properties upon assembly into these trimetallic assemblies.[39–47] In addition, this structural motif has found application in photoinitiated electron collection,[39,42] solar energy conversion,[39,42] and light-activated DNA cleavage.[44–47] The supramolecular assemblies provide TL-LA-BL-Rh-BL-LA-TL molecular architectures (LA = Ru or Os, X = Cl or Br, TL = 2 bpy ligands, 2 phen ligands, or tpy and Cl ligands, BL = dpp, dpq (2,3-bis(2-pyridyl)quinoxaline), dpb (2,3-bis(2-pyridyl)benzoquinoxaline), or bpm). The trimetallic complexes, including representative examples having the general formula $[\{(bpy)_2M(BL)\}_2RhX_2]^{5+}$ (M = Ru or Os, BL = dpp, dpq, dpb, or bpm, X = Cl or Br) and $[\{(tpy)MCl(BL)\}_2RhCl_2]^{3+}$ (BL = Ru or Os, BL = dpp or bpm), have been synthesized and their electrochemical and photochemical properties investigated.[39–42] The complexes have spectroscopic, redox, and photochemical properties dictated by the components used. The rhodium coordination in these complexes, in contrast to most previously studied systems, includes potentially labile monodentate halide ligands, providing for the possibility of photoreactivity in these assemblies. The synthesis of the complexes follows a building block approach with incorporation of the Rh(III) center being the final step.

ii. Redox Properties of LA-BL-Rh-BL-LA

Electrochemistry of the LA-BL-Rh-BL-LA molecular architectures demonstrates the typical metal-based oxidations and the ligand-based reductions. Table 1 summarizes the electrochemical potentials of the trimetallic complexes. A representative cyclic voltammogram of $[\{(bpy)_2Ru(dpp)\}_2RhCl_2]^{5+}$ is illustrated in Figure 21. Oxidative electrochemistry shows overlapping $Ru^{II/III}$ oxidations at 1.59 V, indicating some degree of electronic isolation of the two ruthenium subunits. The reductive electrochemistry shows an irreversible $Rh^{III/II/I}$ reduction at −0.42 V followed by two reversible $dpp^{0/-}$ reductions at −0.81 and −1.05 V.[39] The oxidative and reductive electrochemistry predicts the Ru(dπ) nature of the HOMO and the Rh(dσ*) nature of the LUMO. Upon changing the BL from dpp to dpq, the reductions move to the more positive potentials −0.17 and −0.36 V, consistent with the lower-energy π* orbitals of dpq relative to dpp. Consistent with the electrochemistry observed for similar complexes, the $Rh^{III//II/I}$ reduction is followed by rapid loss of chlorides.[28] The systems with BL = dpb or bpm display orbital inversion with the $BL^{0/-}$ reductions occurring before the $Rh^{III/II/I}$ reduction.[40,41] The electrochemistry implies that when the BL is dpp or dpq, the LUMO is Rh(dπ*)-based, while for the dpb and bpm systems it is BL(π*)-based. These

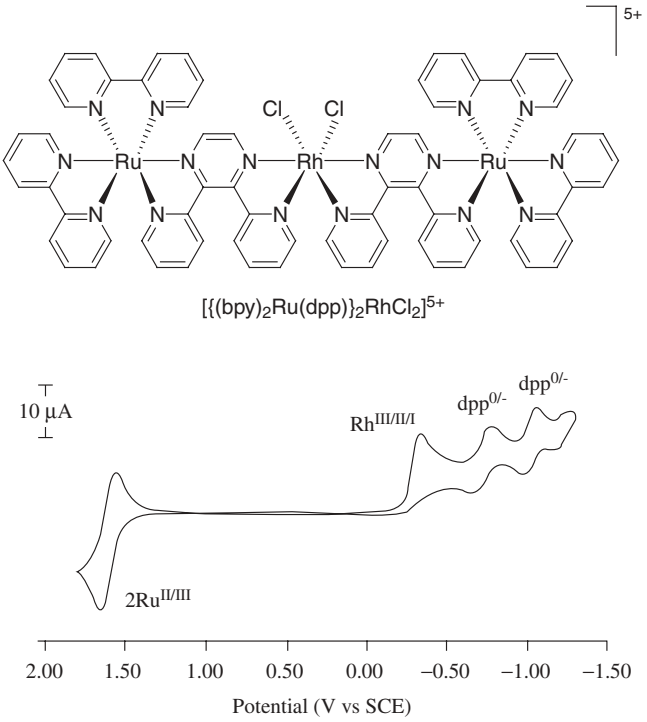

FIGURE 21. Cyclic voltammogram of $[\{(bpy)_2Ru(dpp)\}_2RhCl_2]^{5+}$ (bpy = 2,2′-bipyridine, dpp = 2,3-bis(2-pyridyl)pyrazine).

BL(π^*) and Rh($d\sigma^*$) orbitals can be in very close energetic proximity in this structural motif. Similar to the dpp-based system, the $Ru^{II/III}$ oxidations for the dpq- and dpb-based systems occur as a reversible oxidation at $\sim$1.50 V. The $Ru^{II/III}$ oxidation for the bpm system occurs at 1.66 V. Substitution of the Cl on the rhodium in the dpp-based system with Br affords $[\{(bpy)_2Ru(dpp)\}_2RhBr_2]^{5+}$ having similar electrochemical properties.[42] The $Rh^{III/II/I}$ reduction in $[\{(bpy)_2Ru(dpp)\}_2RhBr_2]^{5+}$ occurs 40 mV more positive than the chloride analog at -0.38 V, consistent with the weaker σ-donor ability of Br^- vs Cl^-.

The tpy ligand provides some stereochemical control in supramolecular complexes by eliminating Δ and Λ isomeric mixtures associated with the tris(bidentate) metal centers. Substitution of the TL, bpy in $[\{(bpy)_2Ru(BL)\}_2RhCl_2]^{5+}$ (BL = dpp or bpm), with tpy and Cl affords $[\{(tpy)RuCl(BL)\}_2RhCl_2]^{3+}$ (BL = dpp or bpm).[43] The $Ru^{II/III}$ oxidation of $[\{(tpy)RuCl(BL)\}_2RhCl_2]^{3+}$ (BL = dpp or bpm) occurs as a reversible couple at a less positive potential than the bpy-based system at 1.08 V. This is consistent

with a more electron rich ruthenium center due to Cl coordination in place of a pyridine ring. The reductive electrochemistry of $[\{(tpy)RuCl(dpp)\}_2RhCl_2]^{3+}$, shows an irreversible $Rh^{III/II/I}$ reduction at -0.53 V followed by two quasi-reversible reductions at -0.92 and -1.25 V due to $dpp^{0/-}$for each BL.[43] It is interesting that the rhodium reduction of $[\{(tpy)RuCl(bpm)\}_2RhCl_2]^{3+}$ appears as two closely spaced irreversible reductions at -0.31 and -0.43 V, respectively, for $Rh^{III/II}$ and $Rh^{II/I}$ reduction process. This indicates some added stability of the Rh(II) oxidation state in this complex. Scanning to more negative potentials reveals the sequential one-electron reductions due to $bpm^{0/-}$ for each BL. The electrochemistry of $[\{(tpy)RuCl(BL)\}_2RhCl_2]^{3+}$ (BL = dpp or bpm) suggests the Ru(dπ) nature of the HOMO and the Rh(dσ*) nature of the LUMO. The electrochemical behavior of $[\{(tpy)RuCl(bpm)\}_2RhCl_2]^{3+}$ with a Rh(dσ*)-based LUMO is in marked contrast to $[\{(bpy)_2Ru(bpm)\}_2RhCl_2]^{5+}$ with a BL(π*)-based LUMO. The differences in the orbital energetics of the LUMOs in the two complexes exemplify the significance of component modulation and the close energetic proximity of the Rh(dσ*) and the BL(σ*) orbitals in these structural motifs. Replacing the light-absorbing ruthenium metal with osmium in $[\{(bpy)_2Ru(dpp)\}_2RhCl_2]^{5+}$ and $[\{(tpy)RuCl(dpp)\}_2RhCl_2]^{3+}$ systems affords $[\{(bpy)_2Os(dpp)\}_2RhCl_2]^{5+}$ and $[\{(tpy)OsCl(dpp)\}_2RhCl_2]^{3+}$.[44,45] Osmium is easier to oxidize than ruthenium due to the higher energy dπ orbitals in osmium. Consistent with this, the $Os^{II/III}$ oxidations of $[\{(bpy)_2Os(dpp)\}_2RhCl_2]^{5+}$ and $[\{(tpy)OsCl(dpp)\}_2RhCl_2]^{3+}$ occur at the less positive potentials of 1.17 and 0.81 V, respectively.[44,45] The $Os^{II/III}$ oxidation for the tpy-based system occurs at the least positive potential, consistent with the more electron rich osmium in $[\{(tpy)OsCl(dpp)\}_2RhCl_2]^{3+}$ due to coordinated Cl. The complexes $[\{(bpy)_2Os(dpp)\}_2RhCl_2]^{5+}$ and $[\{(tpy)OsCl(dpp)\}_2RhCl_2]^{3+}$ possess irreversible first $Rh^{III/II/I}$ reductions at -0.44 and -0.56 V, respectively, followed by sequential reduction of the two dpp BLs at -0.81 and -1.05 V for $[\{(bpy)_2Os(dpp)\}_2RhCl_2]^{5+}$ and -0.91 and -1.25 V for $[\{(tpy)OsCl(dpp)\}_2RhCl_2]^{3+}$. The $Rh^{III/II/I}$ reductions for $[\{(tpy)RuCl(dpp)\}_2RhCl_2](PF_6)_3$ and $[\{(tpy)OsCl(dpp)\}_2RhCl_2](PF_6)_3$ are shifted to more negative potentials of -0.44 and -0.56 V, respectively, than systems with two bpy TLs. The $[\{(bpy)_2M(BL)\}_2RhX_2]^{5+}$ (M = Ru or Os, BL = dpp or dpq, X = Cl or Br) and $[\{(tpy)MCl(BL)\}_2RhCl_2]^{3+}$ (M = Ru or Os, BL = dpp or bpm) systems all possess Ru(dπ) HOMOs and Rh(dσ*) LUMOs. These systems provide a structural motif with an optically populated MLCT state but a lowest-lying ^{3}MMCT state. All systems with lowest-lying ^{3}MMCT states that have been tested are DNA photocleavage agents. They are unique because they cleave DNA in the presence or absence of O_2.[44–46] Furthermore, these systems are able to collect two electrons on the rhodium center, making them important as photoinitiated electron collectors.

iii. Spectroscopic Properties of LA-BL-Rh-BL-LA

The trimetallic complexes coupling two ruthenium or osmium LAs to a central rhodium absorb efficiently throughout the UV and visible regions of the

spectrum with transitions characteristic of each subunit of TL-LA-BL component. The electronic absorption spectra of these complexes display TL- and BL-based $\pi \rightarrow \pi^*$ transitions in the UV region and $M(d\pi) \rightarrow TL(\pi^*)$ and $M(d\pi) \rightarrow BL(\pi^*)$ MLCT transitions in the visible region. The energies of the lowest lying transitions for the trimetallic complexes are given in Table 2. The electronic absorption spectra of $[\{(bpy)_2Ru(BL)\}_2RhCl_2]^{5+}$ (BL = dpp, dpq, dpb, or bpm),[39–41] are similar exhibiting intense $\pi \rightarrow \pi^*$ TL and BL transitions in the UV and $Ru(d\pi) \rightarrow bpy(\pi^*)$ and $Ru(d\pi) \rightarrow BL(\pi^*)$ MLCT transitions in the visible. The $Ru(d\pi) \rightarrow bpy(\pi^*)$ MLCT transition occurs between 410 and 420 nm for all complexes. Consistent with the electrochemical properties and the decreased HOMO-LUMO gap, the $Ru(d\pi) \rightarrow BL(\pi^*)$ MLCT transitions shift to lower energy as the BL is varied from dpp (λ_{max}^{abs} = 520 nm) to dpq (λ_{max}^{abs} = 584 nm) to bpm (λ_{max}^{abs} = 594 nm) to dpb (λ_{max}^{abs} = 662 nm). The electronic absorption spectra of $[\{(bpy)_2Ru(dpp)\}_2RhX_2]^{5+}$ (X = Cl or Br) are virtually identical,[39,42] showing light absorption properties are not greatly affected by substitution of the halide on the rhodium center. The electronic absorption spectra for the tpy-based systems $[\{(tpy)RuCl(BL)\}_2RhCl_2]^{3+}$ (BL = dpp or bpm) are also very similar to the bpy analogs.[43] Significant spectral differences are observed in the visible regions for this series of complexes, consistent with the modulation of the energetics by the TL and BL and as indicated by electrochemistry. The $[\{(tpy)RuCl(bpm)\}_2RhCl_2]^{3+}$ and $[\{(tpy)RuCl(dpp)\}_2RhCl_2]^{3+}$ systems show $Ru(d\pi) \rightarrow bpm(\pi^*)$ and $Ru(d\pi) \rightarrow dpp(\pi^*)$ MLCT transitions at lower energies (λ_{max}^{abs} = 656 and 540 nm, respectively) compared to $[\{(bpy)_2Ru(dpp)\}_2RhCl_2]^{5+}$ (λ_{max}^{abs} = 520 nm) and $[\{(bpy)_2Ru(bpm)\}_2RhCl_2]^{5+}$ (λ_{max}^{abs} = 594 nm).[39–43] The complexes $[\{(bpy)_2Os(dpp)\}_2RhCl_2]^{5+}$and $[\{(tpy)OsCl(dpp)\}_2RhCl_2]^{3+}$ have similar spectroscopies to their ruthenium analogs. The $Os(d\pi) \rightarrow dpp(\pi^*)$ MLCT transitions occur at slightly lower energies, reflective of the higher energy $Os(d\pi)$ orbitals observed in electrochemistry. The electronic absorption spectra of the osmium complexes also show higher intensities in their low-energy tails due to the higher spin-orbit coupling contribution in Os enhancing the ^{3}MLCT absorption.[44–45]

iv. Photochemical and Photophysical Properties of LA-BL-Rh-BL-LA

Emission spectroscopy is used to probe the excited state dynamics of the Ru(II)/Os(II)-Rh(III) trimetallic complexes. Optical excitation of the $Ru/Os(d\pi)$ ^{1}MLCT states in this structural motif, leads to intersystem crossing, populating the ^{3}MLCT states that are often emissive. In systems that possess $Ru/Os(d\pi)$-based HOMOs and $Rh(d\pi^*)$-based LUMOs, the presence of low-lying $Rh(d\sigma^*)$ orbitals affords low-lying ^{3}MMCT states that can be populated by intramolecular electron transfer. Intramolecular electron transfer to populate the ^{3}MMCT states quenches the emission from the ^{3}MLCT states, giving short excited state lifetimes. The complexes $[\{(bpy)_2Ru(dpp)\}_2RhX_2]^{5+}$ (X = Cl and Br)[39,42] display weak emissions from the $Ru(d\pi) \rightarrow dpp(\pi^*)$ ^{3}MLCT states at λ_{max}^{em} = 760 nm ($\Phi^{em} = 7.3 \times 10^{-5}$ and 1.5×10^{-4},

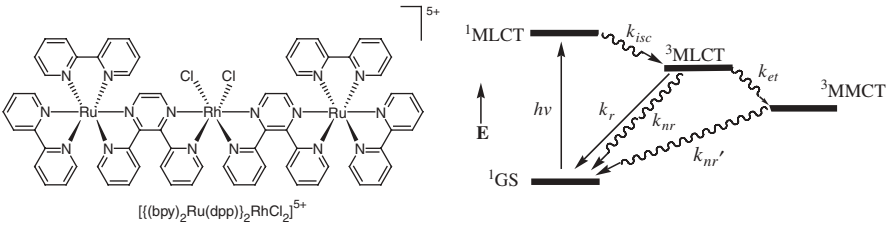

FIGURE 22. State diagram rhodium centered supramolecular assemblies incorporating low-lying ^{3}MMCT states, showing only lowest-lying excited states. GS = ground state; MLCT = metal-to-ligand charge-transfer; k_r = rate constant for radiative decay; k_{nr} = rate constant for non-radiative decay; k_{isc} = rate constant for intersystem crossing.

respectively) at RT in deoxygenated acetonitrile solutions following Ru(dπ)→dpp(π*) ^{1}MLCT excitation at 520 nm. Compared to the model system $[(bpy)_2Ru(dpp)Ru(bpy)_2](PF_6)_4$ without a rhodium electron acceptor (λ_{max}^{em} = 744 nm, $\Phi^{em} = 1.38 \times 10^{-3}$), the emissions from the Ru(dπ)→dpp(π*) ^{3}MLCT state of $[\{(bpy)_2Ru(dpp)\}_2RhCl_2]^{5+}$ and $[\{(bpy)_2Ru(dpp)\}_2RhBr_2]^{5+}$ are reduced by 95% and 89%, respectively (Fig. 22). The rates of electron transfer to populate the ^{3}MMCT states from the ^{3}MLCT states for $[\{(bpy)_2Ru(dpp)\}_2RhCl_2]^{5+}$ and $[\{(bpy)_2Ru(dpp)\}_2RhBr_2]^{5+}$ are similar, $k_{et} = 1.2 \times 10^8$ s^{-1} and 5.2×10^7 s^{-1}, respectively.[39,42] The complex $[\{(bpy)_2Ru(bpm)\}_2RhCl_2]^{5+}$ is weakly emissive at RT in acetonitrile solution (λ_{max}^{em} = 800 nm, τ = 10 ns).[43] The other mixed-metal trimetallic complexes do not display detectable emissions in the visible region. This is not surprising considering the expected lower-energy ^{3}MLCT states in these systems. Generally, lower-energy ^{3}MLCT states display weaker emissions and are shorter lived, consistent with the energy gap law.[25] Table 2 summarizes the electrochemical and photophysical properties of the mixed-metal trimetallic complexes.

v. Photoinitiated Electron Collection on a Rhodium Center

Both $[\{(bpy)_2Ru(dpp)\}_2RhCl_2]^{5+}$ and $[\{(bpy)_2Ru(dpp)\}_2RhBr_2]^{5+}$ in the presence of an ED can undergo photoinitiated electron collection at the rhodium center. These represent the first complexes to undergo light-activated electron collection at a metal center with the molecular assembly remaining intact. In the presence of the electron donor, *N*,*N*-dimethylaniline (DMA), the complexes $[\{(bpy)_2Ru(dpp)\}_2RhCl_2]^{5+}$ and $[\{(bpy)_2Ru(dpp)\}_2RhBr_2]^{5+}$ undergo photoreduction, which is followed by halide loss to produce the coordinatively unsaturated Rh(I) species, $[\{(bpy)_2Ru(dpp)\}_2Rh^I]^{5+}$. Photoinitiated electron collection at the rhodium center allows use of these complexes as photocatalysts.[39,42] The decreased electron withdrawing and increased electron donating ability of the Rh(I) center in $[\{(bpy)_2Ru(dpp)\}_2Rh^I]^{5+}$, destabilizes the dpp(π*) orbitals, shifting the Ru(dπ)→dpp(π*) MLCT band to higher energy (Fig. 23). The electrochemical reduction and the resultant spectroscopy are correlated with

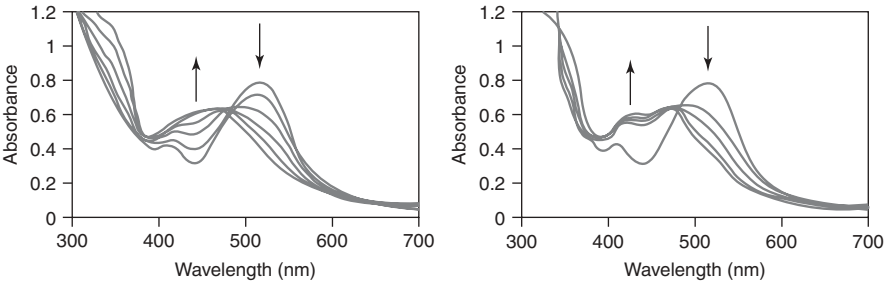

FIGURE 23. Electronic absorption spectra for the conversion of $[\{(bpy)_2Ru(dpp)\}_2RhCl_2]^{5+}$ to the two-electron-reduced form $[\{(bpy)_2Ru(dpp)\}_2Rh^{I}]^{5+}$ electrochemically (a) and photochemically (b). The complexes were photolyzed at 470 nm in the presence of DMA. (bpy = 2,2′-bipyridine, dpp = 2,3-bis(2-pyridyl)pyrazine, DMA = N,N-dimethylaniline).[39]

a photochemical experiment, establishing that this complex is reduced by multiple electrons photochemically at the metal center.[39]

vi. Photochemistry with LA-BL-Rh-BL-LA Architectures

The photochemically reduced Rh(I) species formed by photoinitiated multielectron collection can interact with substrates and participate in light to chemical energy conversion schemes. The complexes $[\{(bpy)_2Ru(dpp)\}_2RhX_2]^{5+}$ (X = Cl and Br) are the first photoinitiated electron collectors to photochemically produce hydrogen from water.[39,46] Photolysis of $[\{(bpy)_2Ru(dpp)\}_2RhX_2]^{5+}$ (X = Cl and Br) in the presence an electron donor affords the Rh(I) complex $[\{(bpy)_2Ru(dpp)\}_2Rh^{I}]^{5+}$ and two halides. In the presence of water, photolysis produces hydrogen.

In addition to the application as a solar hydrogen photocatalyst, $[\{(bpy)_2Ru(dpp)\}_2RhCl_2]^{5+}$is the first supramolecular system shown to photocleave DNA in an oxygen-independent manner.[46] The use of $[\{(bpy)_2Ru(dpp)\}_2RhCl_2]^{5+}$ as a photodynamic therapy agent has also been communicated.[47] DNA photocleavage occurs through a low-lying $Ru(d\pi)\rightarrow Rh(d\sigma^*)$ metal-to-metal charge-transfer (^{3}MMCT) when irradiated with low-energy visible light, with or without molecular oxygen. Similarly, the complexes $[\{(bpy)_2Os(dpp)\}_2RhCl_2]^{5+}$and $[\{(tpy)RuCl(dpp)\}_2RhCl_2]^{5+}$ also possess low-lying $Ru(d\pi)\rightarrow Rh(d\sigma^*)$ ^{3}MMCT states and photocleave DNA when excited with visible light. By contrast, $[\{(bpy)_2Ru(bpm)\}_2RhCl_2]^{5+}$, which does not possess a low-lying $Ru(d\pi)\rightarrow Rh(d\sigma^*)$ ^{3}MMCT state, does not photocleave DNA. This study demonstrated the significance of the $Ru(d\pi)\rightarrow Rh(d\sigma^*)$ ^{3}MMCT in the photocleavage event.[46] The application of the Ru(II)/Os(II)-Rh(III) systems in DNA photocleavage and hydrogen generation show the value of coupling reactive metals to LAs in broad applications.

TABLE 1. Electrochemical Data for Ru(II)-Rh(III) and Os(II)-Rh(III) Complexes Containing Polyazine Light Absorbers[a]

Complex[b]	$E_{1/2}^{ox}$(V vs. SCE)	$E_{1/2}^{red}$ (V vs. SCE)				Reference
		$Rh^{III/II/I}$	BL $^{0/-}$	BL $^{-/2-}$	TL $^{0/-}$	
$[(bpy)_2Ru(dpp)RhH_2(PPh_3)_2]^{3+c}$	1.70 ($Ru^{II/III}$)		−0.66	−1.28	−1.51	24
	1.56 ($Rh^{III/IV}$) E_p^a				−1.73	
$[(bpy)_2Ru(dpq)RhH_2(PPh_3)_2]^{3+c}$	1.71 ($Ru^{II/III}$)		−0.44	−1.26	−1.57	24
	1.56 ($Rh^{III/IV}$) E_p^a				−1.79	
$[(bpy)_2Ru(bpm)RhH_2(PPh_3)_2]^{3+c,d}$	1.65 E_p^a		−0.47	−1.26	−1.52	24
					−1.77	
$[(bpy)_2(CN)Ru(CN)Rh(NH_3)_5]^{3+e,f}$	1.00 ($Ru^{II/III}$)				−1.70	26
$[(bpy)_2Ru\{(CN)Rh(NH_3)_5\}_2]^{6+e,f}$	1.18 ($Ru^{II/III}$)				−1.70	26
$[(bpy)_2(CN)Ru(CN)Rh(NH_3)_4I)]^{2+e,f}$	0.92 ($Ru^{II/III}$)					26
$[(bpy)_2Ru(dpp)Rh(bpy)_2]^{5+c}$		−0.65 E_p^c				27
$[(ttpy)Ru(tpy\text{-}(Ph)_n\text{-}tpy)Rh(ttpy)]^{5+}(n = 0)^g$	1.31 ($Ru^{II/III}$)	−0.54 E_p^c			−1.22	29
					−1.44	
$[(ttpy)Ru(tpy\text{-}(Ph)_n\text{-}tpy)Rh(ttpy)]^{5+}(n = 1)^g$	1.29 ($Ru^{II/III}$)	−0.56 E_p^c			−1.18	29
					−1.41	
$[(ttpy)Ru(tpy\text{-}(Ph)_n\text{-}tpy)Rh(ttpy)]^{5+}$ $(n = 2)^g$	1.27 ($Ru^{II/III}$)	−0.56 E_p^c			−1.20	29
					−1.37	
$[(Me_2phen)_2Ru(Mebpy\text{-}CH_2\text{-}CH_2\text{-}Mebpy)Rh(Me_2bpy)_2]^{5+c}$	1.13 ($Ru^{II/III}$)	−0.92[h]	−1.45		−1.66	31
$[Ru\{(dpp)Rh(ppy)_2\}_3]^{5+i}$	1.25 E_p^a ($Ru^{II/III}$)		−0.48	−1.19		32
			−0.60	−1.37		
			−0.70	−1.60		
$[Os\{dpp)Rh(ppy)_2\}_3]^{5+i}$	0.75 E_p^a ($Os^{II/III}$)		−0.35 E_p^c			32
	1.50 E_p^a ($3Rh^{III/IV}$)		−0.54 E_p^c			
			−0.82 E_p^c			
$[(CN)_4Fe(bpm)Ru(bpy)(bpm)Rh(tpy)(MQ^+)]^{4+c}$		−0.59 E_p^c	−0.30			33
$[(CN)_4Fe(bpm)Ru(bpy)(dpp)Rh(tpy)(MQ^+)]^{4+c}$		−0.60 E_p^c	−0.43			33

$[(CN)_4Fe(dpp)Ru(bpy)(bpm)Rh(tpy)(MQ^+)]^{4+c}$		−0.63 E_p^c	−0.20			33
$[(CN)_4Fe(dpp)Ru(bpy)(dpp)Rh(tpy)(MQ^+)]^{4+c}$		−0.60 E_p^c	−0.20			33
$[(tpy)Ru(tppz)RhCl_3]^{2+c,j}$	1.55 ($Ru^{II/III}$)	−0.28[h]	−0.65	−1.03	−1.45	34
$[\{(bpy)_2Ru(dpp)\}_2RhCl_2]^{5+c,j}$	1.60 ($2Ru^{II/III}$)	−0.42 E_p^c	−0.81			39
			−1.05			
$[\{(bpy)_2Ru(dpq)\}_2RhCl_2]^{5+c,j}$	1.52 ($2Ru^{II/III}$)	−0.17 E_p^c	−0.36			40
$[\{(bpy)_2Ru(dpb)\}_2RhCl_2]^{5+c,j}$	1.52 ($2Ru^{II/III}$)	−0.65 E_p^c	−0.23			40
$[\{(bpy)_2Ru(bpm)\}_2RhCl_2]^{5+c,j}$	1.66 ($2Ru^{II/III}$)	−0.83 E_p^c	−0.18			41
			−0.31			
$[\{(bpy)_2Ru(dpp)\}_2RhBr_2]^{5+c,j}$	1.56 ($2Ru^{II/III}$)	−0.38 E_p^c	−0.77			42
			−1.07			
$[\{(tpy)RuCl(dpp)\}_2RhCl_2]^{3+c,j}$	1.08 ($2Ru^{II/III}$)	−0.52 E_p^c	−0.92			43
			−1.25			
$[\{(tpy)RuCl(bpm)\}_2RhCl_2]^{3+c,j}$	1.08 ($2Ru^{II/III}$)	−0.31 E_p^c	−0.75			43
		−0.43 E_p^c	−1.17			
$[\{(bpy)_2Os(dpp)\}_2RhCl_2]^{5+c,j}$	1.17 ($2Os^{II/III}$)	−0.44 E_p^c	−0.81			44
			−1.05			
$[\{(tpy)OsCl(dpp)\}_2RhCl_2]^{3+c,j}$	0.81 ($2Os^{II/III}$)	−0.56 E_p^c	−0.91			45
			−1.25			

[a] Refer to Figures 6 and 8 for illustrations of the ligands.
[b] Potentials reported vs SCE. E_p^a or E_p^c indicates that only the anodic or cathodic peak was observed.
[c] In acetonitrile with 0.1 M Bu_4NPF_6.
[d] The reported E_p value is a combination of overlapping anodic waves for $Ru^{II/III}$ and $Rh^{III/IV}$.
[e] Converted SSCE to SCE by subtracting 5 mV from the potential vs SSCE.
[f] In acetonitrile with 0.1 M Et_4NClO_4 as supporting electrolyte.
[g] In acetonitrile in 0.1 M Bu_4NBF_4.
[h] Quasireversible.
[i] In dichloromethane with 0.1 M Bu_4NClO_4.
[j] Converted Ag/AgCl to SCE by subtracting 45 mV from the potential vs Ag/AgCl.

TABLE 2. Photophysical Data for Ru(II)-Rh(III) Complexes Containing Polyazine Light Absorbers.[a]

Complex	λ_{max}^{abs} (nm)	λ_{max}^{em} (nm)	Φ^{em}(RT)	τ (RT) (ns)	τ (77 K) (ns)	Reference
$[(bpy)_2Ru(dpp)RhH_2(PPh_3)_2]^{3+b}$	488 425(sh)	776	9.2×10^{-3}	106		24
$[(bpy)_2Ru(dpq)RhH_2(PPh_3)_2]^{3+b}$	572 510(sh) 397					24
$[(bpy)_2Ru(bpm)RhH_2(PPh_3)_2]^{3+b}$	551 515(sh) 413	767	1.9×10^{-3}	41		24
$[(bpy)_2(CN)Ru(CN)Rh(NH_3)_5]^{3+c}$	430	604		310	5700	26
$[(bpy)_2Ru((CN)Rh(NH_3)_5)_2]^{6+c}$	413	576		40	8400	26
$[(bpy)_2(CN)Ru(CN)Rh(NH_3)_4CN)]^{2+c}$	430	606		400	6000	26
$[(bpy)_2(CN)Ru(CN)Rh(NH_3)_4Br)]^{2+c}$	429	620		40 220	5000	26
$[(bpy)_2(CN)Ru(CN)Rh(NH_3)_4I)]^{2+c}$	433	631		350	390	26
$[(bpy)_2Ru(dpp)Rh(bpy)_2]^{5+}$	514[d] 351	778[d]		37[d]	1710[e]	27
$[(ttpy)Ru(tpy\text{-}(Ph)_n\text{-}tpy)Rh(ttpy)]^{5+}(n = 0)$	520[d]	720[f]			12500[e] < 100[f]	29
$[(ttpy)Ru(tpy\text{-}(Ph)_n\text{-}tpy)Rh(ttpy)]^{5+}(n = 1)$	490	655[f]			13000[e] 3000[f]	29
$[(ttpy)Ru(tpy\text{-}(Ph)_n\text{-}tpy)Rh(ttpy)]^{5+}(n = 2)$	490	648[f]			13200[e] 3500[f]	29
$[(Me_2phen)_2Ru(Mebpy\text{-}CH_2\text{-}CH_2\text{-}Mebpy)Rh(Me_2bpy)_2]^{5+}$		610[d]	1.0×10^{-3}	6 30	6800[e]	31
$[Ru\{(dpp)Rh(ppy)_2\}_3]^{5+g}$	471	681	1.8×10^{-2}	330	1050 3400	32

$[Os\{dpp)Rh(ppy)_2\}_3]^{5+g}$	515	821	5.8×10^{-3}	55	620	32
$[(CN)_4Fe(bpm)Ru(bpy)(bpm)Rh(tpy)(MQ^+)]^{4+d}$	609					33
$[(CN)_4Fe(bpm)Ru(bpy)(dpp)Rh(tpy)(MQ^+)]^{4+d}$	544					33
$[(CN)_4Fe(dpp)Ru(bpy)(bpm)Rh(tpy)(MQ^+)]^{4+d}$	540					33
$[(CN)_4Fe(dpp)Ru(bpy)(dpp)Rh(tpy)(MQ^+)]^{4+d}$	521					33
$[(tpy)Ru(tppz)RhCl_3]^{2+d}$	516	830	2.0×10^{-4}	22	330[e]	34
$[\{(bpy)_2Ru(dpp)\}_2RhCl_2]^{5+d}$	520	760	7.3×10^{-5}			39
$[\{(bpy)_2Ru(dpq)\}_2RhCl_2]^{5+d}$	584					40
$[\{(bpy)_2Ru(dpb)\}_2RhCl_2]^{5+d}$	662					40
$[\{(bpy)_2Ru(bpm)\}_2RhCl_2]^{5+d}$	594	800		10		41
$[\{(bpy)_2Ru(dpp)\}_2RhBr_2]^{5+d}$	520	760	1.5×10^{-4}			42
$[\{(tpy)RuCl(dpp)\}_2RhCl_2]^{3+d}$	540					43
$[\{(tpy)RuCl(bpm)\}_2RhCl_2]^{3+d}$	656					43
$[\{(bpy)_2Os(dpp)\}_2RhCl_2]^{5+d}$	530					44
$[\{(tpy)OsCl(dpp)\}_2RhCl_2]^{3+d}$	538					49

[a] Refer to Figures 6 and 8 for illustrations of the ligands.
[b] In acetone.
[c] In DMSO:H_2O.
[d] In acetonitrile.
[e] EtOH-MeOH glass.
[f] 150 K in fluid solution.
[g] In dichloromethane.

III. SUPRAMOLECULAR COMPLEXES COUPLING Ru(II), Os(II) AND Pt(II) POLYAZINE LIGHT ABSORBERS TO REACTIVE METAL CENTERS

The electrochemical and photophysical properties of a variety of mixed-metal supramolecular complexes incorporating Ru/Os(II)-polyazine LA to reactive Pt(II) systems have been investigated.[48–67] Coupling a polyazine LA to a reactive Pt(II) center may impart both the rich redox and photophysical properties of the polyazine LA to the spectroscopic and reactive properties as well as the DNA binding ability of Pt(II). The use of a supramolecular design, allows component modification to enhance device function and light-absorbing properties.

A. Cyanide-Bridged Ru(II)-Pt(II) Complexes: $[(bpy)_2(CN)Ru(CN)Pt(dien)](ClO_4)_2$ and $[(dien)Pt(NC)(bpy)_2Ru(CN)Pt(dien)](ClO_4)_4$

Scandola et al. have investigated the redox and photophysical properties of the Ru(II)-Pt(II) complexes $[(bpy)_2(CN)Ru(CN)Pt(dien)](ClO_4)_2$ and $[(dien)Pt(NC)(bpy)_2Ru(CN)Pt(dien)](ClO_4)_4$ containing the $[Ru(bpy)_2(CN)_2]$ and $[Pt(dien)]^{2+}$ (dien = diethylenetriamine) moieties in 1:1 and 1:2 ratios (Fig. 24).[48] The use of cyanide as a bridge provides strong electronic coupling of the metal centers.

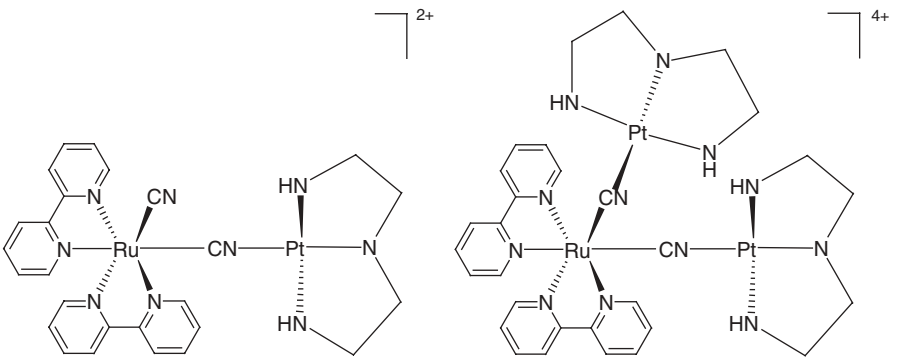

FIGURE 24. Representations of $[(bpy)_2(CN)Ru(CN)Pt(dien)](ClO_4)_2$ and $[(dien)Pt(NC)(bpy)_2Ru(CN)Pt(dien)](ClO_4)_4$ (bpy = 2,2′-bipyridine, dien = diethylenetriamine).

i. Redox Properties of $[(bpy)_2(CN)Ru(CN)Pt(dien)](ClO_4)_2$ and $[(dien)Pt(NC)(bpy)_2Ru(CN)Pt(dien)](ClO_4)_4$

The electrochemistry in DMF shows the typical metal-based oxidations and ligand-based reductions characteristic for ruthenium polyazine complexes (Table 3).[48] The redox couples in the $[(bpy)_2(CN)Ru(CN)Pt(dien)](ClO_4)_2$ and $[(dien)Pt(NC)(bpy)_2Ru(CN)Pt(dien)](ClO_4)_4$ complexes are more positive than

the corresponding redox chemistry of $[Ru(bpy)_2(CN)_2]$. The reductive electrochemistry shows $bpy^{0/-}$ reductions at −1.62, −1.50, and −1.68 V for $[(bpy)_2(CN)Ru(CN)Pt(dien)](ClO_4)_2$, $[(dien)Pt(NC)(bpy)_2Ru(CN)Pt(dien)](ClO_4)_4$, and $[Ru(bpy)_2(CN)_2]$, respectively.[48] The small shift toward positive potentials in the Ru(II)-Pt(II) complexes relative to $[Ru(bpy)_2(CN)_2]$, is attributed to the increase in the positive charge in $[(bpy)_2(CN)Ru(CN)Pt(dien)](ClO_4)_2$ and $[(dien)Pt(NC)(bpy)_2Ru(CN)Pt(dien)](ClO_4)_4$, making the reduction more facile. The oxidative electrochemistry shows reversible $Ru^{II/III}$ oxidations at 1.03, 0.86, and 0.73 V for $[(bpy)_2(CN)Ru(CN)Pt(dien)](ClO_4)_2$, $[(dien)Pt(NC)(bpy)_2Ru(CN)Pt(dien)](ClO_4)_4$, and $[Ru(bpy)_2(CN)_2]$, respectively. The positive shift in the oxidation potential of the Ru(II)-Pt(II) complexes relative to $[Ru(bpy)_2(CN)_2]$ is attributed to the electron-withdrawing ability of platinum, which stabilizes the Ru(dπ) HOMO. The authors suggest the less-positive $Ru^{II/III}$ couple for $[(dien)Pt(NC)(bpy)_2Ru(CN)Pt(dien)](ClO_4)_4$ (0.86 V) relative to $[(bpy)_2(CN)Ru(CN)Pt(dien)](ClO_4)_2$ (1.03 V) as due to the presence of Pt-Pt axial interactions in $[(dien)Pt(NC)(bpy)_2Ru(CN)Pt(dien)](ClO_4)_4$.

ii. Spectroscopic Properties of $[(bpy)_2(CN)Ru(CN)Pt(dien)](ClO_4)_2$ and $[(dien)Pt(NC)(bpy)_2Ru(CN)Pt(dien)](ClO_4)_4$

The Ru(II)-Pt(II) complexes show absorptions throughout the UV and visible regions of the spectrum. The electronic absorption spectra of the complexes were reported in DMF and water and are shown to be solvent dependent. The absorption maxima in the visible region moving to higher energy with increasing number of platinum centers is consistent with the electrochemical properties (Table 4).[48] The visible region of the electronic absorption spectra are dominated by the $Ru(d\pi) \rightarrow bpy(\pi^*)$ MLCT transitions appearing at λ_{max}^{abs} = 460, 426, and 505 nm in DMF for $[(bpy)_2(CN)Ru(CN)Pt(dien)](ClO_4)_2$, $[(dien)Pt(NC)(bpy)_2Ru(CN)Pt(dien)](ClO_4)_4$, and $[Ru(bpy)_2(CN)_2]$, respectively. More subtle changes are observed in aqueous systems with λ_{max}^{abs} ranging between 408 and 428 nm.

iii. Photochemical and Photophysical Properties of $[(bpy)_2(CN)Ru(CN)Pt(dien)](ClO_4)_2$ and $[(dien)Pt(NC)(bpy)_2Ru(CN)Pt(dien)](ClO_4)_4$

Emission spectroscopy was used to study the excited state dynamics in Ru(II)-Pt(II) cyanide-bridged complexes. Emission spectra of the complexes exhibit parallel shifts to absorption. Relative emission intensities of 3 and 1 for $[(bpy)_2(CN)Ru(CN)Pt(dien)](ClO_4)_2$ and $[(dien)Pt(NC)(bpy)_2Ru(CN)Pt(dien)](ClO_4)_4$, respectively, are observed relative to $[Ru(bpy)_2(CN)_2]$. The complexes $[(bpy)_2(CN)Ru(CN)Pt(dien)](ClO_4)_2$, $[(dien)Pt(NC)(bpy)_2Ru(CN)Pt(dien)](ClO_4)_4$, and $[Ru(bpy)_2(CN)_2]$ emit from the $Ru(d\pi) \rightarrow bpy(\pi^*)$ ^{3}MLCT state, with λ_{max}^{em} = 630, 580, and 680 nm; τ = 630, 90, and 205 ns in DMF and λ_{max}^{em} = 590, 580, and 620 nm; τ = 140, 60, and 250 ns in water, respectively, under deaerated conditions at RT.[48] The emission profile for all complexes at RT and 77 K are very similar, suggesting that the bridged platinum does not introduce new low-energy states in the Ru(II)-Pt(II) system.

All three cyanide-bridged complexes are powerful excited state reductants. The emissions from the $Ru(d\pi) \rightarrow bpy(\pi^*)$ ^{3}MLCT states of $[(bpy)_2(CN)Ru(CN)Pt(dien)](ClO_4)_2$, $[(dien)Pt(NC)(bpy)_2Ru(CN)Pt(dien)](ClO_4)_4$, and $[Ru(bpy)_2(CN)_2]$ are efficiently quenched by methylviologen dication in aqueous solutions, in which $k_q = 2.2 \times 10^9$, 7.4×10^8, and 3.5×10^9 $M^{-1}s^{-1}$, respectively. Functionalization through the cyanide bridges modulates the excited and redox properties of $[Ru(bpy)_2(CN)_2]$, while maintaining the original photochemical properties of this complex. Despite the conjugated nature of the small cyanide bridge, many of the desirable properties of the $Ru^{II}(bpy)_2$ subunit are maintained in this structural motif.

B. A Ru(II)-Pt(II) Complex as a Chemodosimeter

The cyano-bridged trinuclear heterobimetallic Ru(II)-Pt(II) complex, $[Ru(phen)_2\{(CN)Pt(DMSO)Cl_2\}_2]^{2+}$ (Fig. 25), was reported as a chemodosimeter for selective sulfhydryl-containing amino acids and peptides by Wong et al.[49] The $[Pt^{II}(DMSO)Cl_2]$ components within the Ru(II)-Pt(II) complex act as electron acceptors, leading to quenching of the emission from the $Ru(d\pi) \rightarrow phen(\pi^*)^3$ MLCT state.[49] Selective binding of the Pt(II) center to the sulfhydryl-containing amino acids and peptides leads to cleavage of the cyano-bridge and the restoration of the $Ru(d\pi) \rightarrow phen(\pi^*)$ ^{3}MLCT emission of the polyazine LA. The proposed $Ru(d\pi) \rightarrow phen(\pi^*)$ MLCT transition occurs at $\lambda_{max}^{abs} = 384$ nm. The MLCT transition is blue shifted from the corresponding transition of $[Ru(phen)_2(CN)_2]$ ($\lambda_{max}^{abs} = 452$ nm). The $Ru(d\pi) \rightarrow phen(\pi^*)$ ^{3}MLCT emission also shifts to higher energy ($\lambda_{max}^{em} = 595$ nm) compared to $[Ru(phen)_2(CN)_2]$ ($\lambda_{max}^{abs} = 621$ nm) with decreased intensity (Table 4). Addition of thiol amino acids shifts the λ_{max}^{em} from 595 to 621 nm, with significant enhancement in intensity. This study demonstrated the use of a Ru(II)-Pt(II) complex in which the Pt(II) center acts as a selective binding site and the Ru(II) center participates in signal transduction.

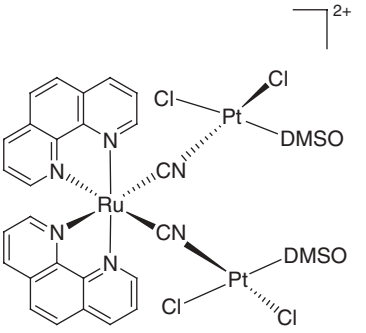

FIGURE 25. Representation of $[Ru(phen)_2\{(CN)Pt(DMSO)Cl_2\}_2]^{2+}$ (phen = 1,10-phenanthroline).

C. Ru(II)-Pt(II) Complexes Bridged by Flexible Spacers

Rillema et al. compared the redox and photophysical properties of the Ru(II)-Pt(II) heterobimetallic complex $[(bpy)_2Ru(Mebpy\text{-}CH_2\text{-}CH_2\text{-}Mebpy)PtCl_2](PF_6)_2$ (Fig. 26) with the monometallic and the homobimetallic complexes, $[(bpy)_2Ru(Mebpy\text{-}CH_2\text{-}CH_2\text{-}Mebpy)](CF_3SO_3)_2$ and $[(bpy)_2Ru(Mebpy\text{-}CH_2\text{-}CH_2\text{-}Mebpy)Ru(bpy)_2](CF_3SO_3)_4$.[50] The use of these flexible unconjugated bridges provides weak coupling of the metals.

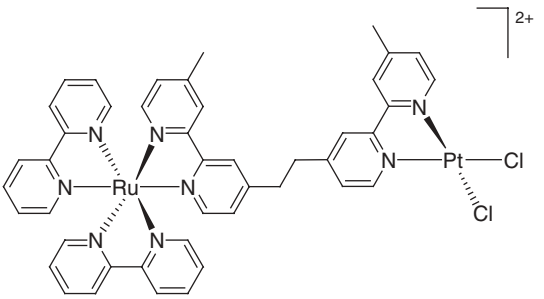

FIGURE 26. Representation of $[(bpy)_2Ru(Mebpy\text{-}CH_2\text{-}CH_2\text{-}Mebpy)PtCl_2]^{2+}$ (2,2′-bipyridine, Mebpy = 4-methyl-2,2′-bipyridine).

i. Redox Properties of $[(bpy)_2Ru(Mebpy\text{-}CH_2\text{-}CH_2\text{-}Mebpy)PtCl_2](PF_6)_2$

The redox chemistry (in propylene carbonate using Et_4NClO_4 as the supporting electrolyte) (Table 3) suggests weak coupling in the Ru(II)-Pt(II) bridged complex. The oxidative electrochemistry of the Ru(II)-Pt(II) complex shows a $Ru^{II/III}$ couple at 1.19 V and the reductive electrochemistry shows $bpy^{0/-}$ couple at −1.39 V.[50] The Ru(II)-Pt(II) complex reveals an additional reduction at −1.28 V due to $Mebpy^{0/-}$ reduction.[50] The electrochemical properties of the Ru(II)-Pt(II) complex predict a Ru(dπ)-based HOMO and a Mebpy(π*)-based LUMO in this structural motif.

ii. Spectroscopic Properties of $[(bpy)_2Ru(Mebpy\text{-}CH_2\text{-}CH_2\text{-}Mebpy)PtCl_2](PF_6)_2$

The Ru(II)-Pt(II) complexes display absorptions characteristic of ruthenium and platinum polyazine complexes. The electronic absorption spectra of the complexes in propylene carbonate are very similar to $Ru(d\pi) \rightarrow ligand(\pi_1^*)$ and $Ru(d\pi) \rightarrow ligand(\pi_2^*)$ MLCT transitions occurring at λ_{max}^{abs} = 457 and 360 nm and ligand-based $\pi \rightarrow \pi^*$ transitions between 250 and 289 nm (Table 4).[50] The homobimetallic complex, $[(bpy)_2Ru(Mebpy\text{-}CH_2\text{-}CH_2\text{-}Mebpy)Ru(bpy)_2](CF_3SO_3)_4$, shows twice the absorptivity of $[(bpy)_2Ru(Mebpy\text{-}Mebpy)](CF_3SO_3)_2$ and $[(bpy)_2Ru(Mebpy\text{-}CH_2\text{-}CH_2\text{-}Mebpy)PtCl_2](PF_6)_2$, consistent with the presence of the two LA units. The absorption at λ_{max}^{abs} = 324 nm

in $[(bpy)_2Ru(Mebpy\text{-}CH_2\text{-}CH_2\text{-}Mebpy)PtCl_2](PF_6)_2$ is attributed to the $Pt(d\pi) \rightarrow ligand(\pi^*)$ MLCT transition. All the complexes display emissions from the $Ru(d\pi) \rightarrow ligand(\Phi^*)$ ^{3}MLCT state with $\Phi \approx 0.06$ and $\tau = 1009$, 1037, and 1034 ns for $[(bpy)_2Ru(Mebpy\text{-}Mebpy)](CF_3SO_3)_2$, $[(bpy)_2Ru(Mebpy\text{-}CH_2\text{-}CH_2\text{-}Mebpy)Ru(bpy)_2](CF_3SO_3)_4$, and $[(bpy)_2Ru(Mebpy\text{-}CH_2\text{-}CH_2\text{-}Mebpy)PtCl_2](PF_6)_2$, respectively. The redox and photophysical properties of these complexes are similar to $[Ru(bpy)_3]^{2+}$, indicating weak coupling, providing the groundwork for additional studies exploiting the properties of the Ru LA and reactive Pt metal subunits.

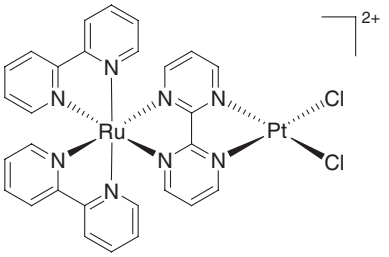

FIGURE 27. Representation of $[(bpy)_2Ru(bpm)PtCl_2]^{2+}$ (bpy = 2,2′-bipyridine, 2,2′-bipyrimidine).

D. A bpm-Bridged Ru(II)-Pt(II) Complex: $[(bpy)_2Ru(bpm)PtCl_2]^{2+}$

Rillema et. al have communicated the Ru(II)-Pt(II) system, $[(bpy)_2Ru(bpm)PtCl_2]^{2+}$(Fig. 27), bridged by a rigid bpm spacer ligand.[51] The bpm bridge provides significant coupling of bridged metals and a symmetric AA chelate to both metals.

i. Redox Properties of $[(bpy)_2Ru(bpm)PtCl_2]^{2+}$

The Ru(II)-Pt(II) complex shows a $Ru^{II/III}$oxidation at 1.35 V (in propylene carbonate using Et_4NClO_4 as the supporting electrolyte) (Table 3).[51] For comparison, the $Ru^{II/III}$oxidation for the monometallic synthon, $[(bpy)_2Ru(bpm)]^{2+}$, occurs at 1.35 V, while the $Ru^{II/III}$oxidation for the homo-bimetallic complex, $[\{(bpy)_2Ru\}_2(bpm)]^{4+}$, occurs as two one electron oxidations at 1.51 and 1.68 V. The oxidative electrochemistry suggests that good communication exists between the two metal centers of $[\{(bpy)_2Ru\}_2(bpm)]^{4+}$, whereas poorer communication exists between the two metal centers of the Ru(II)-Pt(II) complex. The reductive electrochemistry for the Ru(II)-Pt(II) complex shows ligand-based reductions at -0.35 and -1.02 V, corresponding to $bpm^{0/-}$ and $bpm^{-/2-}$, respectively. For comparison, the corresponding reductions for $[(bpy)_2Ru(bpm)]^{2+}$ appear at -1.02 and -1.46 V, whereas they appear at

−0.42 and −1.09 V for $[\{(bpy)_2Ru\}_2(bpm)]^{4+}$. The positive shifts in the reduction potentials for the Ru(II)-Pt(II) complex suggest the stabilization of the bpm ligand orbitals on platinum coordination. The electrochemistry predicts a Ru(dπ)-based HOMO and bpm(π*) LUMO in this complex.

ii. Spectroscopic Properties of $[(bpy)_2Ru(bpm)PtCl_2]^{2+}$

The electronic absorption spectrum for $[(bpy)_2Ru(bpm)PtCl_2]^{2+}$ displays the normal ligand-based $\pi \rightarrow \pi^*$ transition in the UV region and the MLCT transitions in the visible region.[51] The $Ru(d\pi) \rightarrow bpm(\pi^*)$ MLCT transition occurs at $\lambda_{max}^{abs} = 571$ nm, at lower energy than in $[(bpy)_2Ru(bpm)]^{2+}$ ($\lambda_{max}^{abs} = 484$ nm), consistent with platinum coordination. No excited state properties are reported for the Ru(II)-Pt(II) complex. Complexes bridged by bpm are often weakly emissive at best. This bpm-bridged complex, in contrast to the previously discussed systems, displays significant perturbations of the LA properties upon coordination of the Pt(II) reactive metal.

E. Ru(II)-Pt(II) dpp-Bridged Complexes: $[(bpy)_2Ru(dpp)PtMe_2]^{2+}$ and $[(bpy)_2Ru(dpp)PtCl_2]^{2+}$

Yam et al. communicated the redox and photophysical properties of the Ru(II)-Pt(II) complexes $[(bpy)_2Ru(dpp)PtMe_2]^{2+}$ and $[(bpy)_2Ru(dpp)PtCl_2]^{2+}$ (Fig. 28).[52] X-ray crystallographic analysis of $[(bpy)_2Ru(dpp)PtCl_2](PF_6)_2$ revealed a ruthenium center with a distorted octahedral geometry and a platinum center with distorted square planar geometry. The dpp BL is the most widely studied polyazine BL and provides significant coupling of the bridged metals and often emissive LA subunits.

i. Redox Properties of $[(bpy)_2Ru(dpp)PtMe_2]^{2+}$ and $[(bpy)_2Ru(dpp)PtCl_2]^{2+}$

The electrochemistry (in acetonitrile using Bu_4NPF_6 as the supporting electrolyte) revealed ligand-based reductions and metal-based oxidations (Table 3).[52] The reductive electrochemistry of $[(bpy)_2Ru(dpp)PtMe_2]^{2+}$ showed four reversible reductions between −0.84 and −1.83 V, with the least negative

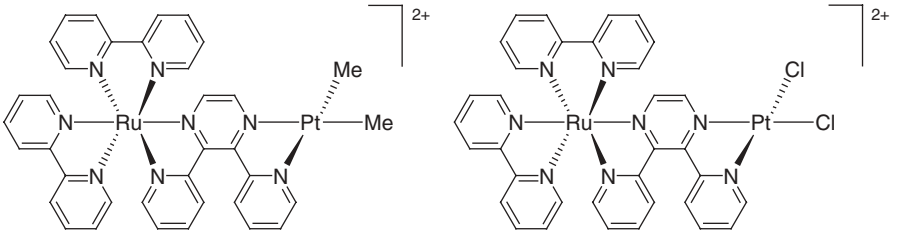

FIGURE 28. Representations of $[(bpy)_2Ru(dpp)PtMe_2]^{2+}$ and $[(bpy)_2Ru(dpp)PtCl_2]^{2+}$ (bpy = 2,2′-bipyridine, dpp = 2,3-bis(2-pyridyl)pyrazine).

reduction at −0.84 V due to $dpp^{0/-}$, followed by $dpp^{-/2}$ and two sequential $bpy^{0/-}$ couples. The stabilization of the dpp(π*) orbitals on metal coordination affords a significant shift in the ligand reduction potentials to more positive values for the Ru(II)-Pt(II) complexes. The reduction potentials of $[(bpy)_2Ru(dpp)PtCl_2]^{2+}$(−0.54 V for $dpp^{0/-}$) are shifted to more positive potentials than the homobimetallic synthon, $[\{(bpy)_2Ru\}_2(dpp)]^{4+}$ (−0.67 V for $dpp^{0/-}$), and the monometallic synthon, $[(bpy)_2Ru(dpp)]^{2+}$ (−1.06 V for $dpp^{0/-}$), consistent with coordination of the more electron deficient $PtCl_2$. The Ru(II)-Pt(II) complexes show an irreversible Pt(II)-based oxidation and reversible $Ru^{II/III}$ oxidation. The $Ru^{II/III}$ couples appear at 1.63 and 1.57 V for $[(bpy)_2Ru(dpp)PtMe_2]^{2+}$ and $[Ru(bpy)_2(dpp)PtCl_2]^{2+}$, respectively. For comparison, the $Ru^{II/III}$ couple of $[(bpy)_2Ru(dpp)]^{2+}$ occurs at a less positive potential of 1.31 V. The electrochemistry predicts a Ru(dπ)-based HOMO and dpp(π*)-based LUMO in these systems.

ii. Spectroscopic Properties of $[(bpy)_2Ru(dpp)PtMe_2]^{2+}$ and $[(bpy)_2Ru(dpp)PtCl_2]^{2+}$

The electronic absorption spectra for the Ru(II)-Pt(II) dpp-bridged systems show the typical absorptions expected for ruthenium and platinum polyazine complexes. Both $[(bpy)_2Ru(dpp)PtMe_2]^{2+}$ and $[(bpy)_2Ru(dpp)PtCl_2]^{2+}$ show intense Ru(dπ)→bpy(π*) and Ru(dπ)→dpp(π*) MLCT transitions in the visible range between λ_{max}^{abs} = 422–440 and 500–524 nm, respectively, with the Ru(dπ)→dpp(π*) MLCT transitions occurring at lower energies (Table 4).[52] The dpp-based MLCT transitions shift to lower energies versus the monometallic synthon, $[(bpy)_2Ru(dpp)]^{2+}$, consistent with the stabilization of the Ru(dπ) orbitals with Pt(II) coordination.

iii. Photophysical and Photochemical Properties of $[(bpy)_2Ru(dpp)PtMe_2]^{2+}$ and $[(bpy)_2Ru(dpp)PtCl_2]^{2+}$

Emission spectroscopy provides a probe into excited state dynamics. Emissions from the Ru(dπ)→dpp(π*) ^{3}MLCT states occur at λ_{max}^{em} = 735 nm; τ = 0.33 μs in acetone for $[(bpy)_2Ru(dpp)PtMe_2]^{2+}$ and λ_{max}^{em} = 800 nm; τ = 0.45 μs in acetonitrile for $[(bpy)_2Ru(dpp)PtCl_2]^{2+}$, compared to λ_{max}^{em} = 682 nm; τ = 0.38 μs for $[(bpy)_2Ru(dpp)]^{2+}$at RT (Table 4).[52] The observed emission energies agree well with the ordering of the dpp(π*) energies detected electrochemically. The lifetimes of the ^{3}MLCT states of the bimetallic complexes are unexpectedly long. In a more detailed study, Yam et al. reported the modulation of the electrochemical and photophysical properties by varying the BL, the substituents on Pt, and the reactive metal.[53] The dpp BL electronically couples the Ru and Pt metal centers and significant changes in the properties are seen relative to the monometallic synthons. In contrast to most bpm-bridged complexes, dpp-bridged LA units often display relatively intense and longer lived emissions from the BL-based ^{3}MLCT states.

F. Ru(II)-Pt(II) Complexes Bridged by a BL Ligand with Two Inequivalent Sites.

Barigelletti et al. investigated the redox and photophysical properties of a pair of isomeric complexes $[(bpy)_2Ru(AB)PtCl_2](PF_6)_2$ and $[(bpy)_2Ru(BA)PtCl_2](PF_6)_2$ (AB = 2,2′:3′,2″:6″,2‴-quaterpyridine) (Fig. 29).[54] The BL AB contains two bipyridyl chelating sites: one that is less sterically hindered, (A), and one that is more sterically hindered (B) (Fig. 8) to which the ruthenium and platinum centers are alternatively coordinated, leading to complexes $[(bpy)_2Ru(AB)PtCl_2](PF_6)_2$ and $[(bpy)_2Ru(BA)PtCl_2](PF_6)_2$.

i. Redox Properties of $[(bpy)_2Ru(AB)PtCl_2](PF_6)_2$ and $[(bpy)_2Ru(BA)PtCl_2](PF_6)_2$

The energetics associated with the frontier orbitals in the Ru(II)-Pt(II) isomeric complexes were probed by electrochemistry. The oxidative electrochemistry of the Ru(II)-Pt(II) complexes in acetonitrile displayed irreversible oxidations that were suggested to be $Ru^{II/III}$-based at 1.35 and 1.48 V for $[(bpy)_2Ru(AB)PtCl_2](PF_6)_2$ and $[(bpy)_2Ru(BA)PtCl_2](PF_6)_2$, respectively (Table 3). The return wave for this $Ru^{II/III}$ oxidation displayed lower current at lower scan rates and became similar in current to the forward wave at fast scan rates.[54] Overlap of the Pt^{II} oxidation may lead to the observed irreversibility. The ruthenium center coordinated to site B is more difficult to oxidize, which implies greater stability of the Ru(dπ) orbitals coordinated to this site. The reductive electrochemistry of $[(bpy)_2Ru(BA)PtCl_2](PF_6)_2$ consists of four reversible ligand-based reductions, at −0.95, −1.30, −1.52, and −1.75 V. The reductive electrochemistry for $[(bpy)_2Ru(AB)PtCl_2](PF_6)_2$ consists of two irreversible reductions at −1.01 and −1.35 V, with the return waves displaying less

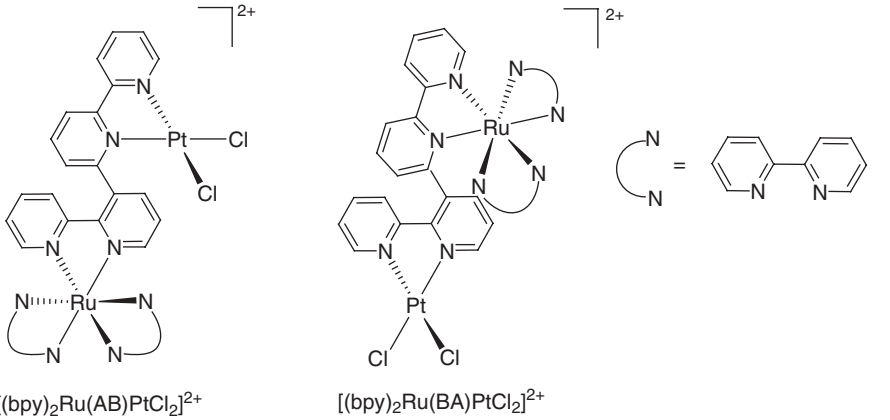

FIGURE 29. Representations of $[(bpy)_2Ru(AB)PtCl_2]^{2+}$ and $[(bpy)_2Ru(BA)PtCl_2]^{2+}$ (bpy = 2,2′-bipyridine, AB = 2,2′:3′,2″:6″,2‴-quaterpyridine).

current, one broad reversible reduction at −1.52 V, followed by a fully reversible reduction at −1.69 V.[54] The first two reductions are attributed to the independent reductions of the bpy-like sites of AB, while the other reductions are due to reduction of the bpy ligands on ruthenium. For comparison, the oxidative electrochemistry of $[(bpy)_2Ru(AB)](PF_6)_2$ consists of a reversible $Ru^{II/III}$ oxidation at 1.33 V, while the reductive electrochemistry consists of three reversible ligand-based reductions at −1.23, −1.46, and −1.69 V, with the reduction at −1.23 V due to reduction of AB. The positive shift in the AB ligand-based reductions in the Ru(II)-Pt(II) complexes is attributed to the greater stabilization of the AB(π*) orbitals with $Pt^{II}Cl_2$ coordination.

ii. Spectroscopic Properties of $[(bpy)_2Ru(AB)PtCl_2](PF_6)_2$ and $[(bpy)_2Ru(BA)PtCl_2](PF_6)_2$

The Ru(II)-Pt(II) positional isomers display absorptions throughout the UV and visible regions of the spectrum. The electronic absorption spectra of the complexes show intense ligand-based absorptions in the UV region and MLCT transition in the visible region. The lowest energy absorption due to the $Ru(d\pi)\rightarrow AB(\pi^*)$ MLCT transition occurs at $\lambda_{max}^{abs} = 455$ and 452 nm for $[(bpy)_2Ru(AB)PtCl_2](PF_6)_2$ and $[(bpy)_2Ru(BA)PtCl_2](PF_6)_2$, respectively (Table 4).[54] For comparison, $Ru(d\pi)\rightarrow AB(\pi^*)$ MLCT transition of $[(bpy)_2Ru(AB)](PF_6)_2$ occurs at $\lambda_{max}^{abs} = 453$ nm. The almost identical absorptions for the Ru(II)-Pt(II) complexes and $[(bpy)_2Ru(AB)](PF_6)_2$ suggest that the $Pt^{II}Cl_2$ has little impact on the light absorption properties. The $Ru(d\pi)\rightarrow AB(\pi^*)$ MLCT transition is slightly red shifted when the ruthenium center is coordinated to site A. The effect of the coordination site of ruthenium is more pronounced in the emissive properties.

iii. Photophysical and Photochemical Properties of $[(bpy)_2Ru(AB)PtCl_2](PF_6)_2$ and $[(bpy)_2Ru(BA)PtCl_2](PF_6)_2$

The excited state properties of the Ru(II)-Pt(II) positional isomers can be determined by emission spectroscopy. Both $[(bpy)_2Ru(AB)PtCl_2](PF_6)_2$ and $[(bpy)_2Ru(BA)PtCl_2](PF_6)_2$ display an emission from the $Ru(d\pi)\rightarrow AB(\pi^*)$ ^{3}MLCT state with $\lambda_{max}^{em} = 640$ and 624 nm; $\Phi = 2.3 \times 10^{-2}$ and 7.5×10^{-4}; and $\tau = 280$ and 13 ns, respectively, in RT acetonitrile (Table 4).[54] The dramatic difference in the excited state properties at RT is attributed to the increased steric hindrance imposed by the B site, which causes the ruthenium metal-centered ^{3}LF states to be destabilized and move closer to the ^{3}MLCT state. The decreased energy gap between the ^{3}LF and the ^{3}MLCT states results in the thermal population of the ^{3}LF states at RT, leading to a weaker emission and a shorter τ in $[(bpy)_2Ru(BA)PtCl_2](PF_6)_2$. At 77 K in butyronitrile, $\tau = 4.8$ and 6.0 μs for $[(bpy)_2Ru(AB)PtCl_2](PF_6)_2$ and $[(bpy)_2Ru(BA)PtCl_2](PF_6)_2$, respectively, and are similar to $[(bpy)_2Ru(AB)](PF_6)_2$ ($\tau = 5.9$ μs).[54] This similarity in τ at 77 K supports the presence of a thermally

accessible ^{3}LF state, as thermal population is limited at 77 K in frozen glass. These studies demonstrated that the asymmetric BL provides positional isomers that have significantly different redox and excited state properties imposed by the inequivalent coordination sites of the BL. Much of the work in Ru(II)-Pt(II) complexes is preliminary. Detailed studies focus on basic chemical and photophysical properties. Their applications in light-activated processes are often not yet explored.

G. DNA Binding of the Ru(II)-Pt(II) Complex: [(tpy)Ru(dtdeg)PtCl]Cl_3

The molecular structure and the coordination to the DNA model base 9-ethylguanine of a Ru(II)-Pt(II) complex, [(tpy)Ru(dtdeg)PtCl]Cl_3 (dtdeg = bis[4′-(2,2′:6′,2″-terpyridyl)]diethyleneglycol ether) have been reported by Reedijk et al.[55] This complex was reported to interact with DNA through electrostatic interactions and covalent binding through the platinum site (Fig. 30). The presence of these multiple modes of DNA interactions are provided by the supramolecular structure. The flexible ether linkage provides weak electronic coupling of the attached metal centers.

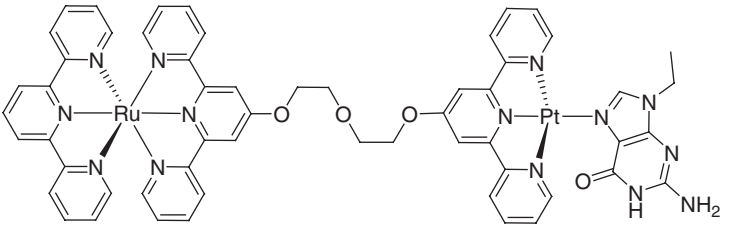

FIGURE 30. Interaction of [(tpy)Ru(dtdeg)PtCl]Cl_3 with 9-ethylguanine (bpy = 2,2′-bipyridine, dtdeg = bis[4′-(2,2′:6′,2″-terpyridyl)]diethyleneglycol ether).

H. Ru(II)-Pt(II) Complexes with Amino Linkages: [(bpy)$_2$Ru(BL)PtCl$_2$](PF$_6$)$_2$ (BL = bpy(CONH(CH$_2$)$_3$NH$_2$)$_2$ and phenNHCO(COOHbpy))

Sakai et. al reported the characterization of Ru(II)-Pt(II) complexes with amino linkages, [(bpy)$_2$Ru(bpy(CONH(CH$_2$)$_3$NH$_2$)$_2$)PtCl$_2$](PF$_6$)$_2$ and [(bpy)$_2$Ru(phenNHCO(COOHbpy)PtCl$_2$](PF$_6$)$_2$ (Fig. 31).[56,57] The applications of these complexes as DNA binding agents as well as hydrogen photocatalysts were investigated.

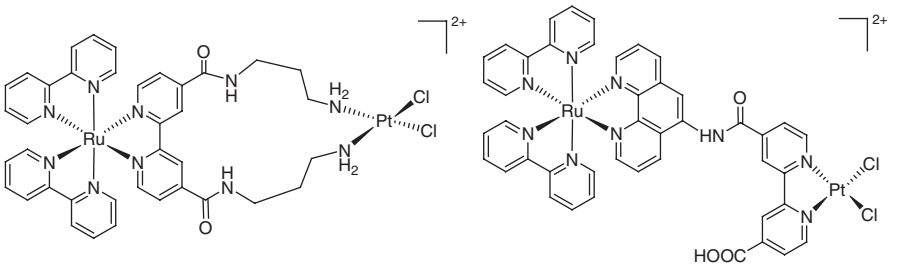

FIGURE 31. Representations of $[(bpy)_2Ru(BL)PtCl_2](PF_6)_2$ (BL = $bpy(CONH(CH_2)_3NH_2)_2$) (left), phenNHCO(COOHbpy) (right) (bpy = 2,2′-bipyridine).

i. Photophysical Properties and DNA Binding Ability of $[(bpy)_2Ru(BL)PtCl_2](PF_6)_2$

The photophysical properties of $[(bpy)_2Ru(BL)PtCl_2](PF_6)_2$ (BL = $bpy(CONH(CH_2)_3NH_2)_2$) were investigated. The electronic absorption spectra of $[(bpy)_2Ru(BL)PtCl_2](PF_6)_2$ and its monometallic synthon with protonated amines, $[(bpy)_2Ru(BL')](CF_3CO_2)_4$ (BL = $bpy(CONH(CH_2)_3NH_3)_2$), are very similar with typical MLCT and ligand-based transitions in the visible and UV regions, respectively.[56] The Ru(II)-Pt(II) complex displays a ruthenium-based emission that is more intense than the corresponding emission of the monometallic synthon. A concurrent increase in τ is observed upon platination (τ = 244 and 518 ns for $[(bpy)_2Ru(BL')](CF_3CO_2)_4$ and $[(bpy)_2Ru(BL)PtCl_2](PF_6)_2$, respectively).[56] The shorter τ in the monometallic synthon is attributed to nonradiative deactivation of the ^{3}MLCT state, which is promoted by the highly flexible ammoniopropyl unit. Upon platination, the formation of the rigid metallocycle retards this deactivation process, leading to enhanced emission and longer τ in the Ru(II)-Pt(II) complex. Enhancement of the ruthenium-based emission intensity of $[(bpy)_2Ru(BL)PtCl_2](PF_6)_2$ is also observed in the presence of guanosine 5′-monophosphate disodium salt (5′-GMP)-, or calf thymus DNA. In addition, studies demonstrated that the photocleavage of pBR322 DNA in the presence of visible light was enhanced in the presence of the Ru(II)-Pt(II) complex, exemplifying the impact of covalently coupling the LA with the reactive metal center.

ii. Photophysical Properties and Photocatalytic Activity of $[(bpy)_2Ru(BL)PtCl_2](PF_6)_2$

Sakai et al. also investigated a Ru(II)-Pt(II) bimetallic system, $[(bpy)_2Ru(BL)PtCl_2]^{2+}$ in which a platinum component is linked to the ruthenium LA through an amide linkage on the phenanthroline ligand, phenNHCO(COOHbpy) (Fig. 8).[57] This complex is capable of photochemically producing hydrogen from water in the presence of the electron donor, ethylenediaminetetraacetic acid (EDTA).[57] The light absorption properties of

the Ru(II)-Pt(II) complex are similar to its monometallic synthon $[(bpy)_2Ru(BL)]^{2+}$ (BL = phenNHCO(COOHbpy)) with typical absorptions in the UV and visible regions. The Ru(II)-Pt(II) system displays a ruthenium-based emission at $\lambda_{max}^{em} = 610$ nm in an air-equilibrated aqueous solution with about one third the intensity of the monometallic synthon. The decreased emission intensity is attributed to intramolecular quenching processes, including electron transfer. Photocatalytic hydrogen production from water occurs with $\Phi \approx 0.01$, and five turnovers in 10 h. Similar Ru(II)-Pt(II) systems investigated by Sakai et al. since then with aliphatic bridging spacers and bridging spacers that retain aromaticity, have shown to be ineffective hydrogen photocatalysts.[58] The mechanism of hydrogen production is unclear and could be due to decomplexation of the platinum to form catalytically active colloidal platinum.[59]

I. Systematic Studies of Ru(II)/Os(II)-Pt(II) Complexes with Polyazine Bridging Ligands

Brewer et al. have designed a series of complexes of the form $[(bpy)_2M(BL)PtCl_2](PF_6)_2$ (M = Ru or Os, BL = dpq or dpb) and $[(tpy)RuX(BL)PtCl_2](PF_6)_n$ (BL = dpp or dpq, *X* = Cl (*n* = 1) or PEt_2Ph (*n* = 2)), incorporating polyazine Ru/Os(II) LAs to bioactive cis-$PtCl_2$ sites through aromatic polyazine BLs (Fig. 32).[60-65] Combining the covalent DNA-binding ability of the Pt(II) center with an aromatic BL capable of intercalating into the planar stacked bases of the DNA double helix affords complexes that represent potential bifunctional DNA binding agents. In addition, coupling of a LA to the Pt(II) center combines the chromophore properties with potential for spectroscopic tagging of DNA or photoactivated reactivity with DNA.

i. Redox Properties of $[(bpy)_2M(BL)PtCl_2](PF_6)_2$

The energetics of the frontier orbitals involved in the electron-transfer processes of Ru(II)/Os(II)-Pt(II) polyazine-bridged complexes can be determined

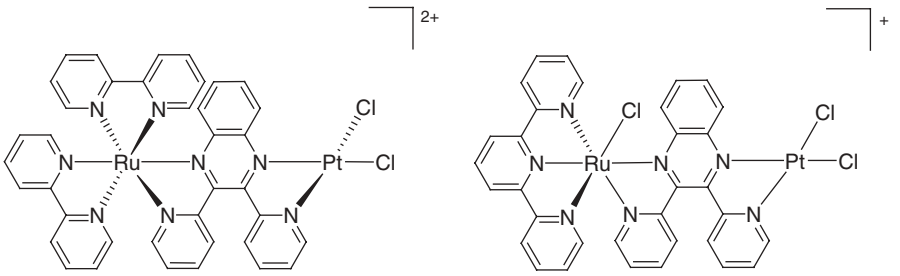

FIGURE 32. Representations of $[(bpy)_2Ru(dpq)PtCl_2](PF_6)_2$ (left) and $[(tpy)RuCl(dpq)PtCl_2](PF_6)$ (right) (bpy = 2,2′-bipyridine, tpy = 2,2′:6′,2″-terpyridine, dpq = 2,3-bis(2-pyridyl)quinoxaline).

through electrochemistry. The electrochemistry of the complexes was recorded in acetonitrile, using Bu_4NPF_6 as supporting electrolyte (Table 3). In the complexes $[(bpy)_2M(BL)PtCl_2](PF_6)_2$ (BL = dpq or dpb; M = Os or Ru), the oxidative electrochemistry displays $Ru^{II/III}$ or $Os^{II/III}$ couples between 1.01 and 1.68, with the $Os^{II/III}$ oxidation occurring at lower potentials.[60] The ruthenium-based systems display an irreversible oxidation that appears as a shoulder, just before the reversible oxidative process. This irreversible oxidation represents the oxidation of the platinum center, $Pt^{II/IV}$. In the osmium bimetallics, the platinum oxidation occurs just before onset of solvent oxidation and after the $Os^{II/III}$ couple. In both the ruthenium and osmium-based systems, the dpb-based systems are easier to oxidize than the dpq systems, suggesting that the dpb ligand can act as a π donor to the ruthenium or osmium center, making the oxidation process more facile. The reductive electrochemistry of $[(bpy)_2M(BL)PtCl_2](PF_6)_2$ (BL = dpq or dpb; M = Os or Ru) displays four ligand-based reductions with the $BL^{0/-}$reductions occurring between −0.16 and −0.35 V and $BL^{-/2-}$ reductions occurring between and −0.80 and −0.97 V, respectively.[60] The $BL^{0/-}$ reductions in the bimetallic systems occur at significantly more positive potentials than their monometallic synthons, $[(bpy)_2M(BL)](PF_6)_2$ (BL = dpq or dpb; M = Os or Ru), consistent with the stabilization of the BL(π*) orbitals upon platinum coordination. In addition, the dpb reductions occur at more positive potentials relative to the dpq reductions, consistent with the lower energy dpb(π*) orbitals.

Substitution of the 2 bpy TLs in $[(bpy)_2M(BL)PtCl_2](PF_6)_2$ with tpy and Cl affords $[(tpy)RuCl(BL)PtCl_2](PF_6)$ (BL = dpp, dpq, or dpb).[61] The complexes $[(tpy)RuCl(BL)PtCl_2](PF_6)$ (BL = dpp, dpq, or dpb) display electrochemistry consistent with their formulation, with the $Ru^{II/III}$ oxidations at 1.09 (dpp), 1.06 (dpq), and 1.08 V (dpb), changing only slightly as the BL is changed. The $Ru^{II/III}$ oxidations of the tpy-based systems, $[(tpy)RuCl(BL)PtCl_2](PF_6)$ (BL = dpp, dpq, or dpb), occur at more negative potentials relative to the bpy-based systems consistent with the presence of a σ-donating chloride ligand in lieu of a bpy making the ruthenium center more electron rich. The reductive electrochemistry displays reversible reductions with the $BL^{0/-}$and $BL^{-/2-}$, followed by the $tpy^{0/-}$ reduction. The $BL^{0/-}$reduction varies as the BL is changed and occurs at −0.55, −0.37, and −0.25 V for BL = dpp, dpq, or dpb, respectively, consistent with the ordering of the BL(π*) energies: dpb(π*) < dpq(π*) < dpp(π*). The reductive electrochemistry establishes the BL(π*) orbitals as the site of localization of the LUMO. In the monometallic synthons $[(tpy)RuCl(BL)](PF_6)$ (BL = dpp, dpq, or dpb), the $BL^{-/2-}$ reduction occurs after the $tpy^{0/-}$ reduction. The occurrence of the $BL^{-/2-}$ reduction before the reduction of $tpy^{0/-}$ reduction in the bimetallic complexes is indicative of the stabilization of the BL(π*) orbitals by coordination to the $PtCl_2$ moiety and a general property of this class of molecules. The reduction potential for this second couple varies dramatically as the BL is changed, shifting to more positive potentials from dpp to dpq to dpb, consistent with its assignment as $BL^{-/2-}$. The third reduction in these bimetallic complexes leads to adsorption to the electrode surface. The potential of this reduction varies little as the BL is changed, consistent with the $tpy^{0/-}$ nature of this couple.

Substitution of the Cl on the ruthenium of $[(tpy)RuCl(BL)PtCl_2](PF_6)$ with a ^{31}P NMR TAG affords TAG-TL-LA-BL-RM (RM = reactive metal) molecular architectures (Fig. 33). The Cl on the ruthenium center can be easily replaced by phosphine groups or other ligands. Complexes of the type $[(tpy)Ru(PEt_2Ph)(BL)PtCl_2](PF_6)_2$ (BL = dpp or bpm) have been characterized.[62] Incorporation of the bpm BL eliminates the cis-trans isomers that result from the AB chelation of the dpp, dpq, or dpb BLs, and affords pure complexes free of isomeric mixtures. The oxidative behavior of these bimetallic complexes is complicated by energetically similar Ru(dπ) and Pt(dπ) orbitals and the irreversible nature of the Pt(II) oxidation. The oxidative electrochemistry of $[(tpy)Ru(PEt_2Ph)(bpm)PtCl_2](PF_6)_2$ displays a quasireversible $Ru^{II/III}$ oxidation at 1.59 V followed by an irreversible $Pt^{II/IV}$ oxidation at 1.78 V. Scanning anodically in a solution of $[(tpy)Ru(PEt_2Ph)(dpp)PtCl_2](PF_6)_2$ shows two overlapping oxidative processes with a much less pronounced reductive process upon switching the scan cathodically. The oxidation at 1.51 V is assigned as a $Ru^{II/III}$ oxidation, whereas the oxidation at 1.66 V is due to oxidation of the Pt(II) center. The $Ru^{II/III}$ oxidation of the $[(tpy)Ru(PEt_2Ph)(dpp)PtCl_2](PF_6)_2$ occurs at a more positive potential relative to $[(tpy)RuCl(dpp)PtCl_2](PF_6)$, consistent with the greater stability of the Ru(dπ) orbitals of $[(tpy)Ru(PEt_2Ph)(dpp)PtCl_2](PF_6)_2$ imposed by the strong field phosphine ligand in place of the weak field chloride. Three reduction waves are observed for each bimetallic complex and are assigned as sequential $BL^{0/-}$, $BL^{-/2-}$, and $tpy^{0/-}$ reductions. The first two reductions of the bpm BL occur at −0.39 and −1.09 V, respectively, whereas the sequential one-electron reductions of dpp occur at more negative potentials, −0.55 and −1.19 V. The electrochemical data of the Ru(II)/Os(II)-Pt(II) complexes predict a Ru(dπ) or Os(dπ)-based HOMO and BL(π*)-based LUMO. Table 3 summarizes the redox potentials of the polyazine-bridged Ru(II)-Pt(II) complexes.

ii. Spectroscopic Properties of $[(bpy)_2M(BL)PtCl_2](PF_6)_2$

The electronic absorption spectra of $[(bpy)_2M(BL)PtCl_2](PF_6)_2$ (BL = dpq or dpb; M = Os or Ru) demonstrate typical ligand-based $n \rightarrow \pi^*$ and $\pi \rightarrow$

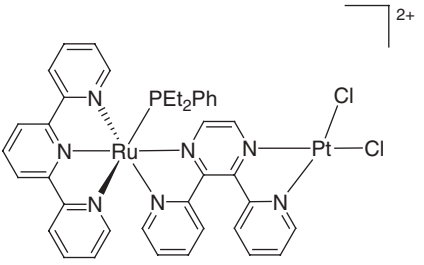

FIGURE 33. Representation of $[(tpy)Ru(PEt_2Ph)(dpp)PtCl_2](PF_6)_2$ (tpy = 2,2′:6′,2″-terpyridine, dpp = 2,3-bis(2-pyridyl)pyrazine).

π* transitions in the UV region and M(dπ)→bpy(π*) and M(dπ)→BL(π*) (BL = dpq or dpb, M = Ru or Os) MLCT transitions in the visible region.[62] The M(dπ)→BL(π*) MLCT transitions occur at 582 (dpq) and 630 (dpb) nm for the ruthenium systems and at 598 (dpq) and 638 (dpb) nm for the osmium systems (Table 4). The transitions in the 410–420 nm region are attributed to M(dπ)→bpy(π*) MLCT transitions. The bpy-based π→π* transitions occur in the UV at ~ 290 nm, whereas BL-based transitions appear between 340 and 350 nm for the dpq systems and between 380 and 390 nm for the dpb-based systems. In $[(bpy)_2Ru(BL)PtCl_2]^{2+}$ (BL = dpq or dpb), the Ru(dπ) and Pt(dπ) orbitals are energetically similar, but the light-absorbing properties of these systems are dominated by the ruthenium chromophore. The platinum component absorbs at a higher energy with a lower absorptivity.

The electronic absorption spectra of $[(tpy)RuCl(BL)PtCl_2](PF_6)$ (BL = dpp, dpq, or dpb) are typical for complexes of this type and show absorptions in much of the UV and visible regions.[61] The UV region is dominated by tpy-based π→π* transitions at 272 and 316 nm. The lowest-energy BL-based π→π* transition shifts as the BL is varied. The dpp or dpq bands appear as low-energy shoulders on the tpy-based peak at 316 nm. The dpb complex displays a distinct π→π* transition at 380 nm. The visible region is dominated by Ru(dπ)→tpy(π*) and Ru(dπ)→BL(π*) MLCT transitions with the Ru(dπ)→BL(π*) MLCT transition occurring at lower energy. The Ru(dπ)→tpy(π*) MLCT transition occurs at 460 nm for all three complexes, whereas the energy of the Ru(dπ)→BL(π*) MLCT transition is modulated by the BL, occurring at λ_{max}^{abs} = 544 nm (dpp), 632 nm (dpq), and 682 nm (dpb). This is consistent with the stabilization of the BL(π*) orbitals through this series. As expected, the Ru(dπ)→BL(π*) MLCT transition for the bimetallic complexes is red shifted relative to those for their monometallic synthons due to the stabilization of the BL(π*) orbitals by platinum coordination. In addition, $[(tpy)RuCl(BL)PtCl_2](PF_6)$ (BL = dpp, dpq, or dpb) displays Ru(dπ)→BL(π*) MLCT transitions that are red-shifted from those of their bpy analogs, $[(bpy)_2Ru(BL)PtCl_2](PF_6)_2$ (BL = dpp, dpq, or dpb).[52,60] This red shift is consistent with the more electron-rich ruthenium center in the tpy-based systems.

The electronic absorption spectra of $[(tpy)Ru(PEt_2Ph)(BL)PtCl_2](PF_6)_2$ (BL = dpp or bpm) display ligand-based and MLCT-based absorptions in the UV and visible regions.[62] The energies of the absorption bands in the visible region of the spectra vary as a function of BL, with the Ru(dπ)→bpm(π*) MLCT transition being red shifted (λ_{max}^{abs} = 560 nm) relative to the Ru(dπ)→dpp(π*) MLCT transition (λ_{max}^{abs} = 506 nm). This is in accord with the electrochemical properties of these complexes. The Ru(dπ)→dpp(π*) MLCT transition (λ_{max}^{abs} = 506 nm) of $[(tpy)Ru(PEt_2Ph)(dpp)PtCl_2](PF_6)_2$ occurs at higher energy relative to that of $[(tpy)RuCl(dpp)PtCl_2](PF_6)$ (λ_{max}^{abs} = 544 nm). The stabilization of the Ru(dπ) upon substitution of the weak field chloride by the strong field phosphine ligand in $[(tpy)Ru(PEt_2Ph)(dpp)PtCl_2](PF_6)_2$ is consistent with observed blue shift in the Ru(dπ)→dpp(π*) MLCT transition

of $[(tpy)Ru(PEt_2Ph)(dpp)PtCl_2](PF_6)_2$. The spectroscopic properties of $[(tpy)RuCl(dpp)PtCl_2](PF_6)$ in the visible region are dominated by $Ru(d\pi) \rightarrow tpy(\pi^*)$ and $Ru(d\pi) \rightarrow dpp(\pi^*)$ MLCT transitions. The $Pt(d\pi) \rightarrow dpp(\pi^*)$ MLCT transition occurs as a high energy shoulder on the lower-energy, more intense $Ru(d\pi) \rightarrow dpp(\pi^*)$ MLCT transition. The complex $[(tpy)Ru(PEt_2Ph)(dpp)PtCl_2](PF_6)_2$ displays an emission from the $Ru(d\pi) \rightarrow dpp(\pi^*)$ ^{3}MLCT state at $\lambda_{max}^{em} = 750$ nm in acetonitrile with $\tau = 56$ ns. For comparison, the monometallic synthon, $[(tpy)Ru(PEt_2Ph)(dpp)](PF_6)_2$, displays an emission from the $Ru(d\pi) \rightarrow dpp(\pi^*)$ ^{3}MLCT state at $\lambda_{max}^{em} = 720$ nm in acetonitrile with $\tau = 6$ ns.[62] This lengthening of τ in the bimetallic complexes relative to the monometallic synthon is attributed to a decreased thermal population of the low-lying ^{3}LF state due stabilization of the emissive ^{3}MLCT with platinum addition. The lowest-lying absorptions in the electronic absorption spectrum of the Ru(II)-Pt(II) complexes are provided in Table 4.

iii. DNA Binding by $[(bpy)_2M(dpb)PtCl_2](PF_6)_2$

The interaction of $[(bpy)_2M(BL)PtCl_2]Cl_2$ (BL = dpb; M = Os or Ru) with DNA has been explored.[63,64] Both $[(bpy)_2Ru(dpb)PtCl_2]Cl_2$ and $[(bpy)_2Os(dpb)PtCl_2]Cl_2$ bind with DNA in a concentration- and time-dependent fashion. The monometallic complex, $[(bpy)_2Ru(dpb)]Cl_2$, does not covalently bind to DNA. This study confirmed the necessity of the Pt(II) center and suggested that the bimetallic complexes form covalent bonds to DNA through the platinum site.[63] The chlorides bound to the Pt(II) center are substitutionally labile, giving these complexes the ability to covalently bind to DNA. The type of covalent interactions were later determined to be primarily intrastrand cross-linking in nature. Such interactions are similar to the type of interactions between DNA and cisplatin.[64] The complexes $[(tpy)RuCl(BL)PtCl_2](PF_6)$ (BL

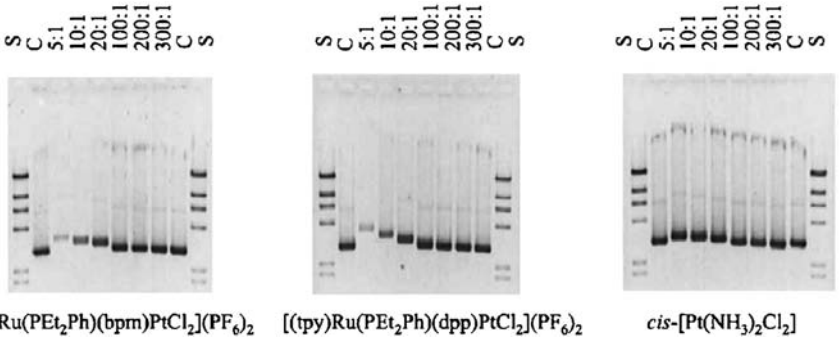

FIGURE 34. DNA-binding study for $[(tpy)Ru(PEt_2Ph)(BL)PtCl_2](PF_6)_2$ (BL = dpp or bpm) by agarose gel electrophoresis using linearized pBluescript DNA. Lane S is the molecular weight standard, 23, 9.4, 6.6, 4.4, 2.3, and 2.0 kb; lane C is the DNA control with no metal complex added. The other lanes are labeled with the basepairs to metal complex ratios, varying from 5:1 to 300:1. Each of these lanes contains 100 ng plasmid DNA.[65]

= dpp, dpq, or dpb) and $[(tpy)Ru(PEt_2Ph)(BL)PtCl_2](PF_6)_2$ (BL = dpp or bpm) were also found to bind to DNA.[61,65] It is interesting that these bimetallic complexes typically bind to DNA more rapidly than cisplatin and affect DNA migration through agarose gels more dramatically. Figure 34 represents a DNA-binding study for $[(tpy)Ru(PEt_2Ph)(BL)PtCl_2](PF_6)_2$ (BL = dpp or bpm) by agarose gel electrophoresis using linearized pBluescript DNA. The agarose gels display increased metal complex binding to DNA binding at small base pair to metal complex ratios.

J. Dendrimeric Ru(II)-Pt(II) Complexes Bridged by Polyazine Bridging Ligands

Few examples of mixed-metal supramolecular complexes incorporating multiple Ru(II) and Pt(II) centers have been reported.[66,67] These systems use dpp or dpq BLs to couple Ru(II) and Pt(II) subunits. The BL provides electronic coupling of the bridged metals.

i. Redox and Spectroscopic Properties of $[Ru\{(dpq)(PtCl_2)\}_3](PF_6)_2$

The electrochemical and photochemical properties of a tetrametallic Ru(II)-Pt(II) complex, $[Ru\{(dpq)(PtCl_2)\}_3](PF_6)_2$ (Fig. 35), were reported by Rillema et al.. This complex incorporated one ruthenium and three platinum centers.[66] The reductive electrochemistry in propylene carbonate is reported, with the BLs being reduced sequentially at −0.08, −0.25, and −0.79 V (Table 3). The electronic absorption spectrum of $[Ru\{(dpq)(PtCl_2)\}_3](PF_6)_2$ in propylene carbonate shows the $Ru(d\pi) \rightarrow dpq(\pi^*)$ MLCT transition in the visible (λ_{max}^{abs} = 553 nm). This transition occurs at a lower energy than in the monometallic

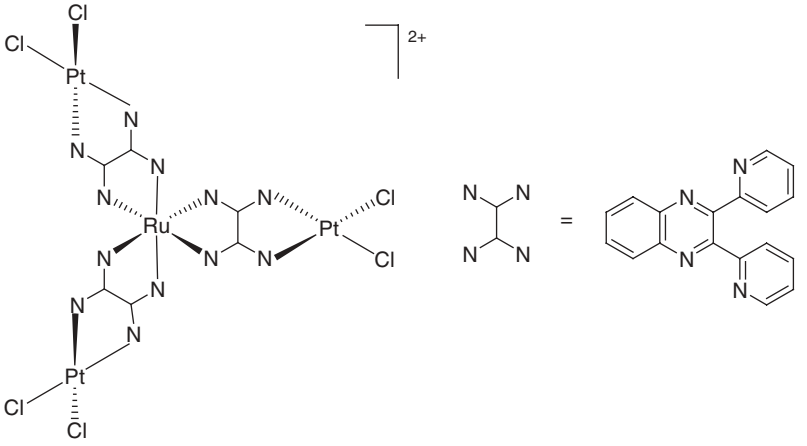

FIGURE 35. Representation of $[Ru\{(dpq)(PtCl_2)\}_3]^{2+}$ (dpq = 2,3-bis(2-pyridyl) quinoxaline).

synthon, $[Ru(dpq)_3](PF_6)_2$ (λ_{max}^{abs} = 502 nm). The red shift in the Ru(dπ)→dpq(π*) MLCT transition for $[Ru\{(dpq)(PtCl_2)\}_3](PF_6)_2$ relative to $[Ru(dpq)_3](PF_6)_2$ is consistent with the stabilization of the dpq(π*) orbitals upon platinum coordination.

ii. Multifunctional DNA Binding and Photocleavage Agent: $[\{(bpy)_2Ru(dpp)\}_2Ru(dpp)PtCl_2](PF_6)_6$

Brewer et al. reported the multifunctional tetrametallic Ru(II)-Pt(II) complex $[\{(bpy)_2Ru(dpp)\}_2Ru(dpp)PtCl_2](PF_6)_6$ exhibiting both DNA binding and photocleavage properties.[67] This complex couples a *cis*-$Pt^{II}Cl_2$ binding site to a three ruthenium polyazine unit (Fig. 36). The complex was characterized by electrochemical and photochemical techniques. The electrochemical properties are dictated by the number and type of subunits with oxidations being metal-based and reductions being ligand-based. The oxidative electrochemistry reveals a reversible $Ru^{II/III}$ oxidation at 1.54 V for the two peripheral metals (Table 3). The reductive electrochemistry shows the dpp reductions between −0.45 and −1.30 V, with the dpp ligands attached to the platinum center being reduced first at −0.45 V. The reductions of the dpps bridging the ruthenium centers occur at −0.65 and −0.75 V. The complex $[\{(bpy)_2Ru(dpp)\}_2Ru(dpp)PtCl_2](PF_6)_6$ is an efficient light absorber throughout the UV and visible regions. The UV contains π→π* transitions for bpy (290 nm) and dpp (320 nm). The Ru(dπ)→bpy(π*) MLCT transition occurs at 416 nm. The absorptions at 520 – 540 nm correspond to the Ru(dπ)→μ-dpp(π*) MLCT transitions. The extinction coefficient for the overlapping MLCT transitions at 542 nm is 35,000 M^{-1} cm^{-1}, consistent with the number of overlapping transitions in this region. Studies demonstrated that

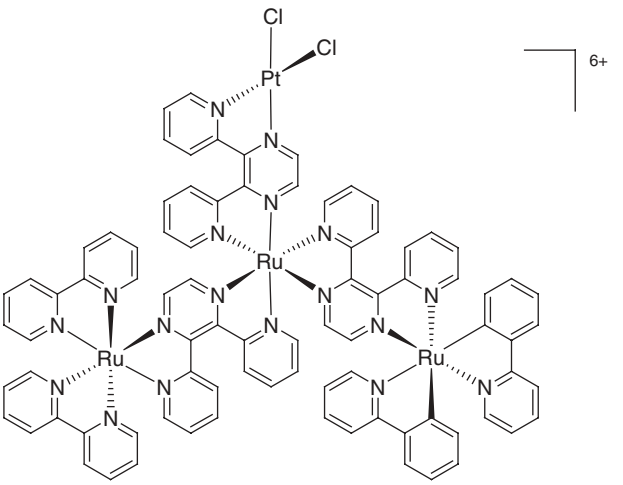

FIGURE 36. Representation of $[\{(bpy)_2Ru(dpp)\}_2Ru(dpp)PtCl_2]^{6+}$ (bpy = 2,2′-bipyridine, dpp = 2,3-bis(2-pyridyl)pyrazine).

$[\{(bpy)_2Ru(dpp)\}_2Ru(dpp)PtCl_2](PF_6)_6$ can interact with DNA through platinum by forming coordinate covalent bonds. Studies also demonstrated that this complex can photocleave DNA through the ruthenium polyazine chromophores in an oxygen-mediated pathway. $[\{(bpy)_2Ru(dpp)\}_2Ru(dpp)PtCl_2](PF_6)_6$ represents the first polyazine supramolecular complex to covalently bind and photocleave DNA.

IV. SUPRAMOLECULAR COMPLEXES COUPLING Ru(II) POLYAZINE LIGHT ABSORBERS TO REACTIVE Pd(II) METAL CENTERS

In the course of constructing molecules for solar energy conversion schemes, some attention has been given to polynuclear systems that combine ruthenium polypyridyl LAs to catalytically active Pd(II) centers. The systems use rigid and flexible spacers that provide electronic coupling between the ruthenium and palladium centers.[53,68–70]

A. Ru(II)-Pd(II) Complexes Bridged by dpp and bpm Ligands: $[(bpy)_2Ru(dpp)PdCl_2](PF_6)_2$ and $[(bpy)_2Ru(bpm)PdCl_2](ClO_4)_2$

Yam et al. reported the electrochemical and photophysical properties of the Ru(II)-Pd(II) complexes, $[(bpy)_2Ru(dpp)PdCl_2](PF_6)_2$ and $[(bpy)_2Ru(bpm)PdCl_2](ClO_4)_2$.[53] The X-ray crystal structure of $[(bpy)_2Ru(dpp)PdCl_2](PF_6)_2$ was also reported.

i. Redox Properties of $[(bpy)_2Ru(dpp)PdCl_2](PF_6)_2$ and $[(bpy)_2Ru(bpm)PdCl_2](ClO_4)_2$

Electrochemistry estimated the energetics of the frontier orbitals involved in electron transfer events of the polyazine ligand bridged Ru(II)-Pd(II) complexes. The electrochemistry of $[(bpy)_2Ru(dpp)PdCl_2](PF_6)_2$ shows a $Ru^{II/III}$ oxidation at 1.56 V and ligand-based reductions between −0.54 and −1.76 V (Table 3).[53] The $dpp^{0/-}$ reduction occurs at the least negative potential of −0.54 V. The electrochemistry of $[(bpy)_2Ru(bpm)PdCl_2](ClO_4)_2$ shows two metal-based oxidations at 1.57 and 1.61 V and ligand-based reductions between −0.32 and −1.71 V. The $bpm^{0/-}$ reduction occurs at the least negative potential of −0.32 V. The $bpm^{0/-}$ reduction occurs at a more positive potential than the $dpp^{0/-}$ potential, consistent with the lower energy bpm(π*) orbitals. Electrochemistry predicts a Ru(dπ)-based HOMO and a bpm(π*) LUMO in this structural motif.

ii. Spectroscopic Properties of $[(bpy)_2Ru(dpp)PdCl_2](PF_6)_2$ and $[(bpy)_2Ru(bpm)PdCl_2](ClO_4)_2$

The electronic absorption spectra of the polyazine-bridged Ru(II)-Pd(II) complexes show the typical ligand-based $\pi \rightarrow \pi^*$ transitions in the UV and

metal-based transitions in the visible.[53] The Ru(dπ)→bpm(π*) MLCT transition of $[(bpy)_2Ru(bpm)PdCl_2](ClO_4)_2$ occurs at a lower energy (λ_{max}^{abs} = 556 nm) relative to the Ru(dπ)→dpp(π*) MLCT transition of $[(bpy)_2Ru(dpp)PdCl_2](PF_6)_2$ (λ_{max}^{abs} = 526 nm) (Table 4).[53] The electronic absorption spectroscopy agrees well with the electrochemical properties of these complexes. Consistent with the stabilization of the BL(π*) orbitals upon metal coordination, the Ru(dπ)→BL(π*) MLCT transition is red shifted in the Ru(II)-Pd(II) complexes relative to those of their monometallic synthons, $[(bpy)_2Ru(BL)](PF_6)_2$ (BL = dpp or bpm). The complex $[(bpy)_2Ru(dpp)PdCl_2](PF_6)_2$ displays an emission from the Ru(dπ)→dpp(π*) ^{3}MLCT excited state (λ_{max}^{em} = 700 nm; τ = 0.37 μs in acetonitrile at RT)[53] at lower energy than the corresponding emission for $[(bpy)_2Ru(dpp)](PF_6)_2$ (λ_{max}^{em} = 682 nm).[52] By contrast, $[(bpy)_2Ru(bpm)PdCl_2](ClO_4)_2$ does not display a detectable emission from the Ru(dπ)→bpm(π*) ^{3}MLCT excited state, consistent with the decreased energy gap due to the lower energy of the bpm(π*) orbitals and the typically weak emissions of bpm complexes. This report is one of the early and few studies of Ru,Pd coupled complexes and shows that the LA properties of the Ru subunit are maintained while still perturbed by Pd coordination.

B. Ru(II)-Pd(II) Complexes Bridged by an Extended Polyazine Ligand: $[(^tBu_2bpy)_2Ru(tpphz)PdCl_2](PF_6)_2$

Rau et al. reported a Ru(II)-Pd(II) bimetallic system, $[(t\text{-}Bu_2bpy)_2Ru(tpphz)PdCl_2](PF_6)_2$ (tpphz = tetrapyridophenazine) (Fig. 37), that photochemically produces hydrogen in the presence of the electron donor, TEA, and also selectively catalyzes the hydrogenation of tolane.[68] The BL, tpphz, connects the LA and a catalytically active Pd center through a polyazine BL with low-lying π* acceptor orbitals. The reductive electrochemistry of $[(t\text{-}Bu_2bpy)_2Ru(tpphz)PdCl_2](PF_6)_2$ in acetonitrile displays a reversible phenazine-based reduction at −0.64 V, an irreversible Pd(II) reduction at −0.83 V,

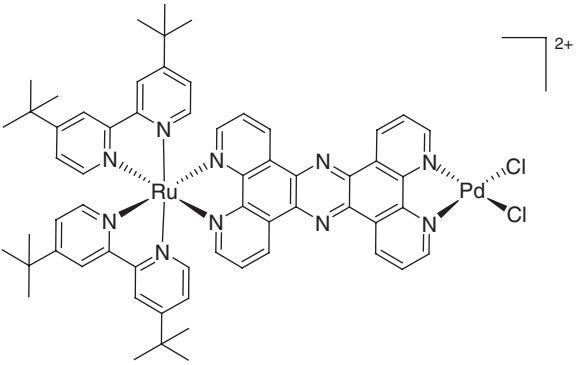

FIGURE 37. Representation of $[(^tBu_2bpy)_2Ru(tpphz)PdCl_2](PF_6)_2$ ($^tBu_2bpy$ = 4,4′-di-tert-butyl-2,2′-bipyridine, tpphz = tetrapyridophenazine).

and reversible bpy-based reductions between −1.09 and −1.43 V (Table 3).[68] The phenazine-based reduction occurs at a slightly less negative potential in the Ru(II)-Pd(II) complex relative to that of its monometallic synthon, $[(t\text{-}Bu_2bpy)_2Ru(tpphz)](PF_6)_2$. This is in accord with the stabilization of the tpphz(π*) orbitals upon metal coordination.

i. Spectroscopic Properties of $[(^tBu_2bpy)_2Ru(tpphz)PdCl_2](PF_6)_2$

The complex $[(^tBu_2bpy)_2Ru(tpphz)PdCl_2](PF_6)_2$ displays the typical ligand-based transitions in the UV region and MLCT transitions in the visible region in the electronic absorption spectrum. The lowest-energy MLCT transition occurs at λ_{max}^{abs} = 445 nm in acetonitrile solutions (Table 4). The Ru(II)-Pd(II) complex displays a weak ruthenium-based emission at 650 nm with τ = 27 ns in an air-saturated acetonitrile solution (Table 4). By comparison, $[(^tBu_2bpy)_2Ru(tpphz)](PF_6)_2$ displays a ruthenium-based emission at 638 nm with τ = 154 ns. The ruthenium-based ^{3}MLCT emission is significantly quenched in the Ru(II)-Pd(II) system. It is proposed that photoexcitation affords a Ru^{III}-phenazine$^{(-)}$-Pd^{II} radical, which is reduced to Ru^{II} by TEA. It is possible that further reduction produces metallic palladium, which acts as the hydrogen evolution catalyst.[69]

C. Ru(II)-Pd(II) Complexes Bridged by bpm Type Ligands: $[(bpy)_2Ru(BL)PdMeCl]^{2+}$

Akita et al. reported the electrochemical and photophysical properties of a series of Ru(II)-Pd(II) complexes including $[(bpy)_2Ru(BL)PdMeCl]^{2+}$ (BL = bpm, Me_2bpm, or Br_2bpm) and their solvated analogs $[(bpy)_2Ru(BL)PdMe(Me_2CO)]^{3+}$ (BL = bpm or Me_2bpm).[70] The electrochemistry (in acetonitrile using Bu_4NClO_4 as the supporting electrolyte) shows typical $Ru^{II/III}$ oxidations and ligand-based reductions. The $Ru^{II/III}$ oxidation of $[(bpy)_2Ru(Br_2bpm)PdMeCl]^{2+}$is not observed in the solvent window. Incorporation of an electron-donating group on the bpm causes a small negative shift in the $Ru^{II/III}$ oxidation, consistent with a ruthenium center that is more easily oxidized. The reductive electrochemistry displayed ligand-based reductions with the $BL^{0/-}$ couple occurring initially, consistent with the stabilization of the BL(π*) orbitals. Introduction of electron-donating or withdrawing substituents on the bpm affords negative or positive shifts, respectively, in the reductive electrochemistry. A unique feature in the Ru(II)-Pd(II) complexes is that significant shifts in the Ru(dπ)→bpm(π*) MLCT transitions are not observed compared to their monometallic synthons $[(bpy)_2Ru(BL)]^{2+}$ (BL = bpm, Me_2bpm, or Br_2bpm). This is in contrast to the reductive electrochemical data. The authors suggest the possibility of the spectroscopic orbitals being different from the redox orbitals. These complexes act as photocatalysts in the dimerization of π-methylstyrene. The Ru(II)-Pd(II) complex containing the Br_2bpm as the BL shows the highest photocatalytic activity. The possible role of metallic Pd formation was not addressed.[69]

D. A Ru(II)-Pd(II) Complex Bridged by a Flexible Polyazine Bridging Ligand: $[(bpy)_2Ru(DMB)PdCl_2]^{2+}$

Hammarström et al. investigated the stability of a Ru(II)-Pd(II) photocatalyst, $[(bpy)_2Ru(DMB)PdCl_2]^{2+}$ (DMB = Mebpy(CH_2)-$C_6H_2(OCH_3)_2$ $(CH_2)_2$Mebpy) (Fig. 38), during photochemical hydrogen production from a proton source.[69]

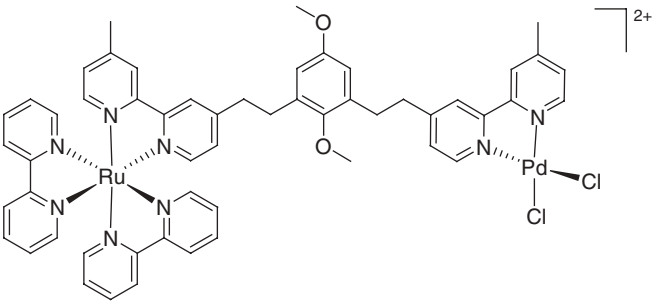

FIGURE 38. Representation of $[(bpy)_2Ru(DMB)PdCl_2]^{2+}$ (DMB = Mebpy(CH_2)-$C_6H_2(OCH_3)_2(CH_2)_2$Mebpy).

i. Redox and Spectroscopic Properties of $[(bpy)_2Ru(DMB)PdCl_2]^{2+}$

The electrochemical and photochemical properties of the complex were investigated. The oxidative electrochemistry revealed a typical $Ru^{II/III}$ oxidation, followed by an irreversible oxidation attributed to $DMB^{0/+}$ oxidation (Table 3).[69] The reductive electrochemistry revealed an irreversible reduction attributed to Pd^{II} reduction. The electronic absorption spectrum revealed the typical absorptions observed for ruthenium polyazine complexes. The Ru(dπ)→bpy(π*) MLCT state energy of the Ru(II)-Pd(II) complex coincides well with that of $[(bpy)_2Ru(DMB)]^{2+}$ at $\lambda_{max}^{abs} = 455$ nm.

ii. Photochemistry of $[(bpy)_2Ru(DMB)PdCl_2]^{2+}$

In the presence of triethylamine, $[(bpy)_2Ru(DMB)PdCl_2]^{2+}$photocatalyzes proton reduction to produce hydrogen.[69] A control experiment using the LAs $[(bpy)_2Ru(DMB)]^{2+}$or $[Ru(bpy)_3]^{2+}$ in the presence of $[Pd(Me_2bpy)Cl_2]$ and triethylamine also afforded comparable amounts hydrogen to the covalently bound Ru(II)-Pd(II) system. This experiment suggested that hydrogen production with the Ru(II)-Pd(II) system is not necessarily an intramolecular process. To investigate the possibility of colloidal Pd formation during photocatalysis, XPS and TEM measurements were carried out on samples of the reaction mixture. The XPS and TEM measurements revealed colloidal Pd, which suggested that the reduction of the Ru(II)-Pd(II) complex produced metallic Pd.[69]

TABLE 3. Electrochemical Data for Ru(II)/Os(II)-Pt(II) Complexes Containing Polyazine Light Absorbers.[a]

Complex[b]	$E_{1/2}^{ox}$ (V vs SCE)	$E_{1/2}^{red}$ (V vs SCE)			Reference
		$BL^{0/-}$	$BL^{-/2-}$	$TL^{0/-}$	
$[(bpy)_2(CN)Ru(CN)Pt(dien)]^{2+c}$	1.03 ($Ru^{II/III}$)			−1.62	48
$[(dien)Pt(NC)(bpy)_2Ru(CN)Pt(dien)]^{4+c}$	0.86 ($Ru^{II/III}$)			−1.50	48
$[(bpy)_2Ru(Mebpy\text{-}CH_2\text{-}CH_2\text{-}Mebpy)PtCl_2]^{2+d}$	1.19 ($Ru^{II/III}$)[e]	−1.28[e]		−1.39[e]	50
$[(bpy)_2Ru(bpm)PtCl_2]^{2+e,f}$	1.35 ($Ru^{II/III}$)	−0.35	−1.02		51
$[(bpy)_2Ru(dpp)PtMe_2]^{2+g}$	1.63 ($Ru^{II/III}$)	−0.84	−1.39	−1.61	52, 53
	0.66 E_p^a			−1.83	
	1.12 E_p^a				
$[(bpy)_2Ru(dpp)PtCl_2]^{2+g}$	1.57 ($Ru^{II/III}$)	−0.54	−1.11	−1.49	53
	1.47 E_p^a				
$[(bpy)_2Ru(AB)PtCl_2]^{2+g,h}$	1.35 ($Ru^{II/III}$)	−1.01		−1.52	54
		−1.35		−1.69	
$[(bpy)_2Ru(BA)PtCl_2]^{2+g,h}$	1.48 ($Ru^{II/III}$)	−0.95		−1.52	54
		−1.30		−1.75	
$[(bpy)_2Ru(dpq)PtCl_2]^{2+j,k}$	1.68 ($Ru^{II/III}$)	−0.33	−0.87		60
$[(bpy)_2Ru(dpb)PtCl_2]^{2+j,k}$	1.57 ($Ru^{II/III}$)	−0.16	−0.80		60
$[(bpy)_2Os(dpq)PtCl_2]^{2+j,k}$	1.07 ($Os^{II/III}$)	−0.35	−0.97		60
$[(bpy)_2Os(dpb)PtCl_2]^{2+j,k}$	1.01 ($Os^{II/III}$)	−0.27	−0.85		60
$[(tpy)RuCl(dpp)PtCl_2]^{+j,k}$	1.09 ($Ru^{II/III}$)	−0.55	−1.09	−1.48	61
$[(tpy)RuCl(dpq)PtCl_2]^{+j,k}$	1.06 ($Ru^{II/III}$)	−0.37	−0.96	−1.55	61
$[(tpy)RuCl(dpb)PtCl_2]^{+j,k}$	1.08 ($Ru^{II/III}$)	−0.25	−0.86	−1.56	61
$[(tpy)Ru(PEt_2Ph)(bpm)PtCl_2]^{2+j,k}$	1.78 ($Pt^{II/IV}$) E_p^a	−0.39	−1.09	−1.50	62
	1.59 ($Ru^{II/III}$)				
$[(tpy)Ru(PEt_2Ph)(dpp)PtCl_2]^{2+j,k}$	1.66 ($Pt^{II/IV}$) E_p^a	−0.55	−1.19	−1.45	62
	1.51 ($Ru^{II/III}$)				

$[Ru\{(dpq)(PtCl_2)\}_3]^{2+d,e}$		−0.08			66
		−0.25			
		−0.79			
$[\{(bpy)_2Ru(dpp)\}_2Ru(dpp)PtCl_2]^{6+j,k}$	1.54 ($2Ru^{II/III}$)	−0.45	−1.17		67
		−0.65	−1.27		
		−0.76	−1.35		
$[(bpy)_2Ru(dpp)PdCl_2]^{2+j}$	1.56 ($Ru^{II/III}$)	−0.54			53
		−0.79			
$[(bpy)_2Ru(bpm)PdCl_2]^{2+j}$	1.57 E_p^a	−0.32			53
	1.61				
$[(^tBu_2bpy)_2Ru(tpphz)PdCl_2]^{2+g,k}$		−0.64		−1.09	68
		−0.83 ($Pd^{II/0}$)			
$[(bpy)_2Ru(DMB)PdCl_2]^{2+h,j}$	1.27 ($Ru^{II/III}$)	−0.92 ($Pd^{II/0}$)			69
	1.46 ($DMB^{0/+}$) E_p^a				

[a] Refer to Figures 6 and 8 for illustrations of the ligands.
[b] Potentials reported vs SCE. E_p^a or E_p^c indicates that only the anodic or cathodic peak was observed.
[c] In DMF.
[d] In propylene carbonate.
[e] Converted SSCE to SCE by subtracting 5 mV from the potential vs SSCE.
[f] In propylene carbonate using Et_4NClO_4 as the supporting electrolyte.
[g] In acetonitrile.
[h] Converted Fc/Fc^+ to SCE by adding 0.430 V to the potential vs Fc/Fc^+.
[i] Quasireversible.
[j] In acetonitrile with 0.1 M Bu_4NPF_6 as supporting electrolyte.
[k] Converted Ag/AgCl to SCE by subtracting 45 mV from the potential vs Ag/AgCl.

TABLE 4. Photophysical Data for Ru(II)/Os(II)-Pt(II) Complexes Containing Polyazine Light Absorbers.[a]

Complex	λ_{max}^{abs} (nm)	λ_{max}^{em} (nm)	Φ^{em}(RT)	τ (RT) (ns)	τ (77 K) (ns)	Reference
$[(bpy)_2(CN)Ru(CN)Pt(dien)]^{2+}$	416[b]	590[b]		140[b]		48
	460[c]	630[c]		630[c]		
$[(dien)Pt(NC)(bpy)_2Ru(CN)Pt(dien)]^{4+}$	408[b]	580[b]		60[b]		48
	426[c]	580[c]		90[c]		
$[Ru(phen)_2\{(CN)Pt(DMSO)Cl_2\}]_2$[d]	384	595				49
$[(bpy)_2Ru(Mebpy\text{-}CH_2\text{-}CH_2\text{-}Mebpy)PtCl_2]^{2+}$[e]	457	620	6×10^{-2}	1034		50
	360					
	324					
$[(bpy)_2Ru(bpm)PtCl_2]^{2+}$[e]	571					51
$[(bpy)_2Ru(dpp)PtMe_2]^{2+}$[f]	437	735		330		52
	524					
$[(bpy)_2Ru(dpp)PtCl_2]^{2+}$[g]	422	800		450		52
	509					
$[(bpy)_2Ru(AB)PtCl_2]^{2+}$[g]	455	640	2.33×10^{-2}	280	4800[h]	54
$[(bpy)_2Ru(BA)PtCl_2]^{2+}$[g]	452	624	7.5×10^{-4}	13	6000[h]	54
$[(bpy)_2Ru(dpq)PtCl_2]^{2+}$[g]	582					60
$[(bpy)_2Ru(dpb)PtCl_2]^{2+}$[g]	630					60
$[(bpy)_2Os(dpq)PtCl_2]^{2+}$[g]	598					60
$[(bpy)_2Os(dpb)PtCl_2]^{2+}$[g]	638					60
$[(tpy)RuCl(dpp)PtCl_2]^{+}$[g]	544					61
$[(tpy)RuCl(dpq)PtCl_2]^{+}$[g]	632					61

$[(tpy)RuCl(dpb)PtCl_2]^{+g}$	682					61
$[(tpy)Ru(PEt_2Ph)(bpm)PtCl_2]^{2+g}$	560					62
$[(tpy)Ru(PEt_2Ph)(dpp)PtCl_2]^{2+g}$	506	750	1.8×10^{-4}	56		62
$[Ru\{(dpq)(PtCl_2)\}_3]^{2+e}$	553					66
$[\{(bpy)_2Ru(dpp)\}_2Ru(dpp)PtCl_2]^{6+g}$	520 – 540					67
$[(bpy)_2Ru(dpp)PdCl_2]^{2+g}$	526	700		370	4000[i]	53
$[(bpy)_2Ru(bpm)PdCl_2]^{2+g}$	556					53
$[(^tBu_2bpy)_2Ru(tpphz)PdCl_2]^{2+g}$	445	650		27[j]		68
$[(bpy)_2Ru(DMB)PdCl_2]^{2+g}$	455					69

[a] Refer to Figures 6 and 8 for illustrations of the ligands
[b] In water.
[c] In DMF.
[d] In DMF/H_2O.
[e] In propylene carbonate.
[f] In acetone.
[g] In acetonitrile.
[h] In butyronitrile.
[i] EtOH-MeOH glass.
[j] Air saturated solvent.

V. CONCLUSIONS

The discovery of the desirable redox and photophysical properties of $[Ru(bpy)_3]^{2+}$ and related chromophores has led to the development of complicated supramolecular assemblies that can absorb light and participate in solar energy conversion schemes. This has lead to a very active area of supramolecular design using ruthenium-based polyazine chromophores in a vast array of structurally interesting complexes. As this area of research has progressed, the molecules have become increasingly complex with an interest in applying these systems in diverse arenas. Much work in the area of polyazine-bridged metal complexes has focused on Ru(II) and Os(II) systems. This area was not reviewed herein. Focus was provided on systems with Ru(II) or Os(II) polyazine light absorbers coupled to reactive Rh(III), Pt(II), and Pd(II) centers. It is interesting that many systems have been prepared and basic properties explored without investigating photoreactivity.

The redox and excited state properties of ruthenium polyazine chromophores can be modulated over a considerable range by component modification. This is a very attractive feature of supramolecular complexes and much that is known results from the aforementioned Ru(II), Os(II) studies. Bridging ligands are used to hold the metal centers together and dictate intercomponent coupling in polymetallic supramolecular assemblies. In supramolecular systems, intramolecular electron or energy transfer quenching is facilitated overcoming the limitations of often inefficient bimolecular electron or energy transfer quenching.

The choice of the bridging ligand plays a pivotal role in the construction of polymetallic assemblies. The structure and orbital energetics of the bridging ligands are crucial to the functioning of the molecules. Variation of the bridging ligands allow control of energy and electronic coupling of excited states in these polymetallic assemblies. Flexible unsaturated bridges provide complexes with redox and spectroscopic properties that are closely approximated by the additive properties of the monometallic synthons. Rigid aromatic bridging ligands provide complexes in which the properties of the synthons are significantly perturbed by the supramolecular assembly.

One attractive area of research is the coupling of ruthenium type polyazine chromophores to reactive metals. This allows the combination of intense visible light-absorbing properties of the chromophore with the favorable reactive properties of the reactive metal center imparting unique properties to the supramolecule. Ru(II) and Os(II) polyazine light absorbers frequently possess emissive ^{3}MLCT states that are discussed herein and used to explain interexcited state dynamics in the coupled reactive metal assemblies.

Coupling of ruthenium or osmium polyazine light absorbers to rhodium has been investigated in some detail. Most of these systems include bis(tridentate) or tris(bidentate) coordination on Rh(III), impeding reactivity at the rhodium site following photoreduction of rhodium. This structural motif has

allowed the exploration of excited state electron transfer to the Rh(III) center without photodecomposition. Given the short time frame of research in this field, very interesting and complex systems are known, many with surprising properties. By contrast, systems in which the rhodium centers contain labile ligands that can be lost after photoreduction of the rhodium center impart reactivity at the rhodium site after photoreduction, facilitating reaction with substrates. Systems have been designed that couple multiple light absorbers to a single rhodium site, with labile monodentate ligands coordinated to rhodium. These unusual molecules allow for multiple excited state electron transfer processes, leading to photoinitiated electron collection at the rhodium center. Loss of the labile ligand on rhodium upon electron collection affords a Rh^{I} species that can interact with substrates leading to rich photochemistry. Such systems have been shown to photocatalyze water reduction to hydrogen, unprecedented in molecular photoinitiated electron collectors. In addition this LA-BL-Rh-BL-LA structural motif has provided a series of visible light activated, oxygen independent PDT agents.

Coupling ruthenium or osmium to reactive platinum or palladium imparts some unique properties to the supramolecules. Multifunctional DNA binding and photocleavage agents have been designed as well as solar energy conversion catalysts. Incorporation of ruthenium or osmium polyazine chromophores and reactive *cis*-$Pt^{II}Cl_2$ sites leads to interesting supramolecules with properties that are sometimes unexpected. Ruthenium(II)-Pt(II)/Pd(II) complexes have been shown to display interesting photoreductions, producing hydrogen from proton sources. The mechanism for proton reduction is a subject of some controversy. Proposals include formation of metallic platinum or palladium or multielectron reductions without platinum or palladium decomplexation using a homogeneous catalyst. Further studies are needed to develop optimized systems to address this very important issue and the promising results, due to the urgent need for alternative energy sources. Much effort is now directed in this field. We hope long-term funding will be committed to energy research and the general field of supramolecular photochemistry, as the potential in energy harvesting and biomedical applications suggest such funding will have significant impact.

Mixed-metal supramolecular complexes incorporating Ru(II)/Os(II) polyazine complexes to reactive metals combine the rich photochemical properties of the polyazine LA to the unique properties of the reactive metal. The basic studies conducted to date on these and related Ru and Os polyazine-bridged assemblies have provided considerable insight into the properties of these supramolecules and the perturbations introduced upon supramolecular assembly. Complexes of the type described herein have potential for making significant advances in solar energy conversion schemes, sensing, anticancer drug development, and PDT. The ability to modulate the electrochemical and photochemical properties of these complexes by component modification is a particularly attractive feature in many applications. Much remains to be learned in this area of supramolecular chemistry, including the role of subunit identity on electronic

coupling, the nature and interaction of excited states, and the mechanism of multielectron photochemistry that can be carried out by these systems. Design of complicated supramolecular assemblies for photoactivated reaction schemes is an exciting and dynamic field that crosses disciplinary lines. Design, development, and study of supramolecular light-absorbing systems that incorporate reactive metals, therefore, remain an important and open area of research.

VI. ACKNOWLEDGMENTS

Acknowledgment is made to all the students and research scientists who have worked in this area in the Brewer Group. Special thanks to Dr. Krishnan Rangan, David F. Zigler, Samantha Hopkins, Avijita Jain, and Joan Zapiter. Acknowledgment is made to the Chemical Sciences, Geosciences and Biosciences Division, Office of Basic Energy Sciences, Office of Sciences, U. S. Department of Energy for their generous support of our research.

VII. REFERENCES

1. V. Balzani, A. Juris, M. Venturi, S. Campagna, and S. Serroni, *Chem. Rev.*, **1996**, *96*, 759, and references therein.
2. A. Juris, V. Balzani, F. Barigelletti, S. Campagna, P. Belser, and A. von Zelewsky, *Coord. Chem. Rev.*, **1988**, *84*, 85.
3. K. Kalyanasundaram, *Coord. Chem. Rev.*, **1982**, *46*, 159.
4. B. Durham, J. V. Caspar, J. K. Nagle, and T. J. Meyer, *J. Am. Chem. Soc.*, **1982**, *104*, 4803.
5. P. A. Anderson, G. F. Strouse, J. A. Treadway, F. R. Keene, and T. J. Meyer, *Inorg. Chem.*, **1994**, *33*, 3863.
6. J. R. Winkler, T. L. Netzel, C. Creutz, and N. Sutin, *J. Am. Chem. Soc.*, **1987**, *109*, 2381.
7. S. R. Johnson, T. D. Westmoreland, J. V. Caspar, K. R. Barqawi, and T. J. Meyer, *Inorg. Chem.*, **1988**, *27*, 3195.
8. M. Beley, J. -P. Collin, J. -P. Sauvage, H. Sugihara, F. Heisel, and A. Miehe, *J. Chem. Soc. Dalton Trans.*, **1991**, 3157.
9. A. J. Bard and M. A. Fox, *Acc. Chem. Res.*, **1995**, *28*, 141.
10. (a) J. -M. Lehn and J. -P. Sauvage, *Nouv. J. Chim.*, **1977**, *1*, 449. (b) M. Kirch, J. -M. Lehn, and J. -P. Sauvage, *Helv. Chim. Acta*, **1979**, *62*, 1345.
11. (a) G. M. Brown, S. -F. Chan, C. Creutz, H. A. Schwarz, and N. Sutin, *J. Am. Chem. Soc.*, **1979**, *101*, 7638. (b) C. Creutz, A. D. Keller, N. Sutin, and A. P. Zipp, *J. Am. Chem. Soc.*, **1982**, *104*, 3618.
12. W. I. Sundquist and S. J. Lippard, *Coord. Chem. Rev.*, **1990**, *100*, 293.
13. E. Wong and C. M. Giandomenico, *Chem. Rev.*, **1999**, *99*, 2451.
14. M. D. Purugganan, C. V. Kumar, N. J. Turro, and J. K. Barton, *Science*, **1988**, *241*, 1645.
15. M. R. Arkin, E. D. A. Stemp, R. E. Holmlin, J. K. Barton, A. Hörmann, E. J. C. Olsen, and P. F. Barbara, *Science*, **1996**, *273*, 475.

16. V. Balzani, L. Moggi, and F. Scandola, in *Supramolecular Photochemistry*, ed., V. Balzani, D. Reidel, Dordrecht, **1987**, 1.
17. D. P. Rillema and K. B. Mack, *Inorg. Chem.*, **1982**, *21*, 3849.
18. (a) C. H. Braunstein, A. D. Baker, T. C. Strekas, and H. D. Gafney, *Inorg. Chem.*, **1984**, *23*, 857. (b) Y. Fuchs, S. Lofters, T. Dieter, W. Shi, R. Morgan, T. C. Strekas, H. D. Gafney, and A. D. Baker, *J. Am. Chem. Soc.*, **1987**, *109*, 2691.
19. D. P. Rillema, D. G. Taghdiri, C. D. Jones, D. S. Worl, T. J. Meyer, L. A. Keller, and H. A. Levy, *Inorg. Chem.*, **1987**, *26*, 578.
20. R. M. Berger, *Inorg. Chem.*, **1990**, *29*, 1920.
21. S. Campagna, C. D. Pietro, F. Loiseau, B. Maubert, N. McClenaghan, R. Passalacqua, F. Puntoriero, V. Ricevuto, and S. Serroni, *Coord. Chem. Rev.*, **2002**, *229*, 67.
22. M. Marcaccio, F. Paolucci, C. Paradisi, S. Roffia, C. Fontanesi, L. J. Yellowlees, S. Serroni, S. Campagna, G. Denti, and V. Balzani, *J. Am. Chem. Soc.*, **1999**, *121*, 10081.
23. C. R. Arana and H. D. Abruna, *Inorg. Chem.*, **1993**, *32*, 194.
24. D. B. MacQueen and J. D. Petersen, *Inorg. Chem.*, **1990**, *29*, 2313.
25. J. V. Caspar, E. M. Kober, B. P. Sullivan, and T. J. Meyer, *J. Am. Chem. Soc.*, **1982**, *104*, 630.
26. Y. Lei, T. Buranda, and J. F. Endicott, *J. Am. Chem. Soc.*, **1990**, *112*, 8820.
27. K. Kalyanasundaram, M. Graetzel, and M. K. Nazeeruddin, *J. Phys. Chem.*, **1992**, *96*, 5865.
28. G. Kew, K. DeArmond, and K. Hanck, *J. Phys. Chem.*, **1974**, *78*, 727.
29. M. T. Indelli, F. Scandola, J. -P. Collin, J. -P. Sauvage, and A. Sour, *Inorg. Chem.*, **1996**, *35*, 303.
30. (a) J. P. Collin, S. Guillerez, J. P. Sauvage, F. Barigelletti, L. DeCola, L. Flamigni, and V. Balzani, *Inorg. Chem.*, **1991**, *30*, 4230. (b) J. P. Collin, P. Laine, J. -P. Launay, J. P. Sauvage, and A. Sour, *J. Chem. Soc., Chem. Commun.*, **1993**, *5*, 434.
31. M. T. Indelli, C. A. Bignozzi, A. Harriman, J. R. Schoonover, and F. Scandola, *J. Am. Chem. Soc.*, **1994**, *116*, 3768.
32. S. Serroni, A. Juris, S. Campagna, M. Venturi, G. Denti, and V. Balzani, *J. Am. Chem. Soc.*, **1994**, *116*, 9086.
33. S. E. Ronco, D. W. Thompson, S. L. Gahan, and J. D. Petersen, *Inorg. Chem.*, **1998**, *37*, 2020.
34. J. -D. Lee, L. M. Vrana, E. R. Bullock, and K. J. Brewer, *Inorg. Chem.*, **1998**, *37*, 3575.
35. S. M. Molnar, G. Nallas, J. S. Bridgewater, and K. J. Brewer, *J. Am. Chem. Soc.*, **1994**, *116*, 5206.
36. (a) R. Konduri, H. Ye, F. M. MacDonnell, S. Serroni, S. Campagna, and K. Rajeshwar, *Angew. Chem. Int. Ed.*, **2002**, *41*, 3185. (b) C. Chiorboli, S. Fracasso, F. Scandola, S. Campagna, S. Serroni, R. Konduri, and F. M. MacDonnell, *Chem. Commun.*, **2003**, 1658. (c) C. Chiorboli, S. Fracasso, M. Ravaglia, F. Scandola, S. Campagna, K. L. Wouters, R. Konduri, and F. M. MacDonnell, *Inorg. Chem.*, **2005**, *44*, 8368.
37. (a) C. C. Chang, B. Pfennig, and A. B. Bocarsly, *Coord. Chem. Rev.*, **2000**, *208*, 33. (b) C. J. Mordas, B. W. Pfennig, E. Schreiber, and A. B. Bocarsly, *Springer Series in Chem. Phys.*, **2003**, *71*, 453. (c) D. F. Watson, H. S. Tan, E. Schreiber, C. J. Mordas, and A. B. Bocarsly, *J. Phys. Chem. A.*, **2004**, *108*, 3261.
38. (a) A. F. Heyduk and D. G. Nocera, *Science*, **2001**, *293*, 1639. (b) J. Rosenthal, J. Bachman, J. L. Dempsey, A. J. Esswein, T. G. Gray, J. M. Hodgkiss, D. R. Manke, T. D. Luckett, B. J. Pistorio, A. S. Veige, and D. G. Nocera, *Coord. Chem. Rev.*, **2005**, *249*, 1316. (c) J. L. Dempsey, A. J. Esswein, D. R. Manke, J. Rosenthal, J. D. Soper, and D. G. Nocera, *Inorg. Chem.*, **2005**, *44*, 6879. (d) A. J. Esswein, A. S. Veige, and D. G. Nocera, *J. Am. Chem. Soc.*, **2005**, *127*, 16641.
39. M. Elvington and K. J. Brewer, *Inorg. Chem.*, **2006**, *45*, 5242.

40. S. M. Molnar, G. E. Jensen, L. M. Vogler, S. W. Jones, L. Laverman, J. S. Bridgewater, M. M. Richter, and K. J. Brewer, *J. Photochem. Photobiol. A: Chem.*, **1994**, *80*, 315.
41. G. N. A. Nallas, S. W. Jones, and K. J. Brewer, *Inorg. Chem.*, **1996**, *35*, 6974.
42. S. M. Arachchige, J. Brown, and K. J. Brewer, *J. Photochem. Photobiol. A: Chem.*, **2008**, *197*, 13.
43. S. Swavey, and K. J. Brewer, *Inorg. Chem.*, **2002**, *41*, 4044.
44. A. A. Holder, S. Swavey, and K. J. Brewer, *Inorg. Chem.*, **2004**, *43*, 303.
45. D. F. Zigler, M. T. Mongelli, M. Jeletic, and K. J. Brewer, *Inorg. Chem. Commun.*, **2007**, *10*, 295.
46. S. Swavey and K. J. Brewer, *Inorg. Chem.*, **2002**, *41*, 6196.
47. A. A. Holder, D. F. Zigler, M. T. Tarrago-Trani, B. Storrie, and K. J. Brewer, *Inorg. Chem.*, **2007**, *46*, 4760.
48. C. A. Bignozzi and F. Scandola, *Inorg. Chem.*, **1984**, *23*, 1540.
49. C. -F. Chow, B. K. W. Chiu, M. H. W. Lam, and W. -Y. Wong, *J. Am. Chem. Soc.*, **2003**, *125*, 7802.
50. R. Sahai, D. A. Baucom, and D. P. Rillema, *Inorg. Chem.*, **1986**, *25*, 3843.
51. R. Sahai and D. P. Rillema, *Inorg. Chim. Acta*, **1986**, *118*, L35.
52. V. W. -W. Yam, V. W. -M. Lee, and K. -K. Cheung, *J. Chem. Soc., Chem. Commun.*, **1994**, 2075.
53. V. W. -W. Yam, V. W. -M. Lee, and K. -K. Cheung, *Organometallics*, **1997**, *16*, 2833.
54. A. M. Barthram, M. D. Ward, A. Gessi, N. Armaroli, L. Flamigni, and F. Barigelletti, *New J. Chem.*, **1998**, *22*, 913.
55. K. Van der Schilden, F. Garcìa, H. Kooijman, A. L. Spek, J. G. Haasnoot, and J. Reedijk, *Angew. Chem. Int. Ed.*, **2004**, *43*, 5668.
56. K. Sakai, H. Ozawa, H. Yamada, T. Tsubomura, M. Hara, A. Higuchi, and M. Haga, *Dalton Trans.*, **2006**, 3300.
57. H. Ozawa, M. Haga, and K. Sakai, *J. Am. Chem. Soc.*, **2006**, *128*, 4926.
58. H. Ozawa, Y. Yokoyama, M. Haga, and K. Sakai, *Dalton Trans.*, **2007**, 1197.
59. P. Du, J. Schneider, F. Li, W. Zhao, U. Patel, F. N. Castellano, and R. Eisenberg, *J. Am. Chem. Soc.*, **2008**, *130*, 5056.
60. M. Milkevitch, E. Brauns, and K. J. Brewer, *Inorg. Chem.*, **1996**, *35*, 1737.
61. R. L. Williams, H. N. Toft, B. Winkel, and K. J. Brewer, *Inorg. Chem.*, **2003**, *42*, 4394.
62. S. Swavey, Z. Fang, and K. J. Brewer, *Inorg. Chem.*, **2002**, *41*, 2598.
63. M. Milkevitch, H. Storrie, E. Brauns, K. J. Brewer, and B. W. Shirley, *Inorg. Chem.*, **1997**, *36*, 4534.
64. M. Milkevitch, B. W. Shirley, and K. J. Brewer, *Inorg. Chim. Acta*, **1997**, *264*, 249.
65. Z. Fang, S. Swavey, A. Holder, B. Winkel, and K. J. Brewer, *Inorg. Chem. Commun.*, **2002**, *5*, 1078.
66. R. Sahai and D. P. Rillema, *J. Chem. Soc., Chem. Commun.*, **1986**, 1133.
67. R. Miao, M. T. Mongelli, D. F. Zigler, B. S. J. Winkel, and K. J. Brewer, *Inorg. Chem.*, **2006**, *45*,10413.
68. S. Rau, B. Schäfer, D. Gleich, E. Anders, M. Rudolph, M. Friedrich, H. Görls, W. Henry, and J. G. Vos, *Angew. Chem. Int. Ed.*, **2006**, *45*, 6215.
69. P. Lei, M. Hedlund, R. Lomoth, H. Rensmo, O. Johansson, and L. Hammarström, *J. Am. Chem. Soc.*, **2008**, *130*, 26.
70. A. Inagaki, S. Yatsuda, S. Edure, A. Suzuki, T. Takahashi, and M. Akita, *Inorg. Chem.*, **2007**, *46*, 2432.

CHAPTER 8

Supramolecular Hybrid Materials—Integrating Functionality with Sensing

Ramón Martínez-Máñez, Félix Sancenón, Ana Belén Descalzo and Knut Rurack

Instituto de Reconocimiento Molecular y desarrollo Tecnológico, Centro Mixto Universidad Politécnica de Valencia-Universidad de Valencia, Spain. Departamento de Química, Universidad Politécnica de Valencia, Camino de Vera s/n, E-46022 Valencia, Spain. CIBER de Bioingeniería, Biomateriales y Nanomedicina (CIBER-BBN).

Div. I.5, BAM Bundesanstalt für Materialforschung und -prüfung, Richard-Willstätter-Strasse 11, D-12489 Berlin, Germany

CONTENTS

Macromolecules Containing Metal and Metal-Like Elements, Volume 9: Supramolecular and Self-Assembled Metal-Containing Materials,
Edited by Alaa S. Abd-El Aziz, Charles E. Carraher Jr., Charles U. Pittman Jr., and Martel Zeldin.

I. INTRODUCTION

This chapter deals with a subject we find especially appealing; the use of supramolecular and hybrid organic–inorganic systems for the development of novel sensing concepts. Supramolecular chemistry is basically devoted to the study of the interaction between molecules, in many cases invoking or adopting concepts and strategies from nature.[1,2] Traditionally, the worlds of supramolecular chemistry and inorganic materials have been poorly interrelated. However, since the turn of the millennium, scientists have begun to explore myriad possibilities and opportunities that the synergistic use of single concepts rooted in these fields might offer. These strategies have led to a rethinking of basic supramolecular strategies and inorganic concepts, resulting in the creation and exploration of so-called hybrid materials.

A particularly exciting direction within the field of functional organic–inorganic hybrid materials, often related to the nanoscopic dimensions involved, is the design of new supramolecular signaling protocols. The concept of "signaling" refers to the transduction of a recognition event through changes of a certain physical property, such as a shift or intensity change in color, fluorescence, or a redox wave, and is the basis of most indicators and sensors. The supramolecular signaling process commonly comprises two steps: (a) selective coordination of the guest by a binding site and (b) transduction of that event by the modulation of a physical or chemical process within the probe. Alternatively, mass sensitive protocols have been developed, relying on quartz crystal microbalances and other piezosensors. Traditionally, this general concept of supramolecular signaling has been applied to the development of chromo-fluorogenic chemosensors following the molecular-based "binding-site–signaling-unit" approach. Although this protocol contains many attractive features, such as the possibility of tailor-made chemosensors for target guests, it also has some limitations, especially with respect to signal amplification and when targeting small organic molecules for which no artificial recognition motif is easily available. In an attempt to overcome these limitations, new concepts

related to the preparation of novel "hetero-supramolecular" hybrid organic–inorganic materials for signaling applications have been reported. As we will see later, these hybrid ensembles usually take advantage of the blending of inorganic materials with classical supramolecular principles. In the sensing of various anionic,[3,4] cationic,[5] or neutral species,[6,7] this simple concept allows for the creation of hybrid sensing ensembles to target analytes for which selectivity is hard to achieve by conventional methods.

The typical examples discussed in this chapter suggest that the wise combination of supramolecular principles and solid structures might lead to novel synergic strategies with unprecedented tunability of the properties of the nanoscopic solids and new perspectives of applicability of supramolecular concepts in relation to signaling. Special attention is paid to cases in which the functional combination of traditional supramolecular chemistry tools, such as the topology and arrangement of functional groups with preorganized solid structures, results in ensembles that are able to show enhanced sensing performance.

This chapter will thus not deal with the synthesis and characterization of hybrid structures[8–11] or with the application of hybrid materials in classical fields, such as separation/extraction, catalysis, or physisorption.[12,13] Instead, new functional sensing concepts having an improved level of performance or sophistication will be highlighted.[14–21] Special attention will be paid to hybrid systems that clearly show synergic functional effects that are not found in molecular-based systems or with unmodified nanoscopic solids alone.

II. ENHANCED COORDINATION BY PREORGANIZATION. SURFACE CHELATE EFFECT AND SIGNALING

Perhaps one of the most common ways to obtain hybrid materials at the nanoscopic scale is to organize (for instance, via anchoring processes) certain functional molecular units on the surface of nanoscopic inorganic scaffoldings, such as nanoparticles (NP) or nanostructured solids. In fact, the processes of functionalization of such surfaces, typically gold and silica as we will see later, is today well understood, and it is possible to choose a large number of commercially available substances for the chemical modification of the surfaces with a number of different organic groups. From a supramolecular point of view, one typical and very remarkable functional effect that is observed upon functionalization of the surface with specific binding groups is the enhancement of guest recognition. This refers to the fact that preorganization of the binding sites results in a significant improvement of guest coordination at the surface in terms of binding constants compared to the free receptor in solution. Examples of surface-assisted enhancement of recognition have been mainly reported for gold nanoparticles (AuNPs) containing suitable ligands. A general scheme for guest coordination with surface functionalized NPs is shown in Figure 1.

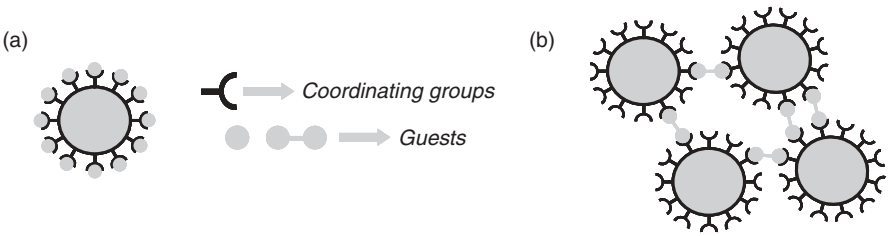

FIGURE 1. Surface-functionalized NPs. (a) NPs with a high density of binding units on its surface. (b) Multidentate coordination with NPs.

This enhancement of guest coordination upon preorganization of binding sites at a surface can be seen, for instance, in an example of Beer et al., who prepared hybrid AuNPs functionalized with zinc metalloporphyrins.[22] These hybrid AuNPs are able to bind chloride and dihydrogen phosphate in DMSO with association constants (log K) of 4.3 and 4.1, respectively. These association constants are two orders of magnitude higher than those measured for the free zinc metalloporphyrin with chloride (<2) and dihydrogen phosphate (2.5). The same effect has been observed for AuNPs functionalized with calix[4]arene derivatives and quaternary ammonium salts.[23] The calix[4]arenes were attached to the nanoparticle surface by the use of alkanethiol chains of two different lengths and hybrid nanoparticles with two different amounts of the appended calix[4]arene were prepared. ^{1}H-NMR titrations in $CDCl_3$ of the different sets of hybrid nanoparticles with quaternary ammonium cations showed that the binding is stronger than that measured with the free calix[4]arene in solution. The authors also observed that the efficiency of binding was enhanced as the number of calix[4]arene units on the surface of the gold nanoparticle increases. The increase in the length of the spacer between the AuNP surface and the calix[4]arene also led to considerably enhanced recognition in a solvent of medium polarity such as $CHCl_3$. This is an interesting case of radial coordination amplification that seems to be an exclusive feature of nanoparticles. In a more recent work, the same authors prepared hybrid nanoparticles functionalized with alkanethiol-containing calix[4]arenes and sulfanylalkyl oligo(ethylene glycol) that works in aqueous environments.[24]

This thermodynamic effect of the enhancement of classical recognition features is basically due to entropic factors related to the preorganization of the coordination sites on the surface that reduce the conformational flexibility of the receptors and increase their effective concentration at the surface. This results in a remarkable improvement of the recognition characteristics. From a molecular viewpoint, surface functionalization creates a multidentate coordination environment that displays a statistical advantage in relation to coordination when compared to the molecular receptor. This effect has also been called the "surface chelate effect" and is not a unique feature of surfaces functionalized with binding sites. It has also been reported for coordinating dendrimers that show a "positive dendritic effect," which is related to

the capability of dendrimers to achieve a better recognition as the generation of the dendrimer increases.[25] The ability to show enhanced coordination is at the heart of the basic concept of supramolecular chemical amplification; the step from the molecule itself to the hetero-supramolecular ensemble thus results in new properties, which are not simply an extrapolation of the solution conduct to the surface, but to its own unique features.

However, the simple enhancement of the coordination, which is driven by the "surface chelate effect," is not sufficient for the preparation of sensing protocols, and the recognition process must be coupled with a signaling event. The mode in which this can be achieved—that is, in which enhanced coordination is coupled with signaling—is exemplified as follows. The support is a solid consisting of a Mobil Composition of Matter mesoporous silica material (MCM-41) that was functionalized with alkylaminoanthracene groups.[26,27] This organic group contains both a secondary amine that acts as an anion coordination site in the protonated state and an anthracene unit anchored to the amino group via a methyl bridge that acts as a reporter unit. The solid was tested in acidic water of pH $\sim$ 2.8. At this pH, the amines are protonated and able to interact via electrostatic and hydrogen bonding forces with a given anion, in this case ATP. The addition of ATP to acidic aqueous suspensions of the solid resulted in remarkable fluorescence quenching. In addition to the MCM-41 support, alkylaminoanthracene groups were also anchored to the surface of fumed silica not possessing a mesoporous structure. It is interesting that it was found that the association constant of the MCM-41 material as measured by fluorescence quenching was larger than that of the silica gel derivative and that of aminomethylanthracene as molecular indicator, respectively. This enhanced ATP response in the ordered mesoporous solid is clearly due to the "surface chelate effect" related to an increase of the effective concentration of binding/signaling units at the surface that results in an enhancement of the signaling of the guest. Such a cooperative effect is not possible when the probe is anchored onto the locally flat surface of the silica gel derivative.

This functional aspect—that is, the enhanced coordination by preorganization—has also been employed for the design of a new generation of materials that show enhanced adsorption capabilities. For instance, removal of Hg^{2+} with thiol-functionalized mesoporous hybrids is remarkably superior to the use of similarly functionalized but "flat" supports.[28] Related to this characteristic of enhanced coordination that is observed in hybrid functionalized mesoporous supports, some recent examples show that this effect can be used to design materials able to perform both signaling and adsorption. A first example involves the use of a mesoporous material that is decorated with thiol groups, which are further reacted with a squaraine dye and resulted in the formation of a 2,4-bis(4-dialkylaminophenyl)-3-hydroxy-4-alkylsulfanylcyclobut-2-enone (APC) derivative that is covalently anchored to the inorganic silica matrix.[29] This hybrid solid behaves as a chemo-dosimeter for Hg^{2+}. Hg^{2+} reacts with the APC fragment resulting in a release of the squaraine dye to the solution, which turns deep blue and fluoresces strongly (Fig. 2). In contrast,

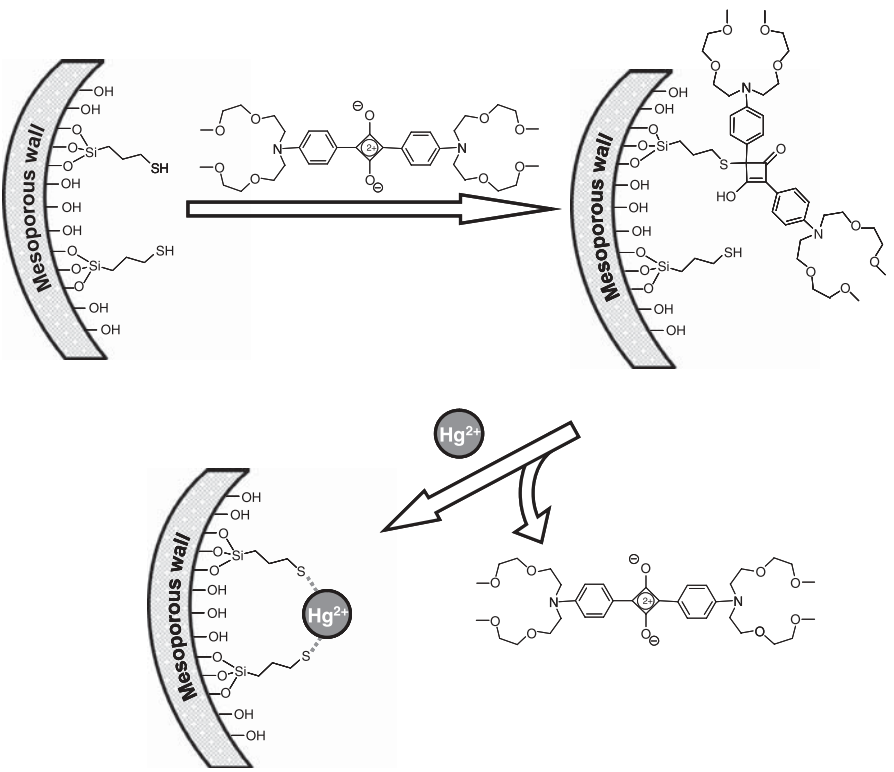

FIGURE 2. Route for the preparation of a dual sorption and sensing material for Hg^{2+} cation (first step) and indication and sorption reaction (second step).

the same solid remains silent in the presence of other thiophilic transition-metal ions, alkali and alkaline-earth metal ions or compulsory water-present anions such as chloride, carbonate, sulfate and phosphate. The solid is not only able to signal the presence of Hg^{2+} down to ppb concentrations but also, at the same time, is an excellent adsorbent for the removal of mercury ions from aqueous solutions. The amount of adsorbed mercury ranges from 0.7 to 1.7 mmol g^{-1}, depending on the degree of functionalization. Model compounds based on silica gel or fumed silica showed no sensing features and points out the functional aspect discussed earlier in relation to the enhanced coordination by preorganization in confined spaces (i.e., the pores). These functionalized solids are a promising new class of polyfunctional hybrid supports that can be used as both remediation and alarm systems via selective signaling and removal of target species of environmental importance. Recently, another example has been reported to act as both a fluorescent chemosensor and adsorbent for Cu^{2+}.[30]

Apart from the previous examples, the recent literature shows an increase in the number of reports dealing with the design of hybrid mesoporous silicas containing chromogenic or fluorogenic probes for the indication of metal ions.

Most of the reported examples involve the use of MCM-41, MCM-48, hydrothermally stable mesoporous molecular sieves (SBA-15) or silica nanotube matrices in which certain selective probe molecules are covalently anchored to the pore walls. In addition, the very low detection limits observed for some of these systems suggest that the "surface chelate effect" also plays a role here. Following this approach, chemosensors for the signaling of Hg^{2+},[31–33] Cu^{2+},[34–36] Fe^{3+},[37] and Zn^{2+} [35,38] have been described. Optical pH sensors using mesoporous structures have also been reported.[39]

In an attempt to avoid complex procedures for the synthesis of reactive indicator precursors for covalent anchoring, Matsunaga[40] and El-Safty[41,42] have prepared a family of optical sensory materials for the detection of certain metal ions in which the probes are electrostatically attached to the pore walls. In a first example, a mesoporous SBA-15 with pores of diameter 5–30 nm was used as a support and was functionalized with an organic spacer carrying a trimethylammonium end group. The negatively charged Cd^{2+} indicator molecule 4-(2-pyridylazo)-resorcinol (PAR) was then electrostatically anchored in the pores. Binding of Cd^{2+} by PAR resulted in a color change from orange-yellow to violet.

In a further work, new nanostructured cage materials were prepared involving the binding of the dyes to the silica surface via electrostatic and hydrogen bonding interactions. For instance, the authors, in a first step, anchored *N*-trimethoxysilylpropyl-*N*,*N*,*N*-trimethylammonium groups into the cavities that, in a second step, were allowed to anchor electrostatically cationic dyes such as pyrogallol red (PR) and tetraphenylporphine tetrasulfonic acid (TPPS). In a somehow similar procedure, cationic dyes such as α, β, γ, δ-tetrakis(1-methylpyridinium-4-yl)porphine (TMPyP) were attached in an electrostatic manner by attaching first $-SO_3^-$ groups onto the nanocage surface. Finally, the neutral dye, dithizone, was anchored into the cages through hydrogen bonding interactions with the silanol groups at the surface (Fig. 3). It was found that these systems could be used for the selective and sensitive detection of Sb^{3+}, Hg^{2+}, Cd^{2+}, and Pb^{2+} at subnanomolar levels. In a later work, the same authors reported the effect of the geometry and shape of the pores and the particle morphology on the colorimetric detection of Sb^{3+}. They prepared similar nanocaged monoliths and used PR as the dye trapped in the nano-size cavities.

Different Cd^{2+} probes in water were prepared by the same authors using TMPyP, diphenlcarbazide (DPC), 4-*n*-dodecyl-6-(2-thiazolylazo)resorcinol (DTAR), and 4-*n*-dodecyl-6-(2-pyridylazo)phenol (DPAR) as signaling units on a mesoporous support. DTAR and DPAR were anchored by simple van der Waals and hydrogen bonding interactions with the abundant hydroxyl groups on the mesoporous surface. In addition to this interaction, the long alkyl chains on these dyes offer the adequate hydrophobicity to prevent leaching of the probes in aqueous solutions. The DPC chromophore was immobilized via the incorporation of the cationic surfactant dilauryldimethylammonium bromide (DDAB) on the mesoporous structure and further reaction with

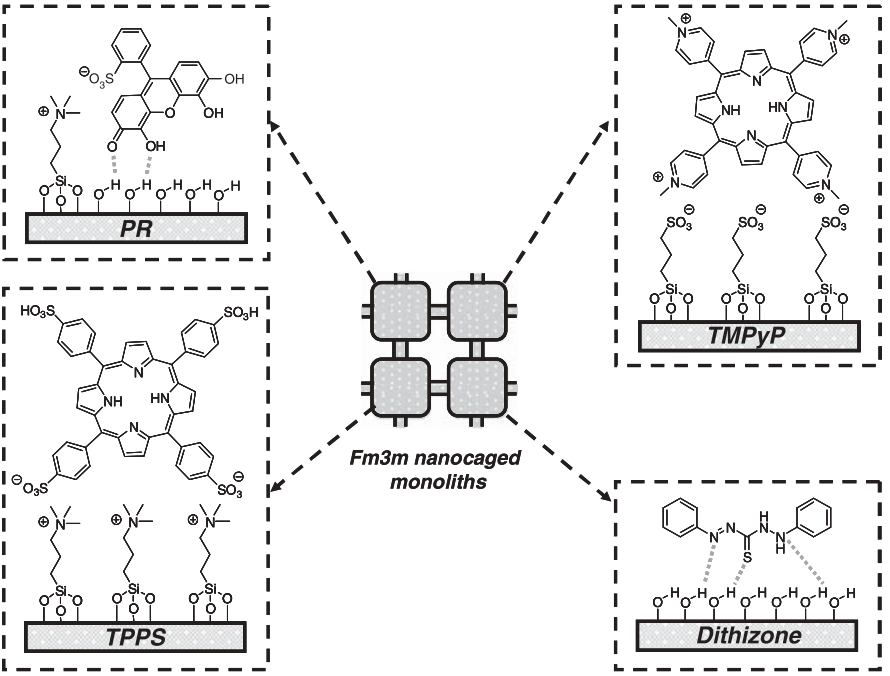

FIGURE 3. Nanocaged monoliths containing selected dyes for the colorimetric signaling of various metal ions.

DPC.[43] Similar mesocaged nanosensors have been prepared for the indication of Bi^{3+} by using a similar inorganic matrix and diphenylthiocarbazone (DZ) as suitable dye.[44]

Enhanced coordination by preorganization in mesoporous solids is also one of the important features of the design of abiotic binding pockets for selective colorimetric displacement assays. The signaling protocol involves several steps: (a) first, the pores are functionalized with adequate binding sites; (b) second, the pores are loaded with a dye that coordinates to these anchored sites; and (c) finally, the presence of a target anion in the solution, which forms a stronger complex with the binding sites and induces the displacement of the dye and diffusion into the bulk solution, enabling the colorimetric detection of the guest (Fig. 4).[45] As in other displacement assays[46–48] a selective response is reached by the adequate choice of binding sites and dye. The stability constant between the binding pockets and the dye has to be lower than that with the target but larger than that with potentially interfering analytes.

A first example reports a mesoporous MCM-41-type solid containing guanidinium groups as binding sites within the mesopores and methylthymol blue as the dye. Guanidinium groups are known to undergo hydrogen bonding interactions with carboxylate groups. A remarkably selective response for citrate was found and indicates that the binding pockets are able to recognize

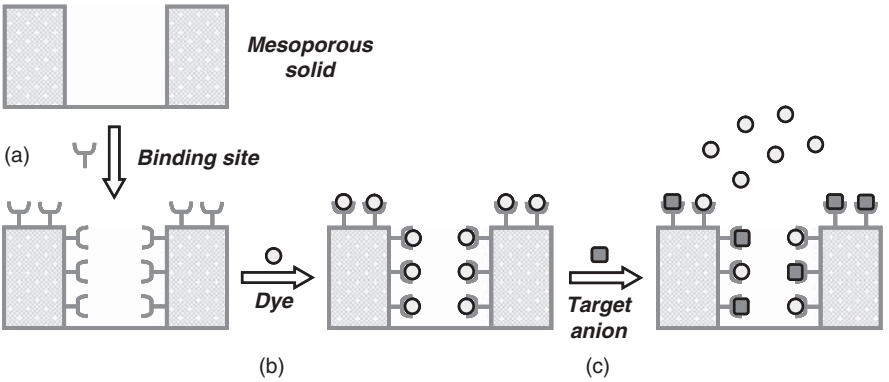

FIGURE 4. Optical detection protocol using displacement assays in bioinspired mesoporous systems. (a) Functionalization of mesoporous walls with selected binding sites. (b) Loading of functionalized material with certain dye. (c) Displacement of the dye with target anion.

this anion through favorable coordination with respect to other carboxylates. As it has been shown, a two-dimensional (2D) silica material that lacks the homogeneous porosity of mesoporous solids functionalized with guanidinium groups and contains a certain amount of adsorbed methylthymol blue shows a very poor response. This behavior stresses the importance of the enhanced coordination observed in this mesoporous three-dimensional (3D) structure in the overall sensing process. In the same paper, similar protocols were developed for the chromogenic sensing of borate. In this case, an MCM-41 solid was functionalized with a mannose derivative that was further treated with a boronic acid dye that can react with a sugar through the formation of a boronic ester bond. In sensing experiments, the addition of borate in water at ppm concentrations induced a partial displacement of the boronic dye and resulted in a simple and selective colorimetric assay for borate in aqueous solution. The solid did not show any sensing feature in the presence of other compulsive water present anions and cations.

Recently, a hybrid material for the colorimetric sensing of phosphate in water using displacement assays was reported.[49] The sensory system consists of suitable nano-size binding pores of an MCM-41-type material functionalized with simple amino binding sites that were then filled with carboxyfluorescein. Addition of phosphate ion to a suspension of the functionalized solid in water resulted in a preferential interaction of the analyte with the tethered amines and displacement of the dye from the pores into the solution. Addition of sulfate ion also induced some color, but to a significantly lesser extension, whereas nitrate and halide anions induced no displacement of the dye. This sensing protocol is undemanding and opens the possibility of developing new chromo-fluorogenic probes by the combination of simple coordination groups and the noncovalent anchoring of dyes to mesoporous materials.

III. ENHANCED SIGNALING BY PREORGANIZATION

Some of the examples reported in this section show clear effects of amplified signaling derived from a collective response of anchored groups. One illustrative example of this effect was reported by Montalti et al. who used silica nanoparticles covered with dansyl moieties on the surface for pH sensing.[50] Clear signs of chemical amplification were found because the protonation of few dansyl moieties resulted in a remarkable quenching of both the protonated and the surrounding unprotonated groups. For instance, they also developed another representative model using silica nanoparticles that were functionalized with a dansyl-polyamine-appended molecule as a binding and signaling unit.[51] For this functionalized hybrid, the addition of the metal ions Cu^{2+}, Co^{2+}, and Ni^{2+} resulted in a strong quenching of the fluorescence at nanomolar concentrations because coordination of a single probe quenches several other probe units in close proximity. Enhanced signaling was demonstrated by the fact that a single Cu^{2+} was able to cause a fluorescence decrease, which corresponded to the total quenching of 13 dansyl moieties. In these two cases, the signal modulation involved a larger number of units than those actually coordinated.

A related supramolecular functional approach relies on the use of additional cooperative effects associated with the independent anchoring of binding sites and signaling units in close proximity to the surface of a support. This allows the coordination of guests at the binding sites to induce quenching of the fluorophore that is closely neighbored on the silica surface (Fig. 5). This approach allows an easy selection of the ligand-fluorophore ratios to tune the final response of the ensemble. In addition, as shown in other examples in this chapter, this approach overcomes synthetic problems connected with the conventional preparation of complex receptors and, at the same time, provides a facile method for the use of combinatorial strategies and the selection of commercially available or simple small molecules for probe preparation.

Tecilla and Tonellato used the same strategy for the development of a fluorescent sensor for Cu^{2+}. In this case, the authors used silica nanoparticles functionalized with both ligands for the selective Cu^{2+} coordination and fluorescent dyes.[52] Binding of Cu^{2+} to the anchored ligands lead to strong fluorescence quenching and allowed the detection of Cu^{2+} concentrations down to the nanomolar level in DMSO-water solutions. As in the earlier case, the authors also confirmed that binding of a single metal ion lead to the quenching of up to 10 fluorescent groups surrounding a receptor unit, thereby producing the amplified signal.

A variation of this approach is the use of dansyl-doped silica nanoparticles synthesized from the co-condensation of tetraethoxysilane and dansyl triethoxysilane derivatives. Addition of Cu^{2+} resulted in coordination of the metal with the acidic silanol groups of the surface and induced fluorescence quenching of the dyes entrapped in the nanoparticle.[53] A similar method has

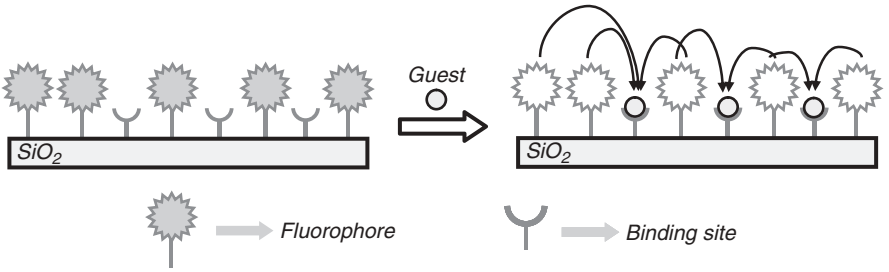

FIGURE 5. A difunctionalized surface ensures the required spatial proximity for communication between binding sites and signaling units. The back arrows indicates quenching induced by the guest.

also been used in sol-gel films.[54] The effect of improved signaling by independent preorganization of ligands and signaling units is not unique for silica nanoparticles, but it has also been realized for polymeric nanoparticles,[55] micellar systems,[56] and in extended surfaces such as in bifunctionalized, self-assembled monolayers or Langmuir-Blodgett films.[57]

Self-assembled monolayers (SAM) on gold or glass are interesting examples of bifunctionalized 2D surfaces in which directional preorganization facilitates communication between the binding group and signaling subunit in a similar way as described earlier. In this respect, the works of Crego-Calama and Reinhoudt were remarkable and have led to the development of chemosensing materials for cations and anions by using a combinatorial approach in which glass monolayers were functionalized with different fluorescent groups and certain types of binding sites.

In a first paper, these researchers self-assembled monolayers of two fluorescent probes (dansyl and coumarin) and certain binding units (amine, amide and urea) on glass and used these fluorescent hybrids for metal ion sensing in organic solvents (Fig. 6).[58] The fluorescence response of this family of bifuctionalized SAMs was quite similar and addition of Pb^{2+}, Zn^{2+}, and Ca^{2+} cations induced different degrees of emission quenching. Specifically, addition of Pb^{2+}, Zn^{2+}, and Ca^{2+} to bifunctionalized monolayers containing dansyl fluorescent units and amine binding sites induced different degrees of fluorescence quenching, the most important one being observed, with Pb^{2+} (92%). On changing to monolayers that were functionalized with coumarin fluorophores and amide binding sites, the same quenching behavior upon addition of metal ions was observed, with Pb^{2+} being the most potent quencher. A different behavior was obtained with a SAM functionalized with coumarin and amine binding sites because an enhancement in emission intensity of 20% was observed upon addition of Zn^{2+}. The dependence of the behavior of the two fluorophores on the choice of the binding site clearly indicates that the ensemble shows a collective response.

Following the same approach mentioned earlier, new SAMs for fluorescence recognition of both metal ions (Cu^{2+}, Co^{2+}, Pb^{2+} and Ca^{2+}) and anions

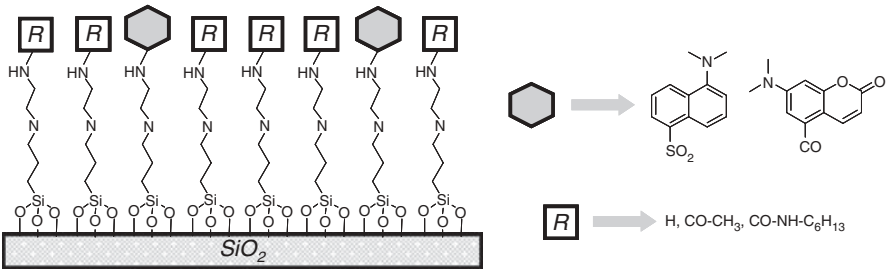

FIGURE 6. Self-assembled monolayers of two fluorescent probes and certain binding units on glass used for metal ion sensing in organic solvents.

(AcO^-, NO_3^-, $H_2PO_4^-$ and HSO_4^-) in organic solvents were developed.[59] Glass monolayers were first functionalized with *N*-[3-(trimethoxysilyl) propyl]ethylenediamine and second with fluorescent (TAMRA, lissamine and TRITC) and coordinating (amino, aryl-urea, alkyl-urea, aryl-amide, alkyl-amide, sulphonamide, urea and thiourea) moieties. Depending on the fluorophore and binding site used, remarkable quenching and enhancement of the emission intensity were observed upon addition of metal ions. As a general trend, addition of Cu^{2+} and Co^{2+} induced quenching, whereas addition of Pb^{2+} and Ca^{2+} induced moderate enhancements of the emission intensity. In a step toward actual sensory applications, microcontact printing techniques were also used for the development of efficient microarrays for sensing. For instance, whereas fluorescent SAMs that were functionalized with anion binding sites showed several degrees of quenching in the presence of acetate and dihydrogen phosphate, hydrogen sulfate triggered an enhanced fluorescence output.

To evaluate potential applications of such microarrays in real aqueous samples, the same authors used a combination approach to prepare a library of sensitive glass SAMs containing different fluorophore-binding sites.[60] The performances of the materials were assessed by measuring the changes in fluorescence intensity upon addition of aqueous solutions of Cu^{2+}, Co^{2+}, Ca^{2+}, and Hg^{2+}. The modified SAMs were prepared in three steps: (a) synthesis of amino-terminated monolayers by functionalization of glass substrates with 1-cyano-11-trichlorosilylundecane followed by reduction of the cyano moiety; (b) immobilization of the fluorophore on the amino-terminated monolayers by reaction with dansyl chloride, 7-dimethylaminocoumarin-4-acetic acid succinimidyl ester, and 5- and 6-carboxytetramethylrhodamine succinimidyl ester (TAMRA); and (c) immobilization of the binding sites on the surface by reaction of the SAMs prepared in the second step with benzenesulfonyl chloride, which produces an aryl-sulfonamide binding site, or 4-isopropylphenyl isocyanate, which produces an aryl-urea binding site. In addition, the SAMs prepared in the second step were used without further functionalization and possess simple amine binding sites. Nine fluorescent SAMs were prepared by this procedure, and their response toward metal ions at submillimolar

concentrations in water was tested. None of the SAMs proved to be selective because all metal ions led to different degrees of quenching. However a "fingerprint" response for each of the metal ions was observed.

IV. ASSEMBLY-DISASSEMBLY

The sensing protocol discussed in this section is based on the ability of functionalized AuNPs to show remarkable optical changes upon guest-induced aggregation processes. This color modulation that is observed upon aggregation is due to a coupling of the dipoles that result in shifts of the plasmon band to the red when the interparticle distances in the aggregates decrease to less than the average particle radius.[61,62] Based on this phenomenon, exponentially increasing attention has been devoted to its use for analyte-induced aggregation/deaggregation sensing protocols. The majority of the examples involving AuNPs realized so far were published in the field of biomacromolecule analysis and will not be reviewed here.[63,64] Instead, we will focus on works dealing with the signaling of inorganic or small-molecule analytes—that is, work related primarily to supramolecular chemistry.

The principle of operation can be seen in the following example designed for the optical detection of K^+ and Na^+. Lin et al. functionalized AuNPs with alkanethiol-appended 15-crown-5 for K^+ sensing. Upon exposure of the functionalized AuNPs to K^+, 2:1 sandwich-type complexes were formed, resulting in the aggregation of AuNPs and a color change from red to blue. This approach avoids the interference of Na^+ because this cation does not tend to form sandwich-type complexes and does not induce aggregation (Fig. 7). The same authors also improved the system by co-attaching thioctic acid and alkanethiol-appended 15-crown-5, again for K^+ sensing, or 12-crown-4, a smaller crown that targets Na^+, onto AuNPs. Apparently, the introduction of carboxylate functions greatly enhances the binding of the cation by cooperative electrostatic forces. Both materials were also tested under realistic conditions for the colorimetric detection of K^+ and Na^+ in urine samples.[65,66]

Lin et al. also used AuNPs functionalized with thioctic acid and alkanethiol-appended 15-crown-5 for the colorimetric signaling of the toxic metal cation Pb^{2+} in methanol-water mixtures. In this medium, the functionalized AuNPs are aggregated most likely due to hydrogen bonding interactions between the carboxylic acid residues appended to its surface. Addition of Pb^{2+} resulted in coordination of this cation by the crown ether and dispersion due to electrostatic repulsion between positively charged nanoparticles.[67] Selective signaling of Pb^{2+} has also been achieved by controlled disassembly of AuNP aggregates involving a Pb^{2+}-specific DNAzyme.[68] Some other examples have been reported for other toxic metal cations such as Hg^{2+}.[69]

Aggregation-amplified colorimetric sensing using AuNPs has also been used for neutral molecules. One example involves the detection of thiols using

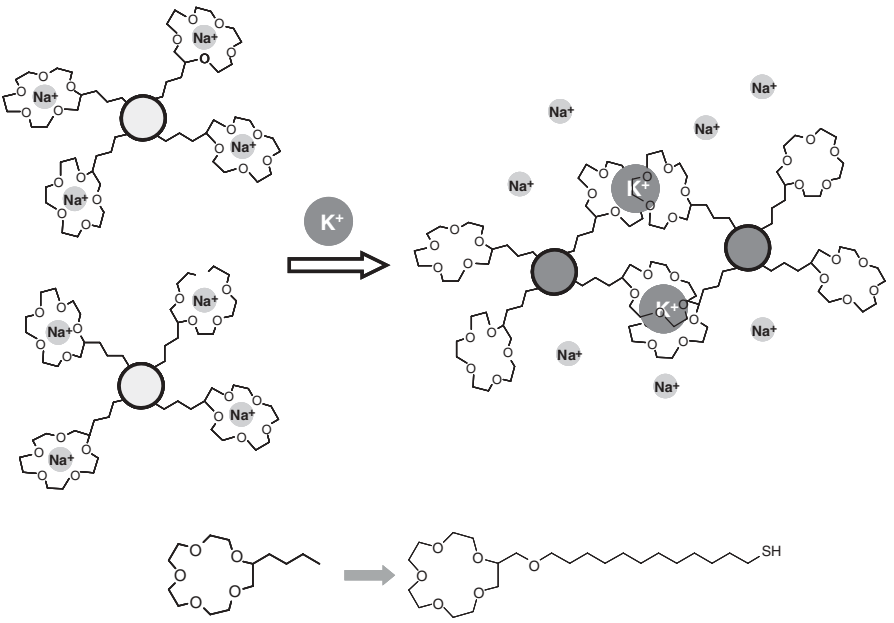

FIGURE 7. Selective potassium-induced aggregation of AuNPs functionalized with crown ether-thiol groups through the formation of sandwich complexes.

citrate-capped AuNPs to which Nile red (NR) was noncovalently adsorbed.[70] The signaling event is related to a displacement assay (fluorescence modulation) that is additionally coupled with an aggregation phenomenon (colorimetric modulation). The as-synthesized NR-AuNPs are not fluorescent because of FRET between NR and AuNPs. When 2-mercaptoethanol is added, the fluorescence is restored as a consequence of the displacement of adsorbed NR units into the solution. At the same time, a color change is observed due to ligand exchange of 2-mercaptoethanol on the surface of the AuNPs and the liberation of citrate. This exchange reduces the electrostatic repulsion among the nanoparticles, which readily aggregate. The authors found that aggregation also occurs with positively charged thiols (e.g., cysteamide), whereas the presence of negatively charged thiols (e.g. mercaptoacetate) did not induce color modulations. The authors proposed that it might be possible to distinguish between certain thiols by the rate at which the color of the NR-AuNPs changes (e.g., slow for reduced glutathione, fast for cysteine and homocysteine, and no change for disulfides such as oxidized glutathione).

AuNPs have also been used for the detection of noncharged nerve agents. However, in this case the sensing protocol relies on a different concept not related to a modification of the aggregation state of the NPs but with their biocatalytic growth.[71] The sensing ensemble uses acetylcholine esterase (AChE). This enzyme is known to hydrolyse acetylthiocholine (ATCh) to yield the

reduction agent thiocholine (TCh). In addition, the presence of TCh stimulates the growth of AuNPs to diameters of 300–500 nm when a certain quantity of $AuCl_4^-$ was present. Upon processing of ATCh by AChE, the plasmon band of the NPs increases in intensity. Moreover, at higher substrate (or enzyme) concentrations, the band also becomes broader and appears at shorter wavelengths, presumably due to the fact that higher processing rates lead to a preferred formation of smaller particles. Because the growth of the AuNPs is controlled by the concentration of ATCh and the activity of the enzyme, the sensory concept is based on the inhibition of the biocatalytic growth in the presence of nerve gases. Thus in the presence of 1,5-bis (4-allyldimethylammoniumphenyl)pentane-3-one dibromide and diethyl-*p*-nitrophenyl phosphate (paraoxon), phosphorylation of the active site of the enzyme occurs and its enzymatic activity is inhibited. The researchers created a colorimetric assay for nerve agents by implementation of AuNP seeds into glass plates.

The use of functionalized AuNPs for anion sensing is less common. An example shows that the addition of certain anions caused dramatic changes in the plasmon band (i.e., intensity decrease and slight red shift in wavelength) of amide-functionalized gold nanoparticles via hydrogen bond formation between the anions and the amide ligands on the particle surface. The authors observed a remarkable chemical amplification effect and an increase of the detection limit of about three orders of magnitude for anions using surface-modified gold nanoparticles in relation to that originally expected for the anion binding ability of the free receptor.[72] In a related work, Kubo et al. used isothiouronium-alkanethiol-capped AuNPs to selectively detect oxoanions such as acetate and HPO_4^{2-} in aqueous methanol solutions.[73]

Another type of inorganic nanoparticles with distinct optical properties, which have received almost exponentially increasing attention in the past few years, are the semiconductor nanocrystals or "quantum dots" (QDs),[74–76] QDs are semiconductor nanoparticles with a diameter typically in the 2–10 nm range and making up as few as 100 to as many as 100,000 atoms. Due to their small size, semiconductor QDs show optical features that are located in between those of discrete molecules and those of bulk semiconductors. The confinement of electrons to a certain small size can be theoretically explained by a general particle-in-a-box quantum mechanical model. The model predicts that the difference in energy between the highest occupied and the lowest unoccupied discrete orbitals of the valence and the conduction band (equivalent to HOMO and LUMO) depends on the size of the box. For instance, a decrease in particle size leads to an increased HOMO-LUMO gap and a shift of the band position to shorter wavelengths (hypsochromic shift). In addition, QDs usually show intense and very broad absorption spectra and very narrow emission spectra. The use of QDs for optical sensing has been recently reviewed.[77–80] Moreover, in most cases QDs are used as "passive" labels in imaging, diagnostics, and bioanalytics[81–84] but have rarely been used as active functional nanoparticles in the sense that AuNPs are commonly used (vide supra).

Chen and Rosenzweig for a specific case of functionalized CdS quantum dots have reported one of the very few examples of analyte-induced aggregation of hybrid nanoparticles that is not based on gold. In their work, CdS QDs capped with L-cysteine showed an increase in the luminescence in the presence of Zn^{2+}, whereas ions such as Cu^{2+}, Ca^{2+}, and Mg^{2+} remained silent. The effect was explained by the formation of QD clusters in the presence of Zn^{2+} as revealed by microfluorometry.[85] Another example involving aggregation was reported by Konishi and Hiratani who observed, upon addition of Cu^{+}, that the band is notably enhanced and red shifted. A positive response was also observed for Cu^{2+} and to some degree for Ag^{+}. The authors suggested that the emission enhancement is due to aggregation through the formation of a multicluster network where Cu^{+} ions act as bridges between CdS clusters.[86]

However, the most common use of QDs as active chemosensors does not involve aggregation. On the contrary, the basic concept underlying the use of QDs in the sensing processes discussed later involve the fact that the emission of QDs is very sensitive to changes at their surface that can occur for instance via coordination or substitution of Cd by other metal cations. For instance, He et al. have reported the use of CdSe QDs modified with mercaptoacetic acid for the selective determination of Ag^{+} by way of quenching of the fluorescence at 543 nm and enhancement in the 570–700 nm range. These changes in emission properties of the QDs are attributed to the chemical displacement of Cd^{2+} for Ag^{+} ions on the surface due to the very low solubility of Ag_2Se.[87] A similar assay was recently realized for Cu^{2+} using CdSe/CdS QDs that were modified with mercaptoethanol groups. The detection depended on the binding of Cu^{2+} onto the surface of QDs, and resulted in a chemical displacement of Cd^{2+} and the formation of CuSe.[88]

Some assays with QDs involve metal ion coordination with the molecules of the appended coating. For instance, CdTe QDs with 3-mercaptopropionic acid have been used for the selective sensing of Cu^{2+}. The signaling event is a partial quenching upon metal coordination to the functionalized surface.[89] A second example was reported by Gattás-Asfura and Leblanc, who designed CdS QDs coated with a pentapeptide. This system demonstrated high selectivity toward Cu^{2+} and Ag^{+} in the presence of other biologically important metal ions. The authors report that complexation of only one of the surface peptides was required to quench the luminescence significantly, thereby showing clear features of signal amplification.[90] Highly luminescent CdTe nanowires have also been used for selective Cu^{2+} sensing in the presence of other relevant cations.[91]

In contrast to metal ion sensing, QDs have been barely used for anion signaling. Toward this objective, Sanz-Medel et al. reported the functionalization of CdSe QDs with *tert*-butyl-*N*-(2-mercaptoethyl)-carbamate for the selective and sensitive detection of cyanide in methanol by analyte-induced luminescence quenching.[92] In a further work, the authors prepared water-soluble CdSe QDs coated with 2-mercaptoethane sulfonate also for cyanide

signaling in aqueous solution.[93] Polyphosphate-containing CdS QDs have also been used for the optical signaling of iodide.[94]

Besides charged species, neutral guests have also been determined with hybrid QDs. By analogy to classic displacement assays of ligand-based ensembles, Singaram et al. used modified QDs in a displacement assay for glucose.[95] These authors prepared an ensemble in which core-shell CdSe/ZnS QDs were functionalized with carboxylate groups and a boronic acid-substituted benzylviologen (BBV). No emission was observed in neutral aqueous solution because electrostatic forces lead to coordination of the BBVs to the QDs. Addition of glucose to the ensemble resulted in the binding of glucose to the BBV through the boronic acid group and liberation of the QDs, thereby recovering luminescence. Water-soluble CdSe/ZnS core-shell QDs carrying tetrahexyl ether derivatives of *p*-sulphonatocalix[4]arene groups on the surface have also been employed for the optical detection of the neurotransmitter acetylcholine.[96]

In a recent example, Kim et al. showed how the combination of several types of nanoparticles could also be wisely used for the design of signaling protocols. They designed a FRET-based inhibition assay to determine the avidin concentration in solution with AuNPs and QDs.[97] The ensemble involves the use of streptavidin-conjugated QDs that interact with biotin-AuNPs through well-known streptavidin-biotin chemistry. This system was not luminescent due to FRET interaction between QDs and AuNPs. Addition of avidin to this ensemble caused the luminescence to increase gradually because the AuNPs were displaced from the streptavidin-functionalized QDs as a consequence of avidin–biotin interactions (Fig. 8).

Finally, after having presented representative examples of particle-based assembly- disassembly protocols, we conclude this section with hybrid signaling systems that show that there is still plenty of room for the design of novel heterosupramolecular ensembles for specific applications. For instance, Suzuki and Kawaguchi immobilized AuNPs and Au/AgNPs in a polymer microgel and managed to swell or shrink the particle-doped polymer in a controlled fashion by simple temperature adjustment.[98] Because the temperature-controlled volume modulations of the organic partner bring the inorganic partners either in closer contact or farther apart, reversible color changes due to a tuning of the interparticle distance and concomitant shifts in the plasmon bands can be achieved. An elaboration of this concept allows the development of a reversible nanothermometer, enabling the precise measurement of temperature down to the nanoscale regime.[99,100] Kotov et al. realized the task by connecting two different NPs, an AuNP and a CdTe quantum dot, through a PEG polymer as a ''molecular spring.'' The system is designed in such a way that the resonance conditions between AuNP plasmon and CdTe exciton lead to luminescence enhancement (instead of the commonly observed quenching). The temperature-based tuning of the distance of the two NPs then modulates the luminescence intensity through the degree of coupling.

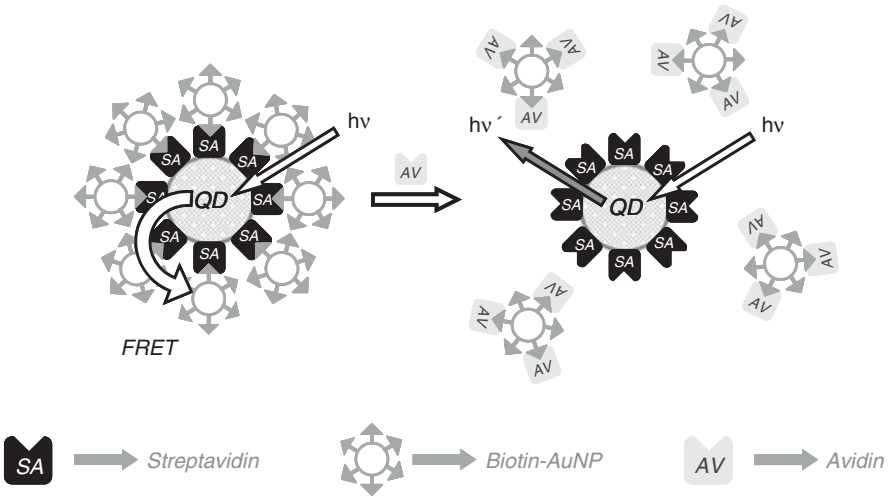

FIGURE 8. Inhibition assay based on the luminescence quenching of streptavidin immobilized QDs by biotin fucntionalized AuNPs. AV is the externally added avidin.

V. SELECTIVITY BY POLARITY AND SIZE. BIOMIMETIC SIGNALING

In this section we discuss how inspiration from nature can lead to the preparation of hybrid systems able to perform a dual functional activity—that is, discriminating between closely related species and at the same time indicating the designated target analytes through chromo-fluorogenic responses. This principle of operation has been mainly realized for biomimetic hybrid systems that are based on preorganized three-dimensional (3D) nanoscopic porous solids. The general idea is to include a suitable binding site into the cavities of a mesoporous solid to form "recognition centers" and then attach additional groups to the walls of the pores that fine-tune the recognition center's polarity. As will be described, these systems show advanced features because, in addition to simple recognition at the binding site, there is additional supramolecular control that is governed by the size and polarity of the nanoscopic pore. This approach usually results in a remarkably enhanced response and selectivity with respect to analogous molecular probes. In terms of bio-inspired concepts, these systems try to mimic the principle of operation of enzymes, which succeed in processing target substrates by extracting them into specific binding pockets. The strategy of mimicking binding pockets, however, is not unique to this field of sensing with mesoporous hybrid materials; another approach tries to simulate the coordination biochemistry involved in metallo-regulatory enzymes.[101] These concepts are embedded in a wider concept of biomimetic chemistry as a part of

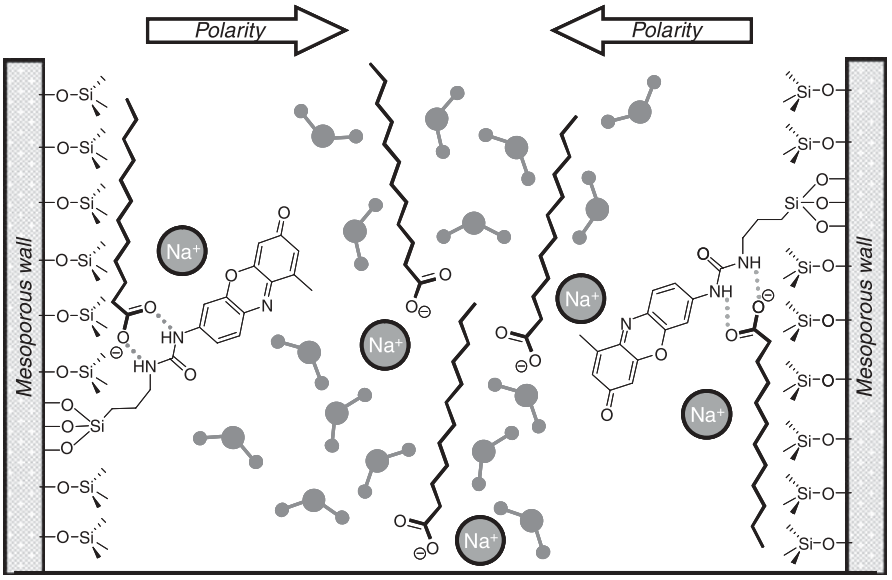

FIGURE 9. Model of a biomimetic material for the sensing of long-chain carboxylates. Hydrophobic forces bind the tail to the wall, enabling hydrogen bonding interactions of the head group of the analyte with the urea group of the phenoxazinone dye. The result is a color and fluorescence modulation.

the science that tries to imitate nature's methods, mechanisms, and processes.[18,102–104]

The basic principle of operation is sketched in the first example (Fig. 9), which was designed to selectively indicate the anions of fatty acids or fatty carboxylates. The hybrid system consisted of a mesoporous MCM-41-type material that was functionalized in two steps. First, a urea-phenoxazinone derivative is anchored onto the surface of the mesoporous solid. Mesoporous materials of the MCM-41-type contain pores of 2–3 nm and a remarkable high specific surface ($\sim$1200 $m^2\ g^{-1}$) that corresponds mainly to the surface of the inner pores. Therefore, the anchoring of the sensor molecule at low concentrations results in a functionalized material that contains the signaling receptor almost exclusively within the pores. The urea-phenoxazinone derivative is the signaling-recognition unit because it is able to act at the same time as an anion receptor through hydrogen bonding between the carboxylate groups of the target guest and the urea group and as the signaling reporter through a modulation of the electron distribution in the phenoxazine group upon carboxylate–urea coordination, which results in changes in absorption and fluorescence. In a second step, the inner surface of the mesoporous support was further functionalized with trimethylsilane with the aim of transforming the hydrophilic inner walls of the silica skeleton into hydrophobic pockets by transformation of OH groups to $Si(Me)_3$ moieties.[105] This solid displays a

remarkable response to fatty- or long-chain carboxylates in water thereby exhibiting a bathochromic shift of the absorption band and an enhancement of the fluorescence emission. The authors demonstrated that short-chain carboxylates; inorganic cations; anions; and biological species such as triglycerides, cholesterol, bile acids, and organic phosphates gave no remarkable response—that is, the solid is highly selective. The performance of the hydrophobic hybrid solid suggests that, after extraction of the fatty carboxylates into the pores, the water content in the hydrophobic layer at the inner wall is presumably reduced so that hydrogen bonding between carboxylate and urea can occur. The integration of functionality and signaling is clearly shown if one takes into account that neither the urea-phenoxazinone probe molecule nor the hybrid material that is solely functionalized with the urea-phenoxazinone probe (but not being hydrophobized) are able to sense the target analytes in water. In biomimetic terms, selective signaling is achieved here in a similar way as many proteins— that is, the substrate is extracted into a hydrophobic pocket in which the active site–substrate complex is shielded from competitive water molecules.

Another example uses a similar mesoporous solid that was first functionalized with a pyrylium derivative, able to undergo color changes in the presence of primary amines, and then reacted with hexamethyldisilazane for passivation.[106] The result is a sensory solid that contains hydrophobized nanoscopic pockets that react in pure water only with medium-chain amines that are hydrophobic enough (such as *n*-octylamine) but do not respond to longer-chain (e.g., *n*-dodecylamine) or hydrophilic (e.g., *n*-propylamine) amines. Apparently, short-chain amines are too hydrophilic to enter into the mesopores and induce a chromogenic reaction. Moreover, long-chain amines appear to close the pores by reaction with the pyrylium groups near the pore openings, thus hampering the diffusion of the analytes due to steric crowding. Again, the integration of functionality and signaling is stressed when one compares the response of the functional solid with that of the pyrylium probe molecule alone and that of simple 2D materials with "flat" surfaces, such as silica gel or fumed silica that are functionalized with the pyrylium dye and passivated by trimethylsilylation but do not possess the mesopores. Whereas the indicator molecule reacts nonspecifically with any primary amine, the latter can discriminate against too hydrophilic short-chain amines but display color modulations with both medium- and long-chain primary amines.

A very similar colorimetric discrimination of amines was reported for a system that employs a dicyanomethylene-2-chloro-3-amino-indene dye as a signaling reporter and a hydrophobized (trimethylsilylated) mesoporous MCM-41-type solid.[107] The same conceptual idea was also followed for a hybrid ensemble that contains a styrylpyrylium derivative anchored at the walls of hydrophobized mesopores. In this case, the sensory material changes its color from blue to red by reaction with primary amines. As a remarkable feature, the styrylpyrylium-appended hydrophobized mesoporous solid was able to react with biogenic amines such as histamine from fish extracts and remained silent in the presence of amino acids or long-chain fatty amines.[108]

Using a similar approach, Lin's group reported two other examples of functional discrimination by size and polarity for enhanced signaling. For example, a mesoporous material was first functionalized with *o*-phthalic hemithioacetal moieties that are able to react with amines to produce a highly fluorescent isoindole chromophore. The solid was then hydrophobized with different groups such as propyl, phenyl, and pentafluorophenyl.[109] It is interesting that some of these solids displayed a remarkably selective and differentiable response to dopamine versus the less lipophilic glucosamine. The authors also demonstrated that this selectivity was not observed when using amorphous silica functionalized with the same organic groups, thereby stressing the importance of the 3D mesoporous structure. In a further interesting study, the authors coated mesoporous materials with poly(lactic acid).[110] This coating acts as a "molecular gate keeper" that is able to regulate the penetration of certain amines into the nanoscopic pores using coulombic forces. A large difference in the diffusion rates into the pores and, therefore, a selective signaling of the neurotransmitter dopamine in relation to tyrosine and glutamic acid was observed. The discrimination relies on the ratio between the charges at neutral pH of the gate keeper (negatively charged) and the charge of the guests—that is, whereas dopamine is positively charged, tyrosine and glutamic acid are negatively charged. Thus the latter are repelled by the negatively charged poly(lactic acid) coating (Fig. 10).

Discrimination by size and polarity in combination with colorimetric signaling was also observed for microporous materials—for example, when a pyrylium derivative is anchored to the inner pores of zeolite Beta. Zeolite Beta is characterized by a 3D channel system for which access to the pore voids is limited by 6.8 Å aperture that is composed of 12 silicon atoms. A size-based discrimination was observed and only amines smaller than the pore openings induce color modulations. For amines of similar size, an additional discrimination by polarity that is induced by the hydrophobic environment of the inner zeolite was also found (Fig. 11).[111]

These results demonstrate that selective molecular recognition can be achieved by integrating functionality related with polarity and size discrimination with a signaling event. In fact, within a biomimetic perspective, the confinement of signaling groups into the modified solid structure leads to additional recognition advantages that take profit of both the extraction of the guest from water that is limited by polarity and size and the selective reactivity of the binding site with the guest. These recognition benefits are especially obvious when one compares the response of the "binding pockets" with the analogous molecular probes or with "flat" non-mesoporous supports (vide ante).

Discrimination by polarity has also been used for the design of robust sensors for vapor detection. For instance, a mesoporous silica material containing a covalently anchored phenoxazinone probe has been used as an optical sensory hybrid for the detection of volatile organic compounds (VOCs). The indication mechanism relies on the property of certain phenoxazinone

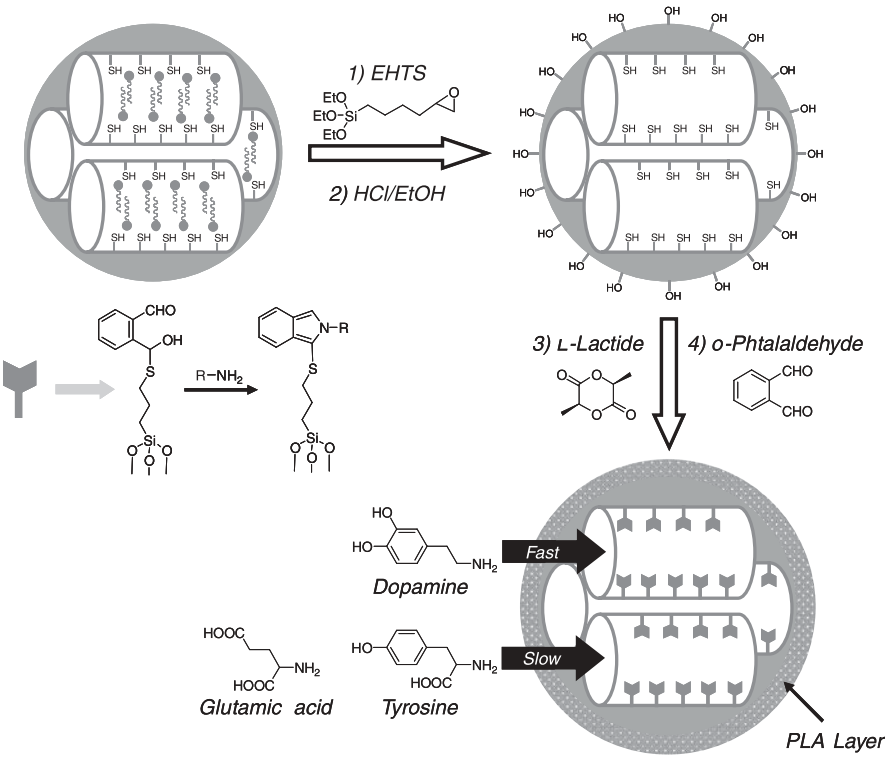

FIGURE 10. The synthesis of a PLA-coated fluorescent sensor material for detection of amine-containing neurotransmitters (dopamine, glutamic acid, and tyrosine).

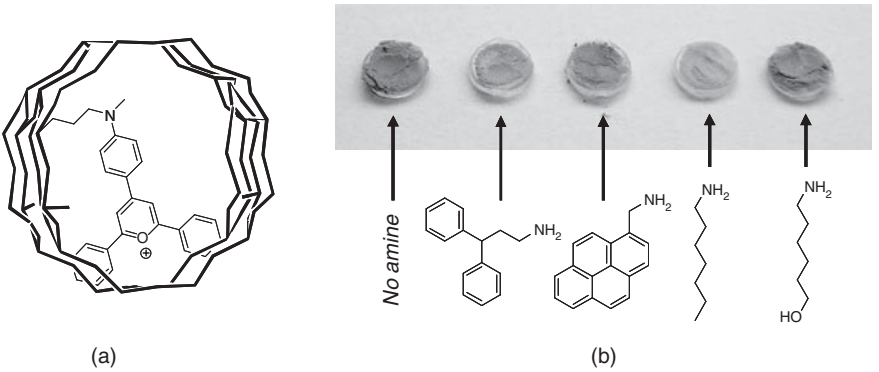

FIGURE 11. (a) A chromogenic hybrid material containing a pyrylium dye anchored on the zeolite Beta walls. (b) The color changes observed in this hybrid material upon addition of certain amines.

derivatives to behave as fluorescent solvatochomic dyes.[112] As in the earlier cases, the mesoporous material was first functionalized with the dye and then refunctionalized with hexamethyldisilazane, which results in a fine control of the inner surface polarity and yields a rather hydrophobic hybrid sensory material. This derivative shows enhanced performance as optical sensor for VOCs when compared with the analogous non-hydrophobized material. For instance, the former allows the indication of VOCs over a larger polarity range, and the color and fluorescence changes distinctly, exceeding those of the latter, hydrophilic material. In addition, the hydrophobic material shows a faster response, better reversibility, and displays minimal interference from environmental humidity. Moreover, when compared with other inorganic hosts for VOCs detection such as zeolites,[113] the mesoporous hybrid has the advantage of larger pore diameters, which enable faster diffusion rates and better surface tailoring. This hybrid approach may also show advantages compared to sensory polymers because of the facile covalent functionalization of inorganic supports, the highly ordered 3D structure and the avoidance of swelling problems.[114,115]

By analogy to the aforementioned, porphyrin-doped mesoporous silica films have been used for the detection of TNT vapors by quenching of the porphyrin emission.[116] The authors demonstrated that the use of mesoporous phases shows distinct advantages in terms of response when compared with functionalized amorphous silica.

VI. SWITCHING, GATING, AND SIGNALING

One of the most exciting areas within hybrid materials research is the anchoring of certain addressable or switchable molecular entities on the surface of (usually porous) inorganic scaffolds that allow the active control of the conformation, physical properties or aggregation state of the organic groups by external stimuli. Following this approach, several materials with controllable wettability,[117] adhesion features,[118] roughness,[119] and biocompatibility[120] have been developed in recent years. In addition, systems for which host–guest complexation at the surface is controlled by electrochemical or photochemical means have also been reported.[121,122] For these systems, the solids are basically modified with switchable molecules that respond to light, redox stimuli, or thermal changes. In many cases, this has been achieved by using polymers and self-assembled monolayers (SAMs), the changes in morphology of which result in modulations of the macroscopic properties of the modified surfaces.

In relation to recognition and signaling with functionalized surfaces, a suggestive approach involves the design of so-called ion channel sensors. These systems usually consist of a conducting solid (e.g., an electrode) and a layer of anchored molecular entities containing certain binding sites. When a certain guest coordinates with the binding sites on the anchored layer there is a change

in the net charge on the layer that results in a regulation of the oxidation or reduction of an electroactive ion (i.e., the redox marker). Thus the coordination of a guest with the anchored substrate determines the accessibility of the electrode surface for the redox marker, which results in an overall guest-controlled switching effect.[123] Also, ion-channel sensors have the inherent possibility of signal amplification because the reduction or oxidation of a greater number of markers can be controlled by the binding of a fewer number of guests to the host monolayer. Since the introduction of this concept by Umezawa's group, considerable interest has been devoted to its use in analytical chemistry, and a number of sensors have been reported for a wide range of species from simple metal ions to complex guests. Organization of the molecular recognition agents or receptors on the surface includes in many cases the formation of SAMs via covalent attachment of receptor molecules. Some representative examples are described in more detail here.

Ion channel sensors (ICSs) have been usefully applied to the recognition and quantification of polyions such as protamine (a polycation with an average charge of +20) and heparine (a polyanion with an average charge of –70). Heparin is extensively employed as anticoagulant, whereas protamine is used to neutralize the anticoagulant activity of heparine. For their determination, gold electrodes were modified by the formation of SAMs of thioctic acid.[124] Upon deprotonation of the anchored thioctic acid molecules, a negatively charged layer on the electrode is generated that induces protamine adsorption through electrostatic forces (Fig. 12a). These sensors could detect protamine levels as low as 0.11 μM when $[Ru(NH_3)_6]^{3+}$ was used as the redox marker. The development of ICSs for heparin was closely related to that prepared for the detection of protamine.[125] Again, SAMs of thioctic acid were prepared on the surface of an electrode. Subsequent treatment with protamine created a positively charged layer able to interact with the negatively charged heparin (Fig. 12b). This interaction provided the electrode surface with an excess of negative charges, thereby repelling the marker ions $[Fe(CN)_6]^{3-}$ and $[Mo(CN)_8]^{4-}$ from the electrode surface. In a solution containing inorganic species at physicological blood concentrations as a background, heparin could be detected in a linear concentration range of 3.3 nM–0.1 μM.

ICSs have also been developed and used for the quantification of metal ions. For these purposes, gold electrodes were modified with a phosphate ester monolayer and showed response toward trivalent and divalent metal ions in the presence of a background of alkali cations.[126] In the absence of metal ions, the surface of the electrode is negatively charged due to the presence of phosphate groups and the reduction of $[Fe(CN)_6]^{3-}$ marker is hindered. Addition of trivalent and divalent metal ions, such as Al^{3+}, La^{3+}, Ba^{2+}, Sr^{2+}, Ca^{2+}, and Mg^{2+}, induced the formation of a positively charged monolayer after bonding of the cations to the phosphate groups. Neutralization of the phosphates permitted access to and reduction of the negatively charged markers at the electrode surface. Trivalent cations could be detected down to submicromolar concentrations. In a similar approach, Gadzekpo et al.

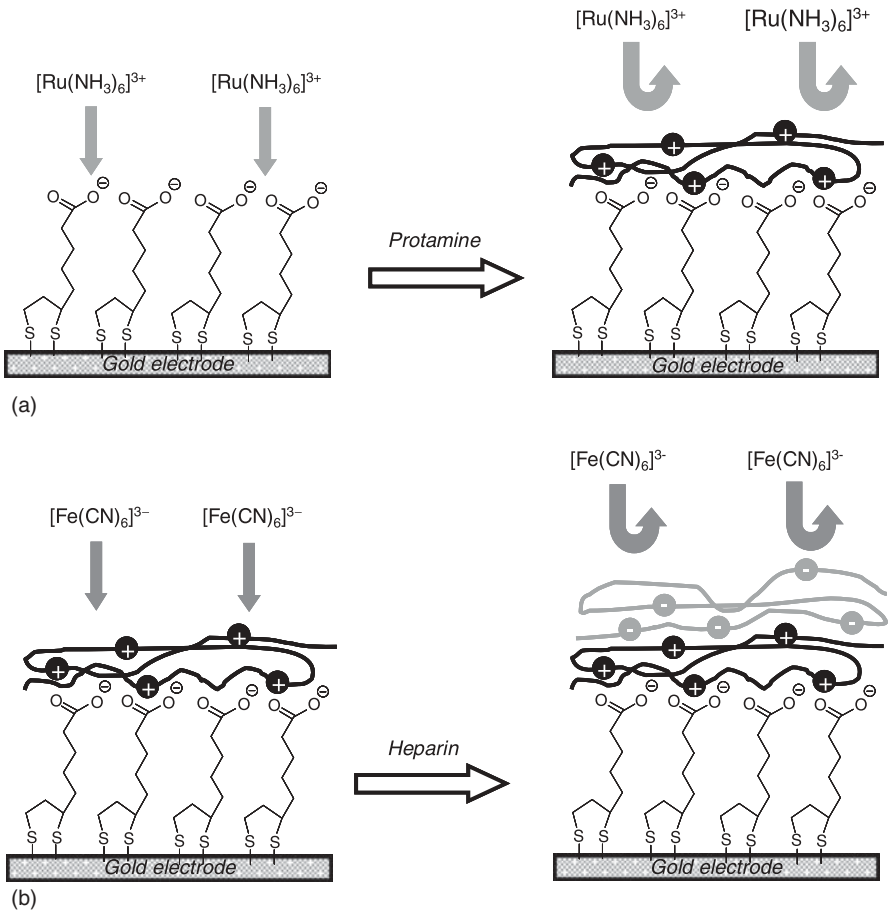

FIGURE 12. (a) Protamine detection with a gold electrode modified with a SAM of thioctic acid and $[Ru(NH_3)_6]^{3+}$ probe. (b) Heparin detection with the protamine–thioctic acid–gold electrode and $[Fe(CN)_6]^{3-}$ probe.

functionalized gold electrodes with thioctic acid and studied the response of the modified electrodes in the presence of alkali, alkaline earth, and trivalent cations by means of cyclic voltammetry.[127] Again, the reduction of $[Fe(CN)_6]^{3-}$ as marker was hindered in the absence of metal ions due to electrostatic repulsion by the carboxylate layer on the surface. The presence of $La^{3+}$and other divalent metal ions then led to an increase in current. Thus ICS showed selectivity toward La^{3+} on a background of divalent and monovalent metal ions with a detection limit of 10 nM.

Selective electrochemical detection of K^+ over Na^+ was achieved by using gold electrodes functionalized with bis-thioctic ester-terminated derivatives of oligoethylene glycol by cyclic voltammetry and impedance spectroscopy.[128]

Functionalization of gold surface with this oligoethylene glycol derivative induced the formation of a SAM, which exhibited a pseudo-18-crown-6 structure. Upon addition of the redox marker $[Ru(NH_3)_6]^{3+}$ to the chemically modified surface of the electrode, a clear anodic process was observed due to reduction of the marker. In the presence of K^+, the anodic process disappeared, indicating that K^+ forms a stable inclusion complex with the pseudo-18-crown-6 moieties on the surface that leads to the repulsion of the positively charged redox marker. On the other hand, addition of Na^+ induced negligible changes in the voltammetric response of the redox marker. In another attempt to selectively and sensitively recognize alkali metal ions, gold electrodes were chemically modified with SAMs of 12-crown-4 and 15-crown-5 macrocycles.[129] Electrochemical impedance spectroscopy was used to monitor the interactions of both crown ether SAMs with Na^+ and K^+, using $[Ru(NH_3)_6]^{3+}$ as the redox marker. The binding of metal ions with crown ether moieties on the surface of the electrodes induced a significant increase in charge transfer resistance that was higher for Na^+ than for K^+ for the electrode modified with 12-crown-4, while the 15-crown-5 SAM showed the opposite trend.

In a more recent example, thiol-derivatized 4-acyl-5-pyrazolone was used to prepare a modified electrode that allowed the selective detection of trivalent metal ions.[130] The chelating group has a typical β-diketone motif suitable for the coordination of "hard" ions (e.g., trivalent lanthanoids) and displays a negative charge at a working pH of 5.5 due to deprotonation of the pyrazolone moiety. Binding of the trivalent lanthanoid ions, La^{3+}, Gd^{3+}, and Yb^{3+} as well as Al^{3+} to the modified electrode surface led to the formation of a positively charged SAM that induced an increase or a decrease in the redox current of $[Fe(CN)_6]^{3-}$ or $[Ru(NH_3)_6]^{3+}$, respectively. Addition of divalent (Mg^{2+}, Sr^{2+}, Ca^{2+}, and Ba^{2+}) and monovalent metal ions (Li^+ and Na^+) revealed negligible changes in the redox current. In a work by Aoki et al., Ca^{2+}-selective detection was achieved with an ICS based on the immobilization of the ionophore, ETH 1001, onto the surface of a gold electrode.[131] The sensory hybrid layer was prepared by functionalization of the surface of a Au electrode with 10-mercaptodecanesulfonate and 11-hydroxy-1-undecanethiol. In a second step, ETH 1001 was immobilized into the mixed SAM through hydrophobic interactions between its alkyl chains and those of the alkanethiol. In the absence of Ca^{2+}, the surface of the gold electrode expressed a high density of negative charges, and as a consequence, the redox reaction of the $[Fe(CN)_6]^{3-}$ marker was inhibited. Upon binding of Ca^{2+} with the surface-confined ETH 1001, a decrease in the global negative charge on the surface took place, allowing access of the redox probe.

ICSs have also been successfully employed for anion sensing. For instance, Umezawa et al. prepared an ion-channel sensor that is selective for phosphate ion in aqueous solution by surface functionalization of a gold electrode with a SAM of a bis-thiourea receptor. They studied the behavior of the material in the presence of several inorganic anions by cyclic voltammetry with $[Fe(CN)_6]^{3-}$ as the redox marker.[132] In the absence of anions, the surface

of the electrode is fully accessible for the redox marker, undergoing a quasi-reversible reduction. Upon addition of phosphate ions, the shape of the cyclovoltammogram changes to that of a more irreversible process. This result clearly indicates that the binding of phosphate with the receptors (through four hydrogen bonds) located on the surface leads to the formation of a negatively charged monolayer that hinders the redox reaction of the marker through electrostatic repulsions. The detection limit of this ICS for phosphate is at the submillimolar level. Moreover, the ICS is virtually insensitive to other inorganic anions such as SO_4^{2-}, AcO^-, NO_3^-, and Cl^-. In a previous work, the same authors prepared an ICS by immobilization of a xanthene derivative that contains two thiourea moieties on a highly oriented pyrolytic graphite electrode, which also showed selectivity for the phosphate anion.[133] In the absence of anions, the electrode's surface is fully accessible for the $[Fe(CN)_6]^{3-}$ marker, whereas binding of phosphate with the receptor inhibited marker oxidation.

Adenosine nucleotides were also electrochemically detected with ICSs.[134] For these purposes, gold electrodes were functionalized by covalent anchoring of macrocyclic polyamines. $[Ru(NH_3)_6]^{3+}$ was used as redox probe for the voltammetric detection of ATP, ADP, and AMP. The response mechanism originates from the inhibition of the redox reaction of the marker upon formation of supramolecular complexes between macrocyclic polyamine hosts and adenine nucleotide guests at the surface of the electrode.

Bioelectronic devices were prepared by the immobilization of certain biomolecules onto a conductive or semiconductive support. Using this approach, ICSs for the electrochemical recognition of cAMP, oligonucleotides, and avidin were prepared. For instance, a peptide receptor for cAMP comprising 17 amino acid residues was adsorbed onto a gold disk electrode and the resulting ICS was tested against the presence of several cyclic nucleotides.[135] A selective response for cAMP was observed because coordination with the adsorbed peptide induced a decrease in the redox current of the $[Fe(CN)_6]^{3-}$ marker due to the formation of a negatively charged monolayer at the electrode surface. Gold electrodes functionalized with SAMs of a 13-mer peptide nucleic acid (PNA) probe and 8-amino-1-octanethiol were used to detect a complementary oligonucleotide.[136] At pH 7.0, the electrode surface was positively charged due to the presence of protonated amines and access for $[Ru(NH_3)_6]^{3+}$ was denied by electrostatic repulsions. Hybridization of PNA probes and negatively charged complementary oligonucleotides then neutralizes the positive charges and also provides an excess of negative charges at the surface, thus facilitating the contact of the marker with the electrode's surface and the redox reaction. This ICS allows the detection of the oligonucleotides at the femtomolar level and, as a general trend, as the number of oligonucleotides in the chain increases, the detection limit is improved. The binding interaction between avidin and biotin has also been monitored with an ICS.[137] A SAM of biotin on the surface of a gold electrode was prepared and the response upon binding with avidin in the presence of $[Fe(CN)_6]^{3-}$ was studied. At pH values

lower than the isoelectric point of avidin, the response of $[Fe(CN)_6]^{3-}$ at the avidin-covered electrode increased because of the electrostatic interaction between avidin entities and $[Fe(CN)_6]^{3-}$ ions. A detection limit as low as 0.29 nM was measured for avidin.

By analogy to layered electrochemical ICSs, highly selective methods of electroanalysis have also been developed on the basis of gold nanotube membranes that mimic ligand-gated ion-channels.[138] A related field of active research is the development of modified protein pores[139] and channels that can act as sensors.[140]

Other interesting developments within the context of this section relate to "adaptive materials." The idea relies on the use of tailored materials that can perform more than one function of a sensor—for example, molecular recognition, self-calibration, activation/passivation, and/or protection. A promising application for adaptive sensor materials resides with electrochemical analysis. The major problem in the praxis of electrochemical sensors is the adsorption of surface-active substances onto the working electrode. Unspecific adsorption causes electrode fouling, which has a negative impact on sensor characteristics. Usually, protective polymer or gel coatings are used to minimize adsorption of unwanted surface-active molecules. An alternative approach relies on the use of adaptive nanowires.[141] For instance, alkanethiol-coated gold nanowires that contain a short magnetic segment (nickel) were used to protect a glassy-carbon disk electrode. This protection was achieved by switching magnetically the surface orientation of the nanowires between vertical (active, open surface) and horizontal (passive, closed surface) position. These "adaptive" electrodes have been successfully employed in the voltammetric determination of Cd^{2+} in the presence of common surfactants (gelatin and polysorbate 80). Whereas bare electrodes display a substantial decrease of the Cd^{2+} peak in the presence of both surfactants, the adaptive nanowire electrode exhibits a highly stable response with negligible changes of the peak current over multiple measurements.

The concept of "adaptive materials" has also been applied to the development of optical sensors. Again, the main idea concerns the protection of the active components of the sensory material from unspecific interferences contained in the bulk solution. Thus the principle of operation includes the activation/passivation of the sensory layer by an external stimulus. Spiropyran and related systems have been used for the development of surface-based adaptive optical sensing materials.[142] For instance, polymethyl methacrylate (PMMA) films were functionalized with spiropyran molecules, rendering the functionalized solid colorless and inactive toward divalent metal ions. Upon irradiation with UV light, the spiropyran isomerizes to its open zwitterionic merocyanine form that is brightly purple and can actively bind certain divalent metal ions through the negatively charged phenolate oxygen atoms. Irradiation with green light leads to the dissociation of the merocyanine-M^{2+} complex and the regeneration of the inactive spiropyran layer (Fig. 13). Accordingly, each state of the system, active and passive, is easily perceptible with the eye. This approach presumably extends the lifetime of sensors and allows one to obtain

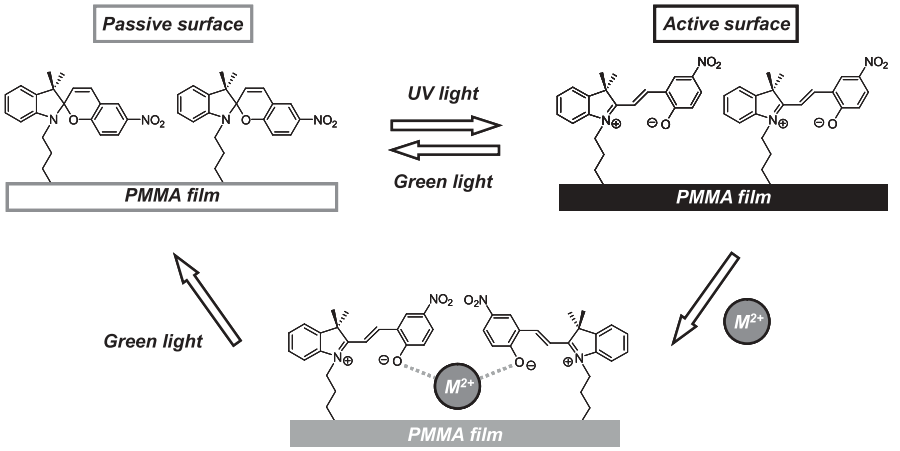

FIGURE 13. The photo-controlled metal cation binding at a spiropyran-modified PMMA film.

reference or zero values at the beginning of each measurement. More sophisticated materials capable of switching reversibly between active and passive forms and simultaneously providing a number of transduction modes for acquiring information about the molecular environment in the vicinity of the binding site in the active mode can also be envisioned.

We finish the chapter with some examples related to the use of nanoscopic gate-like switching mechanisms for the development of new signaling systems using bioinspired hybrid mesoporous materials. A gate-like ensemble here refers to a mesoporous 3D skeleton that is functionalized with molecules that can be switched (by different means) to control either the release of a confined guests from the porous host or the entrance (or access) of molecular species to certain sites or into the pores. The triggers used for switching the state of the gate can be of chemical (e.g., ionic species) or physical nature (e.g., light). Most of these gate-like systems have been developed as scaffoldings for cargo delivery. However, applications in delivery are only one side of the medal. Recent works have demonstrated that nanoscopic gate-like scaffoldings can also be successfully employed in sensing protocols. Inspiration for the designed systems as described later comes from the gating mechanism biological systems employ primarily for trafficking through ligand-gated protein channels. The artificial sensing approach realized so far uses a hybrid architecture that consists of a mesoporous MCM-41 silica support that contains suitable coordination sites at the pore outlets and an indicator dye in the pore voids. In terms of gate-like devices, the sensing protocol is based on the idea that the addition of a certain ''key'' guest ''closes the gate'' and inhibits the delivery of a colored or fluorescent substance from the pores into the bulk solution. These systems are distinctly different from the classical ''binding site-signaling unit''

paradigm because in these gated devices, the complexation of comparatively few guests at the chemical gate posts of the ensemble inhibits the liberation of a large number of dyes, thus showing clear features of signal amplification. This approach detaches the recognition protocol from the signaling event, making signaling independent of the stoichiometry of the guest-binding site complex as usually happens in classical signaling procedures.

A first proof of concept was reported for an MCM-41 mesoporous support containing $[Ru(bpy)_3]^{2+}$ in the inner pores and simple amine groups as gate posts on the external surface. Such polyamine/polyammonium receptors are well-known receptors for anions through a combination of hydrogen bonding and electrostatic interactions. Among several anions tested, ATP and ADP were selectively able to close the gate, whereas other anions such as Cl^-, SO_4^{2-} or GMP were too small or formed too weak complexes with the functionalized surface to effectively close the pore openings and stop leaching of the $[Ru(bpy)_3]^{2+}$ indicator (Fig. 14).[143]

A related approach has been reported for imidazolium-functionalized mesoporous materials also containing the $[Ru(bpy)_3]^{2+}$ dye in the inner pores for the selective colorimetric detection of fatty acids. As in the previous case, again mesoporous MCM-41 with pores of 2.5 nm in diameter was used as the solid scaffolding. $[Ru(bpy)_3]^{2+}$ was included into the pores and imidazolium groups were grafted as simple and suitable binding sites onto the external

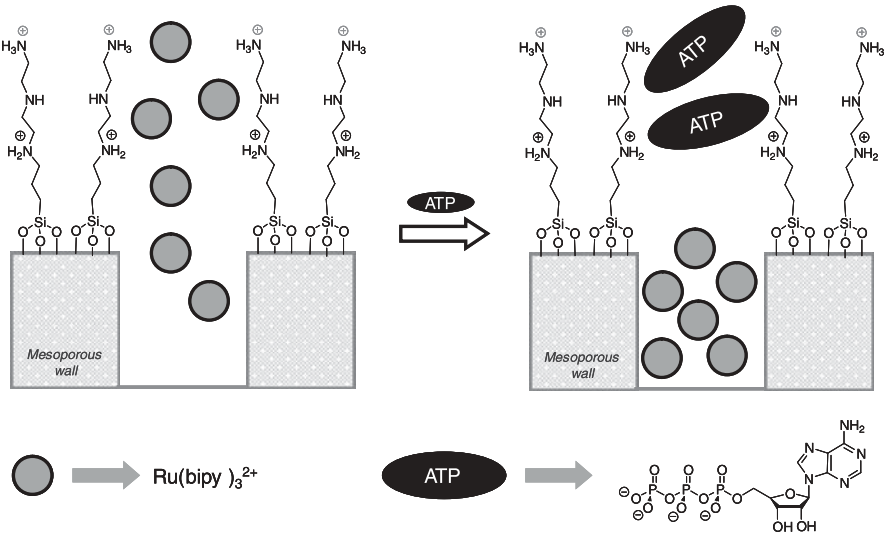

FIGURE 14. ATP signaling protocol via inhibition of dye delivery using nanoscopic gate-like scaffoldings. The mesopores of the system are loaded with a $[Ru(bpy)_3]^{2+}$ dye and polyamines are covalently anchored to the external surface (the gate is open on the left). Addition of ATP results in the inhibition of dye delivery due to strong ATP-polyamine interactions (the gate is closed on the right).

surface.[144] In the absence of carboxylates, the gate is open and dye delivery is observed. Addition of linear carboxylates of different lengths ($CH_3(CH_2)_nCOO^-$, $n = 2, 4, 6, 8, 10$) resulted in a different blockage of the pores. However, gradual pore blockage as a function of the chain length n was not observed but rather an "on-off" behavior—that is, complete dye delivery in the presence of small carboxylates from acetate to octanoate and complete pore blockage for carboxylates with a longer chain. The degree of the closing of the molecular gate-like ensemble upon interaction with the imidazolium groups is most likely due to a combination of two effects related to the size of the carboxylates and the increasingly hydrophobic nature of the object formed in the gating area of the pore outlets upon elongation of the hydrocarbon chain of the carboxylate. Apart from this protocol, a sensing paradigm that uses the opening of pores can also be envisioned. However, the latter would require the equipment of the pore outlets with specific recognition or reactive sites and has not yet been realized. Due to the possible use of different 3D supports, diverse analyte-gate post chemistries and the availability of a wide range of appropriate dyes, a variety of novel signaling systems based on gate-like scaffoldings can be anticipated.

VII. CONCLUSIONS

In this review, an account of representative and authoritative examples published in the field of supramolecular hybrid materials for signaling applications has been given. Sensing concepts arising from the combination of supramolecular functions of suitable molecules and preorganized nanoscopic inorganic supports, often covalently linked, have been introduced and discussed. All the examples have in common synergistic effects that are not achievable at the molecular level or with nanostructured solids alone. In some cases, these hybrid systems yielded improved selectivity and sensitivity; in others they enabled the signaling of targets that are otherwise difficult to achieve with on-site or in situ methods. The main features of the examples in Section II make up enhanced coordination effects observed upon equipping the surface of nanostructured inorganic materials with a high density of one or more binding and/or signaling sites and show how this effect can be coupled with signaling protocols. Section III discussed selected examples that show amplified signaling as a result of the collective response and cooperative effects associated with the independent anchoring of binding sites and signaling units or indicator units in close proximity to the surface of inorganic supports. In all of these cases, optically silent siliceous matrices were used. In contrast, the examples in Section IV are related to the use of gold nanoparticles and quantum dots. For instance, guest-induced aggregation effects that result in remarkable shifts of the plasmon band of AuNPs were shown. The subject of Section V was the selectivity that can be reached by tuning the pore size and

polarity of functionalized porous hybrid materials. The main features presented in Section VI focus on the modification of the morphological aspects of hybrid materials that lead to sophisticated gating and switching mechanisms and how the integration of such functionalities could be used for sophisticated sensing systems. The common feature of all the aforementioned exciting chemistry is the synergistic use of concepts from nanotechnology to biomolecular and supramolecular chemistry that create properties and functions that are difficult to achieve in molecular-based systems or nanoscopic solids alone or that transfer known functions to a higher level of sophistication.

VIII. ACKNOWLEDGMENTS

Financial support from the Ministerio de Ciencia y Tecnologia (project CTQ2006-15456-C04-01) and the European Commission's Human Resources & Mobility Program (Marie Curie Intra-European Fellowship) and the European Commission's EFRE/ProFIT program is gratefully acknowledged.

IX. REFERENCES

1. J. M. Lehn, *Supramolecular Chemistry: Concepts and Perspectives*, VCH, Weinheim, **1995**.
2. J. W. Steed and J. L. Atwood, *Supramolecular Chemistry*, Wiley, Hoboken, N.J., **2000**.
3. I. Stibor, ed., *Top. Curr. Chem.*, **2005**, *255*.
4. P. A. Gale, ed., *Coord. Chem. Rev.*, **2006**, *250*.
5. J. F. Callan, A. P. de Silva, and D. C. Magri, *Tetrahedron*, **2005**, *61*, 8551.
6. G. J. Mohr, *Sens. Actuators B*, **2005**, *107*, 2.
7. G. J. Mohr, *Chem. Eur. J.*, **2004**, *10*, 1082.
8. S. Onclin, B. J. Ravoo, and D. N. Reinhoudt, *Angew. Chem. Int. Ed.*, **2005**, *44*, 6282.
9. A. Vinu, K. Z. Hossain, and K. Ariga, *J. Nanosci. Nanotechnol.*, **2005**, *5*, 347.
10. F. Hoffmann, M. Cornelius, J. Morell, and M. Fröba, *Angew. Chem. Int. Ed.*, **2006**, *45*, 3216.
11. S. Daniel, T. P. Rao, K. S. Rao, S. U. Rani, G. R. K. Naidu, H. Y. Lee, and T. Kawai, *Sens. Actuators B*, **2007**, *122*, 672.
12. D. M. Ford, E. E. Simanek, and D. F. Shantz, *Nanotechnology*, **2005**, *16*, S458.
13. L. He and C. S. Toh, *Anal. Chim. Acta*, **2006**, *556*, 1.
14. G. Cooke, *Angew. Chem. Int. Ed.*, **2003**, *42*, 4860.
15. E. Katz and I. Willner, *Angew. Chem. Int. Ed.*, **2004**, *45*, 6042.
16. A. Verma and V. M. Rotello, *Chem. Commun.*, **2005**, 303.
17. U. Drechsler, B. Erdogan, and V. M. Rotello, *Chem. Eur. J.*, **2004**, *10*, 5570.
18. A. B. Descalzo, R. Martínez-Máñez, F. Sancenón, K. Hoffmann, and K. Rurack, *Angew. Chem. Int. Ed.*, **2006**, *45*, 5924.

19. F. Mancin, E. Rampazzo, P. Tecilla, and U. Tonellato, *Chem. Eur. J.*, **2006**, *12*, 1844.
20. I. Willner, B. Basnar, and B. Willner, *Adv. Funct. Mater.*, **2007**, *17*, 702.
21. L. Basabe-Desmonts, D. N. Reinhoudt, and M. Crego-Calama, *Chem. Soc. Rev.*, **2007**, *36*, 993.
22. P. D. Beer, D. P. Cormode, and J. J. Davis, *Chem. Commun.*, **2004**, 414.
23. A. Arduini, D. Demuru, A. Pochini, and A. Secchi, *Chem. Commun.*, **2005**, 645.
24. T. R. Tshikhudo, D. Demuru, Z. Wang, M. Brust, A. Secchi, A. Arduini, and A. Pochini, *Angew. Chem. Int. Ed.*, **2005**, *44*, 2913.
25. D. Astruc, M.-C. Daniel, and J. Ruiz, *Chem. Commun.*, **2004**, 2637.
26. A. B. Descalzo, D. Jiménez, M. D. Marcos, R. Martínez-Máñez, J. Soto, J. El Haskouri, C. Guillem, D. Beltrán, P. Amorós, and M. V. Borrachero, *Adv. Mater.*, **2002**, *14*, 966.
27. A. B. Descalzo, M. D. Marcos, R. Martínez-Máñez, J. Soto, D. Beltrán, and P. Amorós, *J. Mater. Chem.*, **2005**, *15*, 2721.
28. See for instance: (a) X. Feng, G. E. Fryxell, L.-Q. Wang, A. Y. Kim, J. Liu, and K. M. Kemner, *Science*, **1997**, *276*, 923. (b) L. Mercier and T. J. Pinnavaia, *Adv. Mater.*, **1997**, *9*, 500. (c) M. Etienne, S. Sayen, B. Lebeau, and A. Walcarius, *Stud. Surf. Sci. Catal.*, **2002**, *141*, 615. (d) B. Lee, Y. Kim, H. Lee, and J. Yi, *Microporous Mesoporous Mater.*, **2001**, *50*, 77. (e) R. I. Nooney, M. Kalyanaraman, G. Kennedy, and E. J. Maginn, *Langmuir*, **2001**, *17*, 528. (f) V. Antochshuk and M. Jaroniec, *Chem. Commun.*, **2002**, 258. (g) V. Antochshuk, O. Olkhovyk, M. Jaroniec, I.-S. Park, and R. Ryoo, *Langmuir*, **2003**, *19*, 3031. (h) Y. Kim, B. Lee, and J. Yi, *Sep. Sci. Technol.*, **2004**, *39*, 1427. (i) O. Olkhovyk and M. Jaroniec, *Adsorption*, **2005**, *11*, 685. (j) S. G. Wang and J. L. Li, *Chin. Chem. Lett.*, **2006**, *17*, 221. (k) R. C. Schroden, M. Al-Daous, S. Sokolov, B. J. Melde, J. C. Lytle, A. Stein, M. C. Carbajo, J. T. Fernandez, and E. Rodriguez, *J. Mater. Chem.*, **2002**, *12*, 3261.
29. V. Ros-Lis, R. Casasús, M. Comes, C. Coll, M. D. Marcos, R. Martínez-Máñez, F. Sancenón, J. Soto, P. Amorós, J. El Haskouri, N. Garró, and K. Rurack, *Chem. Eur. J.*, **2008**, *14*, 8267–8278.
30. S. J. Lee, D. R. Bae, W. S. Han, S. S. Lee, and J. H. Jung, *Eur. J. Inorg. Chem.*, **2008**, 1559.
31. M. H. Lee, S. J. Lee, J. H. Jung, H. Lim, and J. S. Kim, *Tetrahedron*, **2007**, *63*, 12087.
32. R. Métivier, I. Leray, B. Lebeau, and B. Valeur, *J. Mater. Chem.*, **2005**, *15*, 2965.
33. S. J. Lee, J.-E. Lee, J. Seo, I. Y. Jeong, S. S. Lee, and J. H. Jung, *Adv. Funct. Mater.*, **2007**, *17*, 3441.
34. L. Gao, J. Q. Wang, L. Huang, X. X. Fan, J. H. Zhu, Y. Wang, and Z. G. Zou, *Inorg. Chem.*, **2007**, *46*, 10287.
35. H. Zhang, P. Zhang, K. Ye, Y. Sun, S. Jiang, Y. Wang, and W. Pang, *J. Lumin.*, **2006**, *117*, 68.
36. L.-L. Li, H. Sun, C.-J. Fang, J. Xu, J.-Y. Jin, and C.-H. Yan, *J. Mater. Chem.*, **2007**, *17*, 4492.
37. J.-Q. Wang, L. Huang, M. Xue, Y. Wang, L. Gao, J. H. Zhu, and Z. Zou, *J. Phys. Chem. C*, **2008**, *112*, 5014.
38. L. Gao, Y. Wang, J. Wang, L. Huang, L. Shi, X. Fan, Z. Zou, T. Yu, M. Zhu, and Z. Li, *Inorg. Chem.*, **2006**, *45*, 6844.
39. G. Wirnsberger, B. J. Scott, and G. D. Stucky, *Chem. Commun.*, **2001**, 119.
40. T. Balaji, M. Sasidharan, and H. Matsunaga, *Anal. Bioanal. Chem.*, **2006**, *384*, 488.
41. T. Balaji, S. A. El-Safty, H. Matsunaga, T. Hanaoka, and F. Mizukami, *Angew. Chem. Int. Ed.*, **2006**, *45*, 7202.
42. S. A. El-Safty, A. A. Ismail, H. Matsunaga, and F. Mizukami, *Chem. Eur. J.*, **2007**, *13*, 9245.

43. S. A. El-Safty, D. Prabhakaran, A. A. Ismail, H. Matsunaga, and F. Mizukami, *Adv. Funct. Mater.*, **2007**, *17*, 3731.
44. S. A. El-Safty, A. A. Ismail, H. Matsunaga, H. Nanjo, and F. Mizukami, *J. Phys. Chem. C*, **2008**, *112*, 4825.
45. M. Comes, G. Rodríguez-López, M. D. Marcos, R. Martínez-Máñez, F. Sancenón, J. Soto, L. A. Villaescusa, P. Amorós, and D. Beltrán, *Angew. Chem. Int. Ed.*, **2005**, *44*, 2918.
46. R. Martínez-Máñez and F. Sancenón, *Chem. Rev.*, **2003**, *103*, 4419.
47. B. T. Nguyen and E. V. Anslyn, *Coord. Chem. Rev.*, **2006**, *250*, 3118.
48. L. Fabbrizzi, N. Marcotte, F. Stomeo, and A. Taglietti, *Angew. Chem. Int. Ed.*, **2002**, *41*, 3811.
49. M. Comes, M. D. Marcos, R. Martínez-Máñez, F. Sancenón, J. Soto, L. A. Villaescusa, and P. Amorós, *Chem. Commun.*, **2008**, 3639.
50. M. Montalti, L. Prodi, N. Zaccheroni, and G. Falini, *J. Am. Chem. Soc.*, **2002**, *124*, 13540.
51. M. Montalti, L. Prodi, and N. Zaccheroni, *J. Mater. Chem.*, **2005**, *15*, 2810.
52. E. Rampazzo, E. Brasola, S. Marcuz, F. Mancin, P. Tecilla, and U. Tonellato, *J. Mater. Chem.*, **2005**, *15*, 2687.
53. M. Arduini, S. Marcuz, M. Montolli, E. Rampazzo, F. Mancin, S. Gross, L. Armelao, P. Tecilla, and U. Tonellato, *Langmuir*, **2005**, *21*, 9314.
54. M. Montalti, L. Prodi, N. Zaccheroni, G. Battistini, S. Marcuz, F. Mancin, E. Rampazzo, and U. Tonellato, *Langmuir*, **2006**, *22*, 5877.
55. R. Méallet-Renault, R. Pansu, S. Amigoni-Gerbier, and C. Larpent, *Chem. Commun.*, **2004**, 2344.
56. E. L. Doyle, C. A. Hunter, H. C. Philips, S. J. Webb, and N. H. Williams, *J. Am. Chem. Soc.*, **2003**, *125*, 4593.
57. Y. Zheng, J. Orbulescu, X. Ji, F. M. Andreopoulos, S. M. Pham, and R. M. Leblanc, *J. Am. Chem. Soc.*, **2003**, *125*, 2680.
58. M. Crego-Calama and D. N. Reinhoudt, *Adv. Mater.*, **2001**, *13*, 1171.
59. L. Basabe-Desmonts, J. Beld, R. S. Zimmerman, J. Hernando, P. Mela, M. F. García Parajó, N. F. van Hulst, A. van den Berg, D. N. Reinhoudt, and M. Crego-Calama, *J. Am. Chem. Soc.*, **2004**, *126*, 7293.
60. R. Zimmerman, L. Basabe-Desmonts, F. van der Baan, D. N. Reinhoudt, and M. Crego-Calama, *J. Mater. Chem.*, **2005**, *15*, 2772.
61. M.-C. Daniel and D. Astruc, *Chem. Rev.*, **2004**, *104*, 293.
62. U. Kreibig and M. Vollmer, *Optical Properties of Metal Clusters*, Springer, Berlin, **1998**.
63. N. L. Rosi and C. A. Mirkin, *Chem. Rev.*, **2005**, *105*, 1547.
64. E. Katz and I. Willner, *Angew. Chem. Int. Ed.*, **2004**, *43*, 6042.
65. S.-Y. Lin, S.-W. Liu, C.-M. Lin, and C.-H. Chen, *Anal. Chem.*, **2002**, *74*, 330.
66. S.-Y. Lin, C. H. Chen, M. C. Lin, and H. F. Hsu, *Anal. Chem.*, **2005**, *77*, 4821.
67. S. Y. Lin, S. H. Wu and C. H. Chen, *Angew. Chem. Int. Ed.*, **2006**, *45*, 4948.
68. J. Liu and Y. Lu, *J. Am. Chem. Soc.*, **2005**, *127*, 12677.
69. C.-C. Huang and H.-T. Chang, *Chem. Commun.*, **2007**, 1215.
70. S.-J. Chen and H.-T. Chang, *Anal. Chem.*, **2004**, *76*, 3727.
71. V. Pavlov, Y. Xiao, and I. Willner, *Nano Lett.*, **2005**, *5*, 649.
72. S. Watanabe, M. Sonobe, M. Arai, Y. Tazume, T. Matsuo, T. Nakamura, and K. Yoshida, *Chem. Commun.*, **2002**, 2866.
73. Y. Kubo, S. Uchida, Y. Kemmochi, and T. Okubo, *Tetrahedron Lett.*, **2005**, *46*, 4369.
74. J. Stangl, V. Holý, and G. Bauer, *Rev. Mod. Phys.*, **2004**, *76*, 725.

75. C. Burda, X. Chen, R. Narayanan, and M. A. El-Sayed, *Chem. Rev.*, **2005**, *105*, 1025.
76. A. L. Rogach, A. Eychmüller, S. G. Hickey, and S. V. Kershaw, *Small*, **2007**, *3*, 536.
77. J. M. Costa-Fernández, R. Pereiro, and A. Sanz-Medel, *Trends Anal. Chem.*, **2006**, *25*, 207.
78. J. M. Costa-Fernandez, *Anal. Bioanal. Chem.*, **2006**, *384*, 37.
79. D. M. Willard, T. Mutschler, M. Yu, J. Jung, and A. V. Orden, *Anal. Bioanal. Chem.*, **2006**, *384*, 564.
80. J. F. Callan, A. P. de Silva, R. C. Mulrooney, and B. McCaughan, *J. Inclusion Phenom. Mol. Recognit. Chem.*, **2007**, *58*, 257.
81. X. Michalet, F. F. Pinaud, L. A. Bentolila, J. M. Tsay, S. Doose, J. J. Li, G. Sundaresan, A. M. Wu, S. S. Gambhir, and S. Weiss, *Science*, **2005**, *307*, 538.
82. I. L. Medintz, H. T. Uyeda, E. R. Goldman, and H. Mattoussi, *Nat. Mater.*, **2005**, *4*, 435.
83. Y. Zhong, N. Kaji, M. Tokeshi, and Y. Baba, *Expert Rev. Proteomics*, **2007**, *4*, 565.
84. Z. B. Li, W. Cai, and X. Chen, *J. Nanosci. Nanotechnol.*, **2007**, *7*, 2567.
85. Y. Chen and Z. Rosenzweig, *Anal. Chem.*, **2002**, *74*, 5132.
86. K. Konishi and T. Hiratani, *Angew. Chem. Int. Ed.*, **2006**, *45*, 5191.
87. J.-G. Liang, X.-P. Ai, Z.-K. He, and D.-W. Pang, *Analyst*, **2004**, *129*, 619.
88. Y. Lai, Y. Yu, P. Zhong, J. Wu, Z. Long, and C. Liang, *Anal. Lett.*, **2006**, *39*, 1201.
89. C. Bo and Z. Ping, *Anal. Bioanal. Chem.*, **2005**, *381*, 986.
90. K.M. Gattás-Asfura and R.M. Leblanc, *Chem. Commun.*, **2003**, 2684.
91. B. Tang, J. Niu, C. Yu, L. Zhuo, and J. Ge, *Chem. Commun.*, **2005**, 4184.
92. W. J. Jin, J. M. Costa-Fernández, R. Pereiro, and A. Sanz-Medel, *Anal. Chim. Acta*, **2004**, *552*, 1.
93. W. J. Jin, T. Fernández-Argüelles, J. M. Costa-Fernández, R. Pereiro, and A. Sanz-Medel, *Chem. Commun.*, **2005**, 883.
94. J. R. Lakowicz, I. Gryczynski, Z. Gryczynski, and C. J. Murthy, *J. Phys. Chem. B*, **1999**, *103*, 7613.
95. D. B. Cordes, S. Gamsey, and B. Singaram, *Angew. Chem. Int. Ed.*, **2006**, *45*, 3829.
96. T. Jin, F. Fujii, H. Sakata, M. Tamura, and M. Kinjo, *Chem. Commun.*, **2005**, 4300.
97. E. Oh, M.-Y. Hong, D. Lee, S.-H. Nam, H. C. Yoon, and H.-S. Kim, *J. Am. Chem. Soc.*, **2005**, *127*, 3270.
98. D. Suzuki and H. Kawaguchi, *Langmuir*, **2006**, *22*, 3818.
99. J. Lee and N. A. Kotov, *Nano Today*, **2007**, *2*, 48.
100. J. Lee, A. O. Govorov, and N. A. Kotov, *Angew. Chem. Int. Ed.*, **2005**, *44*, 7439.
101. E. Rizzarelli and G. Vecchio, *Coord. Chem. Rev.*, **1999**, *188*, 343.
102. O. H. Schmitt, *Paper presented at the Third International Biophysics Congress*, Boston, Aug. 29–Sept. 3, **1969**.
103. Y. Bar-Cohen, *Bioinsp. Biomim.*, **2006**, *1*, P1.
104. J. F. V. Vincent, O. A. Bogatyreva, N. R. Bogatyrev, A. Bowyer, and A.-K. Pahl, *J. R. Soc. Interface*, **2006**, *3*, 471.
105. A. B. Descalzo, K. Rurack, H. Weisshoff, R. Martínez-Máñez, M. D. Marcos, P. Amorós, K. Hoffmann, and J. Soto, *J. Am. Chem. Soc.*, **2005**, *127*, 184.
106. M. Comes, M. D. Marcos, R. Martínez-Máñez, F. Sancenón, J. Soto, L. A. Villaescusa, P. Amorós, and D. Beltrán, *Adv. Mater.*, **2004**, *16*, 1783.
107. S. Basurto, T. Torroba, M. Comes, R. Martínez-Máñez, F. Sancenón, L. Villaescusa, and P. Amorós, *Org. Lett.*, **2005**, *7*, 5469.

108. B. García-Acosta, M. Comes, J. L. Bricks, M. A. Kudinova, V. V. Kurdyukov, A. I. Tolmachev, A. B. Descalzo, M. D. Marcos, R. Martínez-Máñez, A. Moreno, F. Sancenón, J. Soto, L. A. Villaescusa, K. Rurack, J. M. Barat, I. Escriche, and P. Amorós, *Chem. Commun*., **2006**, 2239.
109. V. S.-Y. Lin, C.-Y. Lai, J. Huang, S.-A Song, and S. Xu, *J. Am. Chem. Soc*., **2001**, *123*, 11510.
110. D. R. Radu, C.-Y. Lai, J. W. Wiench, M. Pruski, and V. S.-Y. Lin, *J. Am. Chem. Soc*., **2004**, *126*, 1640.
111. M. Comes, M. D. Marcos, R. Martínez-Máñez, M. C. Millán, J. V. Ros-Lis, F. Sancenón, J. Soto, and L. A. Villaescusa, *Chem. Eur. J*., **2006**, *12*, 2162.
112. A. B. Descalzo, M. D. Marcos, C. Monte, R. Martínez-Máñez, and K. Rurack, *J. Mater. Chem*., **2007**, *17*, 4716.
113. J. L. Meinershagen and T. J. Bein, *J. Am. Chem. Soc*., **1999**, *121*, 448.
114. T. A. Dickinson, J. White, J. S. Kauer, and D. R. Walt, *Nature*, **1996**, *382*, 697.
115. T. A. Dickinson, K. L. Michael, J. S. Kauer, and D. R. Walt, *Anal. Chem*., **1999**, *71*, 2192.
116. S. Tao and G. Li, *Colloid Polym. Sci*., **2007**, *285*, 721.
117. (a) D. Julthogpiput, Y. H. Lin, J. Teng, E. R. Zubarev, and V. V. Tsukruk, *J. Am. Chem. Soc*., **2003**, *125*, 15912. (b) D. Julthogpiput, Y. H. Lin, J. Teng, E. R. Zubarev and V. V. Tsukruk, *Langmuir*, **2003**, *19*, 7832. (c) S. Chia, J. Cao, J. F. Stoddart, and J. I. Zink, *Angew. Chem. Int. Ed*., **2001**, *40*, 2447. (d) R. Wang, K. Hashimoto, A. Fujishima, M. Chikuni, E. Kojima, A. Kitamura, M. Shimohigoshi, and T. Watanabe, *Nature*, **1997**, *388*, 431.
118. (a) E. Raphael and P. G. de Genness, *J. Phys. Chem*., **1992**, *96*, 4002. (b) M. Ruths, D. Johannsmann, J. Ruhe, and W. Knoll, *Macromolecules*, **2000**, *33*, 3860.
119. (a) J. Klein, E. Kumacheva, D. Mahalu, D. Perahia, and L. J. Fetters, *Nature*, **1994**, *370*, 634. (b) A. Berman, S. Steinberg, S. Campbell, A. Ulman, and J. Israelachvili, *Tribol. Lett*., **1998**, *4*, 43.
120. (a) I. Y. Galaev and B. Mattiasson, *Trends Biotechnol*., **1999**, *17*, 335. (b) I. A. Aksay, M. S. Trau, I. Manne, I. Honma, N. Yao, L. Zhou, P. Fenter, P. M. Eisenberger, and S. M. Gruner, *Science*, **1996**, *273*, 892.
121. See for instance: (a) A. K. Boal and V. M. Rotello, *J. Am. Chem. Soc*., **1999**, *121*, 4914. (b) M.-C. Daniel, J. Ruiz, S. Nlate, J. Palumbo, J.-C. Blais, and D. Astruc, *Chem. Commun*., **2001**, 2000. (c) A. M. Allgeier and C. A. Mirkin, *Angew. Chem. Int. Ed*., **1998**, *37*, 894. (d) H. M. Goldston, A. N. Scribner, S. A. Trammell, and L. M. Tender, *Chem. Commun*., **2002**, 416. (e) M. Lahav, E. Katz, A. Doron, F. Patolsky, and I. Willner, *J. Am. Chem. Soc*., **1999**, *121*, 862. (f) M. J. Cook, A.-M. Nygard, Z. Wang, and D. A. Rusell, *Chem. Commun*., **2002**, 1056. (g) K. Kyungpil, W. S. Jeon, J.-K. Kang, J. W. Lee, S. Y. Jon, T. Kim, and K. Kim, *Angew. Chem. Int. Ed*., **2003**, *42*, 2293.
122. See for instance: (a) M. Asakawa, M. Higuchi, G. Mattersteig, T. Nakamura, A. R. Pease, F. M. Raymo, T. Shimizu, and J. F. Stoddart, *Adv. Mater*., **2000**, *12*, 1099. (b) C. P. Collier, G. Mattersteig, E. W. Wong, Y. Luo, K. Beverly, J. Sampaio, F. M. Raymo, J. F. Stoddart, and J. R. Heath, *Science*, **2000**, *289*, 1172. (c) C. P. Collier, J. O. Jeppersen, Y. Luo, J. Perkins, E. W. Wong, J. R. Heath, and J. F. Stoddart, *J. Am. Chem. Soc*., **2001**, *123*, 12632. (d) I. Willner, V. Pardo-Yissar, E. Katz, and K. T. Ranjit, *J. Electroanal. Chem*., **2001**, *497*, 172.
123. (a) P. Bühlmann, H. Aoki, K. P. Xiao, S. Amemiya, K. Tohda, and Y. Umezawa, *Electroanalysis*, **1998**, *10*, 1149. (b) M. Sugawara, A. Hirano, P. Bühlmann, and Y. Umezawa, *Bull. Chem Soc. Jpn*., **2002**, *75*, 187. (c) Y. Umezawa and H. Aoki, *Anal. Chem*., **2004**, *76*, 320A.
124. V. P. Y. Gadzekpo, K. P. Xiao, H. Aoki, P. Bühlmann, and Y. Umezawa, *Anal. Chem*., **1999**, *71*, 5109.
125. V. P. Y. Gadzekpo, P. Bühlmann, K. P. Xiao, H. Aoki, and Y. Umezawa, *Anal. Chim. Acta*, **2000**, *411*, 163.

126. M. Tayaka, P. Bühlmann, and Y. Umezawa, *Mikrochim. Acta*, **1999**, *132*, 55.

127. R. Zugle, J. Kambo-Dorsa, and V. P. Y. Gadzekpo, *Talanta*, **2003**, *61*, 837.

128. K. Bandyopadhyay, H. Liu, S.-G. Liu, and L. Echegoyen, *Chem. Commun*., **2000**, 141.

129. (a) S. Flink, H. Schönherr, G. J. Vancso, F. A. J. Geurts, K. G. C. van Leerdam, F. C. J. M. van Veggel, and D. N. Reinhoudt, *J. Chem. Soc., Perkin Trans*., **2000**, *2*, 2141. (b) S. Flink, B. A. Boukamp, A. van den Berg, F. C. J. M. Van Veggel, and D. N. Reinhoudt, *J. Am. Chem. Soc*., **1998**, *120*, 4652.

130. T. Ito, *J. Electroanal. Chem*., **2001**, *495*, 87.

131. H. Aoki, Y. Umezawa, A. Vertova, and S. Rondinini, *Anal. Sci*., **2006**, *22*, 1581.

132. H. Aoki, K. Hasegawa, K. Tohda, and Y. Umezawa, *Biosens. Bioelectron*., **2003**, *18*, 261.

133. K. P. Xiao, P. Bühlmann, and Y. Umezawa, *Anal. Chem*., **1999**, *71*, 1183.

134. H. Radecka, I. Szymanska, M. Pietraszkiewicz, O. Pietraszkiewicz, H. Aoki, and Y. Umezawa, *Chem. Anal*., **2005**, *50*, 85.

135. Y. Katayama, Y. Ohuchi, H. Higashi, Y. Kudo, and M. Maeda, *Anal. Chem*., **2000**, *72*, 4671.

136. (a) H. Aoki and Y. Umezawa, *Analyst*, **2003**, *128*, 681. (b) H. Aoki and Y. Umezawa, *Electroanalysis*, **2002**, *14*, 1405.

137. H. Kuramitz, K. Sugawara, and S. Tanaka, *Electroanalysis*, **2000**, *12*, 1299.

138. P. Kohli, M. Wirtz, and C. R. Martin, *Electroanalysis*, **2004**, *16*, 9.

139. Y. Jung, H. Bayley, and L. Movileanu, *J. Am. Chem. Soc*., **2006**, *128*, 15332.

140. H. Bayley and C. R. Martin, *Chem. Rev*., **2000**, *100*, 2575.

141. R. Laocharoensuk, A. Bulbarello, S. B. Hocevar, S. Mannino, B. Ogorevc, and J. Wang, *J. Am. Chem. Soc*., **2007**, *129*, 7774.

142. (a) S. Stitzel, R. Byrne, and D. Diamond, *J. Mater. Sci*., **2006**, *41*, 5841. (b) A. Radu, S. Scarmagnani, R. Byrne, C. Slater, K. T. Lau, and D. Diamond, *J. Phys. D, Appl. Phys*., **2007**, *40*, 7238.

143. R. Casasús, E. Aznar, M. D. Marcos, R. Martínez-Máñez, F. Sancenón, J Soto, and P. Amorós, *Angew. Chem. Int. Ed*., **2006**, *45*, 6661.

144. C. Coll, R. Casasús, E. Aznar, M. D. Marcos, R. Martínez-Máñez, F. Sancenón, J. Soto, and P. Amorós, *Chem. Commun*., **2007**, 1957.

CHAPTER 9

Molecular Recognition Processes between Nucleobases and Metal-Oxalato Frameworks

Oscar Castillo, Antonio Luque, Juan P. García-Terán and Pilar Amo-Ochoa

Departamento de Química Inorgánica, Facultad de Ciencia y Tecnología, Universidad del País Vasco, Apartado 644, E–48080 Bilbao, Spain

Departamento de Tecnología Industrial, Universidad Alfonso X "El Sabio", 28691 Villanueva de la Cañada, Madrid, Spain

CONTENTS

Macromolecules Containing Metal and Metal-Like Elements, Volume 9: Supramolecular and Self-Assembled Metal-Containing Materials,
Edited by Alaa S. Abd-El Aziz, Charles E. Carraher Jr., Charles U. Pittman Jr., and Martel Zeldin.

I. INTRODUCTION

The elucidation of the DNA double-stranded helix by Watson and Crick[1] represented not only a breakthrough in the structural biology[2] but also was the starting point for the appealing and flourishing research dedicated to the rational design and elaboration of biomimetic systems based on the interaction of nucleic acids and their building units with a wide range of both organic and inorganic frameworks.[3] The driving force of these multidisciplinary studies has been to gain a wealth of knowledge that helps deepen the understanding of a great diversity of molecular bio-recognition processes and offer a powerful tool for the efficient synthesis of advanced functional materials with tailor-made properties and potential applications for the material sciences[4] and the therapeutic medicine.[5]

Most of the studies concerning DNA/RNA nucleobases have been realized in gas phase[6] or aqueous media,[7] but notable advances have been made in the solid-state chemistry, such as (a) the construction of nanobiological devices,[8] (b) the design and improvement of chemical-biology tools and/or pharmaceutical agents,[9] (c) the stabilization of noncanonical tautomers through interactions with metallic ions[10] and/or hydrogen bonding donor/acceptor species,[11] and (d) the development of artificial receptors for specific DNA/RNA bases recognition for their use as nucleotide sensors or for the determination of low concentrations of therapeutic agents.[12]

Many of the available information obtained to date arises from the knowledge of the structure and reactivity of artificial systems based on transition metal complexes containing nucleobase ligands or analogs.[3c,3d] Most of these complexes are monomers or discrete polymeric species of low nuclearity in which the structural units are held together by means of noncovalent interactions (essentially, hydrogen bonds involving the complementary DNA bases and arene-arene π-stacking of the planar heterocycles of the nucleobases),[13] which are also operative in the control of the conformation and the molecular recognition phenomena of a great diversity of macromolecular biological systems.

A. Molecular Recognition

The term *molecular recognition* refers to the specific interaction between two or more molecules through noncovalent bonding such as hydrogen

bonding, metal coordination, hydrophobic forces, van der Waals forces, π-π interactions, and/or electrostatic effects.

The host and guest involved in molecular recognition processes exhibit molecular complementarity.[14] The design of synthetic receptors for neutral molecules involves π–π stacking and hydrogen-bonding interactions between the host and guest.[15] According to their strength and directional nature compared to other intermolecular noncovalent interactions, hydrogen bonds are the most important and are extremely useful for designing the structure of molecular crystals. However, the binding of such a receptor in aqueous solution finds an important competitor in the solvent itself, which retards the interaction between the host and the guest through forces like H-bonding. Therefore, the alignment of receptor binding sites on a receptor platform must achieve complementary-binding interactions toward a targeted guest. In other words, the chemical and steric features given by a guest molecule have to be matched by a sufficiently predisposed host.[16] Within this context, nucleobase recognition is an important challenge in supramolecular chemistry because of its many biological implications.[17]

The development of artificial receptors for the detection of biologically and environmentally important substrates has received considerable attention in supramolecular chemistry.[18] To achieve this goal in abiotic receptors, a receptor binding unit for the recognition of a guest and a signaling unit are incorporated into the receptor molecule.[19] On the other hand, model studies in molecular recognition have contributed to the development of a wide range of novel molecular devices.[14,20]

B. Nucleobases

The nucleobases are heterocyclic aromatic organic compounds that are basic parts of the nucleic acids. These heterocycles are, in general, the purine bases guanine (G) and adenine (A), and the pyrimidine bases cytosine (C), as well as thymine (T, DNA) or uracil (U, RNA) (Fig. 1).

The nucleobases are quite interesting and versatile ligands due to the large number of donor sites available for metal binding, the H-bonding donor-acceptor sites and the potential for π-π stacking. The use of these noncovalent bonds can be a powerful synthetic tool in the preparation of complex molecular architectures. Figure 2 shows some of the possible noncovalent interactions of adenine that can be employed for the building of supramolecular systems.

The hydrogen bonds are employed by the nucleobases to form base pairs interactions. It is known that there are 28 possible base-pairing motifs that involve at least two hydrogen bonds, which can be formed between the four common nucleobases.[3a] These include reverse Watson-Crick, (Fig. 3a), Hoogsteen and Wobble base pairs (Fig. 3b), and base-triplets (Fig. 3c). In the case of adenine and guanine larger aggregates are also possible.

The nucleobases provide a big number of donor sites that can interact with metal species either directly via coordination to atoms of the heterocycle

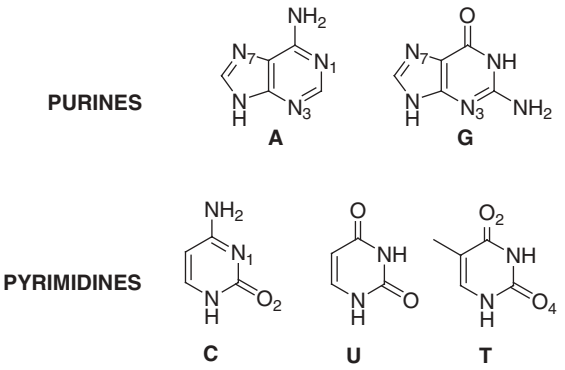

FIGURE 1. Nucleobases.

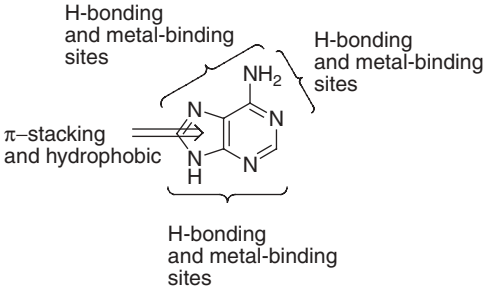

FIGURE 2. Some of the noncovalent interactions present in adenine nucleobase.

(N, C, O), or indirectly via its others ligands. This latter possibility includes hydrogen bond formation—for example, between aqua or amine ligands and suitable acceptors of the nucleobase. A number of excellent reviews have been published about this topic.[3d] Taking into account the direct metal-nucleobase binding, a few general rules can be summarized:

1. The N(7) positions of the purine bases G and A, are major binding sites of metal ions, irrespective of the nature of the metal ion.
2. The floor of the minor groove of double-stranded DNA also presents metal binding sites. Among these, the combination of A-N(3) and T-O(2) is particularly efficient.
3. In the isolated bases, virtually any site of the heterocyclic base can be metalated, including C atoms.
4. Metal binding to sites normally carrying protons (NH, NH_2, CH sites) is possible and does not necessarily require strongly basic reaction conditions.
5. Multiple metalation reactions at nucleobases are quite common and facilitated by initial nucleobase deprotonation. Frequently, metal binding sites are sufficiently close to permit metal–metal interactions.

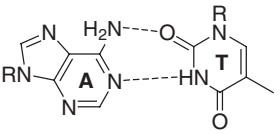

(a) Reverse Watson-Crick basepair

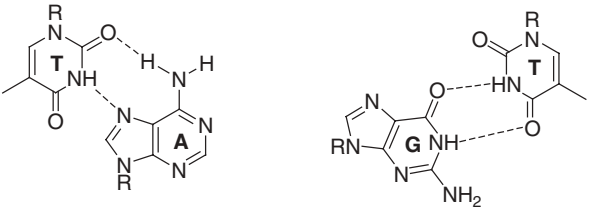

(b) Hoogsteen basepair and Wobble basepairs

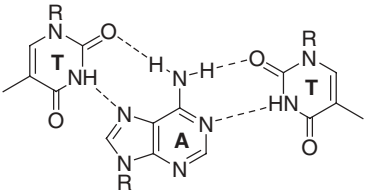

(c) Base-triplets

FIGURE 3. Different hydrogen-bonding modes of nucleobases.

6. Metal complexes of protonated, hence cationic nucleobases are possible.
7. Exocyclic amino groups are metal binding sites only following the removal of one or both protons, hence after deprotonation, or after a shift of a NH_2 proton to another site of the base, which corresponds to a tautomeric change.
8. Metal chelates with nucleobases are also possible.

The study of supramolecular assemblies containing transition-metal ions are of particular interest on account of the functional properties conferred on them by the presence of the metal centers. Metal binding can have a number of effects on the supramolecular chemistry of the nucleobases, for example:

1. Metals bind to the nucleobase and template the formation of special structures.
2. Metals can block the hydrogen bonding site to which they are bound. This result prevents the nucleobase from participating in hydrogen bonding or changes its mode of H-bonding.

3. Metals can have an electronic effect on hydrogen bonding altering the strength of this supramolecular interaction or even result in the formation of rare nucleobase tautomers allowing the stabilization of mismatched basepairs.

Due to the versatility of its binding modes, the nucleobases are extremely useful in the manufacture of supramolecular architectures, either as discrete[21,22] or extended systems.[22] By this way, many and varied examples of supramolecular structures have been designed by the use of metal-nucleobase coordination, hydrogen bonding, and π-π stacking interaction as well.[11,23–25]

C. Oxalate

The oxalato ligand (dianion of oxalic acid; ox) has appeared as a fruitful tecton for the design of a great diversity of homotransition and heterotransition metal compounds, which have played a key role in areas such as inorganic crystal engineering and molecule-based magnetism.[26] The main reasons for the extensive use of this old but evergreen ligand are (a) its remarkable ability to mediate electronic effects between metal centers, affording compounds with a wide range of magnetic properties; and (b) the prevalence of its rigid bischelating bridging mode, providing some degree of predictability with regard to the structural characteristics of the resulting metal-oxalato networks. The topology and dimensionality of polymeric networks based on the oxalato-bridged ligand essentially depend on the shape of the templating counterions, on the features of the auxiliary organic ligands used to complete the metal coordination sphere, or both (Fig. 4).[27–35] The formation of hexagonal two-dimensional $[M^{II}M^{III}(ox)_3]^-$ (M^{II} = V, Cr, Mn, Fe, Co, Ni, Cu, or Zn; M^{III} = V, Cr, or Fe) honeycomb anionic layers is induced by voluminous achiral cations, such as $[XR_4]^+$ (X = N or P; R = phenyl, *n*-propyl, *n*-butyl, or *n*-pentyl), decamethylferrocenium, and tetrathiafulvalene derivatives.[27] The use of chiral tris-chelated transition-metal diimine complexes $[M(L)_3]^{m+}$ (L = 2,2′-bipyridine or phenantroline; m = 2 or 3) favors the formation of helical three-dimensional $[M_2(ox)_3]^{n-}$ networks where cation and anion exhibit inverted chirality.[28] Discrete oligonuclear species (0D) are obtained by using multidentate N- or O- donor ligands that block most of the coordination sites around the metal center, precluding the formation of extended polymeric metal-oxalato systems of higher dimensionality.[29,30,31]

The aim of the present chapter is to look at the structures of transition-metal-oxalate complexes with nucleobases as a valuable source of information on molecular recognition patterns controlling the formation of these systems. Therefore, we focus our attention not only on the metal–nucleobase binding modes but also on the intramolecular interligand interactions, which cooperate with the coordination bond in the stabilization of the resulting mixed-ligand complexes.

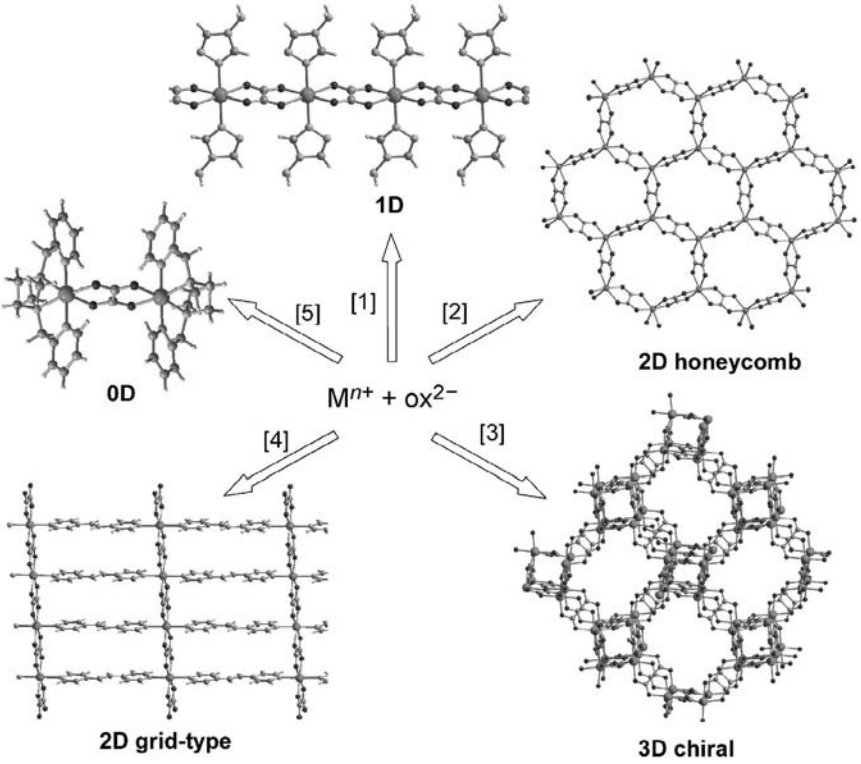

FIGURE 4. Tailoring of metal-oxalato frameworks by using different organic ligands and/or templating counterions: [1] monodentate *N*-containing rings; [2] achiral cations; [3] chiral tris-chelated diimine cationic complexes; [4] bidentate ligands such as 4,4-bipy, piperidine, bpe, and bpa; and [5] multidentate blocking *N*- or *O*-donor ligands.

II. METAL-OXALATO-NUCLEOBASE EXTENDED SYSTEMS

In the framework of our previous research on the chemistry of polymeric complexes based on the oxalato–bridging ligand, we have set up a strategy for the design of one-dimensional complexes with general formula $[M(\mu\text{-ox})(L)_2]_n$ containing substituted pyridine derivatives as terminal ligands.[32,36–38] By using similar synthetic routes, we succeeded in preparing a family of one-dimensional (1D) complexes in which the pyridine bases are replaced by nucleobases, such as purine (pur) and/or adenine (Hade).[35]

The main structural feature common to all compounds is the presence of 1D zigzag chains (Fig. 5) in which *cis*–$[M(H_2O)(L)]^{2+}$ units are sequentially bridged by bis-bidentate centrosymmetric oxalato ligands with dihedral angles

between two consecutive ones of about 90° and 80° for purine and adenine compounds, respectively. The M · · · M intrachain distances across the oxalato bridges vary from 5.236(2) to 5.574(1) Å, depending on the metal center. The metal atoms (placed on a general position) exhibit a distorted octahedral coordination formed by four oxygen atoms from two bridging oxalato ligands, one water molecule and one endocyclic nitrogen atom of the nucleobase in the *cis* position, resulting in a MO_4O_wN chromophore.

The purine itself, without the exo-cyclic N6 amino group, possesses a great coordination versatility, but a scarce number of complexes has been structurally characterized so far, probably because it is not usually present in biopolymers.[39-41] In the isostructural compounds $[M(\mu\text{-ox})(H_2O)(\text{pur-}\kappa N^9)]_n$ (M^{II} = Cu, Co, Mn and Zn), the neutral purine (pur) behaves as a N9-monodentate ligand (Fig. 6).

Other cases of transition-metal ion binding to the imidazole ring N9 atom of the purine ligand have been reported in the monomer $[TiCl(cp)_2(\text{pur-}\kappa N^9)]$ (cp is the cyclopentadienyl anion) with a purinate monoanion[42] and a series of neutral dinuclear and mononuclear gold(I) complexes with phosphine and purin-9-ate synthesized under basic conditions.[43] There are reported examples of Mn(II) binding to N donor sites of nucleobases in biopolymeric systems, but coordinative Mn-N linkages involving isolated nucleobases, as seen in

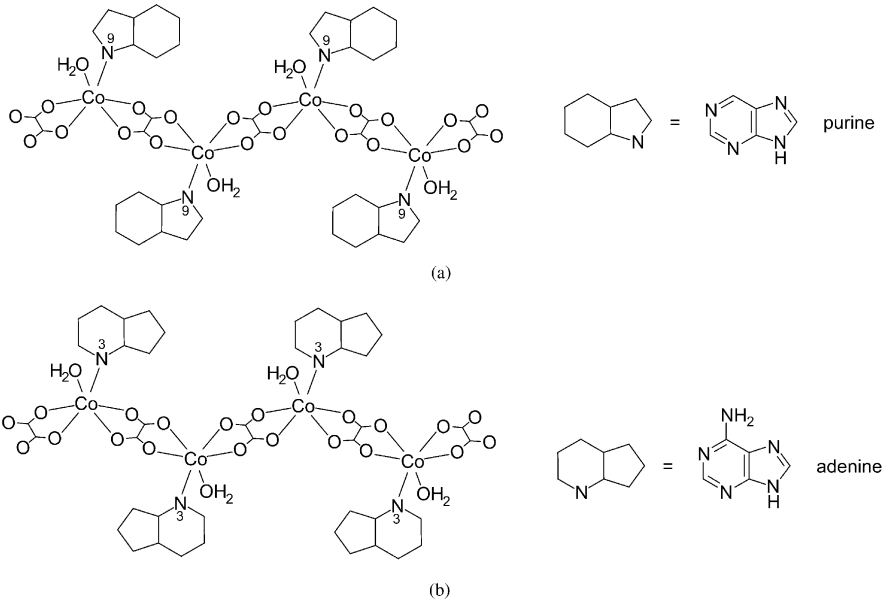

FIGURE 5. The polymeric chains of compounds: (a) $[M(\mu\text{-ox})(H_2O)(\text{pur-}\kappa N^9)]_n$ (M^{II} = Cu, Co, Mn and Zn) and (b) $\{[M(\mu\text{–ox})(H_2O)(7H\text{-ade-}\kappa N^3)] \cdot 2(9H\text{-ade}) \cdot (H_2O)\}_n$ (M^{II} = Co and Zn).

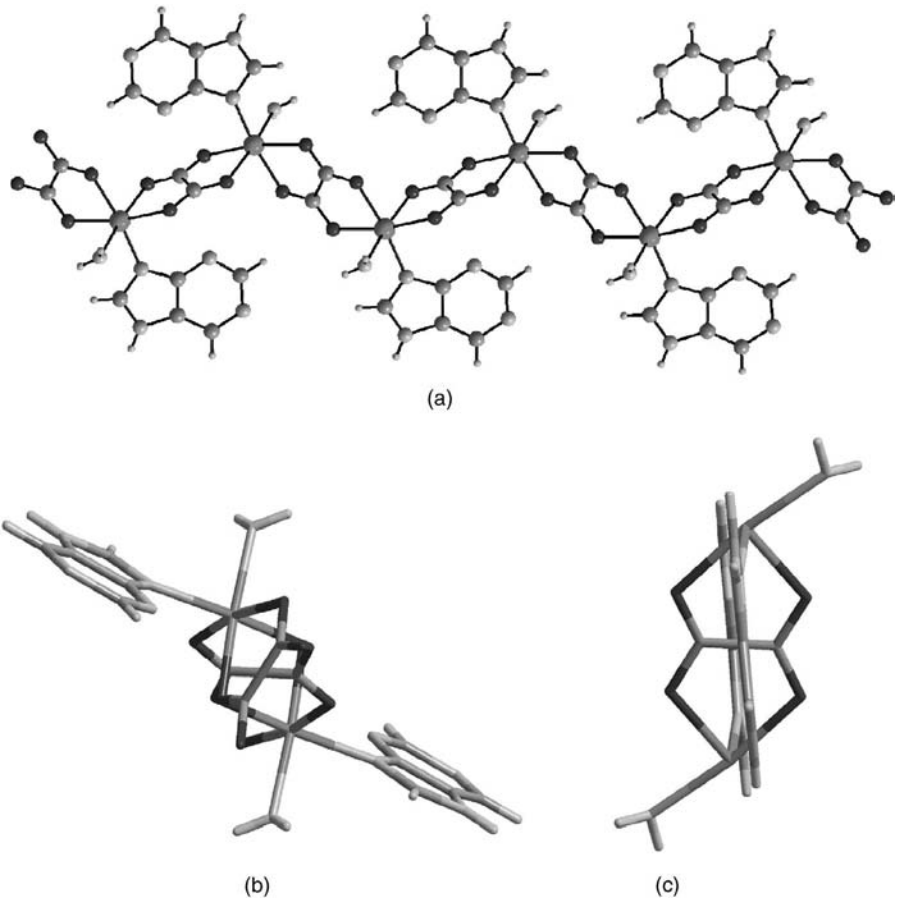

FIGURE 6. (a) A fragment of the polymeric chain of compounds $[M(\mu\text{-ox})(H_2O)(\text{pur-}\kappa N^9)]_n$. (b) and (c) Perspective views showing the arrangement of the purine ligands within the chains.

$[Mn(\mu\text{-ox})(H_2O)(\text{pur-}\kappa N^9)]_n$, are extremely rare in structurally characterized coordination compounds containing isolated nucleobases. Mn(II) is employed as a substitute for Mg(II) in supporting nucleic acid folding and function in vitro[44,45] and it has often been employed to investigate potential metal binding sites in nucleobases. Nevertheless, the coordination details may differ between the two ions[46] because Mg(II) and high-spin Mn(II) are similar but not identical in properties (such as ionic radius, enthalpy of hydration, and coordination preferences).[47] For example, Mn(II) replaced Mg(II) at all sites that included innersphere coordination to the complex folded structure of the group I P4-P6 RNA, but the indirect interactions through aqua ligands of the hydrated Mg(II) ions are only partially replaced by direct coordination

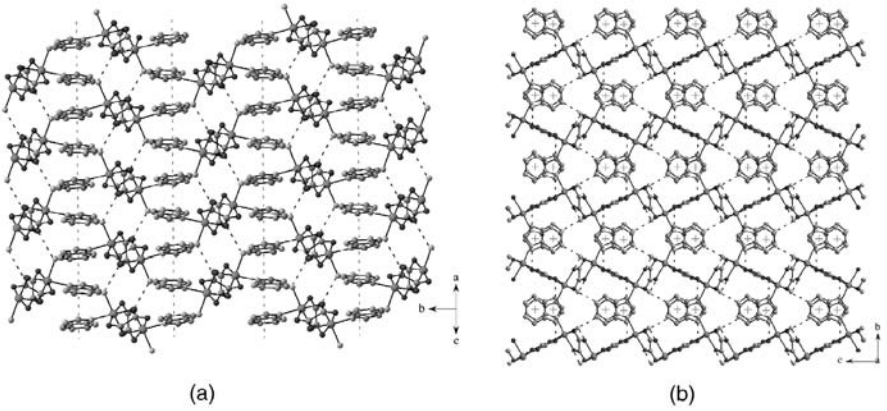

FIGURE 7. Projections of the cristal packing of the compounds with purine ligand showing the noncovalent interactions among the structural units (hydrogen bonds and π-π contacts).

between the Mn and phosphate or nucleid acid base positions.[45] A 10-nt RNA duplex containing sheared adenine:guanine basepairs[48] and the hammer-head rybozyme[46,49] were shown to have a similar Mn(II) binding pattern involving the phosphate oxygen of the adenosine residue and the N7 position of the preceding guanine residue.

The polymeric chains of these compounds run along the [*101*] direction and they are interconnected through short hydrogen bonds of type Ow–H · · · O(ox) giving rise to sheets that spread out along the crystallographic *ac*-plane (Fig. 7). The purine ligands are projected forward to the outside of the layers along the *b*-direction and cross-link adjacent sheets by means of two hydrogen bonds: O5w–H1w · · · N1 (as acceptor) and N7–H7 · · · O2 (as donor). The overall three-dimensional (3D) supramolecular structure is stabilized by significant offset face-to-face π–π stacking interactions between the aromatic rings of purine bases belonging to adjacent layers with interplanar distances of ∼ 3.3 Å.

It should be pointed out that the parallel orientation of the purine ligands with respect to the metal-oxalato framework locates the nonprotonated minor groove N3 atom over the carbon–carbon bond of one centrosymetric oxalato ligand with a mean N3 · · · C distance of 3.0 Å and a dihedral angle between the pyrimidinic ring and the oxalato plane of ∼ 90° (Fig. 8). This fact precludes the involvement of the potential hydrogen-bonding N3 atom in any other interaction.

As seen for compound $[Co(\mu\text{-ox})(H_2O)(\text{pur-}\kappa N^9)]_n$, this crystal structure is flexible enough to allow the random partial subtitution of the purine ligands for adenine ligands giving an isomorphous compound with formula $[Co(\mu\text{–ox})(H_2O)(\text{pur-}\kappa N^9)_{0.76}(7H\text{-ade-}\kappa N^9)_{0.24}]_n$. Its crystallographic parameters are similar, but the orientation of the terminal purine ligands and the partial replacement of purine by adenine (6-aminopurine) with an additional exocyclic

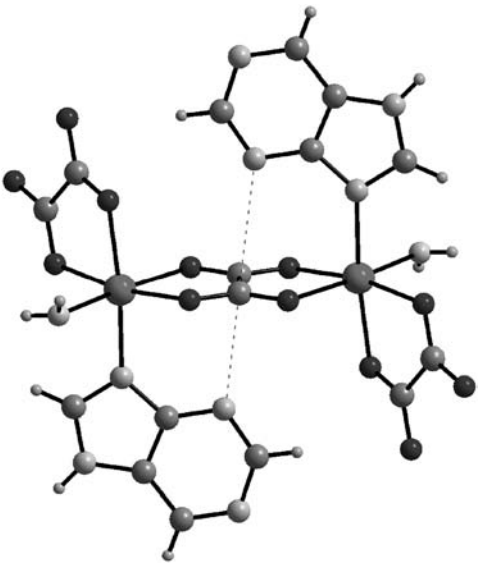

FIGURE 8. Relative arrangement of the purine and oxalato ligands.

amino group results in a slight increase of the distance between the sheets and, as a consequence, the unit cell *b* parameter is longer [16.148(1) vs. 16.457(2) Å]. Figure 9 shows the additional hydrogen bonds involving the exocyclic amino group that are responsible for this elongation.

In the zigzag polymeric chains of compounds $\{[M(\mu\text{–ox})(H_2O)(7H\text{-ade-}\kappa N^3)] \cdot 2(9H\text{-ade}) \cdot (H_2O)\}_n$ (M^{II} = Co, Zn), the adenine nucleobase binds to the metal centres through the less basic pyrimidinic N3 atom (Fig. 10) in contrast to what occurs in the previously described purine compounds where the organic ligands are coordinated through the imidazole N9 atom.

Among the nucleobases, adenine shows the widest range of binding possibilities[3d] because it exhibits at least five donor sites (basicity order: N9 > N1 > N7 > N3 > N6-exocyclic). The binding preference of metal ions to the most basic N9 donor atom of the adenine nucleobase (pKa = 9.8)[50] is largely supported from a structural point of view,[51–53] and the shift of the hydrogen atom to the pyrimidinic N1 atom or the major groove N7 position is observed for neutral ligands. Nevertheless, a great variety of complexes with different metal-ion binding patterns have been reported (Fig. 11).[11]

So far, structurally characterized examples of Co(II)–adenine complexes show a N9-coordination mode of the DNA nucleobase.[10a,52,54] The monodentate coordination mode through the minor groove N3 site is likewise less common and it has been described[10b,55–57] for several compounds containing Cu, Pd, and Ni. It usually stems from steric effects around the metal atom and/or the presence of noncovalent interactions stabilizing the crystal structure.

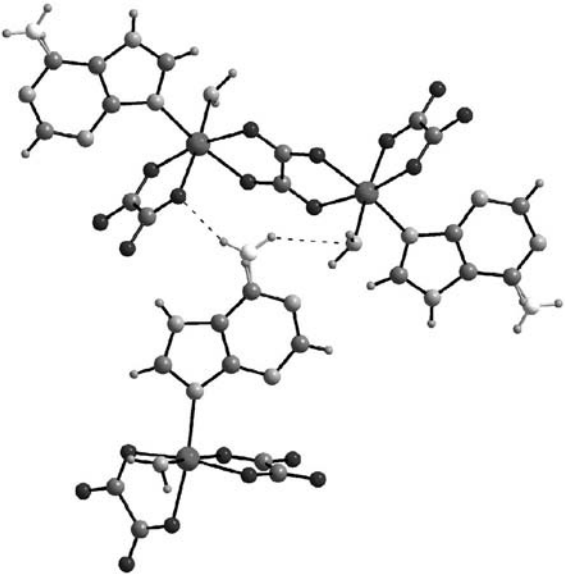

FIGURE 9. Representation of the hydrogen bonding interactions between the exocyclic amino group and the neighboring chain in the purine/adenine compound.

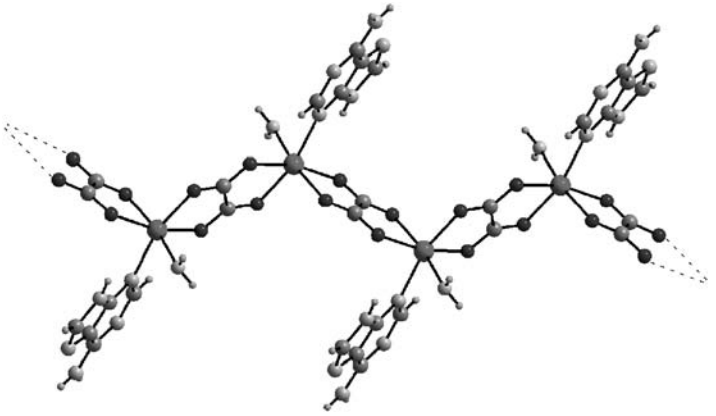

FIGURE 10. Polymeric chain of compound $\{[M(\mu\text{–ox})(H_2O)(7H\text{-ade-}(\kappa N^3)] \cdot 2(9H\text{-ade}) \cdot (H_2O)\}_n$ (M = Co(II), Zn(II)).

One such example is the complex $[Cu(MOBIDA)(7H\text{-ade-}\kappa N^3)(H_2O)] \cdot H_2O$[56] (MOBIDA is the *N*-(*p*-methoxybenzyl)-iminodiacetato(2–) ligand), in which the unusual N3-coordination of the nucleobase is controlled by a molecular recognition process involving the formation of an intramolecular interligand N7(imidazole-like)–H $\cdots$ O(carboxyl) hydrogen-bond and the intermolecular

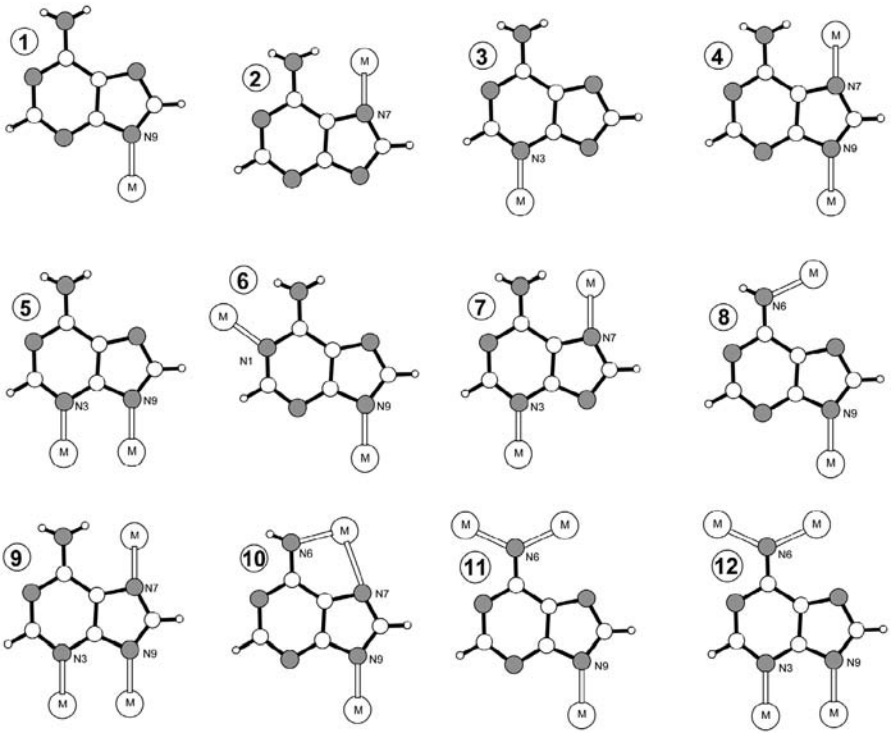

FIGURE 11. Coordination modes for the adenine nucleobase.

interligand π-π stacking interaction between the six-membered rings of benzyl (MOBIDA) and the adenine ligands. This type of binding has not been previously observed for Zn(II)-adenine complexes.[53,58] Hydrated alkali metal ion binding to the N3 position of adenine (in conjunction with O2 of thymine) in the minor groove of DNA has lately received attention in some hydration processes of the B-DNA.[3d] For adenine derivatives, however, there is an increasing number of reports of metal ions binding at this less basic site.[59]

The different coordination sites of the adenine nucleobase generate a markedly different topology of the polymeric chains, relative to the purine complexes. The coordinated adenine molecules are almost perpendicular to the metal-oxalato framework instead of being arranged along the growing axis of the polymeric chain like in the purine complexes. This feature results in the presence of bulkier chains, which leads to a less effective packing with crystallization water molecules and noncoordinated adenine molecules inserted between the chains.

The interplanar distance of 7.52 Å between two consecutive parallel adenine ligands (*HadeA*) in the same side of the polymeric chain permits the insertion of free adenine molecules (*HadeB*) between and aproximately parallel

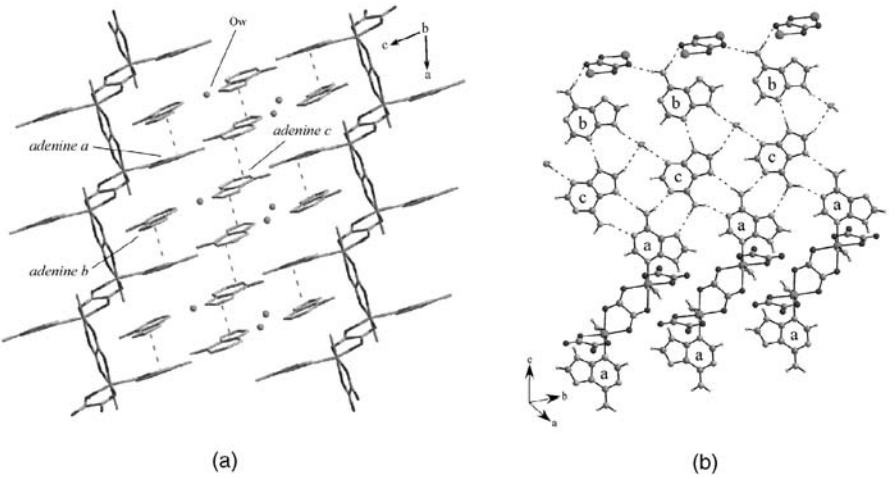

FIGURE 12. Noncovalent interactions among the *9H*-adenine molecules in compounds $\{[M(\mu\text{–ox})(H_2O)(7H\text{-ade-}(N^3)] \cdot 2(9H\text{-ade}) \cdot (H_2O)\}_n$: (a) π-π contacts and (b) hydrogen bonds.

to them with a mean *HadeA-HadeB* separation of 3.22 Å (Fig. 12a). This value is somewhat shorter than that found between two consecutive nucleobases in the B-DNA double helix (3.4 Å). The *HadeB* molecules reinforce the structural cohesiveness of the sheets by means of two hydrogen bonds between the exocyclic amino group and the oxalato O3 oxygen atoms belonging to two adjacent chains placed in the same plane.

In addition, columns of parallel stacked adenine molecules (*HadeC*) are placed between the sheets of polymeric chains and *HadeB* molecules, establishing themselves face-to-face π-π stacking interactions with interplanar distances of about 3.5 Å. Each *HadeC* molecule is surrounded by one uncoordinated *HadeB* molecule and two coordinated *HadeA* ligands. It establishes with them five coplanar hydrogen bonds (Fig. 12b). The N9c–H group forms a strong hydrogen bond to the pyrimidinic N3b atom from a *HadeB* molecule, whereas the interaction with the two *HadeA* ligands implies to the donor and acceptor sites of both Watson-Crick (N1 and N6 atoms) and Hoogsteen (N7 and N6 atoms) edges of the *HadeA* and *HadeC* molecules to give a *zigzag* molecular array. Adenine moieties interacting via Watson-Crick · · · Hoogsteen face hydrogen bonding (N1/HN6 · · · N6/N7) to form a *zigzag* arrangement have been also found in the compound $[Cu(ade\text{-}\kappa N^9)(tren)](ClO_4)$ (tren = tris(2-aminoethyl)amine),[51b] and in Rh(III) and Pt(II) complexes based on N3-bound adenine derivatives.[60] The crystal packing of the polymeric chains and the free adenine molecules generates holes that are occupied by crystallization water molecules. O6w water molecule is surrounded by three coplanar uncoordinated adenine molecules and it is hydrogen-bonded to them. It acts as hydrogen-bond

acceptor for a N9b–H group and behaves as donor for the pyrimidinic N3c atom from a free *HadeC* molecule. Furthermore, it is connected to an adjacent *HadeC* molecule with a weak C8c–H · · · O6w interaction. The quite common distorted tetrahedral geometry around crystallization water molecules is achieved by a strong hydrogen bond formed between the remaining water hydrogen atom and the major groove N7c atom of one *HadeC* molecule placed on a parallel plane. The hydration of DNA bases has been the subject of a large number of theoretical and experimental studies using different methods[61] to gain an insight into the special role that the interaction of nucleobases with water molecules plays in the conformation and activity of biological macromolecules.

Finally, it is interesting to note that the intercalation of the *HadeB* molecules between two *HadeA* ligands places the major groove N7b atom pointing at the carbon–carbon bond of one oxalato bridge with distances to both carbon atoms of 3.039 and 3.068 Å. Indeed, the imidazole N7b atom is not part of the earlier-described network of hydrogen bonds, similarly to the previously described purine bound compounds.

A similar synthetic procedure but using $K_2[Cu(ox)_2] \cdot 2H_2O$ as metal source gives a totally diferent compound $\{[Cu(\mu\text{–}ox)(H_2O)(7H\text{-ade–}\kappa N^9)][Cu(\mu\text{–}ox)(\mu\text{–}H_2O)(7H\text{-ade–}\kappa N^9)] \cdot \sim 10/3H_2O\}_n$.[11] Its structure consists of crystallization water molecules and two crystallographically independent $[Cu(ox)(H_2O)(7H\text{-ade–}\kappa N^9)]$ units, molecule A and molecule B, as shown in Figure 13. In both complex fragments, the Cu(II) atoms are coordinated to two oxygen atoms from a bidentate oxalato ligand, one water molecule, and the imidazole N9 atom from the adenine ligand with Cu1-N9 bond distances of 1.971(5) Å (A) and 1.969(6) Å (B). The CuO_3N chromophores are essentially coplanar and the adenine and oxalato ligands make dihedral angles of 8.8° (A) and 11.3° (B), respectively.

Each complex unit is connected to two symmetric related ones through weaker axial Cu-O interactions to create neutral ribbons with Cu · · · Cu distances coincident with the *a* parameter of the unit cell [3.587(1) Å]. Whereas the metallic atoms of the A chain are bridged only by the coordinated O1 oxygen atom of the oxalato ligand [Cu1A–O1A(i): 2.848(6) Å], the copper centers in the B chain are additionally joined by the bound water oxygen atom [Cu1B–O1B(i): 2.844(7) Å, Cu1B–O5wB(ii): 2.712(6) Å]. The axial Cu-O_{ox} bond distances exceed the equatorial ones by ∼ 0.95 Å and are similar to those reported in analogous oxalato-copper(II) complexes where the $C_2O_4^{2-}$ group acts in a bidentate-monodentate bridging mode (μ–1,1,2-oxalato).[62]

In both chains, all the adenine ligands are located in the same side of the polymeric framework and they are ring-to-ring stacked, suggesting that π-π stacking interactions contribute to the formation of the one-dimensional chains. The planarity of the complex entities is mainly substained by an intramolecular hydrogen bond involving the coordinated water molecule (as donor) and the N3 site of the nucleobase (as acceptor) but also the parallel stacking of the complex entities presumably play an important role. Indeed, DFT calculations on an isolated complex unit gave an optimized model that

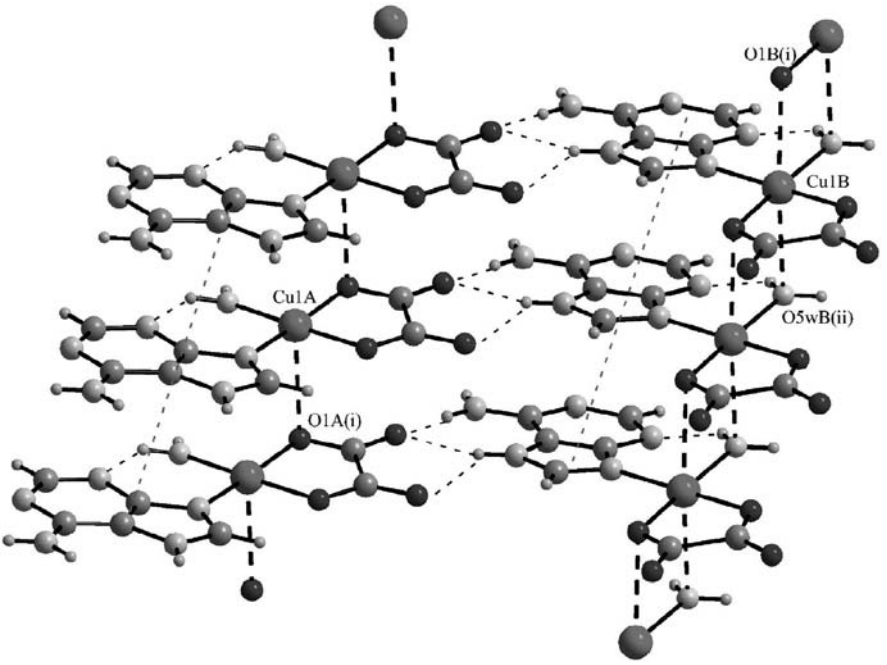

FIGURE 13. One-dimensional chains in compound {[Cu(μ–ox)(H_2O)(*7H*-ade–κN^9)][Cu(μ–ox)(μ–H_2O)(*7H*-ade–κN^9)] · ∼(10/3H_2O}$_n$.

reproduces with acceptable precision the experimental bond distances and angles, and the structural parameters of the intramolecular hydrogen bond. However, the O_3N donor set shows a significant tetrahedral distorsion with a N9-Cu-O bond angle of 158.9°, and the overall structure is clearly nonplanar with a dihedral angle between the oxalato and adenine ligand of 26.0°.

Polymeric one-dimensional chains are further interlinked through an intricate hydrogen bonding network spreading out along the *bc* plane. Watson-Crick-like hydrogen bonds are observed between the adenine moiety (N1 and N6H) and the coordinated oxygen atoms from the oxalato and aqua ligands belonging to the adjacent complex unit. The Hoogsteen donor sites of the nucleobase (N7H and N6H groups) are hydrogen-bonded to two noncoordinated oxygen atoms from one oxalato ligand belonging to another adjacent complex entity. The supramolecular assembling of the structural units, driven by the earlier-described combination of coordinative linkages and hydrogen bonding interactions, creates a 3D porous structure[63] showing two distinct spherical channels along the *a* axis of the unit cell with diameters of about 9 and 7 Å, respectively (Figure 14). The effective volume for inclusion is about 194 $Å^3$/cell, making up 17% of the crystal volume.[64] These parallel cavities are filled by guest water molecules with a high crystallographic disorder.

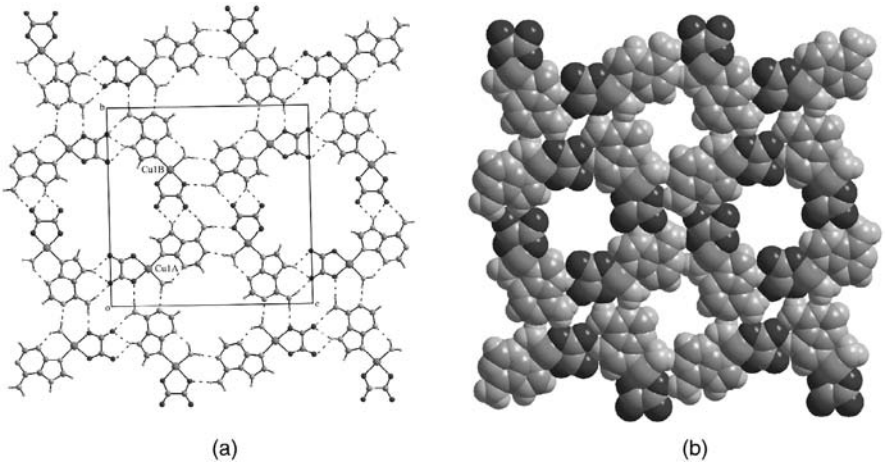

FIGURE 14. (a) Hydrogen bonding interactions among the polymeric chains and (b) channels within the crystal structure of compound $\{[Cu(\mu\text{–ox})(H_2O)(7H\text{-ade–}\kappa N^9)][Cu(\mu\text{–ox})(\mu\text{–}H_2O)(7H\text{-ade–}\kappa N^9)]\cdot\sim(10/3H_2O\}_n$. Crystallization water molecules have been omitted for clarity.

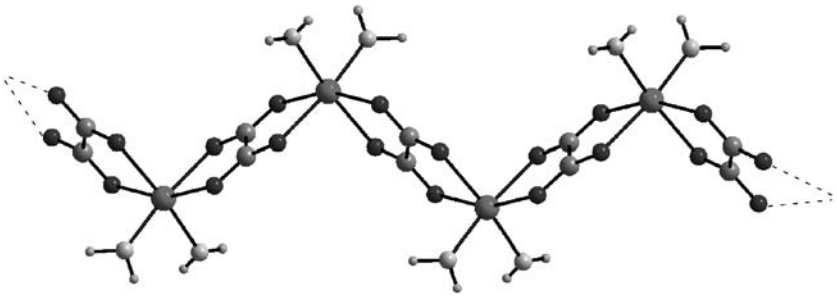

FIGURE 15. Polymeric chain found in compound $\{[Mn(\mu\text{–ox})(H_2O)_2]\cdot(7H\text{-ade})\cdot(H_2O)\}_n$.

All the attempts to obtain 1D chains with the adenine nucleobase being anchored to a manganese(II)-oxalato framework led to the compound $\{[Mn(\mu\text{–ox})(H_2O)_2]\cdot(7H\text{-ade})\cdot(H_2O)\}_n$.[11] Its crystal structure is made up of zigzag chains in which the Mn(II) centers are sequentially bridged by two bis-bidentate centrosymmetric oxalato ligands, but the adenine nucleobase remains free within the crystal building and the metal coordination polyhedron is filled by two water molecules, resulting in a *cis*-$MnO_4(O_w)_2$ chromophore (Fig. 15).

A search in the Cambridge Structural Database[65] revealed that the nucleotide complexes $[Mn(H_2O)_5(5\text{-GMP})]\cdot 2H_2O$ (5-GMP: guanosine-5′-monophosphate)[66] and $[Mn(H_2O)_5(5\text{-IMP})]\cdot 2H_2O$ (5-IMP: inosine-5′-monophosphate)[67] are rare examples of structurally characterized compounds in which an isolated nucleobase

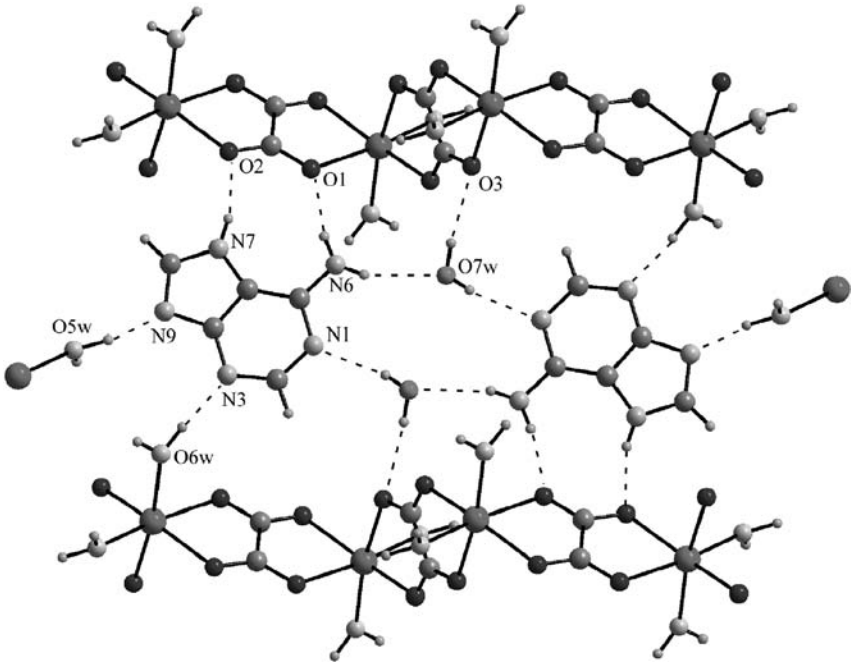

FIGURE 16. Hydrogen-bonded network (dashed lines) around the *7H*-adenine tautomer.

is coordinated to the Mn(II) ion through N donor sites. Mn(II) coordinates the guanine N7 site and five water molecules with through-water mediated indirect hydrogen bonding interactions to the exocyclic carbonyl O6 atom and the phosphate group of the nucleotide. It is interesting that the Mn-ATP and Mn-CMP complexes show only chelation of the metal with oxygen atoms of the phosphate group and/or the cytosine residue.[68] Furthermore, to date, there are only two examples of compounds, characterized in the solid-state, involving direct Mn-N binding between the metal and nonsubstituted nucleobases as ligands.[69] Compound $[Mn(H_2O)_4(7H\text{-ade}–\kappa N^3)_2](ClO_4)_2$ is made up of $[Mn(H_2O)_4(7H\text{-ade}-\kappa N^3)_2]^{2+}$ units, with the Hade molecules directly coordinated to the metal centers through the N3 atoms, while compound $[Mn_2(\mu–H_2O)_2(H_2O)_4(\mu–7H\text{-ade}–\kappa N^3{:}\kappa N^9)_2](NO_3)_4 \cdot 2H_2O$ contains complex dimers, with the Hade molecules directly coordinated through the N3 and N9 atoms. In the monomer $\{[Mn(quin2\text{-}c)_2(H_2O)_2] \cdot 2(9H\text{-ade})\}$ (where quin2-c = quinoline-2-carboxilato), the nucleobase, with only N donor sites, is out of the coordination sphere of the metal ion.[70]

Based on these data, the existence of solely uncomplexed adenine molecules in the crystal building of the $\{[Mn(\mu\text{–ox})(H_2O)_2] \cdot (7H\text{-ade}) \cdot (H_2O)\}$ compound is not surprising. The nucleobase forms centrosymmetric adenine $\cdots$ $(H_2O)_2$ $\cdots$ adenine aggregates (Fig. 16) in which the Watson-Crick edges of each adenine

interact with two symmetry-related water molecules by means of strong hydrogen bonds. The two adenine moities and the water molecules are essentially coplanar and the N6-H61 group acts as hydrogen-bond donor to the O7w water molecule, which in turn is bonded to the N1 acceptor atom from the centrosymmetric moiety.

The adenine nucleobase exists in the lattice in its 7H-amino form due to the efficient stabilization of this noncanonical tautomer by means of a molecular recognition process among the nucleobase, the water molecules, and the manganese-oxalato framework. The proton transfer from N9 to N7 favors the formation of a hydrogen bonded R_2^2 (9) ring between the Hoogsteen face of the nucleobase as donor and the oxygen atoms of carboxylate group belonging to an oxalato bridge as acceptors. The structural parameters for this almost planar nine-membered ring are within the lower range of values reported for hydrogen bonds involving the N7–H group of both neutral and cationic adenine moities (N7 $\cdots$ O: 2.617-3.060 Å, H7 $\cdots$ O: 1.612-2.389 Å, N7–H7$\cdots$O: 149-174°).[65] Analogous structural synthons involving the adenine Hoogsteen face have been reported for the ligands of the complexes (adeninium)$_2$[Co(-$H_2O)_2$(7*H*-ade–κN^9)$_2$](SO$_4$)$_2 \cdot 6H_2O$[54] and [Cu$_2$(7*H*-ade–κN^3,N^9)$_4$ (H_2O)$_2$](ClO$_4$)$_4 \cdot 2H_2O$[71], and for the sulphate[72] and nitrate[73] salts of the 9H,1H,7H-adeninium cation. Indeed, nine-membered rings formed by doubly hydrogen-bonded interactions of the Hoogsteen face are common in both artificial[74] and biological systems, but most of them imply O/N–H $\cdots$ N7 interactions with the N7 site as H-bond acceptor. Hoogsteen AT base-parings found in different structures of DNA and RNA,[75] and the Asn/Glu-adenine interaction in protein-nucleic acid complexes are substained by this kind of hydrogen-bonded rings.[76]

The 7H-adenine tautomer is additionally stabilized by two strong Ow–Hw $\cdots$ N hydrogen bonding interactions involving the N9 and N3 acceptor positions of the nucleobase and coordinated water molecules from adjacent inorganic chains. This compound represented the first X-ray crystallography characterization of the 7H-amino tautomer of the adenine nucleobase as free molecule (without metal coordination). Recently, Mastroprieto et al. have isolated the 7H-adenine tautomeric form in compounds [Mg(H_2O)$_6$]X$_2$ $\cdot$ 2(7*H*-ade) (X = Cl$^-$ and Br$^-$).[69] As in compound {[Mn(μ–ox)(H_2O)$_2$] $\cdot$ (7H-ade) $\cdot$ (H_2O)}$_n$, the most basic imidazole N9 atom is not protonated or involved in metal coordination; their N3 and N9 atoms are also engaged in strong hydrogen bond interactions with coordinated water molecules, which determine the noncovalent stabilization of the adenine tautomer.

It is well known that DNA bases can undergo proton shifts while keeping their neutrality and form different tautomers. Each tautomer has a specific H-bonding donor and acceptor pattern, which increases the posibility of mispairing of purine and pyrimidine bases in DNA, leading to spontaneous point mutations in the genome.[77] Due to its biological impact, the tautomerism of nucleobases has been largely studied using a variety of experimental and theoretical methods.[78] Factors such as excitation, chemical modification, metal

ion interaction, electron attachment, and irradiation have been found to be responsible for the equilibrium between the most stable tautomer and the remaining forms of DNA bases. In addition, hydration plays a significant role in the tautomeric processes, and the water molecules may dramatically change the stability of different tautomeric forms of DNA bases through hydrogen bonding interactions, increasing the populations of the noncanonical tautomers. For adenine, a large number of studies have shown that the 9H-tautomer is energetically favored both in vacuo and water solution.[79–83] The major 9H-adenine tautomer is 7–8 Kcal/mol more stable than the minor 7H-adenine form in gas phase,[79] but the inclusion of bulk electrostatic interactions (such as the presence of polar solvent molecules) significantly stabilizes the 7H-adenine tautomer to approximately 2 Kcal/mol above the 9H-tautomer,[80] due to the much higher dipole moment of the 7H-adenine.[81] A total dipole moment of $\sim$ 7.0 D has been computed for the optimized 7H-adenine tautomer in gas phase (6.2–6.8 D)[79–82] which substantially increases in water solution up to $\sim$ 10.2 D.[83] For comparison, a dipole moment of 2.4 D has been obtained for the 9H-adenine tautomer in solid state,[35] a value that matchs those reported for this tautomeric form in vacuo (2.4–2.7 D),[80–82] and it is slightly lower than the values reported in solution ($\sim$ 3.2 D).[83]

Based on these findings, previous studies have suggested that the 7H-adenine tautomer might be present in a relatively large concentration in aqueous solution ($\sim$20%) and biological systems.[84] Nevertheless, most of the known solid-state structures containing noncoordinated adenine molecules have a hydrogen atom at N9.[35,70,72,73,85,86] The proton is only transferred to the N7 site of the neutral adenine in transition-metal complexes where the nucleobase behaves as either N9-monodentate or N9, N3-bridging ligand and the resulting tautomer is commonly stabilized through a seven-membered ring maintained by means of simultaneous hydrogen bonds of the N7–H and N6–H groups to either chloride ion or water molecule as acceptor.[10a,51a,87,88] Similarly, the rare 1H-[10d] and 3H-amino[10b] tautomers have been characterized only as N9,N7-bidentate ligands.

The deprotonation of the adenine molecule increases its donor positions providing a route to a further polymerization of the entities. This is the case of the 3D polymeric compound $\{[Cu_4(\mu_3\text{-ade-}\kappa N^8{:}\kappa N^7{:}\kappa N^9)_4(ox)_2(H_2O)_4]\cdot \sim 14H_2O\}_n$, whose X-ray crystal structure analysis revealed the presence of an unique 3D framework with two distinct types of neutral building blocks, dimeric $[Cu_2(\mu\text{-ade})_4(H_2O)_2]$ units and mononuclear $[Cu(ox)(H_2O)]$ entities.[23] A perspective view of a fragment of the polymeric structure is given in Figure 17. The dimeric fragment is centrosymmetric and is made up of two Cu(II) atoms bridged by four adeninate anions in a windmill-shaped arrangement with a copper $\cdots$ copper distance of 2.938(2) Å. The basal positions of the distorted square-pyramidal coordination around the copper atom are occupied by two imidazole N9*x* atoms and two pyrimidinic N3*x* atoms of the deprotonated adeninate ligands with regular Cu-N bond distances of about 2.00 Å. Each dimeric fragment is linked to four neighboring monomeric entities via the N7*x*

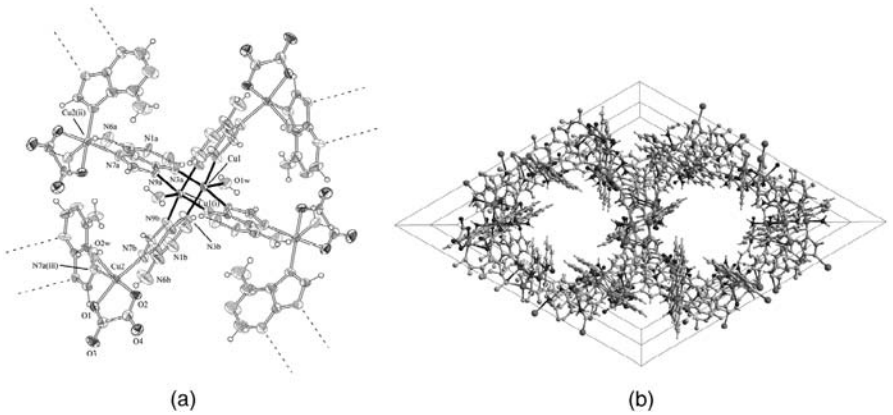

FIGURE 17. (a) A fragment of the polymeric compound showing the coordination mode of the adeninato bridge. (b) Perspective view of the 3D framework along the *c*-axis, showing the presence of nanochannels.

atom from the imidazole ring of the adeninato ligands. Therefore, adeninato anions behave as tridentate μ-N3,N7,N9 bridging ligands.

The self-assembly process directed by the metal-adeninate linkages creates nanotubular channels along the crystallographic *c*-axis with a diameter of about 13 Å, and the effective volume for inclusion is greater than 4916 $Å^3$/cell, making up 40.4% of the crystal volume. Many guest water molecules are trapped in the parallel tubes. The solvated water molecules are engaged themselves and anchored to the inner walls of the nanotubes essentially via hydrogen bonds involving the coordinated water molecules, the uncoordinated oxygen oxalato atoms and the amino groups of the adeninato bridges.

A similar synthetic approach has been also employed to obtain a discrete hexameric $\{(H_2O)_2Cu_2(\mu_3\text{-ade-}\kappa N^8{:}\kappa N^7{:}\kappa N^9)_4[Cu(oda)(H_2O)]_4\} \cdot 6H_2O$ (oda = oxydiacetato) entity, in which the central dimeric core is bonded to four monomeric units.[89] The 3D polymerization is precluded by the blocking tridentate oda ligands.

III. OTHER METAL-NUCLEOBASE 1D EXTENDED SYSTEMS

Examples of *n*-dimensional (*n*D, $n = 1$–3) metal–organic coordination networks based solely on coordinative bonds and containing natural nucleobases as bridging or terminal ligands are quite limited, despite the high scientific interest that such complexes, resembling to DNA double helix dimensionality, might show. To the best of our knowledge, only two 1D polymers containing nonsubstituted purine nucleobases (purine, adenine, and guanine)

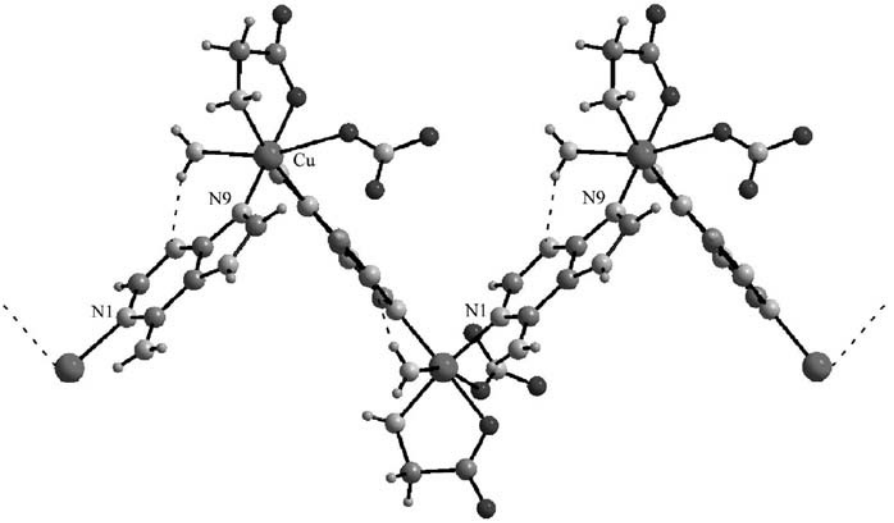

FIGURE 18. 1D chain of compound $\{[Cu(glycine)(\mu\text{–}7H\text{-ade-k}N^1\text{:k}N^9)(H_2O)]NO_3\}_n$.

were structurally characterized up to the beginning of our current program on molecular recognition processes between nucleobases and metal-oxalato frameworks: the compound $\{[Cu(\mu\text{-pur-}\kappa N^7\text{:}\kappa N^9)(H_2O)_4]SO_4 \cdot 2H_2O\}_n$[39] in which the nucleobase acts as a N7,N9 bridging ligand, and the compound $[Cu_2Cl_6(1H,9H\text{-pur-}\kappa N^3)]^n$,[40,90] in which the purinium dication is attached to the metal in N3-monodentate form with a distance of 2.561(3) Å, which is 0.53 Å longer than the average Cu-N3 bond distance found for nucleic-acid constituents containing purine bases.[3d] Recently, a copper(II) coordination polymer has been synthesized in the form of an infinite zigzag chain where each metal is bonded to one glycine, two adenine, one nitrate anion, and a water molecule giving a distorted octahedral coordination geometry with a N_3O_3 donor set (Fig. 18). Adenine molecule acts as a bridging ligand and it is tethered in a zigzag way by copper ions coordinated to N1 and N9 positions, propagating the polymeric chain along the crystallographic *b*-axis, to reveal a structure resembling the periodicity of single stranded nucleic acids. This compound not only shows facile chemical nuclease activity for pBR322 supercoiled DNA but also can be reused keeping its scission activity unchanged.[91]

The compounds $\{[Cu(gua\text{-}\kappa N^3\text{:}\kappa N^7)(H_2O)_3](BF_4)(SiF_6)_{1/2}\}_n$ and $\{[Cu(gua\text{-}\kappa N^3\text{:}\kappa N^7)(H_2O)_3](CF_3SO_3)_2 \cdot H_2O\}_n$ show an unprecedented coordination of neutral guanine.[92] Their crystal structures contain uniform copper(II) chains of formula $[Cu(gua\text{-}\kappa N^3\text{:}\kappa N^7)(H_2O)_3]_n^{2n+}$, where the copper atoms are bridged by guanine ligands coordinated via N3 and N7 (Fig. 19). The values of the copper–copper separation across the bridging guanine ligand are 7.183(1) and 7.123(1) Å, respectively.

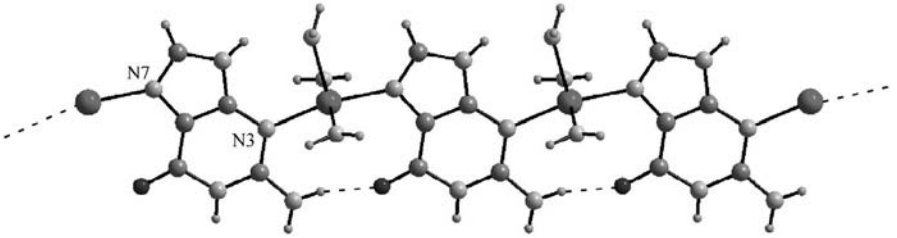

FIGURE 19. Fragment of the polymeric chain of compound $[Cu(gua\text{-}\kappa N^3{:}\kappa N^7)(H_2O)_3]_n^{2n+}$.

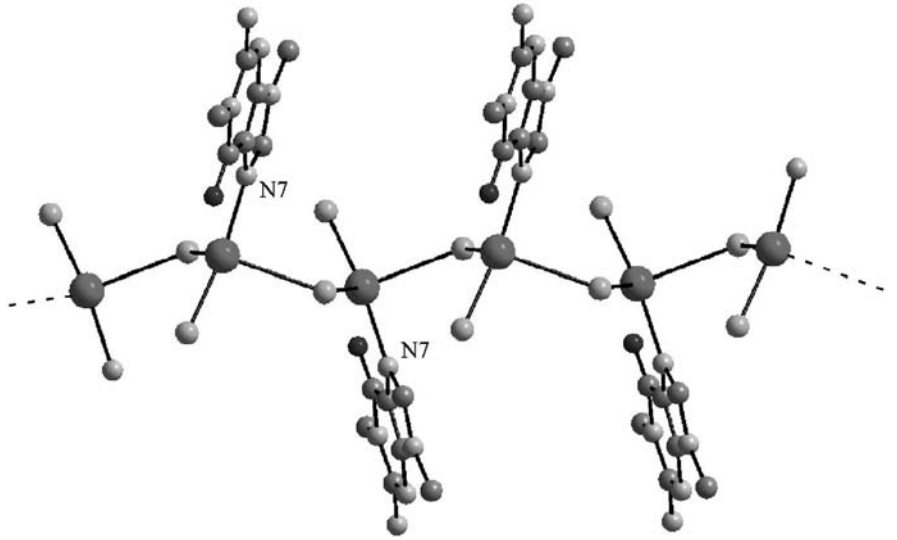

FIGURE 20. Polymeric chain found in compound $\{[HgCl_2(1,9\text{-Megu-}\kappa N^7)] \cdot 2HgCl_2\}_n$.

Other research groups have reported a handful of 1D compounds containing nonnatural nucleobases as terminal or bridging ligands. Stanley and co-workers presented two monodimensional coordination chains of Cd(II) with N6-substituted adenine derivatives (N6-furfuryladenine and N6-benzyladenine). In these structures, the Cd(II) ions present a distorted octahedral geometry formed by the N9 position of the adenine derivatives and five chlorine ions. Two edge chloride ions bridge the two successive Cd(II) atoms. In both complexes, supramolecular hydrogen bonding 2D sheets have been observed.[93]

Lippert and co-workers synthesized a 1D polymeric Hg(II)-nucleobase complex with a guanine derivative (1,9-DiMeG = 1,9-dimethylguanine) by the reaction of $HgCl_2$ with the guanine ligand in a water-alcohol mixture (Fig. 20). The Hg(II) ion is coordinated to one guanine (via N7 position) and three

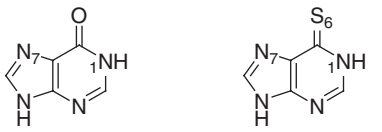

6-oxopurine 6-mercaptopurine

FIGURE 21. 6-Oxopurine and its structural analog 6-mercaptopurine.

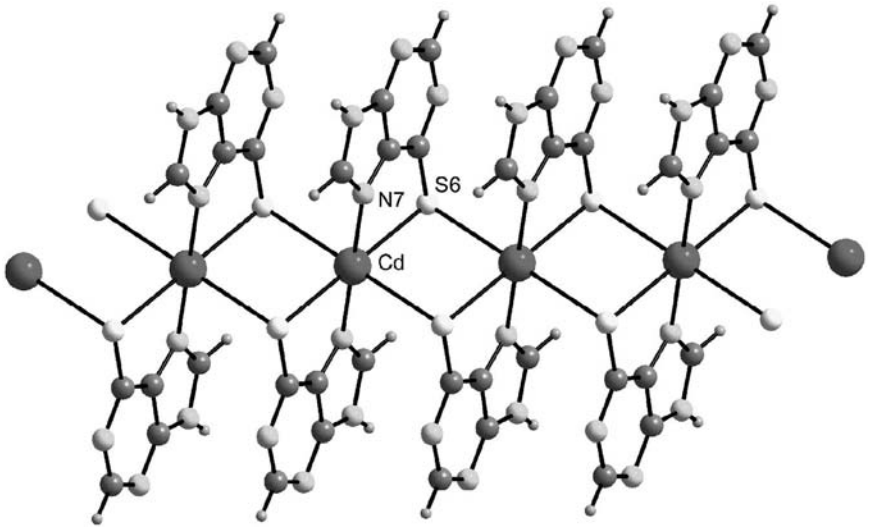

FIGURE 22. Structure of the 1D coordination polymer $[Cd(\mu\text{-}9H\text{-}MP^{-}\text{-}\kappa S^{6},N^{7}\text{:}\kappa S^{6})_2]_n$.

Cl ligands. Two of these Cl act as bridging ligands. The polymeric structure is co-crystallized with $HgCl_2$ molecules.[94]

Zamora and co-workers employed the synthetic ''thio'' analog of the neutral purine hypoxanthine, 6-mercaptopurine ($C_5H_4N_4S$, MP), to obtain a rich family of 1D coordination polymers. 6-mercaptopurine (Fig. 21) has been studied for years because of its interesting applications as an antineoplastic (treatment of human leukemias), immunosuppressive and anti-inflammatory drug.[95] This fact has motivated new research toward the synthesis and biological studies of metal coordination compounds based on MP.

The direct reaction between $Cd(NO_3)_2$ and MP (6-mercaptopurine) leads to formation of the coordination polymer $[Cd(\mu\text{-}9H\text{-}MP^{-}\text{-}\kappa S^{6},N^{7}\text{:}\kappa S^{6})_2 \cdot 2H_2O]_n$ (Fig. 22).[96] Its X-ray structure consists of infinite chains of cadmium atoms octahedrally coordinated by four S6 and two N7 atoms of the μ-mercatopurinate-$\kappa S^{6},N^{7}\text{:}\kappa S^{6}$ ligands. The metal to metal distance within the chain is 3.918 Å. The water molecule does not coordinate to the cadmium atom but it is involved in two strong hydrogen bonds to two other water oxygen atoms and in a hydrogen bond to N3 of the MP^{-} ligand.

The structural analogies between $[Cd(\mu\text{-}9H\text{-}MP^{-}\text{-}\kappa S^{6},N^{7}\text{:}\kappa S^{6})_2]_n$ and M-DNA (Fig. 23) and the most simple and well-known structure of the coordination polymer motivated its electrical characterization as a single molecule on the surface. Even though $[Cd(MP^{-})_2]_n$ behaves as insulator, this work opened new alternative strategies toward the potential use of DNA and coordination polymers as molecular wires. By means of ultrasound it was possible to isolate single chains of $[Cd(MP^{-})_2]_n$ on mica. Atomic force microscopy (AFM) allowed its morphological characterization on surface.[97] The electrical characterization of the $[Cd(MP^{-})_2]_n$ coordination polymer showed that these chains behave as insulators. To re-design similar coordination polymers with electrical capabilities, density functional theory (DFT) was applied to know the electronic structure of a family of coordination polymers of formula $[M(MP)_2]_n$ with different 3d metal ions. DFT calculations suggest stable polymeric structures for Fe(II), Ni(II), Co(II), and Cu(II). Moreover, the polymers with Fe(II), Ni(II), and Co(II) show ferromagnetic semiconductor behavior while with Cu(II) shows a Peierls-unstable paramagnetic metallic phase that undergoes a transition to a ferromagnetic semiconductor one under small stretching.[98]

The deprotonation of the N9 position of the MP^{-} ligands in $[Cd(\mu\text{-}9H\text{-}MP^{-}\text{-}\kappa S^{6},N^{7}\text{:}\kappa S^{6})_2 \cdot 2H_2O]_n$ leads to formation of the polyanionic coordination polymer $[Cd(\mu\text{-}MP^{2-}\text{-}\kappa S^{6},N^{7}\text{:}\kappa S^{6})_2]_n^{2n-}$.[96] This polymer crystallizes in the presence of Ca(II) to form the interesting $[Cd(MP^{2-})_2]_n[Ca(H_2O)_6]_n$ compound (Fig. 24).

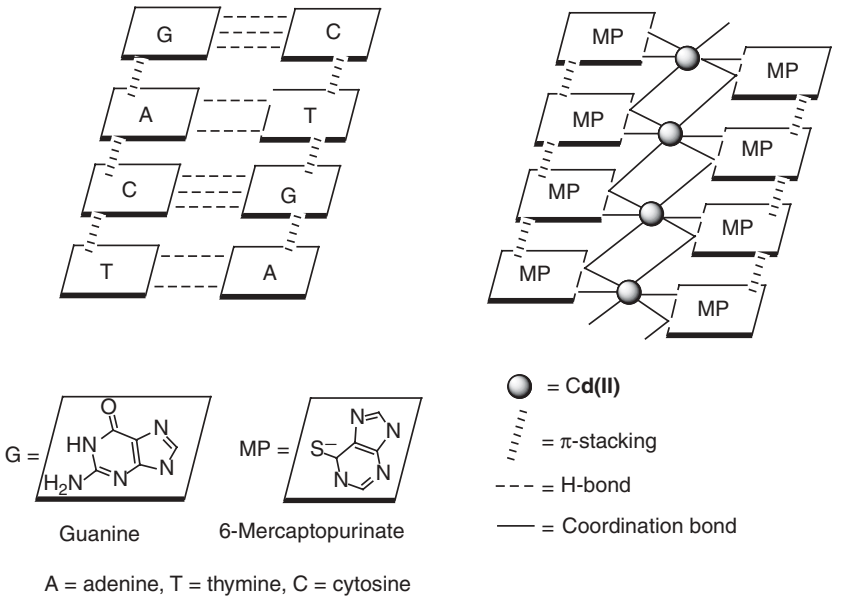

FIGURE 23. The structural analogies between DNA and $[Cd(\mu\text{-}9H\text{-}MP^{-}\text{-}\kappa S^{6},N^{7}\text{:}\kappa S^{6})_2]_n$. complex.

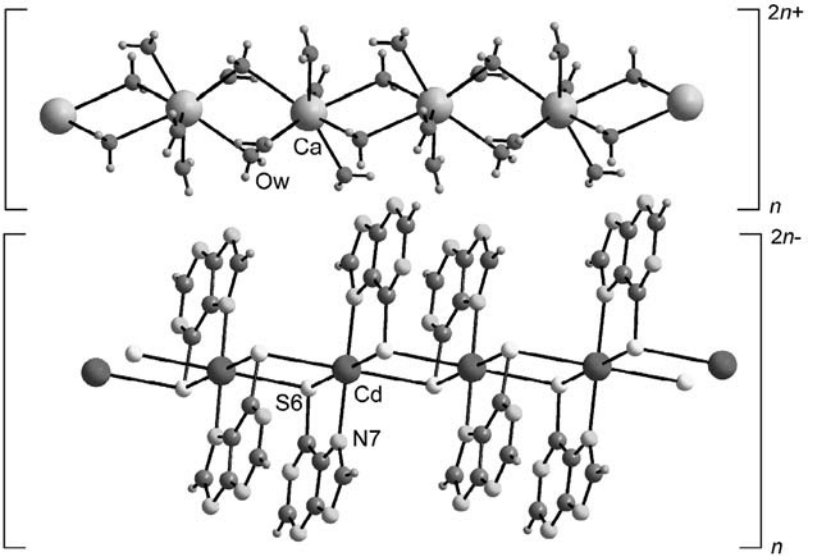

FIGURE 24. Structure of the 1D coordination polymer $[Cd(\mu\text{-}MP^{2-}\text{-}\kappa S^6,N^7{:}\kappa S^6)_2]_n$ $[Ca(H_2O)_6)]_n$.

Its structure consists of parallel anionic chains of $[Cd(\mu\text{-}MP^{2-}\text{-}\kappa S^6,N^7{:}\kappa S^6)_2]_n^{2n-}$ and cationic chains of $[Ca(H_2O)_6]_n^{2n+}$, which are joined together by means of electrostatic interactions and hydrogen bonds. The one-dimensional anionic polymer is based on stacked centrosymmetric $[Cd(MP^{2-})_2]$ entities, which are linked to each other through Cd-S bonds, forming a one-dimensional chain. The ligand coordinates to the cadmium as in the former case. The distance between metal centers of consecutive entities is 4.139(1) Å. An interesting issue is the different shapes of the two polymeric chains and the prevalence of the *trans*-disposition in the $[Cd(MP)_2]$ entities. The main difference between the two linear chains is the establishment of intramolecular $\pi\cdots\pi$ interactions between adjacent MP ligands. In the polyanion the presence of these interactions is hampered by the repulsive electrostatic force between the doubly deprotonated mercatopurines, which leads to a chain arrangement that minimizes it. Another effect of the increased negative charge is the elongation of $M\cdots M$ distance: 4.139(1) Å for $[Cd(MP^{2-})_2]_n[Ca(H_2O)_6)]_n$, versus 3.918(3) Å for $[Cd(MP)_2]_n$.

Recently, Dubler et al. synthesized an interesting Cd(II) coordination polymer with MP: $[Cd_2(\mu\text{-}1H,9H\text{-}MP\text{-}\kappa S^6,N^7{:}\kappa N^3)_2Cl_4]_n[Cd(1H,9H\text{-}MP\text{-}\kappa S^6,N^7)_2Cl_2]$.[99] The structure of this new compound shows two different metal entities. The first one consist of a one-dimensional coordination polymer $[Cd_2(MP)_2Cl_4]_n$ in which the MP is acting as a bridging ligand via the S6 and N7 sites, forming a chelate with one Cd(II) and through N3 to another Cd(II) center (Fig. 25).

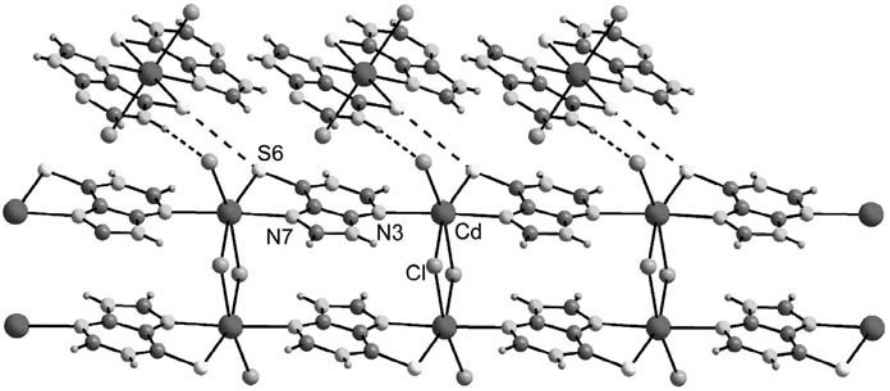

FIGURE 25. One-dimensional coordination polymer of $[Cd_2(\mu\text{-}1H,9H\text{-}MP\text{-}\kappa S^6,N^7{:}\kappa N^3)_2Cl_4]_n$ stabilized by the presence of hydrogen bonds between its terminal chlorines and the monomeric $[Cd(1H,9H\text{-}MP\text{-}\kappa S^6,N^7)_2Cl_2]$ complex.

IV. HYBRID SYSTEMS BASED ON METAL-OXALATO AND PROTONATED NUCLEOBASES

The metal-oxalato matrix has demonstrated a high efficiency not only to permit the covalent anchoring of nucleobases but also to embed supramolecular nucleobase architectures by means of molecular recognition processes involving noncovalent interactions such as those in the organic–inorganic hybrid compounds (1H, 9H ade)$_2$[Cu(ox)$_2$(H$_2$O)][100] and (1H,3H-cyt)$_2$[M(ox)$_2$(H$_2$O)$_2$][101] (M(II) = Mn, Co, Cu, Zn). Their supramolecular architectures are quite similar and their overall crystal packing can be regarded as a lamellar network built up of anionic sheets of metal-oxalato-water complexes and cationic nucleobase layers among them (Fig. 26). Each wide organic layer serves as ''double-sided adhesive tape'' to tightly join adjacent inorganic layers by means of electrostatic forces and a strong hydrogen bonding network.

The asymmetric unit of the adeninium compound consist of one oxalato-containing Cu(II) complex and two crystallographically independent adeninium cations (A and B) with protons at the N1 and N9 sites. The anionic complexes are joined by means of short hydrogen bonds O_{1w}- H $\cdots$ O_{ox}, giving rise to sheets that spread out along the crystallographic *ab*-plane (Fig. 27a). 1H,9H-adeninium cations are inserted between the anionic sheets and they are sequentially arranged to form polymeric ribbon-like 1D supramolecular aggregates (Fig. 27b). These positively charged ribbons are sustained by means of two different types of intermolecular interactions. The Hoogsteen faces (N6H, N7) of two neighboring A and B adeninium cations are doubly N6-H $\cdots$ N7 hydrogen bonded to give a base pair (I), whereas the opposite faces of

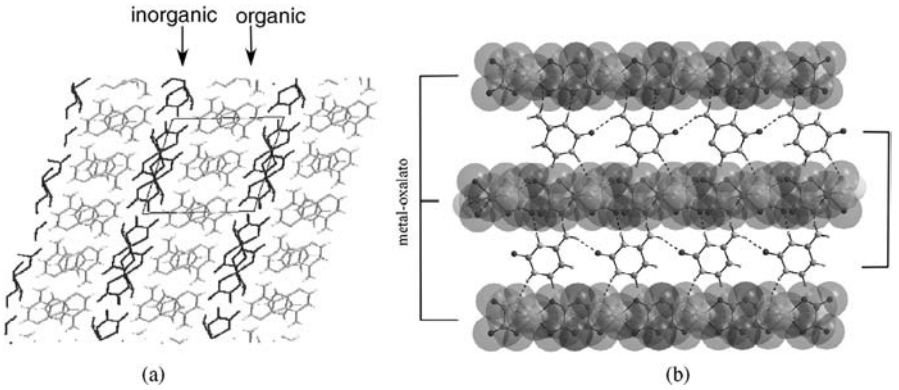

FIGURE 26. Crystal packing of compounds: (a) (*1H,9H*-ade)$_2$[Cu(ox)$_2$(H$_2$O)] and (b) (*1H,3H*-cyt)$_2$[M(ox)$_2$(H$_2$O)$_2$] (M(II) = Mn, Co, Cu, Zn) showing the alternative inorganic–organic sheets.

the dimeric aggregates are linked to the adjacent 1H,9H-ade$^+$ cations through one pair of N9-H $\cdots$ N3 hydrogen bonds in a $R_2^2(8)$ pattern (II),[102] which is a usual base-pairing mode found for adenine and its derivatives.[103,104] The other feasible adenine-adenine interaction[105] simultaneously involving two Watson-Crick faces is precluded by the protonation of the N1 site.

It should be emphasized that ribbon or layer arrangements of nucleobase pairs are common,[106] and both types of adeninium-adeninium self-association base pairs are also suitable for adeninium-adenine and even adenine-adenine pairing. Indeed, the same pattern of ribbon structure has been found in the crystals of the (1H,9H-ade)$_2$SO$_4 \cdot 2$H$_2$O[107] and (9H-ade)(1H,9H-ade)$X \cdot 2$H$_2$O (X = BF_4^-, ClO_4^-)[103,108] compounds, but we have found only one crystal structure with ribbons consisting solely of neutral adenine molecules with both Watson-Crick and Hoogsteen faces involved in the hydrogen bonding system within the ribbon.[70] Nevertheless, a similar spatial arrangement constructed out of dimers of neutral adenine molecules was used as the model for monolayers and bilayers deposited on graphite surfaces, studied by scanning tunneling microscopy, and for the usually complicated superstructures of nucleic acid molecules (e.g, 1D filaments and 2D monolayers) formed at ultra high vacuum conditions on the Cu and Ag terminated Si surfaces, examined by the RAIRS method.[109]

In the crystal structure, the organic ribbons are connected to the complex entities containing copper through hydrogen bonds involving the Watson-Crick faces (N6H, N1H) of both adenine moieties as donors and the oxalato oxygen atoms as acceptors. Molecules A and B are engaged to O-C-O and O-Cu-O frameworks, respectively, leading to $R_2^2(8)$ hydrogen bond motifs in a clear example of a molecular recognition process that directs the supramolecular architecture of the compound (Fig. 27c).

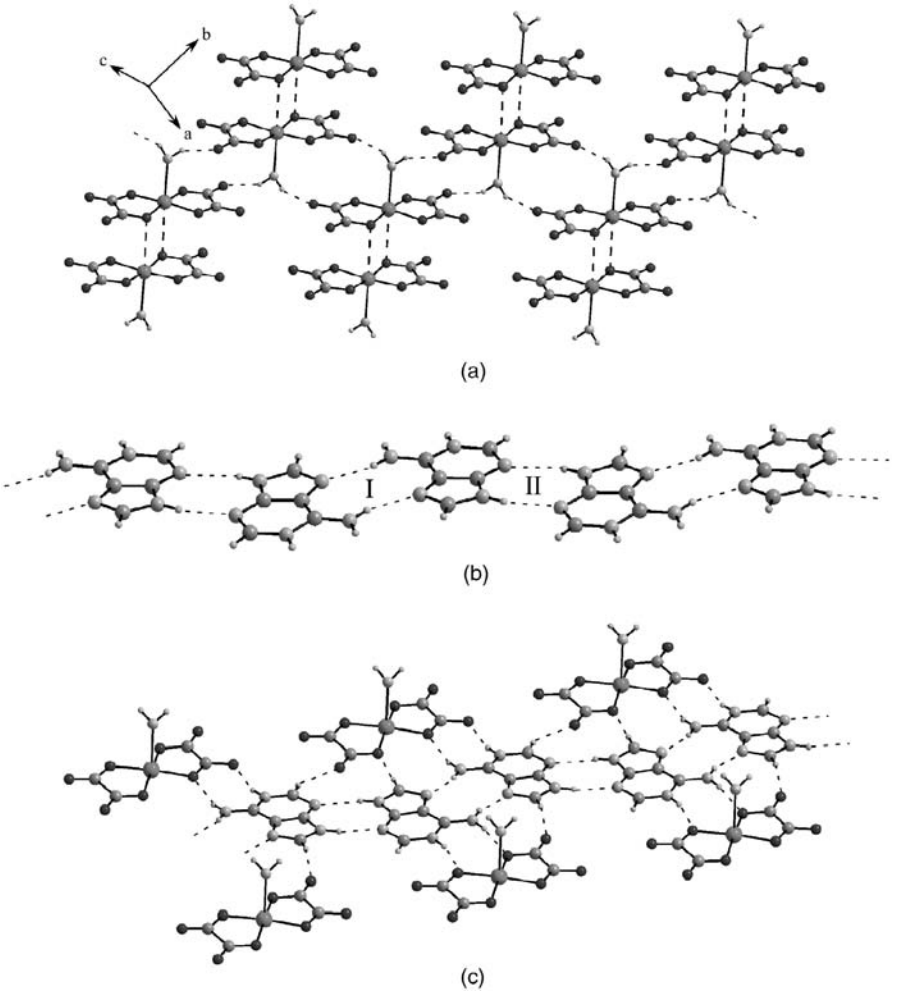

FIGURE 27. Ball and stick representation of (a) the inorganic sheets, (b) the one-dimensional adeninium chain, and (c) the inorganic–organic hydrogen bonding interactions in compound $(1H,9H\text{-ade})_2[Cu(ox)_2(H_2O)]$.

To get a deeper insight into the interaction of the 1H,9H-adeninium tautomer with a metal-oxalato fragment, we optimized the most plausible arrangements between an adeninium cation and a $[Cu(ox)_2]^{2-}$ complex anion. The results indicate that the interaction implying the Watson-Crick edge with the O-Cu-O fragment is the most favorable, with an energy difference of 10.32 Kcal/mol with respect to that involving the O-C-O group with the observed arrangement in the experimental structure. The presence of the second type of interaction in the crystal packing can be attributable to the periodicity constraints of the anionic sheets.

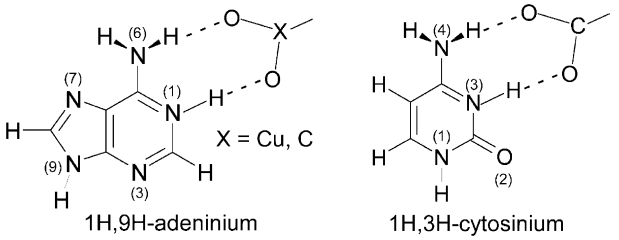

FIGURE 28. Fork-like interactions involving the Watson-Crick faces of 1H,9H-adeninium and 1H,3H-cytosinium.

We have chosen cytosine replacing adenine as organic building block to construct analogous hybrid materials for the following reasons. First, the inorganic–organic interaction in the $(1H,9H\text{-adeninium})_2[Cu(ox)_2(H_2O)_2]$ compound is essentially maintained by two eight-membered hydrogen-bonded $R_2^2(8)$ rings involving the N6H and N1H sites of the Watson-Crick face of the nucleobase as donors and the oxalato-O atoms from O-Cu-O and O-C-O moieties as acceptors (Fig. 28). Experimental and theoretical analysis on the interaction of DNA/RNA constituents and protein building blocks[76] have shown that the last charge-assisted hydrogen bond motif exists in adeninium systems,[110] but it is also a dominant association pattern of the protonated cytosine in both biological[111] and artificial systems,[112] implying the N4H/N3H edge of the nucleobase and the carboxylate groups of the amino acid.

Second, a perusal of the crystallographic information concerning high-dimensional aggregates of the cytosine nucleobase shows that the two previously reported homomeric self-assembling 1D patterns[113,114] for cytosinium cations are sustained by a single interaction via the exocyclic O-atom and one hydrogen atom of the N4 amino group, leaving the N4H and N3H sites as free hydrogen bonding positions to afford fork-like interactions with the carboxylate-O atoms (Fig. 29).

Third, density functional theory calculations, including the presence of one $[M(ox)_2]^{2-}$ fragment in all of its possible dispositions around the cytosinium cation, seem to indicate that the structural synthons found in the adeninium compound are also quite robust for assembling the cytosinium and oxalato-containing complexes.

Cytosinium compounds display the desired layered supramolecular structure in which homomeric cationic ribbon-like 1D supramolecular aggregates are inserted between 2D hydrogen-bonded sheets of metal-oxalato complexes. Nevertheless, the projected fork-like interactions are absent owing to the distinctive features of the self-assembling pattern of the nucleobase ribbons.

In the case of 1H,9H-adeninium compound, the protonated Watson-Crick face of the cations (H6-N6-C6-N1-H) is alternately placed in both sides of the one-dimensional aggregate with a distance of 11.649 Å between two

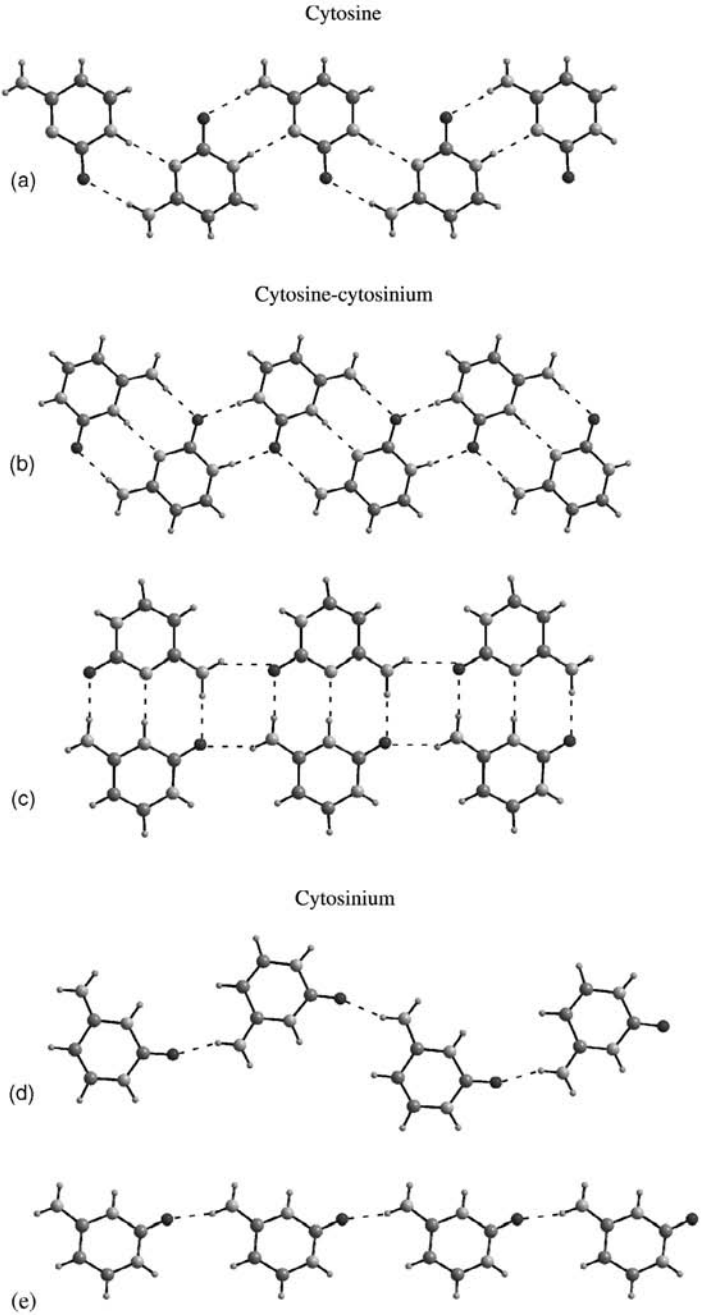

FIGURE 29. Cytosine and/or 1H,3H-cytosinium 1D aggregates.

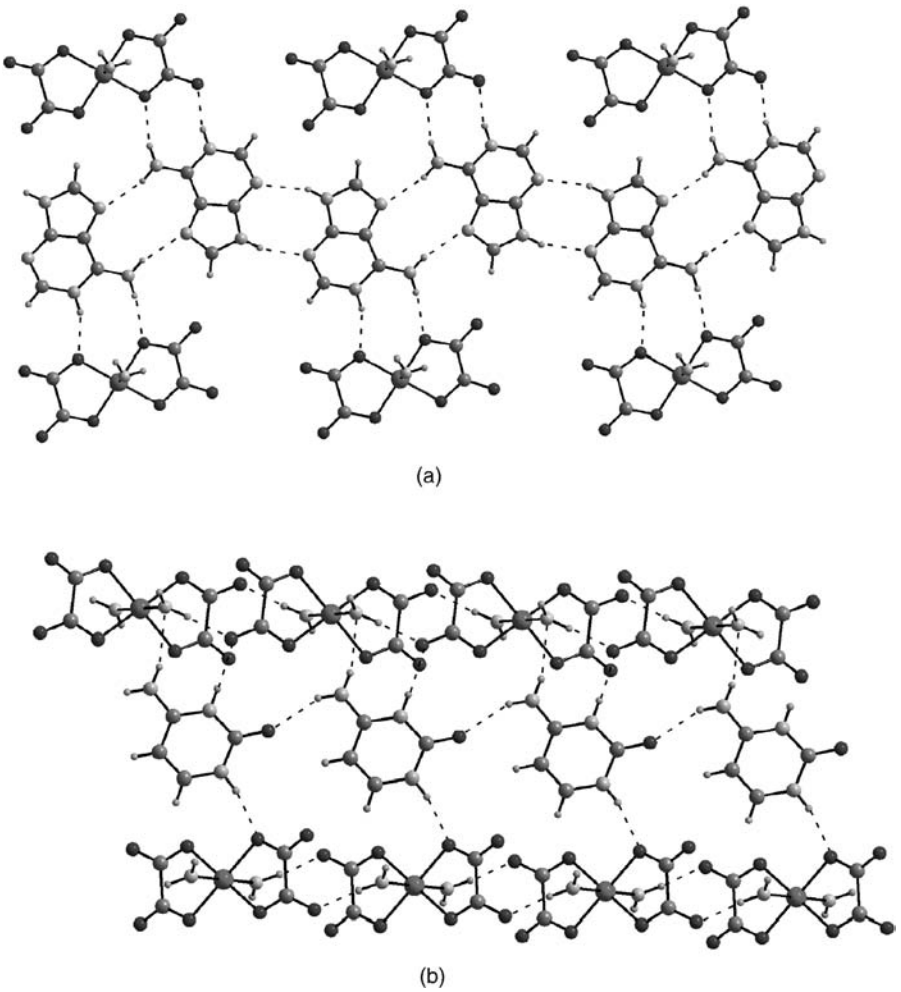

FIGURE 30. Noncovalent interactions between the organic and inorganic building blocks in compounds (a) (1H,9H-ade)$_2$[Cu(ox)$_2$(H$_2$O)] and (b) (1H,3H-cyt)$_2$[M(ox)$_2$ (H$_2$O)$_2$].

consecutive ones, which allows the coplanar stacking of the [Cu(ox)$_2$] fragments close to both sides of the nucleobase ribbon (Fig. 30a). The length of a [M(ox)$_2$] fragment is $\sim$ 10.5 Å, and monomer-monomer distances ranging from 11.0 to 12.0 Å have been previously reported for crystal structures with a coplanar stacking of diaquabis(oxalato)metallate anions.[115] The coplanar organic–inorganic disposition makes easier the establishment of fork-like interactions with both sides of the ribbon, one of them linked to the O_{ox}-Cu-O_{ox} fragments and the opposite one attached to O-C-O carboxylato groups of the adjacent inorganic sheet.

At first sight, a type-D ribbon pattern of cytosinium would then be adequate to provide a coplanar stacking of the structural entities because the N4H/N3H edges are also alternately placed along the one-dimensional aggregate with a distance of 13.5 Å between two consecutives ones.[114] Nevertheless, cytosinium compounds show a 1D aggregate of type E in which the N4H/N3 faces of the cytosinium cations are located on the same side of the ribbon with a distance of $\sim$ 7.0 Å (coincident with the crystallographic *b*-parameter). This value matches very well with those found for other chains of this type (ranging from 6.870 to 7.110 Å),[113] and it is not long enough to allow the coplanar stacking of $[M(ox)_2]$ fragments along the nucleobase ribbon. So that, the nearest anionic complexes are twisted to avoid steric hindrances, and dihedral angles between the planar ribbons and the $[M(ox)_2]$ fragments of around 30° are observed, precluding the anticipated fork-like hydrogen-bonding interactions with the O-C-O and O-M-O units. N4-H and N3-H sites of the cytosinium cation act as hydrogen bonding donors toward oxygen atoms from one oxalato ligand and one water molecule of a neighboring anionic complex belonging to the same inorganic sheet. The oxygen atoms are hydrogen bonded one to each other to complete a cyclic $R_3^2(8)$ ring. The adhesive-tape role of the organic ribbons is completed by a N-H $\cdots$ Oox interaction between the N1-H group of the cytosinium cation and one oxalato oxygen atom from the adjacent anionic sheet (Fig. 30b).

Strategies for creating reliable, reproducible inorganic–organic solid networks often depend on the combination of components that contain complementary hydrogen-bonded functionalities.[116] However, there are still many challenges to realize these tailor-made hybrid materials, because the structural control is often thwarted by the delicate balance of all covalent and noncovalent forces present in the crystal building and a slight modification of a molecular component may result in the failure to achieve the desired supramolecular interactions or even the overall 3D architecture.[117]

The observed hydrogen-bonded $R_3^2(8)$ interaction around the cytosinium moiety has been reported only in the 1H,9H-adeninium chloroanilate dihydrate, and it resembles to that found in the end cap of the binding pocket of the vaccinia VP39 virus protein[118] used to discriminate alkylated from nonalkylated nucleobases.

In conclusion, the supramolecular structure of these inorganic–organic hybrids is created by three types of molecular recognition: between complex anions, between cationic nucleobases, and between ribbons of nucleobases and layers consisting of oxalato-complexes. Molecules of complexes located within the parallel layers are joined by hydrogen bonds. The second interaction between the base molecules results in the hydrogen bonding recognition unit and leads to the ribbon form. Finally, the third group of hydrogen bonds completes the very effective set of interactions and builds the closely packed structure.

Inorganic–organic supramolecular recognition patterns of cytosinium and adeninium compounds are both quite effective because the compounds

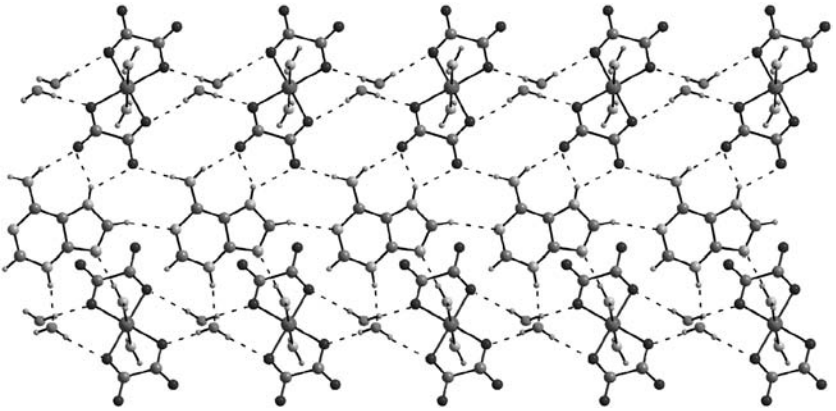

FIGURE 31. Ball and sticks representation of the inorganic–organic hydrogen bonding interactions in compounds $(3H,7H\text{-ade})_2[M(ox)_2(H_2O)_2]\cdot 2H_2O$ [M(II) = Co and Zn].

show a close crystal packing with high values of the crystal density (1.90 and 1.92 g cm^{-3} for the copper(II) complexes of cytosinium and adeninium, respectively). They do not exhibit the presence of crystallization water molecules in contrast to what usually occurs in the crystal building of compounds with discrete *trans*-$[M(ox)_2(H_2O)_2]$ entities in which solvation molecules are filling the channels or holes generated by the arrangement of the structural units.[119,120] The robustness of the overall supramolecular 3D architecture is confirmed by the high thermal stability of the compounds for which thermal degradations in synthetic air take place $> 170^{\circ}C$ without clear discrimination of the lost weight attributable to the coordinated water molecules and the pyrolysis of the organic molecules.

On the other hand, compounds $(3H,7H\text{-ade})_2[M(ox)_2(H_2O)_2]\cdot 2H_2O$ [M(II) = Co and Zn] also show an inorganic–organic layered structure. Crystallization water molecules occupy the interstitial space between anionic metal-oxalato complexes (Fig. 31) and display hydrogen contacts to the coordinated ones and to the oxalato oxygen atoms to form anionic inorganic sheets. The nucleobase cations undergo association through intermolecular hydrogen bonding between the C8H proton of an adeninium entity and the deprotonated N1 position of the adjacent one, leading to infinitely long ribbons that are inserted among the anionic sheets. Intermolecular hydrogen bond formation between CH groups of nucleobases and endocyclic N atoms is common in synthetic systems but it is still extremely rare in nucleic acid chemistry.[121] Moreover, in both artificial and natural structures, the weak C-H$\cdots$N interbase interactions usually reinforce strong neighboring N-H$\cdots$N/O hydrogen bonds, but an analysis of the contacts reveals that the almost linear C8-H$\cdots$N1 hydrogen bond is the only one between neighboring adeninium cations, and their structural parameters indicate a relative strong interaction with values clearly below the ranges found for this

structural motif in crystal structures retrieved from the CSD database.[65] All the remaining donor and acceptor sites of the nucleobases are engaged in hydrogen bond formation between the ribbons and the inorganic sheets.

One of the interesting structural aspects is the protonation of the nucleobase in the N7 and N3 sites. The N7-H is hydrogen bonded to two noncoordinated oxygen atoms from one oxalato ligand, whereas the N3 atom is close to the crystallization water molecule whose hydrogen atoms are attached to two oxalato oxygen atoms.

Previous reports on gas-phase ab initio quantum mechanical calculations have determined that the energy order of the low-lying tautomers is 1H,9H- < 3H,7H- < 3H,9H- < 7H,9H- < 1H,7H-, with a very small energy difference of 0.46 Kcal/mol between the 1H,9H- and 3H,7H-adeninium forms.[122] However, this noncanonical tautomer is unprecedented in nucleobase solid-state chemistry so far. Indeed, because the N3 site of the adenine is known to be the least basic relative to protonation, adenine moieties carrying proton at the N3 site are rare, and it has been solely observed in the crystal structure of the dimer (μ-ade-κN^7:κN^9)[Cu(H_2O)(bzimdi)]$_2$[10b] and in several N7-[123]and N6-gathered adenine species.[124]

To verify the feasible stabilization of noncanonical forms of the protonated adenine nucleobase, we extended our B3LYP/6-31G(d) calculations to the study of the tautomeric forms of isolated cations on a water-simulated dielectric medium and including different metal-oxalato surroundings simulating those experimentally found in the compounds.

The dielectric media of the solvent slightly stabilizes the *1H,9H-* form with a difference of 0.52 Kcal/mol with respect to the *3H,7H*-adeninium cation. This stabilization is more pronounced for the *1H,7H*-tautomer for which the energy-difference energy (4.41 Kcal/mol) is substantially smaller than that found on gas phase (10.87 Kcal/mol) owing to its higher dipole moment. The high dipole moment enables it to establish strong noncovalent interactions with good hydrogen bonding donors/acceptors that could stabilize this tautomeric form such as it has been observed in the crystal structure of the earlier mentioned (1H,7H-ade)$_2$(I_3)$_2$(I_2)$_5$(H_2O)$_2$, (1H,7H-ade)$_4$(calix) · 14H_2O[125] and (1H,7H-ade)$_2$Cl[$ZnCl_3$(1H,9H-ade-κN^7] · H_2O[58c] compounds.

On the other hand, the arrangement of adjacent hydrogen bond donor/acceptor sites surrounding the adenine moiety constrains the hydrogen bonding pattern and therefore, the protonation sites of the nucleobase (Fig. 32). The Watson-Crick and Hoogsteen edges of the 1H,7H-tautomer are protonated, whereas the N3/N9 edge acts as a double acceptor group. In contrast, the 1H,9H- and 3H,7H-adeninium cations (with a quite similar donor/acceptor disposition) exhibit one double hydrogen bonding donor edge, the Watson-Crick face (N1-H/N6-H) for the former and Hoogsteen face (N6-H/N7-H) for the second one, and the remaining two edges act both as donor and acceptor sites. As a consequence of the different hydrogen bonding pattern of the 1H,7H-tautomer with respect to those of *1H,9H-* and *3H,7H*-adeninium forms, it could be the preferent option for some environments, but a not extremely

rigid supramolecular environment well designed to interact with the 3H,7H-tautomer will also be appropriate for the 1H,9H-form, and as this latter tautomer is the most stable one and presents a slightly higher dipole moment, it would be the preferred one.

Calculations including the presence of one $[Cu(ox)_2]^{2-}$ fragment in all of its possible dispositions around the adeninium cation show that the energy order of 1H,9H- and 3H,7H- tautomers is not altered. However, when two $[Cu(ox)_2]^{2-}$ fragments with the experimental disposition of compounds are included, the 3H,7H-adeninium cation becomes the most stable (Fig. 33). This fact is due to the demanding conditions for an efficient hydrogen bonding interaction that are better fulfilled by the 3H,7H-adeninium cation than by the

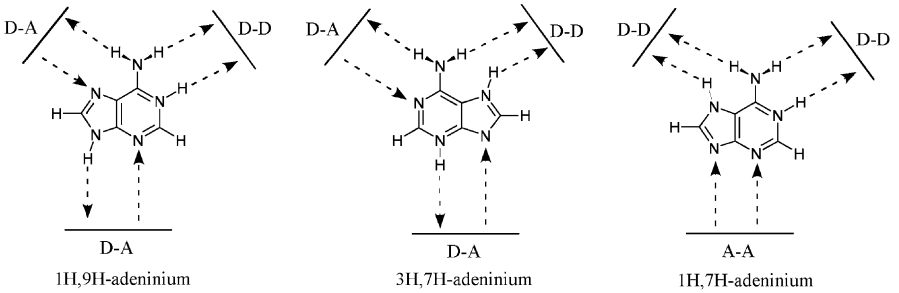

FIGURE 32. Hydrogen bonding sites of several adeninium forms.

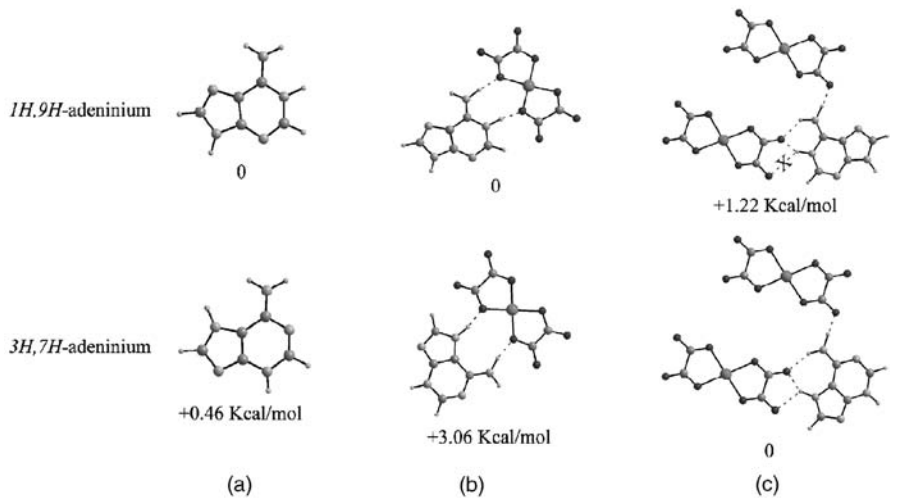

FIGURE 33. Relative energies between the 1H,9H– and 3H,7H–adeninium forms for different environments: (a) gas phase, (b) interacting with a $[Cu(ox)_2]^{2-}$ fragment, and (c) interacting simultaneously with two $[Cu(ox)_2]^{2-}$ fragments.

1H,9H-form. The optimized structural parameters of the hydrogen bonds around the *3H,7H*-adeninium entity agree well with those obtained from the X-ray diffraction analysis, and they are within the range usually found for N—H $\cdots$ O hydrogen bonds. The optimized *1H,9H*-adeninium entity establishes only three hydrogen bonds with the $[Cu(ox)_2]^{2-}$ fragments, indicating a less efficient hydrogen bonding stabilization.

V. CONCLUSIONS

This chapter has provided an overview of the aspects of the molecular recognition processes that take place between nucleobases and artificial receptors, focused in this case on metal-oxalato frameworks. The metal-oxalato fragments present a great efficiency to act as receptors of neutral and cationic nucleobases and even of supramolecular nucleobase aggregates. The anchoring to these receptors takes place by coordinative bonding to the metal centers through any of the endocyclic nitrogen atoms or by means of hydrogen bonding interactions between the organic bases and the inorganic fragments. This work has revealed that the chemical environment surrounding the nucleobase plays a crucial role in stabilizing different tautomeric forms of both the neutral and cationic adenine nucleobases. In fact, the rigid supramolecular environment provided by the metal-oxalato frameworks has allowed the solid-state isolation for first time of the noncanonical 7H–adenine and 3H,7H–adeninium forms.

VI. REFERENCES

1. J. D. Watson and F. H. C. Crick, *Nature*, **1953**, *171*, 737.
2. (a) S. Neidle, ed., *Oxford Handbook of Nucleic Acid Structure*, Oxford University Press, Oxford, **1999**. (b) G. M. Blackburn and M. J. Gait, eds., *Nucleic Acids in Chemistry and Biology*, Oxford University Press, Oxford, **1996**.
3. (a) S. Sivakova and S. J. Rowan, *Chem. Soc. Rev.*, **2005**, *34*, 9. (b) V. J. Derose, S. Burns, M. K. Kim, and M. Vogt, in *Comprehensive Coordination Chemistry II*, *vol.8,* eds. J. A. McCleverty and T. J. Meyer, Elsevier, University of Bern, Switzerland, **2004**, p. 787. (c) J. A. R. Navarro and B. Lippert, *Coord. Chem. Rev.,* **2001**, *222*, 219. (d) B. Lippert, *Coord. Chem. Rev.,* **2000**, *200–202,* 487.
4. (a) F. C. Simmel and B. Yurke, in *Encyclopedia of Nanoscience and Nanotechnology*, *vol. 2*, ed. H. S. Nalwa., American Scientific Publishers, California, **2004** p. 495. (b) S. S. Santoso and S. Zhang, in *Encyclopedia of Nanoscience and Nanotechnology*, *vol. 9*, ed. H. S. Nalwa, American Scientific Publishers, California, **2004**, p. 459. (c) G. Gottarelli, S. Masiero, E. Mezzina, G. P. Spada, P. Mariani, and M. Recanatini, *Helv. Chim. Acta*, **1998**, *81*, 2078.
5. (a) G. Natile and L. G. Marzilli, *Coord. Chem. Rev.*, **2006**, *250*, 1315. (b) K. E. Erkkila, D. T. Odom, and J. K. Barton, *Chem. Rev.*, **1999**, *99*, 2777.
6. (a) C. Fonseca-Guerra, F. M. Bickelhaupt, S. Saha, and F. J. Wang, *Phys. Chem. A* **2006**, *110*, 4012. (b) A. K. Vrkic, T. Taverner, P. F. James, and A. J. O'Hair, *Dalton Trans.*, **2004**, 197.

7. M. Hanus, M. Kabelac, J. Rejnek, F. Ryjacek, and P. J. Hobza, *Phys. Chem. B*, **2004**, *108*, 2087.
8. E. Mezzina, P. Mariani, R. Itri, S. Masiero, S. Pieraccini, G. P. Spada, F. Spinozzi, J. T. Davis, and G. Gottarelli, *Chem. Eur. J.*, **2001**, *7*, 388.
9. M. Legraverend and D. S. Grierson, *Bioorgan. Med. Chem.,* **2006**, *14*, 3987.
10. (a) T. Suzuki, Y. Hirai, H. Monjushiro, and S. Kaizaki, *Inorg. Chem.,* **2004**, *43*, 6435. (b) P. X. Rojas-González, A. Castiñeiras, J. M. González-Pérez, D. Choquesillo-Lazarte, and J. Niclós-Gutiérrez, *Inorg. Chem.,* **2002**, *41*, 6190. (c) F. Zamora, M. Kunsman, M. Sabat, and B. Lippert, *Inorg. Chem.,* **1997**, *36*, 1583. (d) W. S. Sheldrick, H. S. Hagen-Eckhard, and S. Hebb, *Inorg. Chim. Acta*, **1993**, *206*, 15.
11. J. P. García-Terán, O. Castillo, A. Luque, U. García-Couceiro, G. Beobide, and P. Román, *Dalton Trans.,* **2006**, 902.
12. (a) S. C. Lee, M. A. Ruegsegger, and M. Ferrari, in *Encyclopedia of Nanoscience and Nanotechnology*, *vol. 1* ed. H. S. Nalwa, American Scientific Publishers, California, **2004**, p. 309. (b) F. Mancin, and J. Chin, *J. Am. Chem. Soc.,* **2002**, *124*, 10946.
13. (a) K. M. Guckian, B. A. Schweitzer, R. X. F. Ren, C. J. Sheils, D. C. Tahmassebi, and E. T. Kool, *J. Am. Chem. Soc.,* **2000**, *122*, 2213. (b) C. Janiak, *J. Chem. Soc., Dalton Trans.,* **2000**, 3885. (c) S. Yoshizawa, G. Kawai, K. Watanabe, K. Miura, and I. Hirao, *Biochemistry* **1997**, *36*, 4761. (d) X.- F. Ren, B. A. Schweitzer, C. J. Sheils, and E. T. Kool, *Angew. Chem., Int. Ed. Engl.*, **1996**, *35*, 743.
14. J.-M. Lehn, *Supramolecular Chemistry Concepts and Perspectives*; VCH, Weinheim, **1995**.
15. (a) F. Diederich, *Cyclophanes*, The Royal Society of Chemistry, Cambridge, UK, **1991**. (b) J. Rebek, Jr. *Acc. Chem. Res.,* **1990**, *23*, 399.
16. Y. Hisamatsu, H. Takami, N. Shirai, S.-I. Ikeda, and K. Odashima, *Tetrahedron Lett.*, **2007**, *48*, 617.
17. (a) R. Guther, M. Nieger, and F. Vogtle, *Angew. Chem., Int. Ed. Engl.,* **1993**, *32*, 601. (b) M. M. Conn, G. Deslongchamps, J. de Mendoza, and J. J. Rebek, *J. Am. Chem. Soc.,* **1993**, *115*, 3548. (c) K. S. Jeong, T. Tjivikua, A. Muehldorf, G. Deslongchamps, M. Famulok, J. Rebek, Jr. *J. Am. Chem. Soc.,* **1991**, *113*, 201. (d) S. C. Zimmerman, W. Wu, and Z. J. Zeng, *Am. Chem. Soc.,* **1991**, *113*, 196. (e) S. Goswami, A. D. Hamilton, and D. Van Engem, *J. Am. Chem. Soc.,* **1989**, *111*, 3425. (f) J. C. Adrian, Jr. and C. S. Wilcox, *J. Am. Chem. Soc.,* **1989**, *111*, 8055. (g) K. Williams, B. Askew, P. Ballester, C. Buhr, K. S. Jeong, S. Jones, and J. Rebek, Jr., *J. Am. Chem. Soc.*,, **1989**, *111*, 1090.
18. J. L. Atood, J. E. D. Davies, D. D. MacNicol, and F. Vogetle, *Comprehensive Supramolecular Chemistry* eds., Elsevier, Exeter, **1996** and references cited therein.
19. (a) E. A. Katayev, Y. A. Ustynyuk, and J. L. Sessler, *Coord. Chem. Rev.*, **2006**, *250*, 3004. (b) F. P. Schmidtchen, *Coord. Chem. Rev.*, **2006**, *250*, 2918. (c) P. A. Gale, *Acc. Chem. Res.*, **2006**, *39*, 465. (d) V. Amendola, D. Esteban-Gomez, L. Fabbrizzi, and M. Licchelli, *Acc. Chem. Res.*, **2006**, *39*, 343. (e) J. Yoon, S. K. Kim, N. J. Singh, and K. S. Kim, *Chem. Soc. Rev.*, **2006**, *35*, 355. (f) K. Bowman-James, *Acc. Chem. Res.*, **2005**, *38*, 671. (g) P. A. Gale, *Coord. Chem. Rev.*, **2003**, *240*, 167. (h) J. L. Sessler, S. Camiolo, and P. A. Gale, *Coord. Chem. Rev.*, **2003**, *240*, 17.
20. (a) J. P. Desvergne and A. W. Czarnik, *Chemosensors of Ion and Molecule Recognition*, Kluwer, Dordrecht, **1997**. (b) A. W. Czarnik, ed.; *Fluorescent Chemosensors for Ion and Molecule Recognition*, American Chemical Society, Washington, DC, **1992**. (c) J. M. Lehn, *Angew. Chem. Int. Ed. Engl.*, **1990**, *29*, 1304.
21. J. A. R. Navarro, and B. Lippert, *Coord. Chem. Rev.*, **1999**, *185–186,* 653.
22. P. J. Sanz-Miguel, P. Amo-Ochoa, O. Castillo, A. Houlton, and F. Zamora, in Metal Complexes-DNA Interactions, eds. N. Hadjiliadis and E. Sletten, Blackwell, Chichester, **2009**, p. 95
23. J. P. García-Terán, O. Castillo, A. Luque, U. García-Couceiro, P. Román, and L. Lezama, *Inorg. Chem.*, **2004**, *43*, 4549.
24. W. Brüning, E. Freisinger, M. Sabat, R. K. O Sigel, and B. Lippert, *Chem. Eur. J.*, **2002**, *8*, 4681.

25. C. S. Purohit and S. Verma, *J. Am. Chem. Soc.,* **2007**, *129*, 3488.
26. (a) M. Pilkinton, and S. Decurtins, in *Comprehensive Coordination Chemistry II*, *vol. 7*, ed. J. A. McCleverty, T. J. Meyer, Elsevier, University of Berne, Switzerland, **2004** p. 214. (b) C. N. R. Rao, S. Natarajan, and R. Vaidhyanathan, *Angew. Chem. Int. Ed.,* **2004**, *43*, 1466.
27. (a) E. Coronado, J. R. Galán-Mascarós, C. J. Gómez-García, E. Martínez-Ferrero, S. Van Smaalen, *Inorg. Chem.*, **2004**, *43*, 4808. (b) E. Coronado, J. R. Galán-Mascarós, C. J. Goméz-García, and V. Laukhin, *Nature* **2000**, *408*, 447. (c) S. G. Carling, C. Mathoniére, P. Day, K. M. A Malik, S. J. Coles, and M. B. Hursthouse, *J. Chem. Soc. Dalton Trans.*, **1996**, 1839. (d) L. O. Atovmyan, G. V. Shilov, R. N. Lyubovskaya, N. S. Ovanesyan, Y. G. Moronov, S. I. Pirumova, and I. G. Gusakovskaya, *JETP Lett.* **1993**, *58*, 818. (e) H. Tamaki, Z. J. Zhong, N. Matsumoto, S. Kida, M. Koikawa, N. Achiwa, Y. Hashimoto, and H. Okawa, *J. Am. Chem. Soc.*, **1992**, *114*, 6974.
28. (a) G. Ballester, E. Coronado, C. Giménez-Saiz, and F. M. Romero, *Angew. Chem. Int. Ed.*, **2001**, *40*, 792. (b) E. Coronado, J. R. Galán-Mascarós, C. J. Gómez-García, and J. M. Martínez-Agudo, *Inorg. Chem.*, **2001**, *40*, 113. (c) S. Decurtins, H. W. Schmalle, P. Schneuwly, and H. R. Oswald, *Inorg. Chem.*, **1993**, *32*, 1888.
29. D. Cangussu, H. O. Stumpf, H. Adams, J. A. Thomas, F. Lloret, and M. Julve, *Inorg. Chim. Acta*, **2005**, *358*, 2292.
30. A. L. Fuller, R. W. Watkins, K. R. Dunbar, A. V. Prosvirin, A. M. Arif, and L. M. Berreau, *Dalton Trans.*, **2005**, 1891.
31. P. Román, P. C. Guzmán-Miralles, A. Luque, J. I. Beitia, J. Cano, F. Lloret, M. Julve, and S. Alvarez, *Inorg. Chem.*, **1996**, *35*, 3741.
32. O. Castillo, A. Luque, P. Román, F. Lloret, and M. Julve, *Inorg. Chem.*, **2001**, *40*, 5526.
33. U. García-Couceiro, D. Olea, O. Castillo, A. Luque, P. Román, P. J. de Pablo, J. Gómez-Herrero, and F. Zamora, *Inorg. Chem.*, **2005**, *44*, 8343.
34. U. García-Couceiro, O. Castillo, A. Luque, J. P. García-Terán, G. Beobide, and P. Román, *Eur. J. Inorg. Chem.*, **2005**, 4280.
35. J. P. García-Terán, O. Castillo, A. Luque, U. García-Couceiro, P. Román, and F. Lloret, *Inorg. Chem.*, **2004**, *43*, 5761.
36. O. Castillo, A. Luque, F. Lloret, and P. Román, *Inorg. Chim. Acta,* **2001**, *324*, 141.
37. O. Castillo, A. Luque, M. Julve, F. Lloret, and P. Román, *Inorg. Chim. Acta*, **2001**, *315*, 9.
38. M. Pilkington and S. Decurtins, in *Comprehensive Coordination Chemistry II Vol. 7*, eds J. A. McCleverty and T. J. Meyer, Elsevier, University of Berne, Switzerland, **2004**, p. 177.
39. P. I. Vestues and E. Sletten, *Inorg. Chim. Acta*, **1981**, *52*, 269.
40. E. Sletten, J. Sletten, and N. A. Froystein, *Acta Chem. Scand.*, **1988**, *A42*, 413.
41. (a) H. L. Laity, and M. R. Taylor, *Acta Crystallogr.*, **1995**, *C51*, 1791. (b) W. S. Z. Sheldrick, *Naturforsch. Teil B* **1982**, *37*, 653.
42. A. L. Beauchamp, D. Cozak, and A. Mardhy, *Inorg. Chim. Acta*, **1984**, *92*, 191.
43. U. E. I. Horvath, S. Cronje, J. M. McKenzie, L. J. Barbour, and H. G. Z. Raubenheimer, *Naturforsch. B: Chem. Sci.*, **2004**, *59*, 1605.
44. H. Shi, and P. B. Moore, *RNA*, **2000**, *6*, 1091.
45. K. Junean, E. Podell, D. J. Harrington, and T. R. Cech, *Structure*, **2001**, *9*, 221.
46. W. G. Scott, J. B. Murray, J. R. P. Arnold, B. L. Stoodard, and A. Klug, *Science*, **1996**, *274*, 2065.
47. A. L. Feig, *Met. Ions Biol. Syst.*, **2000**, *37*, 157.
48. K. J. Baeyens, H. L. de Bondt, A. Pardi, and S. R. Holbrook, *Proc. Natl. Acad. Sci. USA* **1996**, *93*, 12851.

49. (a) N. Kisseleva, A. Khvorova, E. Westhof, O. Schiemann, *RNA* **2005**, *11*, 1. (b) L. M. Hunsicker and V. J. deRose, *J. Inorg. Biochem.*, **2000**, *80*, 271. (c) H. W. Pley, K. M. Flaverty, and D. B. McKay, *Nature*, **1994**, *372*, 68.
50. M. M. Taqui-Khan, and C. K. Krishnamoorhy, *J. Inorg. Nucl. Chem.*, **1971**, *42*, 1417.
51. (a) A. C. Morel, D. Choquesillo-Lazarte, C. Alarcón-Payer, J. M. González-Pérez, A. Castiñeiras, and J. Niclós-Gutiérrez, *Inorg. Chem. Comm.*, **2003**, *6*, 1354. (b) M. A. Salam, and K. Aoki, *Inorg. Chim. Acta*, **2001**, *314*, 71. (c) A. Marzotto, A. Ciccarese, D. A. Clemente, and G. Valle, J.*Chem. Soc., Dalton Trans.*, **1995**, 1461. (d) E. R. T. Tiekink, T. Kurucsev, and B. F. Hoskins, *J. Crystallogr. Spectrosc. Res.*, **1989**, *19*, 823. (e) Y. Rosopulos, U. Nagel, and W. Beck, *Chem. Ber*, **1985**, *118*, 931. (f) J. -P. Charland and A. L. Beauchamp, *Croat. Chem. Acta*, **1984**, *57*, 679. (g) L. Prizant, M. J. Olivier, R. Rivest, and A. L. Beauchamp, *Can. J. Chem.*, **1981**, *59*, 1311. (h) W. M. Beck, J. C. Calabrese, and N. D. Kottmair, *Inorg. Chem.*, **1979**, *18*, 176. (i) H. Sakaguchi, H. Anzai, K. Furuhata, H. Ogura, Y. Titaka, T. Fujita, and T. Sakaguchi, *Chem. Pharm. Bull.*, **1978**, *26*, 2465. (j) D. B. Brown, J. W. Hall, H. M. Helis, E. G. Walton, D. J. Hodgson, and W. E. Hatfield, *Inorg. Chem.*, **1977**, *16*, 2675. (k) P. De Meester, A. C. Skapski, *J. Chem. Soc. Dalton Trans.*, **1973**, *4*, 424.
52. T. J. Kistenmacher, *Acta Crystallogr.*, **1974**, *B30*, 1610.
53. D. Badura and H. Vahrenkamp, *Inorg. Chem,*, **2002**, *41*, 6013.
54. P. De Meester and A. C. Skapski, *J. Chem. Soc., Dalton Trans.*, **1973**, 1596.
55. (a) J. E. Kickam, S. J. Loeb, and S. L. Murphy, *Chem. Eur. J.*, **1997**, *3*, 1203. (b) A. Marzotto, D. A. Clemente, A. Ciccarese, and G. Valle, *J. Crystallogr. Spectrosc.*, **1993**, *23*, 119.
56. M. J. Sánchez-Moreno, D. Choquesillo-Lazarte, J. M. González-Pérez, R. Carballo, A. Castiñeiras, and J. Niclós-Gutiérrez, *Inorg. Chem. Comm.*, **2002**, *5*, 800.
57. E. Bugella-Altamirano, D. Choquesillo-Lazarte, J. M. González-Pérez, M. J. Sánchez-Moreno, R. Marín-Sánchez, J. D. Martín-Ramos, B. Covelo, R. Carballo, A. Castiñeiras, and J. Niclós-Gutiérrez, *Inorg.Chim. Acta*, **2002**, *339*, 160.
58. (a) M. R. Taylor, L. M. Vilkins, and M. J. McCall, *Acta Crystallogr.*, **1989**, *C45*, 1625. (b) P. T. Muthiah, S. K. Mazumdar, and S. Chaudhuri, *J. Inorg. Biochem.*, **1983**, *19*, 237. (c) M. R. Taylor and J. A. Westphalen, *Acta Crystallogr.*, **1981**, *A37*, 63. (d) M. R. Taylor, *Acta Crystallogr.*, **1973**, *B29*, 884.
59. (a) M. A. Shipman, C. Price, M. R. Elsegood, W. Clegg, and A. Houlton, *Angew. Chem. Int. Ed.*, **2000**, *39*, 2360. (b) J. E. Kickham, S. J. Loeb, and S. L. Murphy, *Chem. Eur. J.*, **1997**, *3*, 1203. (c) C. Meiser, B. Song, E. Freisinger, M. Peilert, H. Sigel, B. Lippert, *Chem. Eur. J.*, **1997**, *3*, 388.
60. (a) D. Amantia, C. Price, M. A. Shipman, M. R. J. Elsegood, W. Clegg, and A. Houlton, *Inorg. Chem.* **2003**, *42*, 3047. (b) A. E. Gibson, C. Price, W. Clegg, and A. Houlton, *J. Chem. Soc., Dalton Trans.,* **2002**, 131.
61. (a) O. S. Sukhanov, O. V. Shishkin, L. Gorb, Y. Podolyan, and J. Leszczynski, *J. Phys. Chem. B* **2003**, *107*, 2846. (b) A. F. Jalbout and L. Adamowicz, *J. Phys. Chem. A.,* **2001**, *105*, 1033.
62. H. Nuñez, J. J. Timor, J. Server-Carrió, L. Soto, and E. Escrivá, *Inorg. Chim. Acta*, **2001**, *318*, 8, and references therein.
63. S. Kitagawa and K. Uemura, *Chem. Soc. Rev.*, **2005**, *34*, 109.
64. A. L. Spek, *Acta Crystallogr.*, **1990**, *A46*, C34.
65. F. H. Allen, *Acta Crystallogr.*, **2002**, *B58*, 380.
66. (a) C. G. Hoogstraten, C. V. Grant, T. E. Horton, V. J. DeRose, and R. D. Britt, *J. Am. Chem. Soc*, **2002**, *124*, 834. (b) P. de Meester, D. M. L. Goodgame, T. J. Jones, and A. C. Skapski, *Biochem. J.*, **1974**, *139*, 791.
67. M. V. Capparelli, D. M. L. Goodgame, P. B. Hayman, and A. C. Skapski, *Inorg. Chim. Acta,* **1986**, *125*, L47.

68. (a) G. de Munno, M. Medaglia, D. Armentano, J. Anastassopoulou, and T. Theophanides, *J. Chem. Soc., Dalton Trans.*, **2000**, 1625. (b) C. V. Grant, V. Frydman, and L. Frydman, *J. Am. Chem. Soc*, **2000**, *122*, 11743. (c) M. Sabat, R. Cini, T. Haromy, and M. Sundaralingham, *Biochemistry*, **1985**, *24*, 7827. (d) K. J. Aoki, *J. Chem. Soc., Chem. Commun.*, **1976**, 748.
69. T. F. Mastroprieto, D. Armentano, N. Marino, and G. De Munno, *Polyhedron*, **2007**, *26*, 4945.
70. D. Dobrzynska and L. B. Jerzykiewicz, *J. Am. Chem. Soc.*, **2004**, *126*, 11118.
71. A. Terzis, A. L. Beauchamp, and R. Rivest, *Inorg. Chem.*, **1973**, *12*, 1166.
72. V. Langer and K. Huml, *Acta Crystallogr.*, **1984**, *A40*, C86.
73. G. L. Hardgrove, J. R. Einstein, B. E. Hingerty, and C. H. Hei, *Acta Crystallogr.*, **1983**, *C39*, 88.
74. (a) Z. Travnicek, J. Marek, K. Dolezal, and M. Z. Strnad, *Kristallogr*, **1997**, *212*, 538. (b) J. Maixner, J. Zachova, and K. Huml, *Collect. Czech. Chem. Commun.*, **1993**, *58*, 861. (c) V. Langer, K. Humo, and J. Zachova, *Acta Crystallogr.*, **1979**, *B35*, 1148.
75. E. Cubero, N. G. A. Abrescia, J. A. Subirane, F. J. Luque, and M. Orozco, *J. Am. Chem. Soc.*, **2003**, *125*, 14603.
76. A. C. Cheng and A. D. Frankel, *J. Am. Chem. Soc.*, **2004**, *126*, 434.
77. M. F. Goodman, *Nature*, **1995**, *378*, 237.
78. J. Sponer, J. Leszczynski, and P. Hobza, *Biopolymers*, **2002**, *61*, 3.
79. Y. Huang and H. Kenttamma, *J. Phys. Chem.*, **2004**, *A108*, 4485, and references therein.
80. J. Gu and J. Leszczynski, *J. Phys. Chem.*, **1999**, *A103*, 2744.
81. S. P. Perun, A. L. Sobolewski, and W. Domcke, *J. Am. Chem. Soc.*, **2005**, *127*, 6257.
82. (a) L. M. Salter and G. M. Chaban, *J. Phys. Chem.*, **2002**, *A106*, 4251. (b) A. L. Laxer, D. J. Mayor, H. E. Gottlied, and B. Fischer, *J. Org. Chem.,* **2001**, *66*, 5463.
83. B. Mennucci, A. Toniolo, and J. Tomasi, *J. Phys. Chem.,* **2001**, *A105*, 4749.
84. C. E. Crespo-Hernández, B. Cohen, P. M. Hare, and B. Holher, *Chem. Rev.,* **2004**, *104*, 1977.
85. S. M. Tretyak, V. V. Mitkevich, and L. F. Sukhodub, *Crystallogr. Rep.*, **1987**, *32*, 1268.
86. (a) M. A. Serra, B. K. Corner, and M. E. Silver, *Acta Crystallogr.*, **1992**, *C48*, 1957. (b) C. M. Weeks, D. C. Rohrer, and W. L. Duax, *Science,* **1975**, *190*, 1096.
87. P. de Meester and A. C. Skapski, *J. Chem. Soc. Dalton Trans.*, **1972**, 2400.
88. P. de Meester and A. C. Skapski, *J. Chem. Soc. A, Dalton Trans.*, **1971**, 2167.
89. J. M. González-Pérez, C. Alarcón-Payer, A. Castiñeiras, T. Pivetta, L. Lezama, D. Choquesillo-Lazarte, G. Crisponi, and J. Niclós-Gutiérrez, *Inorg. Chem.*, **2006**, *45*, 877.
90. W. S. Sheldrick, *Acta Crystallogr.*, **1981**, *B37*, 945.
91. S. Das, C. Madhavaiah, S. Verma, and P. K. Bharadwaj, *Inorg. Chim. Acta*, **2005**, *358*, 3236.
92. T. F. Mastropietro, D. Armentano, E. Grisolia, C. Zanchini, F. Lloret, M. Julve, and G. de Munno *Dalton Trans.*, **2008**, 514.
93. N. Stanley, P. T. Muthiah, P. Lugar, M. Weber, and S. J. Geib, *Inorg. Chem. Comm.*, **2005**, *8*, 1056.
94. S. Menzer, E. C. Hillgeris, and B. Lippert, *Inorg. Chim. Acta*, **1993**, *211*, 211.
95. U. Kela, and R. Vijayvargiya, *Biochem. J.*, **1981**, *193*, 799.
96. P. Amo-Ochoa, and M. I. Rodríguez-Tapiador, O. Castillo, D. Olea, A. Guijarro, S. S. Alexandre, J. Gómez-Herrero, and F. Zamora, *Inorg. Chem.*, **2006**, *45*, 7642.
97. D. Olea, S. S. Alexandre, P. Amo-Ochoa, A. Guijarro, F. de Jesus, J. M. Soler, P. J. de Pablo, J. Gómez-Herrero and F. Zamora, *Adv. Mater.*, **2005**, *17*, 1761.

98. S. S. Alexandre, J. M. Soler, P. J. Sanz, R. W. Nunes. F. Yndurain, J. Gómez-Herrero, and F. Zamora, *Apply Phys Lett*., **2007**, *90*, 193107.
99. E. Glyr, H. W. Schamalle, and E. Dubler, *private communication*, **2004**.
100. J. P. García-Terán, O. Castillo, A. Luque, U. García-Couceiro, G. Beobide, and P. Román, *Inorg. Chem*., **2007**, *46*, 3593.
101. J. P. García-Terán, O. Castillo, A. Luque, U. García-Couceiro, G. Beobide, and P. Román, *Cryst. Growth Des*., **2007**, *7*, 2594.
102. (a) J. Bernstein, R. E. Davis, L. Shimoni, and N. L. Chang, *Angew. Chem. Int. Ed. Engl*., **1995**, *34*, 1555. (b) M. C. Etter, *Acc. Chem. Res*., **1990**, *23*, 120.
103. Y. J. Cheng, Z. M. Wang, C. S. Liao, and C. H. Yan, *New J. Chem*., **2002**, *26*, 1360.
104. A. C. M. Young, J. C. Dewan, and A. J. Edwards, *Acta Crystallogr*., **1991**, *C47*, 580.
105. R. E. A. Kelly, Y. J. Lee, and L. N. J. Kantorovich, *Phys. Chem. B*, **2005**, *109*, 11933.
106. G. A. Jeffrey and W. Sanger, *Hydrogen Bonding in Biological Structures*, Springer-Verlag, Berlin, **1994**.
107. V. Langer, K. Huml, and L. Lessinger, *Acta Crystallogr*., **1978**, *B34*, 2229.
108. V. Zelenak, Z. Vargova, and I. Cisarova, *Acta Crystallogr*., **2004**, *E60*, 742.
109. (a) R. E. A. Kelly and L. N. J. Kantorovich, *Mat. Chem*., **2006**, *16*, 1894. (b) M. Preuss, W. G. Schmidt, and F. Bechstedt, *Phys. Rev. Lett*., **2005**, *94*, 236102. (c) K. Shinoda, W. Shinoda, C. C. Liew, S. Tsuzuki, Y. Morikawa, and M. Mikami, *Surf. Sci*., **2004**, *556*, 109. (d) A. McNutt, S. Haq, and R. Raval, *Surf. Sci*, **2003**, *531*, 131.
110. (a) T. Johansson, C. Oswald, A. Pedersen, S. Törnroth, M. Okvist, G. Karlsson, J. Rydström, and U. J. Krengel, *Mol. Biol*., **2005**, *352*, 299. (b) G. Smith, U. D. Wermuth, and P. C. Healy, *Acta Crystallogr*., **2004**, *E60*, o1573. (c) E. Serrano-Padial, D. Choquesillo-Lazarte, E. Bugella-Altamirano, A. Castiñeiras, R. Carballo, and J. Niclós-Gutiérrez, *Polyhedron*, **2002**, *21*, 1451. (d) M. A. Salam and K. Aoki, *Inorg. Chim. Acta*, **2000**, *311*, 15. (e) F. Takusagawa, H. M. Bergman, M. Dabrow, and R. K. Robins, *Acta Crystallogr*., **1985**, *C41*, 400.
111. (a) L. Yao, S. Sklenak, H. Yan, and R. J. Cukier, *J. Phys. Chem. B*, **2005**, *109*, 7500. (b) H. K. Song, S. H. Sohn, and S. W. Suh, *EMBO*, **1999**, *18*, 1104.
112. (a) K. Bouchouit, N. Benali-Cherif, S. Dahaoui, E. E. Beneif, and C. Lecomte, *Acta Crystallogr*., **2005**, *E61*, o2755. (b) M. Doi, Y. Nakamoto, and A. Asano, *Acta Crystallogr*., **2005**, *C61*, o577. (c) G. Smith, U. D. Wermuth, and P. C. Healy, *Acta Crystallogr*., **2005**, *E61*, o746. (d) R. G. Davies, V. C. Gibson, M. B. Hursthouse, M. E. Light, E. L. Marshall, M. North, D. A. Robson, I. Thompson, A. J. P. White, D. J. Williams, and P. J. Williams, *J. Chem. Soc. Perkin Trans. 1* **2001**, 3365. (e) T. Balsubramanian, P. T. Muthiah, and W. T. Robinson, *Bull. Chem. Soc. Jpn*., **1996**, *69*, 2919.
113. (a) S. Bouacida, A. Merazig, A. Beghidja, and C. Beghidja, *Acta Crystallogr*., **2005**, *E61*, m2072. (b) C. H. Gorbitz and E. Sagstuen, *Acta Crystallogr*., **2004**, *E60*, o1945. (c) S. Jaworski, H. Schollborn, P. Eisenmann, U. Thewalt, and B. Lippert, *Inorg. Chim. Acta*, **1988**, *153*, 31. (d) P. E. Bourne and M. R. Taylor, *Acta Crystallogr*., **1983**, *C39*, 430. (e) K. Ogawa, K. Nishitani, T. Fujiwara, S. Shirotake, and K. Tomita, *Acta Crystalogr*., **1979**, *B35*, 965.
114. (a) M. Bagieu-Beucher, *Acta Crystallogr*., **1990**, *C46*, 238. (b) B. L. Kindberg and E. L. Amma, *Acta Crystallogr*., **1975**, *B31*, 1492. (c) M. Ohki, A. Takenaka, H. Shimanouchi, and Y. Sasada, *Bull. Chem. Soc. Jpn.,* **1975**, *48*, 848.
115. (a) C. A. Murphy, T. S. Cameron, M. W. Cooke, and M. A. S. Aquino, *Inorg. Chim. Acta*, **2000**, *305*, 225. (b) I. E. Grey, I. C. Madsen, K. Sirat, and P. W. Smith, *Acta Crystallogr*., **1985**, *C41*, 681.
116. A. M. Beatty, B. A. Helfrich, G. A. Hogan, and H. A. Redd, *Cryst. Growth Des*., **2006**, *6*, 122.
117. X. J. Zhao, Z. H. Zhang, Y. Wang, and M. Du, *Inorg. Chim. Acta*, **2007**, *360*, 1921.
118. G. Hu, P. D. Gershon, A. E. Hodel, and F. A. Quiocho, *Proc. Natl. Acad. Sci. USA*, **1999**, *96*, 7149.

119. P. Román, C. Guzmán-Miralles, and A. Luque, *Acta Crystallogr.*, **1993**, *C49*, 1336.
120. T. D. Keene, M. B. Hursthouse, and D. J. Z. Price *Anorg. Allg. Chem.*, **2004**, *630*, 350.
121. K. Shi, R. Biswas, S. Nath Mitra, and M. J. Sundaralingam, *Mol. Biol.*, **2000**, *299*, 113.
122. C. Marian, D. Nolting, and R. Weinkauf, *Phys. Chem. Chem. Phys.*, **2005**, *7*, 3306.
123. C. L. Price, and M. R. Taylor, *Acta Crystallogr.*, **1996**, *C52*, 2736.
124. (a) Z. Travnicek, A. Klanicova, I. Popa, and J. Roicik, *J. Inorg. Biochem.*, **2005**, *99*, 776. (b) Z. Travnicek, I. Popa, and K. Dolezal, *Acta Crystallogr.*, **2004**, *C60*, 662. (c) N. Stanley, P. T. Muthiah, and S. J. Geib, *Acta Crystallogr.*, **2003**, *C59*, 27.
125. Z. Wang, Y. Cheng, C. Liao, and C. Yan, *CrystEngComm.*, **2001**, *50*, 1.

CHAPTER 10

Crystal Engineering of Coordination Polymers

Marius Andruh and Catalina Ruiz-Pérez

Inorganic Chemistry Laboratory, Faculty of Chemistry, University of Bucharest, str. Dumbrava Rosie nr. 23, Bucharest, Romania

Laboratorio de Rayos X y Materiales Moleculares, Departamento de Física Fundamental II, Facultad de Física, Universidad de La Laguna, Avda. Astrofísico Francisco Sánchez s/n, 38071 La Laguna, Tenerife, Spain

CONTENTS

Macromolecules Containing Metal and Metal-Like Elements, Volume 9: Supramolecular and Self-Assembled Metal-Containing Materials,
Edited by Alaa S. Abd-El Aziz, Charles E. Carraher Jr., Charles U. Pittman Jr., and Martel Zeldin.

I. INTRODUCTION

First of all, we have to define coordination polymers and highlight the differences between them and traditional polymers. Coordination polymers are constructed from metal ions connected through bridging ligands via coordination bonds (most frequently M–N and M–O bonds, but no M–C ones). They are also known as metal-organic frameworks (MOFs) or metal-organic coordination networks (MOCNs).[1] The metal ions can be connected either by purely inorganic bridges (HO^-, halides, NCS^-, NO_3^-, NO_2^-, CO_3^{2-}, N_3^-, etc.), or by organic species, with the donor atoms separated by at least one carbon atom. In the first case, various organic molecules are coordinated to the metal ions as terminal ligands.[1] With few exceptions, coordination polymers are not soluble as such, and their structures are not preserved in solution (upon "dissolution" they transform into various mononuclear and/or oligomeric species).[1,2] Consequently, they are characterized only in the solid state, by means of single crystal X-ray diffraction, the growth of single crystals thus being crucial. Upon heating, they decompose rather than melt. On the other hand, organometallic polymers, in which the metal ions are linked via covalent M–C bonds, preserve most of the properties of the "classical" polymers. Actually, the classification of the metal-containing polymers (coordination and metalorganic polymers) follows the dichotomy between classical (Werner-ian) coordination chemistry and organometallic chemistry. The cyano group, CN^-, is an inorganic ligand, and although it coordinates to metal ions through

the carbon atom, the resulting complexes belong to classical coordination chemistry.

The design of coordination polymers lies at the interface of coordination and supramolecular chemistry and is a part of crystal engineering, whose ultimate goal is to obtain solids with technologically useful functionalities (molecular magnetic materials, conducting solids, zeolite-like materials, catalysts, luminescent materials, etc.).[3] The metal ions exert a *structural* role (directing and sustaining the solid-state architecture) and a *functional* one (carrying magnetic, optical, or redox properties).

Coordination polymers can be simply classified according to their dimensionality: one-dimensional (1-D) two-dimensional (2-D), and three-dimensional (3-D). They can be homometallic (containing only one type of metal ions) and heterometallic (containing at least two types of metal ions).

An important question concerning the general architecture of crystals containing coordination polymers is the way they pack. The packing of coordination networks generates voids, cavities, or channels, which may account for more than half of the crystal volume.[4] A major factor to be considered for infinite systems is the tendency for solids to minimize void space within their structures. The empty space resulting from the packing of coordination polymers can be filled (a) by hosting the anions, solvent molecules, uncoordinated ligand molecules, etc. or (b) interpenetration—that is, the voids associated with one framework are occupied by one or more independent frameworks. From a practical point of view, porous MOFs are extremely attractive, but difficult to make; the interpenetration of independent frameworks drastically reduces the empty voids and, consequently, their ability to act as zeolite-like materials (porous hosts for guest storage and separation, catalytic systems). Scheme **1** illustrates the interpenetration of two diamondoid nets. Concrete examples are presented in the subsequent sections of this chapter.

II. SYNTHETIC APPROACHES

The general strategy in obtaining coordination polymers consists of self-assembly processes involving metal ions (assembling cations) and bridging ligands. The assembling cations are complex species that resulted by dissolving the metal salt in water or in nonaqueous solvents. The metal ions can also carry ancillary ligands (usually chelating ligands) that block part of the coordination sites of the metal ion. The blocking ligands are employed to control the dimensionality of the coordination polymers and the topology of the metal centers.

The condensation proceeds through the substitution of the water (solvent) molecules coordinated to the metal ions by the bridging ligands.

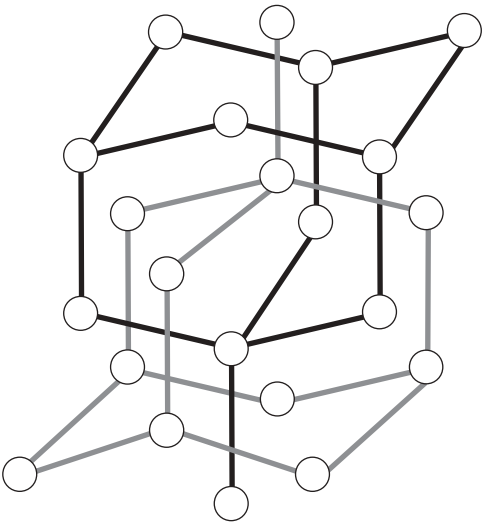

SCHEME 1

Such processes occur either under ambient conditions, or under hydrothermal (or, more generally, solvothermal) conditions. An intuitive mechanism for the formation of metal-organic frameworks was recently proposed by Ramanan and Whittingham.[5] The key step within this mechanism that leads to neutral MOFs is the formation of point zero charge molecules (*pzc*) at the isoelectric point. The *pzc* species assemble and condense through the elimination of the aqua molecules and subsequent coordination of the bridging ligand. Scheme **2** illustrates the formation of a 2D square grid coordination polymer, [Fe(azpy)$_2$(NCS)$_2$], from an octahedral mononuclear complex, [Fe(azpy)(H$_2$O$_3$(NCS)$_2$]; the three aqua ligands are substituted by the azpy ligands from another complex, and so on. In the case of ionic MOFs, the molecular organization is believed to occur around ion pairs.

A. The Node-and-Spacer Paradigm

Originating from Robson's seminal papers published in 1990,[6] the node-and-spacer approach became a widely used strategy for the construction of a large variety of coordination polymers.[7] It relies on the strong directionality of the coordination bonds established between the metal ions (nodes, connectors) and the *exo*-dentate ligands (spacers, linkers). The network topology can be controlled by choosing the appropriate metal ion (coordination number and geometry, charge, HSAB behavior) and the suitably designed bridging ligand (denticity, shape, size, HSAB behavior).[8] Thus the coordination and stereochemical algorithm of metal center nodes coupled to the structural features and directionality of *exo*-dentate ligands that act as spacers and linkers, are crucial

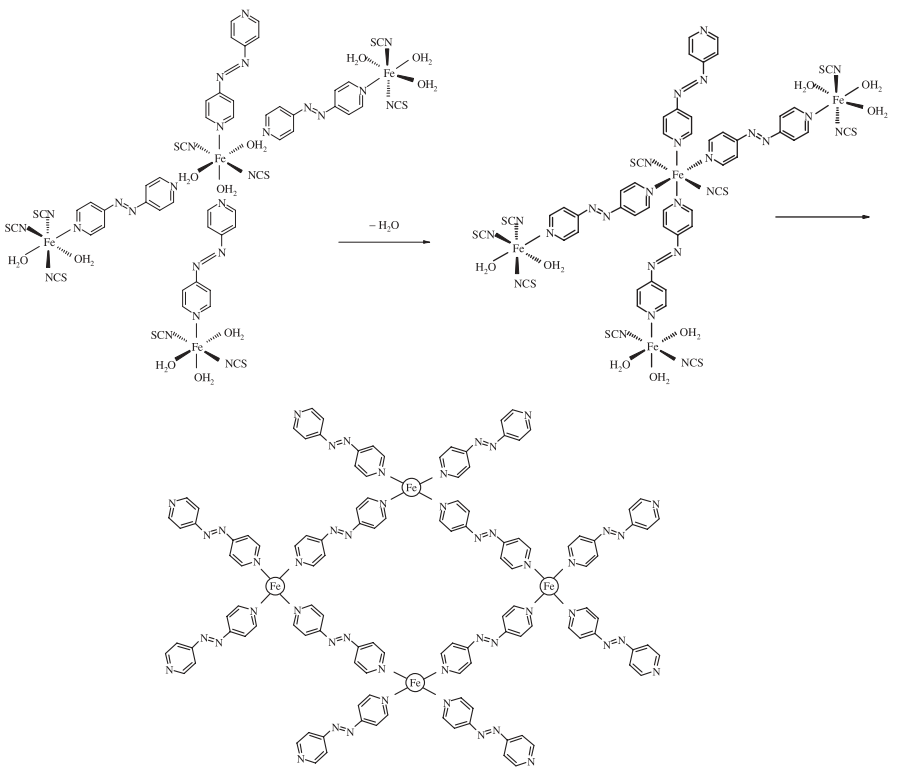

SCHEME 2

factors in the assembly of multimetallic complexes. Over the past 15 years, careful analysis of coordination polymers has led to coherent classifications of their network topologies,[9] and these are constantly being expanded with the discovery of new materials incorporating novel and intriguing structures. Noncovalent interactions such as hydrogen-bonds, π-π or d^{10}-d^{10} (aurophilic/argentophilic) interactions also play an important role in sustaining these supramolecular solid-state architectures,[10] and the understanding and appreciation of these interactions coupled to metal-ligand coordinate bonding allows the synthesis and development, in a deliberate way, of materials with interesting properties and useful functions. Of course, the solvent molecules and the counterions also influence the final crystal architecture

i. Bridging Ligands

Numerous *exo*-dentate (divergent) ligands with specific binding strength and directionality have been used to obtain a rich variety of coordination polymers. Scheme **3** presents several representative bridging ligands. The simplest bridging ligands are the halide ions. However, their binding functions

(a)

F^-, Cl^-, Br^-, I^-, HO^-, CN^-, SCN^-, N_3^-

(b)

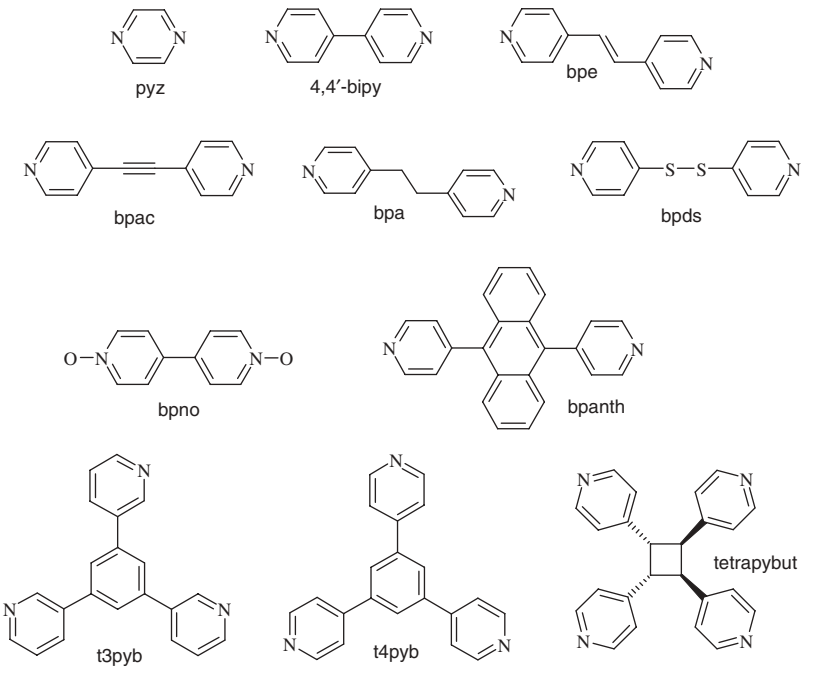

(c)

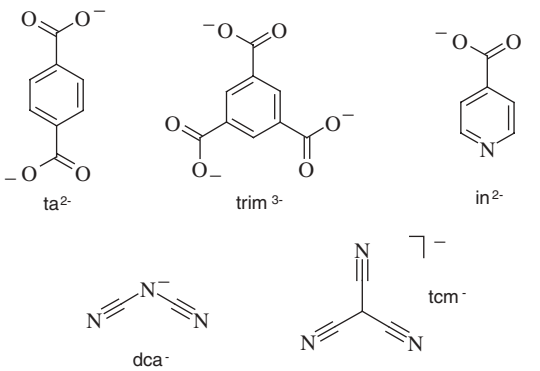

SCHEME 3. (a) Inorganic ligands. (b) Neutral organic ligands. (c) Anionic organic ligands.

(terminal vs. bridging) are not easily controlled. Other purely inorganic bridging ligands, (CN^- and NCS^-), are rarely used as such, but their anionic complexes, $[M(CN)_m]^{p-}$ and $[M(NCS)_m]^{q-}$, are very efficient building blocks in designing especially heterometallic coordination polymers (see Section II.C.iii). The organic ligands offer a larger diversity. The relative position of the donor atoms (directionality) as well as the distance between them, which finally controls the distance between the metal centers, can be efficiently tuned by organic synthesis.

Among the most popular *exo*-bidentate ligands, we recall pyrazine and 4,4′-bipyridine. The stoichiometry of divergent ligand:metal is a key factor in determining the dimensionality of the resulting systems. A 1:1 ligand-to-metal ratio leads to either linear or zigzag chains (Scheme **4**). By altering the stoichiometry—namely by increasing the ligand-to-metal ratio—2D and 3D architectures can be obtained. The formation of 1D chains is favored by the presence of ancillary ligands in the coordination sphere of the metal ion, whereas 2D or 3D structures are obtained by using "naked" (actually hydrated) metal ions. If the 2D or 3D extended structures are based only on the metal-coordination, the resulting network topology is directly influenced by the coordination geometry of the metal ions (templates). So, for a 2:1 L:M stoichiometry, diamondoid networks are obtained by using Ag^I or Cu^I as assembling cations, both with a marked preference for the tetrahedral coordination (Scheme **5a**), whereas square grid networks are obtained using metal ions as templates, which can easily adopt the octahedral stereochemistry (Scheme **5b**). For a 1:1.5 metal-to-ligand ratio the following architectures, based solely on metal-ligand coordinative interactions, were observed: infinite ladder, brick wall, honeycomb, and bilayer (Scheme **6**).

A higher content of bridging ligand does not necessarily mean a higher dimensionality of the coordination polymers: the organic molecule (e.g., 4,4′-bipyridine) can accomplish various functions in the crystal: bridging, terminal, uncoordinated. The last two functions are unfavorable for expanding the structure into a second or third dimension through metal-ligand bonds. On the other hand, the terminal and uncoordinated ligands are involved in other noncovalent interactions (especially hydrogen bonds and π-π stacking) that are important organizing forces of the supramolecular crystal architecture. Let us discuss two examples $[Ni(4,4'\text{-bipy})_{2.5}(H_2O)_2](ClO_4)_2 \cdot 1.5(4,4'\text{-bipy}) \cdot 2H_2O$,[11] and $[Fe(bipy)(H_2O)_3(ClO_4)]ClO_4 \cdot 1.5(4,4'\text{-bipy}) \cdot H_2O$.[12] Formally, the first compound belongs to the 1:4 stroichiometry, but 1.5 mol of 4,4′-bipy do not participate in the construction of the framework. Its structures consists of linear railroad double chains constructed from bridging and terminal 4,4′-bipy ligands. Large pores (11 × 11 Å) are formed. The terminal organic ligands further extend the structure through π-π contacts with identical terminal ligands (3.77 Å) from adjacent chains (Scheme **7**). The 2D supramolecular sheets are stacked in registry, resulting in an extended 1D channel network with large pores along the crystallographic *a*-axis. The pores are occupied by hydrogen bonded hydrated anions and 4,4′-bipy guests. The supramolecular

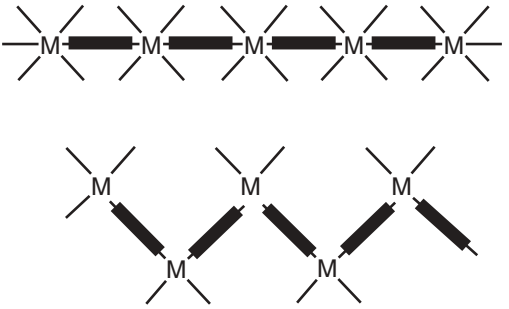

SCHEME 4

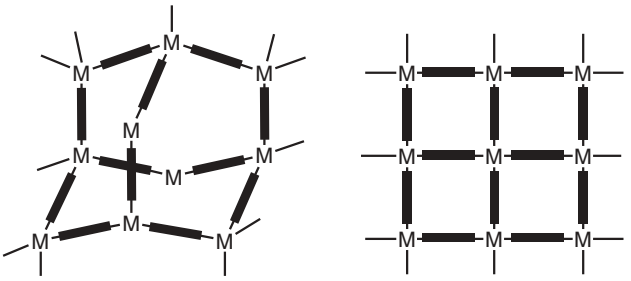

SCHEME 5

architecture of the second compound consists of linear coordination chains, [· · · {$(ClO_4)(H_2O)_3Fe$}-(4,4′-bipy)-{$Fe(HeO)_3(ClO_4)$}-(4,4-bipy)- · · ·], which are hydrogen bonded alternatively by single and double "bridges" (Scheme **8**).

Let us come back to 4,4′-bipyridine complexes with metal-to-ligand ratio of 1:2, and both organic molecules acting as bridges. We mentioned that square grids layers are formed when the metal ion prefers an octahedral geometry, and the 4,4′-bipy molecules connects the metal ions through their equatorial positions. One of the very first examples in this field was reported by Robson et al.: $[Zn(4,4\text{-bipy})_2(H_2O)_2]SiF_6$.[6a] The apical positions of the zinc ions are occupied by aqua ligands. The three-dimensional structure of the crystal results from the inclined interpenetration of the grid layers (each mesh of a sheet has one rod of an inclined sheet passing through it) (Fig. 1). The hexafluorosilicate anions are hydrogen bonded to the aqua ligands. The interpenetration prevents the formation of large channels. The alternative packing of the 2D layers—that is, their superposition in registry—with every zinc atom from one layer disposed exactly above and below the zinc atoms from adjacent layers, should generate channels, with dimensions corresponding to the distance between the zinc ions within the square meshes ($\sim$ 11 Å). This is possible by assembling

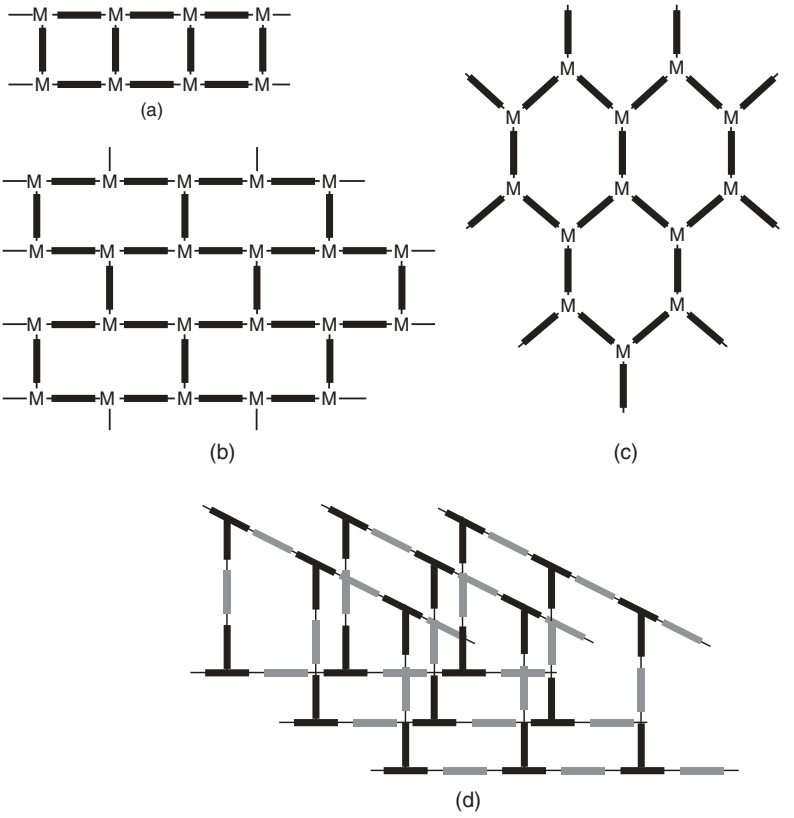

SCHEME 6

the grids starting from anhydrous starting materials. Indeed, the reaction between anhydrous zinc hexafluorosilicate and 4,4′-bipyridine, in DMF/1,4-dioxane, leads to $[Zn(4,4'\text{-bipy})_2SiF_6]$, which crystallizes in the tetragonal space group $P4/mmm$. The zinc atoms from adjacent square grid layers are connected by SiF_6^{2-} ions, which act as linear spacers and coordinate into the apical positions of the zinc ions. A three-dimensional network is constructed by connecting parallel layers through SiF_6^{2-} pillars (Fig. 2a).[13] Large square channels are generated parallel to the crystallographic *c*-axis (Fig. 2b). The volume of the channels is $\sim$ 50% of the total volume. This is a very elegant solution of a problem in crystal engineering. The space group can be regarded as a direct manifestation of the point group symmetry (D_{4h}).

Another interesting case in crystal engineering is the one of interpenetrated cyano-bridged diamondoid networks. Zinc(II) easily adopts a tetrahedral geometry, so the solid-state structure of $Zn(CN)_2$ is quite predictable: tetrahedral zinc ions are connected by cyano groups generating a diamond-like net, with double interpenetration (Scheme1). The cadmium derivative,

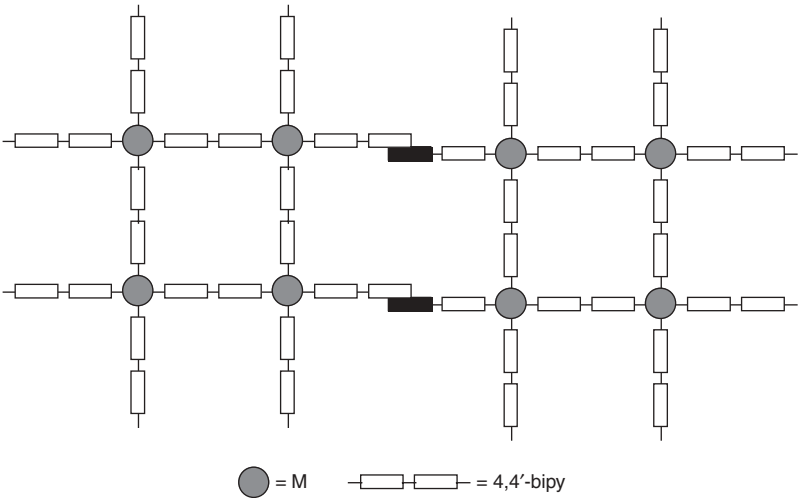

SCHEME 7

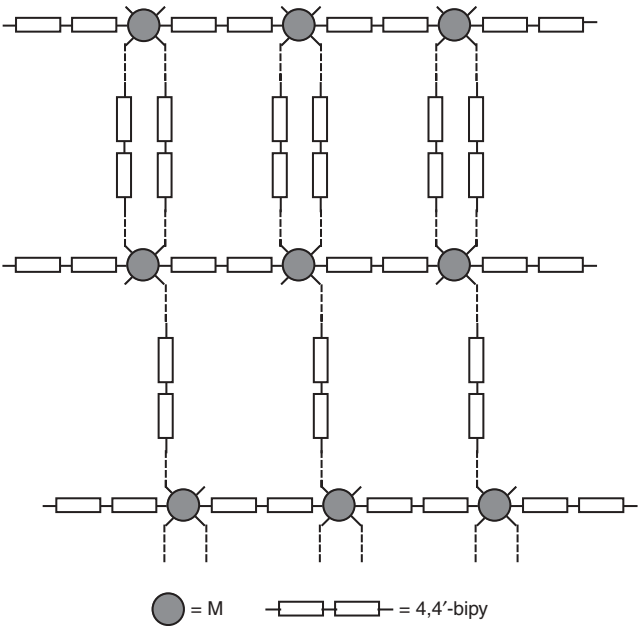

SCHEME 8

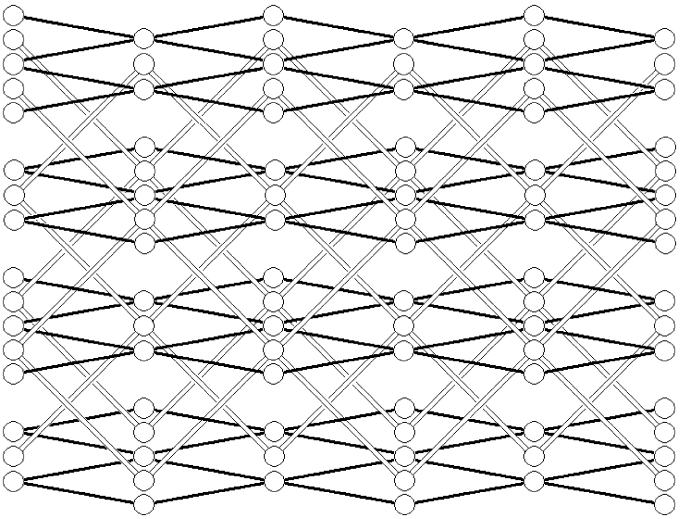

FIGURE 1. The interpenetrating networks in $[Zn(4,4'\text{-bipy})_2(H_2O)_2]SiF_6$.

$Cd(CN)_2$, is isomorphous. To prevent the interpenetration, relatively large species must be hosted into the diamondoid network. Indeed, the mixed metal complex $NMe_4[Cu^{I}Zn^{II}(CN)_4]$ shows no interpenetration because the tetramethylammonium cations, whose size fits to that of the adamantane-like cavity, occupy half of these cavities (both Cu^{I} and Zn^{II} ions are tetracoordinated). The interpenetration of neutral $M(CN)_2$ nets (M = Zn, Cd) can be hindered by hosting neutral molecules, structurally similar to NMe_4^+. The solution of this problem is obvious and elegant: The crystallization of $Cd(CN)_2$ in the presence of Me_4C leads to a single diamond-like net.[6b]

It is also possible to combine two different spacers to generate coordination polymers. For example, the self-assembly process among Cu^{II}, dicyanamido (dca^-), and nicotinato (na^-) ions affords a 1D coordination polymer, $[Cu_3(na)_4(dca)_2(H_2O)_8] \cdot 2H_2O$. Its structure consists of infinite chains, built up by copper(II) ions interconnected through two types of bridges: the nicotinato and the dicyanamido ligands (Fig. 3).[14] Each chain can be viewed as a ladder, in which the rungs are formed by a triad of copper(II) ions linked by two na^- bridges. The ladder sides are formed by dca^- ligands connecting the terminal copper atoms from each triade.

ii. Oligonuclear Complexes as Nodes

Coordination polymers can be constructed from oligonuclear nodes as well.[15] The metal ions interact with the divergent ligand through their easily accessible coordination sites. The presence of two or more metal ions (identical or different) confers a higher geometrical flexibility to the node. Moreover, the metal-metal intranode and internode interactions can lead to new redox,

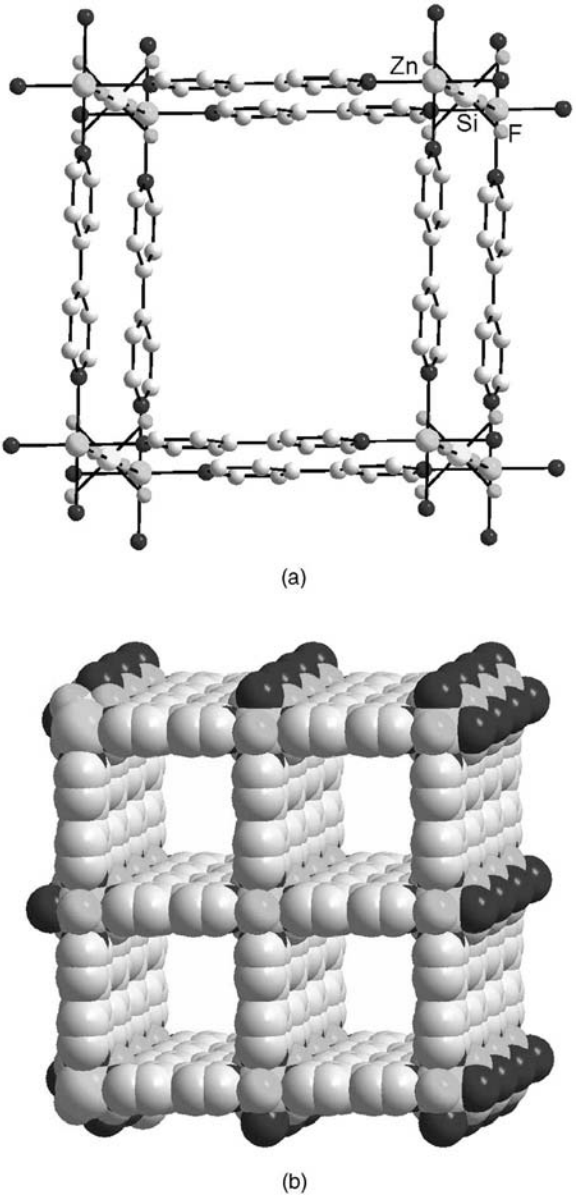

FIGURE 2. (a) Connection of the square-grid layers through SiF_6^{2-} ions in $[Zn(4,4'\text{-bipy})_2]SiF_6$; (b) Packing diagram showing the formation of channels.

electric or magnetic properties. The incorporation of the oligonuclear complexes into extended frameworks occurs through (a) formation of the nodes in a preliminary step, followed by the reaction with appropriate spacers; (b) formation of the nodes as a result of the interaction of the metal ions with

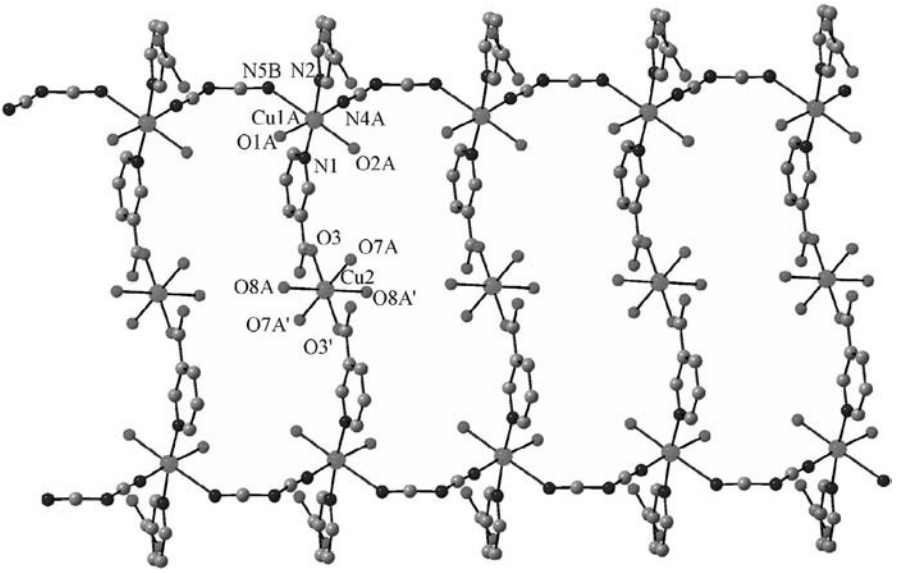

FIGURE 3. Perspective view of a ladder-like coordination polymer, $[Cu_3(na)_4(dca)_2(H_2O)_8]\cdot 2H_2O$, constructed from two different bridging ligands (nicotinato and dicyanamido).

the spacer; and (c) serendipitous assembly of the metal ions into clusters that are then interconnected by spacer molecules.

a. Alkoxo-Bridged Binuclear Copper(II) Complexes as Nodes

The binuclear copper(II) alkoxo-bridged nodes result spontaneously, through the deprotonation of the OH group, when reacting a copper(II) salt with the amino-alcohol and the *exo*-dentate ligand. The following amino-alcohols have been employed to generate binuclear alkoxo-bridged species: triethanolamine (H_3tea), diethanolamine (H_2dea), monoethanolamine (Hmea) and monopropanolamine (Hpa).[16] The aminoalcohols with higher denticity (H_3tea, H_2dea) favor the formation of 1D coordination polymers. Conversely, to obtain coordination polymers with higher dimensionality, aminoalcohols with lower denticity (Hmea, Hpa) have to be used (Scheme **9**). The resulting nodes, $[Cu_2(mea)_2]^{2+}$ and $[Cu_2(pa)_2]^{2+}$, generate 2D coordination polymers, provided that the anions do not coordinate to the copper ions. In this respect, copper(II) perchlorate is more appropriate as a starting material. Conversely, when using copper(II) nitrate, the dimensionality of the resulting coordination polymers is reduced because the nitrato ions coordinate to the metal centers as well, preventing the binding of a second linker molecule.

The reaction between copper(II) perchlorate diethanolamine, H_2dea, and 4,4-bipyridine affords a 1D coordination polymer: $[Cu_2(Hdea)_2(4,4'\text{-bipy})]$

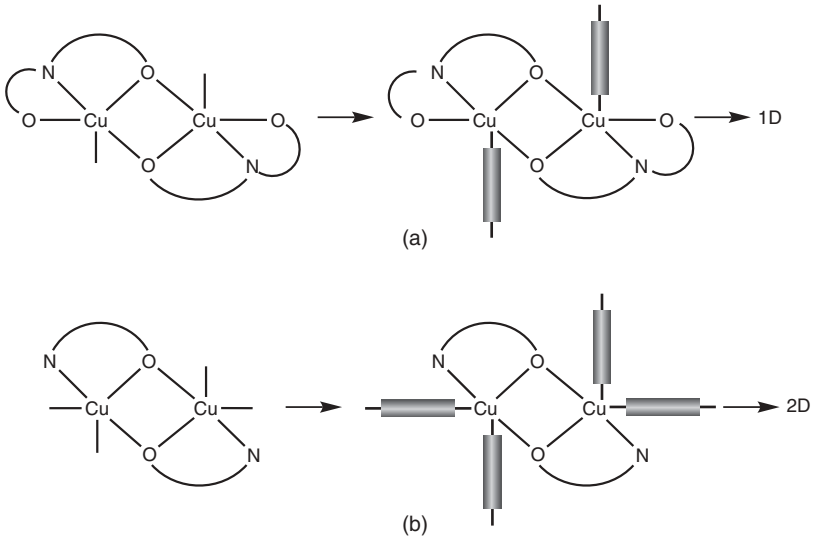

SCHEME 9

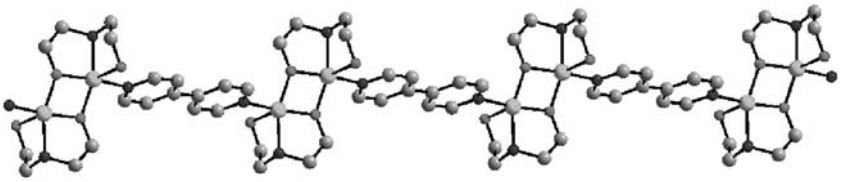

FIGURE 4. View of a 1D chain constructed from alkoxo-bridged nodes in $[Cu_2(Hdea)_2(4,4\text{-bipy})](ClO_4)_2$.

$(ClO_4)_2$ (Fig. 4).[16a] Each copper atom exhibits a distorted square pyramidal stereochemistry. The basal plane is formed by two alkoxo oxygen atoms, one amino nitrogen, and one nitrogen atom from the bridging 4,4-bipy ligand. The fifth coordination site is occupied by the oxygen atom from the OH group of the aminoalcohol. The alternate Cu $\cdots$ Cu distances within the chain, across the alkoxo and 4,4′-bipy bridges, are, respectively, 2.9880(5) and 11.0310(5) Å. As mentioned by employing bidentate amino-alcohols (monoethanolamine, propanolamine), 2D grid-like polymers can, in principle, be obtained. Let's discuss several such examples that exhibit different packing of the grids in the crystals: $[Cu_2(pa)_2(4,4'\text{-bipy})_2](ClO_4)_3 \cdot (4,4'\text{-bipy}) \cdot (H_2pa) \cdot (H_2O)$, $[Cu_2(mea)_2(bpanth)_2](ClO_4)_2 \cdot 2.5(CH_3OH)$ (bpanth = 9,10-bis(4-pyridyl)anthracene,[16b]

$[Cu_2(mea)_2(bpe)_2](ClO_4)_2$ (bpe = bis(4-pyridyl)ethylene), and $[\{Cu_2(pa)_2\}\{Au(CN)_2\}_2]$.[16c]

The structure of the cationic coordination polymer $[Cu_2(pa)_2(4,4'\text{-bipy})_2]_n^{n+}$ is illustrated in Figure 5a. The 2-D coordination networks for this compound stack parallel to one another generating parallel channels, which are marked in Figure 5b by arrows. Each channel is filled by an interesting hydrogen-bonded polymer constructed from uncoordinated 4,4′-bipy and water molecules, H_2pa^+ (monoprotonated aminopropanol species), and perchlorate ions. The second compound, $[Cu_2(mea)_2(bpanth)_2](ClO_4)_2 \cdot 2.5(CH_3OH)$, shows an interlocked structure resulting from the inclined interpenetration of grid-like sheets in which every square incorporates one net passing through it (Fig. 6). The third grid in $[Cu_2(mea)_2(bpe)_2](ClO_4)_2$ is constructed from a less bulky spacer, bpe, which allows a higher degree of interpenetration (twofold interpenetrating nets) (Fig. 7).

The fourth compound, $[\{Cu_2(pa)_2\}\{M(CN)_2\}_2]$,[16d] and the 4,4′-bipy derivative discussed earlier, $[Cu_2(pa)_2(4,4'\text{-bipy})_2](ClO_4)_3 \cdot (4,4'\text{-bipy}) \cdot (H_2pa) \cdot (H_2O)$, are constructed from similar nodes, which are connected through linear anionic linkers, $[Au(CN)_2]^-$ and 4,4′-bipy, respectively. Similar grid-like layers are formed. However, their packing diagrams are different. The 2-D cationic coordination networks in the 4,4′-bipy derivative also stack parallel to one another but with a slight offset, generating channels that accommodate the anions and the uncoordinated molecules. On the other hand, compound $[\{Cu_2(pa)_2\}\{Au(CN)_2\}_2]$ consists of neutral polymeric networks, without anions or neutral molecules to be hosted. The packing of the layers, as described, is driven by aurophilic interactions, the gold atoms from one layer being disposed exactly above the gold atoms from another layer (Fig. 8). The resulting channels are smaller than those existing in the 4,4′-bipy derivative.

An interesting case is the one observed with the Cu(II)–monoethanolamine–$[Au(CN)_2]^-$ system, in which the heterometallic complex $[\{Cu_4(mea)_4\}\{Au(CN)_2\}_4 \cdot H_2O]$ is obtained.[16d] It is constructed from tetranuclear $\{Cu_4(mea)_4\}$ nodes connected through $[Au(CN)_2]^-$ spacers. The pseudotetrahedral disposition of the copper ions within the node as well as the linearity of the spacer, $[Au(CN)_2]^-$, fulfills the necessary condition for the construction of a diamondoid topology (Fig. 9). The $\{Cu^{II}{}_4O_4\}$ heterocubane moiety can act as a tetrahedral synthon (Fig. 9a). As expected, a 3-D diamondoid net is assembled. The analysis of the packing diagram reveals a fourfold interpenetration of the diamondoid networks (Fig. 9b). Again, the aurophilic interactions intervene in sustaining the supramolecular architecture. Apart from the $[Au(CN)_2]^-$ groups acting as linkers, there are two $[Au(CN)_2]^-$ groups per tetranuclear cluster that act as terminal ligands. The interpenetrating diamondoid nets are connected through aurophilic interactions established between the dangling $[Au(CN)_2]^-$ ligands from adjacent nets. Infinite chains of gold atoms are thus formed (Fig. 9c). This is a unique case of fourfold interpenetrating nets that are interconnected through aurophilic interactions.

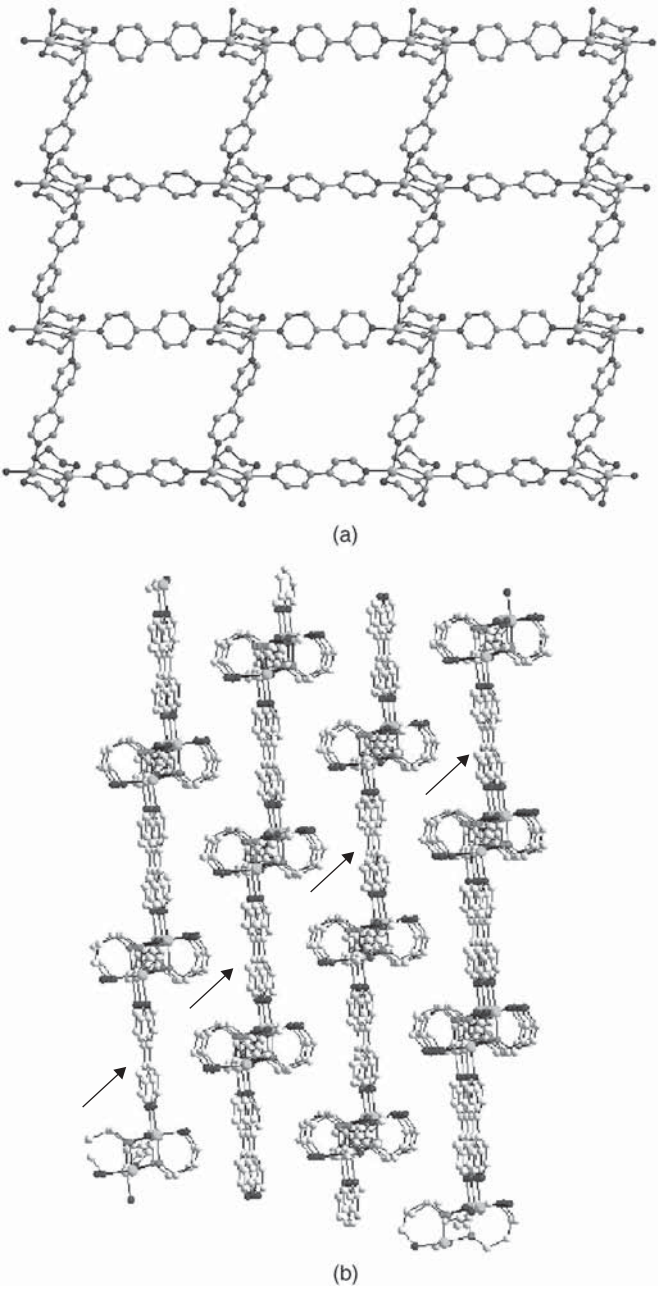

FIGURE 5. (a) View of a cationic layer in $[Cu_2(pa)_2(4,4\text{-bipy})_2](ClO_4)_3 \cdot (4,4\text{-bipy}) \cdot (H_2pa) \cdot (H_2O)$.; (b) Packing diagram showing the formation of channels.

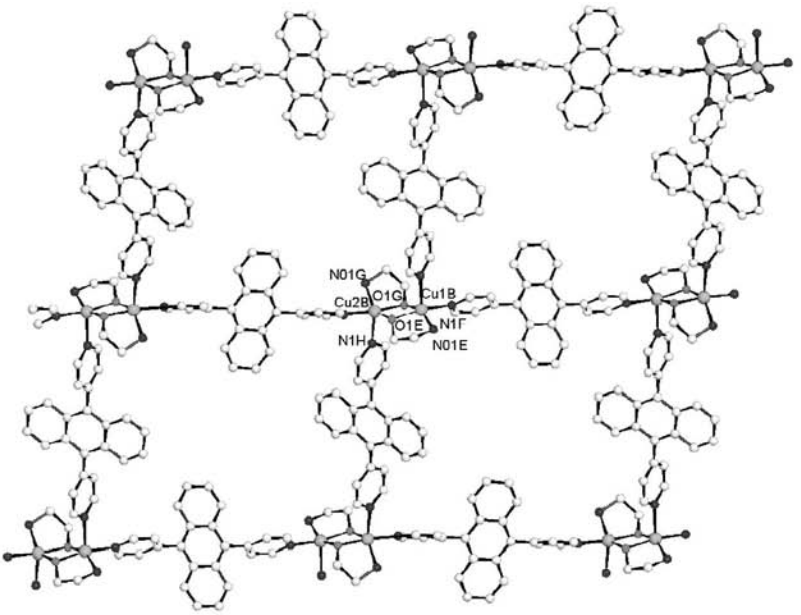

(a)

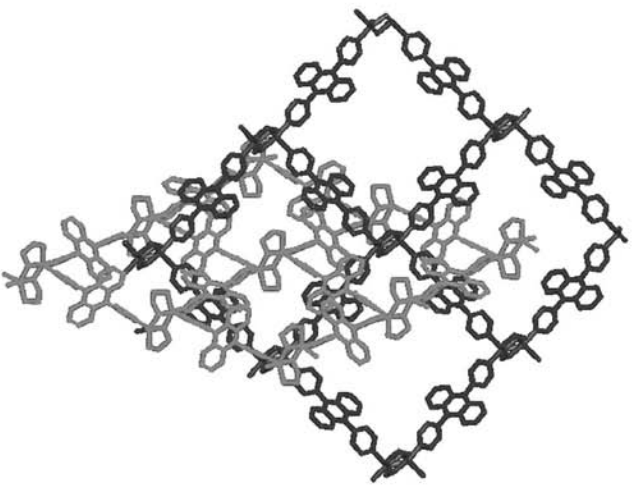

(b)

FIGURE 6. (a) Perspective view of a grid-like layer constructed from alkoxo-bridged nodes and bpanth spacers in $[Cu_2(mea)_2(bpanth)_2](ClO_4)_2 \cdot 2.5(CH_3OH)$.; (b) Packing diagram showing the interpenetration of the 2D layers.

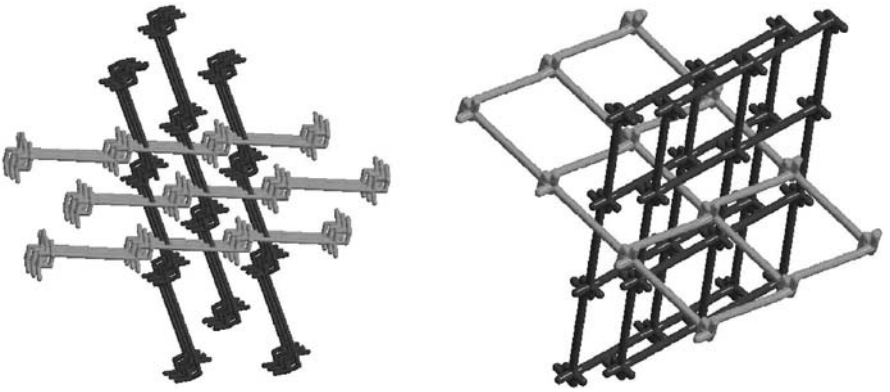

FIGURE 7. Perspective views of the interpenetrating nets in $[Cu_2(mea)_2(bpe)_2](ClO_4)_2$.

The prediction of structures for networks derived from flexible divergent ligands such as bis(4-pyridyl)ethane (bpa), bis(4-pyridyl)propane (bpp), or bis(4-pyridyl)disulfide (bpds) is less precise than for more rigid linkers. However, this flexibility has afforded interesting solid-state architectures. The reaction between copper(II) triflate, monoethanolamine, bpds yields a 2D coordination polymer with an original topology, $[Cu_2(mea)_2(bpds)_2](CF_3SO_3)_2 \cdot 2CH_3OH$ (Fig. 10).[16b] The structure can be viewed as Cu(II) centers connected by the bpds ligands in helicoidal chains, which are then interconnected by the alkoxo bridges to form layers. A view through each layer along the *b*-axis reveals nano-size channels of 10×10 Å filled with methanol molecules (Fig. 10b). Analysis of the channels confirms that each one is constructed exclusively either from left- or right-handed helices with each layer containing alternating helices of opposite chirality (Fig. 10c).

b. Homobinuclear Complexes with Compartmental Ligands as Nodes

The compartmental Schiff-base ligands derived from 2,6-diformyl-4-cresol (end-off and macrocyclic) are very popular in the chemistry of polynuclear complexes (Scheme **10**). They are nice examples showing how the nuclearity can be controlled. The two metal ions are hosted into the two compartments, their apical positions being available for the interaction with the spacer molecules. Let us first consider the macrocyclic ligand resulting from the condensation of 2,6-diformyl-4-methyl-phenol with 1,3-diamino-propane and its copper(II) and zinc(II) complexes. The reaction of the binuclear cooper complex with the dianion of the acetylenedicarboxylic acid leads to a linear coordination polymer. The copper atoms are quadruply bridged: two preexisting phenoxo oxygen atoms arising from the macrocyclic ligand, and two carboxylato groups, exhibiting the classical syn-syn bridging mode (Fig. 11).[17] The copper(II) ions exhibit an elongated octahedral geometry. By employing the zinc complex as a

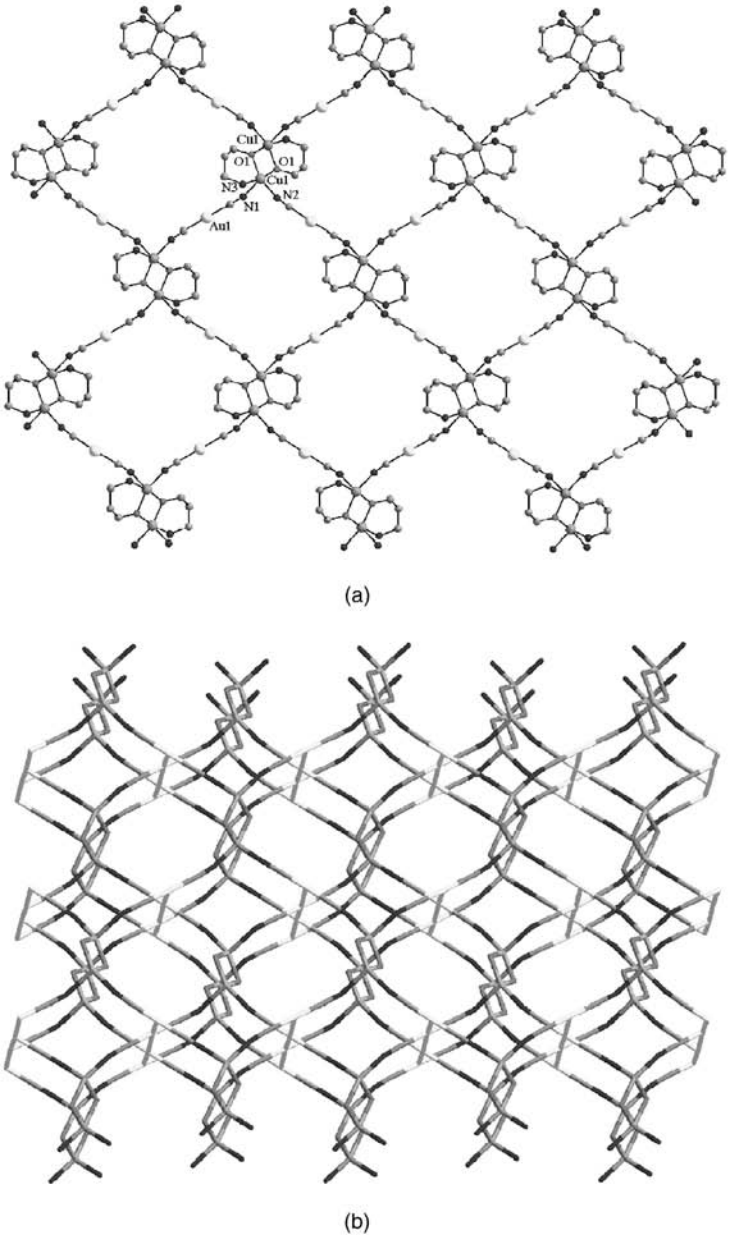

FIGURE 8. (a) Two-dimensional layer constructed from $[Cu_2(pa)_2]^{2+}$ nodes connected through $[Au(CN)_2]^-$ spacers. (b) Packing diagram showing the gold-gold interactions established between adjacent layers.

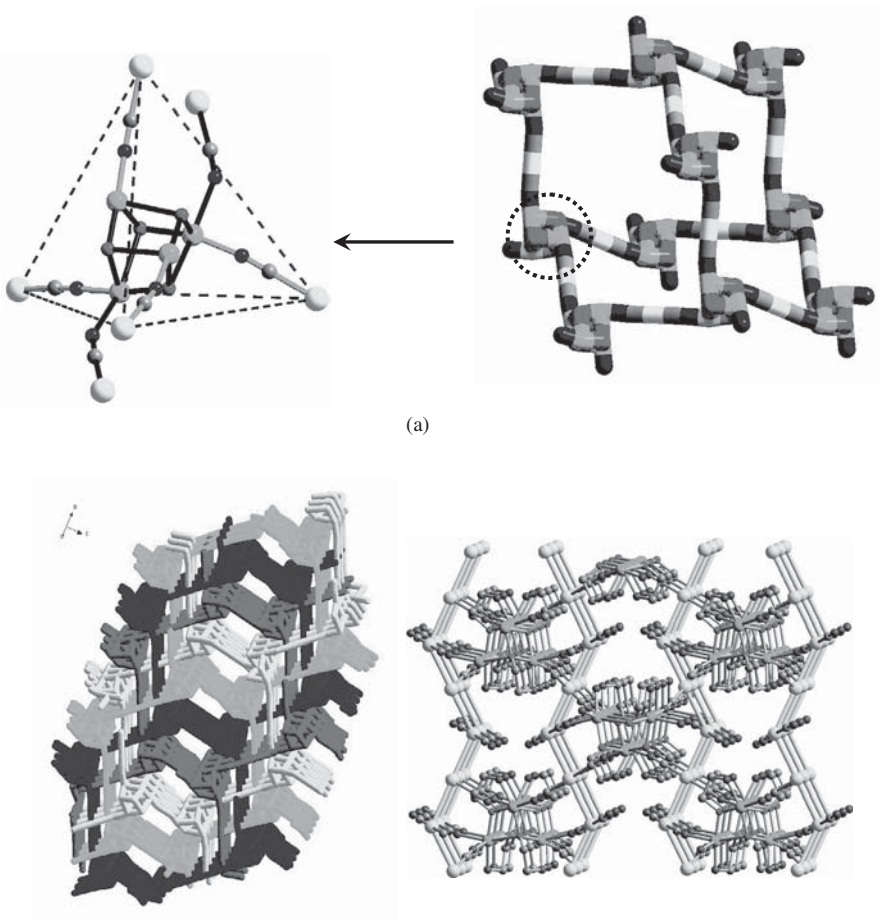

FIGURE 9. (a) The tetrahedral synthon in $[\{Cu_4(mea)_4\}\{Au(CN)_2\}_4 \cdot H_2O]$. Shown is an adamantane-like unit in the structure, and one tetranuclear node is highlighted. For clarity, the carbon atoms from organic ligands and the water molecules have been removed. (b) Packing diagram showing the fourfold interpenetration. (c) Aurophilic interactions connecting the interpenetrating nets.

node and 4,4′-bipy as a linker, ladder-like 1D coordination polymers with $\{Zn_2\}$ platforms are obtained (Scheme **11**).[18]

This kind of complex deserves particular attention. The short Zn · · · Zn distance within the coordination polymers generated by these bimetallic nodes is imposed by compartmental ligand, being ∼ 3.2 Å. When the bridging ligand is *trans*-1,2-bis(4-pyridyl)ethylene (bpe), then two bridging ligands connecting the

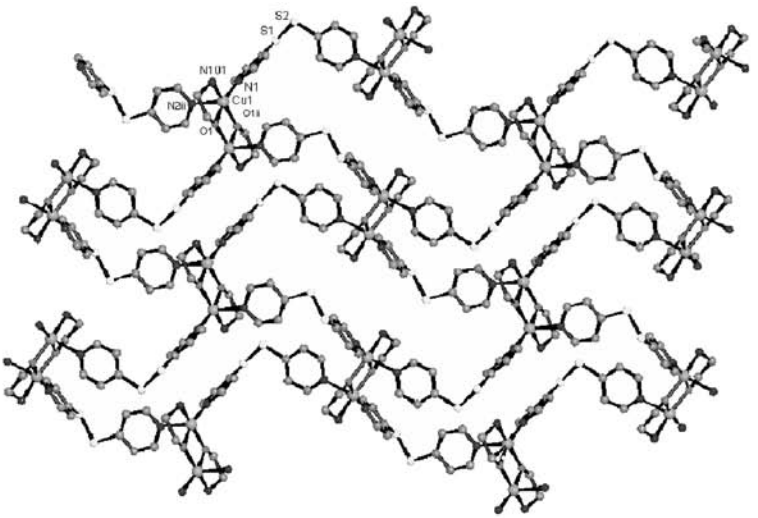

(a)

(b)

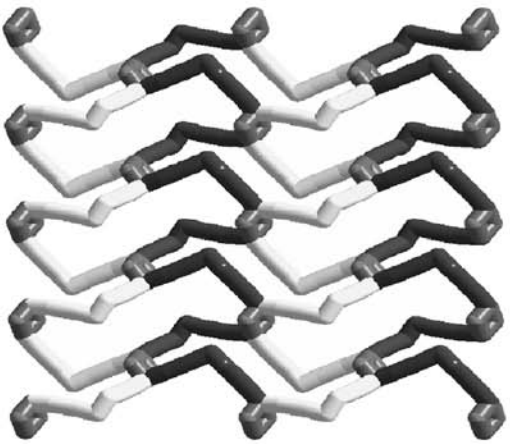

(c)

FIGURE 10. (a) View of a layer in $[Cu_2(mea)_2(bpds)_2](CF_3SO_3)_2 \cdot 2CH_3OH$. (b) View of layered structure and channels; (c) View of helices of opposite chiralities resulting from binding of Cu(II) with with bpds.

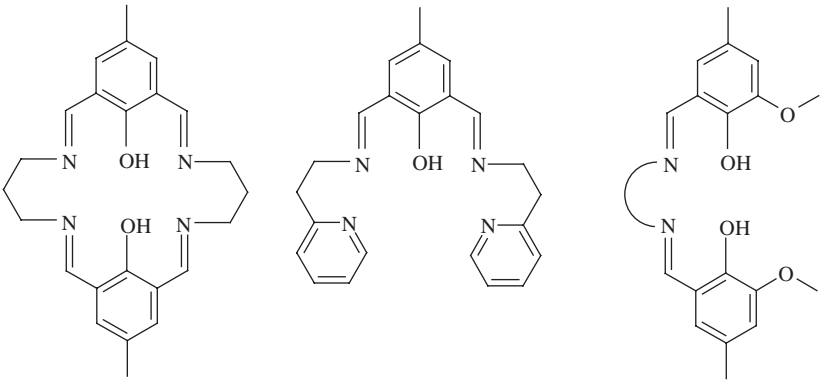

SCHEME 10

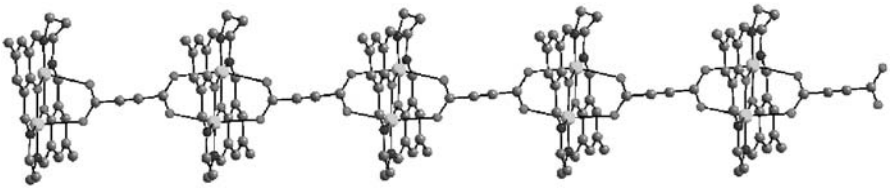

FIGURE 11. Perspective view of the chain resulted by connecting binuclear zinc(II) nodes with acetylenedicarboxylato spacers.

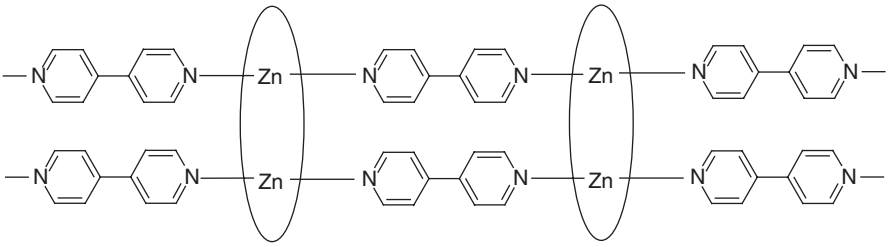

SCHEME 11

binuclear nodes are parallel and separated by about 3.6 Å. This short intermolecular distance is favorable for a [2 + 2] photodimerization in the solid state. The reaction between binuclear zinc(II) complex with the end-off Schiff-base ligand (Scheme **10a**) yields a 1D coordination polymer (Scheme **12**). The UV-irradiation of a powdered crystalline sample produced a coordination polymer in which the zinc(II) platforms are connected by tetra-(4-pyridyl)-cyclobutane, resulting from the photodimerization process (Scheme **12**).[19]

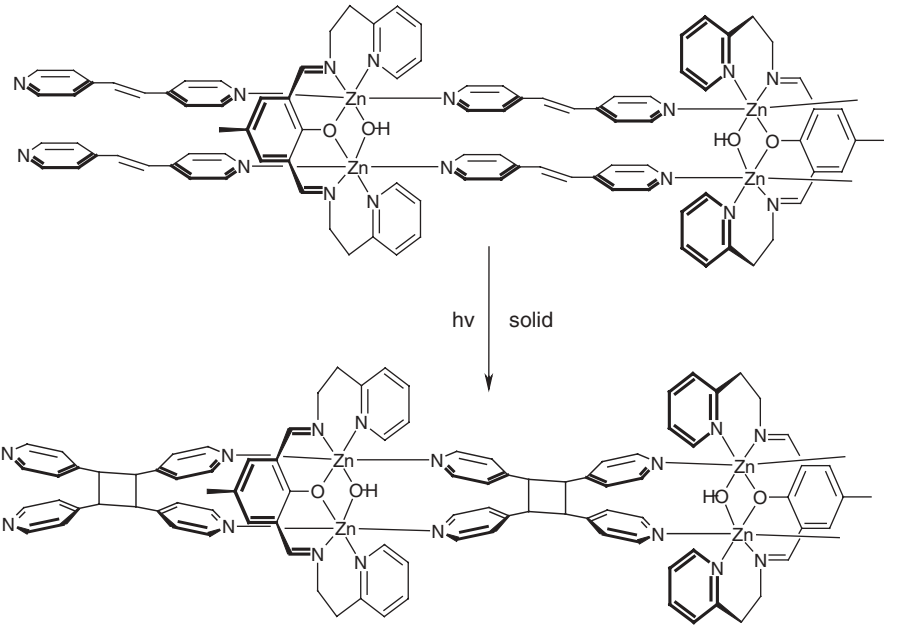

SCHEME 12

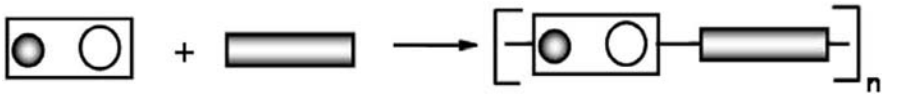

SCHEME 13

c. Heterobinuclear Complexes as Nodes

The main interest in heterometallic complexes arises from their magnetic properties. The combination of metal ions carrying different spins is an important chapter in modern molecular magnetism.[20] The classical synthetic approach toward heterometallic complexes consists of self-assembly processes between anionic complexes acting as ligands and assembling cations. An alternative way to obtain heterometallic coordination polymers is based on heterometallic binuclear complexes that can act as nodes. These nodes are easily obtained using compartmental ligands (Scheme **13**), which are readily accessible and allow good control over the number and the nature of the metal ions.

The compartmental ligands derived from 3-methoxy-salicylaldehyde and a diamine (Scheme **10c**) have been specially designed to obtain binuclear 3d-4f complexes.[21] Their exceptional versatility as building blocks is due to the presence of two metal ions that differ drastically in their chemical behaviour: the rare-earth cations are hard acids, with a strong oxophilic character and high

FIGURE 12. A 1D coordination polymer in $[LCu^{II}Gd^{III}(acdca)_{1.5}(H_2O)_2]\cdot 13H_2O$ formed by connecting [CuGd] nodes with the dianion od the acetylenedicarboxylic acid.

coordination numbers, whereas copper(II) is a borderline acid with a marked tendency to adopt a more or less distorted square-pyramidal geometry. Consequently, they can interact selectively with various spacers.

The *exo*-dentate ligands with oxygen donor atoms are supposed to interact preferentially with the oxophilic rare earths cations, whereas the exo-dentate ligands bearing nitrogen atoms will prefer the copper(II) ions.[22] Indeed, when reacting $[LCu^{II}Gd^{III}(NO_3)_3]$ with the dianion of acetylenedicarboxylic acid, $acdca^{2-}$, a 1D coordination polymer, $^{1}_{\infty}[LCu^{II}Gd^{III}(acdca)_{1.5}(H_2O)_2]\cdot 13H_2O$, is formed, in which the spacer interacts only with the gadolinium ions (Fig. 12). The {LCuGd} entities are alternatively bridged by one and two dicarboxylato ligands having different connectivity modes: With the single bridge, the acetylenedicarboxylato ligand acts as a bis-chelating ligand toward two gadolinium ions, whereas with the double bridge each carboxylato group acts as an unidentate ligand.

A very interesting case is the one resulting from using ligand simultaneously bearing nitrogen and oxygen donor atoms; isonicotinic acid. A 2D coordination polymer, $[LCu^{II}Pr^{III}(NO_3)_2(in)]$, has been obtained by employing the isonicotinate ion, in^-, as a linker with two different coordination sites.[23] The heterobinuclear units, $[LCuPr(NO_3)_2]^+$, are connected through the unsymmetrical *exo*-bidentate ligands, leading to an extended structure (Fig. 13). The building principle is based on the selective interaction of the spacer, in^-, which coordinates with the carboxylato group to the oxophilic Pr^{III} ions and, with the nitrogen atom, to the Cu^{II} ion.

The compartmental ligands derived from 3-methoxy-salicylaldehyde are appropriate for obtaining 3d-3d′ complexes as well, which can be further employed as nodes. The heterobinuclear nodes $[LCuM]^{2+}$, are obtained by reacting the mononuclear complex, [LCu] with a salt of the second metal ion (Mn^{2+}, Co^{2+}).[24] The spacers can interact with only one type of metal ions from different nodes (Scheme **14a**), or they can connect one type of metal ion from a node with another type from the next node (Scheme **14b**). The network topology is also influenced by the number of the connecting groups

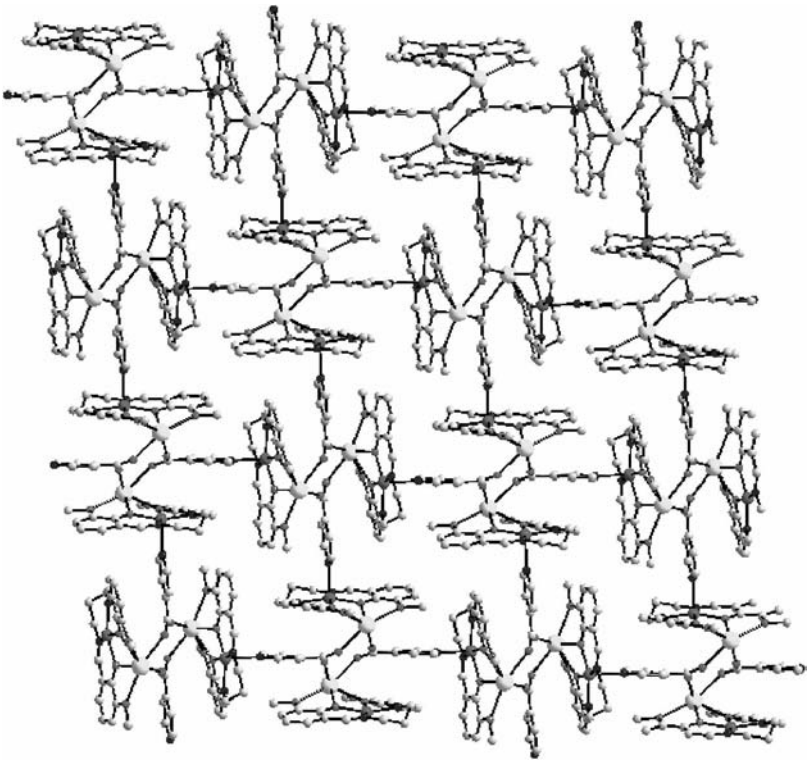

FIGURE 13. View of the 2D coordination polymer, $[LCu^{II}Pr^{III}(NO_3)_2(in)]$, formed by connecting [CuPr] nodes with the isonicotinato anion.

and their spatial orientation. Let's discuss first the crystal structures of two coordination polymers constructed from {LCuMn} tectons and the anions of the pyrazole-3,5-dicarboxylic and trimesic acids. The structure of $[LCuMn(pzdc)(CH_3OH)(H_2O)] \cdot H_2O$ consists of chains with {LCuMn} nodes connected by the pyrazole-dicarboxylato spacers. The $pzdc^{2-}$ ion coordinates through one nitrogen and one oxygen atom from the vicinal carboxylato group to the manganese ion from a node, and with an oxygen atom from the other carboxylato group to the manganese ion from the neighboring node (Fig. 14).

The trimesate anion, $trim^{3-}$, is currently employed in crystal engineering. The self-assembly process involving the mononuclear copper complex, [CuL], Mn^{II} ions and the trimesate ion leads to $[LCuMn(trim)_{2/3}(CH_3OH)_{2/3}(H_2O)_{1/3}] \cdot 0.66(H_2O) \cdot 0.66(CH_3OH)$, a 1D coordination polymer with a unique topology (Fig. 15). There are three crystallographically independent copper ions and three independent manganese ions. Two of the copper ions, Cu1 and Cu3, do not interact with the spacer. The three types of manganese ions are coordinated as follows: Mn1 surrounded by eight oxygen atoms, four from the

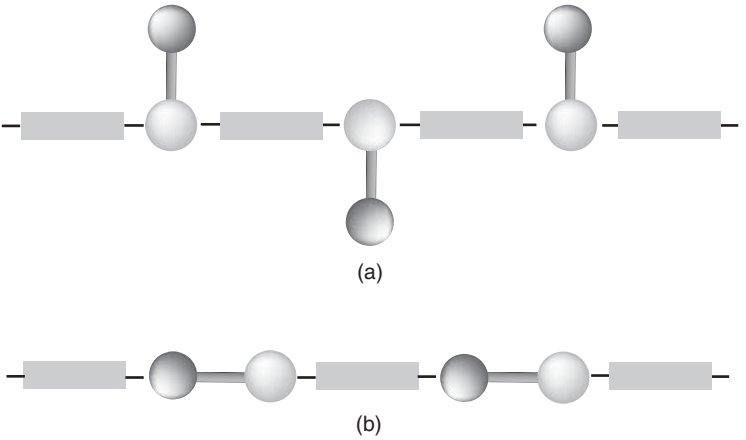

SCHEME 14

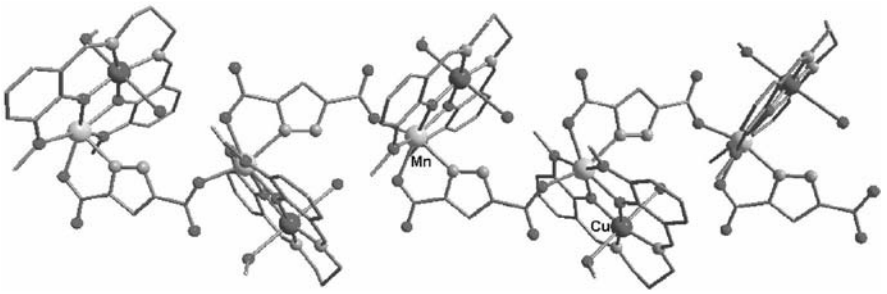

FIGURE 14. Perspective view of a chain in$[LCuMn(pzdc)(CH_3OH)(H_2O)] \cdot H_2O$.

external compartment of the ligand and four from two chelating carboxylato groups arising from two spacers. Mn2 is heptacoordinated with four oxygen atoms from the compartmental ligand, two oxygen atoms from a chelating carboxylato group, and an aqua ligand. Finally, Mn3 is also heptacoordinated, by seven oxygen atoms; four from the Schiff-base, two from a chelating carboxylate, and a seventh one from a monodentate carboxylate arising from another spacer. The coordination polymer is constructed from two types of $trim^{3-}$ spacers, **A** and **B** (Fig. 15a). The parallel chains are formed by [Cu1Mn1] and [Cu3Mn3] nodes, whereas the ladder steps are formed by the [Cu2Mn2] ones. The **A** trimesate ions coordinate only to manganese ions (each carboxylato group acts as a chelate towards Mn1, Mn2, and Mn3, respectively). The three carboxylato groups of the **B** trimesate ions are involved in coordination as follows: one carboxylato group acts as a chelate toward Mn1, the second one is coordinated to Mn3 through one oxygen, while the third one interacts through one oxygen atom to Cu2. Short and

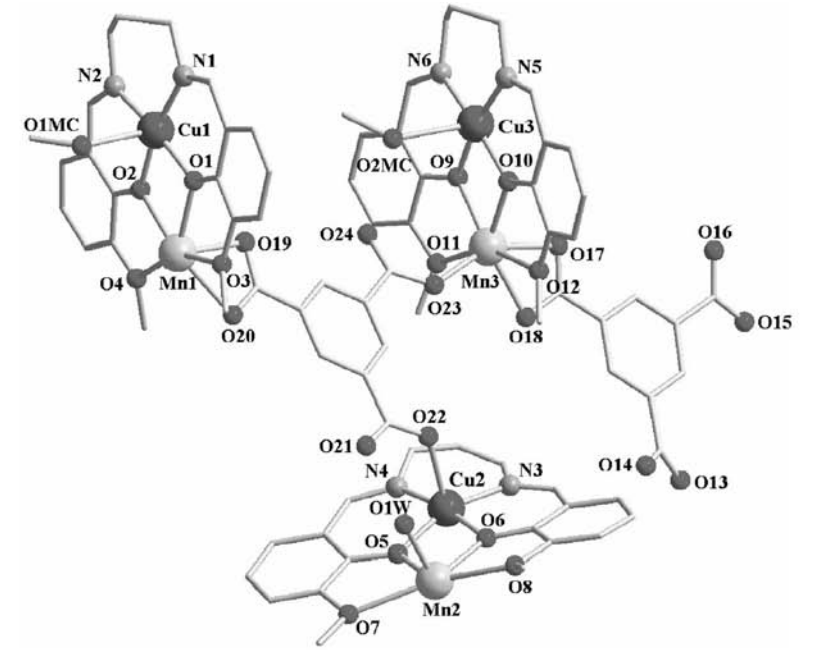

(a)

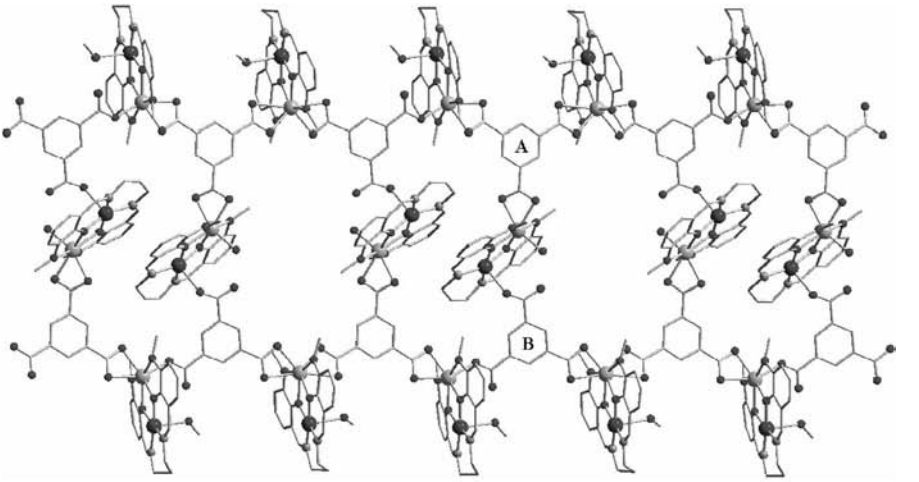

(b)

FIGURE 15. (a) Perspective view of the crystallographically independent nodes in $[LCuMn(trim)_{2/3}(CH_3OH)_{2/3}(H_2O)_{1/3}] \cdot 0.66(H_2O) \cdot 0.66(CH_3OH)$; (b) View of a ladder-like polymer.

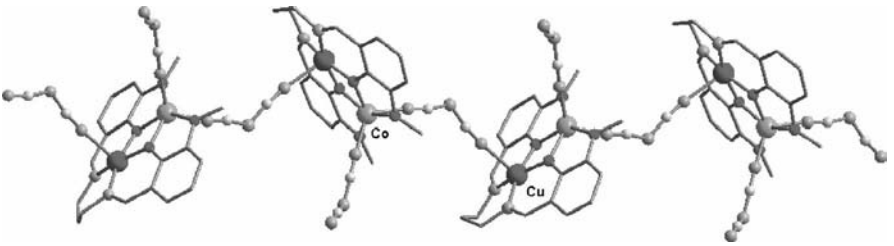

FIGURE 16. View of the dicyanamido-bridged chain in[LCuCo$(dca)_2$].

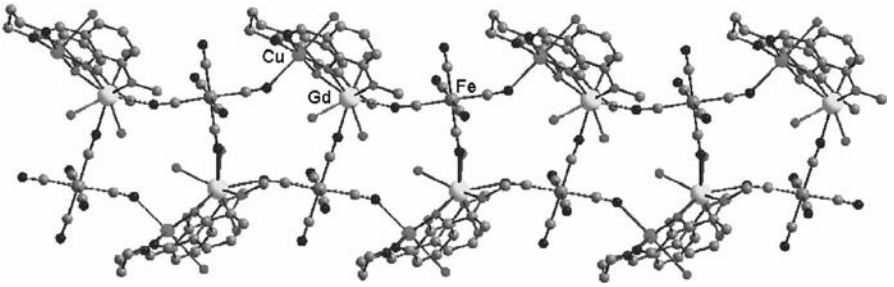

FIGURE 17. Perspective view of the heterotrimetallic chain [{LCu}Gd$(H_2O)_3${Fe$(CN)_6$}] $\cdot$ $4H_2O$.

long distances between the rungs alternate along the ladder (e.g., the alternate distances between the Cu2 ions belonging to adjacent steps are 6.573 and 15.377 Å).

The dicyanamido-bridged polymer [LCuCo$(dca)_2$] crystallizes from a solution containing [CuL], cobalt nitrate, and sodium dicyanamide. Its crystal structure consists of linear chains, which result from connecting the [CuCo] nodes through single $\mu_{1,5}$-dca bridges (one end of the dca bridge is coordinated into the apical position of the copper ion from a node, and the other one to the cobalt ion from the next node) (Fig. 16).

d. Heterotrimetallic Coordination Polymers

The heterobinuclear complexes are useful precursors for obtaining heterotrimetallic coordination polymers. The [LCuLn$(NO_3)_3$] complexes are again suitable precursors: The nitrato ligands can be replaced by connectors carrying the third metal ion, for example hexacyano complex anions, $[M(CN)_6]^{3-}$ (M = Cr, Fe, Co). A family of isomorphous heterotrimetallic chains, [{LCu}Ln$(H_2O)_3${M$(CN)_6$}] $\cdot$ $4H_2O$, has been obtained.[25] The $[M(CN)_6]^{3-}$ ion connects three metal ions (two Cu^{II} and one Ln^{III}), through three meridially disposed cyano groups, resulting in a ladder-type topology built up from distorted {Gd_2Cr_2Cu} pentagons sharing the CrGd edges (Fig. 17).

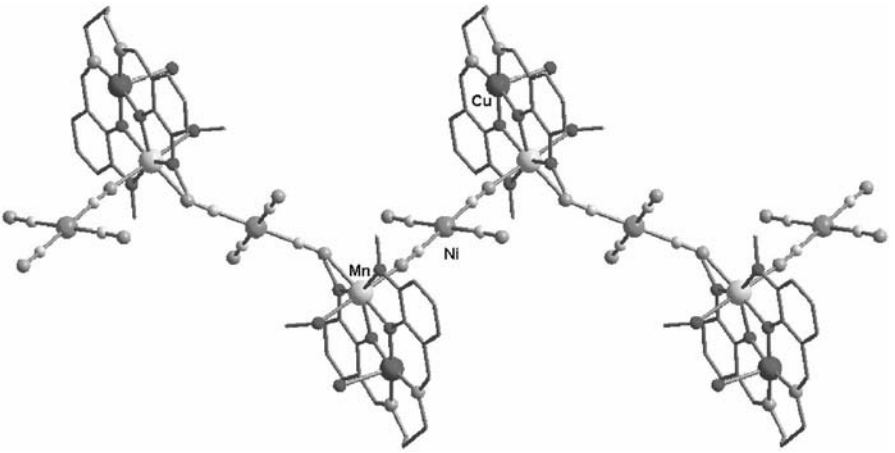

FIGURE 18. Perspective view of the heterotrimetallic chain in [{LCu(CH_3OH)(H_2O)Mn}{Ni($CN)_4$}] · (H_2O)(CH_3CN).

A [$Cu^{II}Co^{II}Ni^{II}$] coordination polymer, [{LCu(CH_3OH)(H_2O)Mn}{Ni($CN)_4$}] · (H_2O)(CH_3CN), which consists of linear zigzag chains constructed from {LCuMn} nodes connected by $[Ni(CN)_4]^{2-}$ spacers (Fig. 18) has been obtained.[24b] The $[Ni(CN)_4]^{2-}$ ions interact only with the manganese(II) ions from two nodes through two *trans* CN groups.

B. Flexible Ligands Approach: Polycarboxylates as Anionic Linkers. A Case Study—Malonato Complexes

Several recent reviews have projected about the gigantic rise in the number of publications about coordination polymers per year since 1990.[26] In the majority of coordination polymers, either the O-atoms of anions (carboxylates, nitrates, sulfates, phosphates, phenolates) and/or the N-atoms of cyanates, cyanides, amines, pyridines engage in coordination bonds with transition-metal atoms (Tr–O and Tr–N). A Cambridge structural database (CSD) search indicates that the coordination polymers propagated by Tr–O (7074 hits) are the major portion compared to those of Tr–N (6392 hits). In about 53% of the Tr–O type, the O-atom belongs to carboxylates, whereas in about 40% of the Tr–N kind, the N-atom belongs to pyridine.[27] These statistics indicate the importance of carboxylate and pyridine moieties in generating coordination polymers.

The simple rod-like exo-bidentate organic ligands such as 4,4′-bipyridil, as we have seen, have the single greatest influence in determining the type and topology of the product.[28–32] These spacers serve to link metal sites and to propagate structural information as expressed in the metal coordination

preferences through the extended structure. Properties of organic spacers, such as solubility, coordination ability, length, geometry, and relative orientation of the donor group, play very important roles in dictating the polymer framework topology and even in affecting the formation of polymer vs. oligomer vs. molecule.[29–33] Generally, these intensively investigated ligands can lead to more predictable crystal structures, but their diversity has been limited to some extent due to the fact that little or no conformational changes can be observed for these kinds of ligand when treated with metal ions. By contrast, flexible ligands can adopt different conformations and coordination modes according to the geometric requirements of different metal ions and may afford unpredictable and interesting coordination networks. Thus rich topologies, including coordination modes, packing fashions, and dimensionalities of coordination solids, may result from these ligands. Their coordination chemistry has been less explored and the investigation of metal-organic frameworks is still a great challenge.[34]

While the rigid ligands with fixed bridging angles discussed in the previous sections are suitable candidates for a more rational design of network structures, conformationally flexible ligands as spacers preclude prediction and control of the resultant structures. However, they are well suited to accommodate a wide variety of architectures and offer a high degree of adaptability—for example, the inclusion of counterions or other guest molecules.

As flexible spacers, some polycarboxylate ligands are a very good choice because the carboxylate group is one of the most widely used bridging ligands for designing polynuclear complexes. The diversity of these organic groups offers great potential to modulate structural architectures and the use of different synthetic conditions considerably enlarges the range of possible arrangements arising from a metal and an organic molecule.

Polycarboxylate ligands as anions possess several interesting characteristics: (a) they have carboxylic groups that, after partial or full deprotonation, can coordinate to the metal ions in a wide variety of coordination modes leading to high dimensional structures; (b) they can act not only as hydrogen-bond acceptors but also as hydrogen bond donors, depending on the number of deprotonated carboxylic groups; and (c) depending on the geometry, the ligands may connect metal ions in different directions.

Taking into account their great diversity, carboxylates seem to be a good election for constructing novel materials with interesting properties such as porosity, chirality or magnetism. Thus much still remains to be understood in this field, although it is clear that very simple organic molecules can lead to the most remarkable frameworks.

i. Dicarboxylates

Many compounds containing the dicarboxylate $[OOC(CH_2)_nCOO]^{2-}$ dianion have been prepared and characterized.[35] In fact, the conformational flexibility of the aliphatic dicarboxylate-type ligands is reflected in the diversity of their connecting modes that lead to novel frameworks. In general, aliphatic

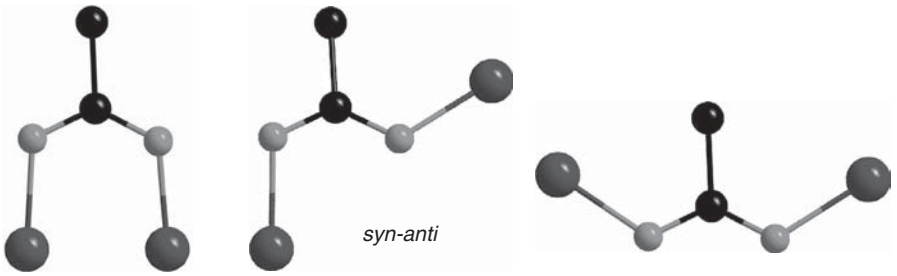

SCHEME 15

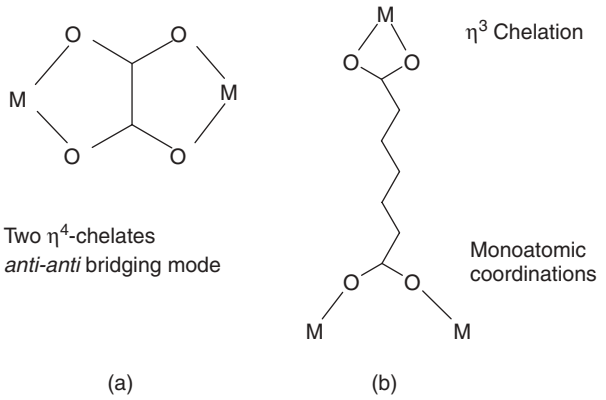

SCHEME 16

carboxylates exhibit the following features when considering their complexing ability: (a) monodentate and bidentate coordination modes; (b) *syn-syn*, *anti-anti*, or *syn-anti* conformations (Scheme **15**); (c) tricoordinated oxygen-atom connectivity; (d) pillaring of the metal-oxygen layers or networks; and (e) and generation of secondary building units (SBUs) by acting as capping agents through their carboxylate moieties.

The most widely studied dicarboxylic ligand is the oxalate $(C_2O_4)^{2-}$ anion in its characteristic coordination mode, the η^4-chelation, acting as a bisbidentate ligand, bridging the metal centers in an *anti-anti* fashion (Scheme **16a**).[36] The higher members of the dicarboxylic series exhibit the characteristic chelate coordination of the CO_2^- group, the η^3-chelation, which can be accompanied by one or two monoatomic coordinations; other chelate modes are forbidden for steric reasons (Scheme **16b**).[37]

ii. The Case of Malonate

The ability of flexible dicarboxylate ligands to build up coordination polymers has been checked with the thorough study of the complexation of the malonate ligand (where *malonate* stands for the dianion of the propanedioic acid, H_2mal, hereafter noted as mal). This ligand has a methylene group between the two carboxylates and a minimal change with respect to the rigid oxalate; it has a great influence in its flexibility and versatility. The malonate dianion can then exhibit a great variety of coordination modes (Scheme **17**),[38a] leading to a high ability to form high-dimensional frameworks. In contrast with the predictable crystal structures rationally designed with the oxalate complex, the work with a more flexible ligand often gives unexpected results, new coordination modes, and unpredictable behavior, the starting points for new polymers with new properties. As an example of these, the magnetic behavior of oxalato-complexes is determined by the η^4-chelation; however, many scenarios are possible with the malonate ligand. The most usual coordination mode toward the copper(II) metal ion is the bidentate-monodentate with the carboxylate-bridge in out-of-plane *anti-syn* conformation (Scheme **17c**); therefore, the observed magnetic interaction is ferromagnetism, with J exchange coupling constants on the order of $+12$ cm^{-1}.[38b]

From a synthetic point of view, the variety of coordination modes represents a challenge. The flexibility of the ligand does not allow the formation of a determined pattern in the coordination that can be repeated synthesis after synthesis. Moreover, the subtle variation of different features of the synthetic procedure could afford different crystal structures.

iii. Influence of the Synthetic Conditions

The copper(II)-malonate system is paradigmatic of the flexibility of the ligand and the different structures it can achieve. Five crystal structures of copper(II) complexes that contain only malonate and water as ligands are known; their formulas are $[Cu(H_2O)_6]\cdot[Cu(mal)_2(H_2O)_2]$,[39] $\{[Cu(H_2O)_4][Cu(mal)_2(H_2O)]\}$,[40] $\{[Cu(H_2O)_4]_2[Cu(mal)_2(H_2O)]\}[Cu(mal)_2(H_2O)_2]\{[Cu(H_2O)_4][Cu(mal)_2(H_2O)_2]\}$,[41] $\{[Cu(H_2O)_3][Cu(mal)_2(H_2O)]\}_n$,[41] and $\{[Cu(H_2O)_3][Cu(mal)_2]_2\cdot 2H_2O\}_n$.[42]

The structure of the $[Cu(mal)_2]^{2-}$ anion as either a sodium[43] or alkaline-earth salt is known.[44] Previous studies of complex formation in aqueous solution between malonic acid and Cu(II) as a function of pH revealed the stepwise formation of the species $[Cu(Hmal)]^+$, [Cu(mal)], and $[Cu(mal)_2]^{2-}$.[45] From the synthetic work, it can be observed that the isolated dimer $\{[Cu(H_2O)_4][Cu(mal)_2(H_2O)]\}$ is obtained from highly concentrated, hot solutions containing basic carbonate with an excess of malonic acid. The ionic salt $[Cu(H_2O)_6]\cdot[Cu(mal)_2(H_2O)_2]$ is formed by the slow evaporation of diluted aqueous solutions containing basic carbonate and malonic acid in a 1:1 molar ratio. The final pH of these solutions must be kept at ~ 3, through the careful addition of a poorly coordinating base. At higher pH values (obtained by further addition of NaOH or Na_2CO_3), the concentration in solution of

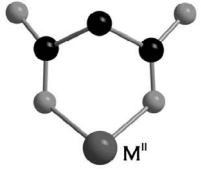

(a) M^{II} = Cu(II), Co(II), Mn(II), Ni(II), Zn(II)

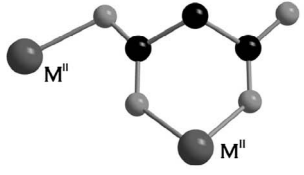

(b) M^{II} = Cu(II)

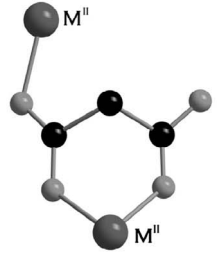

(c) M^{II} = Cu(II), Mn(II)

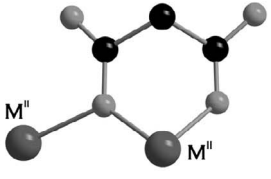

(d) M^{II} = Cu(II)

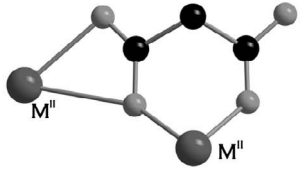

(e) M^{II} = Cu(II)

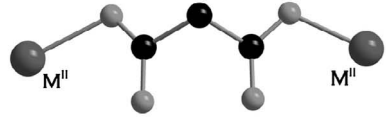

(f) M^{II} = Zn(II)

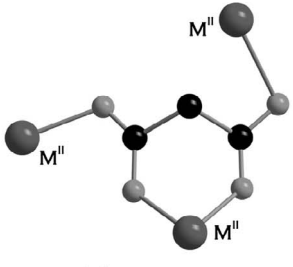

(g) M^{II} = Cu(II), Mn(II)

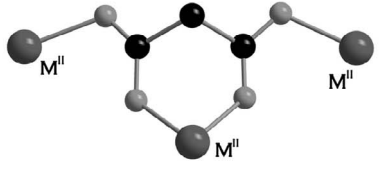

(h) M^{II} = Cu(II), Co(II), Mn(II), Ni(II), Zn(II)

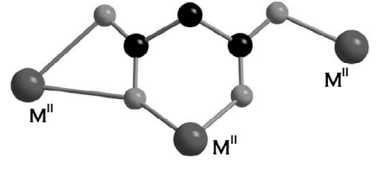

(i) M^{II} = Cu(II)

SCHEME 17

$[Cu(mal)_2]^{2-}$ becomes significant, and the precipitation of $Na_2[Cu(mal)_2]$ takes place.[46] If the concentration of Cu(II) exceeds that of malonate, then mixed basic copper(II) salts are obtained. The use of complexing but less-basic bases, such as 4,4′-bipyridine and pyridine, allowed us to obtain $\{[Cu(H_2O)_4]_2[Cu(mal)_2(H_2O)]\}[Cu(mal)_2(H_2O)_2]\{[Cu(H_2O)_4][Cu(mal)_2(H_2O)_2]\}$ and $\{[Cu(H_2O)_3][Cu(mal)_2(H_2O)]\}_n$, respectively, by a smooth increase in the pH without the precipitation of undesired basic salts. It has been observed that the addition of pyridine[47] and other bases[48] causes the formation of a mixed ligand complex [CuL(mal)] that avoids the formation of basic copper(II) salts, minimizes the concentration of free Cu(II), and—because the pH is increased—favors the formation of $[Cu(mal)_2]^{2-}$. This seems to allow the slow growth of complexes $\{[Cu(H_2O)_4]_2[Cu(mal)_2(H_2O)]\}[Cu(mal)_2(H_2O)_2]$ $\{[Cu(H_2O)_4][Cu(mal)_2(H_2O)_2]\}$ and $\{[Cu(H_2O)_3][Cu(mal)_2(H_2O)]\}_n$, instead of $[Cu(H_2O)_6]\cdot[Cu(mal)_2(H_2O)_2]$ and $\{[Cu(H_2O)_4][Cu(mal)_2(H_2O)]\}$. At pH values > 3,[46] the addition of monoethanolamine (mea) to the aqueous coppermalonate solution increased the pH of the reaction medium and favored the formation of $[Cu(mal)_2]^{2-}$ to give $\{[Cu(H_2O)_3][Cu(mal)_2]_2 2H_2O\}_n$. In summary, parameters such as pH, Cu(II):H_2mal molar ratio, total concentration, and temperature are very critical when attempting to prepare malonate-containing copper(II) complexes and compounds with closely associated formulas. However, the variety of results illustrate that good results can be obtained by monitoring these parameters carefully.

The first of the series, $[Cu(H_2O)_6][Cu(mal)_2(H_2O)_2]$, which is obtained at room temperature,[39] is the mononuclear Cu(II) complex described by Pajunen et al.[49] In this compound, the malonate adopts the bidentate (no-bridging, Scheme **17a**) coordination mode, acting as a blocking ligand leading to isolated molecules that are interconnected through hydrogen bonding (Fig. 19a). With a subtle increase of the temperature, inorganic condensation occurs to form the dinuclear molecule $[(H_2O)_4Cu(\mu\text{-mal})Cu(mal)(H_2O)_2]$, (Fig. 19b).[40] The copper(II) ions are linked by carboxylates in an *anti-syn*, η^5 bidentate + unidentate coordination mode (Scheme **17b**). Remarkably, the main $[Cu(mal)_2(H_2O)_2]^{2-}$ motif present in $[Cu(H_2O)_6][Cu(mal)_2(H_2O)_2]$ remains unaltered, just a pendant $[Cu(H_2O)_4]$ group has been added.

A very interesting case is the use of template molecules (4,4′-bpy and pyridine) in the synthesis. A higher degree of condensation occurs as has been exemplified in the third and very rare complex, $\{[Cu(H_2O)_4]_2[Cu(mal)_2(H_2O)]\}$ $[Cu(mal)_2(H_2O)_2]\{[Cu(H_2O)_4]$ $[Cu(mal)_2(H_2O)_2]\}$.[41] The structure is made up of mononuclear, dinuclear, and trinuclear copper(II) units of formulae $[Cu(mal)_2(H_2O)_2]^{2-}$, $\{[Cu(H_2O)_4][Cu(mal)_2(H_2O)_2]\}$, and $\{[Cu(H_2O)_4]_2$ $[Cu(mal)_2(H_2O)_2]\}^{2+}$, respectively, which are linked by electrostatic forces, van der Waals interactions, and an extensive network of hydrogen bonds involving carboxylate groups and water molecules. The trinuclear copper(II) unit is the next condensation of dinuclear unit in which another pendant $[Cu(H_2O)_4]$ group has been symmetrically attached to the central $[Cu(mal)_2(H_2O)_2]^{2-}$ unit (Fig. 19c). Whereas the mononuclear and dinuclear entities could also be obtained under the adequate crystallization conditions,

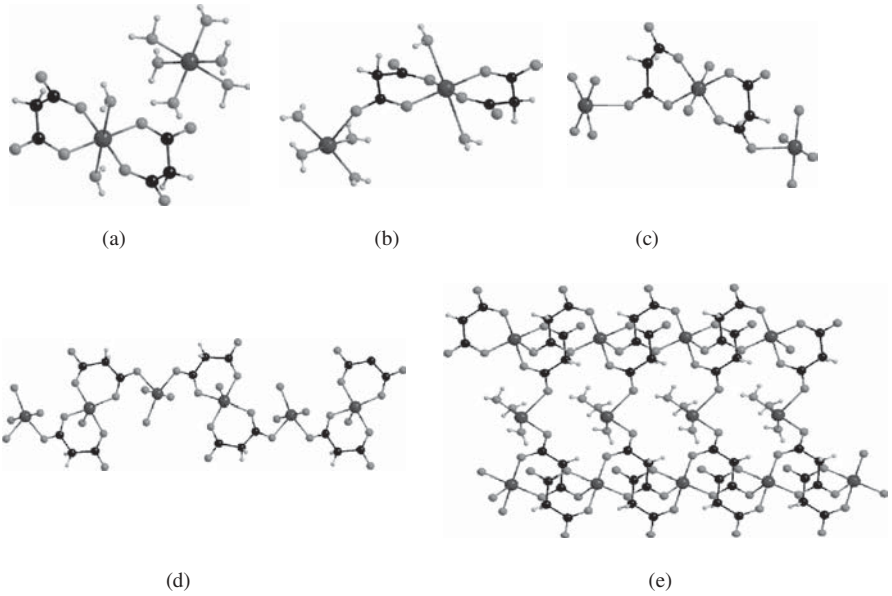

FIGURE 19. The copper(II) Malonate system. (a) Monomeric copper(II) malonate unit in complex $[M^{II}(H_2O)_6][Cu^{II}(mal)_2(H_2O)_2]$ with M = Mn, Co, Ni, Cu and Zn. (b) Perspective view of the dinuclear copper(II) units of compound $[(H_2O)_4Cu(\mu\text{-mal})Cu(mal)(H_2O)_2]$. (c) Perspective view of the trinuclear copper(II) units of compound $\{[Cu(H_2O)_4]_2[Cu(mal)_2(H_2O)]\}$ $[Cu(mal)_2(H_2O)_2]\{[Cu(H_2O)_4][Cu(mal)_2(H_2O)_2]\}$. (d) Perspective view of a fragment of the chain of compound $\{[Cu(H_2O)_3][Cu(mal)_2(H_2O)]\}_n$. (e) Packing diagram of $\{[Cu(H_2O)_3][Cu(mal)_2]_2 \cdot 2H_2O\}_n$.

this situation was never encountered for the trinuclear entity. The third copper(II)-malonate compound is a very rare case, in which three copper(II) complexes of different nuclearity and containing the same ligand coexist in the same crystal. Previous examples in the chemistry of copper(II) were known but only two different entities were present in them.[50]

Changing the template (pyridine instead of 4,4′-bipy) the complete polymerization of the $[Cu(mal)_2(H_2O)_2]^{2-}$ entity is achieved: $\{[Cu(H_2O)_3][Cu(mal)_2(H_2O)]\}_n$ (Fig. 19d).[41] The chain compound is formed by the regular alternation of the $[Cu(mal)_2(H_2O)_2]^{2-}$ moieties and $[Cu(H_2O)_3]^{2+}$ groups linked through *anti-syn* carboxylate bridges. The chain is not the repetition of the trinuclear unit in the third copper(II)-malonate compound; in this fourth complex the intermediate $[Cu(H_2O)_3]^{2+}$ groups are located in *trans*-positions to better accommodate the zigzag sequence. Adjacent chains are interconnected through hydrogen bonds involving the coordination water molecules forming a supramolecular two-dimensional sheet.

Is it possible to get a further condensation of these chains? The appendance of other $[Cu(H_2O)_3]^{2+}$ groups to the main $[Cu(mal)_2(H_2O)_2]^{2-}$ entity to yield a 2D coordination polymer seems to be the next step. However, unexpectedly, the

water molecules coordinated in apical positions to the main $[Cu(mal)_2(H_2O)_2]^{2-}$ moeity were the point of condensation for a 3D coordination network.

The addition of monoethanolamine (mea) to the aqueous copper(II)-malonate solution increases the pH of the reaction medium further than that of the third complex and favors the formation of $[Cu(mal)_2]^{2-}$ to give the complex $\{[Cu(H_2O)_3][Cu(mal)_2]_2 \cdot 2H_2O\}_n$ (Fig. 19e).[42] The structure consists of the same regularly alternated chains observed in $\{[Cu(H_2O)_3][Cu(mal)_2(H_2O)]\}_n$, which intersect in such a way that carboxylate groups of the $[Cu(mal)_2]$ unit in one chain occupy the apical position of the copper atom of the same unit of the adjacent chain.

The structural complexity in these compounds (nuclearity ranging from discrete entities[39–41] to 1D[41] or 3D compounds[42]) is associated with different carboxylato-bridging modes of mal and different structural functions of water molecules. Most of these complexes have been magnetically characterized, and they exhibit ferromagnetic coupling through the carboxylate-malonate bridge.[38,42]

Generally, the diversity in the framework structures greatly depends on the selection of the metal centers and organic spacers as well as on the reaction pathways. Metal ions are involved in the structure, depending on their size, hardness/softness, ligand-field stabilization energy, and coordination geometries (linear, trigonal-planar, T-shaped, tetrahedral, square-planar, square-pyramidal, octahedral, trigonal-prismatic, pentagonal-bipyramidal, or trigonal-bipyramidal). Choosing one or another metal ion means selecting the coordination geometry—that is, the node shape as well as choosing the potentially required properties of the future materials.

The crystal structures of the malonate complexes with other transition metal ions do not exhibit the wide variety of compounds observed with the copper(II) ion. However, it is remarkable that the polymerization suggested for the Cu(II) chain compound $\{[Cu(H_2O)_3][Cu(mal)_2(H_2O)]\}_n$, in which each $[Cu(mal)_2(H_2O)_2]^{2-}$ motif has four pendant $[Cu(H_2O)_x]^{2+}$ groups to yield a 2D structure, is now achieved in the zinc(II), cobalt(II), and nickel(II) malonate series, $\{[M(H_2O)_2][M(mal)_2(H_2O)_2]\}_n$ with M = Zn(II), Ni(II) and Co(II).[51,52] The structure consists of (4,4) networks in which the $[M(mal)_2(H_2O)_2]$ and $[M(H_2O)_2]$ groups act as fourfold connectors and nodes, respectively (Fig. 20a). The former is linked to the latter through *anti-syn* carboxylate bridges in an out-of-plane configuration, leading to the characteristic corrugation of the layers. The case of the manganese(II) complex $[Mn(mal)(H_2O)]_n$ is rather different;[53,54] the $[M(mal)_2(H_2O)_2]$ motif is no longer formed, and the crystal structure is built by sheets of *trans*-diaquamanganese(II) units bridged by carboxylate-malonate groups in the *anti-syn* and *anti-anti* bridging modes (Fig. 20b).

New perspectives were opened when the malonate ligand was partially or totally protonated. Three new compounds containing different anionic malonate species (the neutral H_2mal, the monoanionic $Hmal^-$, and the dianionic mal^{2-}) have been synthesized: one hydrogen malonato-bridged complex of formula $[Cu(Hmal)_2]$ and two polymorphic malonato-bridged complexes of formula $[Cu(H_2O)(H_2mal)(mal)]$, in which the three species of the malonate (H_2mal, $Hmal^-$,

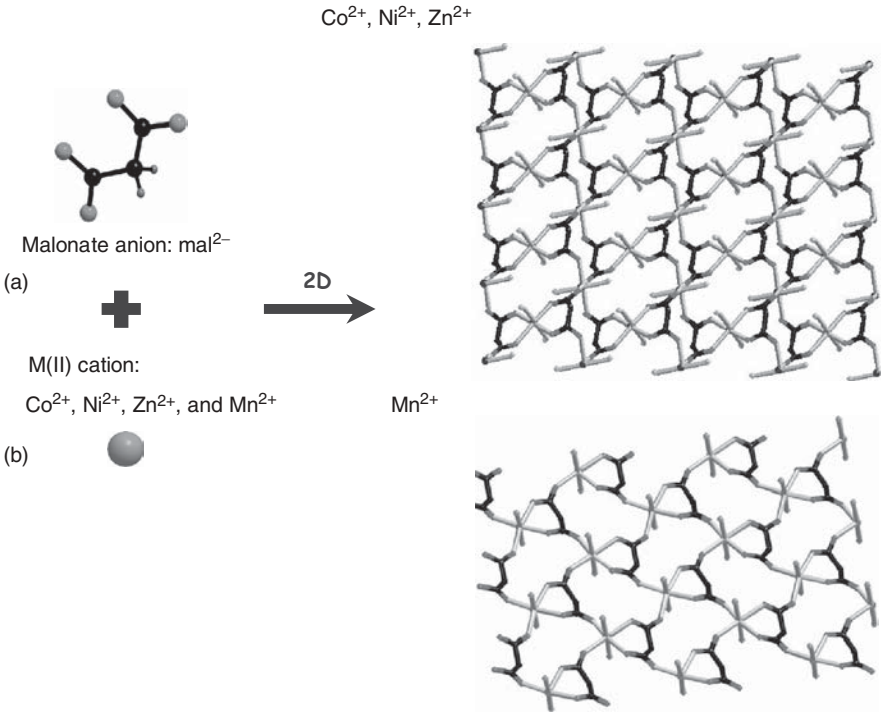

FIGURE 20. (*a*) Co^{2+}, Ni^{2+}, Zn^{2+} Sheet structure of the isostructural $\{[M(H_2O)_2][M(mal)_2(H_2O)_2]\}_n$ with M = Co(II), Ni(II) and Zn(II) compounds. (*b*) Mn^{2+} Sheet structure of compound $[Mn(mal)(H_2O)_2]$.

and mal^{2-}) are present (Figs. 21 and 22).[55] All the compounds have layered structures where hydrogen bonding leads to the three-dimensional network.

The organization of the building blocks (organic ligands and transition metal ions) together can lead to metal-organic frameworks of different dimensionalities: one-, two-, or three-dimensional architectures. Bridging ligands as in Scheme **3** represent the simplest ways of organization to construct the principal architectures types: 1D, 2D, and 3D. In these types, dimensionality is often determined by the nodes (metal centers): In 1D motifs, the metal ion is coordinated with two ligand molecules, metal ions and organic ligands alternate ''infinitely,'' leading to a chain. Two-dimensional compounds are obtained with three or four ligand molecules coordinating around the metal ion, and the elementary motif now expands in two directions. With metal ions of higher coordination number (tetrahedral or octahedral nodes), three-dimensional structures can be built. However, the directionality of elementary units is not always as simple as described before; rather complex situations occur with flexible carboxylate ligands. Considering the huge choice of possible coordination modes of these ligands, one can easily imagine the diversity of new

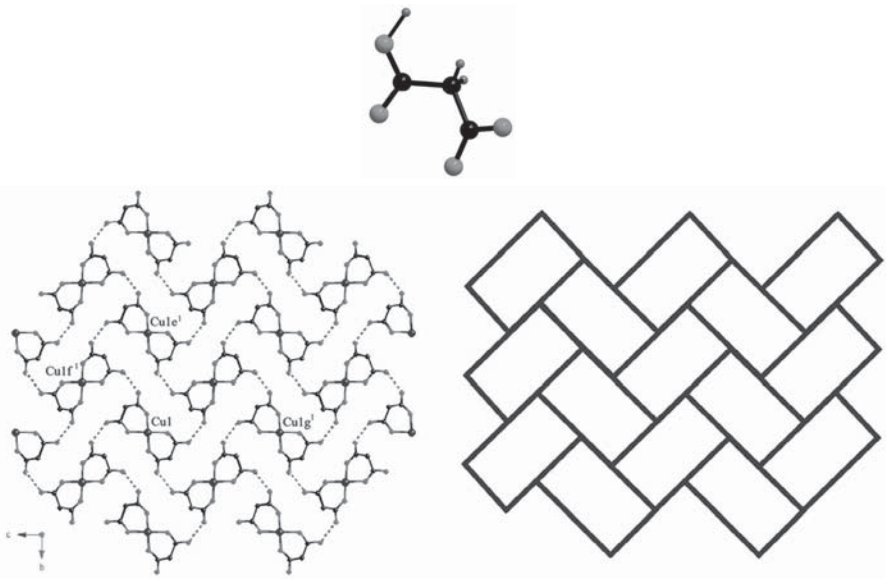

FIGURE 21. Perspective view along the *a*-axis of a fragment of the hydrogen malonate-bridged layer in $[Cu(Hmal)_2]$.

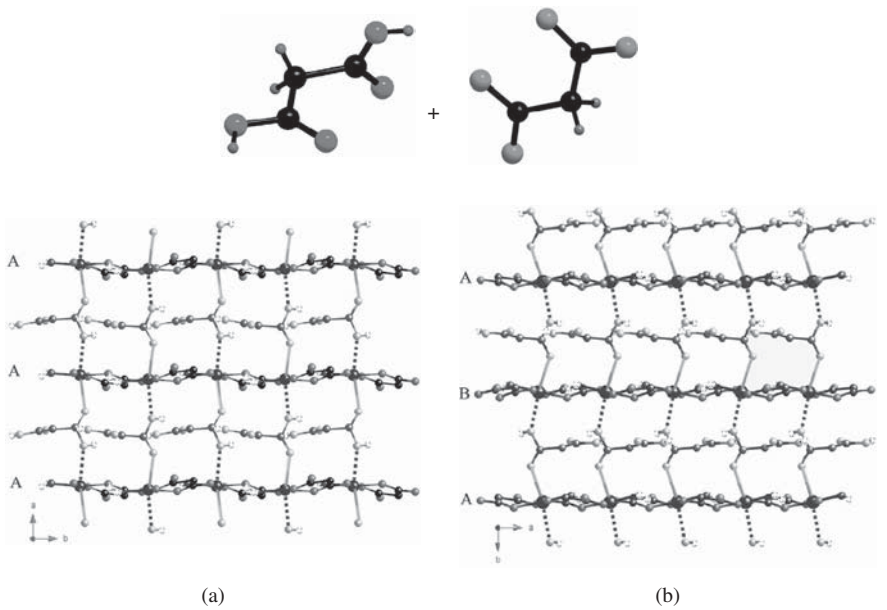

(a) (b)

FIGURE 22. View along the *c*-axis of a fragment of the two polymorphic malonato-bridged complexes [(a) and (b)] of formula $[Cu(H_2O)(H_2mal)(mal)]$ in which the two species of the malonate (H_2mal and mal^{2-}) are present.

synthesizable 1D, 2D, or 3D architectural motifs, depending on the building blocks (organic ligands and metal ions) and the experimental conditions.

It is clear that other interactions also play an important role during the formation of the crystals, but the definition of the final compounds dimensionality is based on the metal complexation. Weak interactions, such as hydrogen bonds, Van der Waals forces, π-type, and hydrophobic and hydrophilic interactions, drive the crystal packing of the coordination polymers. Most frequently encountered weak interactions are hereby shortly described.

Hydrogen bonds are defined by Steiner[56] as follows: *''A D-H · · · A interaction is called a 'hydrogen bond', if (1) it constitute a local bond and (2) D-H acts as proton donor to A''*. For hydrogen bonds of weak to intermediate strengths, they may be described by an ''electrostatic plus van der Waals'' model. For the strongest types of hydrogen bonds (rarely found in coordination polymers), their quasi-covalent nature has to be fully considered. Some systematic studies have been performed, with the use of the structural database (specially the CSD), to understand the strength and the directional preferences of hydrogen bonds.[56–59] The energy of such interactions varies from 15 to 40 $kJmol^{-1}$ for moderate hydrogen bonds.

$\pi \cdot \cdot \cdot \pi$ *interactions* can be of predominant importance during the coordination polymer formation. Janiak reviewed this kind of interaction in metal complexes with aromatic nitrogen-containing ligands.[60] These interactions are based on the sum of several contributions (electrostatic, van der Waals interactions, repulsion, and charge transfer), and the aromatic rings preferentially stack in an optimal way to minimize attraction. The energy of $\pi \cdot \cdot \cdot \pi$ interactions is estimated at 5–10 $kJmol^{-1}$.

iv. The Use of co-ligands

The flexibility of the malonate ligand can be explored by introducing some steric hindrance in the coordination environment of the metal ion in the form of complementary ligands. These co-ligands can act as blocking or bridging ones, contributing to the isolation or the interconnection of the metal atoms. Moreover, the inclusion of these co-ligands can also drive the packing of the coordination polymer through weak interactions.

This situation is illustrated with the use of blocking ligands like 2,2′-bipyridyl (bipy) or imidazole (Im), which can also establish π-type interactions. Their copper(II)-malonate complexes are 1D with formulae $\{[Cu(bipy)(H_2O)][Cu(bipy)(mal)(H_2O)]\}(ClO_4)_2$ and $[Cu(Im)_2(mal)]_n$. Two polymorphic malonato-bridged copper(II) complexes of $\{[Cu(bipy)(H_2O)][Cu(bipy)(mal)(H_2O)]\}(ClO_4)_2$ have been investigated.[61] The $[Cu(bipy)(mal)(H_2O)]$ and $[Cu(bipy)(H_2O)]$ groups are regularly alternated within zigzag chains (Fig. 23), the former unit linked to the latter through carboxylate groups in an *anti-syn* conformation (Scheme **17h**). The inclusion of the bpy ligand in the Cu(II) coordination sphere precludes the formation of the $[M(mal)_2(H_2O)_2]$ motif and drives the crystal packing through π-π staking. The malonate ligands have to bend themselves to incorporate the bulky $[Cu(bipy)(H_2O)]$ groups, resulting in an out-of-plane coordination mode.

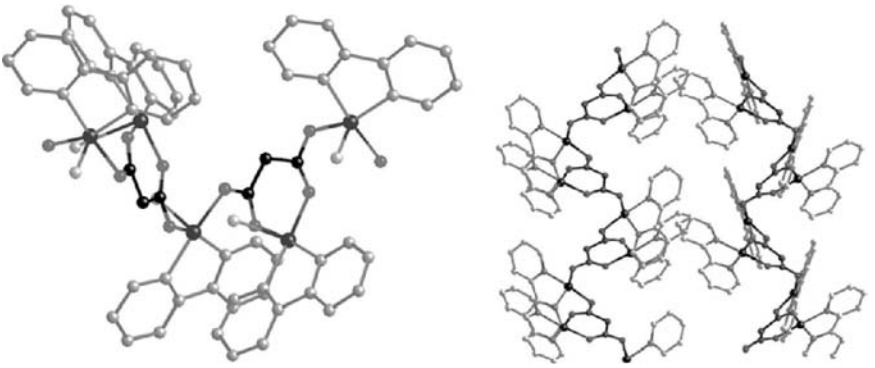

FIGURE 23. View of compound $\{[Cu(bipy)(H_2O)][Cu(bipy)(mal)(H_2O)]\} \cdot (ClO_4)_2$ showing the parallel arrangement of the chains along the *b*-axis. Hydrogen atoms and the perchlorate anions have been omitted for clarity.

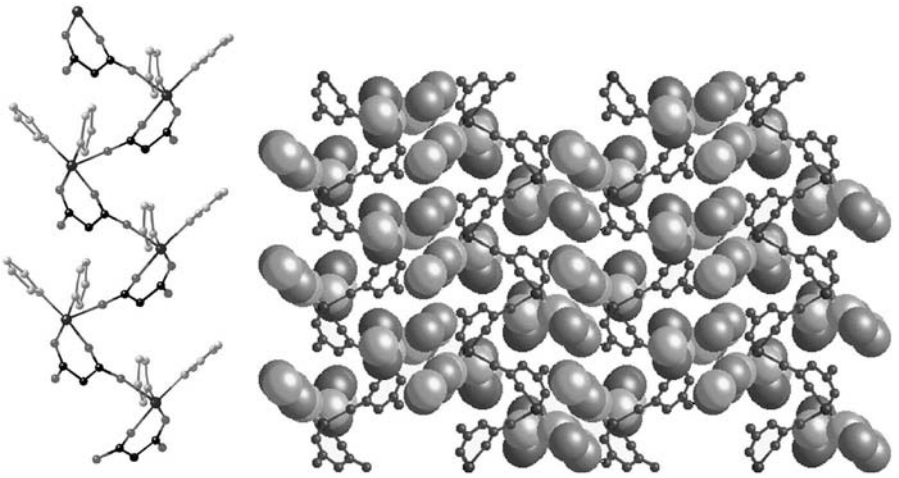

FIGURE 24. Projection of compound $[Cu(Im)_2(mal)]$ down the *a*-axis showing the parallel arrangement of the chains.

The structure of complex $[Cu(Im)_2(mal)]_n$ consists also of a regular zigzag chain of $[Cu(Im)_2(mal)]$ units that are linked through one malonate carboxylate group exhibiting the *anti-anti* conformation (Scheme **15c**).[62] Again, the imidazole ligands occupy two positions of the Cu(II) coordination sphere, and the malonate ligand link is one equatorial position with an apical one of adjacent Cu(II) surroundings through the carboxylate bridge (Scheme **17c**). The imidazole ligands drive the crystal packing of these zigzag chains, exhibiting a parallel columnar arrangement (Fig. 24).

These results have shown the degree of flexibility of the malonate ligand to accommodate bulky groups as co-ligands. However, at the same time, this

flexibility has a major disadvantage: the unpredictability of the coordination modes. Thus the resulting networks cannot be rationally designed a priori and a different strategy has to be proposed. A synthetic pathway hatched in steps has been developed, a first approximation in the form of a trial synthesis has to be studied to decide, in a second step, which co-ligand, counterion, metal center… could improve the results.

This strategy can be tested with the 2D coordination networks $\{[M(H_2O)_2][M(mal)_2(H_2O)_2]\}_n$ with M = Zn(II), Ni(II), and Co(II) presented previously. A reasonable approach to build 3D structures based on layered structural motifs is to control the packing by organic pillars of changeable lengths and/or type. When those homometallic malonate complexes react with *N*-exo pyridyl ligands such as pyrimidine (pym), pyrazine (pyz) or 4,4′-bipyridine (4,4′-bipy), 3D pillared coordination polymers $[M_2(mal)_2(L)(H_2O)_2]_n \cdot n(H_2O)$ M = Mn(II), Co(II), Zn(II), and Ni(II) are formed.[54,63] Although the intralayer coordination framework is different from those of the complexes without co-ligand, the final objective is achieved (Scheme **18**). The rod-like co-ligand occupies the apical positions at metal environments of adjacent layers, linking them. In this way, the separation between the sheets can be controlled, depending on the length of the co-ligand (Fig. 25).

The inclusion of the adequate secondary co-ligand can improve the dimensionality of the complex and the properties they will exhibit. Another example which illustrates this situation is the copper(II) malonate complex with the 2,4′-bipyridine (2,4′-bipy) $[Cu_4(mal)_4(H_2O)_4(2,4\text{-bipy})_4] \cdot 2H_2O$.[64] The structure consists of tetranuclear units forming a small square of dimensions $\sim 4.7 \times 4.7$ Å^2 with the copper(II) ions and the malonate ligands located on the corners and edges, respectively (Fig. 26a). The four copper(II) ions are linked through out-of-plane *anti-syn* carboxylate bridges (Scheme **15**), and they are ferromagnetically coupled, yielding a spin state of S = 2 at 3.0 K. The 2,4′-bipy acts as a blocking ligand, occupying one equatorial position of the metal environment, precluding further polymerization and isolating the ferromagnetic tetranuclear units. The supramolecular network are stabilized by the π-π stacking among the 2,4′-bipy ligands of different tetranuclear units.

From this crystal structure, it seems easy to polymerize the tetranuclear units to get a 2D coordination network. Instead of the blocking 2,4′-bipy, a rod-like connecting 4,4′-bipy ligand is used to synthesize the $[Cu_4(mal)_4(H_2O)_4(4,4'\text{-bipy})_2]$ complex.[64,65] The resultant 2D coordination polymer exhibits a (4,4) network in which the $[Cu_4(mal)_4(H_2O)_4]$ units and the 4,4′-bipy ligands act as fourfold nodes and connectors, respectively (Fig. 26b). This situation leads to the formation of large squares of 15.8×15.8 Å^2 in which each edge is shared by one malonate group and one 4,4′-bipy molecule. The layers are stacked parallel but in a staggered manner on each other along the tetragonal axis with an interplanar separation of 3.850 Å and angle of 56.3°, indicating weak π-π stacking interactions. The tetranuclear units fit exactly into the large squares of the adjacent sheet, precluding the formation of pores or cavities, and no solvent molecules are clathrated in the structure.

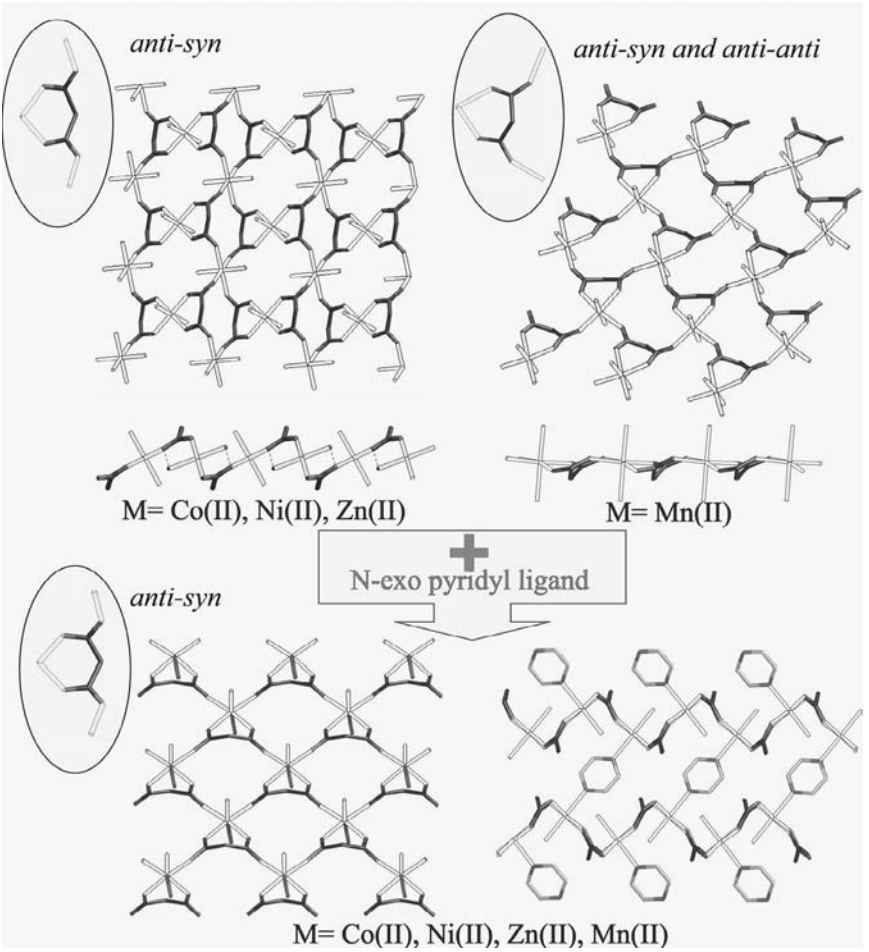

SCHEME 18

Following the same synthetic strategy, the separation between tetranuclear units can be shortened using a small rod-like ligand (i.e. pyrazine).[64] The structure of the $[Cu_4(mal)_4(pyz)_2] \cdot 4H_2O$ complex (Fig. 26c) is very similar to that obtained with the 4,4-bipy ligand. A 2D (4,4) coordination network with $[Cu_4(mal)_4]$ units linked through pyrazine ligands is formed. The shorter separation between them leads to their connection to tetramers of the adjacent layers. By this new link the layers are interconnected leading to a 3D structure. Each malonate uses its four oxygen atoms to coordinate the copper atoms: within each layer, the malonate simultaneously adopts the bidentate (at one copper atom) and unidentate (at another copper atom) coordination modes; the fourth carboxylate-oxygen atom also acts as unidentate because it is bound to a further copper atom from a neighboring layer.

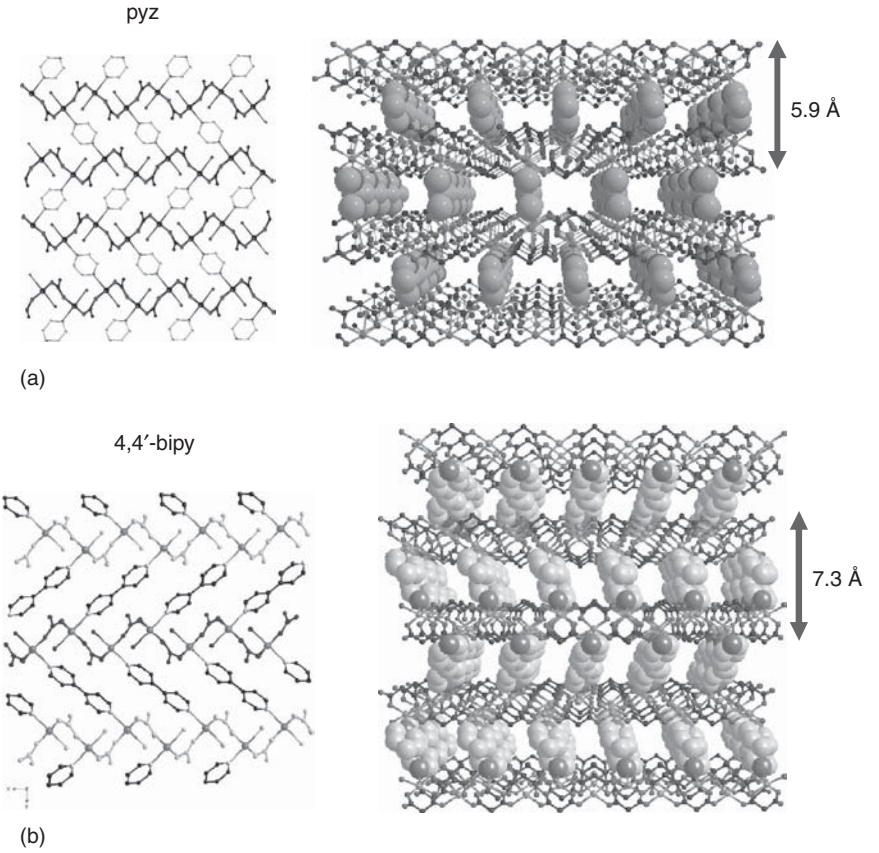

FIGURE 25. A layer of crystal structure showing the [M(mal)(H_2O)] sheets cross-linked by (*a*) pyrazine ligands in the [M(mal)(pyz)(H_2O)]$_n$ (M(II) = Co, Zn) and (*b*) 4,4′-bipy ligands in [Mn(mal)(4,4′-bipy)$_{1/2}$(H_2O)]$_n$ complexes.

v. Ligand Adaptation

The inclusion of co-ligands not only modifies the coordination environment of the metal ion, blocking or extending the polymerization, but also dramatically affects the crystal packing through weak interactions, mainly π-π interactions in the examples reviewed here. To exert some degree of control into the packing of the coordination polymers, subtle modifications, which are able to establish weak interactions with the surroundings could be introduced in the polycarboxylate ligand. The malonate ligand has a methylene carbon atom susceptible to accept hydrogen substitutions by other groups like phenyl, benzyl . . . even aliphatic chains (methyl, ethyl . . .). To illustrate this, the case of the phenylmalonate ligand (dianion of the phenylmalonic acid, H_2Phmal) is shown here. The presence of a phenyl ring on the methylene carbon group could induce different conformations of the malonate bridging modes due to geometrical constraints and would make

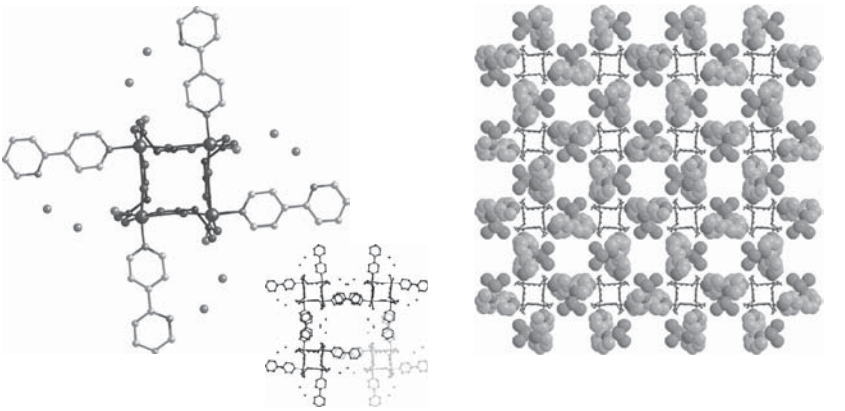

(a) 2,4′-bipy

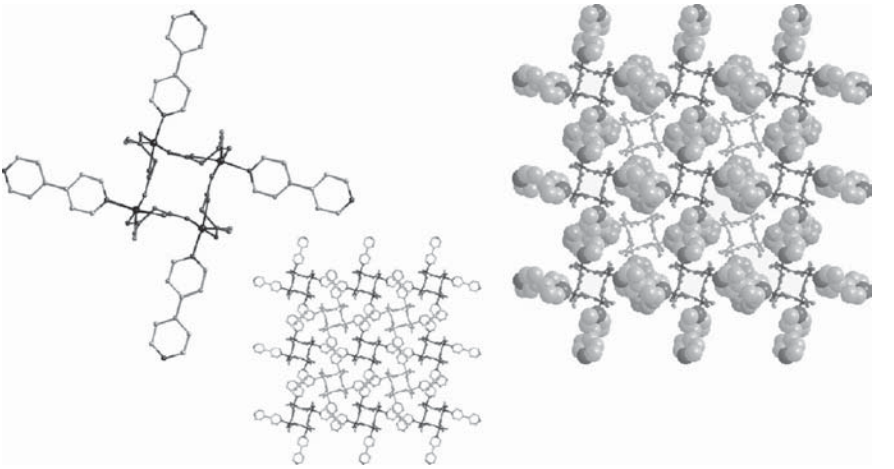

(b) 4,4′-bipy

FIGURE 26. (a) Perspective view of the tetramer unit of $[Cu_4(mal)_4(H_2O)_4(2,4\text{-bipy})_4] \cdot 2H_2O$ together with the stacking of the compound along the *c*-axis. (b) View of the two types of square channels of $[Cu_4(mal)_4(H_2O)_4(4,4\text{-bipy})_2] \cdot 2H_2O$ along the *c*-axis when only the odd layers are considered together with a view of the layers stacked along the tetragonal *c* axis. (c) The Cu/malonate framework in compound $[Cu_4(mal)_4(pyz)_2] \cdot 4H_2O$ along the *c* axis with a view of the 3D structure in which the square grid layers are stacked along the *c*-axis showing the $\pi \cdots \pi$ overlap between pairs of pyrazine molecules.

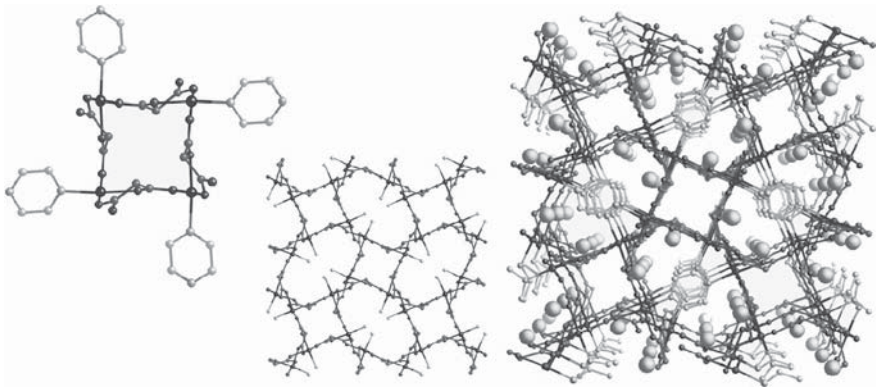

(c) pyz

FIGURE 26. (*Continued*)

possible specific attractive interactions between phenyl rings, which would contribute to the overall stability of the resulting compound. Their role in molecular recognition, and more generally in supramolecular chemistry, has now been widely examined.[66–72] The aim of this study is to analyze the influence that factors such as the withdrawing effect, the rigidity, and the possibility of specific attractive interactions between phenyl rings can exert on the structure and magnetic coupling of phenylmalonate-containing copper(II) complexes.[73–76] The complex $\{[Cu(H_2O)_3][Cu(Phmal)_2]\}_n$ has a sandwich-like structure with two well-separated areas, the hydrophobic layer where the phenyl groups of the Phmal ligands of adjacent layers are located and the more hydrophilic one, where the copper(II) surroundings are constrained (Fig. 27a). The phenyl substituent of the malonate ligand has driven the layered crystal packing, although the coordination polymer formed consists of chains similar to that of the $\{[Cu(H_2O)_3][Cu(mal)_2(H_2O)]\}_n$ complex, which polymerize into sheets through μ-oxo bridges between the $[Cu(Phmal)_2]$ units. Introduction of a co-ligand like pym, $[Cu(pym)(Phmal)]_n$ keeps the sandwich-like crystal packing unaltered, although the coordination mode of the Phmal ligand is completely modified (Fig. 27b).[75]

The separation between aromatic groups in this second compound is longer enough that π-type interactions are precluded. Thus the layered system observed is the result of hydrophobic interactions, similar to those that form micellar systems, and steric constrains, inherent in the presence of the bulky aromatic group. The study of whether smaller substituents can generate such crystal packing has been carried out with the methylmalonate derivative (H_2Memal = methylmalonic acid).[76,77]

The use of the methylmalonate as ligand toward the copper(II) ions affords a neutral sheet-like coordination polymer of formula $[Cu(Memal)(H_2O)]_n$ (Fig. 28a).[77] The layers are sandwich-like packed as occurs with the Phmal-complex, but due to the small size of the methyl substituent, the

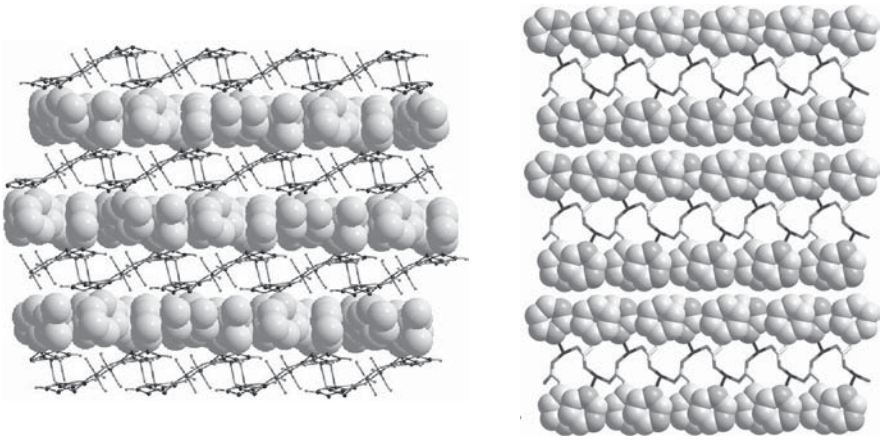

(a) (b)

FIGURE 27. (a) A view of the crystal structure of complex $\{[Cu(H_2O)_3][Cu(Phmal)_2]\}_n$ along the *b*-axis showing the interlayer $\pi \cdots \pi$ interactions. (b) Projection of the crystal packing of $[Cu(pym)(Phmal)]_n$ through the *a*-axis.

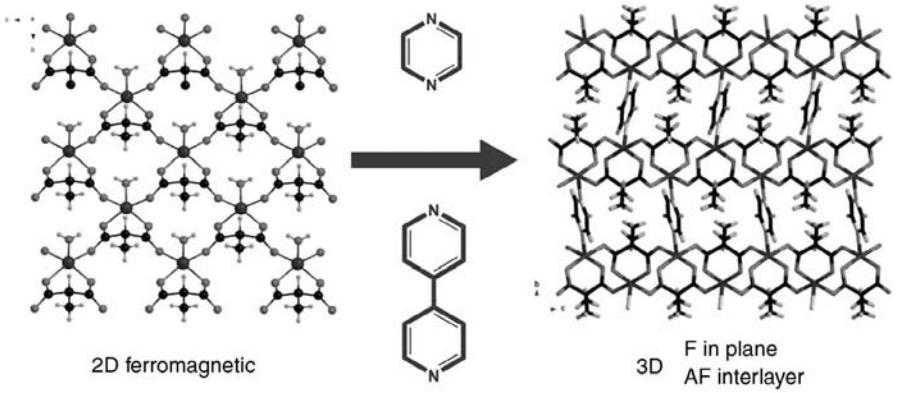

FIGURE 28. (*a*) A perspective view of a fragment of the carboxylate-bridged square grid of the copper atoms in $[Cu(Memal)(H_2O)]_n$ extending in the *bc*-plane. (*b*) Perspective views of the crystal packing of $[Cu_2(pyz)(Memal)_2]_n$.

separation between layers is shorter ($\sim$ 6.2 Å). This distance could be controlled introducing rod-like spacers, such as pyrazine (pyz) and 4,4′-bipyridine (4,4′-bipy), affording the compounds $[Cu_2(pyz)(Memal)_2]_n$ and $[Cu_2(4,4\text{-bpy})(Memal)_2(H_2O)_2]_n$ (Fig. 28b). They are 3D coordination polymers, constructed in a rational way, which exhibit the sheet-like structure observed for the

$[Cu(Memal)(H_2O)]_n$ complex, but pillared with the pyz and 4,4-bipy co-ligands (the new interlayer separations are 6.7 and 8.3 Å, respectively). This family of compounds is a nice example of crystal engineered 3D structures.[77]

vi. Perspectives

This section and these few examples illustrate the versatility of the malonate ligand in crystal engineering. The self-assembly of dicarboxylate flexible ligands with transition metal ions has been demonstrated to be a good approach for preparing new and exciting structures. Their coordination chemistry is a mature field that afforded complexes exhibiting all types of magnetic situations needed for the design of new materials.

The substituted-malonate ligands open a wide area of investigation; some control can be exerted over the weak interactions such as $\pi \cdots \pi$ stacking, hydrophobic, or steric repulsion. Because these intermolecular interactions are the leading forces for the aggregation of the molecules in the crystal, it is possible to make some guidance over the crystal packing and hence, over the properties (e.g., magnetic) of the material. This is an exciting idea which deserves to be investigated.

C. The Building-Block Approach

The building-block strategy is particularly useful for obtaining hetero-metal coordination polymers and consists of self-assembly processes involving anionic or neutral metal complexes (metalloligands) with potentially binding sites and aqua complexes of a second metal ion (Scheme **19**). Such coordination polymers, when the metal ions are different and both paramagnetic, are of high interest in molecular magnetism. To be employed as ligands, the anionic (or neutral) complexes must fulfill an important condition: They have to be relatively stable toward substitution reactions. Otherwise, their interaction with the second metal ion will lead to intractable mixtures of complexes. Therefore, the best-suited metal ions for generating anionic building blocks are metal ions with a high crystal field stabilization geometry (Cr^{III}, low-spin Fe^{III}, 4d and 5d transition metal ions). An alternative way to get stable metalloligands consists of the use of anionic chelating ligands. For example, the coordination of the bis(2-pyridylcarbonyl)amine anion, $pbca^-$, to various metal ions generate numerous bis-chelated complexes, $[M^{II}(bpca)_2]$, that can coordinate to a second metal ion via the carbonyl oxygen atoms. Bimetallic chains are assembled in the absence of blocking ligands attached to the second metal ion. A family of compounds, with the general formula $[\{Ln(O_2NO)(H_2O)_3\}\{Ni(bpca)_2\}](NO_3)_2 \cdot 3H_2O$, were obtained by self-assembly processes involving

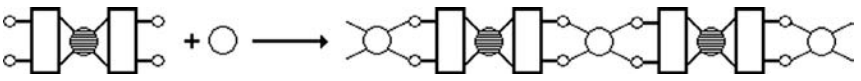

SCHEME 19

neutral $[Ni(bpca)_2]$ building blocks and Ln^{3+} ions.[78] The Ln^{III} ions are connected by $[Ni(bpca)_2]$ complexes acting as bridging bis-bidentate ligands (Fig. 29).

The most important categories of complexes used as metalloligands are oxalato-complexes, cyano-complexes, and bisoxamidato complexes. Let's discuss several representative examples from each category.

i. Oxalato-Bridged Coordination Ploymers

The oxalate ion is a good bridging ligand. Most of the insoluble transition-metal oxalates are actually coordination polymers, with the metal centers connected by bis-chelating oxalato groups.

The oxalate ion cannot be employed to obtain heterometallic complexes through one-pot procedures—that is, by reacting two different metal ions with the oxalate anion, because these reactions lead most frequently to mixtures of compounds. Conversely, anionic complexes such as $[Cr(C_2O_4)_3]^{3-}$, $[Co(C_2O_4)_3]^{3-}$, and $[Ru(C_2O_4)_3]^{3-}$, are enough stable to allow good control over the reaction products.[79] In the absence of ancillary ligands attached to the assembling cations, 2D and 3D networks are formed. For example, the reactions between $cat_3[M(C_2O_4)_3]$ ($cat^+ = NR_4^+, PR_4^+$) and divalent cations, M'^{2+}, yield bimetallic networks with the general formula $\{cat^+ [M'M(C_2O_4)_3]^-\}_n$, which are composed of an anionic sublattice, $\{[M'M(C_2O_4)_3]^-\}_n$ and the cationic counterpart. The two metal ions, M and M′, are connected by bis-chelating oxalato

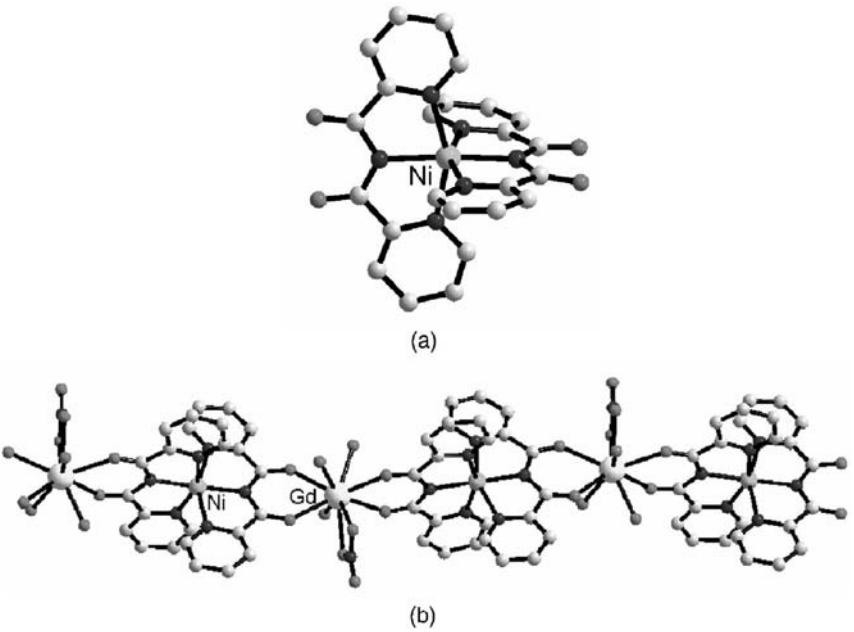

FIGURE 29. (a) The $[Ni(bpca)_2]$ building block; (b) The heterobimetallic cationic chain in $[\{Ln(O_2NO)(H_2O)_3\}\{Ni(bpca)_2\}](NO_3)_2 \cdot 3H_2O$.

groups. It is important to recall here that $[M(C_2O_4)_3]^{3-}$ species exhibit a propeller-like chirality (Δ and Λ). Within the heterometal network both metal centers are chiral. If the chiralities of the connected centers are different, [ΔM; ΛM] or [ΛM; ΔM], then the resultant coordination polymers are 2D with a honeycomb topology (Fig. 30).[80] The crystal is racemic, because it contains an equal number of layers constructed from either Δ or Λ chromium units. By employing only one enantiomer, Δ-$[Cr(C_2O_4)_3]^{3-}$ or Λ-$[Cr(C_2O_4)_3]^{3-}$, Andrés et al. obtained 2D optically active Mn^{II}-Cr^{III} polymers—that is, crystals containing only one type of bimetallic layer, (ΔCr^{III}, ΛMn^{II}) or (ΛCr^{III}, ΔMn^{II}).[81] If both metal centers exhibit the same chirality, 3D networks are formed, with a helical organization.[82]

The reaction between $[Cr(C_2O_4)_3]^{3-}$ complexes and trivalent lanthanide ions leads to chains, $[Ln^{III}Cr^{III}(C_2O_4)_3(H_2O)_4]\cdot nH_2O$, with a ladder-type motif.[83] The rare earth ions are 10-coordinated: six oxygen atoms from the three bis-chealting oxalato groups and four aqua ligands.

New building-blocks—for example, $[Cr(AA)(C_2O_4)_2]$—with different coordinating abilities are formed when one out of the three oxalato groups from the anionic complex is replaced by a blocking ligand (2,2′-bipyridine, 1,10-phenanthroline).[84] For example, the self-assembly process between $[Cr(bipy)(C_2O_4)_2]^-$ and Mn^{2+} ions affords neutral bimetallic chains with diamond shapes sharing the manganese ions, which exhibit a coordination number of eight (Fig. 31).[84]

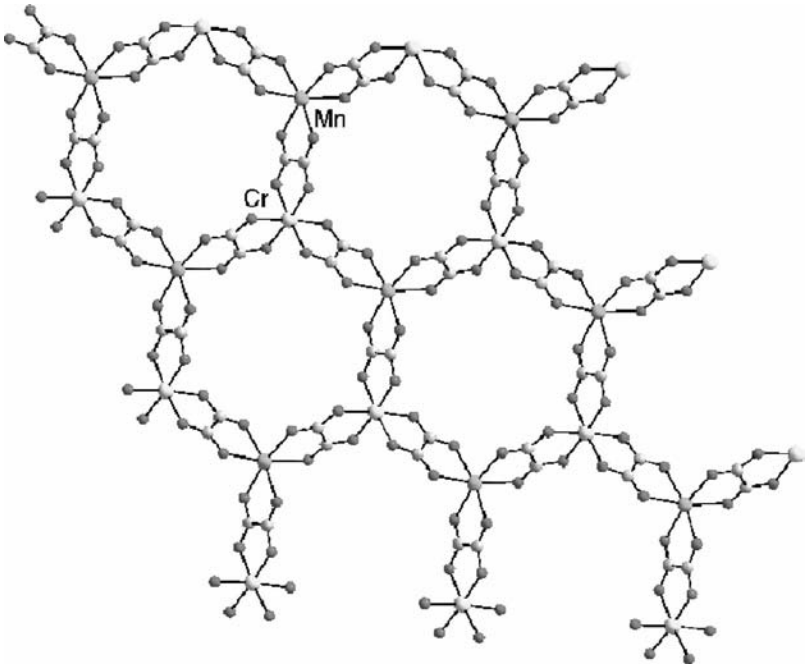

FIGURE 30. Honeycomb anionic layers resulted by assembling Mn^{2+} ions with $[Cr(C_2O_4)_3]^{3-}$ tectons.

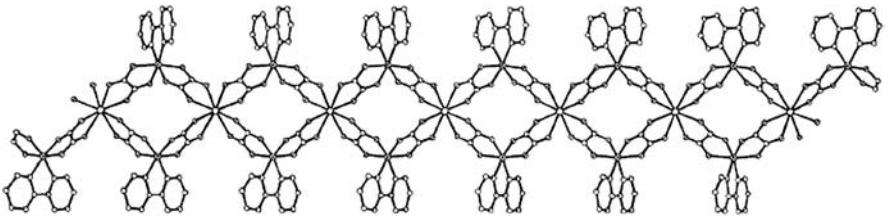

FIGURE 31. Heterobimetallic chain resulted by assembling Mn^{2+} ions and $[Cr(bipy)(C_2O_4)_2]^-$ tectons.

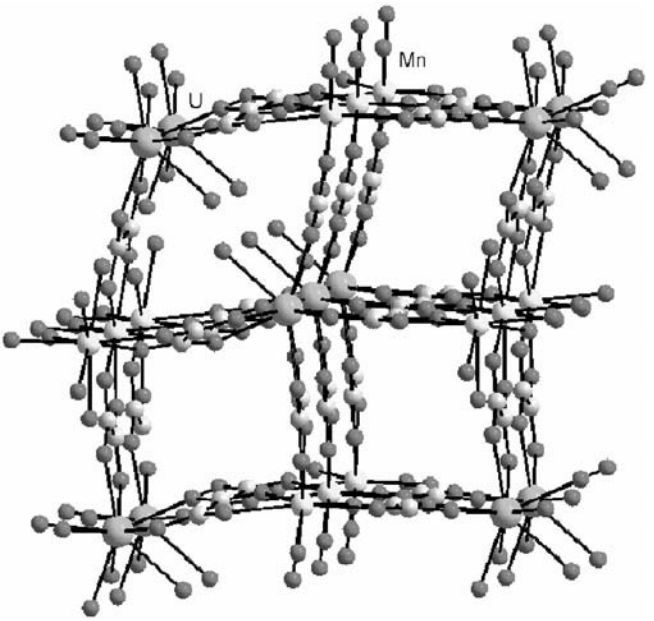

FIGURE 32. Diamondoid network in $K_2Mn[U(C_2O_4)_4(H_2O)_2] \cdot 7H_2O$

The highest number of oxalato groups attached to a metal ion in a mononuclear complex is four: $[M^{IV}(C_2O_4)_4]^{4-}$ (M = Zr, U).[85] The four oxalato ligands are oriented tetrahedrally. The most interesting properties of these species are to act as tetrahedral synthons and to generate, in a deliberate way, diamond-like networks. Indeed, the reaction between $K_4[U(C_2O_4)_4]$ and a manganese(II) salt results in the partial substitution of potassium with manganese(II) ions: $K_2Mn[U(C_2O_4)_4(H_2O)_2] \cdot 7H_2O$.[85a] Each uranium(IV) ion is linked to four manganese ions via the oxalato ligands. The coordination sphere of the manganese ion also consists of four oxalato bridges (the manganese ions are octacoordinated). Every metal ion is linked four times by oxalato bridges to the other metal ion, resulting in a 3D diamondoid network (Fig. 32).

ii. Bisoxamidato Complexes as Building Blocks

The chemistry based on bisoxamido complexes has been developed under the strong impulse of molecular magnetism because of their exceptional ability to generate homometailc and especially heterometallic coordination polymers with tunable magnetic properties.[20,86] Bisoxamides are prepared by reacting a diamine with ethyl-oxalyl chloride (Scheme **20a**). The corresponding oxamato complexes result from the copper-assisted hydrolysis of the primary amide in aqueous solution (Scheme **20b**). The dianionc mononuclear complexes can act as bis-bidentate ligands toward other metal ions generating 1D or 2D bimetallic coordination polymers (Scheme **20c**).

iii. Cyano-Bridged Coordination Polymers

Perhaps the richest chemistry in the realm of heterometal complexes is the one based on self-assembly processes involving polycyanometallate tectons and various assembling complex cations. Indeed, a huge number of heterometallic complexes have been synthesized over the last 15 years.[87] Cyano-bridged coordination polymers are obtained following the same general procedure, consisting of self-assembly processes involving anionic polycyanometallates and various assembling cations. The rich structural variety of these arises from two sources: the availability of numerous homoleptic polyanometallates and the nature of the ancillary ligands attached to the assembling cations. The following anionic

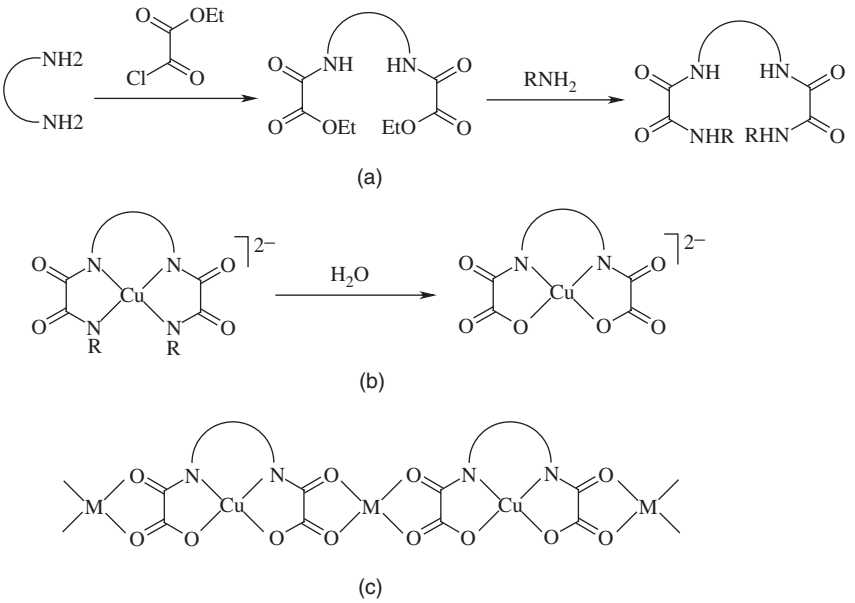

SCHEME 20

cyano-complexes are currently used as templates: $[M^{I}(CN)_2]^{-}$ (M = Ag, Au), $[M^{II}(CN)_4]^{2-}$ (M = Ni, Pd, Pt), $[M^{III}(CN)_6]^{3-}$ (M = Cr, Fe, Co, Ru), $[Mo^{III}(CN)_7]^{4-}$, and $[M(CN)_8]^{q-}$ (M = Nb^{IV}, Mo^{IV}, W^{IV}, Mo^{V}, W^{V}). The number of organic molecules that can be used to block several coordination sites at the assembling cations is unlimited. They can have various denticities, ranging from monodentate to pentadentate and can be linear, tripodal or macrocyclic. Their main role is to control the number of available coordination sites of the assembling cation and their relative position.

When the assembly process involves hexacyanometallates and fully solvated metal ions, Prussian-blue phases are obtained, which are cubic 3D networks.[87a] Figure 33 shows the crystal structure of such a 3D cyano-bridged coordination polymer: $NaMnCr(CN)_6$.[88]

Usually, by attaching blocking ligands to the assembling cations, the dimensionality of the resulting polymers is reduced. The denticity of the blocking ligands and the stereochemical preference of the second metal ion are crucial factors that determine the architecture of the cyano-bridged coordination polymers. Although a huge number of cyano-bridged coordination polymers have been synthesized and characterized, the network topologies, with few exceptions, are difficult to predict, especially when the number of cyano groups within the anionic template is six or higher. From the plethora of coordination polymers synthesized to date, we have selected several representative examples.

The dicyano-complexes, $[M(CN)_2]^{-}$, currently generate linear or zigzag heterobimetallic chains.

The formation of chains, by employing hexacyanometallates as templates was rather serendipitous. One of the very first 1D coordination polymers was

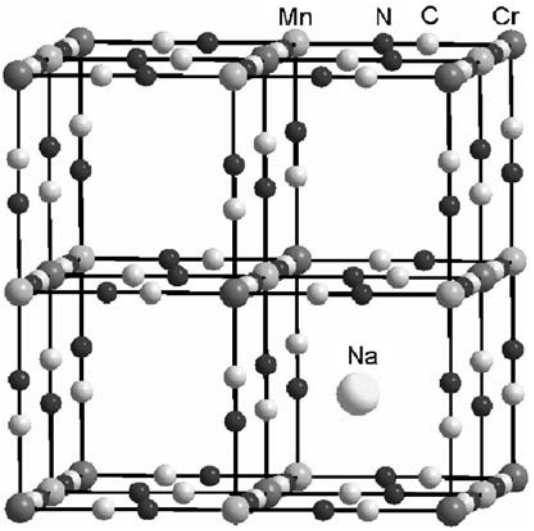

FIGURE 33. Perspective view of the 3D lattice in $NaMnCr(CN)_6$.

obtained by reacting $[Ni(en)_3]^{2+}$ cations (en = ethylene diamine) with $[M(CN)_6]^{3-}$ anions (M = Fe^{III}, Mn^{III}, Cr^{III}, Co^{III}). During the reaction, the tris-chelate nickel complex dissociates into bis-chelated species, $[Ni(en)_2(H_2O)_2]^{2+}$, in which the aqua ligands are substituted by the cyano bridges, resulting in bimetallic chains, $[\{Ni(en)_2\}_3\{M(CN)_6\}_2]\cdot 2H_2O$.[89] The structure consists of a rope-ladder arrangement (Fig. 34). The nickel moieties are present in two configurations: in the first one the bridging groups are disposed in *trans* positions, and in the second one in *cis* positions. This family of complexes displays interesting magnetic properties. When M = Fe, Mn, Cr, the metal ions within the chain are antiferromagnetically coupled, due to the strict orthogonality of the magnetic orbitals of the adjacent Ni^{II} and M^{III} ions.

Another interesting type of chain is obtained by assembling $[Cu(dien)]^{2+}$ and $[M(CN)_6]^{3-}$ ions: $[\{Cu(dien)_2\{M(CN)_6\}]_n\cdot n[\{Cu(dien)(H_2O)\}\{M(CN)_6]\cdot 5H_2O$ (M = Cr^{III}, Fe^{III}, Co^{III}).[90] The structure consists of two ionic units: 1D cationic chains, $[\{Cu(dien)_2\{M(CN)_6\}]_n^{n+}$, whose charges are counterbalanced by $[\{Cu(dien)(H_2O)\}\{M(CN)_6]^-$ ions. A view of the cationic chain is represented in Figure 35. Four equatorial cyano groups from the $[M(CN)_6]^{3-}$

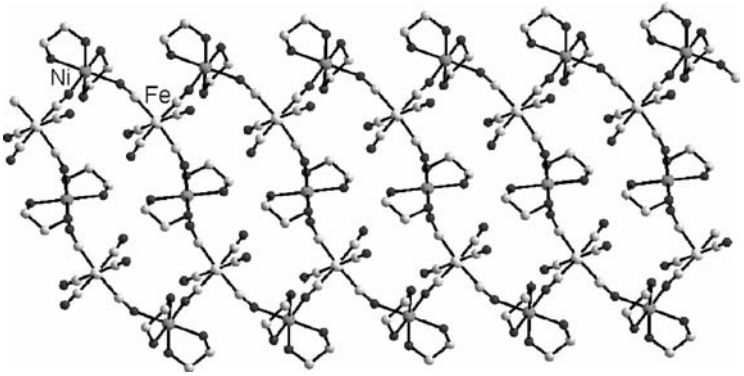

FIGURE 34. Rope-ladder chain in $[\{Ni(en)_2\}_3\{M(CN)_6\}_2]\cdot 2H_2O$.

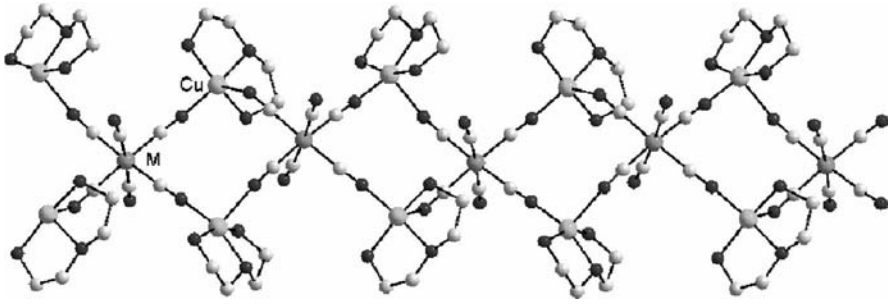

FIGURE 35. Perspective view of the cationic chain $[\{Cu(dien)_2\{M(CN)_6\}]_n^{n+}$

building block are coordinated to four copper ions, while the two axial cyano groups are terminal ligands.

The square-planar tetracyano complexes, $[M(CN)_4]^{2-}$, when the four cyano groups are employed as bridges, generate grid-like sheets. Particularly interesting are Hoffmann clathrates, $M(NH_3)_2Ni(CN)_4 \cdot 2G$ ($M = Ni^{II}$, Cu^{II}), with grid-like layers constructed from square planar nickel centers connected through four cyano groups to four octahedral nickel centers (the apical positions are occupied by the ammonia ligands). The guest molecules ($G = C_6H_6$, C_4H_5N, $C_6H_5NH_2$) are hosted between the layers.[87a]

Macrocyclic ligands, *mac*, are usually coordinated into the equatorial plane of the metal ions, the axial positions being occupied by weakly bonded ligands, which can be replaced by the cyano bridges. The self-assembly process involving *trans*-$[M'(mac)(H_2O)_2]^{2+}$ and $[M(CN)_6]^{3-}$ ions yields 2D $[M'_3M_2]$ networks. Within a layer, each $[M'(mac)]^{2+}$ moiety is linked to two $[M'(CN)_6]^{3-}$ ions in *trans* positions, and each $[M(CN)_6]^{3-}$ ion is surrounded by three $[M(mac)]^{2+}$ units. If the three M(*mac*) units adopt a *facial* configuration around the M ion, then layers with a stair-shaped honeycomb architecture are formed (*mac* stands for cyclam, 1,4,8,11-tetraazacyclotetradecane) (Fig. 36).[91] A *meridial* arrangement of the three $[M'(mac)]^{2+}$ moieties leads to flat brick-wall-like layers (*mac* = 3,10-diethyl-1,3,5,8,10,12-hexaazacyclotetradecane (Fig. 37).[92]

The enormous synthetic potential of the anionic polycyanometallates in designing heterometal complexes has been further exploited by attaching blocking ligands not only to the assembling cations but also to the anionic units, by replacing two or three cyanide groups by bidentate or tridentate ligands—for example $[M(AA)(CN)_4]^-$ ($M = Cr^{III}$, Fe^{III}; AA = 2,2-bipy, 1,10-

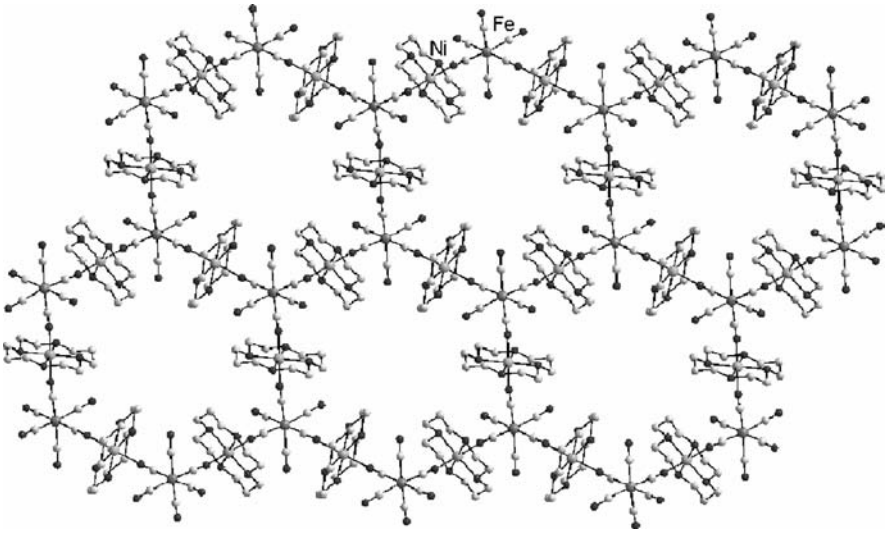

FIGURE 36. Honeycomb layers resulted from $[Ni(mac)]^{2+}$ and $[Fe(CN)_6]^{3-}$ ions (*mac* = 1,4,8,11-tetraazacyclotetradecane (see text)).

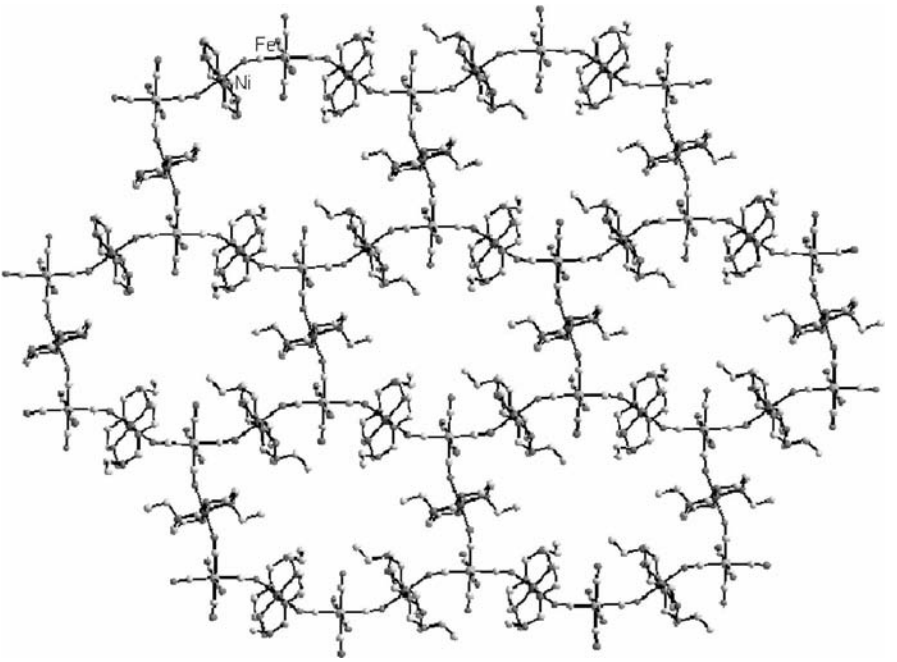

FIGURE 37. Brick-wall layers resulted from $[Ni(mac)]^{2+}$ and $[Fe(CN)_6]^{3-}$ ions (*mac* = 3,10-diethyl-1,3,5,8,10,12-hexaazacyclotetradecane (see text)).

phen, ethylenediamine, 2-aminomethyl-pyridine), $[M(BBB)(CN)_3]^-$ (BBB = tridentate monoanionic ligands: $bpca^-$ = bis(2-pyridylcarbonyl)amidate $HB(pz)_3^-$ = hydrotris(1-pyrazolyl)borate), and *trans*-$[Ru^{III}(acac)_2(CN)_2]^-$ (acac = acetylacetonate).[93,94] Such building blocks are particularly useful in designing 1D coordination polymers with interesting magnetic properties, including single chain magnets (molecular magnetic materials exhibiting a slow relaxation of the magnetization). One example in this family is the heterobimetallic ribbon-like chain obtained by assembling [Fe(2,2′-bipy)$(CN)_4]^-$ anions with fully hydrated cobalt(II) ions: $[\{Fe(2,2'\text{-bipy})(CN)_4\}_2\text{-}Co(H_2O)_2] \cdot 4H_2O$ (Fig. 38).[94] This compound exhibits intrachain ferromagnetic coupling, a slow relaxation of the magnetization and hysteresis effect.

The large field of cyano-bridged coordination polymers is covered by several recent excellent reviews.[87]

III. CONCLUSIONS AND PERSPECTIVES

Crystal architecture is the result of the hierarchic organization determined by the primary structure, resulting from metal-ligand bonds that generate the coordination polymer, and the secondary one, that is determined by a concert

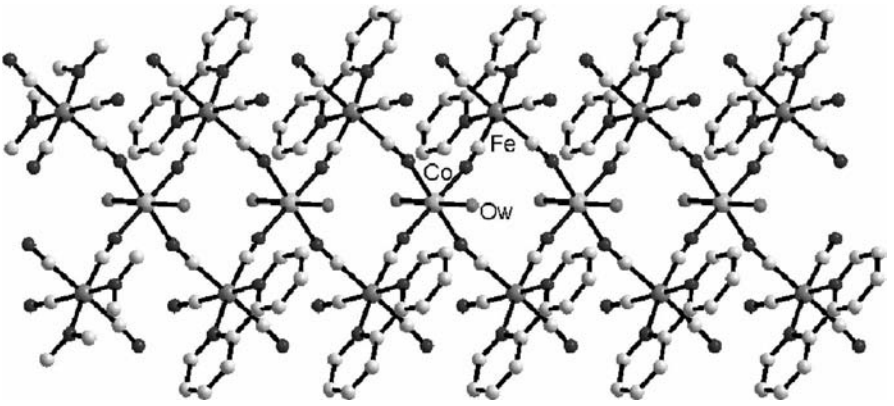

FIGURE 38. Perspective view of a bimetallic chain constructed by using $[Fe(bipy)(CN)_4]^-$ as a building block.

of electrostatic and other non-covalent forces (hydrogen bonds, π-π stacking, metallophilic interactions, secondary bonds). Their subtle interplay makes the prediction of the final structure difficult. Many compounds that exhibit fascinating structures and interesting properties have been serendipitously obtained. Their retrospective analysis, which is also a goal in crystal engineering, provides chemists the necessary knowledge and means for designing crystal structures with desired structures, properties and functions.

We have an increasing interest in coordination polymers due to their potential applications. The syntheses, in the late 1980s of the first molecular magnets (coordination polymers exhibiting spontaneous magnetization below a critical temperature), by Kahn and co-workers,[95] represent beautiful examples of crystal engineering. The synthesis of 1D coordination polymers exhibiting slow relaxation of magnetization (single chain magnets) with high blocking temperatures, is a challenge in molecular magnetism. A new generation of materials emerged recently, by combining magnetic properties with other useful properties (multifunctional materials): porous magnets,[96] chiral magnets,[97] and conducting and superconducting molecular magnets.[98] The field is open and interesting results are expected.

Porosity is another important and desired property in crystal engineering; it confers potential catalytic and sorption properties.[8a,15d,99] There are several examples that encourage the pursuit of research in this direction.[1,100] Chiral networks, with enantioselective host-guest functions, are expected to perform chiral separations and catalysis, as shown by recent works.[101] Another area of intense research is the development of coordination networks as materials for gas uptake (Ar, N_2, CO_2, CH_4), particularly H_2.[102] Last, but not least, coordination polymers attract chemists through their intrinsic beauty and intriguing structural diversity.

IV. ACKNOWLEDGMENTS

M. A. expresses his gratitude to his co-workers, colleagues, and students for their enthousiastic work (Drd. D. Branzea, Dr. R. Gheorghe, Dr. A. M. Madalan, Drd. G. Marin, Dr. C. Paraschiv, Dr. V. Tudor). Financial support from the CEEX (Project D11-17) and CERES (Project 4/130) Programs is gratefully acknowledged. C. R.-P. is specially grateful to many colleagues and co-workers whose skill and enthusiasm contributed to the results described in this chapter, and specially to Dr. J. Pasán for the helpful discussions in preparing this manuscript. Funding for this work is provided by the Ministerio Español de Educación y Ciencia through projects MAT2004-03112, MAT2007-60660 and "Factoría de Cristalización" (Consolider-Ingenio2010, CSD2006-00015).

V. REFERENCES

1. C. Janiak, *Dalton Trans*., **2003**, 2781.
2. V. A. Friese, and D. G. Kurth, *Coord. Chem. Rev*., **2008**, *251*, 199.
3. (a) N. R. Champness, *Dalton Trans*., **2006**, 877. (b) A. S. Abd-El-Aziz, C. E. Carraher Jr., C. U. Pittman Jr., and M. Zeldin, eds., *Metal Coordination Polymers, Macromolecules Containing Metal and Metal-like Elements*, *vol. 5,* Wiley-Interscience, Wiley, New York, **2005**.
4. S. R. Batten, and R. Robson, *Angew. Chem., Int. Ed*., **1998**, *37*, 1461.
5. A. Ramanan, and M. S. Whittingham, *Cryst. Growth & Des*., **2006**, *6*, 2419.
6. (a) R. W. Gable, B. F. Hoskins, and R. Robson, *J. Chem. Soc., Chem. Commun*., **1990**, 1677. (b) B. F. Hoskins, and R. Robson, *J. Am. Chem. Soc*., **1990**, *112*, 1546.
7. R. Robson, *J. Chem. Soc., Dalton Trans*, **2000**, 3735.
8. (a) S. Kitakawa, R. Kitaura, and S. Noro, *Angew. Chem., Int. Ed*., **2004**, *43*, 2334. (b) S. Kitagawa, and M. Kondo, *Bull. Chem. Soc. Jpn*., **1998**, *71*, 1739.
9. (a) L. Carlucci, G. Ciani, and D. M. Proserpio, *Coord. Chem. Rev*., **2003**, *246*, 247. (b) S. Batten, *Cryst. Eng. Comm*. **2001**, *18*, 1. (c) R. J. Hill, D.-L. Long, N. R. Champness, P. Hubberstey, and M. Schröder, *Acc. Chem. Res*., **2005**, *38*, 337. (d) J. Jia, X. Lin, C. Wilson, A. J. Blake, N. R. Champness, P. Hubberstey, G. Walker, and M. Schröder, *Chem. Comm*. **2007**, 840.
10. (a) H. W. Roesky, and M. Andruh, *Coord. Chem. Rev*., **2003**, *236*, 91. (b) K. Biradha, *CrystEngComm*., **2003**, *5*, 374. (c) A. M. Madalan, N. Avarvari, and M. Andruh, *Cryst. Growth & Des*., **2006**, *6*, 1671. (d) S. Nastase, F. Tuna, C. Maxim, C. A. Muryn, N. Avarvari, R. E. P. Winpenny, and M. Andruh, *Cryst. Growth. Des*., **2007**, *7*, 1825.
11. O. M. Yaghi, and H. Li, T. L. Groy, *Inorg. Chem*. **1997**, *36*, 4292.
12. L. Carlucci, G. Ciani, D. M. Proserpio, and A Sironi, *J. Chem. Soc. Dalton Trans*., **1997**, 1801.
13. S. Subramanian, and M. J. Zaworotko, *Angew. Chem. Int. Ed. Engl*., **1995**, *34*, 2127.
14. A. M. Madalan, C. Paraschiv, J.-P. Sutter, M. Schmidtmann, A. Müller, and M. Andruh, *Cryst. Growth Des*., **2005**, *5*, 707.
15. (a) F. A. Cotton, C. Lin, C. A. Murillo, *Acc. Chem. Res*., **2001**, *34*, 759. (b) M. Andruh, *Pure App. Chem*., **2005**, *77*, 1685. (c) M. Andruh, *Chem. Commun*., **2007**, 2565; (d) J. L. C. Rowsell, and O. M. Yaghi, *Micropor. Mesopor. Mater*., **2004**, *73*, 3. (e) M. Eddaoudi,

D. B. Moler, H. Li, B. Chen, T. M. Reineke, M. O'Keeeffe, and O. M. Yaghi, *Acc. Chem. Res.*, **2001**, *34*, 319.

16. (a) V. Tudor, G. Marin, G.; V. Kravtsov, Y. A. Simonov, J. Lipkowski, M. Brezeanu, and M. Andruh, *Inorg. Chim. Acta*, **2003**, *353*, 35. (b) G. Marin, M. Andruh, A. M. Madalan, A. J. Blake, C. Wislon, N. R. Champness, and M. Schröder, *Cryst. Growth. Des*, in press (c) G. Marin, V. Tudor, V. C. Kravtsov, M. Schmidtmann, Y. A. Simonov, A. Müller, and M. Andruh, *Cryst. Growth Des.*, **2005**, *5*, 279. (d) C. Paraschiv, M. Andruh, S. Ferlay, M. W. Hosseini, N. Kyritsakas, J.-M. Planeix, and N. Stanica, *Dalton Trans.* **2005**, 1195. (e) G. Marin, V. Kravtsov, Y. A. Simonov, V. Tudor, J. Lipkowski, and M. Andruh, *J. Molec. Struct.* **2006**, *796*, 123.
17. M. Pascu, M. Andruh, A. Müller, and M. Schmidtmann, *Polyhedron*, **2004**, *23*, 673.
18. W. Huang, S. Gou, D. Hu, S. Chantrapromma, H.-K. Fun, and Q. Meng, *Inorg. Chem.*, **2001**, *40*, 1712.
19. G. S. Papaefstathiou, I. G. Georgiev, T. Friščić, and R. L. MacGillivray, *Chem. Commun.*, **2005**, 3974.
20. (a) O. Kahn, *Adv. Inorg. Chem.*, **1995**, *43*, 179. (b) O. Kahn, *Acc. Chem. Res.*, **2000**, *33*, 647.
21. J.-P. Costes, F. Dahan, A. Dupuis, and J.-P. Laurent, *Inorg. Chem.*, **1996**, *35*, 2400.
22. R. Gheorghe, P. Cucos, M. Andruh, J.-P. Costes, B. Donnadieu, and S. Shova, *Chem. Eur. J.*, **2006**, *12*, 187.
23. R. Gheorghe, M. Andruh, A. Müller, and M. Schmidtmann, *Inorg. Chem.*, **2002**, *41*, 5314.
24. (a) J.-P. Costes, R. Gheorghe, M. Andruh, S. Shova, and J.-M. Clemente Juan, *New J. Chem.*, **2006**, *30*, 572. (b) D. G. Branzea, A. Guerri, O. Fabelo, C. Ruiz-Pérez, L.-M. Chamoreau, C. Sangregorio, A. Caneschi, and M. Andruh, *Cryst. Growth Des.*, in press.
25. R. Gheorghe, M. Andruh, J.-P. Costes, and B. Donnadieu, *Chem. Commun.*, **2003**, 2778.
26. (a) S. L. James, *Chem. Soc. Rev.*, **2003**, *32*, 276 (b) M. J. Rosseinsky, *Microporous Mesoporous Mater.*, **2004**, *73*, 15 (c) N. W. Ockwig, O. Delgado-Friedrichs, M. O'Keeffe, and O. M. Yaghi, *Acc. Chem. Res.*, **2005**, *38*, 176.
27. (a) F. H. Allen, and O. Kennard, *J. Chem. Soc., Chem. Comm.*, **1994**, 1325. (b) K. Biradha, M. Sarkar, and L. Rajput, *Chem. Comm.*, **2006**, 4169.
28. (a) Y. Sano, M. Tanaka, N. Koga, K. Matsuda, H. Iwamura, P. Rabu, and M. Drillon, *J. Am. Chem. Soc.*, **1997**, *119*, 8246. (b) S. Karasawa, Y. Sano, T. Akita, N. Koga, T. Itoh, H. Iwamura, P. Rabu, and M. Drillon, *J. Am. Chem. Soc.*, **1998**, *120*, 10080. (c) Y. Ishimaru, M. Kitano, H. Kumada, N. Koga, and H. Iwamura, *Inorg. Chem.*, **1998**, *37*, 2273. (d) S. Karasawa, H. Kumada, N. Koga, and H. Iwamura, *J. Am. Chem. Soc.*, **2001**, *123*, 1387. (e) A. Kamiyama, T. Noguchi, T. Kajiwara, and T. Ito, *Inorg. Chem.*, **2002**, *41*, 507.
29. F. M. Tabellion, S. R. Seidel, A. M. Arif, and P. J. Stang, *J. Am. Chem. Soc.*, **2001**, *123*, 7740.
30. F. M. Tabellion, S. R. Seidel, A. M. Arif, and P. J. Stang, *Angew. Chem., Int. Ed.*, **2001**, *40*, 1529.
31. R. Horikoshi, T. Mochida, and H. Moriyama, *Inorg. Chem.*, **2001**, *40*, 2430.
32. (a) D. Zhang, W. Liu, W. Xu, X. Jin, and D. Zhu, *Inorg. Chim. Acta*, **2001**, *310*, 84. (b) M. Tanaka, Y. Hosokoshi, A. S. Markosyan, K. Inoue, and H. Iwamura, *Synth. Met.*, **2001**, *122*, 463. (c) M. J. Plater, M. R. S. J. Foreman, and A. M. Z. Slawin, *Inorg. Chim. Acta*, **2000**, *303*, 132.
33. Y.-B. Dong, M. D. Smith, R. C. Layland, and H.-C. zur Loye, *Inorg. Chem.*, **1999**, *38*, 5027.
34. (a) M. Fujita, S. Nagao, and K. Ogura, *J. Am. Chem. Soc.*, **1995**, *117*, 1649. (b) B. F. Abrahams, S. R. Batten, M. J. Grannas, H. Hamit, B. F. Hoskins, and R. Robson, *Angew. Chem. Int. Ed.*, **1999**, *38*, 1475. (c) M. C. Hong, Y. J. Zhao, W. P. Su, R. Cao, M.

Fujita, Z. Y. Zhou, and A. S. C. Chan, *Angew. Chem. Int. Ed.*, **2000**, *39*, 2468. (d) C. Y. Su, Y. P. Cai, C. L. Chen, F. Lissner, B. S. Kang, and W. Kaim, *Angew. Chem. Int. Ed.*, **2002**, *41*, 3371. (e) J.-P. Costes, F. Dahan, and F. Nicodeme, *Inorg. Chem.*, **2003**, *42*, 6556. (f) S. Y. Wan, Y. Z. Li, T. Okamura, J. Fan, W. Y. Sun, and N. Uevama, *Eur. J. Inorg. Chem.*, **2003**, 3183. (g) C. Y. Su, Y. P. Cai, C. L. Chen, M. D. Smith, W. Kaim, and H. C. zur Loye, *J. Am. Chem. Soc.*, **2003**, *125*, 8595. (h) W. Zhao, Y. Song, T. A. Okamura, J. Fan, W. Y. Sun, and N. Ueyama, *Inorg. Chem.*, **2005**, *44*, 3330.

35. C. N. R. Rao, S. Natarajan, and R. Vaidhyanathan, *Angew. Chem. Int. Ed.*, **2004**, *43*, 1466.
36. M. Hernández-Molina, P. A. Lorenzo-Luis, and C. Ruiz-Pérez, *CrystEngComm.*, **2001**, *3*, 60.
37. (a) C. Hornick, P. Rabu, and M. Drillon, *Polyhedron*, **2000**, *19*, 259. (b) P. Rabu, J. M. Rueff, Z. L. Huang, S. Angelov, J. Souletie, and M. Drillon, *Polyhedron*, **2001**, *20*, 1677.
38. (a) F. S. Delgado, *Development of New Molecular Magnets Based on the Malonate Ion*, University of La Laguna, Tenerife, Spain, **2006**. (b) J. Pasán, F. S. Delgado, Y. Rodríguez-Martín, M. Hernández-Molina, C. Ruiz-Pérez, J. Sanchiz, F. Lloret, and M. Julve, *Polyhedron*, **2003**, *22*, 2143.
39. (a) G. I. Dimitrova, A. V. Ablov, G. A. Kiosse, G. A. Popovich, T. I. Malinovskii, I. F. Burshtein, *Dokl. Akad. Nauk SSSR*, *216*, 1055 **(1974)**. (b) Y. Rodríguez-Martín, J. Sanchiz, C. Ruiz-Pérez, F. Lloret, M. Julve, *CrystEngComm.*, *4*, 631 **(2002)**.
40. D. Chattopadhyay, S. K. Chattopadhyay, P. R. Lowe, C. H. Schwalbe, S. K. Mazumder, A. Rana, and S. Ghosh, *J. Chem. Soc. Dalton Trans.*, **1993**, 913.
41. C. Ruiz-Pérez, J. Sanchiz, M. Hernández-Molina, F. Lloret, and M. Julve, *Inorg. Chem.*, **2000**, *39*, 1363.
42. V. T. Yilmaz and E. Senel, *Trans. Metal Chem.* **2004**, *29*, 336.
43. M. J. Schmelz, I. Nagakawa, S. Mizushima, and J. V. Quagliano, *Inorg.Chem.*, **1959**, *81*, 287.
44. I. Gil de Muro, F. A. Mautner, M. Insausti, L. Lezama, M. I. Arriortua, and T. Rojo, *Inorg. Chem.*, **1998**, *37*, 3243.
45. (a) R. M. Smith, and A. E. Martell, *Critical Stability Constants*, *vol. 2.*, Plenum Press, New York, **1975**, p. 165. (b) R. M. Smith, and A. E. Martell, *Critical Stability Constant*, *Vol. 5.*, Plenum Press, New York, **1982**, p. 308.
46. M. J. Schmelz, I. Nagakawa, S. Mizushima, and J. V. Quagliano, *Inorg. Chem.*, **1959**, *81*, 287.
47. V. Mihailova, and M. Bonnet, *Bull. Soc. Chim. Fr.*, **1969**, *12*, 4258.
48. M. Bonnet, and R. A. Paris, *Bull. Soc. Chim. Fr.*, **1966**, 747.
49. A. Pajunen, and E. Nasakkala, *Finn. Chem. Lett.*, **1977**, 189.
50. A. Gleizes, M. Julve, M. Verdaguer, J. A. Real, J. Faus, and X. Solans, *J. Chem. Soc. Dalton Trans.* **1992**, 3209.
51. N. J. Ray, *Acta Crystallogr. Sect. B*, **1982**, *38*, 770.
52. F. S. Delgado, M. Hernández-Molina, J. Sanchiz, C. Ruiz-Pérez, Y. Rodríguez-Martín, T. López, F. Lloret, and M. Julve, *CrystEngComm.*, **2004**, *6*, 106.
53. T. Lis, and J. Matuszewski, *Acta Cryst. Sect .B*, **1979**, *35*, 2212.
54. Y. Rodríguez-Martín, M. Hernández-Molina, J. Sanchiz, C. Ruiz-Pérez, F. Lloret, and M. Julve, *J. Chem. Soc. Dalton Trans.* , **2003**, 2359.
55. F. S. Delgado, J. Sanchiz, C. Ruiz-Pérez, F. Lloret, and M. Julve, *CrystEngComm.*, **2004**, *6*, 443.
56. T. Steiner, *Angew. Chem. Ed. Engl.*, **2002**, *41*, 48.
57. A. Nangia, *CrystEngComm.*, **2002**, *4*, 93.
58. G. Aullon, D. Bellamy, A. G. Orpen, L. Brammer, and E. A. Bruton, *Chem. Comm.*, **1998**, 653.
59. G. R. Desiraju, *Acc. Chem. Res.*, **1996**, *29*, 441.

60. C. Janiak, *J. Chem. Soc. Dalton Trans.*, **2000**, 3885.
61. C. Ruiz-Pérez, M. Hernández-Molina, P. Lorenzo-Luis, F. Lloret, J. Cano, and M. Julve, *Inorg. Chem.*, **2000**, *39*, 3845.
62. J. Sanchiz, Y. Rodríguez-Martín, C. Ruiz-Pérez, A. Mederos, F. Lloret, and M. Julve, *New J. Chem.*, **2002**, *26*, 1624.
63. F. S. Delgado, J. Sanchiz, C. Ruiz-Pérez, F. Lloret, and M. Julve, *CrystEngComm.*, **2003**, *5*, 280.
64. Y. Rodríguez-Martín, M. Hernández-Molina, F. S. Delgado, J. Pasán, C. Ruiz-Pérez, J. Sanchiz, F. Lloret, and M. Julve, *CrystEngComm.*, **2002**, *4*, 440.
65. Y. Rodríguez-Martín, C. Ruiz-Pérez, J. Sanchiz, F. Lloret, and M. Julve, *Inorg. Chim. Acta*, **2001**, *318*, 159.
66. (a) S. O. H. Gutschke, D. J. Price, A. K. Powell, and P. T. Wood, *Angew. Chem. Int. Ed.*, **2001**, *40*, 1920. (b) R. Kuhlman, G. L. Schimek, and J. W. Kolis, *Inorg. Chem.*, **1999**, *38*, 194.
67. M. C. Etter, *J. Phys. Chem.*, **1991**, *95*, 4601.
68. S. K. Burley, and G. A. Petsko, *Science*, **1985**, *229*, 23.
69. J. Singh, and J. M. Thornton, *FEBS Lett.*, **1985**, *191*, 2989.
70. C. A. Hunter, J. Singh, and J. M. Thornton, *J. Mol. Biol.*, **1990**, *211*, 595.
71. L. F. Lindoy, and I. M. Atkinson, *Self-Assembly in Supramolecular Chemistry*, Royal Society of Chemistry, Cambridge, UK, **2000**.
72. I. Dance, in *The Crystal as a Supramolecular Entity*, ed. G. R. Desiraju, Wiley, Chichester, UK, **1996**.
73. J. Pasán, J. Sanchiz, C. Ruiz-Pérez, F. Lloret, and M. Julve, *New J. Chem.*, **2003**, *27*, 1557.
74. J. Pasán, J. Sanchiz, C. Ruiz-Pérez, F. Lloret, and M. Julve, *Eur. J. Inorg. Chem.*, **2004**, 4081.
75. J. Pasán, J. Sanchiz, C. Ruiz-Pérez, J. Campo, F. Lloret, and M. Julve, *Chem. Comm.*, **2006**, 2857.
76. J. Pasán, *Molecular* Magnetic Materials: Influence of the Weak Interactions in the Structural and Magnetic Behaviour of Malonate Complexes, University of La Laguna, Tenerife, Spain, **2006**.
77. J. Pasán, J. Sanchiz, F. Lloret, M. Julve, and C. Ruiz-Pérez, *CrystEngComm.*, **2007**, *9*, 478.
78. A. M. Madalan, K. Bernot, F. Pointillart, M. Andruh, and A. Caneschi, *Eur. J. Inorg. Chem.*, **2007**, 5533.
79. (a) R. Clément, S. Decurtins, M. Gruselle, C. Train, in *Molecular Magnets. Recent Highlights*, ed. W. Linert, and M. Verdaguer, Springer, Wien, **2003**, p. 1, (b) J. Larionova, B. Mombelli, J. Sanchiz, and O. Kahn, *Inorg. Chem.*, **1998**, *37*, 679.
80. (a) L. O. Atovmyan, G. V. Shilov, R. N. Lyobovsaya, E. L. Zhilyaeva, N. S. Ovanesyan, S. I. Pirumova, I. G. Gusa Kovskaya, and Y. K. Morozov, *JETP Lett* **1993**, *58*, 766. (b) S. Decurtins, H. W. Schmalle, H. R. Oswald, A. Linden, J. Ensling, P. Gütlich, and A. Hauser, *Inorg. Chim. Acta.*, **1994**, *216*, 65.
81. R. Andrés, M. Gruselle, B. Malézieux, M. Verdaguer, and J. Vaissermann, *Inorg. Chem.*, **1999**, *38*, 4637.
82. S. Decurtins, H. W. Schmalle, P. Schneuwly, J. Ensling, P. Gütlich, and A. Hauser, *J. Am. Chem. Soc.*, **1994**, *116*, 9521.
83. S. Decurtins, M. Gross, H. W. Schmalle, and S. Ferlay, *Inorg. Chem.*, **1998**, *37*, 2443.
84. F. D. Rochon, R. Melanson, and M. Andruh, *Inorg. Chem.*, **1996**, *35*, 6086.
85. (a) K. P. Mörtl, J.-P. Sutter, S. Golhen, L. Ouahab, and O. Kahn, *Inorg. Chem.*, **2000**, *39*, 1626. (b) I. Imaz, G. Bravic, and J.-P. Sutter, *Chem. Commun.*, **2005**, 993. (c) I. Imaz, G. Bravic, and J.-P. Sutter, *Dalton Trans.*, **2005**, 2681.

86. R. Ruiz, J. Faus, F. Lloret, M. Julve, and Y. Journaux, *Coord. Chem. Rev.*, **1999**, *193–195*, 1069.
87. (a) K. R. Dunbar, and R. A. Heintz, *Progr. Inorg. Chem.* **1997**, *45*, 283. (b) M. Verdaguer, A. Bleuzen, V. Marvaud, J. Vaissermann, M. Seuleiman, C. Desplanches, A. Scuiller, C. Train, R. Garde, G. Gelly, C. Lomenech, I. Rosenman, P. Veillet, C. Cartier, and F. Villain, *Coord. Chem. Rev.* **1999**, *190–192*, 1023. (c) M. Ohba, and H. Ōkawa, *Coord. Chem. Rev.* **2000**, *198*, 313. (d) J. Černák, M. Orendáč, I. Potočňák, J. Chomič, A. Orendáčová, J. Skoršepa, and A. Feher, *Coord. Chem. Rev.* **2002**, *224*, 51. (e) O. Kahn, J. Larionova, and L. Ouahab, *Chem. Commun.* **1999**, 945. (f) P. Przychodzeń, T. Korzeniak, R. Podgajny, and B. Sieklucka, *Coord. Chem. Rev.* **2006**, *250*, 2234.
88. W. Dong, L.-N. Zhu, H.-B. Song, D.-Z. Liao, Z.–H. Jaing, S.-P. Yan, P. Cheng, and S. Gao, *Inorg. Chem.*, **2004**, *43*, 2465.
89. M. Ohba, N. Fukita, and H. Ōkawa, *J. Chem. Soc. Dalton Trans.* **1997**, 1733.
90. (a) G. O. Morpurgo, V. Mosini, and P. Porta, *J. Chem. Soc. Dalton Trans.*, **1981**, 111. (b) M. Ferbinteanu, S. Tanase, M. Andruh, Y. Journaux, F. Cimpoesu, I. Strenger, and E. Rivière, *Polyhedron*, **1999**, *18*, 3019.
91. E. Colacio, J. M. Dominguez-Vera, M. Ghazi, R. Kivekäs, F. Lloret, J. M. Moreno, and H. Stoeckli-Evans, *Chem. Commun.*, **1999**, 987.
92. H.-Z. Kou, S. gao, B.-Q. Ma, and D.-Z. Liao, *Chem. Commun.*, **2000**, 1309.
93. R. Lescouëzec, L. M. Toma, J. Vaissermann, M. Verdaguer, F. S. Delgado, C. Ruiz-Pérez, F. Lloret, and M. Julve, *Coord. Chem. Rev.*, **2005**, *249*, 2691.
94. L. M. Toma, L. D. Toma, F. S. Delgado, C. Ruiz-Pérez, J. Sletten, J. Cano, J. M. Clemente-Juan, F. Lloret, and M. Julve, *Coord. Chem. Rev.*, **2006**, *250*, 2176.
95. Y. Pei, M. Verdaguer, O. Kahn, O.; J. Sletten, and J.-P. Renard, *J. Am. Chem. Soc.* **1986**, *108*, 428.
96. J. Milon, M.-C. Daniel, A. Kaiba, P. Guionneau, S. Brandes, and J.-P. Sutter, *J. Am. Chem. Soc.*, **2007**, *129*, 13872.
97. (a) M. Gruselle, C. Train, K. Boubekeur, P. Gredin, and N. Ovansyan, *Coord. Chem. Rev.*, **2006**, *250*, 2491. (b) A. Beghidja, G. Rogez, P. Rabu, R. Welter, and M. Drillon, *J. Mter. Chem.*, **2006**, *16*, 2715.
98. E. Coronado, J. R. Galan-Mascaros, C. J. Gomez-Garcia, and V. Laukhin, *Nature*, **2000**, *408*, 447.
99. (a) C. N. Rao, S. Natarajan, and R. Vaidhyanathan, *Angew. Chem., Int. Ed.*, **2004**, *43*, 1466. (b) C. L. Bowles, G. A. Ozin, *Adv. Mater.* **1996**, *8*, 13. (c) S. Kitagawa, S. Noro, and T. Nakamura, *Chem. Commun.* **2006**, 701. (d) C. J. Keppert, *Chem. Commun.*, **2006**, 695.
100. (a) M. Fujita, Y. J. Kwon, S. Washizu, and K. Ogura, *J. Am. Chem. Soc.*, **1996**, *116*, 1151. (b) S. Hasegawa, S. Horike, R. Matsuda, S. Furukawa, K. Machizuki, Y. Kinoshita, and S. Kitagawa, *J. Am. Chem. Soc.*, in press. (c) M. Kawano,and M. Fujita, *Coord. Chem. Rev.*, **2007**, *251*, 2592. (d) S. Kitagawa, and R. Matsuda, *Coord. Chem. Rev.*, **2007**, *251*, 2490. (e) A. N. Pârvulescu, G. Marin, K. Suwinska, V. C. Kravtsov, M. Andruh, V. Pârvulescu, and V. I. Pârvulescu, *J. Mater. Chem.*, **2005**, *15*, 4234.
101. C. D. Wu, A. Hu, L. Zhang, and W. B. Lin, *J. Am. Chem. Soc.*, **2005**, *127*, 8940.
102. See, for example: (a) M. Eddaoudi, J. Kim, N. Rosi, D. Vodak, J. Wachter, M. O'keeffe, and O. M. Yaghi, *Science*, **2002**, *295*, 469. (b) B. Kesanli, Y. Cui, M. R. Smith, E. W. Bittner, B. C. Bockrath, and W. Lin, *Angew, Chem., Int. Ed.*, **2005**, *44*, 72. (d) W. Yang, X. Lin, J. Jia, A. J. Blake, C. Wilson, P. Hubberstey, N. R. Champness, and M. Schröder, *Chem. Commun.*, **2009**, 359, and references therein.

Index

Macromolecules Containing Metal and Metal-Like Elements,
Volume 9: Supramolecular and Self-Assembled Metal-Containing Materials,
Edited by Alaa S. Abd-El Aziz, Charles E. Carraher Jr., Charles U. Pittman Jr., and Martel Zeldin.